

OXFORD

Stochastic Methods in Neuroscience

Edited by Carlo Laing and Gabriel J. Lord

Stochastic Methods in Neuroscience

This page intentionally left blank

Stochastic Methods in Neuroscience

Edited by

Carlo Laing

Massey University, Auckland, NZ

and

Gabriel J. Lord

Heriot-Watt University, Edinburgh, UK

OXFORD
UNIVERSITY PRESS

OXFORD
UNIVERSITY PRESS

Great Clarendon Street, Oxford OX2 6DP

Oxford University Press is a department of the University of Oxford.
It furthers the University's objective of excellence in research, scholarship,
and education by publishing worldwide in

Oxford New York

Auckland Cape Town Dar es Salaam Hong Kong Karachi
Kuala Lumpur Madrid Melbourne Mexico City Nairobi
New Delhi Shanghai Taipei Toronto

With offices in

Argentina Austria Brazil Chile Czech Republic France Greece
Guatemala Hungary Italy Japan Poland Portugal Singapore
South Korea Switzerland Thailand Turkey Ukraine Vietnam

Oxford is a registered trade mark of Oxford University Press
in the UK and in certain other countries

Published in the United States
by Oxford University Press Inc., New York

© Oxford University Press 2010

The moral rights of the authors have been asserted
Database right Oxford University Press (maker)

First Published 2010

All rights reserved. No part of this publication may be reproduced,
stored in a retrieval system, or transmitted, in any form or by any means,
without the prior permission in writing of Oxford University Press,
or as expressly permitted by law, or under terms agreed with the appropriate
reprographics rights organization. Enquiries concerning reproduction
outside the scope of the above should be sent to the Rights Department,
Oxford University Press, at the address above

You must not circulate this book in any other binding or cover
and you must impose the same condition on any acquirer

British Library Cataloguing in Publication Data
Data available

Library of Congress Cataloging in Publication Data
Data available

Typeset by Newgen Imaging Systems (P) Ltd., Chennai, India
Printed in Great Britain
on acid-free paper by
MPG Books Group in the UK

ISBN 978-0-19-923507-0

1 3 5 7 9 10 8 6 4 2

CONTENTS

Introduction	vii
Nomenclature	xx
List of Contributors	xxii
1 A brief introduction to some simple stochastic processes <i>Benjamin Lindner</i>	1
2 Markov chain models of ion channels and calcium release sites <i>Jeffrey R. Groff, Hilary DeRemigio, and Gregory D. Smith</i>	29
3 Stochastic dynamic bifurcations and excitability <i>Nils Berglund and Barbara Gentz</i>	65
4 Neural coherence and stochastic resonance <i>André Longtin</i>	94
5 Noisy oscillators <i>Bard Ermentrout</i>	124
6 The role of variability in populations of spiking neurons <i>Brent Doiron</i>	153
7 Population density methods in large-scale neural network modelling <i>Daniel Tranchina</i>	181
8 A population density model of the driven LGN/PGN <i>Marco A. Huertas and Gregory D. Smith</i>	217
9 Synaptic ‘noise’: Experiments, computational consequences and methods to analyse experimental data <i>Alain Destexhe and Michelle Rudolph-Lilith</i>	242
10 Statistical models of spike trains <i>Liam Paninski, Emery N. Brown, Satish Iyengar, and Robert E. Kass</i>	272
11 Stochastic simulation of neurons, axons, and action potentials <i>A. Aldo Faisal</i>	297

12	Numerical simulations of SDEs and SPDEs from neural systems using SDELab <i>Hasan Alzubaidi, Hagen Gilsing, and Tony Shardlow</i>	344
	Index	367

INTRODUCTION

Computational and mathematical neuroscience is an active research area attracting the interest of specialist researchers as well as the general public. It involves the intersection between neuroscience and mathematical/computational techniques. Its current popularity is due to several factors, among them being rapid increases in computing power, increases in the ability to record large amounts of neurophysiological data, and a realization amongst both neuroscientists and mathematicians that each can benefit from collaborating with the other.

The effects of stochastic forcing on physical systems is another area of research under active development. Interest stems from the fact that stochastic models of physical processes tend to be more realistic; in particular it offers a way to model the interactions between different scales. The growth of computer power has enabled numerical investigations of systems which in turn has led to further developments in the theory.

There is considerable overlap between the topics of neuroscience and stochastic systems. At a molecular level, the opening of ion channels and synaptic transmission are inherently probabilistic. At a cellular level, neurons often fire unreliably and the effects of noise on the dynamical system used to model single neurons is of interest. The role of noise in networks of neurons has recently been studied, with the development of population density methods over the last decade. And it is well-known that recordings of neurons *in vivo* are quite irregular, even though there is no external input.

This book presents a series of self-contained chapters on these major aspects of noise and neuroscience, each written by an expert or experts in their particular field. These range over Markov chain models for ion-channel release, stochastically forced single neurons and populations of neurons, statistical methods for parameter estimation and the numerical approximation of these models. The area of mathematical and computational neuroscience attracts researchers from a wide range of backgrounds. This can be seen in the mix of notation in the different chapters of this book, for example

$$\int ds f(s) \equiv \int f(s)ds \quad \text{and} \quad \partial_x \equiv \frac{\partial}{\partial x}.$$

The intended readership is PhD students, postdocs, and other researchers in the area of computational neuroscience, and neuroscientists who want to learn more about recent advances in the modelling and analysis of noisy neural systems. Researchers in the area of stochastic systems and mathematics will also be interested in the book as a source for interesting applications and an introduction to neuroscience.

A brief introduction to neuroscience and models

Models

A number of common models arise throughout the book over a range of scales from individual ion channels, to single neurons, and populations of neurons.

On a small scale, individual ion channels provide the mechanism for signalling between neurons and hence inputs into a neuron. Individual ion channels can be modelled as being in one of a small number of states at any given moment in time. The switching between states is apparently random, and single ion channels are often modelled as a continuous-time, discrete-state Markov chain (see Chapter 2). Simulating such systems involves repeatedly drawing random numbers from appropriate distributions and using these to determine when a particular channel changes state (see also Chapters 1 and 11). Gillespie's algorithm (Gillespie, 1976) is commonly used for such simulations (for a recent review see Higham, 2008). These ion channels can also be modelled by ordinary differential equations (ODEs) – essentially governing the evolution in time of the probability of the channel being open; see Chapter 2. This signalling between cells is achieved by ions diffusing across membranes and such probabilistic models are simpler models than a description of the diffusion process with the full geometry.

The ion channels form a key part of a single neuron. There are a large number of individual models of single neurons. The Hodgkin–Huxley equations are a set of four coupled nonlinear ordinary differential equations, often used to model a single neuron (Hodgkin and Huxley, 1952). One of the four equations is a current-balance equation of the form

$$C \frac{dV}{dt} = \text{sum of currents} \quad (0.1)$$

where C is the cell membrane capacitance, V is the voltage of the interior of a cell relative to its exterior, and the currents are a result of ions (sodium, potassium, calcium) flowing into or out of the cell through ion channels in the cell membrane. The other three ODEs govern the dynamics of voltage-dependent conductances, which in turn affect the currents flowing into or out of a cell. Typical dynamics are either quiescence or periodic oscillations. During one period of oscillation there is normally a rapid rise and then fall of V , termed an action potential.

Since the Hodgkin–Huxley equations show either quiescence or periodic behaviour (when parameters are fixed), it should be possible to qualitatively reproduce their dynamics with a two-variable ODE model. The FitzHugh–Nagumo (FitzHugh, 1961, Nagumo, Arimoto, and Yoshizawa, 1962) and Morris–Lecar (Morris and Lecar, 1981) equations are both models motivated by this idea. One main advantage of these two-variable models is that their dynamics can be understood and visualized using their two-dimensional phase space, or phase plane.

Neural models such as these are often classified by the bifurcations they undergo as the current injected into them is increased, and their behaviour

switches from quiescent to periodic. Type I neurons start firing at an arbitrarily low frequency as the injected current is increased, while Type II neurons start firing at a frequency bounded away from zero. This difference is related to the bifurcations they undergo as the current is increased: Type I neurons often undergo a saddle-node-on-a-circle or homoclinic bifurcation, while Type II neurons often undergo a Hopf bifurcation, or a saddle-node bifurcation of periodic orbits. This qualitative difference between neuron types is thought to underlie the differences in their neurocomputational properties (Izhikevich, 2000).

If solutions of ODEs are allowed to be discontinuous, only one Cartesian variable is required in order to get oscillatory dynamics. This is the idea behind integrate-and-fire (IF) models and their variants. The simplest of these is the integrate-and-fire model:

$$C \frac{dV}{dt} = I, \quad (0.2)$$

together with the rule that when V reaches a fixed threshold value, V_{th} , it is ‘reset’ to a lower value, and the differential equation (0.2) continues to govern the dynamics of V . The leaky-integrate-and-fire (LIF) neuron model is of the same form, but with an additional ‘leak’ term:

$$C \frac{dV}{dt} = -\frac{V}{R} + I, \quad (0.3)$$

where the same reset rule applies. This model is more realistic than the integrate-and-fire, in that it has an input current threshold, so that the dynamics are periodic only for $I > V_{\text{th}}/R$. Both of these models can have absolute refractory periods included, so that the voltage is reset and then held at a constant value for a fixed amount of time after firing, before continuing to evolve.¹ In this book these models are used to examine populations of neurons as in Chapters 6 and Chapter 8, and the fitting of IF models to data is discussed in Chapter 10.

Both of the integrate-and-fire variants have the advantage of being piecewise-linear, and this is often exploited in their analysis. However, they suffer from several disadvantages. The LIF model, having discontinuous flow, does not start firing (as I is increased) through a bifurcation seen in continuous models. Also, it does not generate action potentials, and these must be ‘pasted on’ if required (Chow and Kopell, 2000).

Other minimal models include the ‘theta neuron’ (or ‘Ermentrout–Kopell canonical model’) and the related quadratic-integrate-and-fire neuron (QIF, see Chapter 4), the absolute-integrate-and-fire neuron (Karbowski and Kopell, 2000) and the recently proposed model in Chapter 8 of Izhikevich (2007).

These models treat the single neuron as a point processor. The Hodgkin–Huxley ODEs actually model the behaviour of a space-clamped nerve, where the

¹Note that some authors, both in this volume and elsewhere, use the term ‘integrate-and-fire’ as an abbreviation for ‘leaky-integrate-and-fire’.

voltage has been forced to be the same at all spatial points. However, relaxing this restriction leads to the Hodgkin–Huxley partial differential equation (PDE) which can be used to study the propagation of action potentials in space as time evolves. There are numerous other PDE and spatially extended models for neurons, parts of neurons, and populations of neurons.

Networks

Neurons do not function in isolation but as part of a network, with inputs which may be from other neurons (referred to as ‘presynaptic’), and sending outputs to other neurons (referred to as ‘postsynaptic’), or, for example, to muscles. The two main forms of communication between neurons are via gap junctions and chemical synapses. If neurons i and j are connected via gap junctions, equation (0.1) is modified to

$$C \frac{dV_i}{dt} = \text{sum of currents} + g(V_j - V_i) \quad (0.4)$$

where $V_{i/j}$ is the voltage of neuron i/j and g (a conductance) is the strength of the coupling. The equation for V_j is modified similarly.

Synaptic transmission of a signal from neuron j to neuron i is more complicated, but generally involves modifying an equation of the form (0.1) to

$$C \frac{dV_i}{dt} = \text{sum of currents} + g(E - V_i) \quad (0.5)$$

where E is the reversal potential of the particular neurotransmitter concerned, and g is now time-dependent, transiently rising and then falling, with the start of the rise coinciding with the firing of an action potential by neuron j . The rate of change of g is used to classify neurotransmitters as either ‘fast’ or ‘slow’. If E is more positive than typical values of V_i the synapse is referred to as excitatory, since the firing of neuron j will result in V_i increasing, making neuron i more likely to fire. Conversely, if E is more negative than typical values of V_i , the synapse is referred to as inhibitory. The four main neurotransmitters in the central nervous system are AMPA (fast and excitatory), NMDA (slow and excitatory), GABA_A (fast and inhibitory), and GABA_B (slow and inhibitory). Some of the approximations made in modelling synapses include assuming that g changes infinitely fast, or that the dependence on V_i of the last term in equation (0.5) can be ignored, so that a presynaptic neuron just injects current into a postsynaptic neuron upon firing (see Chapters 7 and 8). These network type models can be extended to neural field type models of integro-differential equations where the kernel determines the connectivity (Wilson and Cowan, 1972, 1973), briefly mentioned in Chapter 7.

Noise in neural models

For ODE models, one may want to include the effects of noise to obtain more realistic models. Mathematically, the simplest way to do this is to add a Gaussian

white noise term to one or more of the ODEs, leading to a set of stochastic differential equations (SDEs). Adding the noise can be thought of as modelling the effects of individual ion channels opening and closing in a stochastic way, or (if the term is added to the current balance equation (0.1)) the effects of randomly arriving input from presynaptic neurons. Mathematically very similar to Gaussian white noise is coloured noise, resulting from an Ornstein–Uhlenbeck (OU) process (see Chapters 1, 4, and 9). Other ways of introducing randomness include choosing the amplitude and/or time course of g in (0.5) from particular distributions, and randomly choosing the arrival times of inputs from presynaptic neurons (see Chapters 7 and 8). Modelling ion channels by a Markov chain is inherently noisy. Adding spatio-temporal noise to a spatially extended PDE model results in a stochastic partial differential equation (SPDE) as considered in Chapters 11 and 12.

A brief introduction to stochastics

Probability

Recall that the mean or expected value $\mathbb{E}[X]$ of a random variable X gives the average behaviour. If we have a probability density p then

$$\Pr(X \in [a, b]) = \int_a^b p(x) dx \quad \text{and} \quad \mathbb{E}[X] = \int_{-\infty}^{\infty} xp(x) dx.$$

The variance is a measure of how a variable changes against itself over time

$$\text{Var}(X) := \mathbb{E}[(X - \mathbb{E}[X])^2] = \mathbb{E}[X^2] - (\mathbb{E}[X])^2.$$

The covariance is a measure of how a variable X changes against a different variable Y

$$\text{Cov}(X, Y) := \mathbb{E}[(X - \mathbb{E}[X])(Y - \mathbb{E}[Y])] = \mathbb{E}[XY] - \mathbb{E}[X]\mathbb{E}[Y].$$

Correlation examines the linear dependence between two random variables and is the covariance scaled by the variance. Autocorrelation (autocovariance) examines the correlation of a random variable in time and so is the covariance of a time-shifted variable and itself. Such terms are introduced in more detail and the links between them are discussed in Chapter 1.

When we talk about noise being ‘white’ noise it is characterized by having all frequencies f equally represented and there is no correlation. So white noise has a power spectrum of $1/f^\alpha$ with $\alpha = 0$, the autocorrelation is the Dirac delta function.

For two events x and y , their joint probability density is $p(x, y)$. If the events are independent, we have $p(x, y) = p(x)p(y)$. The conditional probability of x , given y , is written $p(x|y)$, and is given by

$$p(x|y) = \frac{p(x, y)}{p(y)}. \tag{0.6}$$

Interchanging x and y in Eqn (0.6) leads to Bayes' theorem:

$$p(x|y) = \frac{p(y|x)p(x)}{p(y)}$$

which is of fundamental importance to Bayesian inference and parameter estimation (see Chapter 10). In this form, $p(x)$ is known as the ‘prior’, $p(y|x)$ is the ‘likelihood’, and $p(x|y)$ is the ‘posterior’.

Stochastic DEs

We want to look at the evolution of currents, voltages, etc. in continuous time and how these are perturbed by the effects of noise. For this we need the following definition. A stochastic process $W = (W(t))_{t \geq 0}$ is called a (standard) *Brownian motion* or a *Wiener process* if

1. $W(0) = 0$.
2. The random variables $W(t_1) - W(t_0), W(t_2) - W(t_1), \dots, W(t_n) - W(t_{n-1})$, are independent for any sequence of time points $0 \leq t_1 \leq t_2 \leq \dots \leq t_n$.
3. For $0 \leq s < t$ the increment $W(t) - W(s)$ is normally distributed with mean zero and variance $t - s$.
4. For each realization, $W(t)$ is continuous in t .

Note that in the probability and stochastic literature, time dependence is usually denoted as a subscript, so that $W(t) \equiv W_t$. We have not adopted this notation as it may lead to confusion with partial derivatives.

SDEs, Itô, and Stratonovich integrals

Often a noise term is introduced into an already existing deterministic model to get a stochastic differential equation (SDE)

$$\frac{dv}{dt} = f(v) + g(v) \frac{dW}{dt} \quad (0.7)$$

where the forcing dW/dt is formally a derivative in time. Models of this form are considered throughout the book. In some chapters SDEs are written in a slightly different way as

$$\frac{dv}{dt} = f(v) + g(v)\xi(t)$$

and $\xi(t)$ is Gaussian white noise (see, for example, Chapters 1, 4, and 6). The deterministic term f is called the drift and the stochastic term g is called the diffusion. When g is simply a constant we have additive noise or extrinsic noise and we are modelling with noise the effects of external fluctuations. When g depends on the variable v we have multiplicative or intrinsic noise – this is often noise on a parameter in the system. When uncorrelated in time, the Wiener process or Brownian motion is too rough to have well-defined time derivatives and the SDE should be interpreted in integral form

$$v(t) = v(0) + \int_0^t f(v(s)) ds + \int_0^t g(v(s)) dW(s),$$

where the last term is a stochastic integral. For a more detailed treatment see for example Øksendal (1985); an accessible introduction can also be found in Higham (2001).

Let's examine in a formal manner how to understand the stochastic integral with respect to a one-dimensional Wiener process $W(t)$:

$$I(t) = \int_0^t h(s)dW(s).$$

As with a deterministic (Riemann) integral we can define a partition of the interval $[0, t]$, $\{0 = t_0, t_1, \dots, t_n = t\}$ and look at convergence as $n \rightarrow \infty$. Let's define a time step $\Delta t_k := t_k - t_{k-1}$. In the deterministic case it does not matter at what point in the partition we evaluate h and so it is equally valid to take the mid-point or the left-hand end-point, i.e.

$$\begin{aligned} \int_0^t h(s)ds &= \lim_{n \rightarrow \infty} \sum_{k=1}^n h(t_k)\Delta t_k \quad \text{and} \\ \int_0^t h(s)ds &= \lim_{n \rightarrow \infty} \sum_{k=1}^n h\left(\frac{1}{2}(t_{k-1} + t_k)\right)\Delta t_k. \end{aligned}$$

However, for the stochastic integral it *does* matter at which point in the integral we evaluate h . We define the Brownian increment as $\Delta W_k = (W(t_k) - W(t_{k-1}))$; this is the analogy of the time step Δt_k . The Itô and Stratonovich integrals correspond to the limit based on the left-hand point and mid-point, respectively.

The Itô integral The Itô integral is based on evaluating at the left-hand end-point of each partition. If we define

$$I^n(t) = \sum_{k=1}^n h(t_{k-1})\Delta W_k$$

then for suitable functions h we have uniform convergence to a limit as $n \rightarrow \infty$ independent of the partition, and this limit defines the Itô integral

$$I(t) = \int_0^t h(s)dW(s).$$

For the Itô integral an important restriction on h is that it is non-anticipative so that at time t , $h(t)$ must be independent of values of $W(s)$ for $s > t$.

The Itô integral satisfies a number of nice properties. One of these is the martingale property that

$$\mathbb{E} \left[\int_0^t h(s)dW(s) \right] = 0.$$

Another nice property of the Itô integral is the Itô isometry, given in one dimension by

$$\mathbb{E} \left[\left(\int_0^t h(s) dW(s) \right)^2 \right] = \int_0^t \mathbb{E} [h(s)^2] ds.$$

This is useful for converting a stochastic into a deterministic integral. However, there is a price to pay and an Itô integral does not follow the standard rules of calculus. A standard illustration of this (see for example Øksendal, 1985, Higham, 2001) is to show

$$\int_0^t W(s) dW(s) = \frac{1}{2} W(t)^2 - \frac{1}{2} t$$

contrary to the deterministic case. This is why, for example, in Chapter 4, Section 4.3.4 comments on the change of variables for the stochastic theta neuron, and in Chapter 5, Section 5.1.2, the case of a white noise perturbation is remarked upon.

For Itô integrals we need to modify the chain rule. In one dimension this is given by the following Itô formula. Let $v(t)$ be an Itô process that satisfies in differential form

$$dv = f(v)dt + g(v)dW,$$

which we interpret as the integral equation

$$v(t) = v(0) + \int_0^t f(v(s))ds + \int_0^t g(v(s))dW(s).$$

Suppose we are given $u(v(t))$. Then

$$du = \frac{\partial u}{\partial t} dt + \frac{\partial u}{\partial v} dv + \frac{1}{2} \frac{\partial^2 u}{\partial v^2} g^2 = \left(\frac{\partial u}{\partial t} + \frac{\partial u}{\partial v} f + \frac{1}{2} \frac{\partial^2 u}{\partial v^2} g^2 \right) dt + \frac{\partial u}{\partial v} g dW.$$

This SDE can be interpreted in terms of (Itô) integrals as

$$u(v(t)) = u(v(0)) + \int_0^t \left(\frac{\partial u}{\partial t} + \frac{\partial u}{\partial v} f + \frac{1}{2} \frac{\partial^2 u}{\partial v^2} g^2 \right) ds + \int_0^t \frac{\partial u}{\partial v} g dW(s) \quad \text{a.s.}$$

In practice most authors do not use the integral representation and the interpretation in this way is simply understood. Naturally all of the above results can be extended to arbitrary dimensions and indeed for SPDEs (for example Chapter 12 considers space-time white noise).

Stratonovich integral The Stratonovich integral is based on evaluating at the mid-point of intervals. So if we define

$$I^n(t) = \sum_{k=1}^n h \left(\frac{1}{2}(t_{k-1} + t_k) \right) \Delta W_k$$

then the corresponding limit as $n \rightarrow \infty$ is the Stratonovich integral

$$I(t) = \int_0^t h(s) \circ dW(s).$$

Unlike the Itô integral the Stratonovich integral does not have zero mean; however it does follow the standard rules for calculus so that if we are given

$$dv = f(v)dt + g(v) \circ dW$$

and $u(v(t))$ then

$$du = \frac{\partial u}{\partial t} dt + \frac{\partial u}{\partial v} \circ dW.$$

Itô versus Stratonovich The Itô integral does not assume any knowledge in the future which is not true of the Stratonovich integral. Because of this the Itô form is widely used in finance where one does not want future knowledge of the market. Often the Stratonovich integral is taken where the noise and model is thought to be some approximation over a small interval of some other microscopic process – one interpretation of the mid-point is of an average of noise over a step.

We can convert between the Itô and Stratonovich interpretations by changing the drift term. Suppose we have the Itô SDE

$$dv = f(v)dt + g(v)dW.$$

Then this is equivalent to the Stratonovich equation

$$dv = \left(f(v) - \frac{1}{2}g(v)\frac{\partial g(v)}{\partial v} \right) dt + g(v) \circ dW.$$

This is often called the Itô–Stratonovich drift correction and further details on this can be found in Øksendal (1985). Thus for additive (extrinsic) noise this difference in Itô or Stratonovich calculus is not so important as solutions of the two are the same, which is not the case for multiplicative noise. The authors in this book have typically taken noise in the Itô sense (Chapters 3, 5, 7, 11, and 12) or looked at additive noise.

An example SDE A Langevin equation describes the motion of a particle in a potential energy well. The Ornstein–Uhlenbeck equation is an example of such an equation

$$dv = \mu v dt + \sigma dW$$

where μ and σ are real constants and the solution is called the OU process (see Chapters 1, 5, 4, and 9 for a conductance model, and Chapter 10). With $\mu < 0$ the purely deterministic dynamics ($\sigma = 0$) decays to the zero solution, whereas here with $\sigma \neq 0$ the effects of some external fluctuation is being added. This process has expectation and variance

$$\mathbb{E}[v(t)] = v(0)e^{-\mu t}, \quad \text{Var}(v(t)) = \frac{\sigma^2}{2\mu}(1 - e^{-2\mu t}).$$

This OU noise is often used to investigate the effects of correlation (see the discussion in Chapter 4).

Noise and potential wells Suppose we have a potential energy well – think of a neuron in a stable rest state – or a bistable system. We can consider how long it would take with noisy perturbations to escape from the potential well and leave the neighbourhood of the rest state. With small noise this activation time (or Kramer’s time) is exponentially long – see Chapter 4. Large deviation theory examines the probability of rare events and so, for example, can be used to estimate the probability that a particular path (or solution of an SDE) deviates from the mean path. Freidlin–Wentzell theory (Freidlin and Wentzell, 1998, Berglund and Gentz, 2005) applies this idea and looks at the most probable exit paths from a potential well and can characterize the expected escape time as scaling like $\exp(2M/\sigma^2)$ where M is the size of the potential to overcome and σ is the strength of the noise. These ideas are extended in Chapter 3 where the time spent close to either slow or fast manifolds is examined.

Fokker–Planck equation Suppose we have the Itô SDE

$$dv = f(v)dt + \sigma g(v)dW$$

with smooth functions f and g and we want to know how an initial density of initial conditions varies in time. The Fokker–Planck equation (or Kolmogorov forward equation) describes the evolution of the probability density $\rho(v, t)$, see for example Risken (1996), Gardiner (2004), Berglund and Gentz (2005). In one dimension ρ satisfies

$$\frac{\partial}{\partial t}\rho = \frac{1}{2} \frac{\partial^2}{\partial v^2}(g\rho) - \frac{\partial}{\partial v}(f\rho).$$

For example with $f \equiv 0$ and $g \equiv 1$ corresponding to evolution by white noise, we get the standard diffusion equation as expected. The Fokker–Planck equation is discussed further in Chapter 1 and in Chapters 5–10. Related to the Fokker–Planck equation, the master equation is a set of ODEs that describes the evolution of the probability of a system to be in each one of a discrete set of states (and is considered in Chapter 2).

Numerical simulation A standard way to generate (quasi) random numbers is to use a linear congruential generator which uses a recurrence relation

$$X^{n+1} = (aX^n + b) \bmod M,$$

for some prime M , and a, b, X^0 such that $0 \leq a, b, X^0 < M$. This approximates a uniformly distributed variable on $[0, M]$ which can then be transformed to other distributions; a brief review is given at the end of Chapter 1. To obtain a Gaussian random variable many codes, such as MATLAB, now use the Ziggurat method (Marsaglia and Tsang, 1984).

To solve Itô SDEs such as (0.7) many of the authors in this book use the Euler–Maruyama method. Numerical methods are considered in detail in Kloeden and Platen (1999) and from a more heuristic view in Higham (2001). To numerically approximate (0.7) in one dimension the Euler–Maruyama method is given by

$$v^{n+1} = v^n + \Delta t f(v^n) + g(v^n) \Delta W^n, \quad v^0 = v(0)$$

where $\Delta t > 0$ is the time step and ΔW^n the Brownian increment. The increments ΔW^n are independent Gaussian random variable with mean zero and variance Δt and so each $\Delta W^n = \sqrt{\Delta t} \xi^n$ where ξ^n is Gaussian with mean 0 and variance 1.

To examine convergence (see Kloeden and Platen, 1991) we need to decide how the error is measured. Strong convergence asks that each noise path is approximated and the average is then taken. For the Euler–Maruyama method with **multiplicative** noise this error estimate is given by

$$\mathbb{E} [\|v(T) - v^N\|] \leq C\sqrt{\Delta t}$$

for some constant $C > 0$, and $T = N\Delta t$. When the noise is **additive** this strong estimate can be improved:

$$\mathbb{E} [\|v(T) - v^N\|] \leq C\Delta t.$$

Weak error estimates ask, for example, that the paths are on average correct. For Euler–Maruyama we have

$$\|\mathbb{E}[v(T)] - \mathbb{E}[v^N]\| \leq C\Delta t.$$

An alternative form of convergence is pathwise convergence; for the Euler–Maruyama method see Gyöngy (1998) and more recent work (Kloeden and Neuenkirch, 2007). When we are only interested in weak approximations and the statistics of a simulation the Euler–Maruyama scheme can be made slightly more efficient by taking $\Delta W^n = \sqrt{\Delta t} \operatorname{sign}(1 - \xi^n)$ where ξ^n is a uniform random variable on $[0, 1]$; there is no need to change the distribution to Gaussian. This is called a weak approximation.

To numerically simulate a Stratonovich SDE it is possible to either use the drift correction to convert to an Itô SDE or to compute using the stochastic Heun method (Kloeden and Platen, 1999).

When the system is spatially extended, for example a SPDE, then these methods can be adapted and this is discussed in Chapters 11 and 12.

Outline

We next provide a list of the abbreviations that are used throughout the book with an appropriate page reference. These include terms that are widely used in both the stochastic and neuroscience community so we hope this will be an aid for researchers unfamiliar with a particular area.

Chapter 1 gives an introduction to some stochastic processes in general and makes a good starting point for readers who are not so familiar with probabilities, correlation, white noise, and OU noise.

In Chapter 2 individual ion channels are modelled as a stochastic process – at its simplest a channel is either open or closed with some probability. In particular the chapter examines the role of calcium and coupling of release sites.

The following three chapters examine SDEs: Chapter 3 takes ordinary differential equation models of neural dynamics with noise and exploits a slow–fast structure to examine the dynamics of neuronal models. Chapter 4 looks at coherence resonance where noise may enhance the regularity of firing of the neuron and stochastic resonance where noise may allow a subthreshold signal to be encoded by the neuron. Chapter 5 covers the role of noise in synchronizing and desynchronizing a pair and then a population of coupled oscillators.

Chapter 6 examines stochasticity in a population of neurons and the effects on signal coding, looking at the inputs and outputs in the presence of noise. Chapter 7 examines large-scale networks of noisy neurons using population density methods and population firing rates. Chapter 8 uses these methods to examine a large-scale network of the lateral geniculate nucleus/perigeniculate nucleus (LGN/PGN) in the thalamus.

Chapter 9 considers experimental measurements of synaptic noise, and modelling of synaptic noise by conductance-based stochastic processes. The computational consequences are examined and models compared to experiments. In Chapter 10 statistical analysis of spike trains is developed based on integrate-and-fire (IF) neurons. The probabilistic tools are used for scientific inference.

The modelling and simulation of the stochastic nature of neurons, axons, and action potentials is reviewed in Chapter 11. In Chapter 12 numerical methods are examined for a stochastic Hodgkin–Huxley and spatially extended FitzHugh–Nagumo equations with space-time white noise.

References

- Berglund, N. and Gentz, B. (2005). *Noise-Induced Phenomena in Slow-Fast Dynamical Systems. A Sample-Paths Approach*. Probability and its Applications. Springer-Verlag, London.
- Chow, C. C. and Kopell, N. (2000). Dynamics of spiking neurons with electrical coupling. *Neural Computation*, **12**(7), 1643–1678.
- FitzHugh, R. (1961). Impulses and physiological states in models of nerve membrane. *Biophys. J.*, **1**, 445–466.
- Freidlin, M. I. and Wentzell, A. D. (1998). *Random Perturbations of Dynamical Systems* (2nd edn). Springer-Verlag, New York.
- Gardiner, C. W. (2004). *Handbook of Stochastic Methods for Physics, Chemistry, and the Natural Sciences* (3rd edn). Springer, Berlin.

- Gillespie, D. T (1976). A general method for numerically simulating the stochastic time evolution of coupled chemical reactions. *Journal of Computational Physics*, **22**, 403–34.
- Gyöngy, I. (1998). A note on Euler's approximations. *Potential Anal.*, **8**(3), 205–216.
- Higham, D. (2008). Modelling and simulating chemical reactions. *SIAM Review*, **50**, 347–368.
- Higham, D. J. (2001). An algorithmic introduction to numerical simulation of stochastic differential equations. *SIAM Review*, **43**(3), 525–546.
- Hodgkin, A. L. and Huxley, A. F. (1952). Quantitative description of membrane current and its application to conduction and excitation in nerve. *J. Physiol. (London)*, **117**, 500–544.
- Izhikevich, E.M. (2007). *Dynamical Systems in Neuroscience: The Geometry of Excitability And Bursting*. MIT Press, Cambridge MA.
- Izhikevich, E. M. (2000). Neural excitability, spiking and bursting. *Internat. J. Bifur. Chaos Appl. Sci. Engrg.*, **10**(6), 1171–1266.
- Karbowksi, J. and Kopell, N. (2000). Multispikes and synchronization in a large neural network with temporal delays. *Neural Computation*, **12**(7), 1573–1606.
- Kloeden, P. E. and Platen, E. (1999). *Numerical Solution of Stochastic Differential Equations*. Springer-Verlag, Berlin.
- Kloeden, P. E. and Neuenkirch, A. (2007). The pathwise convergence of approximation schemes for stochastic differential equations. *LMS J. Comput. Math.*, **10**, 235–253 (electronic).
- Marsaglia, G. and Tsang, W. W. (1984). A fast, easily implemented method for sampling from decreasing or symmetric unimodal density functions. *SIAM J. Sci. Statist. Comput.*, **5**(2), 349–359.
- Morris, C. and Lecar, H. (1981). Voltage oscillations in the barnacle giant muscle fiber. *Biophys. J.*, 193–213.
- Nagumo, J. S., Arimoto, S., and Yoshizawa, S. (1962). Active pulse transmission line simulating nerve axon. *Proc. IRE*, **50**, 2061–2070.
- Øksendal, B. (1985). *Stochastic Differential Equations*. Springer-Verlag, Berlin.
- Risken, H. (1996). *The Fokker–Planck Equation: Methods of Solutions and Applications*. Springer-Verlag, New York.
- Wilson, H. R. and Cowan, J. D. (1972). Excitatory and inhibitory interactions in localized populations of model neurons. *Biophysical Journals*, **12**, 1–24.
- Wilson, H. R. and Cowan, J. D. (1973). A mathematical theory of the functional dynamics of cortical and thalamic nervous tissue. *Kybernetik*, **13**, 55–80.

NOMENCLATURE

AchR	acetylcholine receptor, page 32
AMPA	Alpha-amino-3-hydroxy-5-methyl-4-isoxazolepropionic acid, page 238
AP	Action potential, page 230
Ca	Calcium, page 29
CA1	Cornu ammonis 1, one of four areas on the hippocampus, page 264
CR	Coherence resonance, page 92
CV	Coefficient of variation, page 22
EEG	Electroencephalogram, page 122
EPSP	Excitatory post-synaptic potential, page 207
ER	Endoplasmic reticulum, page 29
FHN	FitzHugh–Nagumo, page 97
GABA	Gamma-aminobutyric acid, page 213
HH	Hodgkin–Huxley, page 1
IF	Integrate-and-fire, page viii
IFB	Integrate-and-fire-or-burst, page 208
IMI	Inhomogeneous Markov interval, page 259
IP ₃ R	Inositol 1,4,5-trisphosphate receptor, page 29
ISI	Interspike interval, page 21
LFP	Local field potential, page 122
LGN	Lateral geniculate nucleus, page 207
LIF	Leaky integrate and fire, page 116
MI	Mutual information, page 161
Na	Sodium, page 30
NMDA	<i>N</i> -methyl- <i>D</i> -aspartic acid, page 194
ODE	Ordinary differential equation, page 123
OU	Ornstein–Uhlenbeck, page 7
PDE	Partial differential equation, page 281
PDF	Probability density function, page 176
PGN	Perigeniculate nucleus, page 208
PIR	Post-inhibitory rebound, page 210
PPT	Pedonculopontine tegmentum (brain stem), page 230
PRC	Phase resetting curve, page 123
PSD	Power spectral density, page 248
PSP	Post-synaptic potential, page 236
QIF	Quadratic integrate and fire, page 103
RE	Reticular, page 207
REM	Rapid eye movement, page 246
RGC	Retinal ganglion cell, page 207
RyR	Ryanodine receptor, page 29

SDE	Stochastic differential equation, page xi
SNIC	Saddle node on an invariant circle, page 125
SNR	Signal to noise ratio, page 112
SPDE	Stochastic partial differential equation, page ix
SR	Stochastic resonance, page 92
STA	Spike time average, page 245
TC	Thalamocortical, page 207
TRRP	Time-rescaled renewal process, page 259
TTX	Tetrodotoxin, page 231
V1	Primary visual cortex, page 176

LIST OF CONTRIBUTORS

- Benjamin Lindner
*Max Planck Institute for the Physics of Complex Systems,
Department of Biological Physics,
Nöthnitzer Strasse 38,
01187 Dresden, Germany*
- Jeffrey R Groff et al:
*Department of Applied Science,
The College of William & Mary,
Williamsburg, VA 23185, USA*
- Nils Berglund
*MAPMO - CNRS, UMR 6628
Bâtiment de mathématiques
Route de Chartres
Université d'Orléans,
B.P. 6759
F-45067 Orléans cedex 2
France*
- Barbara Gentz
*Faculty of Mathematics,
University of Bielefeld,
33501 Bielefeld,
Germany*
- André Longtin
*Department of Physics and Center for Neural Dynamics,
University of Ottawa,
Ontario, K1N 6N5, Canada*
- G. Bard Ermentrout
*Department of Mathematics,
University of Pittsburgh,
Pittsburgh, PA 15260, USA*
- Brent Doiron
Department of Mathematics and Center for the Neural Basis of Cognition,
- University of Pittsburgh,
Pittsburgh, PA 15260,
USA*
- Daniel Tranchina
*Department of Biology,
Courant Institute of Mathematical Sciences, and Center for Neural Science,
New York University, USA*
- Marco A. Huertas and Gregory D. Smith
*Department of Applied Science,
College of William & Mary,
Williamsburg, VA 23185, USA*
- Alain Destexhe and Michelle Rudolph-Lilith
*Integrative and Computational Neuroscience Unit (UNIC),
UPR2191, CNRS,
Gif-sur-Yvette, France*
- Liam Paninski
*Department of Statistics and Center for Theoretical Neuroscience,
Columbia University, USA*
- Emery N. Brown
*Department of Anesthesia and Critical Care,
Massachusetts General Hospital,
Harvard Medical School, and
Department of Brain and Cognitive Sciences,
Harvard-MIT Division of Health Sciences and Technology,
Massachusetts Institute of Technology, USA*

Satish Iyengar

*Center for the Neural Basis of
Cognition,
Department of Statistics,
University of Pittsburgh, USA*

Robert E. Kass

*Department of Statistics and Center
for the Neural Basis of Cognition,
Carnegie Mellon University, USA*

A. Aldo Faisal

*Computational and Biological
Learning Group,
Dept. of Engineering,
University of Cambridge, UK*

Hasan Alzubaidi

*School of Mathematics,
University of Manchester,
M13 9PL, UK*

Hagen Gilsing

*Institut fuer Mathematik,
Humboldt Universitaet zu Berlin,
Berlin 10099, Germany*

Tony Shardlow

*School of Mathematics,
University of Manchester,
M13 9PL, UK*

This page intentionally left blank

A BRIEF INTRODUCTION TO SOME SIMPLE STOCHASTIC PROCESSES

Benjamin Lindner

There is a variety of different sources of fluctuations which affect various variables in neural systems. Consequently, there are different types of stochastic processes relevant for a quantitative modelling of stochastic neural activity. Take, for instance, the behaviour of ion channels, which are the key players in the neural dynamics for action potential generation. Only many channels together generate the behaviour modelled in the deterministic Hodgkin–Huxley (HH) system – a single channel switches stochastically between open and closed states possibly going through a cascade of substates. In the simplest modelling approach this would be an example of a *two-state process* – a function that attains only two discrete values $\{\sigma_-, \sigma_+\}$ and switches stochastically (randomly) between them with rates r_- and r_+ according to the scheme

$$\begin{array}{ccc} r_- & & \\ \sigma_- & \rightleftharpoons & \sigma_+ \\ r_+ & & \end{array} \quad (1.1)$$

Taking into account the summed effect of many such channels and their effect on the potential difference of a small patch of neural membrane we come to another stochastic process: the membrane potential, which can vary continuously and is driven by synaptic noise (shot noise) and channel noise. Approximating the conductance fluctuations by current fluctuations and neglecting any spiking mechanism (voltage-dependent conductance), the membrane fluctuations obey the simple stochastic differential equation (formally equivalent to the Ornstein–Uhlenbeck process from statistical physics)

$$\tau_{\text{membrane}} \dot{V} = -(V - V_L) + \xi(t) \quad (1.2)$$

where the effective membrane time-scale is, in the simplest case, $\tau_{\text{membrane}} = C/g_L$ (with C and g_L being the capacitance and the leak conductance of the patch of membrane) or which may also include contributions from the synaptic conductance. All the driving fluctuations are lumped into $\xi(t)$ and assumed to be Gaussian and uncorrelated (white) noise. We will see how to extract statements about the statistics of $V(t)$ that are only based on this kind of knowledge.

Going one level further, noise and external signals (injected currents, evoked synaptic activity, etc.) together lead to the generation of stereotypical action

potentials which encode information in the spiking times only. In Eqn (1.2) this could be modelled by adding voltage-dependent conductances or simply a threshold for spike generation (leaky integrate-and-fire model). The generation of stereotypical spikes naturally leads to the notion of the *point process* – a random sequence of time instances $\{t_i\}$. The spike train can be represented by a series of δ functions

$$x(t) = \sum_{\{t_i\}} \delta(t - t_i) \quad (1.3)$$

with a certain (possibly time-dependent) rate r . The statistics of the point process can be based on the spike train statistics or on the statistics of the intervals between firing times (interval statistics) – both are related in a non-trivial way as we will see.

Basic concepts of the stochastic theory have already been introduced in the Introduction (p. x). Here, we present a detailed overview of methods to simulate, measure, and analytically determine the most common probability measures for the three simple processes introduced above and illustrated in Fig. 1.1. We start by introducing our notation for moments, probability densities, correlation functions, power spectra, and give definitions for the characteristics of a fluctuating function (correlation time, noise intensity). We then discuss simple continuous, two-state, and point processes with special emphasis on the relation between different statistics (e.g. power spectra and interval densities). Possibly unexpected relations among the three processes are given in the last section.

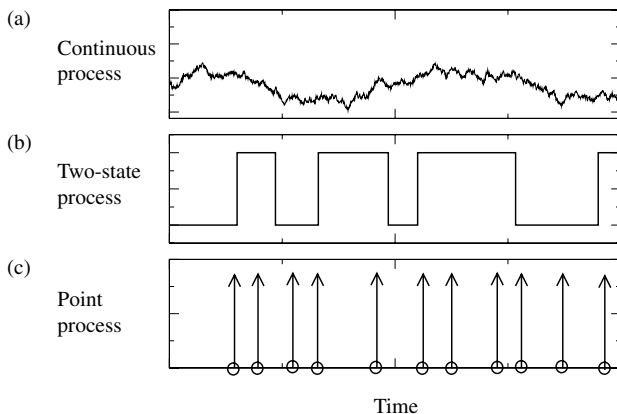


FIG. 1.1: The three classes of stochastic processes discussed in this chapter: (a) a continuous process (Ornstein–Uhlenbeck process according to Eqn (1.2), see Section 1.2); (b) a discrete process (random telegraph noise according to the scheme in Eqn (1.1), see Section 1.3); (c) a point process indicated by the circles and the associated δ spike train according to Eqn (1.3) shown by arrows (see Section 1.4).

This chapter can in no way replace a thorough introduction to probability theory and the theory of stochastic processes as given, for instance, in the following monographs: continuous systems are covered by Papoulis (1965), Stratonovich (1967), Risken (1984), Gardiner (1985), and van Kampen (1992). Gardiner (1985) and van Kampen (1992) also study discrete systems in more detail; useful results on point processes are covered in the books by Cox (Cox, 1962, Cox and Lewis, 1966) and Stratonovich (1967). Many useful results (some of which are rederived here) can be found in textbooks on stochastic processes in the neuroscience by Holden (1976), Ricciardi (1977), Tuckwell (1988), Tuckwell (1989), and more recently Gerstner and Kistler (2002).

1.1 Statistics of stochastic variables and stochastic processes

Averaging Having an ensemble of N independent samples $\{x_i\}$ of a stochastic variable x , we can estimate the average of any function $f(x)$ by

$$\langle f(x) \rangle \stackrel{\text{def}}{=} \frac{1}{N} \sum_{i=1}^N f(x_i) \quad (1.4)$$

which becomes exact for $N \rightarrow \infty$. In particular, we can ask for the mean of x

$$\langle x \rangle = \frac{1}{N} \sum_{i=1}^N x_i \quad (1.5)$$

and its variance

$$\langle \Delta x^2 \rangle = \langle (x - \langle x \rangle)^2 \rangle = \langle x^2 \rangle - \langle x \rangle^2 = \frac{1}{N} \sum_{i=1}^N x_i^2 - \langle x \rangle^2. \quad (1.6)$$

If x is not only a variable but a stochastic function (or process) of time $x(t)$, we can ask for averages over functions of $x(t_i)$ at different times $\{t_i\}$ that are defined by

$$\langle f(x(t_1), x(t_2), \dots) \rangle = \frac{1}{N} \sum_{i=1}^N f(x_i(t_1), x_i(t_2), \dots). \quad (1.7)$$

The averages obviously depend on the ensemble from which we pick the values $x_i(t_k)$ at a certain time $t = t_k$ and they will depend (via the temporal evolution of this ensemble) on the time instants t_1, t_2, \dots . We may define a *stationary* ensemble, by requiring that all possible averages Eqn (1.7) depend only on the time differences $t_2 - t_1, t_3 - t_1, \dots$ but not on the absolute time. For other (weaker) kinds of stationarity, see Papoulis (1965).

Probability densities A very important average gives us the probability density of the stochastic variable or function. For a stochastic function $x(t)$ this density is given by

$$P(X, t) = \langle \delta(X - x(t)) \rangle. \quad (1.8)$$

If we know this density for a continuous process, $P(X, t)\Delta X$ with a small increment ΔX gives us the probability to observe $x(t) \in [X - \Delta X/2, X + \Delta X/2]$. Once we know the probability density, we can calculate the average of any function $f(x(t))$ by

$$\begin{aligned} \langle f(x(t)) \rangle &= \left\langle \int_{-\infty}^{\infty} dX f(X) \delta(x(t) - X) \right\rangle = \int_{-\infty}^{\infty} dX f(X) \langle \delta(x(t) - X) \rangle \\ &= \int_{-\infty}^{\infty} dX f(X) P(X, t) \end{aligned} \quad (1.9)$$

which still may depend on the time t as a parameter.

The definition of the probability density can be easily extended to values at different times yielding a multivariate distribution (joint probability density), formally defined by

$$P_n(X_1, t_1; X_2, t_2; \dots; X_n, t_n) = \langle \delta(X_1 - x(t_1)) \delta(X_2 - x(t_2)) \dots \delta(X_n - x(t_n)) \rangle. \quad (1.10)$$

The stochastic process is described in more and more detail by a hierarchy of probability densities of increasing order n . However, it is generally also more complicated to measure or calculate densities of higher order.

A conditional probability density assumes a certain knowledge about values of the process at time instants t_1, \dots, t_k (say, we know, for instance, that $x(t_1) = X_1$) and gives us the probability of values at other times under this condition. The conditional density (everything following the bar is the condition) is defined by

$$P(X_{k+1}, t_{k+1}; \dots; X_n, t_n | X_1, t_1; \dots; X_k, t_k) = \frac{P_n(X_1, t_1; \dots; X_k, t_k; \dots; X_n, t_n)}{P_k(X_1, t_1; \dots; X_k, t_k)}. \quad (1.11)$$

Markov process An important class of processes is defined by the property that the evolution of their probability density depends only on the present state but not on the past. Thus if we deal with a density $P_n(X_1, t_1; \dots; X_n, t_n)$ (where $t_1 < t_2 < \dots < t_n$) and ask for the lower-order probability conditioned on k values, then only the condition at the latest instant in time will matter

$$P(X_{k+1}, t_{k+1}; \dots; X_n, t_n | X_1, t_1; \dots; X_k, t_k) = P(X_{k+1}, t_{k+1}; \dots; X_n, t_n | X_k, t_k). \quad (1.12)$$

Knowledge about $x(t_k) = X_k$ at $t = t_k$ (which is the present time) determines the density at later times $t_{k'} > t_k$; knowledge about values in the past at $t_{k''} < t_k$ does not improve our statistical knowledge about the future.

For a Markov process, any multivariate probability density can be expressed by one specific conditional probability density $P(X, t|X_0, t_0)$ which is called the transition probability and is the central quantity of interest for a Markov process.

Correlation function In order to characterize the stationary time-dependent features of the dynamics, one can use the autocorrelation function (or short correlation function)

$$C(\tau) = \lim_{t \rightarrow \infty} [\langle x(t)x(t + \tau) \rangle - \langle x(t) \rangle^2], \quad (1.13)$$

telling us essentially how much two values of the trajectory which are lagged by an interval τ have in common. The second term in Eqn (1.13) takes care of what we may expect for statistically independent values and the limit $t \rightarrow \infty$ is taken in order to achieve independence on the initial value $x(0)$. The correlation function for vanishing lag corresponds to the stationary variance of the random variable $x(t)$.

If we know the two-times probability density $P(X_0, t_0; X_1, t_1)$ or, equivalently, the conditional probability density $P(X_1, t_1|X_0, 0)$ together with the steady-state density $P_0(X)$ we can express the correlation function as follows:

$$\begin{aligned} C(\tau) &= \lim_{t \rightarrow \infty} \int_{-\infty}^{\infty} dX_0 \int_{-\infty}^{\infty} dX_1 X_0 X_1 [P(X_0, t; X_1, t + \tau) - P_0(X_0)P_0(X_1)] \\ &= \int_{-\infty}^{\infty} dX_0 \int_{-\infty}^{\infty} dX_1 X_0 X_1 P_0(X_0) [P(X_1, \tau|X_0, 0) - P_0(X_1)]. \end{aligned} \quad (1.14)$$

This formula is also useful if we know a differential equation for $P(X_1, \tau|X_0, 0)$: multiplying this equation by $X_0 X_1$ and integrating yields a potentially useful relation for $C(\tau)$.

Power spectrum An alternative way to quantify the fluctuations and their dynamics is to ask how the variance (in electrical systems proportional to the power of the process) is distributed with respect to frequency. The latter appears naturally by Fourier analysis. Defining the Fourier transform of $x(t)$ by

$$\tilde{x}(f) = \int_0^T dt x(t) e^{2\pi i f t} \quad (1.15)$$

we obtain a new (complex-valued) random variable that depends on the frequency f as a parameter. For a stationary time series $x(t)$ the mean value at finite frequency will vanish, that is $\langle \tilde{x}(f > 0) \rangle = 0$. The variance grows with the simulation time T ; the factor of proportionality is given by the *power spectrum*

$$S(f) = \lim_{T \rightarrow \infty} \frac{\langle \tilde{x}\tilde{x}^* \rangle}{T} \quad (1.16)$$

where \tilde{x}^* denotes the complex conjugate of \tilde{x} . In order to see that this has anything to do with the variance in the time domain let us consider the latter relation in more detail (assuming $\langle x \rangle = 0$, for simplicity):

$$\begin{aligned}
\frac{\langle \tilde{x}\tilde{x}^* \rangle}{T} &= \frac{1}{T} \int_0^T dt \int_0^T dt' e^{2\pi if(t-t')} \langle x(t)x(t') \rangle \\
&= \frac{1}{T} \int_0^T dt \int_{t-T}^t d\tau e^{2\pi if\tau} C(\tau) \\
&= \frac{1}{T} \int_{-T}^0 d\tau e^{2\pi if\tau} C(\tau) \int_0^{T+\tau} dt + \frac{1}{T} \int_0^T d\tau e^{2\pi if\tau} C(\tau) \int_\tau^T dt \\
&= \int_{-T}^T d\tau e^{2\pi if\tau} C(\tau) - \int_{-T}^T d\tau e^{2\pi if\tau} C(\tau) \frac{|\tau|}{T}.
\end{aligned} \tag{1.17}$$

Here, we have introduced a new variable τ , used the autocorrelation function $C(\tau)$, and exchanged the order of integration. For most processes of interest, the correlation function $C(\tau)$ decays sufficiently strongly at large times that the integral $\int d\tau C(\tau)\tau$ remains finite. Hence, for $T \rightarrow \infty$ the second term in the last line vanishes and we thus obtain the important relation

$$S(f) = \int_{-\infty}^{\infty} d\tau e^{2\pi if\tau} C(\tau) \tag{1.18}$$

called the Wiener–Khinchin theorem (Risken, 1996, Gardiner, 1985). The relation is sometimes used as a definition of the spectrum: the power spectrum is the Fourier transform of the autocorrelation function. As for any Fourier transform, the reverse is also true: The correlation function is the (inverse) Fourier transform of the spectrum:

$$C(\tau) = \int_{-\infty}^{\infty} df e^{-2\pi if\tau} S(f). \tag{1.19}$$

In particular for $\tau = 0$ we obtain

$$C(0) = \langle \Delta x^2 \rangle = \int_{-\infty}^{\infty} df S(f). \tag{1.20}$$

Thus as promised the integrated spectrum gives the variance (the power) and the spectrum shows how this power is distributed over frequencies.

The Wiener–Khinchin theorem offers a fast numerical way to estimate the correlation function: One measures or simulates many independent realizations of the process $x_i(t)$ for a sufficiently long time window T , calculates the fast Fourier transform, and determines the frequency-dependent variance of the resulting ensemble. Dividing by the time window T yields an estimate of the power spectrum and applying an additional Fourier back-transformation on the function gives the autocorrelation function $C(\tau)$.

Correlation time In order to estimate the time over which a trajectory is correlated, different definitions of a correlation time can be used. If the process' correlation function does not show oscillations and remains positive we may use the integral over the normalized autocorrelation function that is also simply related to the power spectrum at vanishing frequency:

$$\tau_{\text{corr}} = \int_0^\infty d\tau C(\tau)/C(0) = \frac{S(0)}{2C(0)}. \quad (1.21)$$

In other cases an integral over the absolute value (see, for instance, Hänggi and Jung 1995) or the square of the autocorrelation function yields a more meaningful estimate of a correlation time.

Noise intensity The intensity or strength of the process is *not* just given by the variance of its steady-state density. A widely used definition of the noise intensity of a process with non-negative correlation function is as follows:

$$D = \int_0^\infty d\tau C(\tau) = \frac{S(0)}{2} = \langle \Delta x^2 \rangle \tau_{\text{corr}}. \quad (1.22)$$

In the last step we have related the noise intensity to the variance and the correlation time of the process using Eqns (1.20) and (1.21). This illustrates that it matters not only *how large* typical amplitudes of the noise are (as quantified by the variance) but also for *how long* the noise acts with roughly the same value (as quantified by the correlation time). As is clear from the discussion of the correlation time, the definition of the noise intensity is also meaningful for processes with monotonically decaying correlation but does not apply to processes with a strongly oscillating correlation function.

In order to illustrate these rather dry definitions we turn to our standard examples. We will also use this opportunity to introduce simple simulation algorithms for the three classes of stochastic systems.

1.2 The Ornstein–Uhlenbeck process

As an example of a continuous stochastic process we consider the Ornstein–Uhlenbeck process (or OU process) which is also known in the mathematical

literature as a mean-reverting process. It appears in a number of chapters in this book; see Chapters 4, 5 and 9 for a conductance model, and Chapter 10. It obeys the Langevin equation (Uhlenbeck and Ornstein, 1930, Risken, 1996)

$$\dot{v} = -\gamma v + \sqrt{2D}\xi(t) \quad (1.23)$$

where $\xi(t)$ is a Gaussian white noise with average zero and a δ correlation in time

$$\langle \xi(t) \rangle = 0, \quad \langle \xi(t)\xi(t') \rangle = \delta(t-t'). \quad (1.24)$$

The intensity of the driving noise $\sqrt{2D}\xi(t)$ is (according to Eqn (1.22)) D , and its correlation time is zero as expected for an uncorrelated process. The power spectrum is flat, $S(f) = 2D$, which led to the name ‘white’ noise in analogy with the spectrum of white light. The fact that this *driving* noise has infinite variance and vanishing correlation time (unlike any function in the real world) is a mathematical abstraction leading to the very useful Markov property of the *driven* process. We note that the Gaussian property is used when dealing with increments of the process (which are also Gaussian).

We have seen that the voltage across a passive membrane obeys the same dynamics as Eqn (1.23) (with $\tau_{\text{membrane}} = 1/\gamma$ and a proper rescaling of the noise strength). In the above form, however, the model describes the velocity of a Brownian particle of unit mass by Newton’s law with the acceleration term on the left-hand side and a sum of a friction force (Stokes friction with coefficient γ) and a random stochastic force $\sqrt{2D}\xi(t)$ on the right-hand side. It was introduced 100 years ago by Langevin (Langevin, 1908) and later in detail studied by Uhlenbeck and Ornstein (Uhlenbeck and Ornstein, 1930). In neuroscience it has immense importance because, supplemented with a fire-and-reset condition, Eqn (1.23) is mathematically equivalent to the often-used leaky integrate-and-fire model.

The OU process is a Markov process. This might not be obvious since although we deal with a first-order equation in Eqn (1.23) that is (in the autonomous case) determined only by its initial condition (i.e. by the present time), we have time-dependent driving (the noise). The noise is, however, uncorrelated and thus does not introduce a statistical dependence on the past that would contradict the Markov property in Eqn (1.12).

Simulation algorithm A simple algorithm for this process is obtained by iterating its discretized version in a simple Euler procedure

$$v_{i,j+1} = v_{i,j}(1 - \gamma\Delta t) + \sqrt{2D\Delta t}\eta_{i,j}, \quad i = 1, \dots, N \quad (1.25)$$

where the first index i denotes the realization and the second index j the time $t = j\Delta t$; $\eta_{i,j}$ are independent Gaussian random numbers (see Section 1.6) with

zero mean and unit variance¹ $\langle \eta_{i,j} \eta_{i',j'} \rangle = \delta_{i,i'} \delta_{j,j'}$ (where we have used the Kronecker symbol).

In order to measure an example of a time-dependent probability density $P(V, t)$, we start every realization at $v_{i,0} = v_0$ and so, of course, the initial probability density would be $P(V, t=0) = \delta(V - v_0)$; $P(V, t)$ is then the transition probability of the process. Performing NK iterations of Eqn (1.25) we may find an estimate of the density $P(V, t = K\Delta t)$ at time $t = K\Delta t$ by making a histogram of the N values $v_{i,K}$ ($i = 1, \dots, N$). The whole procedure is shown in Fig. 1.2. An estimate of the probability density is given by

$$P(V, t = K\Delta t) \approx \frac{1}{N\Delta v} \sum_{i=1}^N \Theta(V + \Delta v/2 - v_{i,K}) \Theta(v_{i,K} - (V - \Delta v/2)) \quad (1.26)$$

where the product of Heaviside functions $\Theta(\cdot)$ ensures that $v_{i,K}$ only contributes to the estimate if it falls into the interval $[V - \Delta v/2, V + \Delta v/2]$. Clearly, the density estimated by Eqn (1.26) depends on the time. In the example we have chosen there is a drift of the whole probability density towards the origin – for short times the histogram is biased towards the initial value (which is positive in our numerical example). For longer times ($t \gg \tau$) the probability density becomes independent of time and reaches a stationary limit $P(V, t) \rightarrow P_0(V)$ which means that the initial value (or the initial distribution) is forgotten. In many cases of importance (ergodic processes) this steady-state density would coincide with a time-average of the process itself. This means that instead of a large ensemble of trajectories we may just average a single trajectory over a longer time (bottom panel in Fig. 1.2b). Indeed, this yields the same density as the ensemble average at long times.

We can calculate the probability density analytically and compare it to our simulation result. For the Langevin equation there exists a corresponding Fokker–Planck equation that governs the evolution of the probability density

$$\partial_t P(V, t) = \partial_V [\gamma V + D \partial_V] P(V, t). \quad (1.27)$$

The first term on the right-hand side is the *drift term* (resulting from the friction term in the Langevin equation) and the second one is the *diffusion term* (resulting from the stochastic driving). The correct boundary conditions for a freely evolving Ornstein–Uhlenbeck process are natural boundary conditions

$$\lim_{V \rightarrow \infty} P(\pm V, t) = \lim_{V \rightarrow \infty} \partial_V P(\pm V, t) = 0. \quad (1.28)$$

¹Please note the uncommon scaling of the stochastic term with $\sqrt{\Delta t}$ which can be understood as follows: integrating Eqn (1.23) over the time step Δt , we get the increment $\Delta W = \int_t^{t+\Delta t} dt' \xi(t')$ of a Wiener process which is Gaussian, has vanishing mean, and a variance $\langle (\Delta W)^2 \rangle = \int_t^{t+\Delta t} \int_t^{t+\Delta t} dt' dt'' \langle \xi(t') \xi(t'') \rangle = \Delta t$; hence the standard deviation is $\sim \sqrt{\Delta t}$.

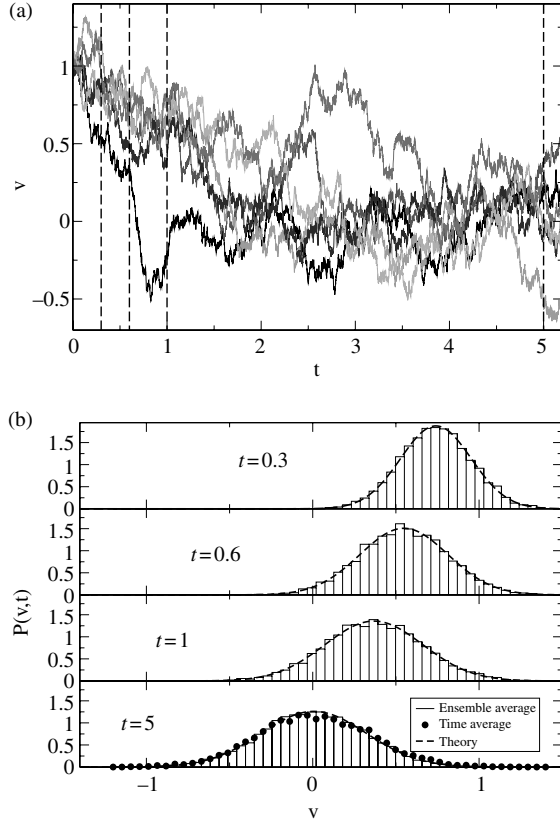


FIG. 1.2: Time-dependent probability densities of an Ornstein–Uhlenbeck (OU) process for $D = 0.1$ and $\gamma = 1$. $N = 10^4$ trajectories were started at $v(t = 0) = 1$ and simulated according to the scheme Eqn (1.25) (time step $\Delta t = 0.01$) and the density was estimated via Eqn (1.26). In (a) the first six trajectories are shown; the dashed lines indicate the instants at which snapshots of the density are shown in (b): the density is initially centred around a positive value (top panel in (b)), for later times it is centred around zero (bottom panel in (b)). Also shown by dots is the density obtained from a long time average ($T = 10^3$) which agrees nicely with the long-time ensemble average (bottom panel in (b)). Theory (dashed lines) is given in Eqn (1.29).

We note in passing that a Fokker–Planck equation can also be found when there is a nonlinear drift term and state-dependent noise (also called multiplicative noise) and that it can also be generalized to more than one variable; for derivation(s) of the Fokker–Planck equation and further applications see Risken (1996). For the OU process it is possible to find the full time-dependent solution with the

initial condition $P(V, 0) = \delta(V - v_0)$ and natural boundary conditions, yielding the transition probability (see Risken 1996)

$$P(V, t) = \frac{1}{\sqrt{2\pi\langle\Delta v^2(t)\rangle}} \exp\left[-\frac{(V - \langle v(t) \rangle)^2}{2\langle\Delta v^2(t)\rangle}\right] \quad (1.29)$$

where the time-dependent mean and variance read

$$\langle v(t) \rangle = v_0 e^{-\gamma t}, \quad (1.30)$$

$$\langle\Delta v^2(t)\rangle = \frac{D}{\gamma}[1 - e^{-2\gamma t}]. \quad (1.31)$$

Equation (1.29) has been plotted in Fig. 1.2; the shape of the histograms reproduce this formula quite well.

For long times ($t \rightarrow \infty$) the mean and variance approach $\langle v \rangle \rightarrow 0$ and $\langle\Delta v^2\rangle \rightarrow D/\gamma = k_B T$ (the latter relation is called the Einstein relation (Risken, 1996)) and in this limit the steady-state density is a so-called Maxwell distribution (Risken, 1996)

$$P_0(V) = \frac{e^{-V^2/(2k_B T)}}{\sqrt{2\pi k_B T}}. \quad (1.32)$$

The time-dependent density (either simulated or calculated) could be used to calculate the autocorrelation function of the OU process. However, we want to illustrate the calculation of the second-order statistics in different ways. First of all, we can determine the correlation function via the power spectrum and fast Fourier transform from simulations. Secondly, we can analytically calculate the correlation function using (i) the Fokker–Planck equation; (ii) the formal solution of Eqn (1.23); and (iii) the Fourier transform of the power spectrum which is obtained by Rice’s method.

Simulations are shown in Fig. 1.3: a single trajectory $v(t)$ (a) is Fourier transformed to \tilde{v} (b); many such realizations are used to estimate the power spectrum (variance of \tilde{v} divided by simulation time) shown in (d); a back-transformation into the time domain yields the autocorrelation function shown in (c). For an Ornstein–Uhlenbeck process the correlation function decays with a single rate (the friction coefficient) and the power spectrum displays a Lorentzian shape with a corner frequency determined by the friction coefficient, that is the power spectrum attains half its maximal value at $2\pi f_{\text{corner}} = \gamma$ (see below, Eqn (1.37)).

Calculation of the correlation function using the Fokker–Planck equation First, it is instructive to calculate the stationary variance $\langle v^2 \rangle$ from the Fokker–Planck equation (1.27), that is the correlation function at vanishing lag $C(0)$. To this end, we set the time derivative on the left-hand side to zero (implying that we

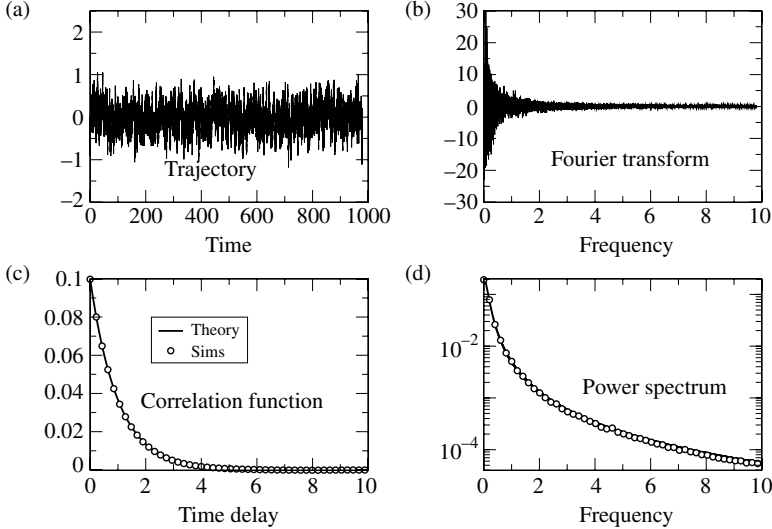


FIG. 1.3: Second-order statistics of the Ornstein–Uhlenbeck process. A single realization shown in (a) is Fourier transformed according to Eqn (1.15); the real part of this complex-valued stochastic quantity is shown as a function of frequency in (b). From many such realizations ($N = 1000$) one obtains the variance of the Fourier transform and from the latter one can determine the power spectrum (d) via Eqn (1.16). The Fourier back-transformation of the power spectrum yields, through Eqn (1.19), the correlation function (c) which shows an exponential decay. Theory is given in Eqn (1.35) (correlation function) and Eqn (1.37) (power spectrum). Numerical parameters: $D = 0.1$, $\gamma = 1$, $\Delta t = 0.001$, $T = 1000$.

now deal with the stationary density $P_0(V)$), multiply both sides by $V^2/2$, and integrate V over the real axis. Multiple integrations by parts (using Eqn (1.28)) yield

$$0 = -\gamma \int_{-\infty}^{\infty} dV V^2 P_0(V) + D \int_{-\infty}^{\infty} dV P_0(V) = -\gamma \langle v^2 \rangle + D$$

$$\Rightarrow \langle v^2 \rangle = C(0) = \frac{D}{\gamma}. \quad (1.33)$$

In order to derive an equation for the correlation function we proceed as follows. We multiply the Fokker–Planck equation (1.27) by $V V_0 P_0(V_0)$ and perform a double integral over V_0 and V . Using (i) the relation between correlation function and time-dependent density Eqn (1.14); (ii) the fact that the stationary mean value vanishes, that is $\langle v \rangle = \int dV_0 V_0 P_0(V_0) = 0$; (iii) all probability densities

and their derivatives vanish at infinity, one obtains after multiple integrations by parts on the right-hand side, the equation

$$\frac{d}{dt}C(t) = -\gamma C(t), \quad t > 0 \quad (1.34)$$

(here the partial derivative with respect to time turns into an ordinary derivative). From the initial condition in Eqn (1.33) and the fact that the correlation function is an even function in τ , we find

$$C(\tau) = \frac{D}{\gamma} e^{-\gamma|\tau|}. \quad (1.35)$$

This formula shows excellent agreement with our simulation data in Fig. 1.3(c). *Calculation of the correlation function using the formal solution* If we know the value of $v(t)$ at $t = 0$, i.e. $v(t = 0) = v_0$, we can formally solve the Langevin equation (it is a linear inhomogeneous first-order differential equation). We obtain

$$v(t) = v_0 e^{-\gamma t} + \sqrt{2D} \int_0^t dt' e^{-\gamma(t-t')} \xi(t'). \quad (1.36)$$

It is easily seen that the stationary mean value must vanish:

$$\langle v \rangle_{\text{st}} = \lim_{t \rightarrow \infty} \left[v_0 e^{-\gamma t} + \sqrt{2D} \int_0^t dt' e^{-\gamma(t-t')} \langle \xi(t') \rangle \right] = 0$$

where we have used the fact that the white noise has a zero mean at all times. The autocorrelation function is obtained as follows. For $t \rightarrow \infty$ any term involving the initial condition (the first term on the right-hand side in Eqn (1.36)) decays to zero; dropping the respective terms we obtain for positive increment $\tau > 0$

$$\begin{aligned} \langle v(t)v(t+\tau) \rangle &= 2D \int_0^t dt' \int_0^{t+\tau} dt'' e^{-\gamma(2t+\tau-t'-t'')} \langle \xi(t') \xi(t'') \rangle \\ &= 2D \int_0^t dt' e^{-\gamma(2t+\tau-2t')} = \frac{D}{\gamma} [e^{-\gamma\tau} - e^{-\gamma(2t+\tau)}]. \end{aligned}$$

Doing the same calculation with negative τ , we can generalize this formula and recover in the limit $t \rightarrow \infty$ the autocorrelation function (1.35).

Analytical calculation of the power spectrum using Rice's method It suffices to perform a Fourier transformation of the Langevin equation as follows:

$$\begin{aligned} \int_0^T dt e^{2\pi i f t} \dot{v} &= -\gamma \int_0^T dt e^{2\pi i f t} v + \sqrt{2D} \int_0^T dt e^{2\pi i f t} \xi(t) \\ v(T)e^{2\pi i f T} - v_0 - 2\pi i f \tilde{v} &= -\gamma \tilde{v} + \sqrt{2D} \tilde{\xi} \\ \Rightarrow \tilde{v} &= \frac{\sqrt{2D} \tilde{\xi} - v(T)e^{2\pi i f T} + v_0}{\gamma - 2\pi i f}. \end{aligned}$$

Multiplying by the complex conjugated Fourier transform \tilde{v}^* and dividing by T , the last two terms in the numerator vanish and only the white-noise spectrum remains ($\langle \tilde{\xi} \tilde{\xi}^* \rangle / T = S_\xi = 1$). By averaging we obtain

$$S(f) = \frac{2D}{\gamma^2 + (2\pi f)^2} \quad (1.37)$$

which agrees with the Fourier transform of the correlation function (1.35) in full accordance with the Wiener–Khinchin theorem (1.18).

Noise intensity and correlation time The noise intensity of the OU process is

$$D_{\text{OU}} = D\gamma^{-2}. \quad (1.38)$$

Its correlation time is easily calculated via Eqn (1.21):

$$\tau_{\text{corr}} = S(0)/[2C(0)] = \gamma^{-1} \quad (1.39)$$

which is independent of the parameter D . For the OU process we can nicely separate and control the intensity and the correlation time of the noise, e.g. by scaling $D = Q\gamma^2$; then Q and γ^{-1} are the intensity and the correlation time, respectively. This is in general not possible for processes generated by nonlinear stochastic differential equations (SDEs).

1.3 Two-state process

A switching between two states can result from complicated dynamics and is in general characterized by the sequence of residence times (the random periods spent in the two possible states). A very simple process is the Markovian two-state process in which transitions from one state to the other are entirely determined by a switching rate and do not depend on the whole history of previous switchings. This was the case illustrated in Eqn (1.1). We start with the statistics of such a simple process and then present the slightly more general case in which the residence times are drawn from two arbitrary probability densities.

1.3.1 Markovian telegraph noise (dichotomous noise)

Simulation algorithm A simple algorithm for simulating a two-state Markov process with rates r_+ (for leaving the state $x = \sigma_+$) and r_- (for leaving the state $x = \sigma_-$) would consist of the following steps:

1. draw a uniformly distributed random number $a_j \in [0, 1]$;
 2. for $x(t) = \sigma_{\pm}$: if $a_j < r_{\pm} \Delta t \Rightarrow x(t + \Delta t) = \sigma_{\mp}$
 else $\Rightarrow x(t + \Delta t) = \sigma_{\pm}$
- update time $t \rightarrow t + \Delta t$ and return to 1.

Here we have to use a time step $\Delta t \ll r_{\pm}^{-1}$ in order to keep the probability of multiple transitions within one time step negligibly small.

Probability density and master equation For the telegraph noise above with states $x \in \{\pm 1\}$ the ‘density’ in this case reduces to

$$P(X, t) = p_+(t)\delta(X - \sigma_+) + p_-(t)\delta(X - \sigma_-) \quad (1.40)$$

where $p_{\pm}(t)$ are governed by the master equation

$$\partial_t p_{\pm}(t) = r_{\mp} p_{\mp} - r_{\pm} p_{\pm}. \quad (1.41)$$

On the right-hand side we have two terms for gain and loss of probability or in other words, for influx and efflux of probability. These fluxes are proportional to the switching rate and the probability of the state that is left. The term $r_{+}p_+$, for instance, gives the efflux of probability from the plus state (the trajectories switching from σ_+ to σ_-) and is, of course, equal to the influx to the minus state.

Residence times Before we come to the full solution of Eqn (1.41) we may answer a simple question: What is the distribution of residence times in one of the states? To answer this we just have to set the initial probability say in the σ_+ state to 1 and the influx term in the master equation to zero; then the efflux of probability describes the fraction of realizations that leave σ_+ at time t *for the first time* (leaving the gain term in the equation the same efflux term would describe the fraction of *all* the realizations that leave σ_+ at time t). Without the gain term, the equations reduce to only one and we obtain for the residence time density $\rho_+(t)$

$$\dot{\rho}_+ = -r_+ p_+ \text{ with } p_+(0) = 1 \Rightarrow p_+(t) = e^{-r_+ t} \Rightarrow \rho_+(t) = r_+ e^{-r_+ t} \quad (1.42)$$

and by a completely equivalent calculation $\rho_-(t) = r_- e^{-r_- t}$. The mean residence time is easily calculated and reads $\tau_{\pm} := \int_0^{\infty} dt t \rho_{\pm}(t) = r_{\pm}^{-1}$. The waiting time densities permit an alternative simulation algorithm: instead of drawing random numbers in each time step and asking whether a transition has occurred, we can draw random residence times from the respective exponential distribution – in between these switching times, the process is simply a constant (for the generation of exponentially distributed random numbers see Section 1.6).

Probability density Turning again to the two-state process, we can use Eqn (1.41) to calculate the time-dependent probability density and from it any desired statistics. Since Eqn (1.41) is a simple linear differential equation, we obtain by standard methods an exponential solution that can (for arbitrary initial conditions $p_+(0), p_-(0) = 1 - p_+(0)$) be written as

$$p_{\pm}(t) = p_{\pm}^0 \pm [p_+(0) - p_+^0] e^{-(r_+ + r_-)t}. \quad (1.43)$$

The first term is the steady-state solution that is approached for long times

$$p_{\pm}^0 = \lim_{t \rightarrow \infty} p_{\pm}(t) = \frac{r_{\mp}}{r_+ + r_-}. \quad (1.44)$$

The other terms in Eqn (1.43) describe the decay of the initial condition. In particular, from $p_+(0) = 1$ and $p_-(0) = 0$ we can obtain the four conditional probabilities to be in two specific states at time zero and at time t , i.e. the transition probabilities of the random telegraph noise

$$p_{\pm|+} = p_{\pm}^0 \pm p_-^0 e^{-(r_- + r_+)t}, \quad (1.45)$$

$$p_{\pm|-} = p_{\pm}^0 \mp p_+^0 e^{-(r_- + r_+)t}. \quad (1.46)$$

These conditional probabilities multiplied by the respective steady-state probability give the two-times probability needed for calculating the autocorrelation function via Eqn (1.14).

Correlation function As for the OU process there are different ways to calculate the correlation function. Here we use Eqn (1.14) (but for the discrete-state process the integrals turn into sums over the two states). We obtain

$$C(\tau) = \sum_{i,j=+,-} \sigma_i \sigma_j p_j^0 [p_{i|j}(\tau) - p_i^0]. \quad (1.47)$$

It is a simple exercise to calculate from Eqns (1.44)–(1.47) the autocorrelation function

$$C(\tau) = \frac{r_- r_+ (\sigma_+ - \sigma_-)^2}{(r_- + r_+)^2} e^{-(r_- + r_+)|\tau|}. \quad (1.48)$$

So, as for the Ornstein–Uhlenbeck process, we obtain a purely exponential correlation function for the Markovian telegraph noise. Hence the power spectrum is again a Lorentzian as for the OU process:

$$S(f) = \frac{2(\sigma_+ - \sigma_-)^2 / (r_+^{-1} + r_-^{-1})}{(r_+ + r_-)^2 + (2\pi f)^2}. \quad (1.49)$$

Noise intensity and correlation time The intensity of the two-state fluctuations is given by

$$D_{\text{dicho}} = \frac{S(0)}{2} = \frac{(\sigma_+ - \sigma_-)^2}{(r_+^{-1} + r_-^{-1})(r_+ + r_-)^2}. \quad (1.50)$$

The noise intensity vanishes, in particular, if one of the rates goes to infinity or zero (with the other rate and the amplitudes σ_{\pm} being fixed). In the symmetric case ($r_+ = r_- = r$), the intensity is $D_{\text{dicho}} = (\sigma_+ - \sigma_-)^2/(8r) = \langle \Delta\sigma^2 \rangle/(2r)$.

The decay rate of the correlation function (1.48) is simply the sum of the two transition rates r_{\pm} . The correlation time of the process is

$$\tau_{\text{corr}} = \frac{1}{r_- + r_+} = \frac{1}{1/\tau_+ + 1/\tau_-}. \quad (1.51)$$

Here we have used the residence (or waiting) times $\tau_{\pm} = r_{\pm}^{-1}$ in the two states. It is amusing to note that the correlation time τ_{corr} is dominated by the *smaller* of the two times. So if we have a very asymmetric two-state process, i.e. a pulse train, then the correlation time will be close to the pulse width rather than to the interpulse interval. This makes sense: for very small pulse width this two-state process approaches the limit of a Poisson spike train which has no temporal correlations at all.

1.3.2 Renewal two-state processes

In general two-state processes do not follow Markovian dynamics. Switching rates, for instance, do depend on the past and not only on the current state of the system. In some comparably simple cases we can still relate statistics of different kinds. For instance, if the system is ergodic and stationary, we can relate by time-averaging the mean residence times τ_{\pm} of the two states and the steady-state probabilities

$$p_{\pm}^0 = \frac{\tau_{\pm}}{\tau_+ + \tau_-} \quad (1.52)$$

which is true in particular for the random telegraph noise as can be checked by Eqn (1.44). Also, the mean and variance of the process can be expressed in a simple way using τ_{\pm} and σ_{\pm} :

$$\langle \sigma \rangle = \frac{\tau_+ \sigma_+ + \tau_- \sigma_-}{\tau_+ + \tau_-}, \quad \langle \Delta\sigma^2 \rangle = \frac{\tau_+ \tau_-}{(\tau_+ + \tau_-)^2} (\sigma_+ - \sigma_-)^2. \quad (1.53)$$

In the following we consider a comparably simple kind of non-Markovian process: the renewal state process. For such a process the switching probability depends only on the time that has passed since the last switching event. The Markovian

telegraph noise is included as a special case for which the residence time densities are purely exponential.

Simulation of a renewal two-state process If we know that the residence times in each of the two states are independent of each other and distributed according to two waiting time densities $w_+(t), w_-(t)$ with mean waiting times τ_{\pm} , we can simulate the process by simulating alternating piecewise constant parts of the process $x(t) = \sigma_{\pm}$, the lengths of which are drawn from $w_{\pm}(t - t_i)$ (here t_i denotes the instant of last switching).

Power spectrum and residence time densities Knowing the Fourier transforms of the residence time densities \tilde{w}_{\pm} , we can calculate the power spectrum of the two-state process with the Stratonovich formula (cf. Stratonovich 1967, Vol. I, Eqn (6.121)):

$$S(f) = \frac{2(\sigma_+ - \sigma_-)^2}{(\tau_+ + \tau_-)(2\pi f)^2} \operatorname{Re} \left[\frac{(1 - \tilde{w}_+)(1 - \tilde{w}_-)}{1 - \tilde{w}_- \tilde{w}_+} \right]. \quad (1.54)$$

For the special case of Markovian telegraph noise, the waiting times are exponential $w_{\pm}(t) = \tau_{\pm}^{-1} \exp[-t/\tau_{\pm}]$ and their Fourier transforms read $\tilde{w}_{\pm} = 1/(1 - 2\pi i f \tau_{\pm})$ from which we obtain the Lorentzian spectrum (1.49).

More interestingly is a non-Markovian case that is more regular (more periodic) than random telegraph noise. Suppose, for instance, equal residence time statistics in both states with the single time being a sum of a fixed dead time τ_D in which no transition is possible and an exponentially distributed time τ . Clearly, this setup contains a symmetric random telegraph noise as the limit case $\tau_D = 0$. Dead times, also known as refractory periods, are quite common in neural systems, for instance, as the finite duration of the spike (~ 1 ms). The Fourier transform of the residence time is now $\tilde{w} = \exp(2\pi i f \tau_D)/[1 - 2\pi i f \tau]$ and the power spectrum according to Eqn (1.54) reads

$$S(f) = \frac{1}{2} \times \frac{(\sigma_+ - \sigma_-)^2 \tau^2 / (\tau + \tau_D)}{1 + \cos(2\pi f \tau_D) - 2\pi f \tau \sin(2\pi f \tau_D) + 2(\pi f \tau)^2}. \quad (1.55)$$

For $\tau_D \rightarrow 0$ this agrees with the Markovian case in Eqn (1.49). In the other limiting case of very small exponential waiting time τ , the process becomes very regular and consequently the spectrum approaches a series of δ peaks at $f = (2\tau_D)^{-1} + n/\tau_D$ ($n = 0, 1, \dots$). Sample trajectories, waiting time densities of the two states, and the power spectrum of the resulting two-state processes are illustrated in Fig. 1.4. As the refractory period increases we start seeing oscillatory features in the power spectrum (bottom panels).

We note that a trajectory with strong oscillatory component, as indicated by a pronounced spectral peak, will generally result in a correlation function with damped oscillations (not shown). Correlation time and noise intensity defined by integrals of the correlation function can no longer be used in such a case.

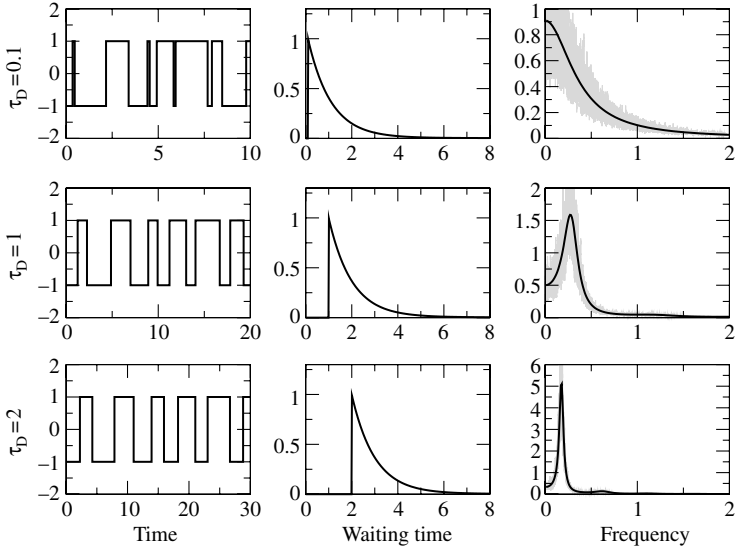


FIG. 1.4: Example of a two-state renewal process that is more regular than the Markovian telegraph process. The left column shows sample trajectories for the three different values of the refractory period τ_D (indicated at the left side): with increasing τ_D (top to bottom) the trajectory looks more regular. Middle column: probability densities which are exponential functions shifted to the right by the increasing values of the refractory period. Right column: power spectrum according to Eqn (1.55) which develops from an almost Lorentzian shape (top panel) to a pronounced peak roughly at the inverse of twice the refractory period (bottom panel). The peak in the power spectrum at a finite frequency indicates an almost regular, i.e. oscillatory, behaviour as also seen in the trajectory on the left. Parameters: $\sigma_{\pm} = \pm 1$, $\tau = 1$.

1.4 Point processes

Here we start with considerations that apply to general stationary point processes, continue with the simplest process, the Poisson process, and finally discuss renewal processes.

1.4.1 General spike train and interval statistics

Probability density as spike rate Consider the δ spike train

$$x(t) = \sum_{t_i} \delta(t - t_i) \quad (1.56)$$

associated with a point process $\{t_i\}$, e.g. as illustrated in Fig. 1.1. Does it make sense to study probability densities for this object? At first glance it does not,

since this pulse train attains only zero (with probability one) or infinity (with probability zero since the spike lasts only an infinitesimal period). However, this is not true in more than one sense. First of all, we can identify the probability of observing at least one spike in $[t - \Delta t/2, t + \Delta t/2]$ which gives us, after dividing by Δt , a probability density² – the well-known spike rate (of neural firing, for instance).

For a specific realization $x_i(t)$ we would get an indicator function over the interval by simply integrating $x_i(t)$ over the short interval Δt . In order to estimate the firing probability density we have to sum over an ensemble and divide by the number of realizations and by the interval, yielding

$$r(t) = \lim_{\Delta t \rightarrow 0} \frac{1}{N\Delta t} \sum_{i=1}^N \int_{t-\Delta t/2}^{t+\Delta t/2} dt' x_i(t') = \langle x(t) \rangle. \quad (1.57)$$

The spike rate is thus the mean value of the spike train.

Another interpretation of a probability density can be achieved by considering the number of spikes in an interval $(0, t)$ given by the *spike count*

$$N(t) = \int_0^t dt' x(t') \quad (1.58)$$

with respect to which we may ask for a probability density $P(N, t)$. The latter is defined on a discrete space as is the telegraph noise. However, in the case of the spike count there are infinitely many discrete states and there is apparently no steady state (for a stationary spike train, the spike count never stops growing in time).

The third aspect in which probability density may be important for spike train statistics is when the spike train is passed through a linear filter and instead of the δ peaks we have a series of exponentially decaying pulses also referred to as shot noise. Synaptic noise is very often modelled in this way; in this case the variable y is proportional to a conductance change and obeys the dynamics

$$\tau_F \dot{y} = -y + \varepsilon x \quad \Rightarrow \quad y(t) = \frac{\varepsilon}{\tau_F} \sum \Theta(t - t_i) \exp \left[-\frac{(t - t_i)}{\tau_F} \right]. \quad (1.59)$$

The probability density $P(y, t)$ for this continuous variable is an important characteristic of the shot noise. In the problem of synaptic conductance it is essential in order to understand the membrane fluctuations which are caused by synaptic input.

²We emphasize that this probability density is a density with respect to time which was only a parameter in the previous cases.

Correlation function Higher order probability densities (always with respect to time!) are obtained from averaged products of the spike train. These in turn are related to correlation functions of the spike train:

$$r_2(t_1, t_2) = \lim_{\Delta t \rightarrow 0} \frac{1}{N \Delta t} \sum_{i=1}^N \int_{t-\Delta t/2}^{t+\Delta t/2} dt'_1 \int_{t-\Delta t/2}^{t+\Delta t/2} dt'_2 x_i(t'_1) x_i(t'_2) = \langle x(t_1) x(t_2) \rangle. \quad (1.60)$$

Furthermore, $r_2(t_1|t_0) = r_2(t_0, t_1)/r(t_0)$ gives us the probability of observing a spike at t_1 if we know that we had a spike at $t = t_0$. The correlation function of a stationary spike train with constant rate r can be expressed as

$$C(\tau) = r[r_2(\tau|0) - r]. \quad (1.61)$$

Interval statistics and its general relation to the power spectrum We can also base our characterization of the point process on the intervals between events (spikes) see Fig. 1.5. The best known is the interspike interval (ISI), the interval between adjacent spikes. Intervals that consist of the sum of n adjacent ISIs are known as n th-order intervals T_n . If we know the probability densities $\rho_n(T_n)$ of all n th-order intervals, the statistics of the associated stationary spike train is completely determined. For instance, the conditional probability density can be expressed as follows (see, for instance, Holden, 1976)

$$r_2(\tau|0) = \delta(\tau) + \sum_{n=1}^{\infty} \rho_n(\tau). \quad (1.62)$$

The first term reflects the sure event that we have a spike at $\tau = 0$ (which is our condition); the other terms sum over the probabilities to have the n th spike at finite τ . Using Eqn (1.62) in Eqn (1.61) relates the correlation function to the n th-order interval density, i.e. relates spike train statistics to interval statistics.

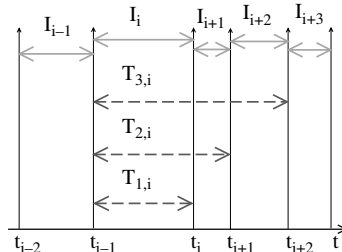


FIG. 1.5: Interval statistics. A spike train indicated by arrows (pointing up); the intervals between adjacent spikes, i.e. the interspike intervals ($\{I_i\}$) are shown with solid lines; the sum of n adjacent ISIs form the n th order intervals $T_{n,i}$ (dashed lines).

More useful is this relation in the Fourier domain relating the power spectrum to the Fourier transform of the n th-order interval density $\tilde{\rho}_n$ as follows (see Holden, 1976)

$$\begin{aligned} S(f) &= 2\text{Re} \int_0^\infty d\tau e^{2\pi i f \tau} r \left[\delta(\tau) + \sum_{n=1}^{\infty} \rho_n(\tau) - r \right] \\ \Rightarrow S(f) &= r \left[1 - r\delta(f) + \sum_{n=1}^{\infty} \tilde{\rho}_n(f) + \tilde{\rho}_n^*(f) \right]. \end{aligned} \quad (1.63)$$

A general remark on the characteristics of the shot noise in Eqn (1.56) is that since a δ spike train has infinite variance, the correlation time defined by Eqn (1.21) is always zero. This is so even if there is some memory in the spiking, i.e. for firing with a strong refractory period.

1.4.2 Poisson process

The simplest process is obtained if we say that the spiking depends only on the spike rate $r(t)$ and not on the past. Let us assume that this rate is a constant.

Three different simulation algorithms The Poisson statistics suggest three approaches. (i) In each time step we draw a random number $a_i \in [0, 1]$; if $a_i < r\Delta t$ a spike is assigned to this time step, i.e. $x_i(t_i) = 1/(\Delta t)$; (ii) starting at time t_0 , we draw exponentially distributed intervals I_i with mean $\langle I \rangle = 1/r$ and obtain the spike times recursively from $t_i = t_{i-1} + I_i$; (iii) we take a large interval $[0, T]$ and distribute $N \approx rT$ points randomly and uniformly on this interval; for a much shorter interval $T' \ll T$, the points form a Poisson process in $[0, T']$.

Probability density The probability density $P(N, t) = \sum p_n(t)\delta(N - n)$ of the spike count $N(t)$ obeys the master equation

$$\dot{p}_n = rp_{n-1} - rp_n, \quad p_0(0) = 1. \quad (1.64)$$

Again we deal with a gain term (from realizations with $n - 1$ spikes up to time t and one additional spike occurring with probability $r\Delta t$) and a loss term (having spiked n times, an additional spike will result in leaving the state $x = n$). We can determine the interspike interval density by asking what the fraction of probability is that leaves $n = 0$ at t by determining the probability current rp_0 (the efflux out of the state). With $p_{-1}(t) \equiv 0$ we obtain – not surprisingly – a simple exponential decay $\rho(I) = r \exp[-rI]$ as we did for the two-state residence time density of one single state. The mean is given by the inverse rate ($\langle I \rangle = 1/r$) and the coefficient of variation CV of the ISI (which is the relative standard deviation of the ISI and a measure for the randomness of the interval) is one, $\text{CV} = \sqrt{\langle \Delta I^2 \rangle / \langle I \rangle} = 1$.

We can also determine the general solution of the spike count's probability (using $p_n(0) = 0$ for $n \geq 1$):

$$p_n(t) = r \int_0^t dt' e^{-r(t-t')} p_{n-1}(t') + \delta_{n,0} e^{-rt} = \frac{(rt)^n}{n!} e^{-rt} \quad (1.65)$$

(the latter relation can be proven by induction). This is the famous Poisson distribution. We obtain from it the n th-order interval density by calculating the current from the $(n-1)$ th to the n th state:

$$\rho_n(T_n) = r p_{n-1}(T_n) = r \frac{(rT_n)^{(n-1)}}{(n-1)!} e^{-rT_n} \Rightarrow \tilde{\rho}_n(f) = \frac{1}{(1 - 2\pi i f / r)^n}. \quad (1.66)$$

Correlation function and power spectrum of the spike train From the independence of the spike generation on the past it follows that the conditional distribution is simply $p(\tau|0) = \delta(\tau) + r$ and thus we obtain (using Eqn (1.61)) for the Poisson process' correlation function and its Fourier transform, i.e. the power spectrum

$$C(\tau) = r\delta(\tau) \Rightarrow S(f) = r. \quad (1.67)$$

The spectrum is flat and does not depend on frequency at all. The same result is obtained when using the Fourier transform of the n th-order interval density (1.66) in Eqn (1.63).

1.4.3 More general renewal process

Non-Poissonian firing is observed for many neurons. One reason is the refractory period of neural firing which makes neural firing more regular than Poissonian and results in an unimodal ISI density with a peak at finite ISI. Some other neurons show bursting, which can lead to a bimodal ISI density (indicating the most probable interburst and intraburst intervals) and correlations among interspike intervals. Ignoring the latter, we can describe and model more experimental data by just assuming independent intervals given by a (generally non-exponential) density $\rho(I)$.

Simulation algorithm Such a renewal process can be simulated by drawing independent random numbers I_i according to the given ISI density $\rho(I)$. The spiking times are then $t_i = t_{i-1} + I_i$.

Formula for the power spectrum For a renewal spike train, the n th-order interval density is just the probability for a sum of identically distributed *independent* random numbers which is given by the n -fold convolution of the ISI density. Even more convenient, its Fourier transform turns into the n -fold product of the Fourier transform $\tilde{\rho}(f)$ of the ISI density $\rho(T)$. In Eqn (1.63) we then get a

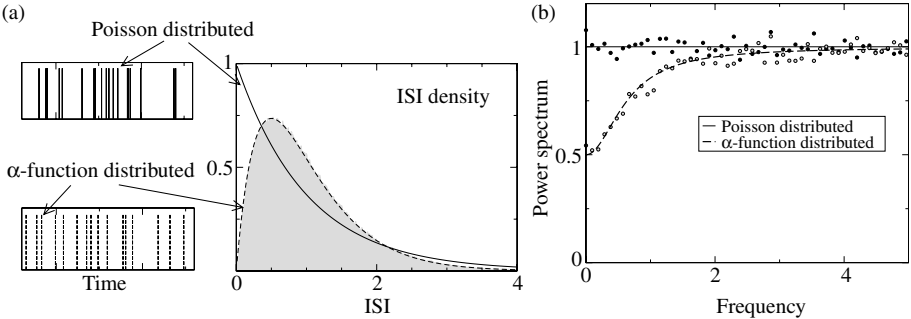


FIG. 1.6: Different renewal spike trains as indicated. ISI densities (a) and power spectra of spike trains (b). Symbols in (b) indicate results of numerical simulations. Both spike trains have a rate of $r = 1$.

simple geometric series that can be summed and yields

$$S(f) = r \frac{1 - |\tilde{\rho}(f)|^2}{|1 - \tilde{\rho}(f)|^2}. \quad (1.68)$$

A simple example As the ISI density we choose a so-called alpha function

$$\rho(I) = 4r^2 I \exp(-2rI) \quad (1.69)$$

which has the realistic feature of having a relative refractory period, as also observed in the firing of many neurons: very short intervals are unlikely. The ISI density starts at zero and attains its maximum at a finite ISI, unlike the exponential ISI density in the Poissonian case. We can generate intervals by adding up two exponentially distributed numbers³ with mean $(2r)^{-1}$. Samples of a Poissonian and an α -function spike train together with the ISI probability densities of these two processes are shown in Fig. 1.6(a); the respective power spectra are displayed in Fig. 1.6(b). An increased regularity in the spiking is already visible in the α -function spike train. This increased regularity leads to a drop of power at low frequencies in the power spectrum. The power spectrum can be calculated from the Fourier transform of the ISI density via Eqn (1.68) and reads

$$S(f) = r \left[1 - \frac{2r^2}{4r^2 + (\pi f)^2} \right]. \quad (1.70)$$

³The density (1.69) is the convolution of two exponential densities each with a rate $2r$; it agrees with the n th-order interval density of the Poisson process (1.66) for $n = 2$ and r replaced by $2r$.

Choosing an even more peaked ISI density, the spectrum will show even more reduced power at low frequencies and, additionally, a finite width peak around the inverse mean ISI and possibly smaller peaks at multiples of this frequency. Clustering of spikes, at the other extreme, will result in increased power at low frequency.

1.5 Relating the three processes

It is instructive to see formal mathematical relations between the three processes we have studied in this chapter. This also gives good intuition about many approximation schemes for stochastic systems.

Two-state process → spike train Consider an asymmetric two-state process with $\sigma_- = 0$, $\sigma_+ = \tau_+^{-1}$, and fixed pulse width, i.e. $w_+(\tau) = \delta(\tau - \tau_+)$ ($\tilde{w}_+ = \exp(i\omega\tau_+)$); let the pulse width τ_+ go to zero. Then we obtain a spike train that clearly has an associated point process. If we neglect one of the time-scales in the two-state problem, we obtain the simpler point process. In this limit the formula for the power spectrum of the two-state process (Eqn (1.55)) turns into that for the spectrum of a renewal spike train (Eqn (1.68)).

Two-state process → Ornstein–Uhlenbeck process It is also possible to obtain the Ornstein–Uhlenbeck process by means of the telegraph noise. If we add up many independent symmetric processes ($\langle \sigma_i(t) \rangle = 0$)

$$y_N = \frac{1}{N} \sum_{i=1}^N \sigma_i(t) \quad (1.71)$$

then for large N (as a consequence of the central limit theorem) the resulting sum will have approximately Gaussian (normal) statistics. A little more surprising perhaps is that the temporal structure of the correlations is maintained as the following simple calculation shows

$$\begin{aligned} C_Y(\tau) &= \langle y_N(t + \tau) y_N(t) \rangle = \frac{1}{N^2} \sum_{i,j=1}^N \langle \sigma_i(t) \sigma_j(t + \tau) \rangle \\ &= \frac{1}{N^2} \sum_{i=1}^N \langle \sigma_i(t) \sigma_i(t + \tau) \rangle = \frac{1}{N} C(\tau) \end{aligned} \quad (1.72)$$

where we have used the fact that $\sigma_i(t)$ and $\sigma_j(t)$ are independent and thus uncorrelated ($\langle \sigma_i(t) \sigma_j(t + \tau) \rangle = 0$ if $i \neq j$). Thus, the correlation function of the sum is just $1/N$ times the single process' correlation function. The resulting process has Gaussian statistics and has exponential correlation – it also approximates more and more accurately a continuous process since a single step changes the sum by only $1/N$. The only continuous process with Gaussian density and exponential correlation function is the Ornstein–Uhlenbeck process according to Doob's theorem. Numerical studies show that for many purposes $N \sim 12$ already yields statistics quite close to normal.

Poisson spike train → white Gaussian noise Increasing the number of spikes and subtracting the mean of the spike train, we obtain a rapidly oscillating ‘spiky’ function, which is largely similar to that of Gaussian white noise. So if we take the original Ornstein–Uhlenbeck process and drive it with white Poissonian noise instead of white Gaussian noise we find

$$\dot{v} = -\gamma v + \varepsilon \left(\sum \delta(t - t_i) - r \right) \quad (1.73)$$

where we have subtracted the mean of the spike train, which is the steady-state spike rate ($\langle \sum \delta(t - t_i) \rangle = r$), and ε is an amplitude. We may interpret the equation by imagining that the particle is kicked around at random times t_i with each kick having the same impact ε . The density equation for this problem approaches the Fokker–Planck equation of an Ornstein–Uhlenbeck process if we set $\varepsilon = \sqrt{2D/r}$ and let r go to infinity. In this sense, the Poissonian shot noise with high rate and white Gaussian noise are very similar. Since the Fokker–Planck equation is a generalized diffusion equation, replacing the shot noise at a finite rate by Gaussian white noise is called the diffusion approximation. This is employed in neuroscience when dealing with subthreshold membrane fluctuations that are caused by synaptic shot noise. The latter can be, to a certain extent, approximated by white Gaussian noise.

1.6 Generation of random numbers

General idea Suppose we have a simple random number generator that provides uniformly distributed numbers x_i between 0 and 1 with $p_{\text{uni}}(x) = 1$ and we want to generate numbers y_i according to a distribution $p(y)$ (in general on $(-\infty, \infty)$). It should be possible to substitute the x_i into a nonlinear function, the corresponding values of which are then distributed with density $p(y)$. To get this function we first find a relationship between the two densities p_{uni} and $p(y)$ via the normalization integral

$$1 = \int_0^1 dx p_{\text{uni}} = \int_{-\infty}^{\infty} dy \left| \frac{dx}{dy} \right| p_{\text{uni}}(x(y)) = \int_{-\infty}^{\infty} dy p(y) \quad (1.74)$$

from which we get

$$\frac{dx}{dy} = p(y) \quad \Rightarrow \quad x(y) = F(y) = \int_{-\infty}^y dz p(z) \quad (1.75)$$

where $F(y)$ is the cumulative distribution telling us how probable a value *below* y is. By inverting (either numerically or analytically) the latter relation we obtain a way to generate the random numbers y_i from the uniformly distributed numbers x_i

$$y(x) = F^{-1}(x). \quad (1.76)$$

Exponentially distributed numbers Suppose we want to generate numbers according to $p(y) = r \exp(-ry)$. In this case it is easy to obtain $F(y) = 1 - \exp(-ry)$ and furthermore to invert this relation to obtain

$$y = -r^{-1} \ln(1 - x). \quad (1.77)$$

Equivalently, we could use $y = -r^{-1} \ln(x)$ because of the symmetry of x .

Gaussian numbers The formulas above can be generalized to multidimensional densities, which is particularly useful for generating Gaussian numbers. In this case we need *two* independent uniformly distributed random numbers x_1 and x_2 in order to obtain *two* independent Gaussian numbers y_1 and y_2 . The transformation is called the Box–Müller formula and reads

$$y_1 = \sqrt{2 \ln(x_1)} \cos(2\pi x_2) \quad (1.78)$$

$$y_2 = \sqrt{2 \ln(x_1)} \sin(2\pi x_2). \quad (1.79)$$

If these variables are normally distributed, the Jacobian (which replaces the simple derivative in the normalization integral) should yield a two-dimensional Gaussian, as can be checked by inserting

$$\left| \frac{\partial(x_1, x_2)}{\partial(y_1, y_2)} \right| = \frac{1}{\sqrt{2\pi}} e^{-y_1^2/2} \frac{1}{\sqrt{2\pi}} e^{-y_2^2/2} = p(y_1, y_2). \quad (1.80)$$

References

- Cox, D.R. (1962). *Renewal Theory*. Methuen, London.
- Cox, D. R. and Lewis, P. A. W. (1966). *The Statistical Analysis of Series of Events*. Methuen, London.
- Gardiner, C. W. (1985). *Handbook of Stochastic Methods*. Springer-Verlag, Berlin.
- Gerstner, W. and Kistler, W. (2002). *Spiking Neuron Models: Single Neurons, Populations, Plasticity*. Cambridge University Press.
- Hänggi, P. and Jung, P. (1995). Colored noise in dynamical systems. *Adv. Chem. Phys.*, **89**, 239.
- Holden, A. V. (1976). *Models of the Stochastic Activity of Neurones*. Springer-Verlag, Berlin.
- Langevin, P. (1908). Sur la theorie du mouvement brownien. *Comptes Rendus Acad Sci. (Paris)*, **146**, 530–533.
- Papoulis, A. (1965). *Probability, Random Variables, and Stochastic Processes*. McGraw-Hill, New York.
- Ricciardi, L. (1977). *Diffusion Processes and Related Topics in Biology*. Springer.
- Risken, H. (1984). *The Fokker–Planck Equation*. Springer, Berlin.
- Risken, H. (1996). *The Fokker–Planck Equation: Methods of Solutions and Applications*. Springer-Verlag, New York.

- Stratonovich, R. L. (1967). *Topics in the Theory of Random Noise*. Routledge, New York.
- Tuckwell, H. (1989). *Stochastic Processes in the Neurosciences*. SIAM, Philadelphia.
- Tuckwell, H. C. (1988). *Introduction to Theoretical Neurobiology*. Cambridge University Press, Cambridge.
- Uhlenbeck, G. E. and Ornstein, L. S. (1930). On the theory of the Brownian motion. *Phys. Rev.*, **36**, 823.
- van Kampen, N. G. (1992). *Stochastic Processes in Physics and Chemistry*. North-Holland, Amsterdam.

MARKOV CHAIN MODELS OF ION CHANNELS AND CALCIUM RELEASE SITES

Jeffrey R. Groff, Hilary DeRemigio, and Gregory D. Smith

2.1 Introduction

The time course of membrane voltage in neurons and other cell types reflects the average behaviour of a large number of ion channels. Such changes are conventionally modelled using deterministic ordinary differential equations (ODEs). For example, both the Hodgkin–Huxley model (Hodgkin and Huxley, 1952) of action potentials in the squid giant axon and the Morris–Lecar model (Morris and Lecar, 1981) of voltage oscillations in the barnacle giant muscle fibre are sets of nonlinear ODEs that include a current balance equation and several ‘gating variables’ representing the state of ion channels (closed, open, inactivated, etc.). In an electrotonically compact neuron, a large number of plasma membrane ion channels experience essentially the same time-course of membrane voltage. This creates the intellectually satisfying situation where Hodgkin–Huxley-like gating variable equations can be derived from Markov chain models of single channel gating, a process that begins by writing a master equation for a collection of N channels that are globally coupled to the same membrane voltage (Fox and Lu, 1994, Smith, 2002b, Gardiner, 2004).

In most cell types, the endoplasmic/sarcoplasmic reticulum (ER/SR) has integrative and regenerative properties analogous to the excitable membranes of neurons (Berridge 1993, 1997, 1998). Considerable insight has been obtained through the analogy of plasma membrane electrical excitability and ER Ca^{2+} excitability using whole cell models of Ca^{2+} signalling that include Hodgkin–Huxley-like gating variables for the dynamics of intracellular Ca^{2+} release channels such as the inositol 1,4,5-trisphosphate receptor (IP_3R) and ryanodine receptor (RyR) (Keizer *et al.*, 1995, Jafri *et al.*, 1998). However, the disparity between electrical length-scales (100–200 μm) and the range of action of intracellular Ca^{2+} (i.e. a *chemical* length-scale of 1–2 μm) (Allbritton *et al.*, 1992, Zador and Koch, 1994, Neher, 1998, Smith *et al.*, 2001) means that intracellular Ca^{2+} channels experience radically different local Ca^{2+} concentrations, even during global Ca^{2+} responses, and clusters of IP_3Rs and RyRs are in fact only *locally* coupled via the buffered diffusion of intracellular Ca^{2+} . For this reason, investigators interested in localized Ca^{2+} elevations such as Ca^{2+} puffs and sparks (Cheng *et al.*, 1993, Yao *et al.*, 1995, Niggli and Shirokova, 2007) and whole-cell phenomena influenced by microdomain Ca^{2+} (Sobie *et al.*, 2002, Greenstein and Winslow, 2002, Hinch *et al.*, 2006, Williams *et al.*, 2007)

often supplement deterministic ODE models of intracellular Ca^{2+} responses with stochastic modelling approaches.

2.2 Markov chain models of single channel gating

Most of our understanding of the stochastic dynamics of ion channel gating is derived from experiments using the patch clamp technique and single channel recordings from channels reconstituted into planar lipid bilayers (Sakmann and Neher, 1995, Hille, 2001). For example, Fig. 2.1 shows patch clamp recordings of currents through single Na^+ channels in the giant axon of squid (Vandenberg and Bezanilla, 1991). Small current deviations in the negative direction indicate the opening of individual voltage-gated Na^+ channels in response to steps in membrane voltage from a holding potential of -108 mV to test potentials of -48 (left) or 28 mV (right). Notice that two conductance levels of the channel are visible: a closed state with no current flowing and an open state with a unitary current of approximately 2 pA .

Historically, the stochastic dynamics of single channel gating have been successfully modelled using continuous-time discrete-state Markov chains (Colquhoun and Hawkes, 1995); for a review of Markov chains from a mathematical perspective see the monographs by Stewart (1994) and Norris (1997). Markov chain models of single channel gating are most intuitively introduced as state-transition diagrams that enumerate the possible states a channel may occupy, and also indicate the allowed transitions between these states. For example, a state-transition diagram corresponding to a channel with two states and

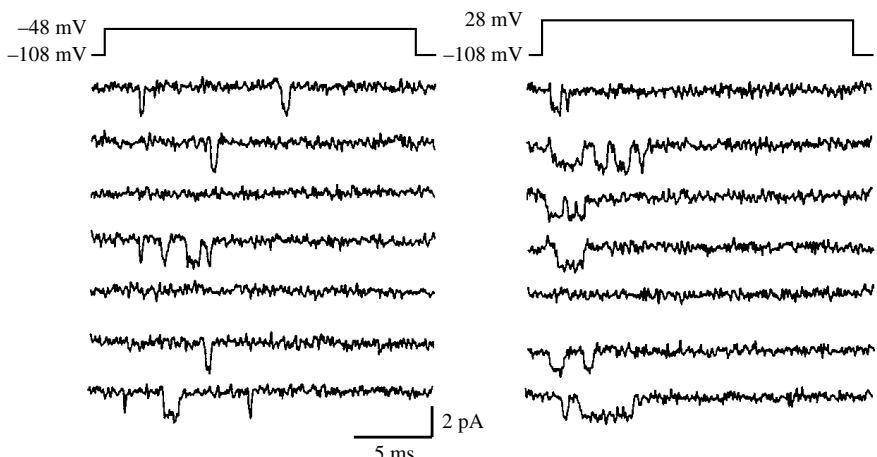


FIG. 2.1: Patch clamp recordings of currents through single Na^+ channels in the giant axon of squid. Adapted with permission from Vandenberg and Bezanilla (1991).

two conductance levels (closed and open) is given by

$$\text{(closed)} \quad \mathcal{C}_1 \xrightleftharpoons[q_{21}]{q_{12}} \mathcal{O}_2 \quad \text{(open)} \quad (2.1)$$

where q_{12} and q_{21} are the rates of the $\mathcal{C}_1 \rightarrow \mathcal{O}_2$ and $\mathcal{O}_2 \rightarrow \mathcal{C}_1$ transitions and have units of time $^{-1}$. When these rates are specified, Eqn (2.1) defines a continuous-time discrete-state stochastic process, $S(t)$, with state space $S \in \{\mathcal{C}_1, \mathcal{O}_2\}$. When the transition rates do not vary with time, Eqn (2.1) corresponds to the well-known telegraph process with infinitesimal generator or Q -matrix given by

$$Q = (q_{ij}) = \begin{pmatrix} -q_{12} & q_{12} \\ q_{21} & -q_{21} \end{pmatrix}. \quad (2.2)$$

Note that rates in the state-transition diagram (Eqn (2.1)) and the off-diagonal elements of the infinitesimal generator matrix (Eqn (2.2)) give the probability per unit time of a transition from state i to state j :

$$q_{ij} = \lim_{\Delta t \rightarrow 0} \frac{P\{S(t + \Delta t) = S_j | S(t) = S_i\}}{\Delta t} \quad (i \neq j).$$

Similarly, the absolute value of the diagonal elements of Eqn (2.2) correspond to the probability per unit time of a transition out of each state:

$$|q_{ii}| = \lim_{\Delta t \rightarrow 0} \frac{P\{S(t + \Delta t) \neq S_i | S(t) = S_i\}}{\Delta t}.$$

If we write the probability of the channel being in each state as a row vector, $\boldsymbol{\pi}(t) = (\pi_{\mathcal{C}_1}, \pi_{\mathcal{O}_2})$, then the time-evolution of this distribution can be found by solving the ODE initial value problem

$$\frac{d\boldsymbol{\pi}}{dt} = \boldsymbol{\pi}Q \quad (2.3)$$

where $\boldsymbol{\pi}(0)$ is an initial probability distribution satisfying conservation of probability, $\pi_{\mathcal{C}_1}(0) + \pi_{\mathcal{O}_2}(0) = 1$, a condition written in general as the inner product $\boldsymbol{\pi}(0)\mathbf{e} = 1$ where \mathbf{e} is a column vector of ones. Note that the diagonal entries of a Q -matrix are given by the negative of the sum of the off-diagonal entries in the same row, that is, $q_{ii} = -\sum_{j \neq i} q_{ij}$ (cf. Eqn (2.2)). This condition ensures conservation of probability for all time, as can be seen by multiplying Eqn (2.3) on the right by \mathbf{e} to give $d(\boldsymbol{\pi}\mathbf{e})/dt = Q\mathbf{e} = \mathbf{0}$.

Markov chain models of ion channel gating found in the literature are often more complex than Eqn (2.1) and include multiple closed and/or open states, as well as transitions that reflect experimentally observed phenomena such as voltage- and ligand-dependent gating. For example, the state-transition diagram for a voltage-gated Na^+ channel shown in Fig. 2.2(a) has four closed states

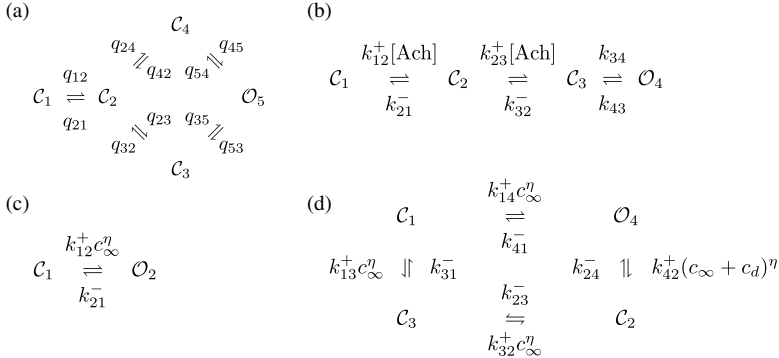


FIG. 2.2: Example single channel models. (a) A five-state model of a voltage-gated Na^+ channel presented by Vandenberg and Bezanilla (1991). (b) A four-state model of the ligand-gated acetylcholine receptor presented by Ogden *et al.* (1997) and Hille (2001). (c) A two-state model of a Ca^{2+} -activated Ca^{2+} channel. (d) A four-state model of a Ca^{2+} -regulated Ca^{2+} channel that includes both Ca^{2+} activation and Ca^{2+} inactivation.

$(\mathcal{C}_1, \mathcal{C}_2, \mathcal{C}_3,$ and $\mathcal{C}_4)$ and one open state (\mathcal{O}_5) . The transition rates $q_{12}, q_{21}, \dots, q_{54}$ are functions of membrane voltage designed to reproduce experimental data such as Fig. 2.1 (Vandenberg and Bezanilla, 1991). Figure 2.2(b) is a state-transition diagram for nicotinic acetylcholine receptor (AChR) gating with three closed states ($\mathcal{C}_1, \mathcal{C}_2$, and \mathcal{C}_3) and one open state (\mathcal{O}_4) (Ogden *et al.*, 1987, Hille, 2001, pp. 183–185). In this single channel model, the $\mathcal{C}_1 \rightarrow \mathcal{C}_2$ and $\mathcal{C}_2 \rightarrow \mathcal{C}_3$ transition rates are functions of the acetylcholine concentration $([\text{Ach}])$ experienced by the channel. For example, $q_{12} = k_{12}^+[\text{Ach}]$ where k_{12}^+ is a bimolecular association rate constant with units of $\text{conc}^{-1}\text{time}^{-1}$, while $q_{21} = k_{21}^-$ is a dissociation rate constant with units of time^{-1} .

2.2.1 Stationary distributions and global balance

Markov chain models of single channel gating have a finite number of states and are *irreducible*, that is, it is possible to move from any state to any other state via one or more transitions. Such Markov chain models have a limiting probability distribution (as can be observed by integrating Eqn (2.3) for a long time) that does not depend on the initial condition $\boldsymbol{\pi}(0)$. This limiting probability distribution is equal to the unique stationary distribution $\bar{\boldsymbol{\pi}}$ satisfying global balance and conservation of probability, that is,

$$\bar{\boldsymbol{\pi}}Q = 0 \text{ subject to } \bar{\boldsymbol{\pi}}\mathbf{e} = 1 \quad (2.4)$$

where Q is the infinitesimal generator matrix, $\bar{\boldsymbol{\pi}}$ is a row vector, and \mathbf{e} is a commensurate column vector of ones (Stewart, 1994). Expanding the first equation

in Eqn (2.4) and rearranging, we see that the condition of global balance can be written as

$$\pi_i \sum_{j \neq i} q_{ij} = \sum_{j \neq i} \pi_j q_{ji} \quad (2.5)$$

for all i , that is, the probability flux into and out of each state is equal.

2.2.2 Analytical solution of stationary distributions

For problems of moderate complexity, analytical solutions of Eqn (2.4) can be most easily obtained using a diagrammatic method introduced by Hill (1989). To illustrate how the method is applied to single channel models without cycles, consider the AchR model of Fig. 2.2(b). Suppressing the rate constants, the topology of this model can be succinctly written as

$$\mathcal{C}_1 \leftrightarrow \mathcal{C}_2 \leftrightarrow \mathcal{C}_3 \leftrightarrow \mathcal{O}_4. \quad (2.6)$$

In Hill's method, a *directional diagram* for state i is a directed graph that spans all of the states of the single channel model and is composed of unidirectional transitions oriented toward state i (i.e. a tree rooted in state i). For example, the directional diagram for state \mathcal{C}_2 is

$$\mathcal{C}_1 \rightarrow \mathcal{C}_2 \leftarrow \mathcal{C}_3 \leftarrow \mathcal{O}_4, \quad (2.7)$$

and with this diagram we can associate the quantity

$$q_{12}q_{32}q_{43} = k_{12}^+ [\text{Ach}] k_{32}^- k_{43}, \quad (2.8)$$

that is, the product of the rate constants corresponding to each arrow. Similar directional diagrams can be computed for closed states \mathcal{C}_1 , \mathcal{C}_3 , and \mathcal{O}_4 . With these definitions, it can be shown (Hill, 1989) that the steady-state probability of being in state i is given by

$$\bar{\pi}_i = \frac{\text{state } i \text{ directional diagram}}{\text{sum of all directional diagrams}}. \quad (2.9)$$

For example, the steady-state probability that the AchR will be in state \mathcal{O}_4 is given by

$$\bar{\pi}_{\mathcal{O}_4} = \frac{\overbrace{\hspace{10em}}^{\rightarrow \rightarrow \rightarrow}}{\underbrace{\hspace{10em}}_{\leftarrow \leftarrow \leftarrow} + \overbrace{\hspace{10em}}^{\rightarrow \leftarrow \leftarrow} + \overbrace{\hspace{10em}}^{\rightarrow \rightarrow \leftarrow} + \overbrace{\hspace{10em}}^{\rightarrow \rightarrow \rightarrow}} \quad (2.10)$$

where for clarity we have dropped the state symbols. If we express Eqn (2.10) in terms of the model parameters and divide the numerator and denominator by $k_{12}^+ k_{23}^+ k_{34}$ we find

$$\bar{\pi}_{\mathcal{O}_4} = \frac{[\text{Ach}]^2}{K_{21}K_{32}K_{43} + [\text{Ach}]K_{32}K_{43} + [\text{Ach}]^2K_{43} + [\text{Ach}]^2} \quad (2.11)$$

where $K_{21} = k_{21}^-/k_{12}^+$ and $K_{32} = k_{32}^-/k_{23}^+$ are dissociation constants (units of concentration) and $K_{43} = k_{43}/k_{34}$ is an equilibrium constant (dimensionless).

Note that for single channel models that contain one or more cycles, a set of direction diagrams for state i are produced that includes every possible ‘spanning tree’ of the state-transition diagram rooted at state i . The steady-state probability of being in state i is in this case given by Eqn (2.9) with the replacement of ‘sum of all state i directional diagrams’ for the numerator. For details see Hill’s monograph (Hill, 1989).

2.2.3 Numerical solution of stationary distributions

In situations where the complexity of the single channel model makes the diagrammatic method intractable, the stationary distribution $\bar{\pi}$ solving Eqn (2.4) can be numerically calculated. One approach is to define the stochastic matrix

$$W = (w_{ij}) = I + Q/\lambda \quad (2.12)$$

where I is an identity matrix and $\lambda > \max_i |q_{ii}|$ so that $w_{ij} \geq 0$, $We = e$, and $\bar{\pi}W = \bar{\pi}$. The stationary distribution $\bar{\pi}$ is then found by numerically calculating the unique eigenvector of W having eigenvalue 1, e.g. using MATLAB’s `eigs` command. Because W is a stochastic matrix with spectral radius 1, $\bar{\pi}$ is the unique Perron vector of W .

An alternate approach is to define an M -by- $(M+1)$ matrix Z and an $(M+1)$ -by-1 column vector b where M is the number of states in the single channel model such that

$$Z = (Q \ e) \quad \text{and} \quad b = \begin{pmatrix} \mathbf{0} \\ 1 \end{pmatrix} \quad (2.13)$$

and solve the overdetermined linear system $\bar{\pi}Z = b$ for $\bar{\pi}$, that is,

$$\bar{\pi} = bZ^T (ZZ^T)^{-1}. \quad (2.14)$$

Note that in some situations, ZZ^T may be ill-conditioned and the pseudo-inverse of Z given by $(ZZ^T)^{-1}$ is difficult to calculate. See Stewart’s monograph (Stewart, 1994) for further discussion.

2.2.4 Dwell times

Markov chain models of single channel gating have the property that the ‘dwell time’ in state i , denoted T_i , is exponentially distributed with expectation

$$\mathbb{E}[T_i] = \frac{1}{\sum_{j \neq i} q_{ij}} \quad (2.15)$$

where the denominator is the total transition rate out of state i . For example, the expected open and closed dwell times for the two-state channel described

by Eqn (2.1) are $E[T_{O_2}] = 1/q_{21}$ and $E[T_{C_1}] = 1/q_{12}$, while the expected open dwell time for the voltage-gated Na^+ channel shown in Fig. 2.2(a) is $E[T_{O_5}] = 1/(q_{53} + q_{54})$.

For single channel models that include multiple states with the same conductance level (e.g. two closed states), the experimentally observable transitions are those between states with different conductance levels, and dwell times at one level are sums of exponential distributions. To see this, consider a single channel model with states partitioned into two aggregate classes $\hat{\mathcal{C}}$ and $\hat{\mathcal{O}}$ (closed and open). Without loss of generality, we will assume that the $M_{\hat{\mathcal{C}}}$ closed states are labelled 1 to $M_{\hat{\mathcal{C}}}$ and the $M_{\hat{\mathcal{O}}}$ open states are labelled $M_{\hat{\mathcal{C}}} + 1$ to $M_{\hat{\mathcal{C}}} + M_{\hat{\mathcal{O}}} = M$ where M is the total number of states. Thus, the M -by- M Q -matrix can be written as

$$Q = \begin{pmatrix} Q_{\hat{\mathcal{C}}\hat{\mathcal{C}}} & Q_{\hat{\mathcal{C}}\hat{\mathcal{O}}} \\ Q_{\hat{\mathcal{O}}\hat{\mathcal{C}}} & Q_{\hat{\mathcal{O}}\hat{\mathcal{O}}} \end{pmatrix} \quad (2.16)$$

where, for example, $Q_{\hat{\mathcal{C}}\hat{\mathcal{O}}}$ is an $M_{\hat{\mathcal{C}}}$ -by- $M_{\hat{\mathcal{O}}}$ matrix that collects rates for transitions from aggregated state $\hat{\mathcal{C}}$ to aggregated state $\hat{\mathcal{O}}$.

Following Ball and Sansom (1989), the probability distribution of dwell times (i.e. sojourn times) in aggregate class $\hat{\mathcal{O}}$ is given by

$$f_{T_{\hat{\mathcal{O}}}}(t) = -\phi_{\hat{\mathcal{O}}} \exp(tQ_{\hat{\mathcal{O}}\hat{\mathcal{O}}})Q_{\hat{\mathcal{O}}\hat{\mathcal{O}}}e_{\hat{\mathcal{O}}} \quad (2.17)$$

where $\exp(tQ_{\hat{\mathcal{O}}\hat{\mathcal{O}}})$ is a matrix exponential and e is a commensurate column vector of ones. The row vector $\phi_{\hat{\mathcal{O}}}$ gives the probabilities that a sojourn in $\hat{\mathcal{O}}$ begins in the various open states and is determined by normalizing the probability flux into each open state from closed states,

$$\phi_{\hat{\mathcal{O}}} = \bar{\pi}_{\hat{\mathcal{C}}} Q_{\hat{\mathcal{C}}\hat{\mathcal{O}}} / \bar{\pi}_{\hat{\mathcal{C}}} Q_{\hat{\mathcal{C}}\hat{\mathcal{O}}} e_{\hat{\mathcal{O}}}, \quad (2.18)$$

where the denominator is a scalar and $\bar{\pi}_{\hat{\mathcal{C}}}$ is the portion of the stationary distribution $\bar{\pi} = (\bar{\pi}_{\hat{\mathcal{C}}} \bar{\pi}_{\hat{\mathcal{O}}})$ corresponding to $\hat{\mathcal{C}}$. The expectation of $T_{\hat{\mathcal{O}}}$ can be found by integrating Eqn (2.17),

$$E[T_{\hat{\mathcal{O}}}] = - \int_0^\infty t \phi_{\hat{\mathcal{O}}} \exp(tQ_{\hat{\mathcal{O}}\hat{\mathcal{O}}})Q_{\hat{\mathcal{O}}\hat{\mathcal{O}}}e_{\hat{\mathcal{O}}} dt = -\phi_{\hat{\mathcal{O}}} Q_{\hat{\mathcal{O}}\hat{\mathcal{O}}}^{-1} e_{\hat{\mathcal{O}}} \quad (2.19)$$

where $E[T_{\hat{\mathcal{O}}}] > 0$. Similar expressions can be written for the dwell time distribution and expected dwell time for aggregate class $\hat{\mathcal{C}}$.

2.2.5 Lumping as a model reduction technique

It is often desirable to reduce the complexity of Markov chain models of ion channel gating by combining or ‘lumping’ states. To combine the M states of a full (unreduced) single channel model and produce a reduced model with \hat{M}

aggregate states, partition the M -by- M generator matrix Q of the full model into \hat{M}^2 blocks,

$$Q = \begin{pmatrix} Q_{11} & Q_{12} & \cdots & Q_{1\hat{M}} \\ Q_{21} & Q_{22} & \cdots & Q_{2\hat{M}} \\ \vdots & \vdots & \ddots & \vdots \\ Q_{\hat{M}1} & Q_{\hat{M}2} & \cdots & Q_{\hat{M}\hat{M}} \end{pmatrix}, \quad (2.20)$$

where Q_{ij} contains the transition rates from lumped state i to lumped state j (Meyer, 1989). Next, partition the stationary distribution of Q in a conformable manner,

$$\bar{\pi} = (\bar{\pi}_1 \bar{\pi}_2 \cdots \bar{\pi}_{\hat{M}}).$$

If each $\bar{\pi}_i$ is normalized to produce a row vector of conditional probabilities,

$$\mathbf{s}_i = \frac{\bar{\pi}_i}{\bar{\pi}_i \mathbf{e}_i}, \quad (2.21)$$

where \mathbf{e}_i is a commensurate column vector of ones, then the elements of the reduced generator matrix, $\hat{Q} = (\hat{q}_{ij})$ are given by $\hat{q}_{ij} = \mathbf{s}_i Q_{ij} \mathbf{e}_j$. When written in matrix form the relationship between the reduced and full models is given by

$$\hat{Q} = S Q V \quad (2.22)$$

where V is an M -by- \hat{M} collector matrix,

$$V = \begin{pmatrix} \mathbf{e}_1 & 0 & \cdots & 0 \\ 0 & \mathbf{e}_2 & \cdots & 0 \\ \vdots & \vdots & \ddots & \vdots \\ 0 & 0 & \cdots & \mathbf{e}_{\hat{M}} \end{pmatrix}, \quad (2.23)$$

the \mathbf{e}_i are column vectors, S is an \hat{M} -by- M distributor matrix given by

$$S = \begin{pmatrix} \mathbf{s}_1 & 0 & \cdots & 0 \\ 0 & \mathbf{s}_2 & \cdots & 0 \\ \vdots & \vdots & \ddots & \vdots \\ 0 & 0 & \cdots & \mathbf{s}_{\hat{M}} \end{pmatrix}, \quad (2.24)$$

and $SV = \hat{I}$, an identity matrix of size \hat{M} (Nicola, 1998).

Note that for this reduction to be performed without approximation, the time-dependent probability distribution of the reduced model that solves $d\hat{\pi}/dt = \hat{\pi}\hat{Q}$ must be related to the time-dependent solution of the full model (Eqn (2.3)) through

$$\hat{\pi}(t) = \pi(t)V.$$

Beginning with the full model solution, $\pi(t) = \pi(0)e^{tQ}$, multiplying on the right by V , and performing multiple substitutions we have

$$\pi(0)e^{tQ}V = \pi(t)V = \hat{\pi}(t) = \hat{\pi}(0)e^{t\hat{Q}} = \pi(0)V e^{t\hat{Q}}.$$

Thus, we require $e^{tQ}V = V e^{t\hat{Q}}$ for the above expression to be valid regardless of initial condition, and using $e^A = \sum_{k=0}^{\infty} A^k/k!$ to expand the matrix exponential, this implies $V\hat{Q} = QV$. Multiplying this expression on the left by S gives $\hat{Q} = SQV$, so that the condition for aggregating states without approximation can be written as

$$VSQV = QV. \quad (2.25)$$

For example, if parameters are chosen for the single channel model shown in Fig. 2.2(a) so that $q_{24} = q_{23}$, $q_{42} = q_{32}$, $q_{45} = q_{35}$, and $q_{54} = q_{53}$, then Eqn (2.25) shows that this five-state model can be reduced without approximation to the four-state model, $\mathcal{C}_1 \leftrightarrow \mathcal{C}_2 \leftrightarrow (\mathcal{C}_4/\mathcal{C}_3) \leftrightarrow \mathcal{O}_5$, where \mathcal{C}_3 and \mathcal{C}_4 are combined.

2.2.6 Fast/slow analysis and model reduction

Another model reduction technique that can often be used when there is a separation of time-scales in a single channel model is quasi-static approximation. Consider the four-state AchR model given in Fig. 2.2(b) and expand Eqn (2.3) to write

$$d\pi_{\mathcal{C}_1}/dt = -k_{12}^+[\text{Ach}]\pi_{\mathcal{C}_1} + k_{21}^-\pi_{\mathcal{C}_2}, \quad (2.26)$$

$$d\pi_{\mathcal{C}_2}/dt = k_{12}^+[\text{Ach}]\pi_{\mathcal{C}_1} + k_{32}^-\pi_{\mathcal{C}_3} - (k_{21}^- + k_{23}^+[\text{Ach}])\pi_{\mathcal{C}_2}, \quad (2.27)$$

$$d\pi_{\mathcal{C}_3}/dt = k_{23}^+[\text{Ach}]\pi_{\mathcal{C}_2} + k_{43}\pi_{\mathcal{O}_4} - (k_{32}^- + k_{34})\pi_{\mathcal{C}_3}, \quad (2.28)$$

and

$$d\pi_{\mathcal{O}_4}/dt = k_{34}\pi_{\mathcal{C}_3} - k_{43}\pi_{\mathcal{O}_4}. \quad (2.29)$$

Under the assumption that the binding and unbinding of Ach to the receptor is a fast process compared to slower transitions between states \mathcal{C}_3 and \mathcal{O}_4 , we may assume states \mathcal{C}_1 , \mathcal{C}_2 , and \mathcal{C}_3 are in rapid equilibrium, that is, $k_{12}^+[\text{Ach}]\pi_{\mathcal{C}_1} \approx k_{21}^-\pi_{\mathcal{C}_2}$ and $k_{23}^+[\text{Ach}]\pi_{\mathcal{C}_2} \approx k_{32}^-\pi_{\mathcal{C}_3}$, or

$$\pi_{\mathcal{C}_1} = \frac{K_{21}}{[\text{Ach}]}\pi_{\mathcal{C}_2} \quad \text{and} \quad \pi_{\mathcal{C}_2} = \frac{K_{32}}{[\text{Ach}]}\pi_{\mathcal{C}_3} \quad (2.30)$$

where $K_{21} = k_{21}^-/k_{12}^+$ and $K_{32} = k_{32}^-/k_{23}^+$. Expressing $\pi_{\mathcal{C}_1}$ and $\pi_{\mathcal{C}_2}$ in terms of $\pi_{\mathcal{C}_3}$ and substituting into $\pi_{\mathcal{C}_1} + \pi_{\mathcal{C}_2} + \pi_{\mathcal{C}_3} = 1 - \pi_{\mathcal{O}_4}$ and Eqn (2.29) gives

$$\frac{d\pi_{\mathcal{O}_4}}{dt} = k_{34} \left(\frac{[\text{Ach}]^2}{K_{21}K_{32} + K_{32}[\text{Ach}] + [\text{Ach}]^2} \right) (1 - \pi_{\mathcal{O}_4}) - k_{43}\pi_{\mathcal{O}_4}. \quad (2.31)$$

Thus, under the assumption of rapid ligand binding, the four-state AchR model (Fig. 2.2b) is well-approximated by the two-state model

$$\frac{k_{*4}}{(C_1/C_2/C_3)} \rightleftharpoons \mathcal{O}_4 \quad (2.32)$$

where $k_{*4} = k_{34}[\text{Ach}]^2 / (K_{21}K_{32} + K_{32}[\text{Ach}] + [\text{Ach}]^2)$ and $k_{4*} = k_{43}$.

2.2.7 Numerical simulations of ion channel gating

The stochastic gating of ion channels modelled as continuous-time discrete-state Markov chains can be simulated using Gillespie's algorithm (Gillespie, 1976), a numerical method with no intrinsic time step. Given the current state i , Gillespie's algorithm requires the non-zero off-diagonal elements of the i th row of the Q -matrix, that is, the rates of all allowed transitions from state i to state j . The dwell time T_i is determined by generating an exponentially distributed pseudo-random number with mean $1/\sum_{j \neq i} q_{ij}$. When there is more than one destination state j , a pseudo-random number X is produced that is uniformly distributed on an interval of length $\sum_{j \neq i} q_{ij}$. This interval is partitioned into subintervals of length $q_{i1}, q_{i2}, \dots, q_{iM}$ (not including q_{ii}) and the $i \rightarrow j$ transition occurs if X falls in the partition associated with j . A record of the channel's state as a function of time is produced by repeating these steps.

For single channel models with transition rates that are not constant but rather known functions of time (i.e. time-inhomogeneous Markov chains), Gillespie's algorithm can be generalized. In this case, the complement of the cumulative distribution function for the dwell time is given by

$$P\{T_i > t\} = \exp \int_0^t q_{ii}(s)ds \quad (2.33)$$

where $q_{ii}(t) = -\sum_{j \neq i} q_{ij}(t)$. Because $\bar{F}(t) = P\{T_i > t\}$ is a continuous function, a pseudo-random T_i can be produced using the inverse transformation method (Ross, 1988, pp. 389–390) in which $T_i = \bar{F}^{-1}(X)$ where X is uniformly distributed on the interval $0 \leq X \leq 1$ (see also Section 1.6).

When single channel models have transition rates that are time-dependent and not known in advance, a first-order accurate solution method can be implemented by defining the stochastic matrix $W(t) = (w_{ij}) = I + Q\Delta t$ where Δt is small enough that $w_{ij}(t) \geq 0$ and $1 - \epsilon < w_{ii}(t) < 1$ where, for example, we might choose $\epsilon = 0.05$ so that with each time step there is 95% chance of no transition occurring. For a channel in state i at time t , the unit interval can be partitioned by the transition probabilities $w_{i1}, w_{i2}, \dots, w_{iM}$, and the state of the channel at time $t + \Delta t$ determined by generating a uniformly distributed random variable (Smith, 2002b).

Using Gillespie's algorithm, Fig. 2.3(a) shows the stochastic gating of a voltage-gated Na^+ channel with the state-transition diagram of Fig. 2.2(a) following a voltage step from -108 to -28 mV at $t = 0$ (parameters as in

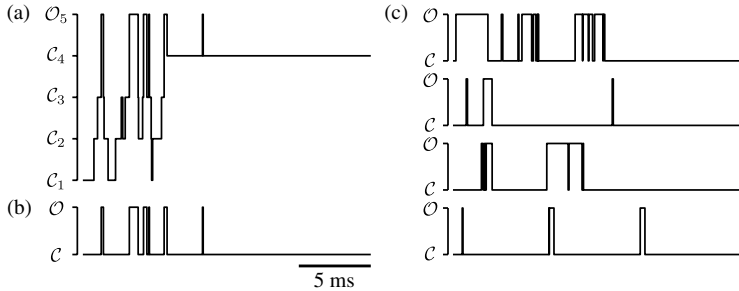


FIG. 2.3: (a) A trajectory showing the stochastic gating of the voltage-gated Na^+ channel of Fig. 2.2(a) following a voltage step from -108 to -28 mV. Model parameters as in Vandenberg and Bezanilla (1991). (b) The simulation in (a) after combining the four closed states (C_1 , C_2 , C_3 , and C_4) into a single experimentally observable closed state C . The single open state is denoted O . (c) Repetitions of the simulation in (a) and (b) yield different stochastic trajectories.

Vandenberg and Bezanilla, 1991). After recognizing that the closed states are indistinguishable (Fig. 2.3b), the trajectory is reminiscent of the experimental records shown in Fig. 2.1. In Fig. 2.3(c), this simulation is repeated four times yielding different stochastic trajectories.

Note that the numerical simulations mentioned above produce an instantiation of the stochastic process described by the Markov chain model of single channel gating. When a simulation of channel gating is not required, but the dynamics of the probability distribution $\pi(t)$ is of interest, Eqn (2.3) can be solved using conventional methods for integrating ODEs (e.g. the first-order Euler's method or the fourth-order Runge–Kutta method). Another numerical algorithm for computing transient probability distributions of continuous-time Markov chains is the uniformization or randomization method (Stewart, 1994, pp. 408–413).

2.2.8 Parameter estimation and model identification

Markov chain models of ion channels are often designed to reproduce salient aspects of channel gating such as voltage- and ligand-dependence of the steady-state open probability, separation of time-scales between activation and inactivation processes, and so on. While constructing phenomenological models in an *ad hoc* fashion is legitimate, there are in principle an infinite number of possible state-transition diagrams and combinations of kinetic parameters to choose from. However, Markov chain models of single channel gating can also be viewed as statistical constructs designed to reproduce the probability distribution of dwell times in the experimentally observable states (Eqn (2.17)) and higher order stochastic dynamics. In this case it may be possible to formalize

the appropriate level of complexity for a single channel model (i.e. the topology of the state-transition diagram). When the topology of the state-transition diagram is prescribed, one can automate the selection of kinetic parameters that best describe experimental data obtained from single channel recording.

A common parameter estimation technique for Markov chain models of single channel gating involves maximization of a likelihood function giving the probability of an experimental data set conditioned on a specific set of kinetic parameters (Yeo *et al.*, 1988, Milescu *et al.*, 2005, Ball and Sansom, 1989, Colquhoun *et al.*, 1996). For example, the likelihood function may be the probability of the dwell time distributions in the experimentally observable states (f_{T_ϕ} and f_{T_c}) conditioned on the model kinetic parameters (θ),

$$L = P\{f_{T_\phi}, f_{T_c} | \theta\}. \quad (2.34)$$

When the single channel model has more than one state corresponding to each experimentally observed conductance level, the kinetic parameters that maximize the likelihood function may not be unique (Edeson *et al.*, 1994).

Identifying a state-transition diagram of appropriate complexity can usually not be accomplished using maximum likelihood techniques alone, because such methods tend to favour models with more states and kinetic parameters. However, model identification can be performed using scoring schemes that reward topologies that best fit experimental data but penalize those that are complex (Ball and Sansom, 1989, Hodgson and Green, 1999). For example, one such technique attempts to maximize the function $Z = -\log_2 L - n_\theta$ where L is a likelihood function as discussed above and n_θ is the number of kinetic parameters (Ball and Sansom, 1989). Because parameter fits using different state-transition diagrams can make identical predictions of steady-state gating statistics, investigators often restrict the topologies explored to a particular canonical form (Kienker, 1989, Larget, 1998, Bruno *et al.*, 2005).

2.2.9 Cycles and thermodynamic constraints

The voltage-gated Na^+ channel model simulated in Fig. 2.3 has a state-transition diagram that includes a cycle (Fig. 2.2a) When rate constants are chosen for such a model, it is important to choose parameters in such a manner that the steady-state probability distribution $\bar{\pi}$ satisfying global balance (Eqn (2.4)) also satisfies detailed balance,

$$\bar{\pi}_i q_{ij} = \bar{\pi}_j q_{ji}. \quad (2.35)$$

Note that the stationary distribution $\bar{\pi}$ of a single channel model that does not include any cycles will satisfy detailed balance regardless of parameters chosen. However, for single channel models that do include cycles, this condition leads to a thermodynamic constraint in which the product of rate constants in the clockwise and counter-clockwise direction around each cycle are equal (Hill, 1977).

For example, in the voltage-gated Na^+ channel model of Fig. 2.2(a), parameters must be chosen to satisfy

$$q_{24}q_{45}q_{53}q_{32} = q_{23}q_{35}q_{54}q_{42}. \quad (2.36)$$

Because one of these transition rates can always be expressed in terms of the other seven, only 9 of the 10 transition rates in this voltage-gated Na^+ channel model can be freely chosen.

2.2.10 Thermodynamic constraints for ligand-gated channels

In the case of ligand-gated channels with cycles, parameters must be chosen so that thermodynamic constraints such as Eqn (2.36) are satisfied when all the binding sites of the channel are exposed to the same ligand concentration (Hill, 1977). Figure 2.2(c) shows a minimal two-state model of a Ca^{2+} -regulated channel that includes Ca^{2+} activation, a phenomenon exhibited in single channel recordings of both IP_3Rs and RyRs (Fill and Copello, 2002, Hagar *et al.*, 1998, Mak and Foskett, 1997, Moraru *et al.*, 1999, Ramos-Franco *et al.*, 1998, Bezprozvanny *et al.*, 1991). In this model, k_{12}^+ is an association rate constant with units $\text{conc}^{-\eta} \text{time}^{-1}$, k_{21}^- is a dissociation rate constant with units time^{-1} , η is the cooperativity of Ca^{2+} binding, and c_∞ is the ‘background’ $[\text{Ca}^{2+}]$ experienced by the regulatory site of the channel. The open probability of this two-state Ca^{2+} -activated channel is an increasing function of c_∞ (not shown), and the $[\text{Ca}^{2+}]$ that leads to half-maximal open probability is given by $c_\infty = K_{21}$ where K_{21} is a dissociation constant and $K_{21}^\eta = k_{21}^-/k_{12}^+$. Because this model includes no cycles, both k_{12}^+ and k_{21}^- are free parameters.

For comparison, Fig. 2.2(d) shows a four-state model with both Ca^{2+} activation and Ca^{2+} inactivation, the latter phenomenon having been repeatedly (but not uniformly) observed in single channel recordings from planar lipid bilayer and nuclear patch experiments (see references in previous paragraph). Because this model includes a cycle, parameters must be chosen to satisfy

$$k_{14}^+k_{42}^+k_{23}^-k_{31}^- = k_{13}^+k_{32}^+k_{24}^-k_{41}^- \quad (2.37)$$

where the Ca^{2+} concentrations experienced by the activation and inactivation binding sites have been cancelled. This leads to the thermodynamic constraint $K_{23}K_{31} = K_{41}K_{24}$, where $K_{ij}^\eta = k_{ij}^-/k_{ji}^+$ are dissociation constants. That is, although there are eight rate constants in this model, only seven are free parameters because $k_{31}^- = k_{13}^+K_{41}K_{24}/K_{23}$.

Notice that the four-state model has a complication in that one of the Ca^{2+} -mediated transitions ($\mathcal{O}_4 \rightarrow \mathcal{C}_2$) occurs when the channel is open (Smith, 2002a). If the channel is conducting Ca^{2+} , then the $[\text{Ca}^{2+}]$ experienced by the Ca^{2+} binding site will be significantly higher than the background $[\text{Ca}^{2+}]$ (c_∞).

Assuming that the formation and collapse of this Ca^{2+} microdomain is a fast process compared to the dwell times of the channel, we can write $c_\infty + c_d$ as

the $[Ca^{2+}]$ determining the rate of the $\mathcal{O}_4 \rightarrow \mathcal{C}_2$ transition in Fig. 2.2(d), where c_d is the ‘domain $[Ca^{2+}]$ ’, the increase in the local $[Ca^{2+}]$ above background experienced by the Ca^{2+} -regulatory site when the channel is open (Sherman *et al.*, 1990, Bezprozvanny and Ehrlich, 1994). Consistent with experimental observations of the type-1 IP₃R (Young and Keizer, 1992, Atri *et al.*, 1993, Bezprozvanny and Ehrlich, 1994, Tang *et al.*, 1996, Kaftan *et al.*, 1997, Swillens *et al.*, 1998, Moraru *et al.*, 1999), the steady state open probability ($\bar{\pi}_{\mathcal{O}_4}$) of the four-state model (not shown) is a bell-shaped function of the background $[Ca^{2+}]$ (c_∞) and is suppressed by increasing the ‘domain $[Ca^{2+}]$ ’ (c_d).

Note that for $c_d > 0$ the stationary distribution $\bar{\pi}$ of the four-state channel that satisfies global balance (Eqn (2.4)) will not satisfy detailed balance (Eqn (2.35)), even when parameters have been chosen to satisfy the thermodynamic constraint (Eqn (2.37)). Indeed, when domain Ca^{2+} -mediated transitions are represented in Ca^{2+} -regulated channel models with cycles, time-irreversibility of channel gating is not unexpected and is a manifestation of the concentration gradient between the cytosol and endoplasmic reticulum that is implicit in the model formulation. It is as though the Ca^{2+} -binding site of the channel is exposed alternately to the cytosolic and luminal ‘baths’ depending on whether the channel is closed or open (Hill, 1977, Keizer, 1987). This situation is analogous to the non-equilibrium steady states that are obtained in models of the glucose transporter in which conformation changes expose the glucose binding site alternately to external and internal glucose concentrations (Marland and Keizer, 2002).

2.3 Coupled gating of calcium-regulated calcium channels

The previous section has discussed Markov chain models of single channel gating and concluded with a presentation of two minimal models of Ca^{2+} -regulated Ca^{2+} channels that reproduce important aspects of the Ca^{2+} -regulation of inositol 1,4,5-trisphosphate receptors (IP₃Rs) and ryanodine receptors (RyRs). This puts us in an excellent position to describe how clusters of interacting ion channels can be modelled using Markov chains. Although there are many examples of co-localized plasma membrane channels (Rasband and Trimmer, 2001, Colledge and Froehner, 1998, Caldwell, 2000, Roberts *et al.*, 1990), and in some cases experimental evidence that these channels gate in a coordinated fashion (Naundorf *et al.*, 2006, Kelesian *et al.*, 2000), we will restrict our presentation to Markov chain models of intracellular Ca^{2+} release sites (Berridge, 1997, Berridge, 2006). For example, clusters of 5–50 IP₃Rs on both the cortical endoplasmic reticulum (Yao *et al.*, 1995, Sun *et al.*, 1998) and outer nuclear membrane (Mak and Foskett, 1997) of immature *Xenopus laevis* oocytes exhibit coordinated gating and give rise to localized Ca^{2+} elevations known as ‘ Ca^{2+} puffs.’ Similarly, localized intracellular Ca^{2+} release events in skeletal and cardiac myocytes known as ‘ Ca^{2+} sparks’ are mediated by clusters of RyRs that are assembled into paracrystalline arrays of 50–250 cooperatively gating channels

(Franzini-Armstrong *et al.*, 1999a, Bers, 2002, Wang *et al.*, 2004, Chen-Izu *et al.*, 2006).

2.3.1 Transition rates for clusters of channels

In a natural extension of the single channel modelling approach, a model Ca²⁺ release site composed of N channels is the vector-valued Markov chain, $\mathbf{S}(t) = \{S_1(t), S_2(t), \dots, S_N(t)\}$, where $S_n(t)$ is the state of channel n at time t (Ball *et al.*, 2000). We will denote release site configurations as the vector $\mathbf{i} = (i_1, i_2, \dots, i_N)$ where i_n is the state of channel n . The transition rate from release site configuration \mathbf{i} to \mathbf{j} denoted by q_{ij} ,

$$(i_1, i_2, \dots, i_N) \xrightarrow{q_{ij}} (j_1, j_2, \dots, j_N), \quad (2.38)$$

is nonzero if the origin (\mathbf{i}) and destination (\mathbf{j}) release site configurations are identical with the exception of one channel – that is, $i_n = j_n$ for all $n \neq n'$ where $1 \leq n'(\mathbf{i}, \mathbf{j}) \leq N$ is the index of the channel changing state – and the $i_{n'} \rightarrow j_{n'}$ transition is included in the single channel model (Nguyen *et al.*, 2005).

More formally, assume that the release site is composed of identical Ca²⁺-regulated Ca²⁺ channels that can be written as

$$Q = K^- + cK^+ \quad (2.39)$$

where the matrices K^- and K^+ collect the dissociation and association rate constants, respectively, have negative diagonal elements, and row sum zero. Note that both the two-state and four-state models of Fig. 2.2(c) and (d) can be expressed in the form of Eqn (2.39), i.e. both have transition rates that are either constant or proportional to the local [Ca²⁺]. The transition rates q_{ij} for a release site composed of N such channels are given by

$$q_{ij} = \begin{cases} \bar{q}_{ij} & \text{if } \mathbf{i} = (i_1, i_2, \dots, i_{n'-1}, i_{n'}, i_{n'+1}, \dots, i_N) \text{ and} \\ & \mathbf{j} = (i_1, i_2, \dots, i_{n'-1}, j_{n'}, i_{n'+1}, \dots, i_N) \\ 0 & \text{otherwise} \end{cases} \quad (2.40)$$

where

$$\bar{q}_{ij} = K^-[i_{n'}, j_{n'}] + K^+[i_{n'}, j_{n'}]c(\mathbf{i}, \mathbf{j})^\eta. \quad (2.41)$$

In this expression, $K^-[i_{n'}, j_{n'}]$ or $K^+[i_{n'}, j_{n'}]$ is the rate constant for the transition being made (only one is non-zero), and $c(\mathbf{i}, \mathbf{j})$ is the relevant [Ca²⁺], that is, the concentration experienced by channel $n'(\mathbf{i}, \mathbf{j})$ in the origin configuration \mathbf{i} . Thus, the infinitesimal generator matrix, $Q = (q_{ij})$, for a model Ca²⁺ release site can be constructed by enumerating transition rates according to Eqns (2.40) and (2.41) and selecting the diagonal elements q_{ii} to ensure the rows sum to zero. In the following section, we show how $c(\mathbf{i}, \mathbf{j})$ depends on

the mathematical representation of the release site ultrastructure and buffered Ca^{2+} diffusion.

2.3.2 Release site ultrastructure and the calcium microdomain

Because intracellular Ca^{2+} channels experience coupling mediated by the buffered diffusion of intracellular Ca^{2+} , a mathematical representation for the landscape of the local $[\text{Ca}^{2+}]$ near the Ca^{2+} release site (the so-called Ca^{2+} microdomain) is required to specify $c(\mathbf{i}, \mathbf{j})$ in Eqn (2.41). In the simulations presented below, we will for simplicity assume that channels are ‘instantaneously coupled’ via the Ca^{2+} microdomain (Nguyen *et al.*, 2005, DeRemigio and Smith, 2005), that is, the formation and collapse of the local peaks in the Ca^{2+} profile are fast compared to the closed and open dwell times of the channels, and we also assume the validity of linearly superposing local $[\text{Ca}^{2+}]$ increases due to individual channels at the release site (Naraghi and Neher, 1997, Smith *et al.*, 2001). We further assume that all channels are localized on a planar section of ER/SR membrane ($z = 0$) so that the position of the pore of channel n can be written as $\mathbf{r}_n = x_n\hat{x} + y_n\hat{y}$. The release site ultrastructure (i.e. the relative location of the channels) will take the form of a Cartesian (Fig. 2.4a) or hexagonal (Fig. 2.4b) lattice.

Assuming a single high concentration Ca^{2+} buffer and using the steady-state solution of the linearized equations for the buffered diffusion of intracellular Ca^{2+} (Naraghi and Neher, 1997), the increase in $[\text{Ca}^{2+}]$ above background at position $\mathbf{r} = x\hat{x} + y\hat{y} + z\hat{z}$ is given by

$$c(\mathbf{r}) = \sum_{n=1}^N \frac{\sigma_n}{2\pi|\mathbf{r}_n - \mathbf{r}|(D_c + \kappa_\infty D_b)} \left[1 + \frac{\kappa_\infty D_b}{D_c} \exp\left(\frac{-|\mathbf{r}_n - \mathbf{r}|}{\lambda}\right) \right] \quad (2.42)$$

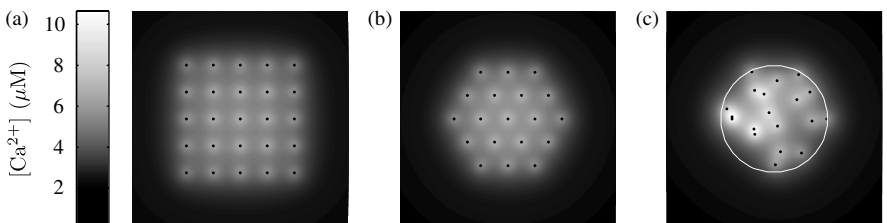


FIG. 2.4: The linearized equations for the buffered diffusion of Ca^{2+} (Eqns (2.42) and (2.43)) give the steady-state $[\text{Ca}^{2+}]$ near ($z = r_d = 30$ nm) a 800×800 nm section of planar ER/SR membrane with a cluster of 25 open channels (black dots) organized on a Cartesian lattice (a), 19 channels on a hexagonal lattice (b), or 19 channels with random spatial locations chosen from a uniform distribution on a disc (white circle) (c). Parameters: release site radius $R = 200$ nm, $i_{\text{Ca}} = 0.04$ pA, $c_\infty = 0.1$ μM , $[B]_T = 300$ μM , $\hat{k}^+ = 100$ $\mu\text{M}^{-1}\text{s}^{-1}$, $\hat{k}^- = 38$ s^{-1} , $D_c = 250$ $\mu\text{m}^2\text{s}^{-1}$, $D_b = 32$ $\mu\text{m}^2\text{s}^{-1}$.

where

$$\frac{1}{\lambda^2} = \frac{1}{\tau} \left(\frac{1}{D_b} + \frac{\kappa_\infty}{D_c} \right), \quad \frac{1}{\tau} = \hat{k}^+ c_\infty + \hat{k}^-, \quad \kappa_\infty = \frac{\hat{K}[B]_T}{(\hat{K} + c_\infty)^2}. \quad (2.43)$$

In these equations, the sum is over all channels at the release site, σ_n is the source amplitude of channel n (number of Ca^{2+} ions per unit time), D_c and D_b are the diffusion coefficients for free Ca^{2+} and the Ca^{2+} buffer respectively, \hat{k}^+ is the buffer association rate constant, \hat{k}^- is the buffer dissociation rate constant, $\hat{K} = \hat{k}^-/\hat{k}^+$, and $[B]_T$ is the total concentration of the Ca^{2+} buffer. Assuming all channels have identical source amplitudes,

$$\sigma_n(t) = \begin{cases} 0 & \text{if channel } n \text{ is closed} \\ \bar{\sigma} & \text{if channel } n \text{ is open,} \end{cases} \quad (2.44)$$

and $\bar{\sigma} = i_{\text{Ca}}/2F$ where i_{Ca} is the unitary current of each channel, 2 is the valence of Ca^{2+} , and F is Faraday's constant.

While Eqns (2.42) and (2.43) define the $[\text{Ca}^{2+}]$ at any position \mathbf{r} for a given release site ultrastructure, $\{\mathbf{r}_n\}$, it is helpful to summarize channel-to-channel Ca^{2+} interactions using an $N \times N$ ‘coupling matrix’ $C = (c_{nm})$ that provides the increase in $[\text{Ca}^{2+}]$ over the background (c_∞) experienced by channel m when channel n is open. If $\mathbf{a}_m = x_m \hat{x} + y_m \hat{y} + r_d \hat{z}$ specifies the position of the Ca^{2+} regulatory site for channel m located a small distance r_d above the channel pore, then

$$c_{nm} = \frac{\bar{\sigma}}{2\pi|\mathbf{r}_n - \mathbf{a}_m|(D_c + \kappa_\infty D_b)} \left[1 + \frac{\kappa_\infty D_b}{D_c} \exp\left(\frac{-|\mathbf{r}_n - \mathbf{a}_m|}{\lambda}\right) \right]. \quad (2.45)$$

Using this expression we can determine the Ca^{2+} concentrations needed to specify the rates of Ca^{2+} -mediated transitions in Eqns (2.40) and (2.41), that is,

$$c(\mathbf{i}, \mathbf{j}) = c_\infty + \sum_{n=1}^N \bar{c}_{nn'} \quad \text{where} \quad \bar{c}_{nn'} = \begin{cases} c_{nn'} & \text{if } i_n \text{ is open} \\ 0 & \text{otherwise,} \end{cases} \quad (2.46)$$

$n'(\mathbf{i}, \mathbf{j})$ is the index of the channel changing state, and i_n is the state of channel n .

2.3.3 Modelling allosteric coupling

While the coupled gating of Ca^{2+} -regulated Ca^{2+} channels can be mediated entirely through the buffered diffusion of intracellular Ca^{2+} , in some situations inter-protein allosteric interactions between neighbouring channels may also contribute to coordinated gating. For example, in skeletal and cardiac myocytes groups of 50–250 RyRs form Cartesian lattices on the surface of the SR membrane (Franzini-Armstrong *et al.*, 1999b, Franzini-Armstrong *et al.*, 1999a, Yin *et al.*, 2005a, Yin *et al.*, 2005b, Serysheva, 2004, Lai *et al.*, 1989, Bers, 2002) (cf. Fig. 2.4a). When reconstituted into planar lipid bilayers to mimic this *in*

situ crystalline lattice, RyRs maintain physical contact with neighbouring channels (Yin *et al.*, 2005a). Physically coupled RyRs sometimes exhibit coupled gating even when Ca^{2+} is not the charge carrier (Marx *et al.*, 1998, Marx *et al.*, 2001).

Following the methodology presented by Stern *et al.* (1999), the Ca^{2+} release site model presented above can be extended to include allosteric interactions between neighbouring channels. We begin by defining dimensionless free energies of interaction ε_{ij} (units of $k_B T$) that specify the change in free energy experienced by a channel in state j when allosterically coupled to a channel in state i . Thus, i - j channel pairs are stabilized when $\varepsilon_{ij} < 0$ and destabilized when $\varepsilon_{ij} > 0$. For convenience we collect these interaction energies in an M -by- M matrix $\mathcal{E} = (\varepsilon_{ij})$ where M is the number of states in the single channel model and $\varepsilon_{ij} = \varepsilon_{ji}$ ($i \neq j$) to satisfy a thermodynamic constraint (cf. Section 2.2.10). For example, for the two-state single channel model presented above (Fig. 2.2c), this matrix takes the form

$$\mathcal{E} = \begin{pmatrix} \varepsilon_{CC} & \varepsilon_{CO} \\ \varepsilon_{OC} & \varepsilon_{OO} \end{pmatrix} \quad (2.47)$$

where $\varepsilon_{CO} = \varepsilon_{OC}$ and the subscripts on C_1 and O_2 have been dropped. Because allosteric interactions require physical contact between neighbouring channels, the model formulation includes a symmetric N -by- N adjacency matrix defined as

$$A = (a_{nm}) = \begin{cases} 1 & \text{if channel } n \text{ and } m \text{ are neighbours} \\ 0 & \text{otherwise} \end{cases} \quad (2.48)$$

where $a_{nn} = 0$ because channels do not experience allosteric interactions with themselves. Normally, the non-zero elements of A would be chosen consistent with release site ultrastructure. For example, when channels are arranged in a Cartesian lattice as in Fig. 2.4(a), allosteric interactions in the horizontal and vertical directions would lead to each channel being influenced by 2–4 neighbours.

To include the effect of allosteric coupling in a release site model, the total allosteric energy experienced by channel $n'(\mathbf{i}, \mathbf{j})$ in the origin and destination configurations of an $\mathbf{i} \rightarrow \mathbf{j}$ transition are calculated as

$$\gamma_{\mathbf{i}} = \sum_{n=1}^N a_{nn'} \varepsilon_{i_n i_{n'}} \quad \text{and} \quad \gamma_{\mathbf{j}} = \sum_{n=1}^N a_{nn'} \varepsilon_{j_n j_{n'}} \quad (2.49)$$

where the sum is over all N channels, $a_{nn'}$ are elements of A , and $\varepsilon_{i_n i_{n'}}$ and $\varepsilon_{j_n j_{n'}}$ are entries of \mathcal{E} . The difference between these total allosteric energies is used to modify the rates of the $\mathbf{i} \rightarrow \mathbf{j}$ and $\mathbf{j} \rightarrow \mathbf{i}$ transitions, that is,

$$q_{ij} = \tilde{q}_{ij} \exp [-\nu_{ij} (\gamma_j - \gamma_i)] \quad \text{and} \quad q_{ji} = \tilde{q}_{ji} \exp [-\nu_{ji} (\gamma_i - \gamma_j)] \quad (2.50)$$

where \tilde{q}_{ij} and \tilde{q}_{ji} denote unmodified rates calculated using Eqns (2.40) and (2.41) and the parameters $0 \leq \nu_{ij} \leq 1$ and $\nu_{ji} = 1 - \nu_{ij}$ partition contributions due to allosteric coupling between the forward (q_{ij}) and reverse (q_{ji}) rates.

2.3.4 A representative three-channel cluster

The simulations shown in Fig. 2.5 demonstrate how coupling via allosteric interactions affect the gating of three two-state Ca^{2+} -activated Ca^{2+} channels (Fig. 2.2c) arranged equidistantly so that the off-diagonal elements of the Ca^{2+} coupling matrix $C = (c_{ij})$ are identical. Simulations are carried out using Gillespie's algorithm and, for simplicity, the configuration of the cluster is summarized by plotting only the number of open channels ($N_{\mathcal{O}}$) as a function of time, that is, the number of channels in state \mathcal{O}_2 . Using $\varepsilon_{ij} = 0$, Fig. 2.5(a) illustrates that allosteric interactions are not required for channels to exhibit collective gating. Rather, channels may exhibit coupled gating that is mediated entirely via the buffered diffusion of local Ca^{2+} , as long as the average Ca^{2+} coupling strength is sufficient (here $c_{ij} = 0.75 \mu\text{M}$, $i \neq j$). Grey bars in Fig. 2.5(a) show the steady-state probability distribution for the number of open channels ($N_{\mathcal{O}}$). The disagreement between these results and the *white bars*, showing a binomial distribution with the same mean, is a signature of the cooperative gating of these channels.

While Fig. 2.5(a) demonstrates that the collective gating of channels can be mediated entirely via Ca^{2+} , Figs. 2.5(b)–(d) show how synchronizing allosteric interactions affect the dynamics of coupled gating. For example, Fig. 2.5(b) demonstrates that when closed channel pairs are stabilized ($\varepsilon_{CC} = -0.8$), the steady-state probability of $N_{\mathcal{O}} = 0$ increases while the probability of $N_{\mathcal{O}} = 3$ decreases relative to Fig. 2.5(a). Conversely, Fig. 2.5(c) shows that when allosteric interactions stabilize open channel pairs ($\varepsilon_{OO} = -0.8$), the probability of $N_{\mathcal{O}} = 3$ increases. In Fig. 2.5(d) allosteric interactions stabilize closed-closed and open-open channel pairs in a balanced fashion ($\varepsilon_{CC} = \varepsilon_{OO} = -0.8$) and the probability of both $N_{\mathcal{O}} = 0$ and $N_{\mathcal{O}} = 3$ increases while the probability of $N_{\mathcal{O}} = 1$ and $N_{\mathcal{O}} = 2$ decreases compared to Fig. 2.5(a).

2.3.5 Calcium coupling, allosteric interactions, and spontaneous sparks

The simulations involving three two-state Ca^{2+} -activated channels shown in Fig. 2.5 demonstrate how the dynamics of coupled gating of intracellular channels may depend on synchronizing allosteric interactions that stabilize closed and/or open channel pairs. Figure 2.6 shows a simulation of a Ca^{2+} release site composed of 25 two-state channels organized on a Cartesian lattice (see Fig. 2.4a). The channels experience both coupling via the buffered diffusion of Ca^{2+} following Eqns (2.42) and (2.43) and nearest-neighbour allosteric coupling such that each channel experiences allosteric interactions with 2–4 other channels. The strength of Ca^{2+} coupling and allosteric interactions that stabilize closed channel pairs are selected to illustrate the phenomenon of ‘stochastic

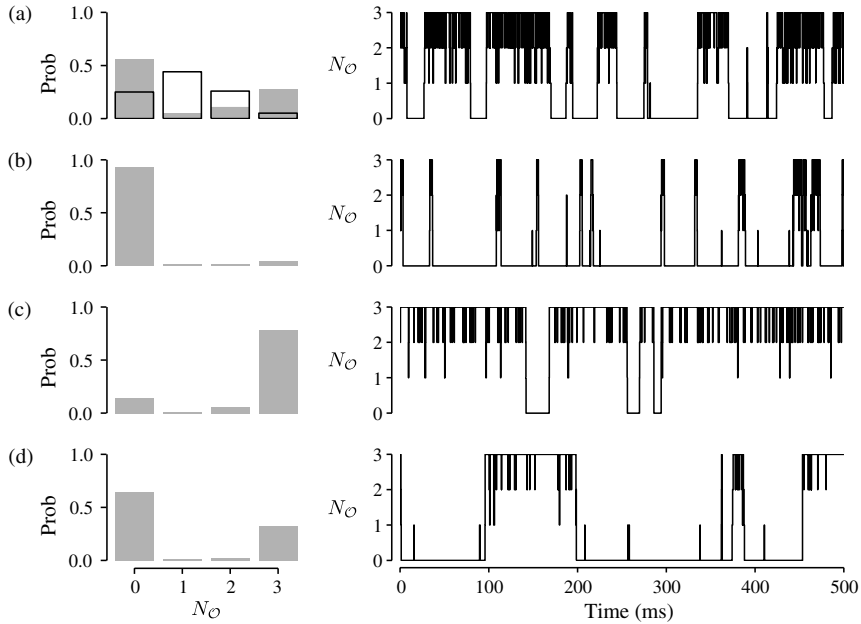


FIG. 2.5: (a) Collective gating of three two-state Ca^{2+} -activated Ca^{2+} channels (Fig. 2.2c) with Ca^{2+} coupling ($c_{ij} = 0.75 \mu\text{M}$, $i \neq j$) but no allosteric interactions ($\varepsilon_{ij} = 0$). Grey bars show the steady-state probability distribution for the number of open channels (N_O) at the release site. White bars give the binomial distribution with the same mean as gray bars; the difference shows that channels do not gate independently. (b), (c), (d) collective gating when in addition to Ca^{2+} coupling, channels experience allosteric interactions that stabilize closed channel pairs (b) ($\varepsilon_{CC} = -0.8$), open channel pairs (c) ($\varepsilon_{OO} = -0.8$), or both in a balanced fashion (d) ($\varepsilon_{CC} = \varepsilon_{OO} = -0.8$). Parameters: $k_{12}^+ = 1.5 \mu\text{M}^{-\eta}\text{ms}^{-1}$, $k_{21}^- = 0.5 \text{ ms}^{-1}$, $\eta = 2$, $c_\infty = 0.1 \mu\text{M}$. Reproduced with permission from Groff and Smith (2008b).

Ca^{2+} excitability' reminiscent of spontaneous Ca^{2+} puffs and sparks. While the channels at the release site are closed most of the time ($N_O < 5$), on occasion the channels simultaneously open ($N_O \approx 25$). In extensive parameter studies similar to Fig. 2.6 (Groff and Smith, 2008b), it has been observed that the puffs and sparks are sensitive to changes in the strength of allosteric and Ca^{2+} coupling experienced by channels (not shown). For example, the release site may become tonically active when allosteric interactions are not included in simulations or when the Ca^{2+} coupling strength is elevated by decreasing the total buffer concentration ($[\text{B}]_T$). On the other hand, puffs and sparks often fail to initiate when the strength of allosteric interactions that stabilize closed channel pairs is increased – ε_{CC} becomes more negative – or $[\text{B}]_T$ is increased. Allosteric

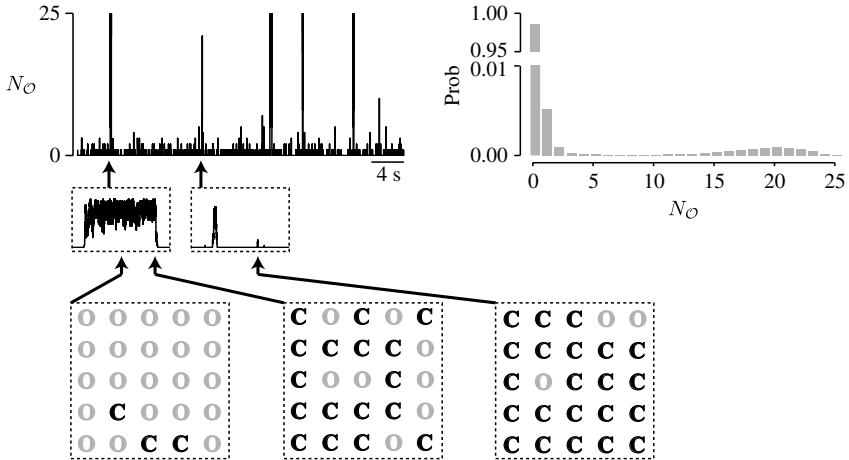


FIG. 2.6: A Ca^{2+} release site simulation involving 25 two-state Ca^{2+} -activated channels arranged in a Cartesian lattice ($R = 60 \text{ nM}$) exhibits stochastic Ca^{2+} excitability reminiscent of spontaneous sparks when channels experience coupling via increases in the local $[\text{Ca}^{2+}]$ and nearest-neighbour allosteric interactions that stabilize closed channel pairs ($\varepsilon_{CC} = -0.2$). Insets expand 50 ms of the simulation beginning at the times indicated by arrows and show ‘snapshots’ giving the states of all 25 channels at the release site. The right panel shows the steady-state probability distribution for the number of open channels (N_O) estimated from a long ($> 20 \text{ s}$) Monte Carlo simulation. Parameters: $k_{12}^+ = 0.04 \mu\text{M}^{-\eta}\text{ms}^{-1}$, $k_{21}^- = 1 \text{ ms}^{-1}$, $[\text{B}]_T = 937.5 \mu\text{M}$. Other parameters as in Figs. 2.4 and 2.5. Reproduced with permission from Groff and Smith (2008b).

interactions that stabilize closed channel pairs may make simulated puffs and sparks less sensitive to variations in the strength of Ca^{2+} coupling between channels. Moreover, the statistics of spontaneous puffs and sparks – such as duration, inter-event interval, and frequency – are less sensitive to the spatial aspect of allosteric interactions than one might expect (Groff and Smith, 2008b).

2.3.6 Stochastic calcium excitability in the absence of allosteric interactions

Figure 2.6 shows stochastic excitability when channels experience coupling via increases in the local $[\text{Ca}^{2+}]$ and nearest-neighbour allosteric interactions. However, simulated Ca^{2+} puffs and sparks are readily observed when the coupling between single channel models is mediated entirely via the buffered diffusion of intracellular Ca^{2+} . For example, Fig. 2.7 shows a stochastic trajectory of a Markov chain model of a Ca^{2+} release site composed of 19 two-state Ca^{2+} -activated channels (Fig. 2.2c) arranged in a hexagonal lattice under the assumption of instantaneous coupling. Because this release site model does

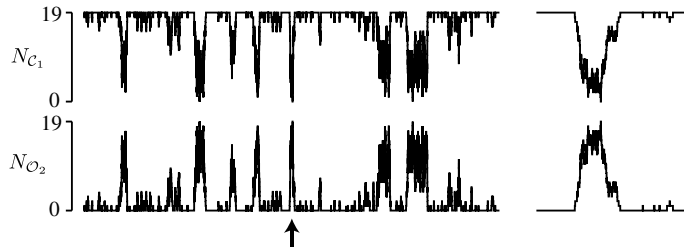


FIG. 2.7: Representative Ca^{2+} release site simulation using 19 two-state channels arranged on a hexagonal lattice that exhibits stochastic Ca^{2+} excitability reminiscent of Ca^{2+} puff/sparks. The time evolution of the number of closed (N_{C_1}) and open (N_{C_2}) channels are plotted. Total time is 2 s (first column) and the arrow indicates an expanded 80 ms epoch (second column). Channels are coupled via changes in the local $[\text{Ca}^{2+}]$ using equations that assume a single high concentration buffer (Smith *et al.*, 2001). Reproduced with permission from Nguyen, Mathias, and Smith (2005).

not include allosteric interactions or slow Ca^{2+} inactivation, we conclude that termination of each localized Ca^{2+} elevation occurs via *stochastic attrition*, i.e. the spontaneous closure of channels (Stern, 1992, Stern and Cheng, 2004). Simulations of instantaneously coupled two-state channels suggest that stochastic attrition is a viable puff/spark termination mechanism for a range of coupling strengths that narrows as the number of channels at the release (N) increases (DeRemigio and Smith, 2005). If the c_{ij} ($i \neq j$) are too large, sparks cannot terminate and the release site is tonically active, but if the c_{ij} are too small, sparks are not initiated and the release site is quiescent. When two-state Ca^{2+} -activated channels are coupled via a time-dependent Ca^{2+} domain as opposed to the instantaneous coupling used in Fig. 2.7, the time constant for Ca^{2+} domain formation and collapse can have a strong effect on both the generation and termination of Ca^{2+} puff/sparks (Mazzag *et al.*, 2005). Slow depletion of luminal Ca^{2+} , i.e. the $[\text{Ca}^{2+}]$ in the ER/SR near the luminal face of the channel, promotes the termination of Ca^{2+} sparks mediated by two-state Ca^{2+} -activated channels (Huertas and Smith, 2007).

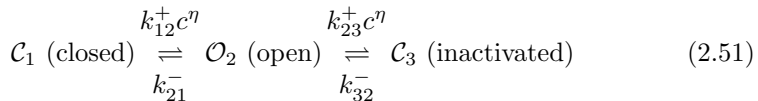
2.3.7 Calcium inactivation and puff and spark termination

Figure 2.7 shows that stochastic attrition may contribute to the termination of Ca^{2+} puffs and sparks. However, the sensitivity of stochastic attrition to variations in the Ca^{2+} coupling strength and the number of channels suggests that an additional negative control mechanism may be required for robust puff and spark termination *in vivo*. Proposed mechanisms include allosteric coupling (Section 2.3.3), depletion of luminal Ca^{2+} , and Ca^{2+} -dependent or activity-dependent inactivation of channels (Stern and Cheng, 2004, Fill, 2003).

Indeed, Ca^{2+} -dependent inactivation may often play a role in the termination of puffs and sparks, because this phenomenon has been repeatedly and directly observed in single-channel recordings of IP_3Rs and RyRs , albeit with affinity and kinetics that vary with receptor subtype (Fabiato, 1985, Bezprozvanny *et al.*, 1991, Bezprozvanny and Ehrlich, 1994, Györke and Fill, 1993, Lukyanenko *et al.*, 1998, Hagar *et al.*, 1998, Moraru *et al.*, 1999, Fill, 2003, Stern and Cheng, 2004).

Figure 2.8 shows a representative simulation of a Ca^{2+} release site composed of 19 four-state channels (Fig. 2.2d) that include a transition representing Ca^{2+} -dependent inactivation (the Ca^{2+} -mediated $\mathcal{O}_4 \rightarrow \mathcal{C}_2$ transition). The four panels summarize the number of channels in each state ($N_{\mathcal{C}_1}$, $N_{\mathcal{C}_2}$, $N_{\mathcal{C}_3}$, $N_{\mathcal{O}_4}$) as a function of time and the puff/spark event indicated by the arrow is expanded in the right column. Notice that the number of inactivated channels ($N_{\mathcal{C}_2}$) gradually increases throughout the duration of puff/sparks, and the corresponding decrease in the number of open channels ($N_{\mathcal{O}_4}$) appears to facilitate puff/spark termination.

Parameter studies have shown that when Ca^{2+} inactivation is included in the single channel model, simulated puffs and sparks are often less sensitive to variations in the size and density of release sites, the source amplitude or channels, and the exact spatial positions of channels (Nguyen *et al.*, 2005, Groff and Smith, 2008a, DeRemigio *et al.*, 2008a). Interestingly, Ca^{2+} inactivation may contribute to puff/spark termination in two distinct manners depending on the rate of Ca^{2+} inactivation. Using a three-state single channel model given by



with moderately fast Ca^{2+} inactivation (k_{23}^+ and k_{32}^-), Fig. 2.9a shows a representative simulation where spark termination is facilitated by the accumulation of inactivated channels throughout the duration of each puff/spark event (similar to Fig. 2.8). For comparison, the simulation of Fig. 2.9(b) includes Ca^{2+} inactivation with ten-fold slower kinetics (both k_{23}^+ and k_{32}^- are reduced). Note that the puff/spark termination in Fig. 2.9(b) does not appear to be due to the recruitment of inactivated channels throughout the duration of puff/spark events (cf. Fig. 2.9a), because the fraction of inactivated channels is relatively constant (*dashed grey line*). However, the ‘sequestering’ of approximately five channels into the inactivated state results in a reduced number of de-inactivated channels (states \mathcal{O}_2 and \mathcal{C}_1) that participate in each puff/spark event, thereby potentiating termination via stochastic attrition.

2.3.8 State space explosion and advanced numerical techniques

In principle, the infinitesimal generator matrix Q corresponding to a Ca^{2+} release site composed of N instantaneously coupled M -state channels can be constructed element-by-element using Eqns (2.40) and (2.41). In this way, release

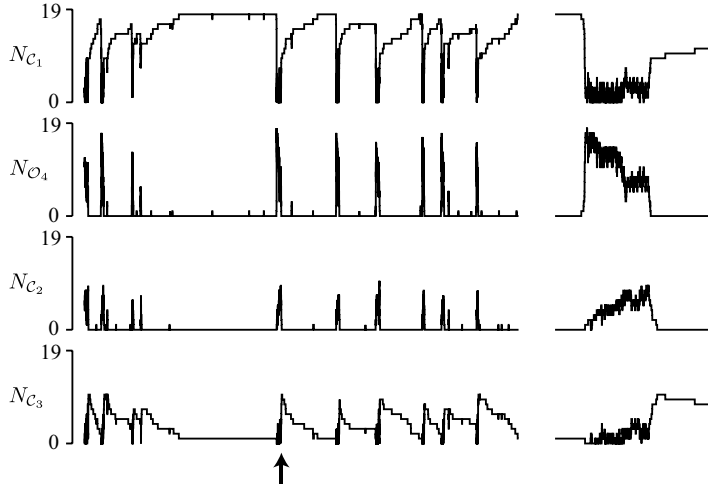


FIG. 2.8: Representative Ca^{2+} release site simulation using 19 four-state channels with Ca^{2+} -dependent inactivation (Fig. 2.2d) arranged on a hexagonal lattice shows robust Ca^{2+} puff/sparks. The time evolution of the number of closed (N_{C_1}), open (N_{O_4}), and inactivated (N_{C_2} , N_{C_3}) channels is shown. Total time is 2 s (first column) and the arrow indicates a 50 ms epoch expanded in the second column. As in Fig. 2.7 channels are coupled using the excess buffer approximation (Smith *et al.*, 2001). Reproduced with permission from Nguyen, Mathias, and Smith (2005).

site statistics such as the distribution of the number of open channels can be calculated directly using methods similar to those presented in Section 2.2.1 in the context of single channel models. However, in practice such direct calculations may be unfeasible because the infinitesimal generator matrix for a release site with M^N states may be too large to be stored in system memory. While the stationary distribution and other puff/spark statistics can always be estimated from Monte Carlo simulations, this is an inefficient approach when the convergence of the occupation measures to the limiting probability distribution is slow. Interestingly, excessive memory requirements and slow convergence can be addressed using a Kronecker representation of the Q -matrix for Ca^{2+} release site models – a stochastic automata network (SAN) descriptor – in conjunction with iterative numerical techniques (Nguyen *et al.*, 2005, DeRemigio *et al.*, 2008b).

In the case of a Ca^{2+} release site composed of N M -state channels coupled via the buffered diffusion of intracellular Ca^{2+} , the SAN descriptor takes the form

$$Q^{(N)} = Q_-^{(N)} + Q_+^{(N)} \quad (2.52)$$

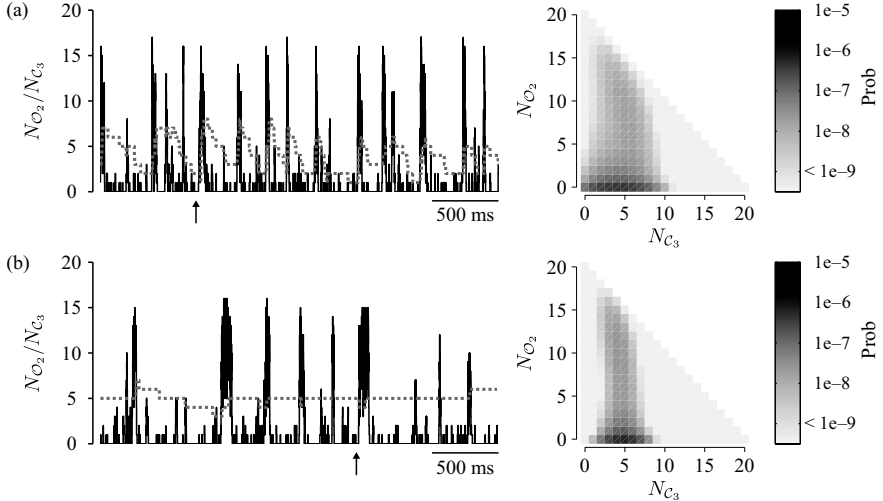


FIG. 2.9: Calcium inactivation can facilitate puff/spark termination in two distinct ways. (a) Ca^{2+} release site simulation with 20 mean-field coupled (see Section 2.3.10) three-state channels and moderately fast Ca^{2+} inactivation showing puff/spark termination facilitated by the recruitment of inactivated channels during puff/spark events. The left panel shows the number of open ($N_{\mathcal{O}_2}$, black line) and inactivated ($N_{\mathcal{C}_3}$, grey dashed line) channels. The right panel shows the steady-state probability of the 231 release site configurations ($N_{\mathcal{C}_1}, N_{\mathcal{O}_2}, N_{\mathcal{C}_3}$), where it is understood that $N_{\mathcal{C}_1} = 20 - N_{\mathcal{O}_2} - N_{\mathcal{C}_3}$. (b) When the kinetics of Ca^{2+} inactivation are reduced ten-fold without changing the affinity of Ca^{2+} inactivation or the Ca^{2+} coupling strength, the number of inactivated channels ($N_{\mathcal{C}_3}$) is nearly constant and puff/sparks terminate without additional recruitment of inactivated channels. Reproduced with permission from Groff and Smith (2008a).

where

$$Q_-^{(N)} = \bigoplus_{n=1}^N K_- = \sum_{n=1}^N I^{(n-1)} \otimes K_- \otimes I^{(N-n)}, \quad (2.53)$$

$$Q_+^{(N)} = c_\infty K_+^{(N)} + \sum_{i,j=1}^N c_{ij} (Y_{ij}^1 Z_{ij}^1 \otimes \cdots \otimes Y_{ij}^N Z_{ij}^N), \quad (2.54)$$

and

$$Y_{ij}^n = \begin{cases} I_{\mathcal{O}} & \text{for } i = n \\ I & \text{otherwise,} \end{cases} \quad Z_{ij}^n = \begin{cases} K_+ & \text{for } j = n \\ I & \text{otherwise.} \end{cases} \quad (2.55)$$

In these expressions, the superscripted quantities in parentheses such as (N) in $Q^{(N)}$ indicate matrix size, $I^{(n)}$ is an identity matrix of size M^n , $I_{\mathcal{O}} = \text{diag}\{\mathbf{e}_{\mathcal{O}}\}$, $\mathbf{e}_{\mathcal{O}}$ is a $M \times 1$ vector indicating open states of the single channel model, $K_+^{(N)} = \oplus_{n=1}^N K_+$, K_{\pm} define the single channel model (Eqn (2.39)), and \otimes and \oplus are the Kronecker product and sum operators (Graham, 1981, van Loan, 2000, Langville and Stewart, 2004). Note that in Eqns (2.52)–(2.55) the Ca^{2+} -dependent and -independent transition rates are separated, and each term in Eqn (2.54) corresponds to Ca^{2+} from channel i potentially influencing the gating of channel j . However, combining Eqns (2.52)–(2.54) and simplifying, $Q^{(N)}$ can be written more compactly as

$$Q^{(N)} = \sum_{i,j=1}^N X_{ij}^1 \otimes \cdots \otimes X_{ij}^N, \quad (2.56)$$

$$X_{ii}^n = \begin{cases} A_d & \text{for } i = n \\ I & \text{otherwise,} \end{cases} \quad \text{and} \quad X_{ij}^n = \begin{cases} I_{\mathcal{O}} & \text{for } i = n \\ A_{ij} & \text{for } j = n \\ I & \text{otherwise} \end{cases} \quad \text{for } i \neq j$$

where $A_d = K_- + c_{\infty}K_+ + c_d I_{\mathcal{O}} K_+$, and $A_{ij} = c_{ij}K_+$. Note that all states of the expanded Markov chain $Q^{(N)}$ are reachable, the matrices I , $I_{\mathcal{O}}$, A_d , A_{ij} , and X_{ij}^n are all $M \times M$, and $2N^2 - N$ of the N^3 matrices denoted by X_{ij}^n are *not* identity matrices.

To give just one example of how the SAN descriptor (Eqn (2.56)) might be employed, consider that the stationary distribution of the Ca^{2+} release site model (Eqn (2.4)) can now be found using an iterative eigenvector solver such as restarted Arnoldi (part of MATLAB's `eigs` command) that requires only the black-box vector-matrix product

$$\mathbf{y} \leftarrow \mathbf{x} + \mathbf{x}Q^{(N)}/\lambda$$

for arbitrary \mathbf{x} (cf. Eqn (2.12)), which can be efficiently calculated using Kronecker identities (Fernandes *et al.*, 1998). Thus, $\bar{\pi}^{(N)}$ solving

$$\bar{\pi}^{(N)} \left(I^{(N)} + Q^{(N)}/\lambda \right) = \bar{\pi}^{(N)}$$

subject to $\bar{\pi}^{(N)} \mathbf{e}^{(N)} = 1$ can be found without forming the $M^N \times M^N$ generator matrix $Q^{(N)}$. For further discussion see DeRemigio *et al.* (2008b).

2.3.9 Use of release site symmetries for model reduction

Much of the complexity of the Markov chain models of puff/sparks discussed above is due to the detailed account of release site ultrastructure represented by the elements of the Ca^{2+} coupling matrix C and allosteric adjacency matrix A

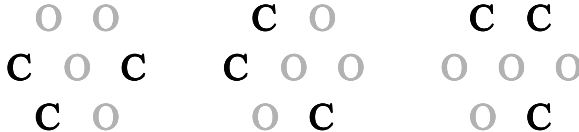


FIG. 2.10: Three configurations of a Ca^{2+} release site composed of seven two-state channels that can be lumped due to the rotational and reflectional symmetry of release site ultrastructure.

(Sections 2.3.2 and 2.3.3). While it is possible to use iterative numerical techniques that leverage the Kronecker structure of the infinitesimal generator matrix Q for a release site composed of N spatially distinguishable M -state channels (Section 2.3.8), direct calculations can often be simplified by performing a contraction of Q that lumps release site configurations based on rotational and/or reflectional symmetry of the release site ultrastructure (cf. Fig. 2.4a and b).

Figure 2.10 shows three configurations of a Ca^{2+} release site composed of seven two-state channels. While the spatial arrangement of four open and three closed channels is unique in each configuration, the strength of Ca^{2+} coupling between any two channels depends only on the distance between them (Eqn (2.45)) and, consequently, these three configurations are equivalent. In fact, due to the reflectional symmetry and six-fold rotational symmetry of the hexagonal lattice, there are 12 unique configurations with three open channels that belong to this symmetry group, and all the corresponding elements of the Q -matrix may be lumped without approximation as discussed in Section 2.2.5. That is, after constructing an M^N -by- \hat{M} collector matrix V (Eqn (2.23)) that maps each of the M^N configurations of the full model to one of \hat{M} unique symmetry groups, the lumpability condition given by Eqn (2.25) is satisfied and the reduced model is given by Eqn (2.22). Note that the distributor matrix in this case is given by Eqn (2.24) where the elements of each s_i are uniformly distributed (i.e. $s_i = e_i^T / e_i^T e_i$), because all the elements of each π_i are identical.

2.3.10 Mean-field simulations of calcium release sites

Because an accurate account of the spatial relationship between channels adds to the complexity of Ca^{2+} release site simulations, a natural question is whether the precise location of channels is important. Indeed, in many situations it may be appropriate to assume ‘mean-field’ coupling where channels interact via Ca^{2+} and allosteric interactions as if they were spatially indistinguishable. While a model of N spatially distinguishable M -state channels has M^N unique configurations, a mean-field formulation that identifies release site configurations by the number of channels in each state without regard for channel position has just $(N + M - 1)!/N!/(M - 1)!$ configurations, one for each way N channels can be assigned to M states.

Each configuration of a mean-field Ca^{2+} release site model can be expressed as a vector of the form (N_1, N_2, \dots, N_M) where N_m is the number of channels

in state m , $1 \leq m \leq M$, and $\sum_{m=1}^M N_m = N$. If the current state of the release site is (N_1, N_2, \dots, N_M) and a valid destination state can be entered by a channel making an $i \rightarrow j$ transition, the transition rate is $N_i k_{ij}^-$ or $N_i k_{ij}^+ c^\eta$ where N_i is the number of channels in state i and k_{ij}^\pm are the transition rates of the single channel model. Extensive parameter studies using model release sites with irregular ultrastructure (Fig. 2.4c) have shown that the validity of mean-field simulations can be enhanced by maintaining a distinction between each channel's substantial influence on its own stochastic gating and the collective contribution of elevated $[Ca^{2+}]$ from neighbouring open channels (Nguyen *et al.*, 2005, DeRemigio *et al.*, 2008a). That is, when employing a mean-field formulation, it is best if c is given by

$$c = \begin{cases} c_\infty + N_{\mathcal{O}} c_* & \text{for } i \text{ closed} \\ c_\infty + c_d + (N_{\mathcal{O}} - 1)c_* & \text{for } i \text{ open} \end{cases} \quad (2.57)$$

where i is the origin state of the channel making the transition, c_d is the previously discussed domain $[Ca^{2+}]$, that is, the self-induced increase in $[Ca^{2+}]$ due to an open channel, c_∞ is the background $[Ca^{2+}]$, $N_{\mathcal{O}}$ is the number of open channels in the origin release site configuration, and c_* is the average of the off-diagonal elements of the Ca^{2+} coupling matrix $C = (c_{nm})$, that is,

$$c_* = \frac{1}{N(N-1)} \sum_n \sum_{m \neq n} c_{nm} \quad \text{and} \quad c_d = c_{nn}. \quad (2.58)$$

Simulations have also demonstrated the validity of mean-field allosteric coupling using transition rates of the form $N_i k_{ij}^- \chi$ and $N_i k_{ij}^+ c^\eta \chi$ where the χ are 'coupling factors' of the form (Sobie *et al.*, 2002, Groff and Smith, 2008b)

$$\chi = \exp \left[-\nu_{ij} a_* \sum_{k=1}^M (N_k - \delta_{ki}) (\varepsilon_{kj} - \varepsilon_{ki}) \right] \quad (2.59)$$

where i and j are the origin and destination state of the channel making a transition, k is an index over channel states, ε_{kj} and ε_{ki} are elements of the allosteric energy matrix \mathcal{E} (Section 2.3.3), ν_{ij} is the previously encountered coefficient that partitions allosteric coupling between forward and reverse transitions between Ca^{2+} release site configurations ($0 \leq \nu_{ij} \leq 1$ as in Eqn (2.50)), δ_{ki} is the Kronecker delta function, and a_* is the average allosteric connectivity experienced by channels, that is,

$$a_* = \frac{1}{N(N-1)} \sum_n \sum_{m \neq n} a_{nm} \quad (2.60)$$

where $A = (a_{nm})$ is the allosteric connectivity matrix (Eqn (2.48)). For details see Groff and Smith (2008b).

2.3.11 Multiscale models of local and global Ca^{2+} signals

While deterministic equations are sufficient to represent whole cell phenomena that involve the gating of a large number of globally coupled ion channels, the stochastic modelling approaches discussed in this chapter are essential to simulate spatially localized subcellular phenomena involving a small number of channels such as Ca^{2+} puffs in immature *Xenopus laevis* oocytes or Ca^{2+} sparks in cardiac myocytes (Cheng *et al.*, 1993, Yao *et al.*, 1995, Niggli and Shirokova, 2007). These techniques are also applicable to neuronal simulations in which localized elevations of intracellular Ca^{2+} often play an important role in information processing (Berridge, 1998). For example, Purkinje neurons of the cerebellum have arborous dendrites that integrate synaptic inputs from thousands of afferent axons. Many of these synapses occur on small protruding sections of the dendritic membrane referred to as dendritic spines. Because they contain a projection of the endoplasmic reticulum membrane on which IP_3Rs are expressed, input specific Ca^{2+} microdomains may be established within the relatively isolated cytosol of dendritic spines. These localized Ca^{2+} microdomains arise due to the stochastic gating of a relatively small number of IP_3Rs and may significantly affect neuronal computation by allowing spines to function as coincidence detectors (Sharp *et al.*, 1993).

Interestingly, whole-cell models of Ca^{2+} responses in some non-neuronal cells require an accurate account of the underlying localized stochastic events from which global events emerge to reproduce important aspects of cellular physiology. For example, models of excitation–contraction coupling in ventricular cardiac myocytes that assume deterministic ‘continuously stirred’ cytosolic and endoplasmic reticulum Ca^{2+} pools readily exhibit the phenomenon of high-gain release, in which a small influx of Ca^{2+} via L-type channels recruits a much larger release of Ca^{2+} from the SR via RyRs. However, such models are unable to reproduce the phenomenon of graded release, in which the amount of released Ca^{2+} is a gradually increasing function of the amount of trigger Ca^{2+} that enters via L-type channels (Hilgemann and Noble, 1987, Stern, 1992). In contrast to common pool models, local control models of excitation–contraction coupling that include a large number of Ca^{2+} release units each composed of stochastically gating channels are able to reproduce high-gain graded Ca^{2+} release (Stern, 1992, Rice *et al.*, 1999, Sobie *et al.*, 2002, Greenstein and Winslow, 2002, Williams *et al.*, 2007, Williams *et al.*, 2008). In an analogous fashion, realistic models of global Ca^{2+} signalling and membrane excitability in neurons may often require an accurate accounting of local Ca^{2+} signals mediated by the collective gating of clusters of Ca^{2+} -regulated Ca^{2+} channels.

Acknowledgments

This material is based upon work supported by the National Science Foundation under Grants No. 0133132 and 0443843. The authors acknowledge stimulating conversations with Peter Kemper.

References

- Allbritton, N. L., Meyer, T., and Stryer, L. (1992). Range of messenger action of calcium ion and inositol 1,4,5-trisphosphate. *Science*, **258**(5089), 1812–1815.
- Atri, A., Amundson, J., Clapham, D., and Sneyd, J. (1993). A single-pool model for intracellular calcium oscillations and waves in the *Xenopus laevis* oocyte. *Biophys. J.*, **65**(4), 1727–1739.
- Ball, F. G., Milne, R. K., and Yeo, G. F. (2000). Stochastic models for systems of interacting ion channels. *IMA Journal of Mathematics Applied in Medicine and Biology*, **17**(3), 263–293.
- Ball, F. G. and Sansom, M. S. (1989). Ion-channel gating mechanisms: model identification and parameter estimation from single channel recordings. *Proc. R Soc. Lond., B, Biol. Sci.*, **236**(1285), 385–416.
- Berridge, M. J. (1993, Jan). Inositol trisphosphate and calcium signalling. *Nature*, **361**(6410), 315–325.
- Berridge, M. J. (1997, Mar). Elementary and global aspects of calcium signalling. *J. Physiol. (Lond.)*, **499**, 291–306.
- Berridge, M. J. (1998, Aug). Neuronal calcium signaling. *Neuron*, **21**(1), 13–26.
- Berridge, M. J. (2006, Oct). Calcium microdomains: organization and function. *Cell Calcium*, **40**(5-6), 405–412.
- Bers, D. M. (2002, Jan). Cardiac excitation-contraction coupling. *Nature*, **415**(6868), 198–205.
- Bezprozvanny, I. and Ehrlich, B. E. (1994, Nov). Inositol (1,4,5)-trisphosphate (InsP_3)-gated Ca channels from cerebellum: conduction properties for divalent cations and regulation by intraluminal calcium. *J. Gen. Physiol.*, **104**(5), 821–856.
- Bezprozvanny, I., Watras, J., and Ehrlich, B. E. (1991, Jun). Bell-shaped calcium-response curves of $\text{Ins}(1,4,5)\text{P}_3$ - and calcium-gated channels from endoplasmic reticulum of cerebellum. *Nature*, **351**(6329), 751–754.
- Bruno, W. J., Yang, J., and Pearson, J. E. (2005, May). Using independent open-to-closed transitions to simplify aggregated Markov models of ion channel gating kinetics. *Proc. Natl. Acad. Sci. U.S.A.*, **102**(18), 6326–6331.
- Caldwell, J. H. (2000, Apr). Clustering of sodium channels at the neuromuscular junction. *Microsc. Res. Tech.*, **49**(1), 84–89.
- Cheng, H., Lederer, W. J., and Cannell, M. B. (1993, Oct). Calcium sparks: elementary events underlying excitation-contraction coupling in heart muscle. *Science*, **262**(5134), 740–744.
- Chen-Izu, Y., McCulle, S. L., Ward, C. W., Soeller, C., Allen, B. M., Rabang, C., Cannell, M. B., Balke, C. W., and Izu, L. T. (2006, Jul). Three-dimensional distribution of ryanodine receptor clusters in cardiac myocytes. *Biophys J.*, **91**(1), 1–13.
- Colledge, M and Froehner, S C (1998, Jun). Signals mediating ion channel clustering at the neuromuscular junction. *Curr Opin Neurobiol*, **8**(3), 357–363.
- Colquhoun, D. and Hawkes, A. G. (1995). A Q-matrix cookbook: how to write only one program to calculate the single-channel and macroscopic

- predictions for any kinetic mechanism. In *Single-Channel Recording* (ed. B. Sakmann and E. Neher). Plenum Press, New York, pp. 589–633.
- Colquhoun, D., Hawkes, A., and Srodzinski, K. (1996, Jan). Joint Distributions of Apparent Open and Shut Times of Single-Ion Channels and Maximum Likelihood Fitting of Mechanisms. *Philosophical Transactions of the Royal Society of London Series A – Mathematical Physical and Engineering Sciences*, **354**(1718), 2555–2590.
- DeRemigio, H., Groff, Jr., and Smith, G. D. (2008a). Calcium release site ultrastructure and the dynamics of puffs and sparks. *Math. Med. and Biol.*, **25**, 65–85.
- DeRemigio, H., Kemper, P., LaMar, M. D., and Smith, G. D. (2008b). Markov chain models of coupled intracellular calcium channels: Kronecker structured representations and benchmark stationary distribution calculations. *Physical Biology*, **5**, 36003.
- DeRemigio, H. and Smith, G. D. (2005, Aug). The dynamics of stochastic attrition viewed as an absorption time on a terminating Markov chain. *Cell Calcium*, **38**(2), 73–86.
- Edeson, R. O., Ball, F. G., Yeo, G. F., Milne, R. K., and Davies, S. S. (1994, Jan). Model properties underlying non-identifiability in single channel inference. *Proceedings of the Royal Society of London Series B – Biological Sciences*, **255**(1342), 21–29.
- Fabiato, A. (1985, Feb). Time and calcium dependence of activation and inactivation of calcium-induced release of calcium from the sarcoplasmic reticulum of a skinned canine cardiac Purkinje cell. *J. Gen. Physiol.*, **85**(2), 247–289.
- Fernandes, P., Plateau, B., and Stewart, W. J. (1998). Efficient descriptor-vector multiplications in stochastic automata networks. *J. ACM*, **45**(3), 381–414.
- Fill, M. and Copello, J. A. (2002, Sep). Ryanodine receptor calcium release channels. *Physiol. Rev.*, **82**(4), 893–922.
- Fill, M. (2003). Mechanisms that turn-off intracellular calcium release channels. *Front. Biosci.*, **8**, d46–d54.
- Fox, R. and Lu, Y. (1994, Jan). Emergent collective behavior in large numbers of globally coupled independently stochastic ion channels. *Physical Review E*, **49**(4), 3421–3431.
- Franzini-Armstrong, C., Protasi, F., and Ramesh, V. (1999a, Dec). Comparative ultrastructure of Ca^{2+} release units in skeletal and cardiac muscle. *Ann. N. Y. Acad. Sci.*, **853**, 20–30.
- Franzini-Armstrong, C., Protasi, F., and Ramesh, V. (1999b, Sep). Shape, size, and distribution of Ca^{2+} release units and couplons in skeletal and cardiac muscles. *Biophys. J.*, **77**(3), 1528–1539.
- Gardiner, C. W. (2004). *Handbook of Stochastic Methods for Physics, Chemistry, and the Natural Sciences* (3rd edn). Springer, Berlin.
- Gillespie, D. T. (1976, Dec). A general method for numerically simulating the stochastic time evolution of coupled chemical reactions. *Journal of Computational Physics*, **22**, 403–434.

- Graham, A. (1981). *Kronecker Products and Matrix Calculus with Applications*. John Wiley and Sons, New York.
- Greenstein, J. L. and Winslow, R. L. (2002, Dec). An integrative model of the cardiac ventricular myocyte incorporating local control of Ca^{2+} release. *Biophys. J.*, **83**(6), 2918–2945.
- Groff, J. R. and Smith, G. D. (2008a). Calcium-dependent inactivation and the dynamics of calcium puffs and sparks. *J. Theor. Biol.*, **253**, 483–499.
- Groff, J. R. and Smith, G. D. (2008b). Ryanodine receptor allosteric coupling and the dynamics of calcium sparks. *Biophys. J.*, **95**, 135–154.
- Györke, S. and Fill, M. (1993, May). Ryanodine receptor adaptation: control mechanism of Ca^{2+} -induced Ca^{2+} release in heart. *Science*, **260**(5109), 807–809.
- Hagar, R. E., Burgstahler, A. D., Nathanson, M. H., and Ehrlich, B. E. (1998, Nov). Type III InsP₃ receptor channel stays open in the presence of increased calcium. *Nature*, **396**(6706), 81–84.
- Hilgemann, D. W. and Noble, D. (1987, Mar). Excitation-contraction coupling and extracellular calcium transients in rabbit atrium: reconstruction of basic cellular mechanisms. *Proc. R. Soc. Lond. B, Biol. Sci.*, **230**(1259), 163–205.
- Hill, T. L. (1977). *Free Energy Transduction in Biology: The Steady-State Kinetic and Thermodynamic Formalism*. Academic Press, New York.
- Hill, T. L. (1989). *Free Energy Transduction and Biochemical Cycle Kinetics*. Springer-Verlag, New York.
- Hille, B. (2001). *Ionic Channels of Excitable Membranes* (3rd edn). Sinauer Associates, Sunderland, MA.
- Hinch, R., Greenstein, J. L., and Winslow, R. L. (2006, Jan). Multi-scale models of local control of calcium induced calcium release. *Prog. Biophys. Mol. Biol.*, **90**(1-3), 136–150.
- Hodgkin, A. L. and Huxley, A. F. (1952, Aug). A quantitative description of membrane current and its application to conduction and excitation in nerve. *J. Physiol. (Lond.)*, **117**(4), 500–544.
- Hodgson, M. and Green, P. J. (1999, Jan). Bayesian choice among Markov models of ion channels using Markov chain Monte Carlo. *Proceedings of the Royal Society of London Series A – Mathematical Physical and Engineering Sciences*, **455**, 3425–3448.
- Huertas, M. A. and Smith, G. D. (2007, May). The dynamics of luminal depletion and the stochastic gating of Ca^{2+} -activated Ca^{2+} channels and release sites. *J. Theor. Biol.*, **246**(2), 332–354.
- Jafri, M., Rice, J., and Winslow, R. (1998, Jan). Cardiac Ca^{2+} dynamics: the roles of ryanodine receptor adaptation and sarcoplasmic reticulum load. *Biophysical Journal*, **74**(3), 1149–1168.
- Kaftan, E. J., Ehrlich, B. E., and Watras, J. (1997, Nov). Inositol 1,4,5-trisphosphate (InsP₃) and calcium interact to increase the dynamic range of InsP₃ receptor-dependent calcium signaling. *J. Gen. Physiol.*, **110**(5), 529–538.

- Keizer, J. E. (1987). *Statistical Thermodynamics of Nonequilibrium Processes*. Springer Verlag, Berlin.
- Keizer, J., Li, Y. X., Stojilković, S., and Rinzel, J. (1995, Aug). InsP₃-induced Ca²⁺ excitability of the endoplasmic reticulum. *Mol. Biol. Cell.*, **6**(8), 945–951.
- Keleshian, A. M., Edeson, R. O., Liu, G. J., and Madsen, B. W. (2000, Jan). Evidence for cooperativity between nicotinic acetylcholine receptors in patch clamp records. *Biophys. J.*, **78**(1), 1–12.
- Kienker, P. (1989, Apr). Equivalence of aggregated Markov models of ion-channel gating. *Proc. R Soc. Lond., B, Biol. Sci.*, **236**(1284), 269–309.
- Lai, F. A., Misra, M., Xu, L., Smith, H. A., and Meissner, G. (1989, Oct). The ryanodine receptor-Ca²⁺ release channel complex of skeletal muscle sarcoplasmic reticulum. Evidence for a cooperatively coupled, negatively charged homotetramer. *J. Biol. Chem.*, **264**(28), 16776–16785.
- Langville, A. N. and Stewart, W. J. (2004). The Kronecker product and stochastic automata networks. *J. Comput. Appl. Math.*, **167**(2), 429–447.
- Larget, B. (1998, Jan). A canonical representation for aggregated Markov processes. *J. Appl. Probab.*, **35**, 313–324.
- Lukyanenko, V., Wiesner, T. F., and Györke, S. (1998, May). Termination of Ca²⁺ release during Ca²⁺ sparks in rat ventricular myocytes. *J. Physiol. (Lond.)*, **507**, 667–677.
- Mak, D. O. and Foskett, J. K. (1997, May). Single-channel kinetics, inactivation, and spatial distribution of inositol trisphosphate (IP₃) receptors in Xenopus oocyte nucleus. *J. Gen. Physiol.*, **109**(5), 571–587.
- Marland, E. S. and Keizer, J. (2002). Transporters and pumps. In *Computational Cell Biology* (ed. C. Fall, E. Marland, J. Wagner, and J. Tyson), Springer-Verlag, pp. 53–76.
- Marx, S. O., Gaburjakova, J., Gaburjakova, M., Henrikson, C., Ondrias, K., and Marks, A. R. (2001, Jun). Coupled gating between cardiac calcium release channels (ryanodine receptors). *Circ. Res.*, **88**(11), 1151–1158.
- Marx, S. O., Ondrias, K., and Marks, A. R. (1998, Aug). Coupled gating between individual skeletal muscle Ca²⁺ release channels (ryanodine receptors). *Science*, **281**(5378), 818–821.
- Mazzag, B., Tignanelli, C. J., and Smith, G. D. (2005, Apr). The effect of residual Ca²⁺ on the stochastic gating of Ca²⁺-regulated Ca²⁺ channel models. *J. Theor. Biol.*, **235**(1), 121–150.
- Meyer, C. D. (1989). Stochastic complementation, uncoupling markov chains, and the theory of nearly reducible systems. *SIAM Review*, **31**(2), 240–272.
- Milescu, L., Akk, G., and Sachs, F. (2005, Jan). Maximum likelihood estimation of ion channel kinetics from macroscopic currents. *Biophysical Journal*, **88**(4), 2495–2515.
- Moraru, I. I., Kaftan, E. J., Ehrlich, B. E., and Watras, J. (1999, Jun). Regulation of type 1 inositol 1,4,5-trisphosphate-gated calcium channels by InsP₃ and calcium: Simulation of single channel kinetics based on ligand binding and electrophysiological analysis. *J. Gen. Physiol.*, **113**(6), 837–849.

- Morris, C. and Lecar, H. (1981, Jul). Voltage oscillations in the barnacle giant muscle fiber. *Biophys. J.*, **35**(1), 193–213.
- Naraghi, M. and Neher, E. (1997, Sep). Linearized buffered Ca^{2+} diffusion in microdomains and its implications for calculation of $[\text{Ca}^{2+}]$ at the mouth of a calcium channel. *J. Neurosci.*, **17**(18), 6961–6973.
- Naundorf, B., Wolf, F., and Volgshev, M. (2006, Apr). Unique features of action potential initiation in cortical neurons. *Nature*, **440**(7087), 1060–1063.
- Neher, E. (1998, Jan). Usefulness and limitations of linear approximations to the understanding of Ca^{++} signals. *Cell Calcium*, **24**(5-6), 345–357.
- Nguyen, V., Mathias, R., and Smith, G. D. (2005, Apr). A stochastic automata network descriptor for Markov chain models of instantaneously coupled intracellular Ca^{2+} channels. *Bull. Math. Biol.*, **67**(3), 393–432.
- Nicola, V. (1998). Lumping in markov reward processes. Technical report, RC14719, IBM Thomas Watson Research Centre, P.O. Box 704, Yorktown Heights, NY 10598.
- Niggli, E. and Shirokova, N. (2007, Jan). A guide to sparkology: the taxonomy of elementary cellular Ca^{2+} signaling events. *Cell Calcium*, **42**(4-5), 379–387.
- Norris, J. R. (1997). *Markov Chains*. Cambridge University Press, Cambridge.
- Ogden, D. C., Colquhoun, D., and Marshall, C. G. (1987). Activation of nicotinic ion channels by acetylcholine analogues. In *Cellular and Molecular Basis of Cholinergic Function* (ed. M. Dowdall and J. Hawthorn). John Wiley, New York, pp. 133–151.
- Ramos-Franco, J., Caenepeel, S., Fill, M., and Mignery, G. (1998, Dec). Single channel function of recombinant type-1 inositol 1,4,5-trisphosphate receptor ligand binding domain splice variants. *Biophys. J.*, **75**(6), 2783–2793.
- Rasband, M. N. and Trimmer, J. S. (2001, Aug). Developmental clustering of ion channels at and near the node of Ranvier. *Dev. Biol.*, **236**(1), 5–16.
- Rice, J. J., Jafri, M. S., and Winslow, R. L. (1999, Oct). Modeling gain and gradedness of Ca^{2+} release in the functional unit of the cardiac diadic space. *Biophys. J.*, **77**(4), 1871–1884.
- Roberts, W. M., Jacobs, R. A., and Hudspeth, A. J. (1990, Nov). Colocalization of ion channels involved in frequency selectivity and synaptic transmission at presynaptic active zones of hair cells. *J. Neurosci.*, **10**(11), 3664–3684.
- Ross, S. (1988). *A First Course in Probability*. Macmillan Publishing Company, New York.
- Sakmann, B. and Neher, E. (ed.) (1995). *Single-Channel Recording* (2nd edn). Springer, New York.
- Serysheva, I. I. (2004). Structural insights into excitation-contraction coupling by electron cryomicroscopy. *Biochemistry Mosc.*, **69**(11), 1226–1232.
- Sharp, A. H., McPherson, P. S., Dawson, T. M., Aoki, C., Campbell, K. P., and Snyder, S. H. (1993, Jul). Differential immunohistochemical localization of inositol 1,4,5-trisphosphate- and ryanodine-sensitive Ca^{2+} release channels in rat brain. *J. Neurosci.*, **13**(7), 3051–3063.

- Sherman, A., Keizer, J., and Rinzel, J. (1990, Oct). Domain model for Ca²⁺(+)-inactivation of Ca²⁺ channels at low channel density. *Biophys. J.*, **58**(4), 985–995.
- Smith, G. D. (2002a). An extended DeYoung-Keizer-like IP₃ receptor model that accounts for domain Ca²⁺-mediated inactivation. In *Recent Research Developments in Biophysical Chemistry, Vol. II* (ed. C. Condat and A. Baruzzi). Research Signpost, pp. 37–55.
- Smith, G. D. (2002b). Modeling the stochastic gating of ion channels. In *Computational Cell Biology* (ed. C. Fall, E. Marland, J. Wagner, and J. Tyson). Springer-Verlag, New York, pp. 289–323.
- Smith, G. D., Dai, L., Miura, R., and Sherman, A. (2001, Aug). Asymptotic analysis of buffered calcium diffusion near a point source. *SIAM Journal of Applied Mathematics*, **61**(5), 1816–1838.
- Sobie, E. A., Dilly, K. W., dos Santos Cruz, J., Lederer, W. J., and Jafri, M. S. (2002, Jun). Termination of cardiac Ca²⁺ sparks: an investigative mathematical model of calcium-induced calcium release. *Biophys. J.*, **83**(1), 59–78.
- Stern, M. D. (1992, Aug). Theory of excitation-contraction coupling in cardiac muscle. *Biophys. J.*, **63**(2), 497–517.
- Stern, M. D. and Cheng, H. (2004, Apr). Putting out the fire: what terminates calcium-induced calcium release in cardiac muscle? *Cell Calcium*, **35**(6), 591–601.
- Stern, M. D., Song, L. S., Cheng, H., Sham, J. S., Yang, H. T., Boheler, K. R., and Rios, E. (1999, Mar). Local control models of cardiac excitation-contraction coupling. A possible role for allosteric interactions between ryanodine receptors. *J. Gen. Physiol.*, **113**(3), 469–489.
- Stewart, W. J. (1994). *Introduction to the Numerical Solution of Markov Chains*. Princeton University Press, Princeton.
- Sun, X. P., Callamaras, N., Marchant, J. S., and Parker, I. (1998, Jun). A continuum of InsP₃-mediated elementary Ca²⁺ signalling events in Xenopus oocytes. *J. Physiol. (Lond.)*, **509**, 67–80.
- Swillens, S., Champeil, P., Combettes, L., and Dupont, G. (1998, Jul). Stochastic simulation of a single inositol 1,4,5-trisphosphate-sensitive Ca²⁺ channel reveals repetitive openings during 'blip-like' Ca²⁺ transients. *Cell Calcium*, **23**(5), 291–302.
- Tang, Y., Stephenson, J., and Othmer, H. (1996, Jan). Simplification and analysis of models of calcium dynamics based on IP₃-sensitive calcium channel kinetics. *Biophysical Journal*, **70**(1), 246–263.
- Vandenberg, C. A. and Bezanilla, F. (1991, Dec). A sodium channel gating model based on single channel, macroscopic ionic, and gating currents in the squid giant axon. *Biophys. J.*, **60**(6), 1511–1133.
- van Loan, C. F. (2000). The ubiquitous Kronecker product. *J. Comput. Appl. Math.*, **123**(1-2), 85–100.

- Wang, S.-Q., Stern, M. D., Rios, E., and Cheng, H. (2004, Mar). The quantal nature of Ca^{2+} sparks and in situ operation of the ryanodine receptor array in cardiac cells. *Proc. Natl. Acad. Sci. USA*, **101**(11), 3979–3984.
- Williams, G. S. B., Huertas, M. A., Sobie, E. A., Jafri, M. S., and Smith, G. D. (2008). Moment closure for local control models of Ca^{2+} -induced Ca^{2+} release in cardiac myocytes. *Biophys. J.*, **95**, 689–703.
- Williams, G. S. B., Huertas, M. A., Sobie, E. A., Jafri, M. S., and Smith, G. D. (2007, Jan). A probability density approach to modeling local control of calcium-induced calcium release in cardiac myocytes. *Biophys. J.*, **92**(7), 2311–2328.
- Yao, Y., Choi, J., and Parker, I. (1995, Feb). Quantal puffs of intracellular Ca^{2+} evoked by inositol trisphosphate in Xenopus oocytes. *J. Physiol. (Lond.)*, **482**, 533–553.
- Yeo, G. F., Milne, R. K., Edeson, R. O., and Madsen, B. W. (1988, Oct). Statistical inference from single channel records: two-state Markov model with limited time resolution. *Proc. R Soc. Lond., B, Biol. Sci.*, **235**(1278), 63–94.
- Yin, C.-C., Blayney, L. M., and Lai, F. A. (2005a, May). Physical coupling between ryanodine receptor-calcium release channels. *J. Mol. Biol.*, **349**(3), 538–546.
- Yin, C.-C., Han, H., Wei, R., and Lai, F. A. (2005b, Feb). Two-dimensional crystallization of the ryanodine receptor Ca^{2+} release channel on lipid membranes. *J. Struct. Biol.*, **149**(2), 219–224.
- Young, G. W. De. and Keizer, J. (1992, Oct). A single-pool inositol 1,4,5-trisphosphate-receptor-based model for agonist-stimulated oscillations in Ca^{2+} concentration. *Proc. Natl. Acad. Sci. USA*, **89**(20), 9895–9899.
- Zador, A. and Koch, C. (1994, Aug). Linearized models of calcium dynamics: formal equivalence to the cable equation. *J. Neurosci.*, **14**(8), 4705–4715.

STOCHASTIC DYNAMIC BIFURCATIONS AND EXCITABILITY

Nils Berglund and Barbara Gentz

3.1 Introduction

Neurons communicate through abrupt changes in the electrical potential across their cell membranes, which propagate along axons and transmit information to the synapses of other neurons. Many models for this so-called action-potential generation involve slow–fast dynamical systems. This is due to the fact that the involved variables (flows of ions such as sodium, calcium, and potassium) typically evolve on well-separated time-scales.

One of the first systems of ordinary differential equations describing action-potential generation is a four-dimensional system, which was introduced by Hodgkin and Huxley in 1952 (Hodgkin and Huxley, 1952). There exist various two-dimensional systems, obtained either by simplifying the Hodgkin–Huxley system and other models, or simply by fitting experimental data.

Example 3.1 (Morris–Lecar model) This model has been derived to describe giant barnacle (*Balanus Nubilus*) muscle fibres (Morris and Lecar, 1981). It can be written in the form

$$\begin{aligned}\varepsilon \dot{x} &= c_1 m^*(x)(1-x) + c_2 y(V_2 - x) + c_3(V_3 - x) , \\ \dot{y} &= (w^*(x) - y) \cosh\left(\frac{x - x_3}{x_4}\right) ,\end{aligned}\tag{3.1}$$

where ε is a small parameter, $m^*(x)$ and $w^*(x)$ are the ‘sigmoidal’ functions

$$\begin{aligned}m^*(x) &= \frac{1}{2} \left[1 + \tanh\left(\frac{x - x_1}{x_2}\right) \right] , \\ w^*(x) &= \frac{1}{2} \left[1 + \tanh\left(\frac{x - x_3}{x_4}\right) \right] ,\end{aligned}\tag{3.2}$$

and the c_i , V_i and x_i are constants.

Example 3.2 (FitzHugh–Nagumo model) This system, which was introduced by FitzHugh (1961) and Nagumo, Arimoto and Yoshizawa (1962) uses the model vector field

$$\begin{aligned}\varepsilon \dot{x} &= x - x^3 + y , \\ \dot{y} &= \alpha - \beta x - \gamma y ,\end{aligned}\tag{3.3}$$

where α , β and γ are constants, and ε is again a small parameter.

In this chapter, we discuss methods allowing one to describe quantitatively the effect of noise on slow–fast systems of the form

$$\begin{aligned}\varepsilon \dot{x} &= f(x, y), \\ \dot{y} &= g(x, y),\end{aligned}\tag{3.4}$$

where $f, g : \mathbb{R}^2 \rightarrow \mathbb{R}$ are (sufficiently smooth) functions. The parameter ε , describing the relative size of the two different time-scales, is assumed to be small, and hence x is called the *fast variable* and y is called the *slow variable*. For simplicity, in the following we will focus on situations where both x and y are one-dimensional. However, many ideas introduced in the $(1+1)$ -dimensional case extend to higher-dimensional systems (Berglund and Gentz, 2003, Berglund and Gentz, 2005).

3.1.1 Fast system, slow manifolds, and nullclines

Deterministic slow–fast systems of the form (3.4) are examples of singularly perturbed systems, which have been extensively studied (for overviews, see for instance the monographs Nayfeh 1973, O’Malley 1974, Wasow 1987, O’Malley 1991 and the proceedings Benoît 1991, Jones 1995).

One way to look at the slow–fast system (3.4) is to slow down time by a factor ε , yielding the equivalent system

$$\begin{aligned}x' &= f(x, y), \\ y' &= \varepsilon g(x, y),\end{aligned}\tag{3.5}$$

where the prime denotes the derivative with respect to the fast time t/ε . This system can then be considered as a small perturbation of the *fast system*, which is the one-parameter family of differential equations

$$x' = f(x, y_0),\tag{3.6}$$

in which y_0 plays the rôle of a fixed parameter. Being one-dimensional, the asymptotic dynamics of the fast system is typically quite simple: the orbits $x(t)$ converge to one of the equilibrium points of the vector field f , that is, points $x_i^*(y_0)$ such that $f(x_i^*(y_0), y_0) = 0$. Typically they converge to asymptotically stable equilibrium points, i.e. equilibrium points at which the derivative $\partial_x f(x_i^*(y_0), y_0)$ is strictly negative. In exceptional cases (bifurcations), orbits may also converge to points at which $\partial_x f(x_i^*(y_0), y_0)$ vanishes.

The slow–fast system (3.5) can be considered as a perturbation of the fast system (3.6) in which the parameter y moves slowly in time. One expects that orbits will tend to follow the slowly moving stable equilibrium points $x_i^*(y)$. This is why an important rôle is played by the so-called *slow manifolds*, that is, collections of equilibrium points of the fast system, also called *equilibrium branches* in this $(1+1)$ -dimensional context.

Another way to see this is by plotting (say) in the (y, x) -plane the *nullclines* of the system, that is, the curves on which $f(x, y) = 0$ or $g(x, y) = 0$. The curves $f(x, y) = 0$ being identical with the slow manifolds, we will henceforth reserve the name nullcline for the curves $g(x, y) = 0$ only. The orbits of the slow–fast system can be sketched with the help of the following rules (Fig. 3.1):

- The equilibrium branches $f(x, y) = 0$ separate the plane into regions where the fast variable x is either increasing or decreasing.
- Away from equilibrium branches, the slope of orbits is large (of order $1/\varepsilon$).
- Orbits which cross equilibrium branches, must cross those horizontally.
- The nullclines $g(x, y) = 0$ separate the plane into regions where the slow variable y is either increasing or decreasing.
- Orbits which cross nullclines, must cross those vertically.
- Intersections of equilibrium branches and nullclines are equilibrium points for the full slow–fast dynamics.

As can be seen in Fig. 3.1, these rules yield orbits tracking stable equilibrium branches with a small delay.

In the models discussed here, the slow manifold is typically S-shaped, that is, it consists of two stable branches and one unstable branch meeting at saddle-node bifurcation points. These points are responsible for the interesting behaviour observed in such systems.

For the FitzHugh–Nagumo model, the slow manifold is given by the equation

$$y = x^3 - x . \quad (3.7)$$

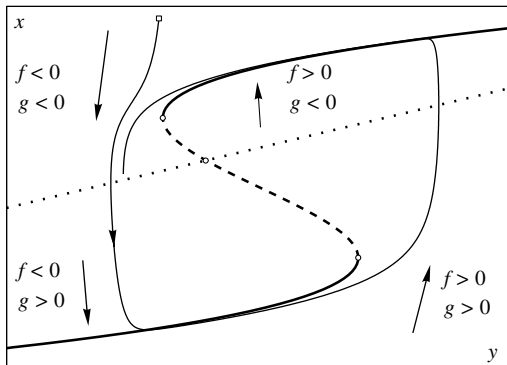


FIG. 3.1: Example of a slow–fast system with stable equilibrium branches (*full heavy curves*), unstable equilibrium branches (*broken heavy curves*), and nullcline (*dotted curve*). The light curve is an orbit of the system, with initial condition marked by a small square. In this example, the system admits a limit cycle.

Since

$$\partial_x f(x, y) = 1 - 3x^2, \quad (3.8)$$

branches lying in the region $|x| < 1/\sqrt{3}$ are unstable, while branches lying in the region $|x| > 1/\sqrt{3}$ are stable. The saddle-node bifurcation points are located at $(x, y) = \pm(1/\sqrt{3}, -2/3\sqrt{3})$, and the nullcline is simply the straight line

$$\beta x + \gamma y = \alpha. \quad (3.9)$$

For the Morris–Lecar model, the slow manifold is given by the equation

$$y = -\frac{c_1 m^*(x)(1-x) + c_3(V_3 - x)}{c_2(V_2 - x)}, \quad (3.10)$$

where the stability of its branches depends on the sign of

$$\partial_x f(x, y) = c_1 \partial_x m^*(x)(1-x) - [c_1 m^*(x) + c_2 y + c_3], \quad (3.11)$$

and the nullcline is given by

$$y = w^*(x). \quad (3.12)$$

We shall see that the dynamics depends strongly on where the nullclines lie relative to the equilibrium branches.

3.1.2 Models for noise

In the present context of continuous-time slow–fast systems, the simplest mathematical model that can be adopted for noise is additive Gaussian white noise, leading to a system of Itô stochastic differential equations (for the general theory of such equations, see e.g. Øksendal, 1985). This is the situation we will consider here. However, we will allow for the amplitude of the noise terms to depend on the state of the system.

The equations we will consider are thus of the form

$$\begin{aligned} dx(t) &= \frac{1}{\varepsilon} f(x(t), y(t)) dt + \frac{\sigma}{\sqrt{\varepsilon}} F(x(t), y(t)) dW_t^{(1)}, \\ dy(t) &= g(x(t), y(t)) dt + \sigma' G(x(t), y(t)) dW_t^{(2)}, \end{aligned} \quad (3.13)$$

where $W_t^{(1)}$ and $W_t^{(2)}$ are two independent Brownian motions, and $F, G : \mathbb{R}^2 \rightarrow \mathbb{R}$ are two given functions (always assumed to be sufficiently smooth). The small parameters σ and σ' measure the intensity of the two noise terms, in the following sense: During a small time interval Δt , the variance of the noise term for the slow variable grows like $(\sigma')^2 G(x(t), y(t))^2 \Delta t$, while the slow drift term moves the slow variable by $g(x(t), y(t)) \Delta t$ along the orbit. Similarly, the variance of the noise term for the fast variable grows like $\sigma^2 F(x(t), y(t))^2 \Delta t / \varepsilon$, while the fast drift term moves the fast variable by $f(x(t), y(t)) \Delta t / \varepsilon$ along the orbit.

The main effect of the noise terms will be that sample paths (which now depend on the realization of the noise) fluctuate in space. As we shall see, near stable equilibrium branches, the size of typical fluctuations is of order σ in the fast direction, and of order σ' in the slow direction, but it may become larger near bifurcation points. Furthermore, transitions between different regions of phase space, which are impossible in the deterministic case, become possible in the presence of additive noise. Typically, they occur very rarely, on time-scales which are exponentially long in $1/\sigma^2$. However, in the vicinity of bifurcation points, these noise-induced transitions may become much more frequent, thus yielding a dynamics which is qualitatively different from the deterministic one.

The main idea in order to describe the behaviour of solutions of the stochastic system (3.13) is to cut the phase space into several pieces, cf. Fig. 3.2, which are then analysed separately, using different methods. These pieces correspond to:

- the dynamics far from equilibrium branches;
- the dynamics near stable equilibrium branches;
- the dynamics near unstable equilibrium branches;
- the dynamics in the vicinity of bifurcation points.

Finally, the global picture is obtained by patching together the results of the different local analyses.

The first situation, namely the dynamics far from equilibrium branches, is quite easily dealt with: In the deterministic case, trajectories have large slopes of order $1/\varepsilon$, and thus usually approach equilibrium branches in a short time of order ε . A rough estimate (Berglund and Gentz, 2005, Theorem 3.1.11) suffices to show that in the stochastic case, sample paths are likely to do the same. We

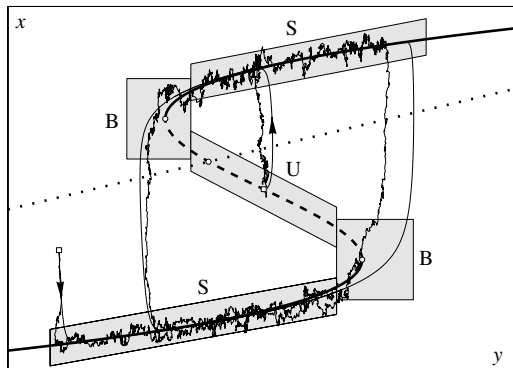


FIG. 3.2: A deterministic trajectory and a stochastic sample path of a slow–fast system. The dynamics is analysed by studying separately the behaviour near stable equilibrium branches (S), near unstable equilibrium branches (U), near bifurcation points (B), and in the remaining phase space, before patching together the results of the local analyses.

shall thus focus on the dynamics near equilibrium branches, by distinguishing stable branches, unstable branches, and bifurcation points.

Here we limit the discussion to saddle-node bifurcations, because they are the most frequent type of bifurcation in models for neuron dynamics as considered here. However, similar ideas can be applied to pitchfork bifurcations (Berglund and Gentz, 2002c), to (avoided) transcritical bifurcations (Berglund and Gentz, 2002d), and to Hopf bifurcations (Berglund and Gentz, 2005, Section 5.3.2).

Let us finally point out that one can be interested in various other types of noise, including

- the same noise acting on slow and fast variables;
- coloured noise, described by an Ornstein–Uhlenbeck process;
- other types of time-correlated noise, derived, for instance, from fractional Brownian motion;
- noise including jumps, derived, for instance, from Lévy processes.

The first two types of noise can be accommodated by an analogous framework, possibly by augmenting the dimension of phase space, see in particular (Berglund and Gentz, 2002a). The other two cases are at the moment much less well understood, and new methods are required in order to quantify their effect.

A major interest of a quantitative study of the effects of different types of noise on the dynamics is that it may help to select the best model for noise relevant in a particular system, by comparison with experimental results.

3.2 Stable equilibrium branches

3.2.1 Deterministic case

We consider general slow–fast systems of the form

$$\begin{aligned} \varepsilon \dot{x} &= f(x, y) , \\ \dot{y} &= g(x, y) , \end{aligned} \tag{3.14}$$

for functions $f, g : \mathbb{R}^2 \rightarrow \mathbb{R}$ (always assumed in the sequel to be as smooth as required by the Taylor expansions used in the analysis). We start by considering the dynamics near stable equilibrium branches, that is, collections of asymptotically stable equilibrium points of the associated fast system $\dot{x} = f(x, y_0)$.

Definition 3.3 Assume there exists an interval $I \subset \mathbb{R}$ and a continuous function $x^* : I \rightarrow \mathbb{R}$ such that

$$f(x^*(y), y) = 0 \quad \forall y \in I . \tag{3.15}$$

Then the set $\mathcal{M}_0 = \{(x^*(y), y) : y \in I\}$ is called an equilibrium branch of the system (3.14). Let

$$a^*(y) = \partial_x f(x^*(y), y) \tag{3.16}$$

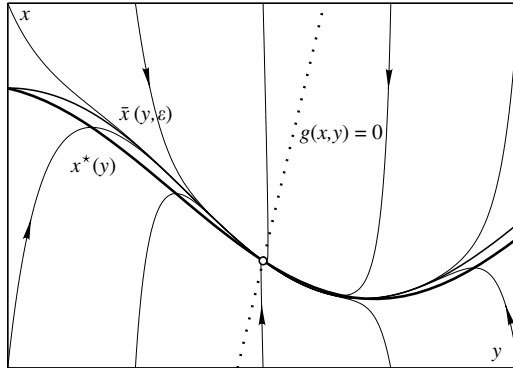


FIG. 3.3: Deterministic dynamics near a stable equilibrium branch $x^*(y)$ (full heavy curve), intersecting a nullcline (dotted line). Orbits are attracted exponentially fast by an invariant curve $x = \bar{x}(y, \varepsilon)$, lying at a distance of order ε of the equilibrium branch (in this example $\varepsilon = 0.1$).

be the linearization of the fast vector field at $x^*(y)$. The equilibrium branch is called (asymptotically) stable if $a^*(y)$ is negative and bounded away from zero, uniformly in $y \in I$.

A first result, due to Tikhonov, states that orbits, starting sufficiently close to a stable equilibrium branch, tend to track that branch up to a small lag of order ε .

Theorem 3.4 (Tikhonov 1952, Gradštejn 1953) *Any orbit starting in a sufficiently small neighbourhood of a stable equilibrium branch \mathcal{M}_0 is attracted exponentially fast to a neighbourhood of order ε of \mathcal{M}_0 .*

A second result, due to Fenichel, makes the picture more precise. It states that all orbits starting near the stable equilibrium branch actually converge to an invariant curve, cf. Fig. 3.3.

Theorem 3.5 (Fenichel 1979) *If the equilibrium branch \mathcal{M}_0 is stable, then there exists a curve \mathcal{M}_ε , which is ε -close to \mathcal{M}_0 and invariant under the flow.¹ The curve \mathcal{M}_ε attracts neighbouring orbits exponentially fast.*

The invariant curve \mathcal{M}_ε admits a parametric equation of the form $x = \bar{x}(y, \varepsilon)$, where $\bar{x}(y, \varepsilon) = x^*(y) + \mathcal{O}(\varepsilon)$. The function $\bar{x}(y, \varepsilon)$ can be computed perturbatively in ε to any desired accuracy. Indeed, substituting in (3.14), we obtain the invariance condition

$$f(\bar{x}(y, \varepsilon), y) = \varepsilon \partial_y \bar{x}(y, \varepsilon) g(\bar{x}(y, \varepsilon), y) . \quad (3.17)$$

¹ \mathcal{M}_ε is called *invariant under the flow*, if $(x(0), y(0)) \in \mathcal{M}_\varepsilon$ implies that $(x(t), y(t)) \in \mathcal{M}_\varepsilon$ as long as $y(t) \in I$ holds.

Looking for a solution in the form of an asymptotic series

$$\bar{x}(y, \varepsilon) = x_0(y) + \varepsilon x_1(y) + \varepsilon^2 x_2(y) + \dots \quad (3.18)$$

(where the existence of such an asymptotic series follows from the centre manifold theorem), we start by inserting the ansatz (3.18) into (3.17). Expanding into powers of ε , and equating like powers allows us to determine the $x_i(y)$. To order ε^0 , one simply gets

$$f(x_0(y), y) = 0 , \quad (3.19)$$

which is the equation defining the equilibrium branch, so that $x_0(y) = x^*(y)$ follows. To order ε^1 , we obtain

$$\partial_x f(x^*(y), y) x_1(y) = \partial_y x^*(y) g(x^*(y), y) . \quad (3.20)$$

The term $\partial_x f(x^*(y), y)$ is the one we denoted $a^*(y)$, so that

$$x_1(y) = \frac{\partial_y x^*(y) g(x^*(y), y)}{a^*(y)} . \quad (3.21)$$

Since $a^*(y)$ is negative for the stable equilibrium branch \mathcal{M}_0 , the invariant curve lies below $x^*(y)$ if $x^*(y)$ is increasing and g is positive, while it lies above $x^*(y)$ if $x^*(y)$ is increasing and g is negative (and vice versa for decreasing $x^*(y)$). If g vanishes at a point $(x^*(y^*), y^*)$, then this point is in fact an equilibrium point of the slow–fast system. Hence \mathcal{M}_ε may contain equilibrium points, and if so, it can consist of stable or unstable manifolds of such points.

The dynamics on the invariant curve \mathcal{M}_ε is governed by the reduced equation

$$\dot{y} = g(\bar{x}(y, \varepsilon), y) . \quad (3.22)$$

Expanding in ε , we can write this equation as

$$\begin{aligned} \dot{y} &= g(x^*(y), y) + \varepsilon \partial_x g(x^*(y), y) x_1(y) + \dots \\ &= g(x^*(y), y) \left[1 + \varepsilon \partial_x g(x^*(y), y) \frac{\partial_y x^*(y)}{a^*(y)} + \dots \right] . \end{aligned} \quad (3.23)$$

We recover the fact that orbits on the invariant curve move to the right if g is positive, and to the left if g is negative.

3.2.2 Stochastic case

We consider now the dynamics of Itô stochastic differential equations of the form

$$\begin{aligned} dx(t) &= \frac{1}{\varepsilon} f(x(t), y(t)) dt + \frac{\sigma}{\sqrt{\varepsilon}} F(x(t), y(t)) dW_t^{(1)} , \\ dy(t) &= g(x(t), y(t)) dt + \sigma' G(x(t), y(t)) dW_t^{(2)} , \end{aligned} \quad (3.24)$$

cf. (3.13), near a stable equilibrium branch. In the first step, we aim at bounds on the deviation

$$\xi(t) = x(t) - \bar{x}(y(t), \varepsilon) \quad (3.25)$$

of the random fast variables from the deterministic invariant curve. By Itô's formula, this deviation satisfies the stochastic differential equation

$$d\xi(t) = dx(t) - \partial_y \bar{x}(y(t), \varepsilon) dy(t) - \frac{1}{2} \partial_{yy} \bar{x}(y(t), \varepsilon) (dy(t))^2, \quad (3.26)$$

where $(dy(t))^2$ is to be computed according to the rules of Itô calculus, yielding

$$\begin{aligned} d\xi(t) = & \frac{1}{\varepsilon} f(x(t), y(t)) dt + \frac{\sigma}{\sqrt{\varepsilon}} F(x(t), y(t)) dW_t^{(1)} \\ & - \partial_y \bar{x}(y(t), \varepsilon) g(x(t), y(t)) dt - \partial_y \bar{x}(y(t), \varepsilon) \sigma' G(x(t), y(t)) dW_t^{(2)} \\ & - \frac{1}{2} \partial_{yy} \bar{x}(y(t), \varepsilon) (\sigma')^2 G(x(t), y(t))^2 dt. \end{aligned} \quad (3.27)$$

Because of the invariance condition (3.17), the coefficient of dt in the above equation vanishes to leading order for $\xi(t) = 0$. Expanding everything in $\xi(t)$, one obtains an equation of the form

$$\begin{aligned} d\xi(t) = & \frac{1}{\varepsilon} [\bar{a}(y(t), \varepsilon) \xi(t) + \mathcal{O}(\xi(t)^2) + \mathcal{O}(\varepsilon(\sigma')^2)] dt \\ & + \frac{\sigma}{\sqrt{\varepsilon}} [F_0(y(t), \varepsilon) + \mathcal{O}(\xi(t))] dW_t^{(1)} \\ & - \sigma' \partial_y \bar{x}(y(t), \varepsilon) [G_0(y(t), \varepsilon) + \mathcal{O}(\xi(t))] dW_t^{(2)}, \end{aligned} \quad (3.28)$$

where we have used the shorthand

$$\begin{aligned} \bar{a}(y, \varepsilon) &= \partial_x f(\bar{x}(y, \varepsilon), y) = a^*(y) + \mathcal{O}(\varepsilon), \\ F_0(y, \varepsilon) &= F(\bar{x}(y, \varepsilon), y) = F(x^*(y), y) + \mathcal{O}(\varepsilon), \\ G_0(y, \varepsilon) &= G(\bar{x}(y, \varepsilon), y) = G(x^*(y), y) + \mathcal{O}(\varepsilon). \end{aligned} \quad (3.29)$$

The idea is now to choose a suitable Gaussian approximation for ξ . Such an approximation can be obtained by approximating the slow variable $y(t)$ by a deterministic variable $y^0(t)$, while choosing a linear approximation $\xi^0(t)$ for $\xi(t)$, yielding the system

$$\begin{aligned} d\xi^0(t) = & \frac{1}{\varepsilon} \bar{a}(y^0(t), \varepsilon) \xi^0(t) dt + \frac{\sigma}{\sqrt{\varepsilon}} F_0(y^0(t), \varepsilon) dW_t^{(1)} \\ & - \sigma' \partial_y \bar{x}(y^0(t), \varepsilon) G_0(y^0(t), \varepsilon) dW_t^{(2)}, \\ dy^0(t) = & g(\bar{x}(y^0(t), \varepsilon), y^0(t)) dt. \end{aligned} \quad (3.30)$$

Assuming that $x(t)$ starts on $\bar{x}(y(t), \varepsilon)$ at time $t = 0$, it follows that $\xi(0) = 0$, and thus we may also assume that $\xi^0(0) = 0$. Therefore, the process $\{\xi^0(t)\}_t$ is Gaussian with zero mean and variance $\sigma^2 v(t)$, where $v(t)$ can be written as an integral, but also as a solution of the deterministic slow–fast system

$$\begin{aligned}\varepsilon \dot{v}(t) &= 2\bar{a}(y^0(t), \varepsilon)v(t) + F_0(y^0(t), \varepsilon)^2 + \varepsilon \left[\frac{\sigma'}{\sigma} \partial_y \bar{x}(y^0(t), \varepsilon) G_0(y^0(t), \varepsilon) \right]^2, \\ \dot{y}^0(t) &= g(\bar{x}(y^0(t), \varepsilon), y^0(t)).\end{aligned}\tag{3.31}$$

By Tikhonov's theorem, we conclude that $v(t)$ approaches exponentially fast a function $\bar{v}(y^0(t), \varepsilon)$ satisfying (if we assume $\sigma' \leq \text{const } \sigma$)

$$\bar{v}(y^0(t), \varepsilon) = -\frac{F_0(y^0(t), \varepsilon)^2}{2\bar{a}(y^0(t), \varepsilon)} + \mathcal{O}(\varepsilon).\tag{3.32}$$

This result is not surprising: It means that the variance of the deviation $\xi^0(t)$ is proportional to the instantaneous variance increase of the noise term, and inversely proportional to the attractivity of the stable equilibrium branch.

The main result is that sample paths of the nonlinear equation are concentrated in a neighbourhood of order $\sigma\sqrt{\bar{v}(y, \varepsilon)}$ of the deterministic invariant curve $\bar{x}(y, \varepsilon)$, provided the diffusion coefficient F is bounded away from zero. We formulate this concentration result by introducing the family of sets

$$\mathcal{B}(h) = \{(x, y) : y \in I, |x - \bar{x}(y, \varepsilon)|^2 < h^2 \bar{v}(y, \varepsilon)\}.\tag{3.33}$$

Each $\mathcal{B}(h)$ is a strip around the deterministic invariant curve, of width proportional to the parameter h and to the standard deviation of the linearized process.

We further introduce two first-exit times:

$$\begin{aligned}\tau_{\mathcal{B}(h)} &= \inf\{t > 0 : (x(t), y(t)) \notin \mathcal{B}(h)\}, \\ \tau_I &= \inf\{t > 0 : y(t) \notin I\}.\end{aligned}\tag{3.34}$$

Both times are random as they depend on the realization of the sample path $(x(t), y(t))$. While τ_I describes the first time the slow variable is found outside the interval of existence of the equilibrium branch, $\tau_{\mathcal{B}(h)}$ gives the first time the sample path exits the strip $\mathcal{B}(h)$, in which we expect sample paths to be concentrated, cf. Fig. 3.4.

The following result states that indeed, for $h \gg \sigma$, sample paths are unlikely to leave $\mathcal{B}(h)$ – unless $y(t)$ leaves the interval I in which the equilibrium branch is defined.

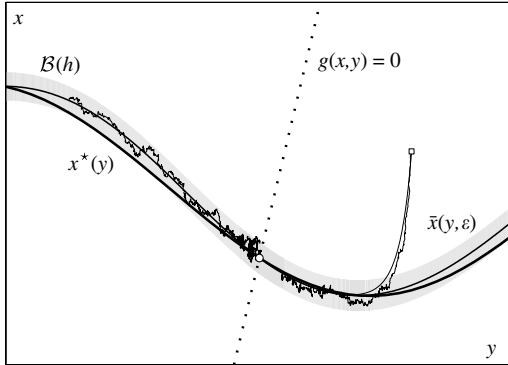


FIG. 3.4: Stochastic dynamics near a stable equilibrium branch $x^*(y)$ (*full heavy curve*), for the same system as in Fig. 3.3 and noise intensities $\sigma = \sigma' = 0.03$. Sample paths are likely to stay in the shaded set $\mathcal{B}(h)$, centred in the curve $\bar{x}(y, \varepsilon)$ (shown here for $h = 3$). Sample paths starting away from the invariant curve stay close to the deterministic solution starting at the same point. Once the deterministic solution and the random sample path have entered the set $\mathcal{B}(h)$, we may continue to study the sample path as if it had started in $\mathcal{B}(h)$.

Theorem 3.6 (Berglund and Gentz 2003) *Assume the initial condition lies on the invariant curve, that is, $x(0) = \bar{x}(y(0), \varepsilon)$ for some $y(0) \in I$. Then there exist constants $h_0, c, L > 0$ such that for all $h \leq h_0$,*

$$\Pr(\tau_{\mathcal{B}(h)} < \min(t, \tau_I)) \leq C(t, \varepsilon) e^{-\kappa h^2/2\sigma^2}, \quad (3.35)$$

where the exponent κ is uniform in time and satisfies

$$\kappa = 1 - \mathcal{O}(h) - \mathcal{O}(\varepsilon(\sigma'/h)^2) - \mathcal{O}(e^{-c/\varepsilon}/h), \quad (3.36)$$

and the prefactor satisfies

$$C(t, \varepsilon) = L \frac{(1+t)^2}{h^2 \varepsilon} \left(1 + \frac{h^2}{\sigma^2} \right). \quad (3.37)$$

As soon as we take h slightly larger than σ , say $h = \text{const } \sigma |\log \sigma|$, the right-hand side of (3.35) becomes very small, unless we wait for very long time spans. For brevity, we will say that sample paths are concentrated in $\mathcal{B}(\sigma)$.

Remark 3.7

1. A matching lower bound for the probability in (3.35), with an exponent differing only in the error terms, and a different prefactor holds, cf. (Berglund and Gentz, 2003, Theorem 2.4), showing that the above bound is sharp in the sense that it captures the correct behaviour of the probability.

2. If the sample path does not start on the invariant curve, but in a sufficiently small neighbourhood of the invariant curve, the upper bound (3.35) remains valid, provided we first wait for a time of order $\varepsilon|\log h|$, after which the sample path is likely to have entered $\mathcal{B}(h)$.
3. We expect the exact prefactor of the probability in (3.35) to grow linearly with time t . This has been established in some particular situations, cf. (Berglund and Gentz 2005, Section 3.1).
4. One can show that on a suitable time-scale, the dynamics is well approximated by its projection on the invariant curve, given by

$$dy(t) = g(\bar{x}(y(t), \varepsilon), y(t)) dt + \sigma' G(\bar{x}(y(t), \varepsilon), y(t)) dW_t^{(2)}. \quad (3.38)$$

5. Note that if the deterministic solution $y^0(t)$ of the deterministic reduced equation $\dot{y}^0 = g(\bar{x}(y^0, \varepsilon), y^0)$ leaves the interval of existence I in a time of order 1, then sample paths of the stochastic equation are likely to leave I in a comparable time, cf. Berglund and Gentz (2003, Theorem 2.6) and Berglund and Gentz (2005, Section 5.1.4).

3.3 Unstable equilibrium branches

3.3.1 Deterministic case

We return to the study of deterministic slow–fast systems of the form (3.14), this time focusing on the dynamics near unstable equilibrium branches.

Definition 3.8 Let $\mathcal{M}_0 = \{(x^*(y), y) : y \in I\}$ be an equilibrium branch of the system (3.14), with linearization $a^*(y)$ of the fast drift term. The equilibrium branch is called unstable if $a^*(y)$ is positive and bounded away from zero, uniformly in $y \in I$.

In this case, Tihonov’s theorem can still be applied, by looking backwards in time. Simply note that an orbit passing through a point chosen close to the equilibrium branch will approach an ε -neighbourhood of this branch when viewed backwards in time.

Again by looking backwards in time, we see that Fenichel’s theorem also holds in the unstable case, i.e. there exists an invariant curve \mathcal{M}_ε in a neighbourhood of order ε of the equilibrium branch. The only difference is that this curve is now repelling neighbouring orbits exponentially fast (looking forward in time). The invariance condition is the same as before, and thus the invariant curve still has an equation of the form $x = \bar{x}(y, \varepsilon)$, where

$$\bar{x}(y, \varepsilon) = x^*(y) + \frac{\partial_y x^*(y)g(x^*(y), y)}{a^*(y)} \varepsilon + \mathcal{O}(\varepsilon^2). \quad (3.39)$$

Since $a^*(y)$ is now positive, the invariant curve lies above the equilibrium branch if $x^*(y)$ is increasing and g is positive, while it lies below if $x^*(y)$ is increasing and g is negative (and vice versa for decreasing $x^*(y)$).

If the initial condition lies at a distance δ_0 from the invariant curve, then the distance will grow roughly like $\delta_0 e^{\text{const} t/\varepsilon}$. The time needed to reach a distance δ from the curve is of order $\varepsilon \log(\delta/\delta_0)$, which can be large for very small δ_0 . Hence, though most orbits are quickly repelled from the invariant curve, one can always find orbits staying near the curve for a long time.

3.3.2 Stochastic case

When noise is added to the slow–fast system, sample paths starting on the deterministic curve or close to it typically leave its vicinity earlier than they would in the deterministic case. This is due to the diffusion term being likely to push sample paths to regions where the drift term is sufficiently large to take over and accelerate the escape.

More precisely, assuming the diffusion coefficient $F(x, y)$ is bounded away from zero near the unstable equilibrium branch, one can show (Berglund and Gentz 2005, Section 3.2) that the following holds:

- Let $\rho(y, \varepsilon) = F_0(y, \varepsilon)/\sqrt{2\bar{a}(y, \varepsilon)}$, where F_0 and \bar{a} are defined as in (3.29). For $h \leq \sigma$, sample paths starting on the invariant curve $\bar{x}(y, \varepsilon)$ are likely to leave a neighbourhood of size $h\rho(y, \varepsilon)$ of this curve in a time of order $\varepsilon h^2/\sigma^2$.
- For small δ up to order 1 in σ , sample paths are likely to leave a neighbourhood of size δ of $\bar{x}(y, \varepsilon)$ in a time of order $\varepsilon \log(\delta/\sigma)$.

Hence, sample paths starting at a distance δ_0 from the invariant curve are likely to reach a distance δ in a time of order $\varepsilon \log(\delta/\max(\delta_0, \sigma))$. Thus the system behaves as if the noise term accounts for an effective initial condition at distance σ from the invariant curve.

3.4 Saddle-node bifurcations

3.4.1 Deterministic case

We consider now the dynamics of the deterministic slow–fast system (3.4) near saddle-node bifurcation points.

Definition 3.9 A point (x^*, y^*) is a saddle-node bifurcation point if the fast vector field satisfies the conditions

$$\begin{aligned} f(x^*, y^*) &= 0, && (\text{equilibrium point}), \\ \partial_x f(x^*, y^*) &= 0, && (\text{bifurcation point}), \\ \partial_{xx} f(x^*, y^*) &\neq 0, && (\text{saddle-node bifurcation}), \\ \partial_y f(x^*, y^*) &\neq 0, && (\text{saddle-node bifurcation}). \end{aligned} \tag{3.40}$$

In this section, we further assume that

$$g(x^*, y^*) \neq 0, \quad (\text{non-zero slow drift speed}). \quad (3.41)$$

Cases in which $g(x^*, y^*)$ vanishes, or nearly vanishes, will be considered in the next section.

One can always translate the origin of the coordinate system to the bifurcation point, which amounts to assuming that $(x^*, y^*) = (0, 0)$. One can further scale x , y and time in such a way that $|\partial_{xx}f(0, 0)| = 2$, $|\partial_y f(0, 0)| = 1$ and $|g(0, 0)| = 1$, as in the simple example

$$\begin{aligned} \varepsilon \dot{x} &= y - x^2, \\ \dot{y} &= -1. \end{aligned} \quad (3.42)$$

This system, which is actually the normal form of (3.14) near a saddle-node bifurcation, admits a stable equilibrium branch $x_-^*(y) = \sqrt{y}$, $y > 0$, with linearization $a_-^*(y) = -2\sqrt{y}$, and an unstable equilibrium branch $x_+^*(y) = -\sqrt{y}$, $y > 0$, with linearization $a_+^*(y) = 2\sqrt{y}$, cf. Fig. 3.5. General systems satisfying (3.40) and (3.41) admit branches with the same asymptotic behaviour as $y \rightarrow 0$, possibly with different signs.

Let us stick to Eqn. (3.42) for simplicity. We know that there exists an invariant curve $x = \bar{x}_-(y, \varepsilon)$ tracking $x_-^*(y)$. A computation shows that it satisfies

$$\bar{x}_-(y, \varepsilon) = \sqrt{y} + \frac{\varepsilon}{4y} - \frac{5}{32} \frac{\varepsilon^2}{y^{5/2}} + \mathcal{O}(\varepsilon^3), \quad (3.43)$$

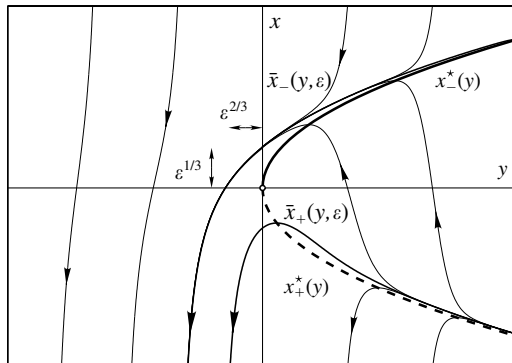


FIG. 3.5: Some orbits of the deterministic slow–fast system (3.42) describing the dynamics near a saddle-node bifurcation point, for $\varepsilon = 0.1$. The invariant curve $x = \bar{x}_-(y, \varepsilon)$, tracking the stable branch $x = x_-^*(y)$ for positive y , crosses the x -axis at a distance of order $\varepsilon^{1/3}$ above the origin, and the y -axis at a distance of order $\varepsilon^{2/3}$ to the left of the origin. Also shown is the invariant curve $x = \bar{x}_+(y, \varepsilon)$, tracking the unstable branch $x = x_+^*(y)$ for positive y .

as long as y is bounded away from zero. As y decreases, however, the expansion becomes ‘disordered’: all terms are of comparable size for $y = \varepsilon^{2/3}$, and the expansion is no longer a valid asymptotic series for $y < \varepsilon^{2/3}$. The curve $\bar{x}_-(y, \varepsilon)$, however, continues to exist, since it can be defined as a particular solution of the slow–fast differential equation. Its fate is described by the following general result (Pontryagin 1957, Haberman 1979, Berglund and Kunz 1999).

Theorem 3.10 *Let (x^*, y^*) be a saddle-node bifurcation point of a slow–fast system satisfying (3.41). Assume (without loss of generality) that the coordinates have been scaled in such a way that $(x^*, y^*) = (0, 0)$, $\partial_{xx}f(0, 0) = -2$, $\partial_y f(0, 0) = -1$ and $g(0, 0) = -1$. Choose an initial condition $(x(0), y(0))$ sufficiently close to the bifurcation point, with $y(0) > 0$ of order 1 and $x(0) - x^*(y(0)) > 0$ of order ε . Then the orbit starting in $(x(0), y(0))$ satisfies²*

$$\begin{aligned} x(t) - x_-^*(y(t)) &\asymp \frac{\varepsilon}{y(t)} \quad \text{for } c_1\varepsilon^{2/3} \leq y(t) \leq y(0) , \\ x(t) &\asymp \varepsilon^{1/3} \quad \text{for } -c_1\varepsilon^{2/3} \leq y(t) \leq c_1\varepsilon^{2/3} , \end{aligned} \quad (3.44)$$

for some constant $c_1 > 0$. Furthermore, $x(t)$ reaches negative values of order 1 when $y(t)$ is still of order $-\varepsilon^{2/3}$.

This result implies that when continued from positive to negative y , the invariant curve $x = \bar{x}_-(y, \varepsilon)$ first crosses the axis $y = 0$ for an x of order $\varepsilon^{1/3}$, then the axis $x = 0$ for a y of order $-\varepsilon^{2/3}$, and finally reaches negative x of order 1, still for a y of order $-\varepsilon^{2/3}$ (Fig. 3.5).

3.4.2 Stochastic case

We turn now to the behaviour of the stochastic differential equation (3.13) near a saddle-node bifurcation point, which we assume to lie at $(0, 0)$. We further assume that

$$F(0, 0) \neq 0 \quad (\text{non-zero noise on fast component}) . \quad (3.45)$$

By continuity, F will be non-zero in a full neighbourhood of the bifurcation point.

One can try to proceed as in the stable case, and define a neighbourhood $\mathcal{B}(h)$ of the invariant curve $\bar{x}_-(y, \varepsilon)$ tracking the stable equilibrium branch $x_-^*(y)$, cf. (3.33). The new feature is that the function $\bar{v}(y, \varepsilon)$ controlling the variance of fluctuations, defined as the solution of the system (3.31), does not remain of

²The notation $a(y, \varepsilon) \asymp b(y, \varepsilon)$ means that two functions a and b behave in the same way, in the sense that $a(y, \varepsilon)/b(y, \varepsilon)$ is bounded above and below by positive constants, independent of y and ε .

order 1. In fact, Theorem 3.10 implies that $\bar{a}(y, \varepsilon) = \partial_x f(\bar{x}_-(y, \varepsilon), y)$ scales like $\max(y^{1/2}, \varepsilon^{1/3})$ and hence

$$\bar{v}(y, \varepsilon) \asymp \frac{1}{\max(y^{1/2}, \varepsilon^{1/3})} \quad (3.46)$$

for $y \geq -c_1 \varepsilon^{2/3}$. It follows that the set $\mathcal{B}(h)$ becomes wider as $y(t)$ approaches the bifurcation point, and reaches a width of order $h \varepsilon^{-1/6}$ near $y = 0$.

If $\sigma < \varepsilon^{1/2}$, we can choose an h satisfying $\sigma < h < \varepsilon^{1/2}$. For such h , the width of $\mathcal{B}(h)$ is still smaller than the distance to the bifurcation point, which has order $\varepsilon^{1/3}$. In this situation, the results of Theorem 3.6 remain valid, and sample paths are concentrated in the corresponding set $\mathcal{B}(h)$ as long as $y(t) > -c_1 \varepsilon^{2/3}$ (Fig. 3.6a).

If $\sigma > \varepsilon^{1/2}$, fluctuations already allow sample paths to reach the unstable branch as soon as $y(t)$ has decreased to order $\sigma^{4/3}$. One then shows that sample paths are likely to overcome the unstable branch, and to reach negative x -values of order 1, for only slightly smaller y , cf. Fig. 3.6(b). These results can be summarized as follows.

Theorem 3.11 (Berglund and Gentz 2002b) *Assume the conditions of Theorem 3.10 hold, as well as (3.45), and that $\sigma' \leq \text{const } \sigma$. Then the following hold:*

- If $\sigma < \sigma_c = \varepsilon^{1/2}$, then sample paths remain in $\mathcal{B}(h)$ with probability larger than $1 - \mathcal{O}(e^{-h^2/2\sigma^2})$ for all h up to order $\varepsilon^{1/2}$, as long as $y(t) > -c_1 \varepsilon^{2/3}$. In particular, the probability that $x(t)$ becomes negative for these $y(t)$ is of order $e^{-\mathcal{O}(\varepsilon/\sigma^2)}$. Furthermore, $x(t)$ is likely to reach negative values of order 1 as soon as $y(t)$ reaches values of order $-\varepsilon^{2/3}|\log \varepsilon|$.

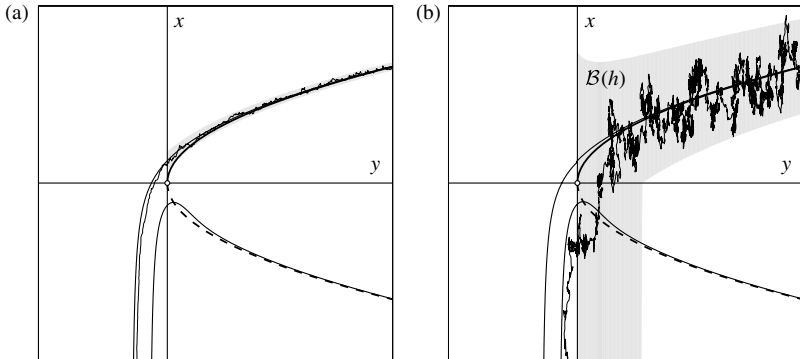


FIG. 3.6: Stochastic dynamics near a saddle-node bifurcation, for $\varepsilon = 0.03$ and (a) $\sigma' = \sigma = 0.03 < \varepsilon^{1/2}$, and (b) $\sigma' = 0.25, \sigma = 0.35 > \varepsilon^{1/2}$. In both cases, the sample paths are likely to stay in the shaded set $\mathcal{B}(h)$, but for strong noise intensity, they may nevertheless overcome the unstable equilibrium branch before $y(t)$ reaches the bifurcation value.

- If $\sigma > \sigma_c = \varepsilon^{1/2}$, then sample paths are likely to cross the unstable branch and reach negative values of order 1 already for $y(t)$ of order $\sigma^{4/3}$. The probability that this does not happen is of order $e^{-\mathcal{O}(\sigma^2/\varepsilon|\log \sigma|)}$.

Thus for $\sigma < \varepsilon^{1/2}$, the situation does not differ notably from the deterministic one: Sample paths feel the bifurcation after a delay of order $\varepsilon^{2/3}$, and then they quickly react by jumping to negative x of order 1. If $\sigma > \varepsilon^{1/2}$, on the other hand, noise induces a new behaviour: Sample paths feel the bifurcation some time before it happens, and thus anticipate the transition to negative x .

3.4.3 The Van der Pol oscillator

As a first illustration of how to patch together the above results in order to get the full picture of the dynamics of a slow–fast system, let us consider the van der Pol oscillator. This oscillator is based on an electric RCL circuit modelling the dynamics of a triode (van der Pol 1920, 1927). In the large-damping case, its dynamics is described by the slow–fast system

$$\begin{aligned}\varepsilon \dot{x} &= y + x - \frac{x^3}{3}, \\ \dot{y} &= -x.\end{aligned}\tag{3.47}$$

This system is equivalent, up to a scaling, to the FitzHugh–Nagumo equations with $\alpha = \gamma = 0$.

The system (3.47) admits two stable and one unstable equilibrium branches, meeting at two saddle-node bifurcation points $\pm(1, -2/3)$. The nullcline is simply the axis $x = 0$. A solution starting anywhere in the plane (except possibly near the unstable branch) will first quickly approach a stable equilibrium branch, which it then tracks at a distance of order ε . Upon reaching the neighbourhood of one of the bifurcation points, it will jump, after a small delay of order $\varepsilon^{2/3}$, to the other stable branch, which it then tracks until reaching the other bifurcation point, cf. Fig. 3.7(a). This alternation of slow and fast motions will repeat periodically, a behaviour that van der Pol called *relaxation oscillations* (van der Pol, 1926). In the (x, y) -plane, the orbits enclose an area $\mathcal{A}(\varepsilon) = \mathcal{A}(0) + \mathcal{O}(\varepsilon^{2/3})$ (Mishchenko and Rozov 1980, Jung *et al.* 1990).

Assume now that noise of intensity $\sigma/\sqrt{\varepsilon}$ is added to the fast variable x . The previous results show that as long as $\sigma < \sqrt{\varepsilon}$, typical sample paths merely fluctuate around the deterministic limit cycle. In particular, the area enclosed by the cycles is concentrated around the deterministic value $\mathcal{A}(\varepsilon) = \mathcal{A}(0) + \mathcal{O}(\varepsilon^{2/3})$. When $\sigma > \sqrt{\varepsilon}$, however, typical cycles are smaller, by an amount of order $\sigma^{4/3}$, than $\mathcal{A}(0)$ (Berglund and Gentz 2002b), cf. Fig. 3.7(b).

One can also analyse the situation when only the slow variable y is subjected to an additive noise term of intensity σ' . Then, a similar transition between large and small cycles occurs at a threshold noise intensity of order $\varepsilon^{1/3}$ (Berglund and Gentz, 2005, Section 6.1.2).

Remark 3.12 As σ further increases, for fixed ε , transitions from one stable branch to the other occur earlier and earlier.

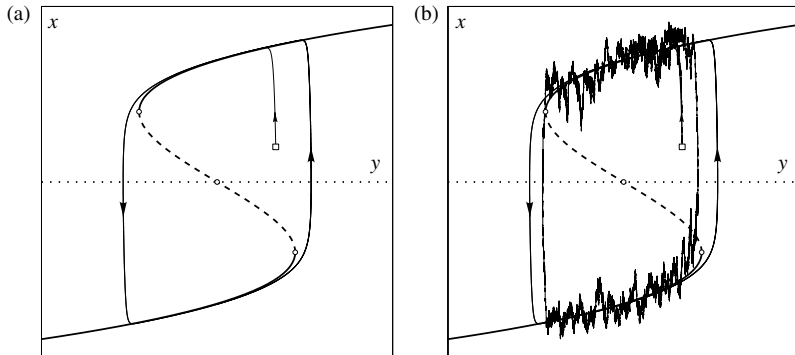


FIG. 3.7: (a) An orbit of the van der Pol oscillator for $\varepsilon = 0.02$. It quickly converges to a limit cycle. (b) When sufficiently strong noise is added to the fast variable x (here $\sigma = 0.3$), sample paths perform noisy cycles which are likely to be a little smaller than the deterministic cycle.

A particular regime, in which transitions are advanced and which can be studied in detail, is the quasi-static regime, in which ε and σ are both small, and satisfy a relation of the form $\varepsilon = e^{-\lambda/\sigma^2}$, where λ is a parameter. (Note that this implies $\sigma = [\lambda/\log(\varepsilon^{-1})]^{1/2} \gg \sqrt{\varepsilon}$.) In that case, for small σ , ε is extremely small and one can consider the slow variable y locally as frozen. This permits one to examine the behaviour of the one-dimensional equation for x , with methods from the theory of large deviations (Freidlin, 2001).

Let $V_{y_0}(x) = -y_0x - \frac{1}{2}x^2 + \frac{1}{12}x^4$ be the double-well potential associated with the frozen system. If the depth of the potential well in which the frozen system is currently sitting is below $\lambda/2$, the state jumps to the other potential well after a time of order $1/\varepsilon$. For values of λ in a certain range, this leads to quasi-deterministic cycles which are smaller, by an amount of order 1, than the cycles obtained without noise.

3.5 Excitability

One of the interesting features of action-potential generation, reproduced by simple slow-fast models, is the phenomenon of *excitability*. A system is excitable if it admits an asymptotically stable equilibrium point, with the particular feature that some orbits passing close by make a large excursion in phase space before returning to the point. In such a case, a small change of the vector field, controlled for instance by a bifurcation parameter, may produce a stable periodic orbit of large amplitude. Noise can have the same effect as a change of the bifurcation parameter, and occasionally move the system away from the stable equilibrium point and towards the periodic orbit. The system then makes a large excursion in phase space, corresponding to a spike, before returning to rest (Longtin, 2000, Kosmidis and Pakdaman, 2003) (see also Chapter 4).

Various types of excitability can be distinguished (Izhikevich, 2000). One possible distinction concerns the period of the periodic orbit:

- In excitability of type I, the period of the orbit diverges as the bifurcation parameter approaches its threshold. It occurs for instance in the case of a saddle-node-to-invariant-circle (SNIC) bifurcation.
- In excitability of type II, the period of the orbit converges to a finite value as the bifurcation parameter approaches its threshold. It occurs for instance in the case of a Hopf bifurcation.

3.5.1 Excitability of type I

Excitability of type I occurs for instance when the nullcline $g(x, y) = 0$ intersects both the stable and unstable equilibrium branch near a saddle-node bifurcation point (in addition to a second intersection with the unstable branch further away). When the nullcline is moved towards the bifurcation point, the two intersection points collapse, and their unstable manifolds are replaced by a periodic orbit. This situation occurs, for instance, in the Morris–Lecar model, when the parameter x_4 is sufficiently small for the nullcline to be close to a step function.

The dynamics in the vicinity of the bifurcation point can be described by the normal form

$$\begin{aligned} \varepsilon \dot{x} &= y - x^2, \\ \dot{y} &= \delta - y. \end{aligned} \tag{3.48}$$

The parameter δ measures the distance to the saddle-node-to-invariant-circle bifurcation. There are two equilibrium branches, a stable one given by $x_-^*(y) = \sqrt{y}$ and an unstable one given by $x_+^*(y) = -\sqrt{y}$. If $\delta > 0$, the nullcline $y = \delta$ intersects the equilibrium branches at $(\sqrt{\delta}, \delta)$, which is an asymptotically stable node, and at $(-\sqrt{\delta}, \delta)$, which is a saddle. If $\delta < 0$, the invariant line $y = \delta$ represents the portion of the periodic orbit lying near the origin (this orbit can only be reproduced when including more nonlinear terms in the normal form).

The invariant curve $x = \bar{x}_-(y, \varepsilon)$, tracking the stable equilibrium branch for larger y , converges to the stable node $(\sqrt{\delta}, \delta)$ as y converges to δ , cf. Fig. 3.8. It has an expansion of the form

$$\bar{x}_-(y, \varepsilon) = \sqrt{y} + \varepsilon \frac{y - \delta}{4y} + \dots \tag{3.49}$$

One can also define an invariant curve $x = \bar{x}_+(y, \varepsilon)$ tracking the unstable equilibrium branch. It coincides with the stable manifold of the saddle point $(-\sqrt{\delta}, \delta)$, while the unstable manifold of the saddle consists of the part of the nullcline $y = \delta$ below the stable node (Fig. 3.8).

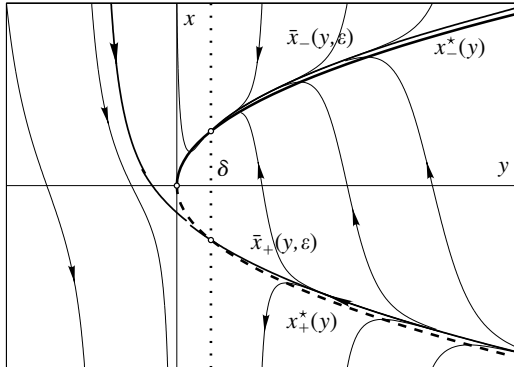


FIG. 3.8: Some orbits of the deterministic slow–fast system (3.48) for $\delta = 0.2$ and $\varepsilon = 0.1$. The curve $x = \bar{x}_+(y, \varepsilon)$, tracking the unstable equilibrium branch $x = x_+^*(y)$, is also the stable manifold of the saddle point $(-\sqrt{\delta}, \delta)$. The unstable manifold of the saddle is contained in the nullcline (*dotted line*).

Consider now the situation where noise is added to the fast variable, i.e. the stochastic differential equation

$$\begin{aligned} dx(t) &= \frac{1}{\varepsilon}(y(t) - x(t)^2) dt + \frac{\sigma}{\sqrt{\varepsilon}} F(x(t), y(t)) dW_t , \\ dy(t) &= (\delta - y(t)) dt , \end{aligned} \quad (3.50)$$

where we assume that $F(x, y)$ is bounded away from zero. In fact, the equation for the slow variable is closed and can be solved:

$$y(t) = \delta + (y(0) - \delta)e^{-t} . \quad (3.51)$$

The system is thus equivalent to the one-dimensional time-dependent equation

$$dx(t) = \frac{1}{\varepsilon}(\delta + (y(0) - \delta)e^{-t} - x(t)^2) dt + \frac{\sigma}{\sqrt{\varepsilon}} F(x(t), \delta + (y(0) - \delta)e^{-t}) dW_t . \quad (3.52)$$

In particular, if $y(0) = \delta$, we simply have the autonomous equation

$$dx(t) = \frac{1}{\varepsilon}(\delta - x(t)^2) dt + \frac{\sigma}{\sqrt{\varepsilon}} F(x(t), \delta) dW_t , \quad (3.53)$$

describing the overdamped motion of a particle in the static potential $V(x) = \frac{1}{3}x^3 - \delta x$. This potential has a local minimum at $x = \sqrt{\delta}$ and a local maximum

at $x = -\sqrt{\delta}$, with a potential difference $\frac{4}{3}\delta^{3/2}$. We thus know that if $\sigma \ll \delta^{3/4}$, sample paths will be trapped near the potential minimum for a time of order $e^{\text{const } \delta^{3/2}/\sigma^2}$. Furthermore, it is known (Day, 1983, Bovier *et al.*, 2004) that for small noise intensity, the law of the escape time is well approximated by an exponential distribution.

If the sample path starts at some $y(0) > \delta$, one can proceed as in the stable case by defining a neighbourhood $\mathcal{B}(h)$ of the deterministic invariant curve $x = \bar{x}_-(y, \varepsilon)$. Similar computations as in Section 3.2 show that $\mathcal{B}(h)$ has a width scaling like $h/y^{1/4}$. If $\sigma \ll \delta^{3/4}$, sample paths are likely to remain in $\mathcal{B}(h)$ for exponentially long time spans, as in the case $y(0) = \delta$, provided we choose $h \gg \sigma$. Otherwise, sample paths are likely to overcome the unstable equilibrium branch as soon as $\mathcal{B}(\sigma)$ reaches a width of order \sqrt{y} , that is, when $y(t)$ is of order $\sigma^{4/3}$. By (3.51), this happens at a time of order $|\log \sigma|$, cf. Fig. 3.9.

Let us now implement this local analysis into the context of the full system (e.g. the Morris–Lecar equations, cf. Fig. 3.10). The parameter δ of the normal form can be computed by expanding the slow component of the vector field around the saddle–node bifurcation point (x^*, y^*) , yielding

$$\delta \simeq \frac{g(x^*, y^*)}{\partial_y g(x^*, y^*)}. \quad (3.54)$$

From the previous analysis, one concludes that

- If $\sigma \ll \delta^{3/4}$, the system will display rare spikes, with approximately exponentially distributed waiting times between spikes (i.e. the spike times follow a Poisson process), with mean of order $e^{\text{const } \delta^{3/2}/\sigma^2}$.

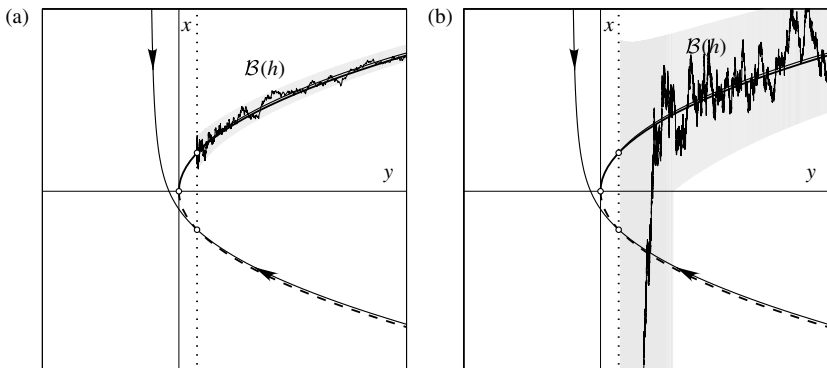


FIG. 3.9: Sample paths of the stochastic differential equation (3.50) for $\delta = \varepsilon = 0.1$, and (a) $\sigma = 0.05 < \delta^{3/4}$, (b) $\sigma = 0.35 > \delta^{3/4}$. In both cases, the sample paths are likely to stay in the shaded set $\mathcal{B}(h)$, but for strong noise intensity, they are likely to overcome the unstable equilibrium branch before reaching the stable equilibrium point.

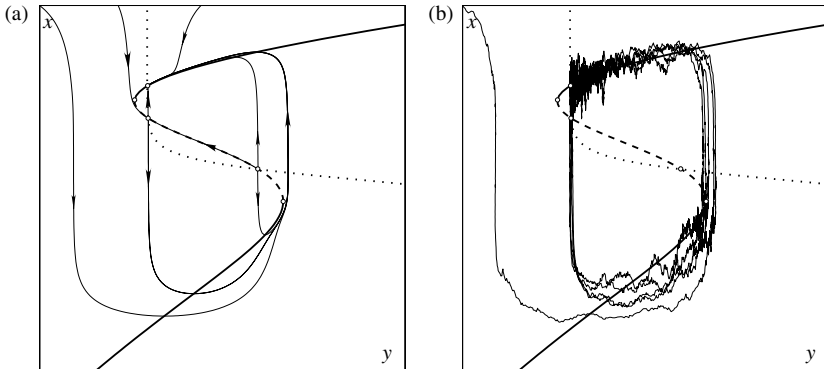


FIG. 3.10: (a) Some orbits of the deterministic Morris–Lecar model. Parameter values are $x_1 = 0.5$, $x_2 = 0.15$, $x_3 = 0.37$, $x_4 = -0.05$, $c_1 = 4.75$, $c_2 = 1$, $c_3 = 5$, $V_2 = 2$, $V_3 = 0$ and $\varepsilon = 0.05$. We show in particular the stable and unstable manifolds of the hyperbolic equilibrium point. Its unstable manifolds both converge to the same stable equilibrium point, but have very different lengths. (b) A sample path of the Morris–Lecar model with the same parameter values as before, and noise of intensity $\sigma = 0.07$ and $\sigma' = 0.05$ added to the slow and fast components, respectively.

- If $\sigma \geq \delta^{3/4}$, the system will spike frequently, the time interval between spikes being of order $|\log \sigma|$ because of the time needed to reach the active zone, in which escape from the local potential minimum is easy.

Fig. 3.11 illustrates these results for different values of the noise intensity.

We expect that this picture will not change significantly when weak noise of intensity σ' is added to the slow variable y , as long as $\sigma' \ll \delta$. For stronger noise, there is the possibility that the system escapes from the stable equilibrium point by turning around the saddle-node bifurcation point.

3.5.2 Excitability of type II

Excitability of type II occurs for instance when the nullcline $g(x, y) = 0$ intersects only the stable equilibrium branch near a saddle-node bifurcation point. This situation occurs, e.g. in the FitzHugh–Nagumo model, when $\beta = 1$, $\gamma = 0$ and $\alpha = 1/\sqrt{3} + \delta$ for small δ : Then the nullcline is the horizontal line $x = 1/\sqrt{3} + \delta$, passing at a distance δ above one of the saddle-node bifurcation points.

The dynamics near the bifurcation point can again be understood through its normal form, given by

$$\begin{aligned}\varepsilon \dot{x} &= y - x^2, \\ \dot{y} &= \delta - x.\end{aligned}\tag{3.55}$$

As before, this system has two equilibrium branches at $x = \pm\sqrt{y}$. The associated invariant curves are shown in Fig. 3.12. Unlike in the case discussed in the

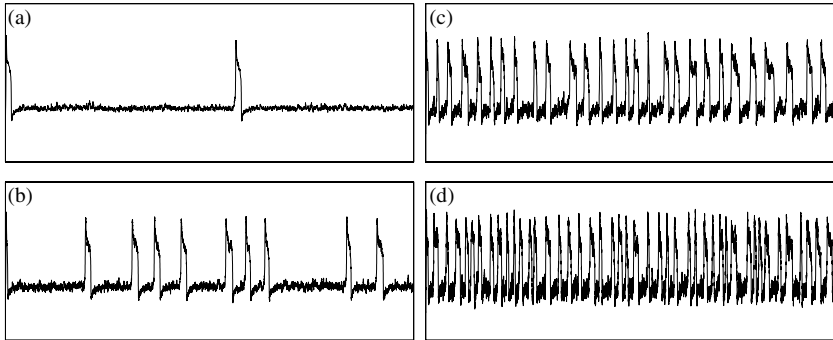


FIG. 3.11: Plot of $-x(t)$ as a function of t for the Morris–Lecar model, showing the different spiking behaviours as the noise intensity increases. Parameter values are the same as in Fig. 3.10, except that $c_1 = 4.7$ and (a) $\sigma = 0.027$, (b) $\sigma = 0.045$, (c) $\sigma = 0.085$, and (d) $\sigma = 0.125$. The behaviour changes from rare random spikes roughly following a Poisson process to frequent, more regularly distributed spikes. For stronger noise, the spikes become irregular again because multiple transitions between equilibrium branches are more likely.

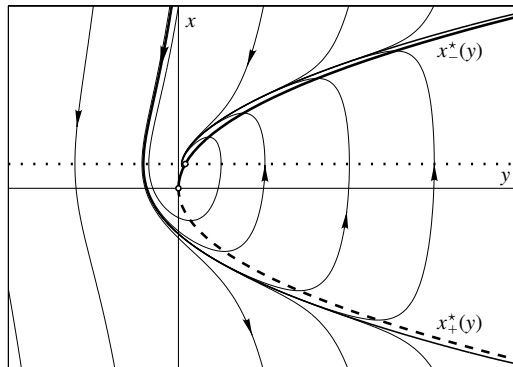


FIG. 3.12: Some orbits of the deterministic slow–fast system (3.55) for $\varepsilon = \delta = 0.2$. The invariant curve tracking the unstable equilibrium branch $x = x_+^*(y)$ for positive y delimits the basin of attraction of the stable equilibrium point (δ, δ^2) .

previous section, there is only a single equilibrium point (δ, δ^2) . The linearization of the vector field at this point is given by the matrix

$$A = \begin{pmatrix} -2\delta/\varepsilon & 1/\varepsilon \\ -1 & 0 \end{pmatrix}, \quad (3.56)$$

which has eigenvalues $(-\delta \pm \sqrt{\delta^2 - \varepsilon})/\varepsilon$. Thus the equilibrium point is a stable node for $\delta > \sqrt{\varepsilon}$, a stable focus for $0 < \delta < \sqrt{\varepsilon}$, an unstable focus for $-\sqrt{\varepsilon} < \delta < 0$ and an unstable node for $\delta < -\sqrt{\varepsilon}$. At $\delta = 0$, the point undergoes a Hopf bifurcation. It is known that such a bifurcation generically corresponds to either the creation of a stable periodic orbit, or the destruction of an unstable periodic orbit. In the present case, a stable periodic orbit is created as δ becomes negative. This orbit has a very particular shape: Starting near the origin, it tracks the unstable equilibrium branch for some time, then quickly jumps to the stable equilibrium branch, which it tracks until returning near the origin, closing the cycle.

Placing this local analysis back into the context of the FitzHugh–Nagumo equations, one sees that

- For $\delta > 0$, all orbits converge to the stable equilibrium point, cf. Fig. 3.13(a).
- As δ becomes negative, the system develops a periodic orbit of particular shape, reminding some authors of the shape of a duck, cf. Fig. 3.13(b). This is why these solutions are often called (French) ducks, or canards (Callot, Diener and Diener, 1978, Eckhaus, 1983).

Canards only exist in an interval of δ -values which is exponentially small in ε . Decreasing δ further, the periodic orbit quickly starts resembling that of the van der Pol oscillator.

Let us now add noise to the system, first by considering only the normal form

$$\begin{aligned} dx(t) &= \frac{1}{\varepsilon}(y(t) - x(t)^2) dt + \frac{\sigma}{\sqrt{\varepsilon}} dW_t^{(1)}, \\ dy(t) &= (\delta - x(t)) dt + \sigma' dW_t^{(2)}. \end{aligned} \quad (3.57)$$

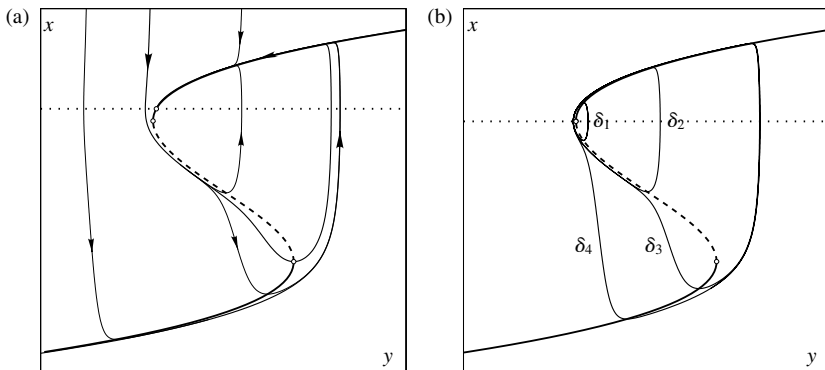


FIG. 3.13: (a) Orbits of the FitzHugh–Nagumo system for $\varepsilon = 0.05$, $\beta = 1$, $\gamma = 0$ and $\alpha = 1/\sqrt{3} + \delta$, with $\delta = 0.1$. The orbit tracking the unstable equilibrium branch has been obtained by starting in the lower right saddle-node bifurcation point, and going backwards in time. (b) Periodic orbits of the same system, for negative δ , taking values $\delta_1 = -0.003$, $\delta_2 = -0.003765458$, $\delta_3 = -0.003765459$ and $\delta_4 = -0.005$.

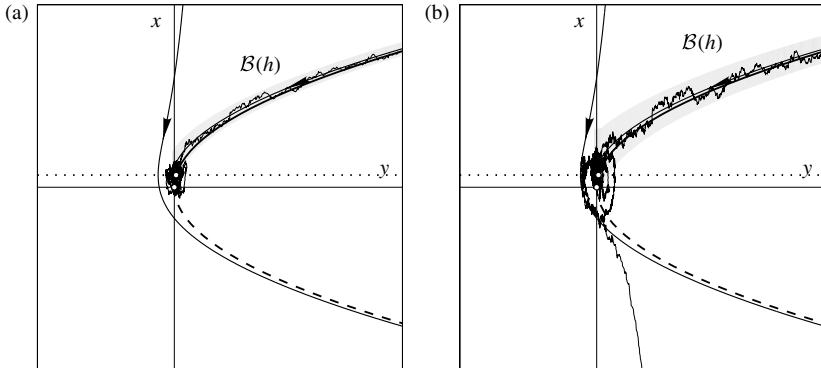


FIG. 3.14: Sample paths of the stochastic differential equation (3.57) for $\varepsilon = \delta = 0.1$, and (a) $\sigma = 0.05$, $\sigma' = 0.02$ and (b) $\sigma = 0.08$, $\sigma' = 0.02$. In both cases, the sample paths are likely to stay in the shaded set $\mathcal{B}(h)$, but for strong noise intensity, they are likely to cross the invariant curve tracking the unstable branch.

Unlike in the case studied in the previous section, we cannot reduce the system to a one-dimensional one, which makes its analysis much harder. In particular, we now have to study where and when sample paths cross the invariant curve tracking the unstable equilibrium branch, which delimits the basin of attraction of the stable equilibrium point (Fig. 3.14).

If $\delta > \sqrt{\varepsilon}$, the equilibrium point (δ, δ^2) is a node, towards which the invariant curve tracking the stable branch converges from the right. We can basically repeat the analysis from the previous section (with δ replaced by δ^2), showing that

- If $\sigma \ll \delta^{3/2}$, the system will display rare spikes, with approximately exponentially distributed waiting times between spikes (i.e. the spike times follow a Poisson process) with mean waiting time of order $e^{\text{const } \delta^3/\sigma^2}$, cf. Fig. 3.15(a).
- If $\sigma \geq \delta^{3/2}$, the system will spike frequently, the time interval between spikes being of order $|\log \sigma|$ because of the time needed to reach the active zone, in which escape from the local potential minimum is easy, cf. Fig. 3.15(b).

If $\delta < \sqrt{\varepsilon}$, the equilibrium point (δ, δ^2) is a focus, around which the invariant curve coming from the right is wound. This situation has been analysed using an approximate constant of motion of the normal form. The result of a rather intricate scaling analysis (Muratov and Vanden-Eijnden, 2008) is that there are now three different regimes, namely

- If $\sigma^2 + (\sigma')^2 \ll (\delta\varepsilon^{1/4})^2$, escape from the stable focus is unlikely, and the system will display rare spikes. The average time elapsing between spikes has order $e^{-(\delta\varepsilon^{1/4})^2/(\sigma^2 + (\sigma')^2)}$.

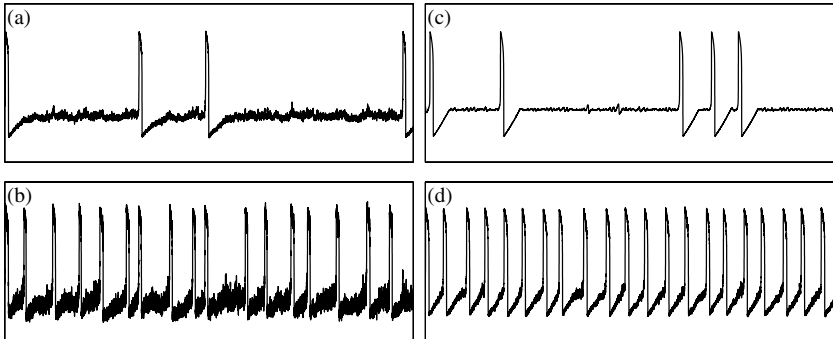


FIG. 3.15: Plot of $-x(t)$ as a function of t for the FitzHugh–Nagumo model, showing the different spiking behaviours. Parameter values are $\varepsilon = 0.01$ and (a) $\delta = 0.15$, $\sigma = \sigma' = 0.04$, (b) $\delta = 0.15$, $\sigma = \sigma' = 0.15$, (c) $\delta = 0.01$, $\sigma = \sigma' = 0.003$, and (d) $\delta = 0.01$, $\sigma = \sigma' = 0.05$.

- If $(\delta\varepsilon^{1/4})^2 \ll \sigma^2 + (\sigma')^2 \ll \delta\varepsilon$, escape from the focus is still unlikely, but there is a certain chance that a spike will immediately be followed by another one, so that the system displays rare sequences of spikes, cf. Fig. 3.15(c).
- If $\sigma^2 + (\sigma')^2 \gg \delta\varepsilon$, the system again displays frequent and more regularly spaced spikes, cf. Fig. 3.15(d).

We did not discuss the distribution of time intervals between spikes, for the reason that not much is known about it. Unlike the case of exit from a potential well, we have to deal here with the problem of noise-induced escape through a characteristic boundary (Day, 1990a, 1992), which does not necessarily follow an exponential law. If, for instance, the boundary is a periodic orbit, *cycling* occurs and the exit location depends logarithmically on the noise intensity (Day, 1990b, 1994, 1996, Berglund and Gentz, 2004). This is related to the fact that a characteristic boundary is not crossed instantaneously the moment a small neighbourhood is reached.

Finally note that the quasi-static regime of exponentially small ε (Freidlin, 2001) can also be treated in this particular situation (DeVille, Vanden-Eijnden and Muratov 2005, Muratov, Vanden-Eijnden and E, 2005, Sowers 2008).

3.6 Concluding remarks

We have shown how to determine the effects of noise on slow–fast differential equations, such as those appearing in models for action-potential generation through neuron membranes. The analysis proceeds by studying separately the dynamics near stable and unstable equilibrium branches, near bifurcation points, and in the remaining phase space, before patching the parts together in order to obtain the global picture.

The dynamics away from bifurcation points is well understood, under very general assumptions. Near bifurcation points, the analysis has to rely on case

studies, and not all cases have yet been described to the same level of accuracy. In particular, in situations leading to excitability of type II (a nullcline intersecting a stable branch near a saddle-node bifurcation point), the relevant scaling regimes have been determined, but little is known on the distribution of exit times. The stochastic dynamics near bifurcation points of higher codimension has also not yet been analysed in sufficient detail.

The models we have considered here, although being relatively simple, are able to reproduce several types of spiking behaviour observed in experiments: rare isolated spikes, frequent, nearly periodic spikes, and rare clusters of spikes (bursts). Comparing the predictions of these theoretical models with experimental results will allow one to determine the noise intensities to be used in the stochastic model equations, thereby improving their accuracy.

Acknowledgement

Support by the German Research Council (DFG), within the CRC 701 ‘Spectral Structures and Topological Methods in Mathematics’, is gratefully acknowledged.

References

- Benoît, E. (ed.) (1991). *Dynamic Bifurcations*, Berlin. Springer-Verlag.
- Berglund, N. and Gentz, B. (2002a). Beyond the Fokker–Planck equation: Pathwise control of noisy bistable systems. *J. Phys. A*, **35**(9), 2057–2091.
- Berglund, N. and Gentz, B. (2002b). The effect of additive noise on dynamical hysteresis. *Nonlinearity*, **15**(3), 605–632.
- Berglund, N. and Gentz, B. (2002c). Pathwise description of dynamic pitchfork bifurcations with additive noise. *Probab. Theory Related Fields*, **122**(3), 341–388.
- Berglund, N. and Gentz, B. (2002d). A sample-paths approach to noise-induced synchronization: Stochastic resonance in a double-well potential. *Ann. Appl. Probab.*, **12**, 1419–1470.
- Berglund, N. and Gentz, B. (2003). Geometric singular perturbation theory for stochastic differential equations. *J. Differential Equations*, **191**, 1–54.
- Berglund, N. and Gentz, B. (2004). On the noise-induced passage through an unstable periodic orbit I: Two-level model. *J. Statist. Phys.*, **114**, 1577–1618.
- Berglund, N. and Gentz, B. (2005). *Noise-Induced Phenomena in Slow–Fast Dynamical Systems. A Sample-Paths Approach*. Probability and its Applications. Springer-Verlag, London.
- Berglund, N. and Kunz, H. (1999). Memory effects and scaling laws in slowly driven systems. *J. Phys. A*, **32**(1), 15–39.
- Bovier, A., Eckhoff, M., Gayrard, V., and Klein, M. (2004). Metastability in reversible diffusion processes. I. Sharp asymptotics for capacities and exit times. *J. Eur. Math. Soc. (JEMS)*, **6**(4), 399–424.
- Callot, J.-L., Diener, F., and Diener, M. (1978). Le problème de la “chasse au canard”. *C. R. Acad. Sci. Paris Sér. A-B*, **286**(22), A1059–A1061.

- Day, M. (1990a). Large deviations results for the exit problem with characteristic boundary. *J. Math. Anal. Appl.*, **147**(1), 134–153.
- Day, M. V. (1983). On the exponential exit law in the small parameter exit problem. *Stochastics*, **8**, 297–323.
- Day, M. V. (1990b). Some phenomena of the characteristic boundary exit problem. In *Diffusion processes and related problems in analysis, Vol. I (Evanston, IL, 1989)*, Volume 22 of *Progr. Probab.*, pp. 55–71. Birkhäuser Boston, Boston, MA.
- Day, M. V. (1992). Conditional exits for small noise diffusions with characteristic boundary. *Ann. Probab.*, **20**(3), 1385–1419.
- Day, M. V. (1994). Cycling and skewing of exit measures for planar systems. *Stochastics*, **48**, 227–247.
- Day, M. V. (1996). Exit cycling for the van der Pol oscillator and quasipotential calculations. *J. Dynam. Differential Equations*, **8**(4), 573–601.
- DeVille, R. E. L., Vandenberghe, E., and Muratov, C. B. (2005). Two distinct mechanisms of coherence in randomly perturbed dynamical systems. *Phys. Rev. E (3)*, **72**(3), 031105.
- Eckhaus, W. (1983). Relaxation oscillations including a standard chase on French ducks. In *Asymptotic analysis, II*, Volume 985 of *Lecture Notes in Math.*, pp. 449–494. Springer, Berlin.
- Fenichel, N. (1979). Geometric singular perturbation theory for ordinary differential equations. *J. Differential Equations*, **31**(1), 53–98.
- FitzHugh, R. (1961). Impulses and physiological states in models of nerve membrane. *Biophys. J.*, **1**, 445–466.
- Freidlin, M. I. (2001). On stable oscillations and equilibriums induced by small noise. *J. Statist. Phys.*, **103**, 283–300.
- Gradštejn, I. S. (1953). Application of A. M. Lyapunov's theory of stability to the theory of differential equations with small coefficients in the derivatives. *Mat. Sbornik N. S.*, **32**(74), 263–286.
- Haberman, R. (1979). Slowly varying jump and transition phenomena associated with algebraic bifurcation problems. *SIAM J. Appl. Math.*, **37**(1), 69–106.
- Hodgkin, AL and Huxley, AF (1952, Aug). A quantitative description of membrane current and its application to conduction and excitation in nerve. *J. Physiol. (Lond.)*, **117**(4), 500–44.
- Izhikevich, E. M. (2000). Neural excitability, spiking and bursting. *Internat. J. Bifur. Chaos Appl. Sci. Engrg.*, **10**(6), 1171–1266.
- Jones, C. K. R. T. (1995). Geometric singular perturbation theory. In *Dynamical systems (Montecatini Terme, 1994)*, pp. 44–118. Springer, Berlin.
- Jung, P., Gray, G., Roy, R., and Mandel, P. (1990). Scaling law for dynamical hysteresis. *Phys. Rev. Letters*, **65**, 1873–1876.
- Kosmidis, E. K. and Pakdaman, K. (2003). An analysis of the reliability phenomenon in the FitzHugh-Nagumo model. *J. Comput. Neuroscience*, **14**, 5–22.
- Longtin, A. (2000). Effect of noise on the tuning properties of excitable systems. *Chaos, Solitons and Fractals*, **11**, 1835–1848.

- Mishchenko, E. F. and Rozov, N. Kh. (1980). *Differential equations with small parameters and relaxation oscillations*. Plenum Press, New York.
- Morris, C and Lecar, H (1981, Jul). Voltage oscillations in the barnacle giant muscle fiber. *Biophys J*, **35**(1), 193–213.
- Muratov, C. B. and Vanden-Eijnden, E. (2008). Noise-induced mixed-mode oscillations in a relaxation oscillator near the onset of a limit cycle. *Chaos* (18), 015111.
- Muratov, C. B., Vanden-Eijnden, E., and E, W. (2005). Self-induced stochastic resonance in excitable systems. *Phys. D*, **210**(3-4), 227–240.
- Nagumo, J. S., Arimoto, S., and Yoshizawa, S. (1962). Active pulse transmission line simulating nerve axon. *Proc. IRE*, **50**, 2061–2070.
- Nayfeh, A. H. (1973). *Perturbation methods*. John Wiley, New York.
- Øksendal, B. (1985). *Stochastic Differential Equations*. Springer-Verlag, Berlin.
- O'Malley, Jr., R. E. (1974). *Introduction to Singular Perturbations*. Academic Press, New York.
- O'Malley, Jr., R. E. (1991). *Singular Perturbation Methods for Ordinary Differential Equations*, Volume 89 of *Applied Mathematical Sciences*. Springer-Verlag, New York.
- Pontryagin, L. S. (1957). Asymptotic behavior of solutions of systems of differential equations with a small parameter in the derivatives of highest order. *Izv. Akad. Nauk SSSR. Ser. Mat.*, **21**, 605–626.
- Sowers, R. B. (2008). Random perturbations of canards. *J. Theoret. Probab.*, **21**, 824–889.
- Tihonov, A. N. (1952). Systems of differential equations containing small parameters in the derivatives. *Mat. Sbornik N. S.*, **31**, 575–586.
- van der Pol, B. (1920). A theory of the amplitude of free and forced triode vibration. *Radio. Rev.*, **1**, 701.
- van der Pol, B. (1926). On relaxation oscillation. *Phil. Mag.*, **2**, 978–992.
- van der Pol, B. (1927). Forced oscillations in a circuit with non-linear resistance. (Reception with reactive triode). *Phil. Mag.*, **3**, 65–80.
- Wasow, W. (1987). *Asymptotic Expansions for Ordinary Differential Equations*. Dover Publications Inc., New York. Reprint of the 1976 edition.

NEURAL COHERENCE AND STOCHASTIC RESONANCE

André Longtin

4.1 Introduction

All neurons in the peripheral and central nervous system exhibit randomness to some extent. Repeated presentations of a given deterministic stimulus does not produce the same response, although these responses may have similar statistical features (Moore, Perkel, and Segundo, 1966). This randomness originates from one or more sources. (Tuckwell, 1989, Lindner, Garcia-Ojalvo, Neiman and Schimansky-Geier, 2004, Stein, Gossen and Jones, 2005). Two sources are particularly important. The first is intrinsic, and arises from conductance fluctuations of ion channels. This includes fluctuations in the associated biochemical machinery that regulates or interacts with them, such as second messengers. These channels are distributed from synapses to dendrites to soma to hillock to axon, and so this is a ubiquitous source of noise. The second source is extrinsic, and comes from the synaptic activity of other cells that drive the synapses of a neuron, and includes here the failure properties of synapses. These inputs produce fluctuating currents which randomize the firing mechanism at the hillock. This influences spike timing – spike shape is unaffected.

While there may be some debate as to the origins of noise in specific cells – and part of it might be deterministic chaos arising from nonlinearity – there is often more debate as to the functionality of noise (Gammaitoni *et al.*, 1998, Stein, Gossen and Jones, 2005). While some noise is likely a nuisance to the brain's operation, it may in fact enhance the regularity of firing. It may express subthreshold activity that would otherwise go unnoticed to post-synaptic neurons. It may break up phase lockings and enable smooth encoding of incoming signals. It may conceal correlations that carry much important information about the level of synchrony in a network or the memory state of its synapses. It may enable the production of smooth motor actions. And in many sensory systems that are driven by near-periodic signals, such as in mechanoreceptors, (Douglass *et al.*, 1993), the hair cells of the auditory system, and the receptors of the electrosensory systems, and even neurons in the primary visual cortices (Longtin, Bulsara, and Moss, 1991), the neurons may fire around a preferred phase of the signal, yet randomly skip cycles of these signals. This behaviour is a form of stochastic phase locking known as skipping.

The purpose of this chapter is to review the mechanisms by which noise can (1) enhance the regularity of firing, an effect known as coherence resonance (CR), (2) produce stochastic phase locking, and under the right circumstances, (3) allow the cell to encode a subthreshold signal via stochastic resonance (SR).

Throughout, special attention is given to the constructive effect of noise, and to the connection between stochastic and deterministic resonances in such systems. We first give some background on excitability, noise, numerical integration, and measures of regularity in Section 4.2. We then discuss coherence resonance in the context of Type II neural dynamics, then Type I dynamics, in Section 4.3. The response to periodic driving and noise is then analysed in Section 4.4 using more rigorous definitions of ‘subthreshold’ and ‘phase locking’. Section 4.5 focuses on SR, first in Type II, then Type I dynamics. We summarize findings on the popular leaky integrate-and-fire model in Section 4.6. The chapter ends with a discussion of generalized coherence and stochastic resonance effects, outstanding problems and potentially fruitful future research directions.

4.2 Excitability, phase locking, and noise

4.2.1 *Excitability versus oscillatory firing*

The behaviour of excitable systems subjected to deterministic and/or stochastic forcing has been the subject of ongoing interest for many decades (Glass and Mackey, 1988, Lindner *et al.*, 2004, Tateno *et al.*, 1995). An excitable system executes a large stereotyped motion in phase space when it is subjected to sufficiently strong forcing. This can be a constant forcing, or a time-varying forcing. When the forcing is too weak, the dynamics of the excitable system are confined to a neighbourhood of a (usually unique) fixed point.

For constant signals, one can define an oscillatory regime as one where the constant ‘bias’ signal causes repeated firings. In contrast, in the excitable regime, the constant bias is insufficient to produce sustained firings. Note that there are many variants of this definition, because any neuron that can fire is often labelled as an excitable system, regardless of whether it is excitable or oscillatory by the definition based on a ‘constant signal.’ The two regimes are usually ‘next’ to each other in parameter space. Hence in the vicinity of this excitable regime, there exists a continuous range of parameters for which the system exhibits oscillatory behaviour associated with a limit cycle attractor (Izhikevich, 2007). The phase space trajectory during the limit cycle is closely related to the stereotyped firing event in the excitable regime. Nevertheless, it is important to distinguish between the ‘excitable’ and ‘oscillatory’ regime for the purpose of understanding noise-induced firing, phase locking to periodic forcing, and the effect of noise on phase locking. The transition point at which the cell starts firing is called rheobase.

For time-varying signals, there are two other regimes that must be distinguished within the excitable regime: subthreshold and suprathreshold forcing. The ability of a time-varying signal to produce spikes is determined by its magnitude and frequency content, as well as where the system lies on the line between excitable and oscillatory behaviour. If the system is close to oscillatory behaviour, the threshold for spiking is low, and a weak forcing signal can make the trajectory cross the threshold. If a given signal produces spiking, it will be referred to

as suprathreshold; otherwise, it is subthreshold. It is important to clearly define these regimes, because they determine the main features of the response of the cell to noise and to periodic input. The frequency is also generally important because the threshold is frequency-dependent, as we will see below. In fact, the mean value of the input, or ‘mean bias’, as well as its frequency and magnitude, are the most important determinants of sub- or suprathreshold behaviour that are under (relatively) easy experimental control.

Our focus in this chapter is on dynamical neuronal models, in contrast to non-dynamical neuron models that abound in the literature (Holden, 1976, Wiesenfeld *et al.*, 1994), and which focus solely on the statistics of the firing events without regard to how events are generated. Some interesting statistics of the firing events and phase locking are revealed by such simplified models, such as the behaviour at low forcing frequency where other time-scales of the neuron do not come into play.

4.2.2 Phase locking

Responses to suprathreshold periodic forcing include $n:m$ phase locking patterns with m firings for n forcing cycles, as well as chaotic firing patterns (Tateno *et al.*, 1995, Glass and Mackey, 1988) arising from the interaction of internal time-scales with the time-scale of the input. Stochastic forcing further turns a quiescent (i.e. non-firing) excitable system into a stochastic oscillator. In the oscillatory regime, noise turns the deterministic oscillator into a noise-perturbed oscillator. This can modify the phase locking structure, and can strongly affect the cell’s frequency sensitivity (‘tuning’). It is also known that noise can smoothen and/or increase the dynamic range of excitable cells by linearizing their stimulus-response characteristics and breaking up phase lockings (Knight, 1972, Glass *et al.*, 1980, Yu and Lewis, 1989, Spekreijse, 1969). Furthermore, other new phenomena arise from stochastic forcing, such as coherence resonance (Pikovsky and Kurths, 1997, Longtin, 1997), stochastic resonance (Gammaitoni *et al.*, 1998), mean frequency locking, and noise-enhanced phase coherence (reviewed in Lindner *et al.*, 2004).

4.2.3 Excitability classes

Type II neurons make a transition from quiescence to periodic firing via a Hopf bifurcation (Izhikevich, 2007). The Hodgkin–Huxley (HH) equations with standard parameters as well as its simplified description in terms of the FitzHugh–Nagumo relaxation oscillator are example of models with Type II dynamics. In contrast, Type I neurons make this transition via a saddle-node on an invariant circle bifurcation (Izhikevich, 2007). Other characteristics differ between the two types, such as latency to fire and phase resetting; they will not concern us here even though they shape responses. Type II dynamics exhibits a resonance in the sense that the membrane potential is highly responsive near a given frequency. Also, the firing frequency jumps abruptly to a finite value when the bias crosses rheobase, i.e. the firing frequency-versus-bias current (‘f-I’ curve) is discontinuous at the onset of firing. In contrast, the f-I curve is continuous for Type I, and arbitrarily low firing rates can occur; and there is no resonance. Note that

things are less clear-cut when many ionic species are present that contribute e.g. to bursting (Izhikevich, 2007). Below we investigate coherence and stochastic resonance for both dynamics. We also review results for the LIF model, which is neither Type I nor Type II, yet used very frequently for neural modelling studies.

4.2.4 Stochastic dynamics

Spike timing reflects noise in the absence of any stimuli. In the presence of a stimulus, spike timing depends on the signal and on the synaptic and other sources of cellular noise. Of course, the stimulus itself may be a stochastic process, such as band-limited ('coloured') Gaussian noise. Also, in the context of stochastic resonance, noise can be added to the external signal (see, e.g. Douglass *et al.* (1993)) or internally via intracellular injections (Stacey and Durand, 2001) or by stimulating afferent fibres (in computational studies this synaptic input can be simulated, see e.g. Rudolph and Destexhe (2001*b*)). From a modelling perspective, one has to decide whether the internal cellular noise and external, perhaps noisy, signals can be lumped together into one term, or enter in different parts of the equations, either as multiplicative (conductance) noise or additive noise. Also, one has to consider the possibility that synaptic noise may be stimulus-dependent (Lindner and Schimansky-Geier, 2001, Lánský and Sacerdote, 2001).

4.3 Coherence resonance

4.3.1 Origins

There are two ways to understand CR: one based on the statistics of activation and excursion times (Pikovsky and Kurths, 1997; Pakdaman, Tanabe and Shimokawa, 2001), the other, on the effect of noise on limit cycles. We begin with the first way, and consider a noiseless excitable system sitting at its subthreshold resting potential V_{rest} (a fixed point). If perturbed just beyond threshold, the voltage will perform a large excursion in phase space and come back to V_{rest} . The total time from threshold to the proximity of V_{rest} is the excursion time t_e , made up of deterministic processes: the absolute refractory period during the spike, and the time to reach V_{rest} . Strictly speaking, this time includes the relative refractory period. Now imagine that noise is present. It will act like the perturbation above, and there will be a distribution of times to cross threshold starting from V_{rest} . We can then define the mean $\langle t_a \rangle$ and variance $\langle \Delta t_a^2 \rangle$ of this 'activation' time t_a . One can also define the mean $\langle t_e \rangle$ and variance $\langle \Delta t_e^2 \rangle$ of the 'excursion' time. The total time between firings is the random interspike interval variable $\text{ISI} = t_a + t_e$. Coherence can be defined by the ratio

$$R = \frac{\sqrt{\langle \Delta \text{ISI}^2 \rangle}}{\langle \text{ISI} \rangle} \quad (4.1)$$

where $\langle \Delta ISI^2 \rangle = \langle ISI^2 \rangle - \langle ISI \rangle^2$. In other words, R is the ratio of the standard deviation to the mean of the ISI, also known as the coefficient of variation of ISIs (CV). It follows that R^2 can be written as a weighted sum of the CVs of t_e and t_a :

$$R^2 = R_a^2 \left(\frac{\langle t_a \rangle}{\langle ISI \rangle} \right)^2 + R_e^2 \left(\frac{\langle t_e \rangle}{\langle ISI \rangle} \right)^2. \quad (4.2)$$

For low noise, activation is a Poisson process, for which $R_a = 1$, a property of processes with low rate of ‘success’ (to cross threshold). As noise increases, t_a drops to zero faster than $\langle ISI \rangle$ does, so R_a goes to zero rapidly. However, the second term increases from zero for two reasons: for zero noise there is no variance in t_e (i.e. $R_e = 0$), as it should be for a deterministic process; further, increasing noise does not affect the excursion time much, but mainly shortens the mean interval. So both R_e and the ratio $\langle t_e \rangle / \langle ISI \rangle$ increase. Thus, there exists a value of optimal noise where R^2 will be minimized, and consequently the CV will be minimized. At this point the spike train can be said to have the highest regularity.

The origins of CR can also be traced to studies of noise effects on autonomous (limit cycle) oscillations (Lindner *et al.*, 2004). Assume there exists a bifurcation between fixed point and limit cycle without noise. There may even be coexistence of a stable fixed point and stable limit cycle over some parameter range. Consider this latter ‘subcritical’ bistable case: if the system is at the fixed point, then noise can kick the state outside the basin of attraction of this fixed point and land on the limit cycle. Likewise, noise can kick the system off the limit cycle back to the fixed point. With ongoing noise, there are transitions between the two basins, with the result that the trajectory is made up partly of oscillations, albeit noisy ones, corresponding to the epochs when the system tries to settle on the limit cycle. For neurons, the limit cycle is associated with repetitive spiking; thus the sequence of spikes will exhibit some of the periodicity of the limit cycle. Too much noise will clearly cause spikes at random times. Now extend this argument to the non-bistable case, and set the parameter to the bifurcation point. Noise will amount to changing the system from fixed point to limit cycle randomly. Below we will define a spectral measure β_{CR} for the sharpness of the limit cycle induced by noise.

4.3.2 Noise: white or coloured?

The Type I model discussed below will be driven by Gaussian white noise. This is the simplest form of noise for simulation purposes and to do theoretical work. Its only characteristic is its intensity D (defined below). In contrast, the Type II model used below will be driven by coloured noise known as an Ornstein–Uhlenbeck (OU) process, which has an intensity D and a correlation time τ_c . This allows one to independently study the effect of intensity as well as frequency content of the noise. This content is related to the time-scale of

synaptic responses. Synaptic input is often modelled as a train of Dirac delta functions

$$I_{\text{syn}}(t) = \sum_{i=1}^N \sum_j J_i \delta(t - t_i^j), \quad (4.3)$$

where the first sum is over all N synapses, and the second, over all firing times t_i^j at each synapse. Here the reversal potential of the synaptic current is neglected (Tuckwell, 1989). The synaptic efficacies J_i are often lumped into one efficiency g . An input spike train causing a sequence of synaptic currents is often assumed to be a Poisson process with mean rate $N\nu$. If ν is large, and the synaptic weights are small, many synaptic events must add up to fire the cell; further if $N\nu \gg 1$, the Poisson process can be approximated by a diffusion process (Gaussian white noise) with the same mean and variance. Thus, synaptic input may be approximated by Gaussian white additive noise on the voltage dynamics. Furthermore, synapses have their own dynamics (instead of delta responses). If the diffusion approximation is valid, the synaptic current dynamics are approximately driven by Gaussian white noise. The synaptic current is then an OU process (see below), which in turn drives the voltage dynamics. This justifies using OU noise for input to analytically and computationally simpler models such as the FitzHugh–Nagumo (FHN) model below (Tuckwell, 1989, Longtin, 1993, Brunel *et al.*, 2001).

4.3.3 Coherence resonance in Type II dynamics

4.3.3.1 FHN model with coloured noise We consider the FitzHugh–Nagumo (FHN) model obtained from the standard Hodgkin–Huxley (HH) model by lumping together the fast voltage and sodium activation channels into the voltage variable V , and the sodium inactivation and potassium activation variables together into a slow recovery variable w . Although technically speaking the FHN system is a relaxation oscillator, it still has realistic aspects of Type II excitable dynamics such as a deterministic resonance. We focus on this model with additive periodic and/or stochastic forcing (Longtin, 1993):

$$\epsilon \frac{dV}{dt} = V(V - 0.5)(1 - V) - w + A \sin(\omega_0 t) + I + \eta(t) \quad (4.4)$$

$$\frac{dw}{dt} = V - w - b \quad (4.5)$$

$$\frac{d\eta}{dt} = -\lambda\eta + \lambda\xi(t). \quad (4.6)$$

The bias current I encompasses the mean external and synaptic currents. A Hopf bifurcation occurs as I increases. Here $\xi(t)$ is Gaussian white noise of mean zero and correlation function $\langle \xi(t)\xi(s) \rangle = 2D\delta(t - s)$. The forcing frequency is $f_0 = \omega_0/(2\pi)$, and its inverse is the forcing period T . The stochastic process

η is OU noise with variance $D\lambda$ and correlation time $t_c \equiv \lambda^{-1}$ (Horsthemke and Lefever, 1984). Note that λ has units of frequency, and gives a measure of the cutoff frequency of the fluctuations of the noise; t_c gives a measure of its autocorrelation time. The effect of intensity is investigated by varying D , as we do in this chapter. Effects of correlation time can also be studied by varying λ , but one then has to decide if the variance of the OU process is kept constant or not.

We should mention that different scalings of the OU process exist, such as

$$\frac{d\eta}{dt} = -\lambda\eta + \sqrt{2\sigma^2\lambda} \xi(t) \quad (4.7)$$

where again the white noise has zero mean but its autocorrelation is $\langle \xi(t)\xi(s) \rangle = \delta(t-s)$. In this case σ^2 directly gives the variance of the OU noise η . One can investigate the effect of the noise correlation, i.e. of its ‘color’, all the while keeping the noise intensity $\sigma^2 t_c$ constant. This means for example that the white noise limit can be investigated by keeping $\sigma^2 t_c$ fixed and letting τ approach zero. It is important to understand the properties of the scaling chosen to avoid problems such as noiseless limits (Hänggi and Jung, 1995).

Note also that the noise has been added to the fast dynamics, but it could be added to the recovery variable, especially if this variable mimics K⁺ channel fluctuations that typically dominate the resting state. Analytic results on CR and SR for Eqns (4.4)–(4.6) have been obtained for white noise and small ϵ , or for a piecewise linear version of the voltage dynamics with slow forcing (Collins, Chow and Imhoff, 1995), and are reviewed by Gammaconi *et al.* (1998) and Lindner *et al.* (2004).

4.3.3.2 Numerics for FHN The system (4.4)–(4.6) can be integrated numerically using any technique for the V and w variables, as long as it coordinates properly with the integration of the Gaussian white noise in the η dynamics. The latter will usually be the limiting step, because the order of algorithms for white noise is smaller than for deterministic processes (Kloeden and Platen, 1992). For example, the simplest – but slowest – method to integrate the η dynamics is given by an Euler–Maruyama technique with time step Δt :

$$\eta(t + \Delta t) = \eta(t) - \lambda\eta(t)\Delta t + \lambda\sqrt{2D\Delta t}\Delta W(t) \quad (4.8)$$

where the $\Delta W(t)$ are independent Gaussian random numbers with unit variance (they are known technically as increments of the Wiener process). This process is thus integrated in parallel with the integration of the deterministic part. It is an order 1/2 fixed-step method, which limits the size of the time step. The resulting slowness is compounded by the fact that simulations have to be run typically for many different realizations of the noise process, in order to get reliable estimates of firing statistics. Some of our results below were actually obtained with an order 3/2 fixed-step method as in Longtin and Chialvo (1998).

A spike is said to occur whenever the voltage variable crosses the threshold in the upward direction, and is separated from a previous one by at least the

absolute refractory time of $T_R = 0.4$ sec (equivalent to $\approx 1\text{--}2$ msec in typical real neurons). This is important because high noise or deterministic forcing may strongly affect the spike shape in simulations, and one spike may unrealistically count as more than one (Longtin, 1993). Interestingly, inclusion of a proper refractory period improves the linear correlation between input signal and output rate (Chialvo *et al.*, 1997). Further, before interpreting statistics at high noise, it is crucial to determine whether the process still has any resemblance to the firings of a real neuron.

4.3.3.3 Results for CR with FHN For CR we consider the excitable regime with zero-forcing $A = 0$. The mean spiking rate as a function of the noise intensity D is shown in Fig. 4.1. The rate is arbitrarily low if one chooses a small value of D .

We next consider the firing patterns at different noise intensities. These are shown in Fig. 4.2. From simple visual inspection, it is clear that the model spikes more regularly for moderate noise compared to the lower noise. This can be further quantified by measuring the ratio R (Eqn (4.2)) for different D ; results are plotted in Fig. 4.3. One sees a clear resonance in the coherence as measured by R , for which a qualitative explanation was given above in terms of the statistics of activation and excursion times. However, caution is required at this point, as one must carefully interpret the realism of the model at higher noise due to spike

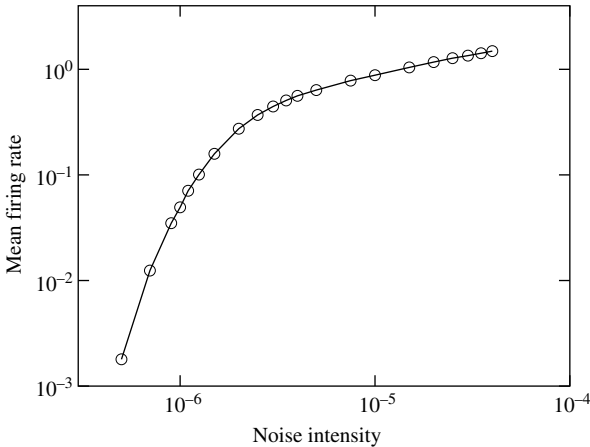


FIG. 4.1: Average firing rate versus noise intensity D for the Fitzhugh–Nagumo model (4.4)–(4.6) with stochastic forcing by Ornstein–Uhlenbeck additive noise. There is no periodic forcing. The reciprocal of this rate is the mean interspike interval $\langle ISI \rangle$, which can also be plotted versus D as in Fig. 4.16 below. The time step is 0.0005 sec, and $I = 0.04, b = 0.15, \epsilon = 0.005, t_c = \lambda^{-1} = 0.001$ and are the same throughout this chapter unless stated otherwise.

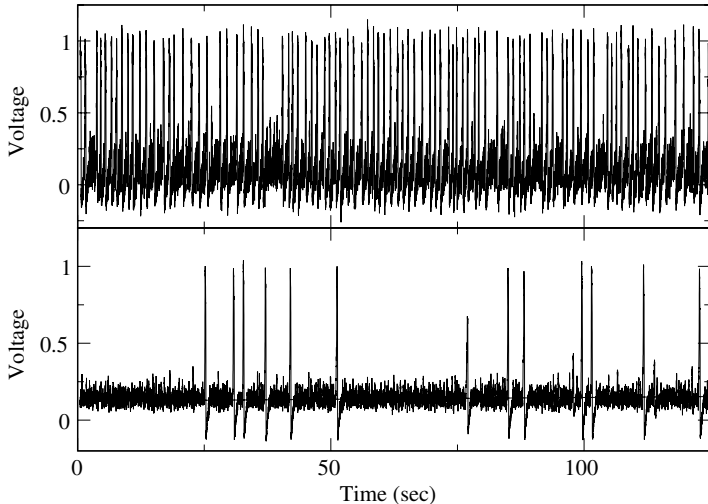


FIG. 4.2: Voltage versus time for the Fitzhugh–Nagumo model (4.4)–(4.6) for two intensities of the OU noise. There is no periodic forcing. The lower panel corresponds to $D = 10^{-6}$, and the upper one to $D = 8 \times 10^{-6}$. The regularity of the spiking is best for the higher noise intensity, as measured by the CV of the interspike interval in Fig. 4.3 below.

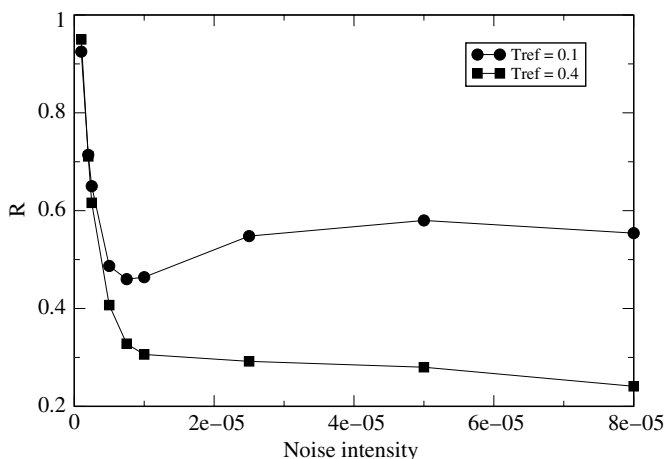


FIG. 4.3: Coefficient of variation (CV) of the interspike interval, denoted R in Eqn (4.2) versus D for the FHN model (4.4)–(4.6). There is no periodic forcing. The regularity of the spiking is best for the moderate noise level, i.e. there is a coherence resonance.

shape distortion. CR from the CV of ISIs viewpoint is seen if the numerically implemented refractory period is made very short (0.1 sec) – this is the minimal interval by which successive threshold crossings have to be separated to be called spikes. If it is set at the value of 0.4 sec – the value chosen for the rate calculation above and all subsequent FHN computations – then there is no CR, but rather just an improvement in regularity as D increases. This latter value is more physiologically plausible because it corresponds to the absolute refractory period of the action potential in the model's units. So before deciding on whether the CV goes back up at higher noise, it is important to ascertain that the simulation is still giving ‘spikes’, and not bumps with multiple peaks due to noise. This will depend also on the choice of ϵ on which the absolute refractory period depends (e.g. $\epsilon = 0.001$ for CR to be seen in Lindner *et al.* (2004) with Gaussian white noise forcing).

Finally, we consider the alternative point of view that emphasizes the temporal coherence of the firings from the spectral point of view, which relates to the autocorrelation point of view used by Pikovsky and Kurths (1997). One first computes the power spectral density of the point process defined by the spike trains, and performs averages over many realizations. This corresponds mathematically to computing the Fourier transform of the autocorrelation function:

$$S(\omega) = \int_{-\infty}^{\infty} d\tau \langle x(t)x(t+\tau) \rangle e^{i\omega\tau}, \quad (4.9)$$

where $x(t)$ is the spike train and the angled brackets denote an average over many realizations of the stochastic process. One can then define the relative width of the peak in such a spectrum as

$$\beta_{\text{CR}} = \frac{S(\omega_{\max})}{\Delta\omega/\omega_{\max}}, \quad (4.10)$$

where ω_{\max} is the frequency of the peak, and $\Delta\omega$ is the distance between two frequencies at which the spectrum has decayed to a fraction of its maximum. This fraction may have to be chosen high since the background under the peak may be too high to see a prolonged decay. The FHN model also exhibits a resonance from this point of view (Lindner *et al.*, 2004). This can be guessed by looking at the power spectra for the different values of D in Fig. 4.4. Note that these spectra exhibit a peak around 1 Hz. There are also other peaks corresponding to a periodic forcing signal, which we will come back to when we discuss SR. These signal peaks can be disregarded in the CR context (the forcing very slightly modifies the background spectrum). It is clear in the left panels, for which the Nyquist cutoff frequency for the spectrum calculation is 12 Hz, that the peak around 1 Hz increases with D . At very high noise, firings are too random to produce any significant peak. Thus at some moderate D , β_{CR} will be strongest (not shown – see Lindner *et al.* (2004)).

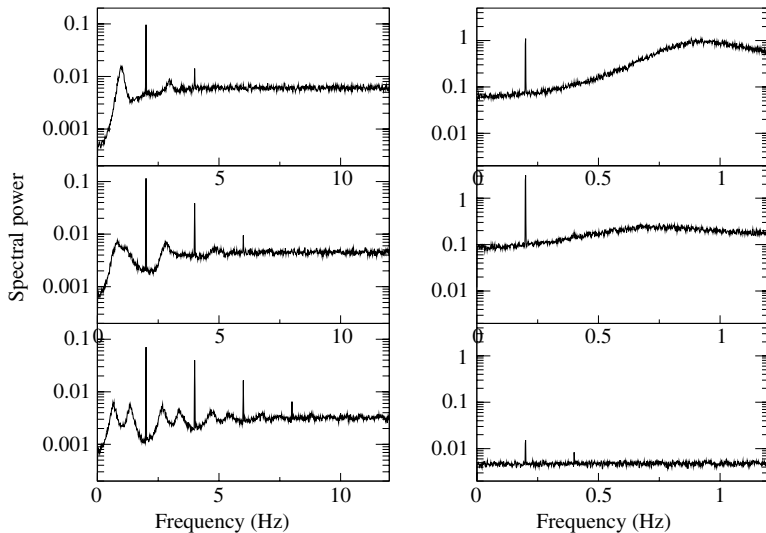


FIG. 4.4: Power spectral densities for the FHN model (4.4)–(4.6) for three intensities of the OU noise. The periodic forcing is $T = 0.5$ sec for the left panels, and $T = 5$ sec for the right panels. The regularity of the spiking is associated with the sharpness of the peak around 1 Hz. The presence of the periodic forcing has little effect on the behaviour of that peak. This figure also shows the increase followed by the decrease of the peak at the driving frequency as the noise increases from bottom to top (the harmonics of this frequency are also seen). This non-monotonic behaviour of the spectral amplification is a manifestation of SR. Noise intensities are $D = 5 \times 10^{-7}$ (bottom panels), 2×10^{-6} (middle panels), and 8×10^{-6} (top panels).

Note that the peak of interest for CR is due to the fact that noise turns the subthreshold system into a *stochastic oscillator*. This can be said of any thresholding system. But it is much more pronounced when the system can sample the limit cycle nearby in parameter space, or relatedly, that the fixed point has complex eigenvalues. In fact, one can see from Fig. 4.5 that the subthreshold response to sinusoidal forcing exhibits a classical resonance. Non-linearity is involved, not surprisingly, as the resonance frequency depends on the amplitude of the forcing. These complex eigenvalues sharpen the time-scale of the stochastic oscillator, and this sharpening is maximal for a finite noise. Other statistics can be used as well to measure CR, such as the correlation time (Pikovsky and Kurths, 1997) or the spike count diffusion (Lindner *et al.*, 2004). The values of noise at which different statistics exhibit the coherence resonance may differ. Some statistics may show CR, others not. Also different noise bandwidths (λ in Eqns (4.4)–(4.6)) may lead to different results.

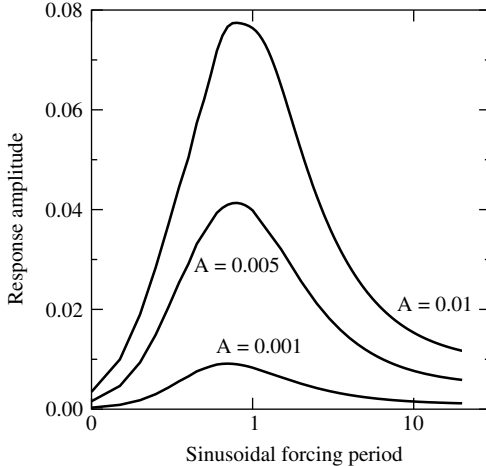


FIG. 4.5: Steady state amplitude of the subthreshold voltage in the FHN system (4.4)–(4.6) as a function of forcing frequency for different forcing amplitudes. There is no noise. This resonant behaviour is characteristic of classical oscillators, and of Type II neural dynamics.

4.3.4 Coherence resonance in Type I dynamics

4.3.4.1 QIF model with white noise We now consider the quadratic integrate-and-fire (QIF) model, the standard defining form for Type I dynamics. The evolution of the voltage is given by:

$$\frac{dV}{dt} = \beta + V^2 + \sqrt{2D}\xi(t) + A \sin(\omega t). \quad (4.11)$$

Here β is considered the mean bias to the cell, and $\xi(t)$ is Gaussian white noise which drives the voltage directly, rather than being first filtered into an OU process. The voltage V is defined on the real line. For $D = 0$, V converges to a stable fixed point (node) when $\beta < 0$. This is the excitable regime; a spike occurs if V exceeds the threshold that lies at the unstable (saddle) point $V_{\text{thr}} = \sqrt{-\beta}$. The trajectory always diverges (in finite time) to $+\infty$ when $\beta > 0$, i.e. in the oscillatory regime. One can map this system onto the behaviour of a Type I neuron by re-injecting the trajectory at $-\infty$ after the divergence. V will then increase, slow down near the origin, and then rapidly escape to $+\infty$. Interestingly one can show by rescaling time $\tilde{t} \equiv t/a$ and voltage $y \equiv V/a$ with $a = \sqrt{|\beta|}$ that the stochastic dynamics really depend on one parameter (Lindner, Longtin, and Bulsara, 2003):

$$\dot{y} = \frac{\beta}{|\beta|} + y^2 + \sqrt{2D/|\beta|^{3/2}}\xi(\tilde{t}) = \begin{cases} +1 + y^2 + \sqrt{2D/|\beta|^{3/2}}\xi(\tilde{t}), & \beta > 0 \\ -1 + y^2 + \sqrt{2D/|\beta|^{3/2}}\xi(\tilde{t}), & \beta < 0. \end{cases} \quad (4.12)$$

Thus only two cases need to be studied, depending on whether the excitable or oscillatory regimes are of interest. This is because the noise intensity D and the bias β are lumped together in a ratio; firing statistics at one D will be the same as at another D with β modified to keep the ratio fixed. The behaviour at three noise intensities is illustrated in Fig. 4.6. Also, the $\beta = 0$ case is somewhat special. The mean firing rate, which is the reciprocal of the mean first passage time from $-\infty$ to $+\infty$, is given by

$$r \approx 0.201D^{1/3}, \quad (4.13)$$

i.e. the rate varies slowly with D . The variance of the first passage time is given by $\langle \text{ISI} \rangle^2/3$. Consequently, and rather surprisingly, the CV is constant and equal to $1/\sqrt{3}$ (see Fig. 4.8 below). For the excitable regime $\beta < 0$, the mean rate at low noise is given by a Kramer's-type formula:

$$r = \frac{|\beta|}{\pi} \exp \left[-\frac{4|\beta|^{3/2}}{3D} \right]. \quad (4.14)$$

Also, if $|\beta|$ is small or the noise is strong, the rate is approximately given by

$$r \approx 0.201D^{1/3} + 0.147\beta D^{-1/3} \quad (4.15)$$

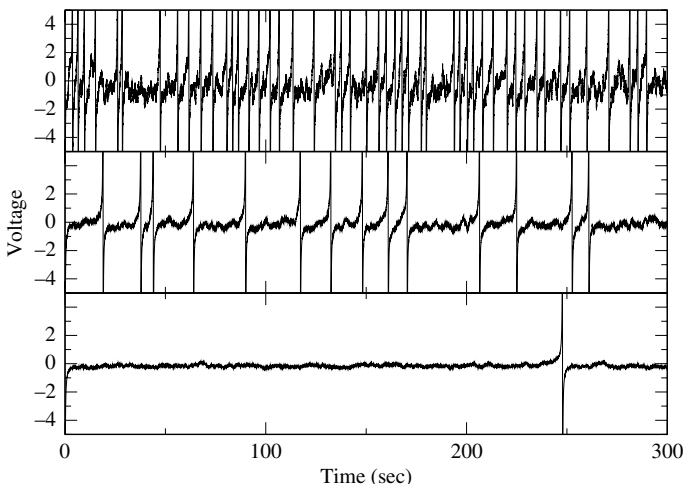


FIG. 4.6: Stochastic firing in the QIF model (4.11) in the absence of periodic forcing ($A = 0$) for $\beta = -1$ and three noise intensities. The CV of interspike intervals is 0.86 for $D = 2 \times 10^{-3}$ (lower panel), 0.68 for $D = 2 \times 10^{-2}$ (middle), and 0.59 for $D = 5 \times 10^{-1}$ (upper). Hence the regularity of the firing increases with D , in agreement with theory. This is the first half of a CR effect. At higher noise, the CV converges to its maximal theoretical value of $1/\sqrt{3}$. The time step is 0.0005 sec.

and the CV by

$$CV \approx 0.578 + 0.250\beta D^{-2/3}. \quad (4.16)$$

Thus these statistics consist of small linear (in β) departures from their values for $\beta = 0$.

4.3.4.2 Numerics for QIF The QIF system can be numerically integrated using a standard Euler–Maruyama technique for stochastic differential equations with time step Δt :

$$V(t + \Delta t) = V(t) + (\beta + V^2(t) + A \sin(\omega t)) \Delta t + \sqrt{2D\Delta t} \Delta W(t) \quad (4.17)$$

where the $\Delta W(t)$ are again independent Gaussian random numbers with unit variance. A smaller time step may be needed at larger noise intensities. The absorption point is set at $V_+ = 500$. After the trajectory has passed this point, it is re-injected at the next time step at the reset point $V_- = -500$. Another popular related form of this model is the theta neuron model. This involves a nonlinear change of variables

$$\theta = 2 \arctan(V) \quad (4.18)$$

which for the noiseless case leads to the dynamics

$$\dot{\theta} = (1 - \cos \theta) + (1 + \cos \theta) \beta. \quad (4.19)$$

One must be careful when applying changes of variables to stochastic differential equations, because the answer will depend on the form of stochastic calculus used (Ito or Stratonovich) – see Lindner, Longtin and Bulsara (2003) for an account of this difference in the context of the theta neuron model. The proper form of the Euler–Maruyama integration scheme for the theta neuron is

$$\begin{aligned} \theta(t + \Delta t) &= \theta(t) + [(1 - \cos \theta(t)) + (\beta - D \sin \theta(t)) (1 + \cos \theta(t))] \\ &\quad + \sqrt{2D\Delta t} (1 + \cos \theta) \Delta W(t). \end{aligned} \quad (4.20)$$

Further, the qualitative behaviour of firing statistics in the QIF model (4.11) may depend on the precise absorption and reset points (Lindner, Longtin, and Bulsara, 2003); see below.

4.3.4.3 Results for CR in QIF For coherence resonance, we study the QIF model with $A = 0$. We focus on the threshold case $\beta = 0$ and excitable case $\beta = -1$. We first consider the mean firing rate as a function of the noise intensity D in Fig. 4.7. As for the FHN system, the noise turns the quiescent system into a stochastic oscillator. For $\beta = 0$ and for $V_{\pm} = \pm\infty$, we find a rate that follows a $D^{1/3}$ power law, as expected from the theoretical results above. For $\beta = -1$, the

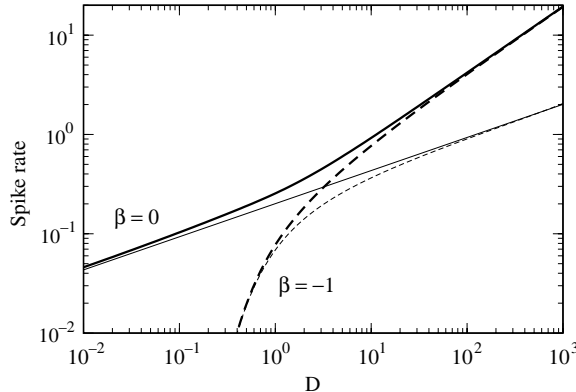


FIG. 4.7: Mean firing rate in the QIF model (4.11) as a function of noise intensity, for the excitable case $\beta = -1$ and the threshold case $\beta = 0$. The thin lines correspond to the absorption and reset points being at $\pm\infty$, respectively, and can be compared to the theory. The thick lines are for finite boundaries $V_{\pm} = \pm 2$.

low noise regime follows a Kramer's-type law (Lindner, Longtin, and Bulsara, 2003), which changes to the $1/3$ power law at large noise. If the boundaries are set low, i.e. $V_{\pm} = \pm 2$, the mean rate increases, as expected intuitively. The effect is small at low noise, but the scaling behaviour at larger noise is altered.

The behaviour of the CV with D is shown in Fig. 4.8. We first consider the case $V_{\pm} = \pm\infty$. One sees that the CV always equals $1/\sqrt{3}$ for $\beta = 0$, as discussed above. For $\beta = -1$, the CV decreases monotonically to the high noise limit of $1/\sqrt{3}$. In other words, the increase in noise produces a regularization of the firings, which is bounded from below by the CV for the threshold case $\beta = 0$. So from this point of view, there is no CR in the QIF model – nor in its theta neuron analogue – but only a partial CR effect. So CR from the CV point of view is not to be universally expected across all neuron models. *However, the more interesting part of CR is still seen: increasing noise decreases CV. There just isn't an optimal noise.*

There is a twist to the story, which leaves the door open. Consider the case now where the boundaries are finite with $V_{\pm} = \pm 2$ in Fig. 4.8. One now sees that the CV for the $\beta = 0$ case increases monotonically, which is drastically different from the previous case. Further, for $\beta = -1$, the CV now exhibits a minimum as a function of D : there is CR! Preliminary numerical results using the Morris–Lecar model suggest that no resonance is seen for additive noise on the voltage dynamic (B. Lindner, personal communication). A more rigorous derivation of the connection between a given ionic Type I model and its normal form is likely needed to pinpoint proper V_{\pm} values. This will influence any theta neuron formulation, which assumes $V_{\pm} = \pm\infty$. So while the QIF model may be a more realistic mimic of Type I behaviour than, say, LIF, there is still work

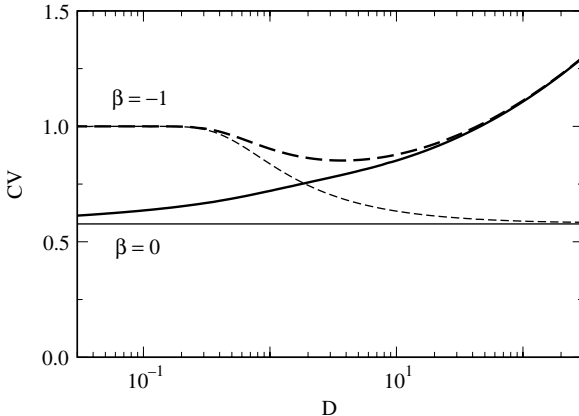


FIG. 4.8: CV of the ISIs for the QIF model (4.11) as a function of D . The thin lines correspond to the absorption and reset points being at $\pm\infty$, and can be compared to the theory. Only regularization by noise (i.e. CV decreases as D increases) is seen in this case. The thick lines are for finite boundaries $V_{\pm} = \pm 2$. There is a full CR in this case.

to do to figure out its spiking statistics in the presence of noise. We can also consider CR from the spectral viewpoint, which we address in Fig. 4.17 below in the section on stochastic resonance.

4.4 Stochastic phase locking

4.4.1 Tuning and noise

The FHN model behaves as an under-damped oscillator. This implies that it takes minimal stimulation at the resonant frequency to get a response. In contrast, the simple LIF model (see Eqn (4.21) below) as well as the QIF model (4.11) are low-pass filters without a resonance. A tuning curve is a plot of the minimal amplitude of forcing to obtain a certain firing pattern as a function of forcing frequency. Figure 4.9 shows tuning curves for the FHN model with and without noise; the firing pattern used is one spike per forcing period (1:1) in the steady state. With noise, this statistic must be understood as meaning ‘on average’. We will see later that this statistic provides a deeper insight into SR across the whole range of forcing frequencies. This figure reveals the familiar V-shape characteristic of Type II cells, i.e. there is a minimal amplitude required to get 1:1 at that ‘preferred forcing period’ (at $T \approx 1.5$ sec here). The subthreshold regime lies below the 1:0 curve, and the suprathreshold regime lies above this curve. The preferred period for 1:1 is close to the period of the limit cycle that is reached for larger bias I , and to the period that produces the largest deterministic subthreshold voltage response as in Fig. 4.5. Also, one sees that the boundary between subthreshold and suprathreshold is frequency-dependent. For example,

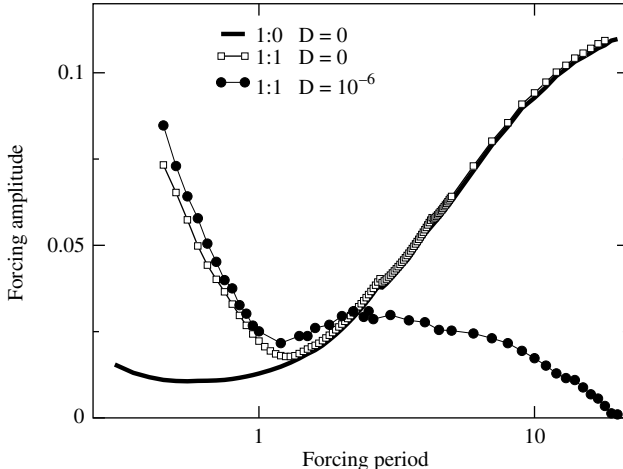


FIG. 4.9: Tuning curves for the FHN model (4.4)–(4.6) with and without noise.

For $D = 0$, each curve gives the minimum value of forcing amplitude A for each forcing period $T = 2\pi/\omega_o$ to produce one spike per forcing period (1:1 firing). For $D \neq 0$, the 1:1 firing is *on average*. Each average minimum value is averaged over three independent determinations of this minimum. The curves exhibit resonant behaviour at low noise, but lose their resonant minimum if the noise is sufficiently high.

a forcing of $A = 0.05$ is subthreshold at $T = 10$, but not at $T = 1$. Between the 1:0 and 1:1 curves one can find the classically arranged deterministic Arnold tongues at intermediate ratios (Glass and Mackey, 1988).

Adding noise changes the shape of the curves at low to mid-frequencies, but not at high frequencies, an effect that may be important to know to explain the shape of measured tuning curves (Longtin, 2000). The noise moves the deterministic Arnold tongues into the subthreshold domain. Each curve can now be interpreted as the set of A - T pairs yielding a given time-averaged phase locking ratio, specifically here $\langle 1 : 1 \rangle$ (Longtin and Chialvo, 1998). For $T < 1.5$, the recovery variable w becomes a key determinant of the firing probability, but theory is still possible (Lindner *et al.*, 2004).

4.4.2 Sinusoidal forcing of the stochastic FHN

Figure 4.10 shows the response of the FHN model (4.4)–(4.6) to zero-mean Ornstein–Uhlenbeck noise and a zero-mean high-frequency sinusoidal forcing (2 Hz in this model’s units). This is a high frequency because it is on the time-scale of the inverse of the refractory period. The amplitude is chosen as $A = 0.01$, which is subthreshold for all frequencies for the chosen model parameters (see Fig. 4.9). The solution would converge to a fixed point for $A = D = 0$. For $A > 0$

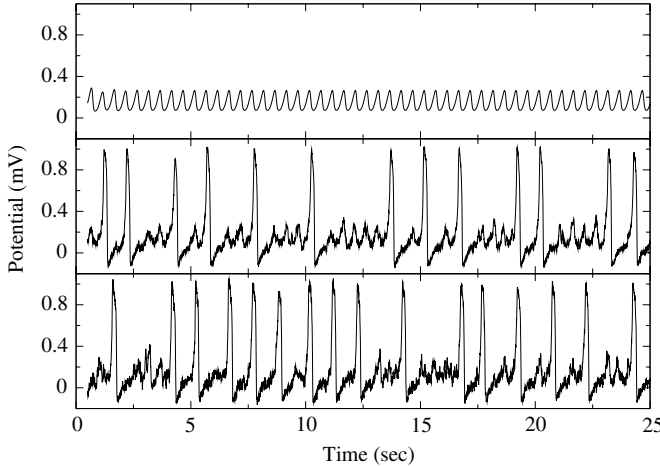


FIG. 4.10: Solutions of the FHN model (4.4)–(4.6) with high-frequency sinusoidal forcing and OU noise ($\lambda^{-1} = 0.001$ sec). The forcing period is $T = 0.5$ sec. $D = 0$ for the upper panel, 7×10^{-7} for the middle panel, and 2×10^{-6} for the lower panel. $A = 0.01$, i.e. the forcing is subthreshold. Transients have been discarded.

and $D = 0$, the voltage executes periodic motion around the fixed point, without spikes. For $A = 0$ and $D > 0$, spikes occur at a rate proportional to D as in Fig. 4.1 (although there is no periodic forcing in Fig. 4.1).

For $A > 0$ and $D > 0$, firings are caused by the combination of noise and periodic forcing. They tend to occur near a preferred phase of the forcing, but there is randomness as well because spikes randomly skip stimulus cycles. We will refer to this form of stochastic phase locking as ‘skipping’. It is also clear that more firings occur as D increases. Stochastic phase locking to a slower forcing is shown in Fig. 4.11. Here one cannot say with confidence that spikes occur near a preferred phase of the forcing; we will see that they do so only for low noise. This is due in part to the fact that the voltage response to this low-frequency forcing is small (Fig. 4.9).

We now consider phase locking in the D – T subspace instead of the usual A – T subspace. Figure 4.12 shows the location of the $\langle 1 : 1 \rangle$ ‘DT’ Arnold tongues for two different forcing amplitudes. The curves are either monotonically decreasing or go through a maximum. For $A = 0.015$, the forcing is always subthreshold for $\langle 1 : 1 \rangle$, and noise is always needed to produce firings; a monotonically decreasing curve results, which parallels the behaviour of the mean firing rate versus D (as we will discuss in Fig. 4.16 below). This basically means that more noise is needed to produce one spike per forcing cycle (on average) when the forcing frequency is high. For $A = 0.03$, noise is needed to achieve $\langle 1 : 1 \rangle$ only when the forcing frequency becomes too low.

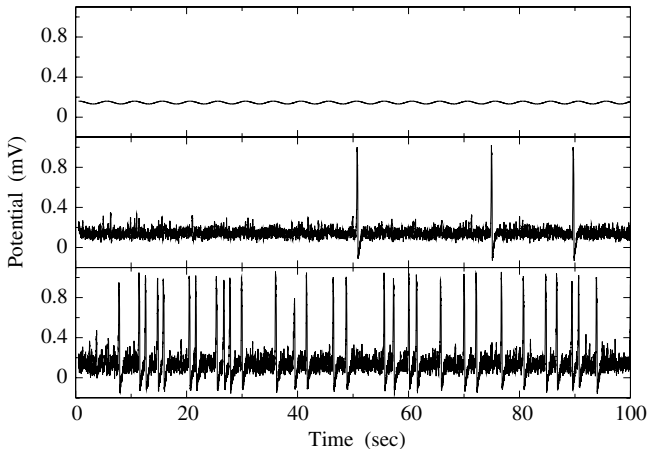


FIG. 4.11: Solutions of the FHN model (4.4)–(4.6) with low-frequency sinusoidal forcing, and broadband stochastic forcing. The forcing period is $T = 5.0$ sec. $A = 0.01$, i.e. forcing is subthreshold at this frequency. The noise intensity is zero for the upper panel, 7×10^{-7} for the middle panel, and 2×10^{-6} for the lower panel.

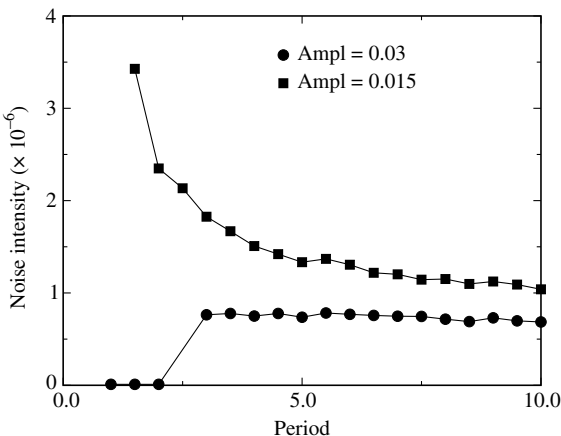


FIG. 4.12: Noise intensity-forcing period boundaries for the $\langle 1 : 1 \rangle$ average phase locking ratios for two forcing amplitudes. Each curve plots, as a function of forcing period, the minimum D needed to produce an average 1:1 phase locking ratio.

4.5 Stochastic resonance (SR)

Stochastic resonance characterizes the synchronization of the response of a system to its time-dependent input when this input is too weak to produce spikes

on its own. It is clear from the foregoing discussion of stochastic phase locking that noise enables responses that are synchronized to some extent with the input.

4.5.1 Type II

4.5.1.1 *ISI histograms, power spectra, cycle histograms* We present a gallery of behaviours for different combinations of noise and forcing period, keeping the amplitude fixed at the subthreshold value (for all periods) of $A = 0.01$. This will allow us to have a global view of the behaviour of an excitable model to different regimes of stochastic and periodic forcing. The terms low, mid- and high frequency are referenced to the preferred deterministic frequency of the model (near $T = 1.5$, a ‘mid’-frequency). Figure 4.13 shows ISI histograms. For the high period (low frequency) $T = 5$ and low noise, a multimodal ISI histogram is seen, as well as at mid-to-high frequencies and low-to-moderate noise levels (Chialvo, Longtin, and Müller-Gerking, 1997). The qualitative similarity between (1) such experimentally observed histograms and (2) those seen for bistable systems forced by noise and subthreshold sinusoids suggested that SR could be at work in excitable systems (Longtin, Bulsara, and Moss, 1991). At

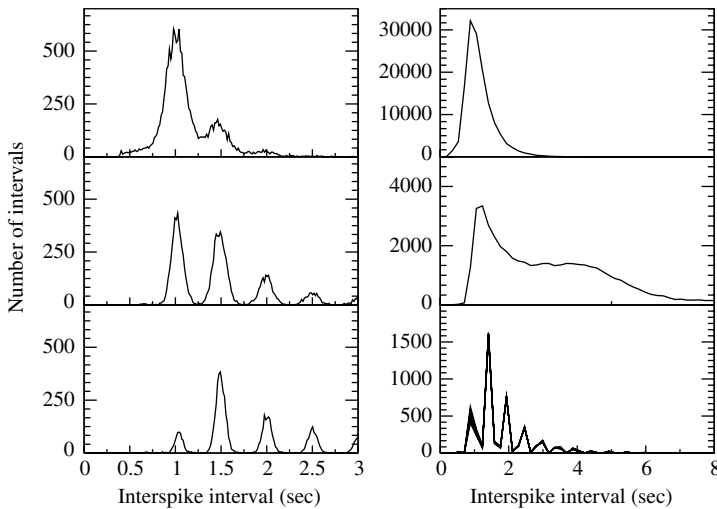


FIG. 4.13: Interspike interval histograms from numerical solutions of Eqns (4.4)–(4.6) for various D and forcing periods T ($T = 0.5$ for left panels, and $T = 5$ sec for the right panels). The forcing amplitude is fixed at $A = 0.01$ (subthreshold) throughout. The ISI histograms are obtained by cumulating into the same 100-bin histogram the intervals from 100 realizations of 340 forcing cycles. The noise intensity is 5×10^{-7} for the lower panels, 2×10^{-6} for the middle panels, and 8×10^{-6} for the upper panels.

high noise, the ISI histogram is unimodal, with little evidence of skipping. At low noise, there is skipping, and between the two, there is some intensity where there is a dominance of firing intervals near the forcing period, a signature of SR (Longtin, 1993).

Figure 4.4, used earlier to illustrate CR in the FHN system, shows spike train power spectra for the same forcing parameter ranges as for the ISI histograms in Fig. 4.13. Apart from the spectral signature of the forcing signal and its harmonics, there is not much other structure for $T = 5$. There is more structure for lower T , relating to the presence of the refractory period; there are also modes at the mean firing rate and its harmonics. And it is clear that as D increases, the peak height at the forcing frequency f_0 (also known as the spectral amplification) goes through a maximum, i.e. SR is seen. One could also look at the ratio of the peak height to noise floor under the peak to get a signal-to-noise ratio – and this SNR also goes through a maximum as D increases (not shown – see Lindner *et al.* (2004) for a review).

The probability of firing as a function of the phase of the forcing signal is known as a ‘cycle histogram’. Such histograms are shown in Fig. 4.14. They have a rectified form at low noise, and become more sinusoidal (reflecting the shape of the stimulus) at higher noise. More noise is needed for the sinusoidal

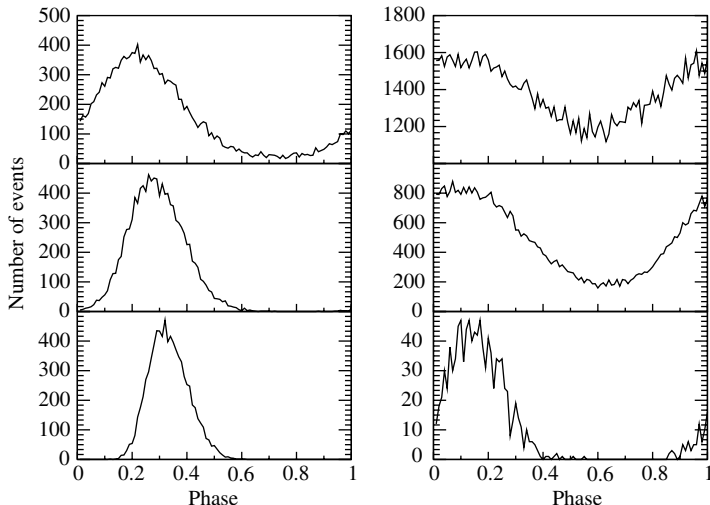


FIG. 4.14: Cycle histograms from solutions as in Fig. 4.13. The period is normalized to one. $T = 0.5$ sec for the left panels, and $T = 5$ sec for the right panels. A histogram is constructed by incrementing one of 100 bins whenever a spike occurs at a phase of the sinusoidal stimulus corresponding to that bin. It represents the unnormalized firing probability as a function of stimulus phase. Results were obtained from 100 realizations of 340 stimulus cycles with $A = 0.01$. Noise intensities are as in Fig. 4.13.

shape to appear when the forcing frequency is high. The transition from rectified to sinusoidal reflects the fact that the f-I curve is linearized by noise (Chialvo, Longtin, and Müller-Gerking, 1997). In fact, the slope of this function, which corresponds to a ‘gain’ for slow signals, goes through a maximum as a function of D and underlies SR at low frequencies (the so-called adiabatic regime (Longtin and Chialvo, 1998)). This linearization makes the firing probability track the forcing signal more faithfully.

4.5.1.2 Optimal noise Figure 4.15 shows the behaviour of the spectral peak as a function of noise intensity for two forcing periods. For $T = 1.0$, we see that there is an optimal noise level where the peak is maximal. This is the hallmark of SR. One could also consider SNR versus noise and also observe a unimodal curve (not shown). We comment below on the behaviour of the peak for $T = 0.6$.

The noise that maximizes a given firing statistic depends on the frequency of the forcing. We have seen in Fig. 4.9 that, at high forcing frequency, a higher noise level is needed to obtain $\langle 1 : 1 \rangle$ firing. Of course, $\langle 1 : 1 \rangle$ firing actually corresponds to a higher firing rate for a higher forcing frequency. Also, a high noise induces a high firing rate without forcing (Fig. 4.1). Since the mean firing period and forcing period are both time-scales, they can be plotted on the same axis. This is done in Fig. 4.16, where we consider SR experiments at many different frequencies and plot in each case the optimal noise D_{opt} , i.e. that at which spectral amplification is maximum. The mean interval curve without forcing is superimposed on the data.

We see that this mean interval parallels the optimal noise-versus-forcing period curves for both statistics of interest over a significant range of forcing

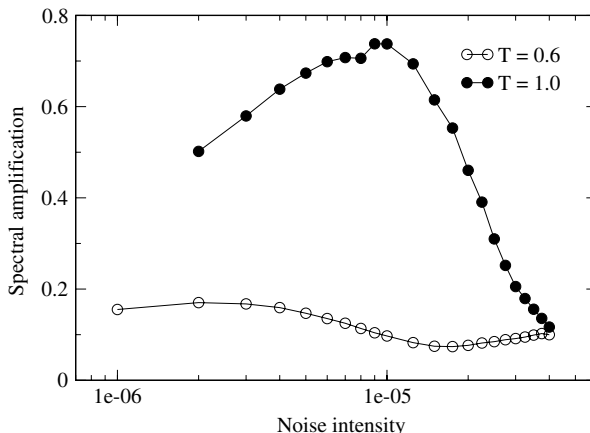


FIG. 4.15: Peak height (spectral amplification) from spike train power spectra as a function of noise intensity for two different periods of sinusoidal forcing for the FHN system. The presence of a maximum is the hallmark of SR. One also sees that more than one maximum may exist.

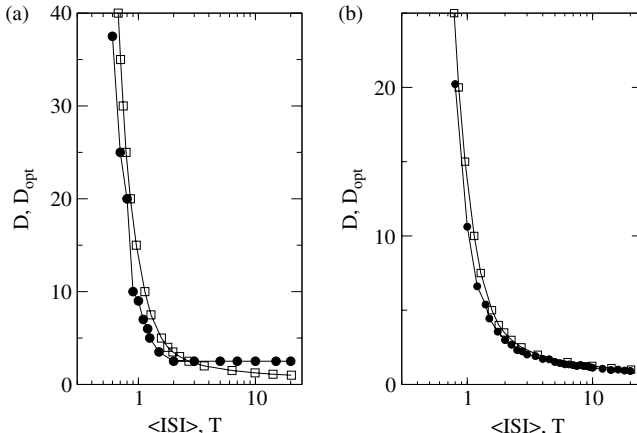


FIG. 4.16: Dependence of noise producing (a) maximal spectral amplification and (b) $\langle 1:1 \rangle$ firing as a function of forcing period for the FHN model (4.4)–(4.6). The same curve (open squares) of mean ISI versus D for $A = 0$ is plotted in each panel (from the reciprocal of the data in Fig. 4.1). The optimal statistics for ISI histogram peaks and the input–output correlation show similar behaviour (not shown; see Longtin and Chialvo (1998)). The statistics with forcing signal parallel the zero-signal mean interval for $T < 3$. For the spectral amplification, a static ('adiabatic') regime occurs for $T > 3$, where D_{opt} is independent of T . Symbols are approximately two standard deviations wide.

periods (Longtin and Chialvo, 1998). For example, at higher forcing frequencies, a higher noise intensity is needed to obtain (1) 1:1 firing on average and (2) a maximal spectral amplification at the forcing frequency. Also, at higher noise, the mean spontaneous firing interval is smaller. This is a manifestation of time-scale matching of SR in excitable systems (Gammaitoni *et al.*, 1998). Note also that at lower forcing frequencies, D_{opt} does not depend on T . This is the ‘non-dynamical’ (or ‘adiabatic’ or ‘static’) regime where the neuron acts as a simple threshold crossing device (Gingl, Kiss and Moss, 1995, Jung 1994); this occurs when the time-scale of the periodic forcing is larger than all internal neuron time-scales. Outside this slow regime, the optimal noise is roughly one that produces one spike per cycle, on average. The mean rate curve forms the backbone of these optimal firing statistics.

Much can be calculated analytically for this model for small ϵ , reviewed by Lindner *et al.* (2004) and Longtin (2000) or slow signals (Collins, Chow and Imhoff, 1995). One finds a maximum as a function of noise for both the spectral amplification and the signal to noise ratio (Lindner, Garcia-Ojalvo, Neiman and Schimansky-Geier, 2004). Further, one finds a maximum in the spectral amplification as a function of driving frequency for a fixed noise. This is not the case for the SNR. Nevertheless, this property has been dubbed stochastic double

resonance (Lindner *et al.*, 2004, Plesser and Geisel, 1999). At higher frequencies $T < 0.9$, multiple stochastic resonances can occur as D increases (Longtin and Chialvo, 1998), as is shown in Fig. 4.15 for the high-frequency forcing ($T = 0.6$). Similar resonances have also been found in bistable systems (Jung and Hänggi, 1991), and are related to the deterministic lockings that exist for suprathreshold forcing, and which are induced by the noise in the subthreshold regime

4.5.2 Type I

Power spectra for the QIF model with periodic forcing are shown in Fig. 4.17 for different noise intensities. The absorption and reset voltages are at $\pm\infty$. One can see that there is a peak that corresponds to the forcing frequency, along with some of its harmonics. As the amplitude of the noise increases from a lower value (bottom curve), the peak height increases, and then goes down. Thus this QIF Type I model exhibits SR. It is also apparent that there is a broader

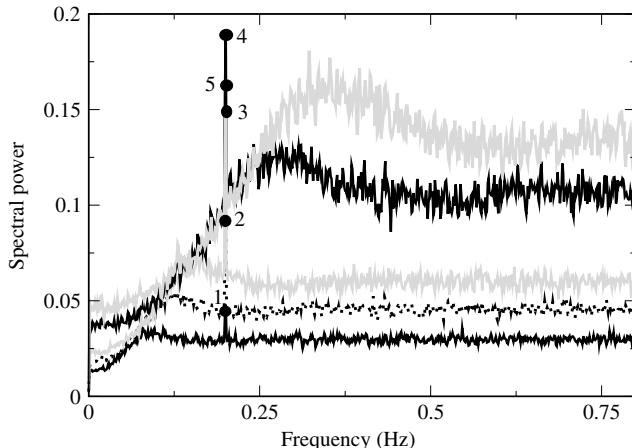


FIG. 4.17: Spike train power spectra at different noise intensities for the QIF model (4.11) with $\beta = -0.03$. The forcing frequency is 0.2 Hz with amplitude $A = 0.15$. The asymptotic background power at higher frequency increases with noise intensity (it is proportional to the mean firing rate (Lindner, Schimansky-Geier and Longtin, 2002)), corresponding to noise intensities $D = 10^{-2}, 5 \times 10^{-2}, 10^{-1}, 5 \times 10^{-1}, 1.0$. The corresponding peaks heights at the forcing frequency are labelled in that order; one thus sees a maximum as D increases, i.e. SR. The broad background peak is also seen without periodic forcing (not shown), and corresponds to the broad frequency scale of the noise-induced oscillation, i.e. the range of firing rates. As D increases, it increases in amplitude and shifts to higher frequencies (since the rate is higher), but seems to preserve its shape relative to the background. The presence of CR from this point of view is again a matter of interpretation.

peak – this peak is almost unaffected by the presence of the periodic forcing. It corresponds to the time-scale of this stochastic oscillator. One sees that as D increases, this peak sharpens a bit at first, but seems to preserve its shape relative to the background up to high noise levels (even beyond those shown here). So while there may be CR at lower noise in the form of a regularization and the appearance of a peak, it is not clear that this peak really sharpens and broadens again, and the CR may just be partial as from the CV point of view (Fig. 4.3). A full investigation of CR in this model is beyond the scope of this chapter.

4.6 CR and SR in the leaky integrate-and-fire model

The leaky integrate-and-fire model (LIF) has been widely used for many decades. With periodic forcing and zero-mean Gaussian white noise ξ , it can be written as:

$$\frac{dV}{dt} = -V + I + A \cos(\omega t) + \sqrt{2D}\xi(t) \quad (4.21)$$

where $\langle \xi(t)\xi(s) \rangle = \delta(t-s)$. Time is in units of the membrane time constant. Starting from an initial condition, this model will evolve until a threshold is reached, here set to $V = 1$. At that point a spike is said to have occurred, and the potential is set to V_{reset} , and the process continues. This model is in the excitable regime when $I < 1$, otherwise it fires repetitively. The statistics of firing for the LIF model with Gaussian white noise are very similar to those of the QIF model seen above. The main difference is that its CV is not bounded from below, but can decrease down to zero.

In the excitable regime, the LIF model has been shown to exhibit maximal coherence in its firing intervals for a finite noise intensity (Pakdaman, Tanabe and Shimokawa, 2001, Lindner, Schimansky-Geier and Longtin, 2002), as measured by the CV of interspike intervals. The optimal noise at which the CR occurs (using the CV measure) decreases monotonically with the bias. For large bias, i.e. near (but below) the onset of the oscillatory regime, the CR is pronounced, and occurs with just a bit of noise. Deep into the excitable regime, however, i.e. for small bias I , the CR is shallow, and occurs at high noise. This model also exhibits CR from the spectral point of view via the measure β_{CR} in Eqn (4.10).

Interestingly, Lindner, Schimansky-Geier and Longtin (2002) also show that this model exhibits a maximal incoherence at a noise intensity that is higher still. This occurs if the model has an absolute refractory period, and if that period is sufficiently small. Otherwise the CV drops from the Poissonian low-noise limit of one down to the high noise limit of zero, where the firings are basically separated by the refractory period. Whether coherence or incoherence maximization can be observed in a real neuron awaits experimental verification and more realistic simulations than those that the models above afford.

The LIF model also clearly exhibits SR from both the spectral amplification and SNR points of view (Shimokawa, Pakdaman and Sato, 1999). In fact, double SR occurs (Plessler and Geisel, 1999) since the spectral amplification

goes through a maximum as a function of noise, but also as a function of forcing frequency (however, not for the SNR in this latter case). Both are purely noise-induced effects. Also, much can be calculated analytically for this model for both CR and SR (Lindner, Schimansky-Geier, and Longtin, 2002, Lindner *et al.*, 2004, Gammaitoni *et al.*, 1998). One interesting feature that is revealed by plotting the spectral amplification as a function of both D and ω is that there exists a global maximum, and this maximum is in the same range where CR is most pronounced. It is as though the noise induces an oscillatory time-scale, and SR occurs in its strongest form when the driving frequency is in the range of this intrinsic noise-induced time-scale, just like for a classical resonance. Finally, there has been much analytical and numerical work aimed at understanding the effect of coloured noise on the LIF model (Brunel *et al.*, 2001), and with noise that increases along with the stimulus, as expected for a large class of point processes (Lindner and Schimansky-Geier, 2001, Lánský and Sacerdote, 2001). And there are ongoing studies of its effect in phase models that can approximate or even be formally derived from these models.

4.7 Generalizations and outlook

4.7.1 Subthreshold+noise+periodic forcing?

One interesting question is whether the stochastic phase locking from the models above matches that seen experimentally (Longtin, Bulsara, and Moss, 1991, Longtin, 1993, Douglass *et al.*, 1993, Rudolph and Destexhe, 2001b, Lindner *et al.*, 2004). This is a modelling question, and the usual techniques (Glass and Mackey, 1988) can be used to assess the validity and predictive power of the model. The interesting questions from the point of view of CR and SR are: Does the noise regularize the firing, with or without periodic forcing? Under what conditions is the periodic forcing best expressed in the output spike train, given that without noise, it is not expressed at all? And is the signal really subthreshold? This in turn can help us understand how aperiodic time-varying signals can be transduced by the system ('aperiodic SR' (Collins, Chow and Imhoff, 1995, Chialvo, Longtin and Müller-Gerking, 1997)) and how the underlying deterministic resonances influence this noise-aided transduction.

At the core of these questions is the issue of pinpointing the regime where a given cell operates, which in turn can lead to hypotheses as to what it is computing. This can be a tricky endeavour. For example, multimodal ISI histograms associated with SR could in principle be obtained with suprathreshold forcing. The notion is that while noise can randomly induce firings on top of a subthreshold periodic signal, it could also randomly delete firings that are otherwise phase locked to a suprathreshold periodic signal. More generally noise can randomize $n : m$ deterministic phase locking patterns to produce skipping (Longtin, 2002). In fact the periodically modulated Brownian motion used by Gerstein and Mandelbrot (1964) to model skipping had a positive drift. This means that the model without noise behaved like the perfect integrate-and-fire model with positive drift, which fires repetitively and is thus suprathreshold.

Such suprathreshold skipping was also shown Longtin (1993) in the FHN model in the oscillatory regime; skipping there resulted from the action of noise on chaotic dynamics. It was also observed in a chaotic map based on excitable dynamics by Kaplan *et al.* (1996).

Consequently, dynamics that produce a skipping pattern do not necessarily exhibit SR, which requires peri- or subthreshold dynamics. For example, current models for electroreceptors (Chacron *et al.*, 2000) reproduce the first and second order firing statistics for the skipping pattern seen experimentally, using a regime of suprathreshold forcing and noise. The dynamics are noise-perturbed deterministic phase locking patterns. Because the dynamics are suprathreshold, there is no enhancement of the periodic driving signal by increasing noise. However, noise can help code aperiodic signals in this suprathreshold regime, because noise disrupts the deterministic phase locking. For example, the noise-free model exhibits 5:1 phase locking over a range of parameters (corresponding to the width of the 5:1 Arnold tongue). The model will not encode a time varying input with amplitudes in that range, since it always gives a 5:1 firing. However, if noise is added, the 5:1 pattern will be perturbed in a way that reflects the amplitude variations, and coding does occur (Chacron *et al.*, 2000). Thus, noise can also help coding in the suprathreshold regime.

This ties in to other studies of computations in the so-called fluctuation-driven regime, i.e. where input mean does not count but input variance does. This variance can be increased in particular by correlations in the inputs to the cell, and SR can follow (Rudolph and Destexhe, 2001a). Thus SR can be brought on by changing the number, activity and cross-correlation of synaptic inputs, and a host of other parameters.

Noise also arises from the fluctuations in conductance of various ionic channels and ionic pumps. There have been a number of studies where this noise can assist signalling (see e.g. Shuai and Jung (2002), Faisal and Loughlin (2007) and a review in Lindner *et al.* (2004)). For example, thermoreceptors are free nerve endings, and their signalling of temperature does not rely on synaptic currents, but rather on the temperature-dependent rates of opening and closing of various channels. Such receptors possess intrinsic tonic or bursting oscillations, even for constant input. Interestingly, noise can express these rhythms if they are subthreshold, leading to a form of coherence resonance based on intrinsic rhythms dubbed ‘autonomous stochastic resonance’ (Longtin, 1997).

4.7.2 Outlook

We have shown that the combination of noise and excitable dynamics brings a new perspective on issues of resonance and tuning. Noise linearizes the transduction function of the neuron, allowing its firing rate to track input signals. It can change the shape of tuning curves. At high frequencies, multiple subthreshold resonances can be seen (Longtin and Chialvo, 1998, Massanés and Pérez Vicente, 1999), appearing as statistical versions of the deterministic suprathreshold phase-lockings. Apart from creating/sustaining/shaping rhythms, noise may enhance

signal detection, or run network oscillations at low metabolic cost (rhythms are expressed with less firing thanks to skipping). Such ideas are worth exploring, as is the interaction of CR and SR with plasticity and synaptic failures, which impose their own fingerprint on firing statistics.

The area of CR and SR will continue to receive attention as long as there is a strong interaction with experiments in neurophysiology and medicine (see examples in Lindner *et al.*, (2004)), such that theorists can be sent back to the drawing board. This is true for single cell manifestations of CR and SR down to the single channel scale (Shuai and Jung, 2002), but also at the network level where the question of the origin of rhythms – intrinsic to the cells or born out of network interactions? – needs to be resolved. And ultimately, the significance of CR and SR will depend on whether postsynaptic neurons care about the degree of regularity or periodicity of presynaptic neurons, a fact that is challenging to establish experimentally. It is certain however that, whether or not there are such postsynaptic neurons that do care, stochastic phase locking is a ubiquitous pattern used in neural coding, and that we now have a better understanding of its genesis.

Acknowledgements

The author gratefully acknowledges support from NSERC Canada and from CIHR Canada.

References

- Brunel, N., Chance, F.S., Fourcaud, N., and Abbott, L.F. (2001). Effects of synaptic noise and filtering on the frequency response of spiking neurons. *Physical Review Letter*, **86**, 2186–2189.
- Chacron, M.J., Longtin, A., St-Hilaire, M., and Maler, L. (2000). Suprathreshold stochastic firing dynamics with memory in p-type electoreceptors. *Physical Review Letters*, **85**(7), 1576–1579.
- Chialvo, D.R., Longtin, A., and Müller-Gerking, J. (1997). Stochastic resonance in models of neuronal ensembles. *Physical Review E*, **55**(2), 1798–1808.
- Collins, J.J., Chow, C.C., and Imhoff, T.T. (1995). Aperiodic stochastic resonance in excitable systems. *Physical Review E*, **52**(4), 3321–3324.
- Douglass, J.K., Wilkens, L., Pantazelou, E., and Moss, F. (1993). Noise enhancement of information transfer in crayfish mechanoreceptors by stochastic resonance. *Nature*, **365**(6444), 337–340.
- Faisal, A.A. and Loughlin, S. (2007). Stochastic Simulations on the Reliability of Action Potential Propagation in Thin Axons. *PLoS Comput Biol.* **3**(5): e79.
- Gammaitoni, L., Hänggi, P., Jung, P., and Marchesoni, F. (1998). Stochastic resonance. *Reviews of Modern Physics*, **70**(1), 223–287.
- Gerstein, G. and Mandelbrot, B. (1964). Random walk models for spike activity of a single neuron. *Biophysical Journal*, **4**, 41–68.
- Gingl, Z., Kiss, L.B., and Moss, F. (1995). Non-dynamical stochastic resonance: Theory and experiments with white and various coloured noises. *Il Nuovo Cimento D*, **17**(7), 795–802.

- Glass, L., Graves, C., Petrillo, G.A., and Mackey, M.C. (1980). Unstable dynamics of a periodically driven oscillator in the presence of noise. *J Theor Biol.*, **86**(3), 455–75.
- Glass, L. and Mackey, M.C. (1988). *From Clocks to Chaos: The Rhythms of Life*. Princeton University Press.
- Hänggi, P. and Jung, P. (1995). Colored noise in dynamical systems. *Adv. Chem. Phys.*, **89**, 239.
- Holden, A. V. (1976). *Models of the Stochastic Activity of Neurones*. Springer-Verlag, Berlin.
- Horsthemke, W. and Lefever, R. (1984). *Noise-Induced Transitions. Theory and Applications in Physics, Chemistry, and Biology. Springer Series in Synergetics vol 15*, Springer-Verlag, Berlin.
- Izhikevich, E. (2007). *Dynamical Systems in Neuroscience*. MIT Press, Cambridge MA.
- Jung, P. (1994). Threshold devices: Fractal noise and neural talk. *Physical Review E*, **50**(4), 2513–2522.
- Jung, P. and Hänggi, P. (1991, Dec). Amplification of small signals via stochastic resonance. *Phys. Rev. A*, **44**(12), 8032–8042.
- Kaplan, D.T., Clay, J.R., Manning, T., Glass, L., Guevara, M.R., and Shrier, A. (1996). Subthreshold dynamics in periodically stimulated squid giant axons. *Physical Review Letters*, **76**(21), 4074–4077.
- Kloeden, P.E. and Platen, E. (1992). *Numerical Solution of Stochastic Differential Equations*. Springer, Berlin.
- Knight, B. W. (1972). Dynamics of encoding in a population of neurons. *Journal of General Physiology*, **59**, 734–766.
- Lánský, P. and Sacerdote, L. (2001). The Ornstein–Uhlenbeck neuronal model with signal-dependent noise. *Physics Letters A*, **285**(3-4), 132–140.
- Lindner, B., Garcia-Ojalvo, J., Neiman, A., and Schimansky-Geier, L. (2004). Effects of noise in excitable systems. *Phys. Rep.*, **392**(6), 321–424.
- Lindner, B., Longtin, A., and Bulsara, A. (2003). Analytic expressions for rate and CV of a type I neuron driven by white Gaussian noise. *Neural Computation*, **15**(8), 1761–1788.
- Lindner, B. and Schimansky-Geier, L. (2001). Transmission of noise coded versus additive signals through a neuronal ensemble. *Physical Review Letters*, **86**(14), 2934–2937.
- Lindner, B., Schimansky-Geier, L., and Longtin, A. (2002). Maximizing spike train coherence or incoherence in the leaky integrate-and-fire model. *Physical Review E*, **66**(3), 31916.
- Longtin, A. (1993). Stochastic resonance in neuron models. *Journal of Statistical Physics*, **70**(1), 309–327.
- Longtin, A. (1997). Autonomous stochastic resonance in bursting neurons. *Physical Review E*, **55**(1), 868–876.
- Longtin, A. (2000). Effect of noise on the tuning properties of excitable systems. *Chaos, Solitons and Fractals*, **11**, 1835–1848.
- Longtin, A. (2002). Phase locking and resonances for stochastic excitable systems. *Fluct. and Noise Lett.*, **2**, 183–211.

- Longtin, A., Bulsara, A., and Moss, F. (1991). Time-interval sequences in bistable systems and the noise-induced transmission of information by sensory neurons. *Physical Review Letters*, **67**(5), 656–659.
- Longtin, A. and Chialvo, DR (1998). Stochastic and deterministic resonances in excitable systems. *Phys. Rev. Lett.*, **81**, 4012–4015.
- Massanés, S.R. and Pérez Vicente, CJ (1999). Nonadiabatic resonances in a noisy Fitzhugh–Nagumo neuron model. *Physical Review E*, **59**(4), 4490–4497.
- Moore, G.P., Perkel, D.H. and Segundo, J.P. (1966). Statistical analysis and functional interpretation of neuronal spike data. *Ann. Rev. Physiol.*, **28**: 493–522.
- Pakdaman, K., Tanabe, S., and Shimokawa, T. (2001). Coherence resonance and discharge time reliability in neurons and neuronal models. *Neural Networks*, **14**(6-7), 895–905.
- Pikovsky, A.S. and Kurths, J. (1997). Coherence resonance in a noise-driven excitable system. *Physical Review Letters*, **78**(5), 775–778.
- Plesser, H.E. and Geisel, T. (1999). Markov analysis of stochastic resonance in a periodically driven integrate-and-fire neuron. *Physical Review E*, **59**(6), 7008–7017.
- Rudolph, M. and Destexhe, A. (2001a). Correlation detection and resonance in neural systems with distributed noise sources. *Physical Review Letters*, **86**(16), 3662–3665.
- Rudolph, M. and Destexhe, A. (2001b). Do neocortical pyramidal neurons display stochastic resonance? *Journal of Computational Neuroscience*, **11**(1), 19–42.
- Shimokawa, T., Pakdaman, K., and Sato, S. (1999). Time-scale matching in the response of a leaky integrate-and-fire neuron model to periodic stimulus with additive noise. *Physical Review E*, **59**(3), 3427–3443.
- Shuai, JW and Jung, P. (2002). Optimal intracellular calcium signaling. *Physical Review Letters*, **88**(6), 68102.
- Spekreijse, H. (1969). Rectification in the goldfish retina: analysis by sinusoidal and auxiliary stimulation. *Vision Res.*, **9**(12), 1461–72.
- Stacey, W.C. and Durand, D.M. (2001). Synaptic noise improves detection of subthreshold signals in hippocampal CA1 neurons. *Journal of Neurophysiology*, **86**(3), 1104–1112.
- Stein, R.B., Gossen, E.R., and Jones, K.E. (2005). Neuronal variability: noise or part of the signal? *Nature Reviews Neuroscience*, **6**(5), 389–397.
- Tateno, T., Doi, S., Sato, S., and Ricciardi, L.M. (1995). Stochastic phase lockings in a relaxation oscillator forced by a periodic input with additive noise: A first-passage-time approach. *Journal of Statistical Physics*, **78**(3), 917–935.
- Tuckwell, H. (1989). *Stochastic Processes in the Neurosciences*. SIAM, Philadelphia.
- Wiesenfeld, K., Pierson, D., Pantazelou, E., Dames, C., and Moss, F. (1994). Stochastic resonance on a circle. *Physical Review Letters*, **72**(14), 2125–2129.
- Yu, X. and Lewis, ER (1989). Studies with spike initiators: linearization by noise allows continuous signal modulation in neural networks. *IEEE Transactions on Biomedical Engineering*, **36**(1), 36–43.

NOISY OSCILLATORS

Bard Ermentrout

Synchronous oscillations occur throughout the central nervous system. Recordings of population activity such as the electroencephalogram (EEG) and local field potential (LFP) often show a strong peak in the power spectrum at certain frequencies. This synchronous activity is sometimes observed across multiple recording sites and over distant brain areas. While local circuitry in the cortex is ideal for the production of local rhythms, the mechanisms for synchronization across different regions are more complex. Furthermore, the rhythms observed in real biological networks are not perfect oscillations. Instead, correlations between cells are often weak and the width of peaks in the power spectrum can also be quite broad. There are many reasons for this imperfect synchronization. Among them are heterogeneities in properties of individual neurons, heterogeneities in the connectivity between cells and their inputs, and finally, intrinsic noise (due, e.g. to channel fluctuations as well as the aforementioned heterogeneities). The goal of this chapter is to analyse the role of noise in synchronising and desynchronising coupled oscillators using a particularly simple class of model oscillators.

There is a long history of the study of noise in oscillators, going back to the work of Stratonovich (1958, 1967) where the interest was in how noise could disrupt oscillatory radio circuits. Our focus in this chapter concerns how noise affects neural oscillators, both in isolation and when coupled to each other. Furthermore, we will mainly consider the behaviour when the noise and coupling are small and the oscillators are nearly identical. This allows one to significantly reduce the dimensionality of the problem and treat each oscillator as a single variable coding its phase. In other chapters of this book (notably Chapter 4 by Longtin), the effects of larger noise is studied on systems which may not even intrinsically oscillate (coherence resonance).

The overall organization of this chapter is as follows. First we consider the general question of perturbed oscillators and introduce the phase resetting curve. We then look at how correlated noise can serve as a synchronising signal for uncoupled oscillators. We study how noise can desynchronize coupled oscillators. We first study a pair and then a large network of globally coupled oscillators using population density methods.

5.1 The phase resetting curve and weak perturbations

5.1.1 Preliminaries

Many authors (particularly in physics) define an oscillator to be any dynamical system which makes repeated (although not necessarily predictable) transits

through some local region in phase space. For example, chaotic systems are often called oscillators. In this chapter, we confine our attention to systems in which there is an underlying attracting limit cycle, $X_0(t)$ such that $X_0(t+T) = X_0(t)$. We suppose that this limit cycle is a solution of an ordinary differential equation (ODE):

$$\frac{dX}{dt} = F(X(t)). \quad (5.1)$$

All autonomously generated limit cycles have an arbitrary phase associated with them. Thus, let us define the phase of the limit cycle to be t modulo T , with $t = 0$ defined as some identifiable point on the cycle. Since our main examples come from neuroscience, the 0 phase is often defined as the time of the spike. Thus a rhythmically firing neuron produces spikes at multiples of T . Now, suppose that we add to this a possibly noisy, time-dependent perturbation, which is ‘weak’ in the sense that it does not destroy the overall shape of the limit cycle. Formally, the limit cycle attractor is a closed orbit in phase space and there is a local tubular neighbourhood of the cycle in which all points are attracted to the limit cycle with a well-defined asymptotic phase. The perturbation should be small enough so as not to leave this neighbourhood. In practice, it can be quite large. Since each point in the neighbourhood has a well-defined phase, there are curves called *isochrons* which parametrize the phase of every point on the limit cycle (Izhikevich, 2007, Kuramoto, 2003, Winfree, 2001, Guckenheimer, 1975). Figure 5.1(a) shows a neighbourhood (dashed ellipses) around a limit cycle with the zero phase, $\theta = 0$ defined to be the maximum in the horizontal direction. Phase increases at a constant rate in the counterclockwise direction. The curve passing through $\theta = 0$ is the 0-phase isochron. Any points on this curve will asymptotically approach the unshifted oscillator. Consider a brief (instantaneous) stimulus in the horizontal direction occurring at phase ϕ . The perturbation will cause the dynamics to leave the limit cycle, but, if it is sufficiently small, it will remain in a neighbourhood where the asymptotic phase is defined. Figure 5.1(a) shows that the perturbation moves the limit cycle from its current phase, ϕ to a new phase, $\hat{\phi}$. The mapping from ϕ to $\hat{\phi}$ is called the phase transition curve. The net change in phase is the phase resetting curve (PRC), $\Delta(\phi) := \hat{\phi} - \phi$. Note that in this example, the change in phase is negative and the time of the next maximum

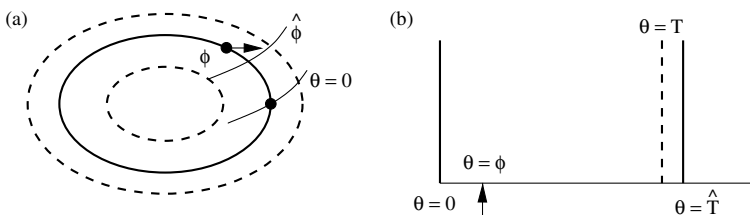


FIG. 5.1: (a) Definition of the phase of an oscillator. Isochrons for $0, \hat{\phi}$ are shown; (b) defining the phase resetting curve.

will be delayed. An alternate way to look at the PRC is through the spike (or event) time. Figure 5.1(b) shows how the PRC is constructed in this manner. The perturbation is given at phase ϕ producing the next spike/event at a time \hat{T} . The PRC is then $\Delta(\phi) := T - \hat{T}$. As above, in this example, the next spike is delayed so the PRC at this value of phase is negative. We should remark that the PRC is often defined in terms of a phase between 0 and 1 or 0 and 2π . In this case, one only needs to divide by the period T and multiply by 2π . We prefer to work using the real time of spike, but it does not matter.

In the above geometric example, the perturbation was a horizontal kick; of course, there could also be a vertical kick which would give a PRC in the y -direction. If the kicks are small, then the effects add linearly, so that we can regard the actual PRC as a vector quantity corresponding to small perturbations in each of the n -directions of an n -dimensional dynamical system. If we parametrize the j th component of the PRC by the amplitude of the perturbation, a_j , where a_j has the dimensions of the given quantity, e.g. voltage for membrane deflections or millimolar for, say, calcium perturbations, then we can define:

$$Z_j(t) = \lim_{a_j \rightarrow 0} \frac{\Delta_j(t, a_j)}{a_j} \quad (5.2)$$

which is called the *adjoint* for the limit cycle; it is also called the infinitesimal PRC. The adjoint is the unique periodic solution of

$$\frac{dZ}{dt} = -D_X F(X_0(t))^T Z(t) \quad (5.3)$$

such that $Z(t)^T X'_0(t) = 1$. (Here $D_X F(X_0(t))$ is the linearization of $F(X)$ with respect to X evaluated at $X_0(t)$ and $Z(t) := (Z_1(t), \dots, Z_n(t))$.) $Z(t)$ can also be defined geometrically. In Fig. 5.1(a), every point in the dashed region can be assigned an asymptotic phase; let $Q(Y)$ be the asymptotic phase of any point Y in the dashed region. Then, $Z(t) = \nabla_X Q(X_0(t))$; that is, Z is the gradient of the asymptotic phase with respect to the vector field evaluated along the limit cycle. This geometric definition is quite intuitive and matches precisely with Eqn (5.2), when the reader recalls the definition of the derivative. The advantage of Eqn (5.3) is that it enables us to calculate $Z(t)$ numerically by solving a linear ODE. Experimentalists measure the PRC in the direct manner illustrated in Fig. 5.1(b), by delivering brief perturbations and measuring the phase shift (Reyes and Fetz, 1993). As we will see in the next sections, the PRC is to limit cycles what the linearization is to fixed points and tells us how the timing of spikes is altered by perturbations.

We close this section with a short discussion on PRCs since they are so important. Figure 5.2 shows some PRCs from a variety of CNS neurons. In each case the zero phase corresponds to the time of the spike. One property which is quite common among neurons is that the PRC vanishes at 0, T corresponding to the times of the spikes. Another aspect of PRCs is that for some cells they are

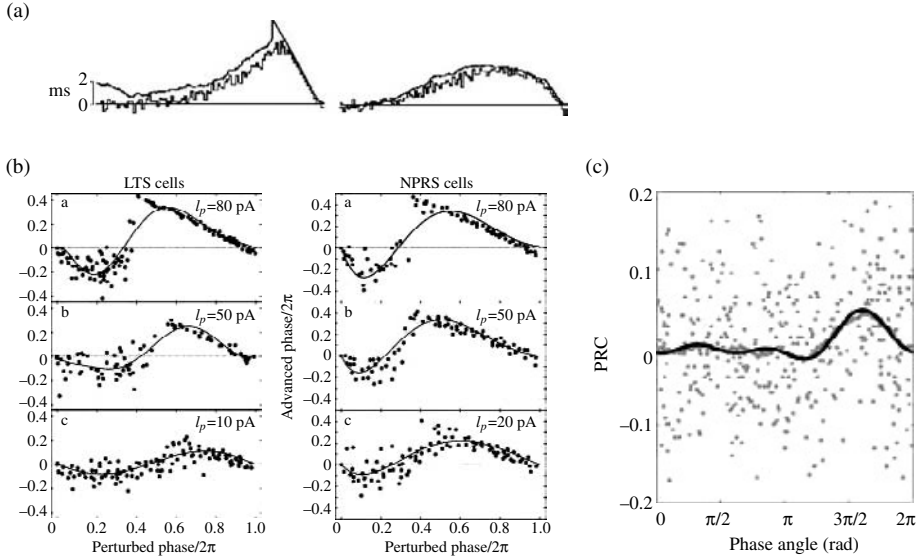


FIG. 5.2: PRCs from different neurons (a) Gutkin, Ermentrout, and Reyes (2005); (b) Tateno and Robinson (2007); (c) Galán, Ermentrout, and Urban (2005). Note that the axes are either between 0 and 1 or 0 and 2π depending on the conventions of the authors.

strictly non-negative while for others they have a negative region which always occurs right after the spike. Several authors have noted that these shapes can be loosely matched to different bifurcations (Ermentrout, 1996, Hansel, Mato, and Meunier, 1995, Brown, Moehlis, and Holmes, 2004). Specifically, the PRC near a saddle-node on a limit cycle (SNIC) (the so-called theta model or quadratic integrate and fire model) has the form $\Delta(t) = K(1 - \cos(2\pi t/T))$ while near a Hopf bifurcation, the PRC has the form $\Delta(t) = K \sin(2\pi t/T)$. Thus, in many of the examples we discuss, we will use different variants of these PRCs. In particular, a nice parameterization has the form

$$\Delta(t) = \frac{\sin(t + \alpha) - \sin(\alpha)}{\sqrt{\pi(2 - \cos(2\alpha))}} \quad (5.4)$$

which has an L^2 norm of 1. By varying α , we can smoothly transition from the PRC associated with the Hopf to that associated with the SNIC.

5.1.2 Perturbations

We now add a small perturbation to Eqn (5.1):

$$\frac{dX}{dt} = F(X(t)) + \epsilon G(X(t), t). \quad (5.5)$$

Here $0 < \epsilon \ll 1$ is a small parameter. Since the perturbation is small, we expect that solutions will stay close to the stable limit cycle attractor and thus there is a well-defined notion of phase. If we introduce the phase variable, $\theta(t)$, and write $X(t) = X_0(\theta(t)) + Y(t)$ where $Y(t)$ represents coordinates orthogonal to the limit cycle, then

$$X'_0(\theta(t)) \frac{d\theta}{dt} + \frac{dY}{dt} = F(X_0(\theta(t))) + D_X F(\hat{X}(t))Y(t) + \epsilon G(X_0(\theta) + Y(t), t)$$

where \hat{X} is close to X_0 and X . If we multiply this equation by $Z(t)^T$, we obtain

$$\frac{d\theta}{dt} = 1 + Z(t)^T[-Y'(t) + D_X F(\hat{X}(t))Y(t)] + \epsilon Z(t)^T G(X_0(t) + Y(t), t).$$

(Note that we have used the fact that $Z(t)^T X_0(t)' = 1$.) This is an *exact* equation for the evolution of the phase; it is not an approximation. However, it still involves $Y(t)$ and $\hat{X}(t)$ which are unknown. Note also that we have not used the smallness of ϵ except to assume that the perturbation remains in a region for which phase is defined. If ϵ is small, $Y(t)$, too, will be of order ϵ and \hat{X} will be close to X_0 . We will exploit this to obtain an approximate equation for the phase. The linear operator, $L(t)Y := -Y' + D_X F(X_0(t))Y$, has a one-dimensional nullspace spanned by $X'_0(t)$ and its adjoint (under the usual inner product for periodic systems) has a nullspace spanned by $Z(t)$. Thus, with the approximation $\hat{X} \approx X \approx X_0$, we obtain the self-contained phase model:

$$\frac{d\theta}{dt} = 1 + \epsilon Z(\theta)^T G(X_0(\theta), t). \quad (5.6)$$

This is the main equation of this chapter and we will use it to analyse the effects of noise and coupling on oscillators. We note that in the case of neuronal models, the perturbations are typically only through the somatic membrane potential so that all but one of the components of G are zero and we can more conveniently write

$$\theta' = 1 + \epsilon \Delta(\theta)g(\theta, t). \quad (5.7)$$

Remarks

1. If the perturbation is a white noise, then we have to be a bit more careful and make sure that we interpret this process correctly since the normal changes of variables that we take need to be adjusted in accordance with the rules of stochastic calculus (Risken, 1996). Thus, if the perturbation is white noise, then the correct version of (5.7) is (Teramae and Tanaka, 2004):

$$d\theta = [1 + \epsilon^2 \Delta'(\theta) \Delta(\theta)/2]dt + \epsilon \Delta(\theta)dW(t) \quad (5.8)$$

where $dW(t)$ is a zero mean unit variance Gaussian.

2. The perturbations incorporated in G in Eqn (5.5) could be the effects of other oscillators to which our example oscillator is coupled via, e.g. synapses or gap junctions. We will consider this in later sections.

5.1.3 Statistics

In this section, we derive equations for the mean and variance of the interspike interval for noisy oscillators as well as show that the variance of the phase-resetting curve is phase-dependent. We first consider the non-white case for which the perturbation is zero mean:

$$\theta' = 1 + \epsilon \Delta(\theta) \xi(t).$$

Here $\xi(t)$ is the ‘noise.’ We look for a solution of the form: $\theta(t) = t + \epsilon \theta_1(t) + \epsilon^2 \theta_2(t) + \dots$ and obtain:

$$\theta_1(t) = \int_0^t \Delta(s) \xi(s) \, ds.$$

Similarly,

$$\theta_2(t) = \int_0^t \int_0^s \Delta'(s) \Delta(s') \xi(s) \xi(s') \, ds \, ds'.$$

The unperturbed period is T , so that we want to find the value of t^* such that $\theta(t^*) = T$. Thus, we expect $t^* = T + \epsilon \tau_1 + \epsilon^2 \tau_2 + \dots$, which results in

$$\tau_1 = - \int_0^T \Delta(s) \xi(s) \, ds$$

and

$$\tau_2 = -\Delta(T) \xi(T) \tau_1 - \int_0^T \int_0^s \Delta'(s) \Delta(s') \xi(s) \xi(s') \, ds \, ds'.$$

Let $C(t) := \langle \xi(0) \xi(t) \rangle$ be the autocorrelation function for the noisy perturbation (which we assume is stationary with zero mean). We see that the expected period of the oscillation is just

$$\bar{T} = T + \epsilon \langle \tau_1 \rangle + \epsilon^2 \langle \tau_2 \rangle.$$

To order ϵ , there is no effect of the signal since the mean of τ_1 is zero. However, there are second-order effects:

$$\langle \tau_2 \rangle = \Delta(T) \int_0^T \Delta(s) C(s-T) \, ds - \int_0^T \int_0^s \Delta'(s) \Delta(s') C(s-s') \, ds \, ds'. \quad (5.9)$$

The variance (to order ϵ^2) is

$$\text{var} = \epsilon^2 \langle \tau_1^2 \rangle = \epsilon^2 \int_0^T \int_0^T \Delta(s) \Delta(s') C(s-s') \, ds \, ds'. \quad (5.10)$$

For a simple low-pass filtered white noise process (Ornstein–Uhlenbeck), $C(t) = \exp(-|t|/\tau)/2$ so that these integrals can be readily evaluated for simple PRCs such as (5.4).

Figure 5.3 shows some numerical as well as analytical results on the effects of the noise colour on the statistics of weakly perturbed oscillators. As noted above, there is a weak effect on the mean period of the oscillator for coloured noise as seen in Fig. 5.3(a) that is well-accounted for by the theoretical expression in Eqn (5.9). For a purely sinusoidal PRC, there is a ‘resonance’ in the variance as a function of the noise colour. That is, the variance has a maximum when the temporal correlations are proportional to the period of the oscillator as seen by the width of the histograms in Fig. 5.3(b). Using Eqn (5.10), we can make

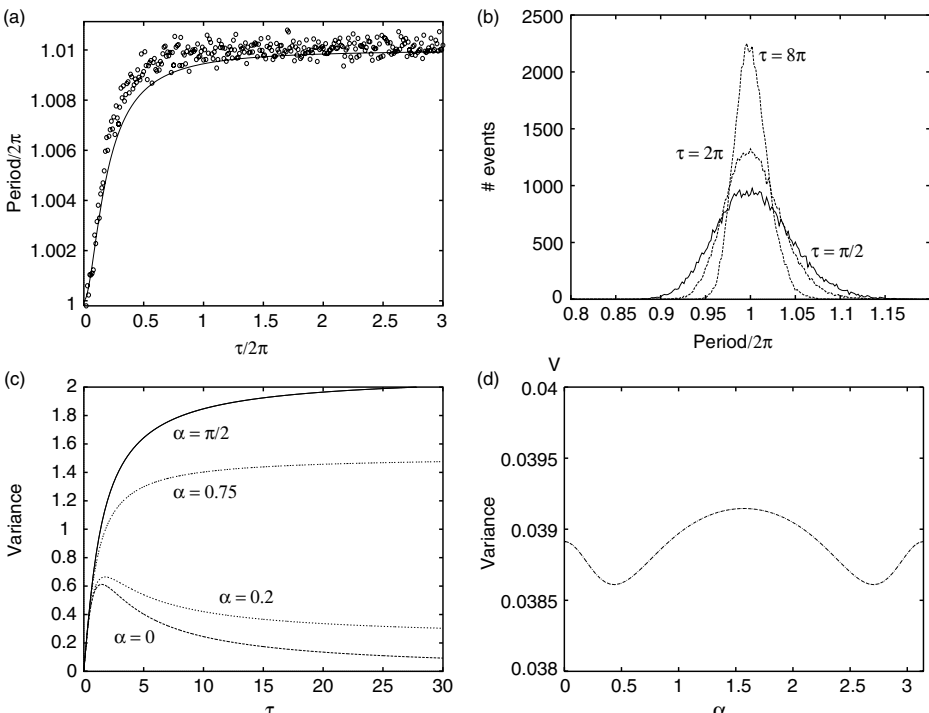


FIG. 5.3: Statistics of a single noisy oscillator as the shape of the PRC varies (α) and the temporal correlation of the noise changes (τ). (a) Mean value of the period for the PRC model, $\Delta(t) = \sin t$ as the correlation time, τ varies for $\epsilon = 0.2$ along with the theoretical value from Eqn (5.9). (b) Histograms of the period of the oscillator for 10 000 firings and different values of τ . (c) Variance from Eqn (5.10) for different shapes of the PRC (using (5.4)) as a function of the noise color. (d) Variance as a function of α for $\epsilon = 0.2$ and white noise.

this more explicit by evaluating the double integrals. Figure 5.3(c) clearly shows a resonance in the variance (here we have scaled out ϵ^2) for PRCs that are nearly sinusoidal (cf. Eqn (5.4) with α small). However as the PRC becomes more like the SNIC case, α near to $\pi/2$, this resonance is lost and the variance increases monotonically with the correlation time, τ . We remark that the PRC for the integrate-and-fire neuron is strictly positive and shows the same monotonic behaviour of variance with respect to noise colour. The key feature shared by both the SNIC and the integrate-and-fire PRCs is the large 0-mode Fourier component. The pure sinusoidal PRC lacks this component.

The case of white noise is more straightforward and does not require perturbation theory since we can write explicit equations for the mean first passage time, T_1 , and second moment, T_2 (Risken, 1996):

$$-1 = [1 + \epsilon^2 \Delta'(t) \Delta(t)] T'_1 + (\epsilon^2/2) \Delta(t)^2 T''_1 \quad (5.11)$$

$$-2T_1 = [1 + \epsilon^2 \Delta'(t) \Delta(t)/2] T'_2 + (\epsilon^2/2) \Delta(t)^2 T''_2. \quad (5.12)$$

Here we assume that $\Delta(t)$ is 1-periodic. These equations have to be solved with the appropriate boundary conditions, which are found by setting $t = 0$ and exploiting the fact that $\Delta(0) = 0$, thus, $T'_1(0) = -1$, $T_1(1) = 0$ and $T'_2(0) = -2T_1(0)$, $T_2(1) = 0$. The mean period is $T_1(0)$ and the variance is $T_2(0) - T_1(0)^2$. Explicit expressions for these quantities could be found (Lindner, Longtin, and Bulsara, 2003), but they involve integrals that are not readily evaluated. Instead, we can solve the boundary value problem by shooting or some other technique and compute how the variance depends on shape of the PRC. Figure 5.3(d) shows this dependence for $\epsilon = 0.2$. The variance remains less than would be the case for a constant PRC ($\text{var} = \epsilon^2 = 0.04$) and is maximal when $\alpha = \pi/2$ corresponding to the SNIC bifurcation.

As a last look at statistics, we can study the effect of noise on the actual calculation of the phase resetting curve. In particular, we consider the following simple model:

$$\frac{d\theta}{dt} = 1 + [\epsilon\xi(t) + \beta\delta(t - \phi)]\Delta(\theta) \quad (5.13)$$

which represents the noise $\xi(t)$ along with a Dirac delta function perturbation for the PRC. Here ϕ is the time of the perturbation and lies between 0 and T , the period. The net gain in phase given $\theta(0) = 0$ is found by evaluating $\theta(T)$. In the absence of any stimuli (noise or experimental perturbations), $\theta(T) = T$. For a completely noise-free system, $\theta(T) = T + \beta\Delta(\phi)$ so that the gain (or loss) in phase is just $\theta(T) - T = \beta\Delta(\phi)$ as it should be; the PRC of the noise-free system should be proportional to $\Delta(\tau)$. With noise, $\theta(T)$ is a random variable. Using perturbation theory, it is possible to show that the mean value of $\theta(T)$

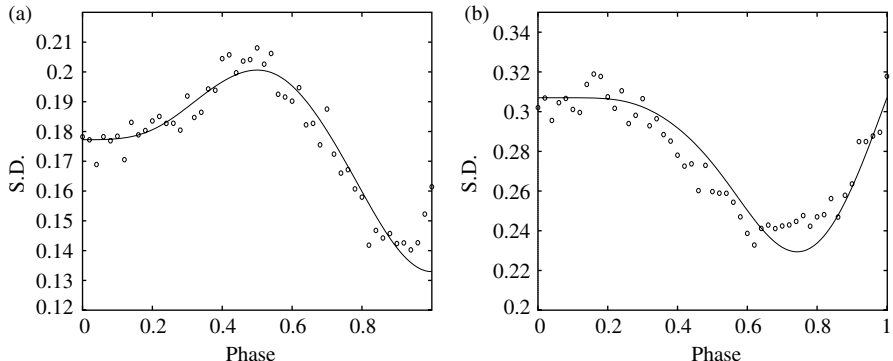


FIG. 5.4: Standard deviation (square root of the variance) of the PRC for (a) $\Delta(t) = \sin 2\pi t$ and (b) $\Delta(t) = 1 - \cos 2\pi t$. Here $\epsilon = 0.1$ and $\beta = 1/(8\pi)$.

is the same as the noise-free case, but that the variance is phase-dependent. In fact, we have shown (unpublished work) that for white noise:

$$\text{var}(\phi) = \epsilon^2 \left([1 + \beta\Delta'(\phi)]^2 \int_0^\phi \Delta^2(s) ds + \int_\phi^T \Delta^2(s + \beta\Delta(\phi)) ds \right). \quad (5.14)$$

That is, the variance is phase-dependent. Figure 5.4 shows the phase-dependence of the PRC for two different phase models. Solid lines are Eqn (5.14) and points are from Monte Carlo simulations of 1000 repetitions of an impulse at each phase point. Phase-dependence of the variance of the PRC was shown experimentally in several papers (Netoff *et al.*, 2005, Reyes and Fetz, 1993, Gutkin, Ermentrout, and Reyes, 2005), and Ermentrout and Saunders (2006) showed how this phase-dependence had interesting consequences for the synchronization of coupled oscillators. We revisit this point in Section 5.3.

In conclusion, by using PRC theory and perturbation theory, we can study how various types of noise affect the regularity of spiking and how the properties of the PRC and the noise factor into these effects. Furthermore, we have provided an explanation for phase-dependence in the variance of the PRC.

5.2 Noise induced synchrony

Suppose that we have a population of nearly identical oscillators which are uncoupled but receiving some kind of common input. A well-known example would be independent oscillators receiving common periodic input. For example, most living organisms contain an internal clock with a period of about 24 hours which is locked to the light-dark cycle as the Earth circles the Sun. Thus, even though these oscillators are not directly coupled, the periodic drive they receive is sufficient for them to partially synchronize. Of course, the frequency of the periodic drive must match that of the individual oscillators in order for this to work. What

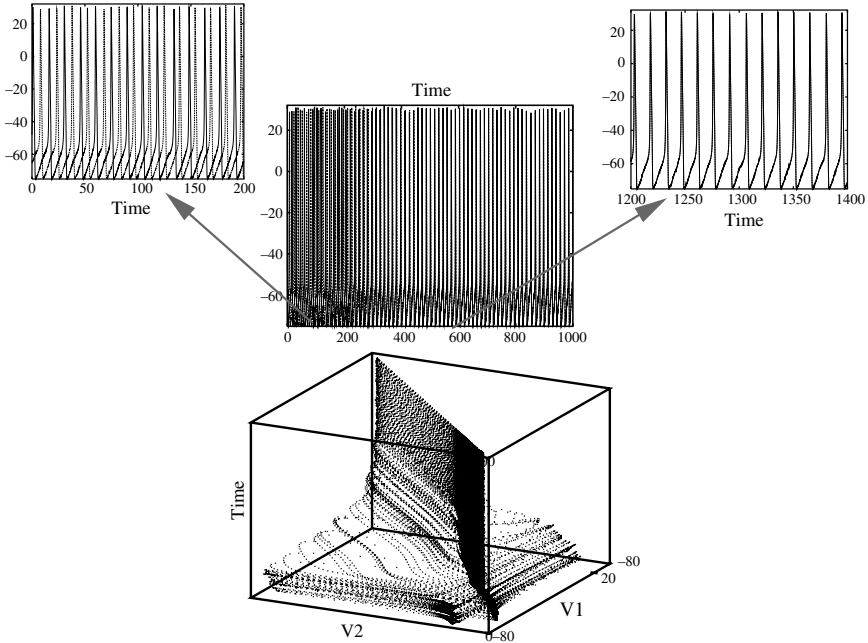


FIG. 5.5: White noise synchronization of two Hodgkin–Huxley oscillators. The oscillators are identical and start at different points in their cycle. Both receive an identical white noise stimulus. Time series and V_1 versus V_2 are shown.

is surprising is that the common signal received by the uncoupled oscillators need not be periodic.

Pikovsky and his collaborators were among the first to describe models and theory for the synchronization of dynamical systems to common noisy input (Goldobin and Pikovsky, 2005, Pikovsky, 1984, Pikovsky, Rosenblum, and Kurths, 2001). These authors look not only at oscillators but also at chaotic systems and other systems with complex dynamics. They have also shown that for strong noise, synchrony is disrupted. Jensen (2002) studied an abstract phase model for oscillators receiving a common signal and Ritt (2003) analysed synchronization of a specific model (the theta model) to white noise. In this section, we will use phase response curves once again to explore synchrony when they are uncoupled but receive a common noisy input. The methods described here are close to those of Teramae and Tanaka (2004).

Figure 5.5 shows an example of a synchronization due to a common input for two Hodgkin–Huxley (HH) oscillators. Voltages are plotted against time in the upper plots and against each other in the three-dimensional plot below. The cells are identical, uncoupled, and start with a phase difference of half a cycle. They are driven by weak white noise and after several cycles, the phase-difference

disappears and the oscillators are completely synchronized. This phenomena is not restricted to neural *models*; Galan *et al.* (2006) demonstrated that filtered white noise stimuli could synchronize mitral cells in the olfactory bulb. This mechanism is called the Moran effect in ecology (Engen and Saether 2005) and has also been suggested as a means to synchronize intracellular signalling oscillations (Zhou, Chen, and Aihara, 2005). The goal in this section is to use phase models to study how noise can synchronize uncoupled oscillators. The mechanism for this type of synchronization is closely related to the issue of spike time reliability as first discussed by Bryant and Segundo (1976) and popularized by Mainen and Sejnowski (1995). To see the connection, suppose that we apply a constant current to a neuron to induce it to fire repetitively and mark the times of the spikes. We repeat this experiment many times and create a histogram of the spike times. In a completely noise-free environment, the spikes will line up perfectly. However, if there is noise and it is uncorrelated from trial to trial, then as time progresses, spikes will occur less and less reliably. In contrast, suppose that in addition to the uncorrelated noise, there is a fast signal (e.g. correlated noise) common to each trial. With this background signal, both of the above experimental groups found that the spike times were considerably more reliable from trial to trial. Figure 5.6 shows an illustration of this effect with the Hodgkin–Huxley equations when there is just extrinsic noise and then when there is an additional signal on top. A single cell model is simulated for 100 trials with uncorrelated noise and starting from identical initial conditions. The right panel has an additional weak frozen white noise signal (it is the same for every trial and plays the role of a stimulus). The histogram of the spike times is much thinner around later spikes when there is a stimulus. The mechanism for reliability and for noise synchronization is the same. If the signal is such

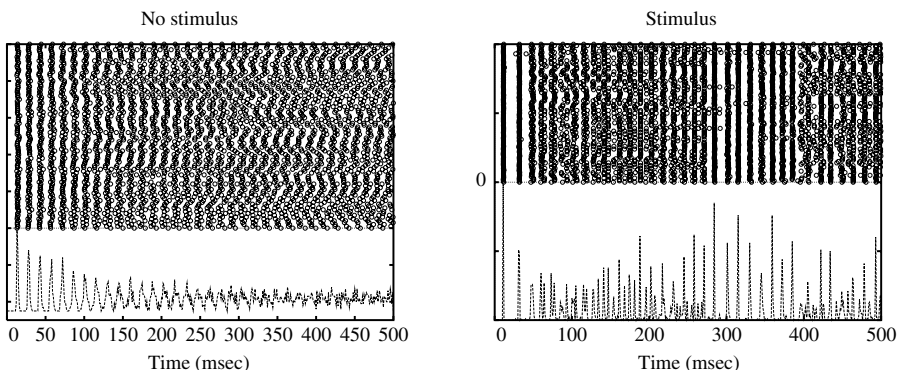


FIG. 5.6: Reliability in the Hodgkin–Huxley model. 100 trials of a constant current injection with uncorrelated noise (amplitude 1) with no stimulus and then with a common white noise stimulus (amplitude = 15). Spike times and histograms (below) are shown.

that the dynamics is an attractor, then nearby initial conditions will fall into the attractor induced by this stochastic force. As it is attractive, it is also robust against small perturbations, such as extrinsic noise. Brette and Guigon (2003) and Brette (2004) analysed these spike-time attractors for the integrate-and-fire model; Troyer (2006) also analysed these attractors in a context similar to that described here. We will formalize the notion of stability in the next several pages and introduce the so-called Lyapunov exponent.

5.2.1 White noise

Pikovsky (1984) was among the first to analyse synchronization to noise when he studied Poisson inputs. More recently, this work has been extended to white noise and to more general synchronization issues. We will follow Teramae and Tanaka for the white noise case and sketch the analysis for the Poisson case as well. We start with a single oscillator driven by white noise and reduced to a phase model. As our motive is to study neuronal oscillations, we will confine ourselves to the case when white noise appears only in the voltage equation. For any regular perturbations, Eqn (5.6) is valid, however, when the noise is white, we have to be careful and make the correct change of variables using the Ito stochastic calculus, so that we start with Eqn (5.8). Solutions to this equation have an invariant density found by solving the steady state Fokker–Planck equation:

$$0 = [(1 + D\Delta'(x)\Delta(x))\rho(x) + D(\Delta(x)^2\rho(x))']'$$

where $D = \epsilon^2/2$ and $\rho(x)$ is the invariant density; that is the probability that $\theta \in [a, b]$ is $\int_a^b \rho(x)dx$. This differential equation must be solved subject to $\rho(x)$ being periodic and $\int_0^T \rho(x) dx = 1$, the normalization. Solutions can be found by integrating or, since D is small, using perturbation theory. For our purposes, the invariant density is close to being uniform when D is small, so we will approximate $\rho(x)$ by $1/T$. Consider two oscillators driven with the same white noise signal:

$$\begin{aligned} d\theta_1 &= [1 + D\Delta'(\theta_1)\Delta(\theta_1)]dt + \epsilon\Delta(\theta_1)dW \\ d\theta'_2 &= [1 + D\Delta'(\theta_2)\Delta(\theta_2)]dt + \epsilon\Delta(\theta_2)dW. \end{aligned} \quad (5.15)$$

We are interested in whether or not they will synchronize. That is, we would like to assess the stability of the state $\theta_2 = \theta_1$. We let $\theta_2 - \theta_1 = y(t)$ and thus study the variational equation which has the form

$$dy = [D\Delta'(\theta)\Delta(\theta)]'ydt + \epsilon\Delta'(\theta)y dW.$$

Here $\theta(t)$ satisfies Eqn (5.8). This is a linear stochastic ODE in $y(t)$ and we would like to solve it. Let $z(t) = \log y(t)$ be a change of variables. Then appealing to Ito's formula, we find that

$$dz = D[(\Delta'(\theta)\Delta(\theta))' - \Delta'(\theta)^2]dt + \epsilon\Delta'(\theta)dW.$$

This is now a standard stochastic equation and we can integrate it to obtain the mean drift in $z(t)$:

$$\lambda := D \lim_{t \rightarrow \infty} \int_0^t [(\Delta'(\theta(s))\Delta(\theta(s)))' - \Delta'(\theta(s))^2] ds.$$

This is the mean rate of growth of $y(t)$, so that if $\lambda < 0$ then $y(t)$ will decay and synchrony will be stable. The quantity λ is called the Lyapunov exponent and since our system is ergodic, we obtain a simple expression:

$$\lambda = D \int_0^T [(\Delta'(x)\Delta(x))' - \Delta'(x)^2]\rho(x) dx.$$

Using the approximation that $\rho(x) \approx 1/T$ and the periodicity of $\Delta(x)$, we find

$$\lambda = \frac{-D}{T} \int_0^T \Delta'(x)^2 dx. \quad (5.16)$$

This is the main result on the stability of synchrony with identical white noise stimuli. It was derived by Teramae and Tanaka (2004) for the white noise case. What it tells us is that the details of the oscillator are irrelevant, the Lyapunov exponent is always negative for weakly forced oscillators.

As we began this section by discussing reliability, it is interesting to relate reliability to the magnitude of the Lyapunov exponent. Galan, Ermentrout and Urban (2008) showed that the reliability (measured as the ratio of the cross-correlation of the output to the autocorrelation) is

$$R = \frac{|\lambda|}{|\lambda| + c}$$

where $c \geq 0$ is the magnitude of the extrinsic noise which is uncorrelated between the neurons. Note that if $c = 0$, then reliability is 1, which is perfect. For small λ , reliability decreases which is why we generally want to maximize the magnitude of λ .

5.2.2 Poisson and coloured noise

Pikovsky (1984) and others (Marella and Ermentrout, 2008) have also studied the case of Poisson inputs. Let θ_n denote the phase of an oscillator right before the n th impulse where the train of impulses obeys some type of distribution. Assuming each has an amplitude ϵ , we obtain a model for the phase:

$$\theta_{n+1} = \theta_n + I_n + \epsilon\Delta(\theta_n) \mod T$$

where I_n is the time between impulses. As with the white noise case, it is possible to write an equation for the invariant density. Let $Q(I)$ denote the density function for the intervals, I_n , modulo the period, T . (Thus, the support of Q is

the interval $[0, T)$.) Then the invariant density for the phase θ , $\rho(x)$, satisfies the linear integral equation:

$$\rho(x) = \int_0^T Q[x - y - \epsilon\Delta(y)]\rho(y) dy.$$

See Lasota and Mackey (1994), Ermentrout and Saunders (2006), Nakao, Arai, and Kawamura (2007). In this case, the Lyapunov exponent satisfies:

$$\lambda_P = \int_0^T \log[1 + \epsilon\Delta'(x)]\rho(x) dx.$$

For ϵ small, $\rho(x)$ is nearly uniform and expanding in ϵ , we find the same expression for λ_P as for the white noise case.

We can use Eqn (5.6) for coloured noise in order to study the stability of synchrony. As in the rest of this section, the single oscillator satisfies

$$\frac{d\theta}{dt} = 1 + \epsilon\Delta(\theta)\xi(t)$$

where $\xi(t)$ is a general process. The variational equation satisfies

$$\frac{dy}{dt} = \epsilon\Delta'(\theta(t))\xi(t)y(t)$$

and the Lyapunov exponent is

$$\lambda_\xi = \epsilon \lim_{t \rightarrow \infty} \frac{1}{t} \int_0^t \Delta'(\theta(s))\xi(s) ds.$$

Using perturbation theory, as above, $\theta(t) = t + \epsilon \int_0^t \Delta(s)\xi(s) ds$ can be substituted into the equation for λ_ξ and we obtain:

$$\lambda_\xi = \lim_{t \rightarrow \infty} \frac{1}{t} \int_0^t \Delta''(s) \int_0^s \Delta(s')C(s-s') ds' ds \quad (5.17)$$

where $C(t)$ is once again the autocorrelation of the common noise. For low-pass filtered noise and $\Delta(t)$ as in Eqn (5.4), we obtain:

$$\lambda_\xi = -\epsilon^2 \frac{1}{2\pi(2 - \cos(2\alpha))} \frac{\tau}{1 + \tau^2}.$$

This shows that the Lyapunov exponent shows ‘resonance’ with respect to the PRC shape. For this model, the minimum occurs when $\tau = 1$. Figure 5.7(a) shows an experimental verification of the dependence of reliability on the correlation time of the signal, $\xi(t)$. Since reliability is a monotonic function of the Lyapunov exponent, this shows that the above calculations hold in realistic settings for both real and model neurons. Reliability is also a monotonic function of the noise amplitude for a given correlation time as can be seen from Fig. 5.7(b).

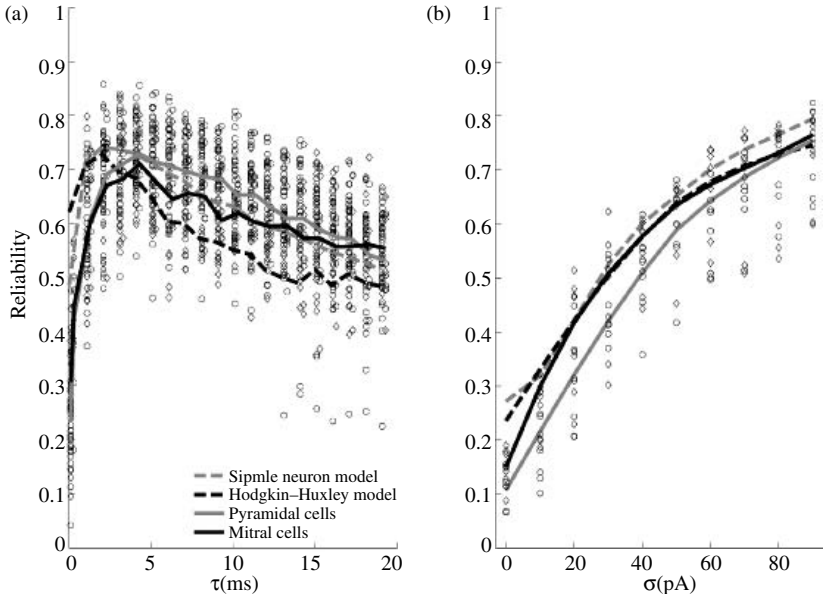


FIG. 5.7: Reliability of real and model neurons (from Galan, Ermentrout, and Urban (2008)). (a) Reliability is a non-monotonic function of the correlation time of the signal for both real (mitral and pyramidal neurons) and model neurons. (b) Reliability increases monotonically with signal amplitude.

5.2.3 Heterogeneity and extrinsic noise

In Fig. 5.5, we showed that perfectly correlated noise produces a perfectly synchronized state. How does this change in the presence of heterogeneities or uncorrelated noise? Nakao, Arai, and Kawamura (2007) consider the white noise problem when there is a mixture of identical and uncorrelated noise. We can generalize that slightly to study the case when there is additionally heterogeneity in the natural frequencies of the oscillators. The generalization of Eqn (5.15) is

$$d\theta_1 = [1 - \hat{\mu}/2 + (\epsilon^2/2)\Delta'(\theta_1)\Delta(\theta_1)]dt + \epsilon\Delta(\theta_1)(\sqrt{q}dW + \sqrt{1-q}dW_1)$$

$$d\theta'_2 = [1 + \hat{\mu}/2 + (\epsilon^2/2)\Delta'(\theta_2)\Delta(\theta_2)]dt + \epsilon\Delta(\theta_2)(\sqrt{q}dW + \sqrt{1-q}dW_2).$$

where $\hat{\mu}$ is the difference in natural frequency and q is the fraction of shared noise. When $q = 1$ and $\hat{\mu} = 0$, the oscillators receive identical noise and have no intrinsic differences, in short, Eqn (5.15). Nakao *et al.* develop an equation for the probability density function (PDF) for the phase difference, $\theta_2 - \theta_1$, for small ϵ when $\hat{\mu} = 0$. If we rescale $\hat{\mu} = \epsilon^2\mu$, then we can generalize their result

and obtain the following equation for the density of the phase differences:

$$\left[\left(1 - c \frac{h(x)}{h(0)} \right) \rho(x) \right]' = K + \mu \rho(x) \quad (5.18)$$

where $c = 2q/(1+q)$ is the correlation,

$$h(x) := \int_0^T \Delta(x+y) \Delta(y) dy$$

and K is an arbitrary constant chosen so that $\rho(x)$ is periodic. An almost identical equation was derived by Marella and Ermentrout (2008) for Poisson inputs. Integrating this equation over one period and using the normalization and periodicity, it is clear that $K = -\mu/T$. When $\mu = 0$, then the density of the phase differences is just

$$\rho(x) = \frac{N}{1 - ch(x)/h(0)}$$

with N a normalization constant. As $c \rightarrow 1$, this density approaches a delta function. The definition of $h(x)$ implies it is an even function so that, in general, the density is symmetric around 0 and has a peak at 0. One could integrate (5.18) to get the general solution for different values of μ , but the formulas are not particularly insightful. Instead, we simply solve the resulting boundary value problem numerically. Figure 5.8 shows the effects of the two kinds of heterogeneity on the phase difference between oscillators. For $c = 0$ and weak noise, the density is flat. As c increases, the density becomes more and more highly peaked. Galán, Ermentrout, and Urban (2007) and Marella and Ermentrout (2008) showed that the degree of this sharpening depends a great deal on the shape of the PRC.

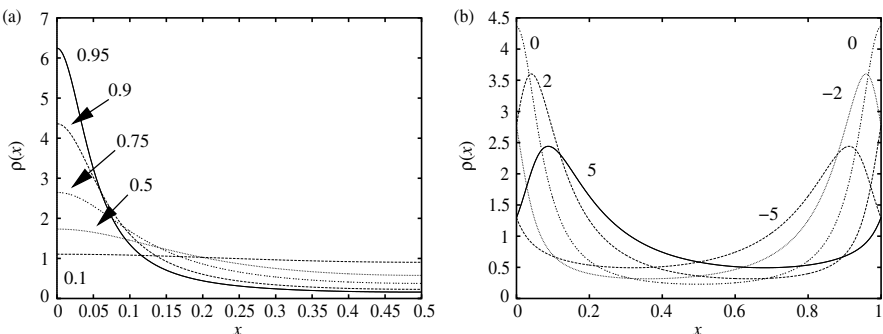


FIG. 5.8: The effect of heterogeneity on noise-induced synchrony. (a) Identical oscillators ($\mu = 0$) as the correlation, c , varies. As the density is symmetric, only $x \leq 0.5$ is shown. $\Delta(x) = \sin 2\pi x$. (b) $c = 0.9$ and the frequency difference, μ , between the oscillators varies.

However, the general shape of the distribution and the general trends are identical. Nakao *et al.* showed more complex forms for the density when the noise in Eqn (5.5) was not simply additive. Figure 5.8(b) fixes the correlation at 90% and varies μ , the difference in frequencies. For $\mu < 0$, oscillator 1 is faster than oscillator 2 and the density of $\theta_2 - \theta_1$ is skewed to the right as expected. For $\mu > 0$, the skew is opposite and oscillator 2 tends to lead oscillator 1. This is exactly what one would expect and is similar for coupled oscillators (see below).

In conclusion, in this section we have shown that noise can induce synchronization between uncoupled oscillators when there are correlations. The rate and degree of synchronization depends on the properties of the noise as well as the amount of the correlation. Understanding of this process can be reduced to the analysis of several integrals and the solutions to some linear boundary-value problems.

5.3 Pairs of oscillators

In the remainder of this chapter, we review the effects of coupling between oscillators. We start with weak coupling with noise and use this to discuss how noise has mild effects on coupling. Then we turn to pulse coupling with stronger noise.

5.3.1 Weak coupling

As in the previous sections, we begin with Eqn (5.6) which is the general equation for the effects of perturbations on an oscillator. We now split the perturbations into two parts, those that come from extrinsic noise and those that arise from coupling to other oscillators. That is, we write $G(X(t), t) = K_j(X_j(t), X_k(t)) + R_j(X_j(t), t)$ where $X_j(t)$ are the state variables for oscillators $j = 1, 2$ and K_j is the coupling and R_j is the noisy perturbation. Each oscillator obeys exactly the same dynamics, Eqn (5.1), when $\epsilon = 0$. While we could do this more generally, it is simpler to split the perturbations into the coupling and noise parts. From the point of view of neural applications, this makes sense as well. Finally, we will assume the noise is white and that the amplitude of the noise is such that the variance of the noise and the strength of the coupling match. Thus, we take the coupling strength to be ϵ and the noise strength to be $\sqrt{\epsilon}\sigma$, where $\sigma = O(1)$, so that they match. We thus obtain

$$d\theta_j = [1 + \epsilon(\Delta(\theta_j)B_j(\theta_j, \theta_k) + \sigma^2\Delta'(\theta_j)/2)]dt + \sqrt{\epsilon}\Delta(\theta_j)dW_j. \quad (5.19)$$

The term B_j represents the voltage component of the coupling, which will generally be some type of synaptic interaction between neurons, either electrical or chemical. We will not go through all the different cases and how the time courses of synapses and their position as well as the shape of the PRC affect the way neurons interact. This, in itself, is a topic for an entire book or at least a lengthy chapter. Our main goal in this chapter is to see how noise affects the interactions and not what the interactions themselves do. Furthermore, in this section, all noise is uncorrelated. (However, the interactions between correlated

noise and coupling are fascinating and the subject of some current research.) We let $\theta_j = t + \psi_j$ be a change of variables and this leads to:

$$d\psi_j = \epsilon \Delta(t + \psi_j) [B_j(t + \psi_j, t + \psi_k) + \sigma^2 \Delta'(t + \psi_j)/2] dt + \sqrt{\epsilon} \Delta(t + \psi_j) dW_j.$$

We average this equation over t to obtain an effective coupling equation:

$$d\psi_j = \epsilon H_j(\psi_k - \psi_j) dt + \sqrt{\epsilon} \|\Delta\|_2 dW_j \quad (5.20)$$

where

$$H_j(\phi) := \frac{1}{T} \int_0^T \Delta(t) B_j(t, t + \phi) dt$$

and $\|\Delta\|_2$ is the L_2 -norm of the PRC. We take this to be 1 without loss of generality. We can now drop the ϵ as we can rescale time. Finally, we let $\phi = \psi_2 - \psi_1 = \theta_2 - \theta_1$ and have now reduced the initially $2n$ -dimensional noisy dynamical system to a single scalar stochastic differential equation:

$$d\phi = [H_2(-\phi) - H_1(\phi)] dt + \sigma dW \quad (5.21)$$

where dW is a white noise process. (We use the fact that the difference between two uncorrelated Gaussian processes is also Gaussian.) This Langevin equation is readily solved and the stationary density function for the phase difference, $\rho(\phi)$ satisfies:

$$K = -[H_2(-\phi) - H_1(\phi)]\rho(\phi) + \frac{\sigma^2}{2}\rho'(\phi)$$

where K is a constant chosen so the solutions are periodic and the density function ρ has a unit integral. At this point, it is convenient to rewrite the drift term. Suppose that the coupling between oscillators is identical (symmetric) and that the only difference between the two oscillators is in their natural frequencies (as in the previous section). We write

$$H_2(-\phi) - H_1(\phi) := -q(\phi) + \mu$$

where $q(\phi)$ is twice the odd part of the coupling function and μ is the difference in natural frequencies.

For simplicity, we assume that the period is 1. Without noise, the dynamics reduces to

$$\frac{d\phi}{dt} = -q(\phi) + \mu.$$

Since q is an odd periodic function, it always has zeros at $\phi = 0$ and at $\phi = 1/2$ corresponding to the synchronous and anti-phase solutions, respectively. Thus, when $\mu = 0$, there are at least two phase-locked fixed points, synchrony and

anti-phase. If $q'(0) > 0$ then synchrony is stable and if $q'(1/2) > 0$, the anti-phase solution is stable. For small values of μ , the fixed points persist and are near 0 or 1/2. However, any continuous periodic function is bounded, so that for sufficiently large values of μ , there will be no fixed point and thus no phase-locked solutions. The noise-free system no longer has a steady state. However, the phase difference does have an invariant density:

$$\rho(\phi) = \frac{N}{\mu - q(\phi)}$$

where N is a normalization constant. Note that this is only valid when $\mu - q(\phi)$ has no zeros; otherwise the oscillators will phase-lock and the density is a sum of Dirac delta functions.

If $q(\phi)$ is odd (as will be the case with symmetric coupling between identical oscillators) and there is no frequency difference, $\mu = 0$, then we can write down a closed form solution for the probability distribution in the presence of noise:

$$\rho(\phi) = N \exp \left[\frac{-2Q(\phi)}{\sigma^2} \right]$$

where $Q(\phi) = \int_0^\phi q(s) ds$. Since q is odd, Q is periodic. Here N is just a normalization constant. Stable roots of $q(\phi)$ (that is, where $q'(\phi) > 0$) correspond to local maxima in the density function and unstable roots correspond to local minima. With heterogeneity, the peak of the density function is shifted as would be expected from the noise-free case. That is, if oscillator 1 is faster than oscillator 2, then $\mu < 0$ and the noise-free phase-locked value of ϕ is negative, thus, the peak

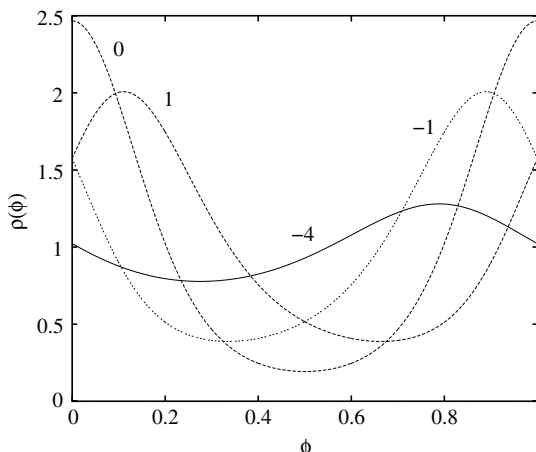


FIG. 5.9: Probability density function (PDF) for the phase difference between a pair of oscillators when $\sigma = 0.5$ and $q(\phi) = \sin(2\pi\phi)$ for different degrees of heterogeneity, μ .

of the density function in the presence of noise is shifted to the left. Figure 5.9 shows how heterogeneity both moves the peak and makes the distribution more uniform.

5.3.2 Correlations

Neuroscientists cannot generally measure phase differences between two coupled neurons. However, they can measure the correlations between spike trains of neurons. Pfeuty *et al.* (2003) showed that there is a relationship between the spike train cross-correlogram and the density function. Suppose that each time $\theta_j(t)$ crosses zero modulo the period, we say that a spike has occurred. We break continuous time into a discrete set of bins of width w and let $S_j(t)$ be $1/w$ if there is a spike in the bin corresponding to t and zero otherwise. The normalized cross-correlation is

$$C(t_2 - t_1) := \frac{\langle S_1(t_1)S_2(t_2) \rangle}{\langle S_1(t) \rangle \langle S_2(t) \rangle}.$$

Here $\langle S(t) \rangle$ is the average of $S(t)$. Pfeuty *et al.* (2003) show that as w gets small,

$$C(\tau) \approx \rho(\tau).$$

Thus, there is simple relationship between the cross-correlation (to lowest order) and the density function of the phase difference.

5.3.3 Pulse coupling

In the above parts of this section, we considered additive noise together with weak coupling of oscillators. However, in an earlier part of this chapter, we also showed that the phase resetting curve is subject to uncertainty in the form of phase-dependent noise. Thus, consider two neurons which are coupled via phase resetting curves, in the sense of Goel and Ermentrout (2002):

$$\theta'_j = \omega + \sum_n B(\theta_j, z_j) \delta(t - t_n^k).$$

Here t_n^k are the times that oscillator k fires (crosses 0 modulo its period). $B(\theta, z)$ is the phase resetting curve parametrized by a random variable, z taken from some distribution. Recall from Eqn (5.14) that the PRC can have phase-dependent variance, so this model might incorporate this variance. If we consider two identical mutually coupled cells, the phase, ϕ , of cell 2 at the moment cell 1 fires satisfies

$$\phi_{n+1} = G(G(\phi_n, z_n))$$

where $G(x, z) = 1 - x - B(x, z)$ (see, for example, Goel and Ermentrout (2002) and Ermentrout and Saunders (2006)). Here we have assumed a period of 1.

Let us write $B(x, z) = \epsilon\Delta(x) + zR(x)$ so that there is possibly phase-dependent noise, R and a deterministic coupling via the PRC, $\epsilon\Delta(x)$. As in Section 5.2.2, we can use the theory of stochastic maps to derive an equation for the invariant density:

$$P(x) = \int_{-\infty}^{\infty} \frac{Q([x + y + \epsilon\Delta(y)]/R(y))}{R(y)} P(y) dy, \quad (5.22)$$

where $Q(z)$ is the density of the variable z defined on the real line. We seek solutions to this equation when $P(x+1) = P(x)$. Notice that we can wrap the line up as a bi-infinite sum over the unit interval using the periodicity of $\Delta(x)$, but for the purposes of analysis, it is much easier to keep the integral over \mathbb{R} . If $R(x) = 1 + \epsilon r(x)$ and ϵ is small, it is possible to write a formula for the invariant density, $P(x)$, in a perturbation expansion in ϵ . For example, if $r(x) = 0$ and $\Delta(x) = b_1 \sin 2\pi x$, then

$$P(x) \approx 1 - \epsilon 2\pi b_1 \frac{q_1}{1 - q_1} \cos(2\pi x)$$

where $q_n = \int_{-\infty}^{\infty} Q(x) \cos 2\pi x dx$. The shape of $P(x)$ is not surprising. If $b_1 > 0$ then there is a peak at $x = 1/2$, corresponding to anti-phase oscillations, while for $b_1 < 0$, the peak is at synchrony. Suppose that the noise amplitude is now phase-dependent and suppose that the coupling tends to push the oscillators toward the anti-phase solution ($x = 1/2$). Let $R(x)$ be such that the variance is minimal near $x = 0, 1$ and maximal near $x = 1/2$. Then, for strong enough noise, one might expect that the anti-phase state might become unstable. That is, even though the deterministic dynamics push the oscillators toward anti-phase, the PRC is so noisy near that state that the oscillators cannot remain there. Figure 5.10 shows an example of this. We take $\Delta(x) = b \sin(2\pi x)$ and $R(x) = 1 + c \cos(2\pi x)$, with $b = 0.05$ so that the deterministic system has a stable anti-phase solution and $c = -0.4$ so that the PRC is noisiest at $x = 1/2$. For low values of noise, $\sigma = 0.1$, Monte Carlo simulations show a peak at $x = 1/2$ as predicted from the deterministic dynamics. However, for $\sigma = 0.35$, the histogram of phases shows peaks at 0, 1 corresponding to synchrony. Using the small ϵ approximation for the invariant density, we find that

$$P(x) = 1 - 2\pi\epsilon \frac{q_1}{1 - q_1} (b + \pi\sigma^2 c) \cos(2\pi x).$$

Whether the peak is at $1/2$ or $0, 1$ depends only on the sign of $b + \pi\sigma^2 c$. Thus, there will be a change in the peak if b, c have opposite signs and the noise is large enough. For our case, the critical value of σ is about 0.25. Figure 5.10(b) shows the stationary solutions to Eqn (5.22) as a function of σ for $\epsilon = 1$ via a colour code. The switch from a peak at $x = 1/2$ to $x = 0, 1$ is evident.

In conclusion, we have shown that for pulse coupling, noise can have a qualitative effect on the steady state phase distribution if there is phase-dependent

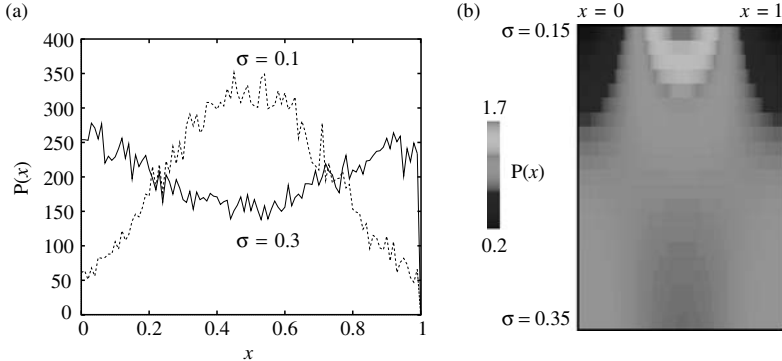


FIG. 5.10: Noise-induced bifurcation in a system with phase-dependent variance. $\Delta(x) = b \sin(2\pi x)$, $R(x) = (1 + c \cos(2\pi x))$ with $b = 0.05$, $c = -0.25$, $\epsilon = 1$ for different values of σ . (a) Monte Carlo simulation of phase equations with 20 000 spikes. (b) Steady state density as σ increases from 0.15 to 0.35. The peak in the middle disappears while a pair of peaks appear at synchrony.

variance in the PRC. For weak coupling, uncorrelated noise does not have more than a quantitative effect on the behaviour of coupled pairs of oscillators. As expected, the phase-differences between the oscillators stay close to the noise-free case in the sense that stable locked states correspond to peaks in the probability density. What is interesting is that the peaks remain in the presence of heterogeneities for cases in which the deterministic dynamics do not have phase-locked solutions, e.g. Fig. 5.9, $\mu = -4$. Interactions between correlated noise and coupling is the subject of some of our recent research and should prove to be interesting.

5.4 Networks of oscillators

We close this chapter with a sketch of the kinds of analysis that can be done with large systems of coupled oscillators in the presence of noise and possibly heterogeneities. Kuramoto (2003) and later Strogatz (2000), Crawford (1994), and more recently, Buice and Chow (2007) have studied the behaviour of globally coupled oscillators in the presence of heterogeneities and noise. Buice and Chow (2007) consider finite size effects, while the others are interested in the infinite size limit. As the latter case is considerably easier to understand and analyse, we only consider this. A very extensive review of the analysis of the Kuramoto model and its generalizations can be found in Acebrón *et al.* (2005). Here, we sketch the population density approach (Strogatz, 2000).

Consider the generalization of Eqn (5.20) after we have averaged and rescaled time:

$$d\psi_j = \left(\omega_j + \frac{1}{N} \sum_{k=1}^N H(\psi_k - \psi_j) \right) dt + \sigma dW_j(t) \quad (5.23)$$

where we assume that all oscillators are symmetrically coupled to each other and that they all have independent noise. As it will be notationally easier, we assume that the period of H is 2π . Kuramoto studies the case in which $\sigma = 0$ and $H(\phi) = \sin \phi$ as well as the case of no heterogeneity but non-zero noise. The review paper by Acebrón *et al.* (2005) references dozens of papers on the analysis of the Kuramoto model and its descendants. As $N \rightarrow \infty$, the ansatz of the population density method is that there is a function, $P(\theta, \omega, t)$, describing the probability of finding the oscillator with natural frequency, ω , at phase θ at time t . A nice history of this method and its development are found in Strogatz (2003, 2000). The sum in Eqn (5.23) is an average over the other phases and as $N \rightarrow \infty$ can be written in terms of the density function P as

$$\lim_{N \rightarrow \infty} \frac{1}{N} \sum_{k=1}^N H(\phi_k - \phi_j) = \int_{-\infty}^{\infty} \int_0^{2\pi} g(\omega) H(\phi - \phi_j) P(\phi, \omega, t) d\phi d\omega := J(\phi_j, t) \quad (5.24)$$

where $g(\omega)$ is the distribution of the frequencies, ω_j . With this calculation, the density satisfies:

$$\frac{\partial P}{\partial t} = -\frac{\partial}{\partial \theta} [J(\theta, t) P(\theta, \omega, t)] + D \frac{\partial^2 P}{\partial \theta^2}, \quad (5.25)$$

where $D = \sigma^2/2$. This equation is a nonlinear, integro-partial differential equation. Unlike the Fokker–Planck equations we previously encountered, the flux, J , is a function of the probability which involves a convolution (so it is non-local). As with most nonlinear equations, there are very few methods for solving them. Here, we will perform a linear stability analysis to get a handle on the types of patterns which are possible. We will not perform a complete bifurcation analysis for the general case, but provide the normal forms for the case with just noise and no heterogeneities. As noise is the main topic of this book and this chapter, we treat D as a parameter. In the original Kuramoto analysis, there is no noise and the bifurcation parameter is the amplitude of the coupling. Another possible parameter is the ‘spread’ of the natural frequencies, ω_j (the variance of the distribution, $g(\omega)$ where defined). Normalization requires that

$$\int_{-\infty}^{\infty} \int_0^{2\pi} g(\omega) P(\phi, \omega, t) d\phi d\omega = 1.$$

A trivial solution to Eqn (5.25) is $P(\theta, \omega, t) = 1/(2\pi)$. Our strategy is to linearize around this trivial fixed point. This state corresponds to the completely asynchronous state with the oscillators effectively uncoupled and a uniform probability of finding them in any state. (As a contrast, suppose that there is no heterogeneity and no noise. The perfectly synchronous state is $P(\theta, \omega, t) = \delta(\theta - \Omega t)$ where Ω is the ‘ensemble’ frequency, $\Omega = \omega_0 + H(0)$ with ω_0 the uncoupled frequency of each oscillator.)

We write $P = 1/(2\pi) + r(\theta, \omega, t)$ and write the linear terms for r :

$$\frac{\partial r}{\partial t} = D \frac{\partial^2 r}{\partial \theta^2} - \frac{\partial}{\partial \theta} (\omega + H_0) + \frac{1}{2\pi} \int_{-\infty}^{\infty} \int_0^{2\pi} g(\omega) H'(\phi - \theta) r(\phi, \omega, t) d\phi d\omega,$$

where H_0 is the average value of H . This is a linear problem which is homogeneous in θ, t but not in ω . The former homogeneity implies that $r(\theta, \omega, t) = \exp(\lambda t + in\theta) f_n(\omega)$ where f_n is an unknown function of ω and n is an integer. If $\text{Re}(\lambda) < 0$ for all n then the asynchronous state is asymptotically stable. We substitute this function into the linearization and find:

$$\lambda f_n(\omega) = -Dn^2 f_n - i(\omega + H_0) n f_n + h_n \bar{f}_n \quad (5.26)$$

where

$$\bar{f}_n = \int_{-\infty}^{\infty} g(\omega) f_n(\omega) d\omega$$

and

$$h_n = \frac{1}{2\pi} \int_0^{2\pi} H'(\phi) \exp(in\phi) d\phi.$$

Note that h_n is the n th Fourier coefficient of the derivative of the H function. We can solve Eqn (5.26) for $f_n(\omega)$:

$$f_n(\omega) = \frac{h_n \bar{f}_n}{\lambda + Dn^2 + in(H_0 + \omega)}.$$

We substitute this into the definition of \bar{f}_n to obtain:

$$\bar{f}_n = \bar{f}_n \int_{-\infty}^{\infty} \frac{g(\omega) h_n}{\lambda + Dn^2 + in(H_0 + \omega)} d\omega.$$

This equation has a non-trivial solution for \bar{f}_n if and only if

$$1 = \int_{-\infty}^{\infty} \frac{g(\omega) h_n}{\lambda + Dn^2 + in(H_0 + \omega)} d\omega := \Gamma(\lambda). \quad (5.27)$$

Equation (5.27) is the eigenvalue equation that must be solved and the values of λ determine stability. The simplest scenario and the only one which we solve here is when all oscillators are identical and $g(\omega)$ is a Dirac delta function at ω_0 . In this case, the integral is easy to evaluate and we find after trivial algebra:

$$\lambda = h_n - Dn^2 - i(\omega_0 + H_0)n. \quad (5.28)$$

There is always a zero eigenvalue ($n = 0$) corresponding to translational invariance of the phases. For $n \neq 0$, since h_n are bounded, for sufficient noise, $D, \text{Re}(\lambda)$

is negative and the asynchronous state is asymptotically stable. (When there is heterogeneity and no noise, the spectral equation is extremely subtle and the analysis complex. As there is always noise in neural systems, we make life easy by assuming $D > 0$.) Suppose that we write

$$H(\phi) = H_0 + \sum_{n=1}^{\infty} [a_n \cos(n\phi) + b_n \sin(n\phi)].$$

Then

$$h_n = -ina_n/2 + nb_n/2.$$

Thus the real part of λ is

$$\text{Re}(\lambda) = -Dn^2 + nb_n/2.$$

The only terms in H which can destabilize the asynchronous state are those for which the Fourier sine coefficients are positive. The critical value of noise is thus

$$D^* = \max_{n>0} \frac{b_n}{2n}.$$

Figure 5.11 shows an example of the application of this analysis to a simulation of 400 globally coupled oscillators. Here $H(\phi) = 0.25 \cos(\phi) - 0.5 \sin(\phi) + \sin(2\phi)$. The critical value of D predicted is $1/4$, corresponding to $\sigma = 1/\sqrt{2}$. We let the simulation run to steady state with $\sigma = 0.8$ (above criticality) and then changed σ to 0.6 which is below the critical value. Figure 5.11(a) shows a space-time plot of the 400 oscillators as a function of time. Their phases relative to oscillator 1 are plotted in a colour code over a time window including the decrease of the noise amplitude. The colour coding shows that after the noise is reduced, oscillators are divided into roughly two clusters (pink and blue) corresponding to 0 and π phase differences. This is a two-cluster state. We introduce so-called ‘order parameters’, which quantify the degree of synchrony between the oscillators:

$$\text{OP}_n := \frac{1}{N} \sqrt{\left(\sum_{j=1}^N \cos(n\theta_j) \right)^2 + \left(\sum_{j=1}^N \sin(n\theta_j) \right)^2}.$$

These pick out the Fourier coefficients of the invariant density, $P(\theta, \omega, t)$, and vanish when the oscillators are asynchronous. If $D < b_n/n$, we expect OP_n to grow. Figure 5.11(b) shows the abrupt change in OP_2 as predicted from the infinite N theory. Figure 5.11(c) shows histograms at the high and low noise levels for one time slice of the 400 oscillators. There are two clear peaks in the low-noise case as predicted from the linear analysis.

A natural, next approach to the equation is to do a full nonlinear bifurcation analysis. This was done in Chapter 5 of Kuramoto (2003). The first step is to subtract off the constant frequency and the constant Fourier term of H . Thus,

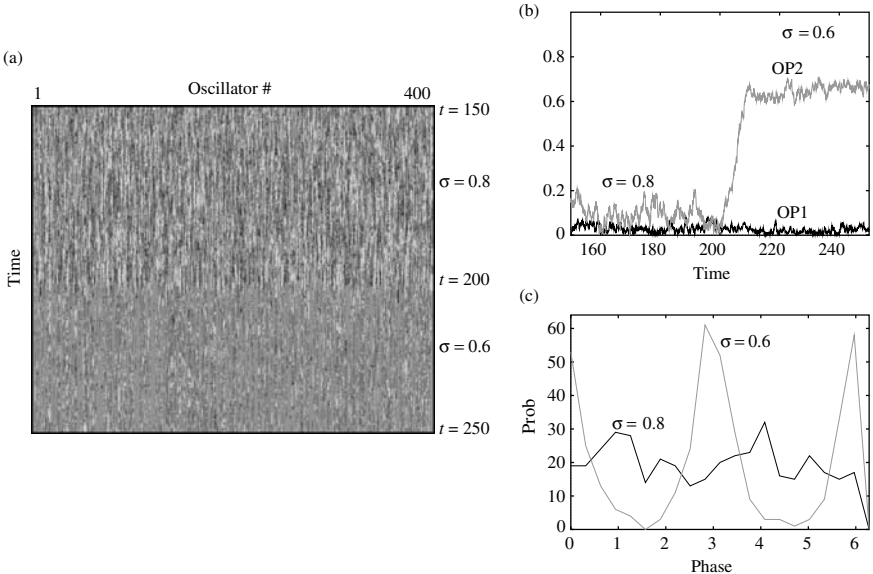


FIG. 5.11: Example of the destabilization of the asynchronous state as the noise is reduced leading to a two-cluster solution. ($H(\phi) = 0.25 \cos(\phi) - 0.5 \sin(\phi) + \sin(2\phi)$, $\sigma^* = 1/\sqrt{2} \approx 0.707$). (a) Space-time plot of the phases relative to oscillator 1. At $t = 200$, the noise is abruptly reduced from $\sigma = 0.8$ to $\sigma = 0.6$. The emergence of a two-cluster state (turquoise/red) is apparent. (b) Order parameters $OP_{1,2}$ showing the two-cluster instability. (c) Histogram of the relative phases during two different points in the simulation corresponding to the two different levels of noise. See Plate 1.

we reduce (5.25) to the following nonlinear equation:

$$\frac{\partial P}{\partial t} = -\frac{\partial}{\partial \theta} \int_0^{2\pi} H(\phi - \theta) P(\theta, t) P(\phi, t) d\phi + D \frac{\partial^2 P}{\partial \theta^2}.$$

Letting m denote the critical wavenumber, the normal form for the bifurcation has the form:

$$\frac{dz}{dt} = z[m^2(D^* - D) + \gamma_2 z \bar{z}]$$

where

$$\gamma_2 = -\frac{m\pi^2}{2} \left(\frac{b_m^2 + a_m^2 + a_m a_{2m} - b_m b_{2m} + i(a_{2m} b_m + a_m b_{2m})}{2b_m - b_{2m} + i(a_{2m} - a_m)} \right)$$

and

$$H(\phi) = \sum_n a_n \cos(n\phi) + b_m \sin(n\phi).$$

The bifurcation is supercritical if the real part of γ_2 is negative. Note that if H contains only odd periodic terms then

$$\gamma_2 = -\frac{mb_m\pi^2}{2} \frac{b_m - b_{2m}}{2b_m - b_{2m}}.$$

Note that the denominator is always positive since $b_m/m > b_{2m}/(2m)$ by hypothesis. For the case illustrated in Fig. 5.11, the bifurcation is supercritical.

In conclusion, we have used the methods of Kuramoto to analyse the effects of noise and coupling on a large population of coupled neurons and shown that only the odd Fourier components of the interaction function contribute to synchronization.

5.5 Summary

Noise interacts with oscillators in complex ways. Correlated noise can act to synchronize uncoupled oscillators. Using perturbation theory and the method of phase reduction, it is possible to reduce the analysis of these high-dimensional systems to simple phase models. Coupled oscillators can be similarly reduced and the effects of noise on them analysed. Methods include using population density equations, Fokker–Planck equations, and the analysis of linear integral operators. There are many unanswered questions, such as what happens with larger noise and how interactions between internal dynamics and correlated inputs change the ability to synchronize.

References

- Acebrón, J.A., Bonilla, LL, Pérez Vicente, C.J., Ritort, F., and Spigler, R. (2005). The Kuramoto model: A simple paradigm for synchronization phenomena. *Reviews of Modern Physics*, **77**(1), 137–185.
- Brette, R. (2004). Dynamics of one-dimensional spiking neuron models. *Journal of Mathematical Biology*, **48**(1), 38–56.
- Brette, R. and Guigon, E. (2003). Reliability of spike timing is a general property of spiking model neurons. *Neural Computation*, **15**(2), 279–308.
- Brown, E., Moehlis, J., and Holmes, P. (2004). On the phase reduction and response dynamics of neural oscillator populations. *Neural Computation*, **16**, 673–715.
- Bryant, H.L., and Segundo, J.P. (1976). Spike initiation by transmembrane current: a white-noise analysis. *The Journal of Physiology*, **260**(2), 279–314.
- Buice, M.A. and Chow, C.C. (2007). Correlations, fluctuations, and stability of a finite-size network of coupled oscillators. *Physical Review E*, **76**(3), 031118.
- Crawford, J.D. (1994). Amplitude expansions for instabilities in populations of globally-coupled oscillators. *Journal of Statistical Physics*, **74**(5), 1047–1084.
- Engen, S. and Saether, B.E. (2005). Generalizations of the Moran effect explaining spatial synchrony in population fluctuations. *American Naturalist*, **166**(5), 603–612.

- Ermentrout, B. (1996). Type I membranes, phase resetting curves, and synchrony. *Neural Computation*, **8**(5), 979–1001.
- Ermentrout, B. and Saunders, D. (2006). Phase resetting and coupling of noisy neural oscillators. *Journal of Computational Neuroscience*, **20**(2), 179–190.
- Galán, R.F., Ermentrout, G.B., and Urban, N.N. (2005). Efficient estimation of phase-resetting curves in real neurons and its significance for neural-network modeling. *Physical Review Letters*, **94**(15), 158101.
- Galán, R.F., Ermentrout, G.B., and Urban, N.N. (2007). Stochastic dynamics of uncoupled neural oscillators: Fokker-Planck studies with the finite element method. *Physical Review E*, **76**(5), 056110.
- Galán, R.F., Ermentrout, G.B., and Urban, N.N. (2008). Optimal time scale for spike-time reliability: Theory, simulations, and experiments. *Journal of Neurophysiology*, **99**(1), 277.
- Galan, R.F., Fourcaud-Trocme, N., Ermentrout, G.B., and Urban, N.N. (2006). Correlation-induced synchronization of oscillations in olfactory bulb neurons. *Journal of Neuroscience*, **26**(14), 3646.
- Goel, P. and Ermentrout, B. (2002). Synchrony, stability, and firing patterns in pulse-coupled oscillators. *Physica D: Nonlinear Phenomena*, **163**(3-4), 191–216.
- Goldobin, D.S. and Pikovsky, A. (2005). Synchronization and desynchronization of self-sustained oscillators by common noise. *Physical Review E*, **71**(4), 45201.
- Guckenheimer, J. (1975). Isochrons and phaseless sets. *Journal of Mathematical Biology*, **1**(3), 259–273.
- Gutkin, B.S., Ermentrout, G.B., and Reyes, A.D. (2005). Phase-response curves give the responses of neurons to transient inputs. *Journal of Neurophysiology*, **94**(2), 1623–1635.
- Hansel, D., Mato, G., and Meunier, C. (1995). Synchrony in excitatory neural networks. *Neural Computation*, **7**(2), 307–337.
- Izhikevich, E. (2007). *Dynamical Systems in Neuroscience*. MIT Press, Cambridge, MA.
- Jensen, R.V. (2002). Synchronization of driven nonlinear oscillators. *American Journal of Physics*, **70**, 607.
- Kuramoto, Y. (2003). *Chemical Oscillations, Waves, and Turbulence*. Courier Dover Publications, New York.
- Lasota, A. and Mackey, M.C. (1994). *Chaos, Fractals, and Noise: Stochastic Aspects of Dynamics*. Springer, Berlin.
- Lindner, B., Longtin, A., and Bulsara, A. (2003). Analytic expressions for rate and CV of a type I neuron driven by white gaussian noise. *Neural Computation*, **15**(8), 1761–1788.
- Mainen, Z. and Sejnowski, T. (1995). Reliability of spike timing in neocortical neurons. *Science*, **268**, 1503–1506.
- Marella, S. and Ermentrout, G.B. (2008). Class-II neurons display a higher degree of stochastic synchronization than class-I neurons. *Physical Review E*, **77**(4), 041918.

- Nakao, H., Arai, K., and Kawamura, Y. (2007). Noise-induced synchronization and clustering in ensembles of uncoupled limit-cycle oscillators. *Physical Review Letters*, **98**(18), 184101.
- Netoff, T.I., Banks, M.I., Dorval, A.D., Acker, C.D., Haas, J.S., Kopell, N., and White, J.A. (2005). Synchronization in hybrid neuronal networks of the hippocampal formation. *Journal of Neurophysiology*, **93**(3), 1197–1208.
- Pfeuty, B., Mato, G., Golomb, D., and Hansel, D. (2003). Electrical synapses and synchrony: The role of intrinsic currents. *Journal of Neuroscience*, **23**(15), 6280.
- Pikovsky, A.S. (1984). Synchronization and stochasticization of the ensemble of autogenerators by external noise. *Radiophys. Quantum Electron.*, **27**(5), 576–581.
- Pikovsky, A., Rosenblum, M., and Kurths, J. (2001). *Synchronization: A Universal Concept in Nonlinear Sciences*. Cambridge University Press, Cambridge.
- Reyes, A.D., and Fetz, E.E. (1993). Effects of transient depolarizing potentials on the firing rate of cat neocortical neurons. *Journal of Neurophysiology*, **69**(5), 1673–1683.
- Risken, H. (1996). *The Fokker-Planck equation: Methods of Solutions and Applications*. Springer-Verlag, New York.
- Ritt, J. (2003). Evaluation of entrainment of a nonlinear neural oscillator to white noise. *Physical Review E*, **68**(4), 041915.
- Stratonovich, R.L. (1958). Oscillator synchronization in the presence of noise. *Radiotekhnika i Elektronika*, **3**(4), 497.
- Stratonovich, R.L. (1967). *Topics in the Theory of Random Noise*. Routledge, New York.
- Strogatz, S.H. (2000). From Kuramoto to Crawford: exploring the onset of synchronization in populations of coupled oscillators. *Physica D: Nonlinear Phenomena*, **143**(1-4), 1–20.
- Strogatz, S. (2003). *Sync: The Emerging Science of Spontaneous Order*. Hyperion.
- Tateno, T. and Robinson, H.P.C. (2007). Phase resetting curves and oscillatory stability in interneurons of rat somatosensory cortex. *Biophysical Journal*, **92**(2), 683.
- Teramae, J. and Tanaka, D. (2004). Robustness of the noise-induced phase synchronization in a general class of limit cycle oscillators. *Physical Review Letters*, **93**(20), 204103.
- Troyer, T.W. (2006). Factors affecting phase synchronization in integrate-and-fire oscillators. *Journal of Computational Neuroscience*, **20**(2), 191–200.
- Winfree, A.T. (2001). *The Geometry of Biological Time*. Springer, New York.
- Zhou, T., Chen, L., and Aihara, K. (2005). Molecular communication through stochastic synchronization induced by extracellular fluctuations. *Physical Review Letters*, **95**(17), 178103.

THE ROLE OF VARIABILITY IN POPULATIONS OF SPIKING NEURONS

Brent Doiron

6.1 Introduction

The brain is often compared to a supercomputer, capable of performing complex computations in a very small amount of time. While it is true that the brain performs impressive calculations, many neurophysiologists would likely disagree with the analogy between brains and standard computers. If a user performs the same task twice on a computer, the current passing through the computer's resistors and semiconductors is almost the same during each trial of the task. The low variability of the electronic components is needed so that the computer's binary representation of the task is identical during both trials. If even one bit is switched during the second trial, the outcome of that trial could be very different from the first, and the computer rendered effectively useless to the user. In contrast, neural recordings from many brain areas have significant trial-to-trial variability during both sensory processing and motor tasks. The paradoxical contrast between the lack of response precision in neural systems at the cellular level, and the sophistication of brain-driven behaviour, is a critical challenge for contemporary neuroscience.

This chapter focuses on the potential impact of trial-to-trial variability in neural coding. We first present experimental evidence for trial-to-trial variability in single cells, and extend this to populations of uncorrelated neurons. We review experimental and theoretical results which show how membrane fluctuations not correlated with a signal can nevertheless manipulate the coding of the signal, or whose time-dependent statistics can themselves carry the signal. We next consider neural variability that is correlated across neurons in a population. A simple paradigm for correlated network activity is presented, and we show that the output correlation of spike train pairs is related to the output firing rate, thereby linking rate based and correlation based coding.

Incorporating variability and co-variability of populations of cells within a plausible framework of brain function is an important step in any theory of neural computation. Accomplishing this would not only answer many open questions in systems neuroscience, but would also uncover potential new forms of computing where component unreliability is an important feature rather than an unwanted nuisance.

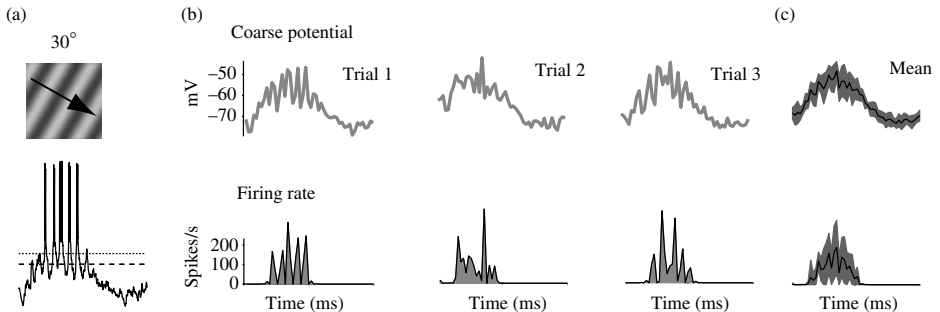


FIG. 6.1: Single neuron variability. (a) A drifting grating stimulus was presented to an anesthetized cat (top). The orientation of the stimulus was chosen to maximize the membrane response of a recorded cell (bottom). The response to one cycle of the grating is shown. (b) Coarse (subthreshold) membrane response (top), and instantaneous firing rate (bottom) computed from the spike response for three separate trials. (c) The trial average for the coarse potential (top) and instantaneous firing rate (bottom) with the shaded area marking two standard deviations. Data and figure generously provided by Matteo Carandini; see Carandini (2004) for details.

6.2 Experimental evidence for single neuron variability

Cortical neurons have a spike response that is tuned for specific features of sensory inputs. As an example, the firing rates of some pyramidal neurons in the visual cortex are sensitive to the orientation of a drifting grating presented to the retina (Hubel and Wiesel, 1959); see Fig. 6.1(a). When the grating orientation is optimal, the neuron will respond with a high-frequency spike discharge. Sub-optimal orientations decrease the firing rate, with orthogonal to optimal orientations often eliciting no response. A typical experiment involves presenting the exact same stimulus grating multiple times, with careful attention paid so that external influences are fixed across all experimental trials. The responses are then averaged across trials and the mean membrane trajectory and spike rate are reported.

Nevertheless, it is well known that neural responses are quite variable across trials (Heggelund and Albus, 1978), meaning that single neuron response within any given trial may differ significantly from the trial averaged response. To illustrate this important observation we review some recent data from Carandini (2004). Figure 6.1 shows intracellular recordings from cortical neurons in the primary visual cortex obtained during presentation of a drifting grating stimulus at the optimal orientation (Fig. 6.1b,c top). The mean neural response is a quasi-sinusoidal membrane trajectory (solid curve in Fig. 6.1c top), and a mean firing rate¹ that resembles a rectified copy of the mean membrane dynamic

¹Firing rate is to be interpreted as $N(t)/\delta t$ where $N(t)$ is the number of spikes in a time window of length δt centred at t .

(solid curve in Fig. 6.1c bottom). However, significant trial-to-trial membrane variability is very apparent (shaded region in Fig. 6.1c), and for comparison purposes we show three trials (Fig. 6.1b). As Carandini (2004) remarks, the trial-to-trial variability of the firing rate is, in a relative sense, much larger than the membrane variability (compare the relative standard deviation in Fig. 6.1c top and bottom). The source of the membrane variability is likely to be a combination of random synaptic bombardment and intrinsic channel variability, with synaptic inputs being the dominant culprit. However, spike train mechanisms exhibit very low variability (Bryant and Segundo, 1976, Mainen and Sejnowski, 1995), raising questions as to the source of the ‘excess’ variability of the spike response. To account for this discrepancy, Carandini (2004) used both detailed and phenomenological neural models to establish that threshold systems (of which neurons are a classic example) act to amplify input fluctuations. This indicates that in interconnected cortical networks, where the output of one cell is the input to another cell, any variability is propagated and amplified.

The above example is just one of many studies characterizing the trial-to-trial variability in single cell recordings (Britten *et al.*, 1993, Softky and Koch, 1993, Shadlen and Newsome, 1998). Neural computations (perception, decisions, etc.) are of course performed on a trial-by-trial basis, and are thought to require significant temporal precision. Furthermore, neurons have the cellular capacity to be both reliable and precise in their response. Nonetheless, the analysis of significant amounts of data has shown that, for some reason, a premium is not placed on single neuron reliability in cortical coding.

6.3 Population of uncorrelated stochastic neurons

6.3.1 Presynaptic spike trains and the diffusion limit

In this section we present the basic mathematical framework used throughout the chapter. The synaptic input afferent to a neuron, $I(t)$, is a linear superposition of excitatory (E) and inhibitory (I) events. Consider a large pool of presynaptic cells whose summed activity produces the post-synaptic input:

$$I(t) = a_E P_E(t) + a_I P_I(t). \quad (6.1)$$

Let $P_\alpha(t) = \sum_k \delta(t - t_k)$ with t_k being random synaptic activation times created from a Poisson generator (possibly inhomogeneous) of intensity $N_\alpha \nu_\alpha(t)$, and each synaptic event is of size a_α ($\alpha = E, I$). N_α is the number of cells in presynaptic pool α and $\nu_\alpha(t)$ is the firing rate of each cell in that pool. Letting $N_\alpha \rightarrow \infty$, and choosing $a_\alpha \rightarrow 0$ in this limit, yields a reasonable approximation (the so-called diffusion approximation) of $I(t)$ as a continuous time stochastic process:

$$I(t) = \mu(t) + \sigma(t)\xi(t). \quad (6.2)$$

The noise term $\xi(t)$ has statistics² $\langle \xi \rangle_t = 0$ and $\langle \xi(t)\xi(t') \rangle_t = \delta(t - t')$, with time-dependent coefficients $\mu(t)$ and $\sigma(t)$ related to the synaptic inputs via:

$$\begin{aligned}\mu(t) &= N_E a_E \nu_E(t) + N_I a_I \nu_I(t), \\ \sigma^2(t) &= N_E a_E^2 \nu_E(t) + N_I a_I^2 \nu_I(t).\end{aligned}\quad (6.3)$$

The interested reader is referred to the books by Tuckwell (1988) and Ricciardi (1977) for a reduction of point process synaptic inputs to a continuous time stochastic process. Sensory inputs cause modulations of the presynaptic population firing rates $\nu_E(t)$ and $\nu_I(t)$, and are conserved across ‘experiment’ trials, carrying information about the stimulus. The trial-to-trial variability is modelled by the noise term $\xi(t)$, where the exact realization of $\xi(t)$ is *not* conserved across trials, representing input fluctuations not correlated with the stimulus.

6.3.2 Spiking dynamics and spike train statistics

A simple caricature of neural spiking dynamics is given by a leaky integrate-and-fire (LIF) neuron model (Tuckwell, 1988, Lapicque, 2007). Consider N LIF neuron models where the membrane potential V_i of the i th cell obeys:

$$C \frac{dV_i}{dt} = -gV_i + I_i(t). \quad (6.4)$$

C and g are the membrane capacitance and conductance respectively, and $\tau_m = C/g$ is the membrane time constant. Equation (6.4) is supplemented with a discontinuous spike-reset rule whereby $V(t^-) = V_T$ implies that $V(t^+) = V_R$; V_T and V_R denote the spike threshold and spike reset, respectively. $I_i(t)$ is given in Eqn (6.2), and is to be interpreted as a current (though see Section 6.4). The temporal expectation of the current variability is given by $\langle \xi_i(t)\xi_j(t') \rangle_t = \delta_{ij}\delta(t - t')$, where δ_{ij} is 1 if $i = j$ and 0 otherwise. The $\delta(t - t')$ term means ξ_i is uncorrelated with itself from one instant to the next, while the δ_{ij} condition makes the within-trial fluctuations experienced by any two cells in the network uncorrelated from one another. We relax this second condition in Section 6.6.2 and consider correlation in the input currents across i and j .

The spike train output from the LIF models is of primary interest, with t_{ik} denoting the k th time that V_i crosses V_T . The spike train from neuron i is then $y_i(t) = \sum_k \delta(t - t_{ik})$, with the spike count from neuron i over a time window $(t, t + T)$ being simply:

$$n_i(t, t + T) = \int_t^{t+T} y_i(t) dt. \quad (6.5)$$

²Throughout the chapter $\langle \cdot \rangle_t$ denotes expectation computed over time, while $\langle \cdot \rangle_i$ denotes expectation computed over the ensemble.

For $\sigma > 0$ it is simple to see that $n_i(t, t + T)$ is a random variable indexed by both t and i . The temporal average of the spike train, called the firing rate, from neuron i is:

$$\begin{aligned}\nu_i &= \langle n_i \rangle_t \\ &= \lim_{T \rightarrow \infty} \frac{n_i(t, t + T)}{T}.\end{aligned}\quad (6.6)$$

For stationary spike trains (i.e time independent μ and σ), the responses ν_i can also be computed directly from the spike train $\{t_k\}$ as:

$$\nu_i = \frac{1}{\langle t_{i(k+1)} - t_{ik} \rangle_k}, \quad (6.7)$$

or in other words ν_i is the reciprocal of the mean waiting time between spikes from neuron i .

Rather than define spike train statistics from temporal averages it is useful to compute averages across the population of N statistically identical cells. The instantaneous firing probability of a representative cell in the population is:

$$p(t) = \lim_{T \rightarrow 0} \lim_{N \rightarrow \infty} \frac{n_p(t, t + T)}{N}, \quad (6.8)$$

where the number of spikes produced by the population over the time window $(t, t + T)$ is:

$$n_p(t, t + T) = \sum_i n_i(t, t + T). \quad (6.9)$$

It is typical to discuss the time-dependent firing rate $\nu(t)$, rather than firing probability

$$\begin{aligned}\nu(t) &= \lim_{N \rightarrow \infty} \frac{1}{N} \sum_i y_i(t) \\ &= \langle y_i(t) \rangle_i.\end{aligned}\quad (6.10)$$

If the fluctuations given to all cells in the network are uncorrelated, $\nu(t)$ converges to a fixed number with probability 1 (law of large numbers). Further, for statistically stationary currents and statistically identical inputs across the population the well-known relation exists (Knight, 1972a):

$$\lim_{t \rightarrow \infty} \nu(t) = \nu_i, \quad (6.11)$$

where the time limit is needed to erase any memory of initial conditions across the population. This is an ergodicity relationship for ensembles of spiking neurons, and is valid for any i . Combining Eqns (6.5), (6.8), and (6.10) shows that $\nu(t)$ is

a probability density, i.e. when integrated against time a probability is obtained. Experimentalists often construct $\nu(t)$ from a trial averaged spike train recorded from a single neuron, while here we have defined the average to be over an ensemble of neurons during one trial. For an unconnected network, and $\xi_i(t)$ and $\xi_j(t)$ uncorrelated ($i \neq j$), these approaches are equivalent.

Finally, the spike response variability across the population is most easily quantified by the Fano factor:

$$\text{FF}(t) = \frac{\langle n^2(t, t+T) \rangle_i - \langle n(t, t+T) \rangle_i^2}{\langle n(t, t+T) \rangle_i}. \quad (6.12)$$

A Poisson process has $\text{FF} = 1$ for all T . In a way analogous to Eqns (6.7) and (6.10), given a stationary renewal spike train, the ensemble average FF is related to a temporal average over one cell via $\lim_{T \rightarrow \infty} \text{FF} = \text{CV}^2$ with CV the coefficient of variability of the inter-spike interval density (Cox and Lewis, 1966).

6.4 Noise induced gain control

6.4.1 *Divisive gain control*

The simplest, and perhaps best studied, framework for neural coding is the transfer between the time averaged firing rate of an excitatory presynaptic population ν_E and the time averaged firing rate of the post-synaptic spike response ν ; here we take ν_E and ν as time independent and use the relation (6.11) to interchange between ensemble and time averaging. In most neurons ν is a monotonically increasing function of ν_E , with vanishingly small firing rates at low ν_E , and large saturating rates at high ν_E . Many theories of neural computation involve a modulation of the input–output transfer of a single neuron or group of neurons. In most cases this amounts to controlling the transfer gain $d\nu/d\nu_E$. A multiplicative shift of $d\nu/d\nu_E$ over a large range of ν_E is a critical component in contemporary theories of attention (McAdams and Maunsell, 1999), receptive field construction (Heeger, 1992), as well as visually guided reaching (Pouget and Sejnowski, 1997); for a review see Salinas and Thier (2000). However, the biophysical mechanisms that multiplicatively (or divisively) modulate $d\nu/d\nu_E$ have been elusive (Holt and Koch, 1997).

Chance *et al.* (2002) and Doiron *et al.* (2001) independently studied the role of conductance based fluctuations on $d\nu/d\nu_E$. To elaborate, we first write $I(t)$ resulting from conductance based synapses which multiply an associated battery term:

$$I(t) = a_I(V_I - V)P_{Ib}(t) + a_E(V_E - V)[P_{Eb}(t) + P_E(t)]. \quad (6.13)$$

V_E and V_I are the respective reversal potentials of excitatory and inhibitory channels ($V_I < V_T < V_E$), and a_E and a_I are conductance increases associated with a single synaptic pulse. This is a more realistic model for synaptic input than the current based approach presented in Eqn (6.1). We assume that relevant stimulus information is contained in the overall firing rate $N_E\nu_E$ of the excitatory

drive $P_E(t)$. In addition to this stimulus input, *balanced* inhibitory (Ib) and excitatory (Eb) components are used, where the term ‘balanced’ implies the mean total current is

$$\langle a_I(V_I - V)P_{Ib}(t) + a_E(V_E - V)P_{Eb}(t) \rangle_t \approx 0 \quad (6.14)$$

over the subthreshold range $V_I \leq V \leq V_T$. In general this can be achieved over a large range of Poisson intensities ν_{Ib} and ν_{Eb} . Even though balanced excitation and inhibition oppose one another so that the mean input is zero, the fluctuations contributed by $P_{Eb}(t)$ and $P_{Ib}(t)$ combine and produce significant input variability that is independent of the stimulus ν_E .

In a series of controlled *in vitro* experiments Chance *et al.* (2002) demonstrated that ν_{Eb} and ν_{Ib} have significant influence on the gain $d\nu/d\nu_E$. With a simulated conductance paradigm (commonly termed ‘dynamic clamp’; see Section 9.4 in this volume) they fixed ν_{Eb} and ν_{Ib} , and then varied ν_E whilst recording the output rate ν . For a given experiment they set $\nu_{Eb} = X\bar{\nu}_{Eb}$ and $\nu_{Ib} = X\bar{\nu}_{Ib}$ where X is a multiplication factor that models an overall increase ($X > 1$) in balanced background activity from a baseline state $\bar{\nu}_{Eb}$ and $\bar{\nu}_{Ib}$ ($X = 1$). Figure 6.2(a) shows that increases in X cause a divisive scaling of $d\nu/d\nu_E$ for a surprisingly large range of output rates ν . This result demonstrates that stimulus independent conductance fluctuations can modulate the transfer of static stimuli ν_E , hence influencing neural processing.

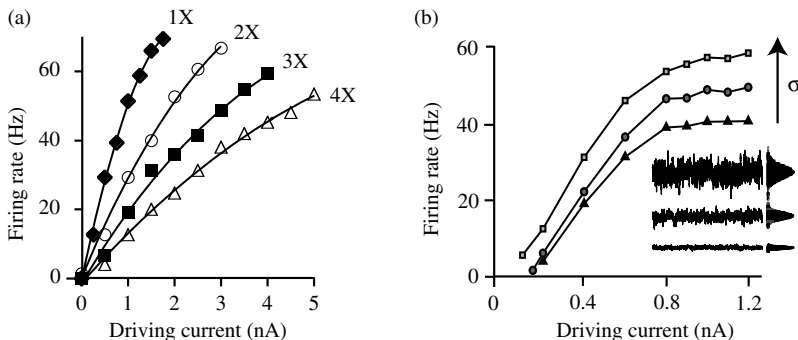


FIG. 6.2: Noise-induced gain control. (a) *In vitro* simulated conductance experiments in somatosensory cortex. Output firing rate ν plotted against the mean input current μ from the unbalanced excitatory drive. Each curve corresponds to balanced synaptic background activity of rate X times a base value. See Chance *et al.* (2002) for experimental details. (b) *In vitro* experiments from layer 5 of prefrontal cortex with input $I(t) = \mu + \sigma\xi(t)$. Each curve was created with a fixed value of σ (see inset). See Arsiero *et al.* (2007) for experimental details. We thank Frances Chance and Michele Giugliano for donation of their figures.

For an explanation of the effect using the LIF neuron model we follow the treatment presented in Burkitt *et al.* (2003), see also Chapter 9, Section 9.3 in this book. With $a_\alpha \propto 1/N_\alpha$ and in the limit $N_\alpha \rightarrow \infty$ ($\alpha = \text{Eb}; \text{Ib}; \text{E}$) a standard mean first-passage time calculation can be performed (Tuckwell, 1988, Burkitt *et al.*, 2003), and the resulting firing rate ν is computed as:

$$\begin{aligned} \nu &= \frac{1}{\tau_e} F \left(\frac{\mu_e - V_T}{\sqrt{2}\sigma_e}; \frac{\sigma_e}{\theta} \right) \\ &= \frac{1}{\tau_e} \left[\int_{-\frac{-\mu_e - V_T}{2\sigma_e}}^{-\frac{\mu_e - V_T}{2\sigma_e}} \sqrt{\pi} \exp(u^2)(1 + \operatorname{erf}(u))du \right]^{-1}, \end{aligned} \quad (6.15)$$

where $\theta = V_T - V_R$ and $\operatorname{erf}(\cdot)$ is the standard error function. Here τ_e , μ_e , and σ_e are the effective time constant, mean applied current, and applied current standard deviation, satisfying:

$$\begin{aligned} \frac{1}{\tau_e} &= \frac{1}{\tau} + r_{10}, \\ \mu_e &= \tau_e (V_R/\tau + r_{11}), \\ \sigma_e^2 &= \frac{\mu_e^2 r_{20} - 2\mu_e r_{21} + r_{22}}{2/\tau_e - r_{20}}, \\ r_{mn} &= (\nu_E + X\bar{\nu}_{\text{Eb}}) a_E^m V_E^n + X\bar{\nu}_{\text{Ib}} a_E^m V_E^n. \end{aligned} \quad (6.16)$$

An increase in the background activity influences ν through two distinct mechanisms. First, from Eqn (6.16) it is straightforward to see that $1/\tau_e$ is a linear function of X , meaning balanced activity multiplicatively scales the $1/\tau_e$ term in Eqn (6.15). This is simply a conductance-induced decrease of the membrane integration time τ_e , facilitating a rapid rise from V_R to V_T in between spikes. Second, if the background fluctuations are balanced (so that μ_e is roughly X independent), then $(\mu_e - V_T)/(\sqrt{2}\sigma_e)$ scales as μ_e/X . This implies that balanced activity divisively scales inputs, an effect expected of a shunting current. For $\sigma_e > 0$ the function $F(a, b)$ has both a nonlinear regime for small to moderate a (akin to power law scaling in a), and a linear regime for large a . When F is in the nonlinear regime the impact of the divisive scaling of the input μ_e/X outweighs the multiplicative scaling of X/τ_e , resulting in an overall division of ν . For large μ_e , the linear regime of F results in the X scalings of μ_e/X and X/τ_e cancelling and $d\nu/d\mu$ is unaffected. The vague nature of a transition from the nonlinear to linear regime in F is one possible reason that conductance induced divisive gain control has been elusive (Holt and Koch, 1997, Doiron *et al.*, 2001, Burkitt *et al.*, 2003, Chance *et al.*, 2002), however, the experimental results presented in Fig. 6.2(a) suggest that the nonlinear regime can be significant.

6.4.2 Other noise-induced influences on $\nu(\mu)$

Doiron *et al.* (2001) and Burkitt *et al.* (2003) replicated fluctuation-induced divisive gain control with a simple conductance based LIF neuron model. However,

many real neurons have spiking dynamics which cannot be captured with such a simple framework. Describing how fluctuations control their spike rate transfer is an important, yet understudied, avenue of research.

As motivation, we present experimental results from Arsiero *et al.* (2007) which show a novel form of noise-dependent gain control. Pyramidal cells were stimulated and recorded in an *in vitro* slice preparation of layer 5 rat prefrontal cortex. Rather than using a simulated conductance input, as was done by Chance *et al.* (2002), they used fluctuating current inputs similar to those in Eqn (6.2). Figure 6.2(b) shows the recorded firing rate ν as a function of μ , for three different values of σ . Current fluctuations clearly have an impact on the shape of $\nu(\mu)$, however, one that is quite distinct from that presented by Chance *et al.* (2002). An increase in σ produces an overall increase in firing rate over all values of ν tested, even for values of μ which saturated ν (i.e. $d\nu/d\mu \approx 0$). Thus, σ determines, in part, the refractory period of the spike dynamics. This behaviour cannot be replicated by the standard LIF model.³

Arsiero *et al.* (2007) used a Hodgkin–Huxley (HH) style neuron model to show how fluctuations facilitate the rapid removal of a slow sodium inactivation, thereby allowing for rapid recovery from past spike discharge. Similar noise-dependent modulation of $\nu(\mu)$ has been associated with fluctuation sensitive recovery from slow after hyperpolarization potassium channels (Higgs *et al.*, 2006). These results depend on the noise-sensitive interaction between the membrane potential and a slow auxiliary channel dynamic which gates spike behaviour, making theoretical progress in this area difficult (although see Lundstrom *et al.* (2008)). Understanding how this form of noise gated transfer shapes neural processing in coupled networks is an important challenge for future research.

6.5 Effects of noise in the coding of time varying stimuli

6.5.1 Noise-enhanced coding of dynamic stimuli

Natural stimuli have specific temporal signatures, which can sometimes have high frequency content. The digitization inherent in a spike train makes it difficult to code high-frequency stimuli with only one spike train. A straightforward solution to this problem is to assume that a population of neurons, rather than a single neuron, code time varying stimuli with their population spike train $\nu(t)$, as defined in Eqn (6.10). In this section we review the proposed influences that the noise intensity σ has on the transfer of a stimulus by a population of neurons. The results are motivated heavily by the work of Stein (1967) and Knight (1972b), with contemporary inspiration from Gerstner (2000), Masuda and Aihara (2002), and van Rossum *et al.* (2002).

Consider the scenario where stimulus information is contained exclusively in the mean current, $\mu(t)$, and the intensity of the input current variability, σ , is

³Arsiero *et al.* (2007) did qualitatively replicate the results with an LIF model with a noise-dependent refractory period. However, a principled derivation of the modification was not given.

both stimulus and time independent. Let $\mu(t)$ vary with a time-scale comparable to the membrane integration time τ_m , meaning that a quasi-static approximation of $\nu(t)$ from a static $\nu(\mu)$ relation (see Fig. 6.2) is insufficient.

To begin with, let σ be small. Since each neuron in the population receives a common time varying term $\mu(t)$ (see bottom panels of Fig. 6.3), and σ is small, the population response shows significant stimulus-induced synchrony. This is evident in the banded structure of the spike train rasters (Fig. 6.3a top) and the ‘pulsatile’ shape of the instantaneous population response $\nu(t)$ (Fig. 6.3a middle). This result mimics the low-noise spike train reliability experiments performed by Bryant and Segundo (1976) and Mainen and Sejnowski (1995).⁴ From a coding perspective this excess synchrony is deleterious because it imparts a redundancy in the population response, making it difficult to extract $\mu(t)$ from observations of $\nu(t)$.

For moderate values of σ the stimulus induced population redundancy reduces, allowing $\nu(t)$ to better copy $\mu(t)$ (Fig. 6.3b). Finally, when σ increases to very large values the copy of $\mu(t)$ by $\nu(t)$ is somewhat degraded (Fig. 6.3c). This is especially apparent when noting that the mean activity of the population has significantly increased (from 5 Hz to 35 Hz) when σ is changed from moderate to large, meaning that the information computed on a per spike basis has drastically diminished. In total, it is evident that a non-zero value of σ can optimize the information transfer in the $\mu(t) \rightarrow \nu(t)$ channel.

The above result uses simulations of stochastically driven leaky integrate-and-fire neurons, however, the essential idea of noise enhanced coding in neural populations is most easily shown in a *non-dynamical* setting with a population of simple threshold units, as previously noted by Stocks (2000). In a neural context a threshold unit is a simplistic neuron model that lacks intrinsic dynamics, having only a binary representation. More specifically, if the total input to unit i , $\mu + \sigma\xi_i$, is bigger than θ then unit i has a state of $y_i = 1$, otherwise its state is $y_i = 0$. The population response is $Y = \sum_{i=1}^N y_i$, which is thus an integer taking values between 0 and the population size N . Figure 6.3(d) shows a schematic of the threshold unit population. The mutual information, MI (Cover and Thomas, 1991), between the population response Y and the stimulus μ can be written as:

$$MI = H(Y) - H(Y|\mu)$$

$$\begin{aligned} &= - \sum_{Y=0}^N P(Y) \log_2 P(Y) - \left(- \int_{-\infty}^{\infty} P(\mu) \sum_{Y=0}^N P(Y|\mu) \log_2 P(Y|\mu) d\mu \right) \\ &= - \sum_{n=0}^N C_n^N P'(Y) \log_2(P'(Y)) - \left(-N \int_{-\infty}^{\infty} P(\mu) \sum_{j=0}^1 P(y|\mu) \log_2(P(y|\mu)) d\mu \right). \end{aligned} \quad (6.17)$$

⁴In the cited studies the stimulus was presented many times in succession to a single neuron recorded *in vitro*, while here we consider the stimulus to be presented simultaneously to a population of uncoupled neurons. Assuming that overall state of the neuron in the experiment does not change very much over the length of the experiment, these scenarios are equivalent.

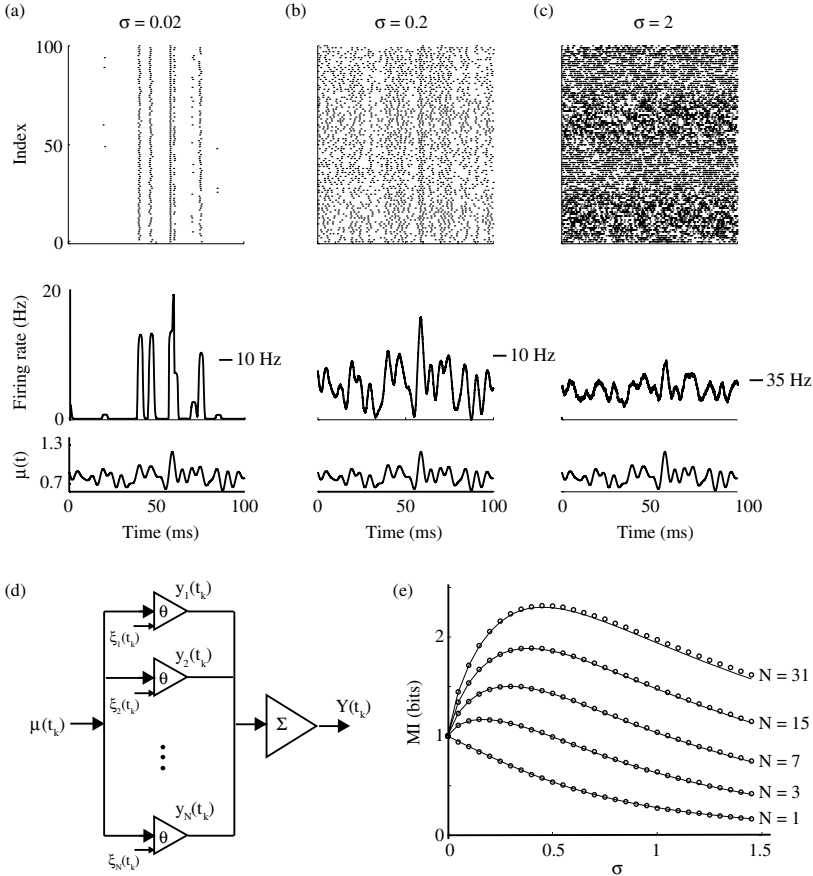


FIG. 6.3: Noise enhanced coding of $\mu(t)$. (a) The top panel is the spike train raster of a fraction of the spiking network in response to a particular realization of a time varying input $\mu(t)$, shown at the bottom. The middle panel is an estimate of the instantaneous firing rate $\nu(t)$, the scale is the same for all panels with the mean rate (over time) indicated to the right of each plot. For presentation purposes we smoothed the data by making $\nu(t) = \frac{1}{N}G(t) * \sum_i \sum_j \delta(t - t_{ik})$ where G is a Gaussian function with standard deviation of 1 ms, and $*$ denotes convolution. Throughout, σ is small. (b) Same as (a), but σ is moderate. (c) Same as (a), but σ is large. (d) Schematic of the population of threshold units. At each time iteration t_i every unit receives the signal $\mu(t_i)$ and a noise source $\sigma\xi_i(t_i)$. The unit outputs, y_k are summed to give the population response $Y(t_i)$. (e) Mutual information, MI, as a function of σ for ensembles of different size N . The open circles are simulations of the threshold unit ensemble, and the curves are theory calculated from Eqn (6.17). Here $\sigma = \sigma_\xi / \sigma_\mu$. We thank Nigel Stocks for the donation of the figure in panel (e).

Here

$$P'(Y) = \int_{-\infty}^{\infty} P(\mu) P(y=1|\mu)^n P(y=0|\mu)^{N-n} d\mu \quad (6.18)$$

with C_n^N the binomial coefficient. The first line of Eqn (6.17) is the definition of MI, the second is a straightforward casting into the threshold unit population, and the third is valid only if all y_i are statistically identical. When the signal distribution $P(\mu)$ is Gaussian with zero mean and standard deviation σ_μ , then

$$P(y=1|\mu) = 1/2\text{erfc}\left[(\theta - \mu)/\sqrt{2\sigma_\xi^2}\right] \quad (6.19)$$

and $P(y=0|\mu) = 1 - P(y=1|\mu)$, where $\text{erfc}(\cdot)$ is the complementary error function. The theoretical expression in Eqn (6.17) is easily computed using standard numerical integration techniques.

Plotting MI against $\sigma = \sigma_\xi/\sigma_\mu$ for $N = 1$ shows that fluctuations exclusively degrade information transmission in single cell computation (Fig. 6.3e). In contrast, for $N > 1$, it is shown that MI is maximized at a non-zero value of σ (Fig. 6.3e). This is because the heterogeneity in the unit response allows a better population sampling of the stimulus. This phenomena has been called suprathreshold stochastic resonance (Stocks, 2000, Stocks and Mannella, 2001). The connection to stochastic resonance is clear since coding is maximized with non-zero fluctuations. However, since for $\sigma = 0$ the signal still drives a response, meaning the signal is not weak, then in contrast to classic stochastic resonance, the signal is labelled suprathreshold. We remark that for $\sigma = 0$ the MI is independent of N since the units are perfectly synchronized. Similar results have been documented in populations of more realistic neurons (Stocks and Mannella, 2001). Related work has been performed in feedforward networks (van Rossum *et al.*, 2002, Masuda and Aihara, 2002).

6.5.2 Noise-coded signals

An important constraint in behaviourally relevant neural coding is that neural activity must be transmitted within a certain time for the code to be useful. Thorpe *et al.* (1996) used a combination of scalp recordings and behavioural experiments to determine that visual processing of complicated images develops in frontal cortex roughly 150 ms after stimulus onset. This observed speed of computation has been difficult to recreate with layered neural structures that are limited by the intrinsic timescale of single neurons (i.e. τ_m) (Knight, 1972*b*), as exemplified in the *in vitro* experiments of Silberberg *et al.* (2004). In brief, a single cell was stimulated many times with a step input current; the current in trial i was:

$$I_i(t) = \mu_{\text{low}} + H(t - t_s)\mu_s + \sigma\eta_i(t). \quad (6.20)$$

$H(t - t_s) = 1$ for $t > t_s$ and is zero otherwise, and $\eta_i(t)$ is a broadband noise process approximating white noise, uncorrelated across trials. This experiment

should be conceived of as an ensemble of uncoupled and uncorrelated cells being stimulated simultaneously at $t = t_s$. Figure 6.4(a) shows the population spike response (top) and the time-dependent firing rate response $\nu(t)$ (middle) to a step change in μ at $t_s = 300$ ms (bottom). It is apparent that the population response $\nu(t)$ lags t_s , due to the integration time τ_m of each neuron in the population.

In contrast to mean coded signals, both Silberberg *et al.* (2004) and Lindner and Schimansky-Geier (2001) considered the step signal encoded via

$$I_i(t) = \mu + (\sigma_{\text{low}} + H(t - t_s)\sigma_s)\eta_i(t). \quad (6.21)$$

The difference here is the variability of the current I_i changes at $t = t_s$ rather than the mean of I_i (compare Fig. 6.4a and b, bottom). The response $\nu(t)$ to the step change in σ is effectively instantaneous, suggesting that rapid processing is

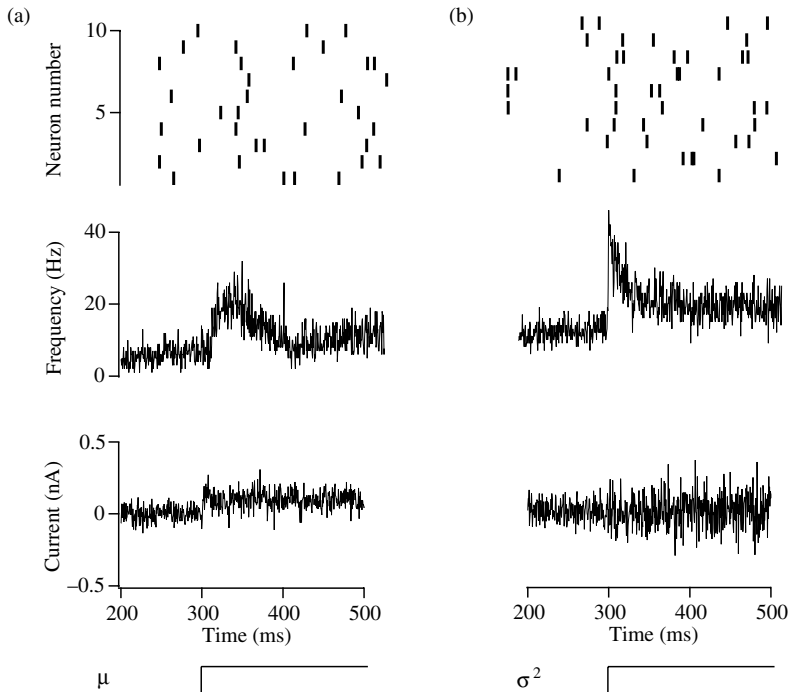


FIG. 6.4: Mean versus noise-coded signals. (a) Sample current trace (bottom) used to drive an neocortical pyramidal cell *in vitro*. Following Eqn (6.20) the mean current changes abruptly at $t_s = 300$ ms, σ remains fixed through the trial. Spike rain rasters (top) for 10 trials, and the population instantaneous firing rate $\nu(t)$ computed from 4000 sequential trials (middle). (b) The same as (a) except the current used in each trial is given by Eqn (6.21). Experimental details are given in Silberberg *et al.* (2004). We thank Matthias Bethge for the donation of the figure.

possible if the signal is coded by the variability of an input current across a large ensemble of neurons.

To understand why the response speed is dramatically enhanced for noise coded signals (Eqn (6.21)) as compared to mean coded signals (Eqn (6.20)) it is useful to write down the evolution equation for the membrane density $P(V, t)$. For an ensemble of LIF neurons described Eqn (6.2)–(6.4) $P(V, t)$ obeys the Fokker–Planck Equation (Risken, 1996):

$$\frac{\partial P(V, t)}{\partial t} = \frac{\partial}{\partial V} \left(V - \mu(t) + \frac{\sigma^2(t)}{2} \frac{\partial}{\partial V} \right) P(V, t) + \nu(t) \delta(V - V_R). \quad (6.22)$$

$P(V, t)$ also satisfies a continuity relation with an effective probability current $S(V, t)$:

$$\frac{\partial P(V, t)}{\partial t} = -\frac{\partial S(V, t)}{\partial V}. \quad (6.23)$$

Combining Eqns (6.22) and (6.23) yield the evolution equation for $S(V, t)$:

$$\frac{\partial S(V, t)}{\partial t} = \left(\mu(t) - V - \frac{\sigma^2(t)}{2} \frac{\partial}{\partial V} \right) P(V, t) - \nu(t) H(V - V_R). \quad (6.24)$$

Any solution $P(V, t)$ of Eqn (6.22) must obey the boundary conditions:

$$\begin{aligned} P(V_T, t) &= 0, \\ \lim_{V \rightarrow -\infty} P(V, t) &= 0. \end{aligned} \quad (6.25)$$

The first boundary condition implies that $V = V_T$ is an absorbing boundary, meaning that once a neuron's membrane potential V_i reaches threshold the dynamics of V_i are momentarily suspended. The LIF spike-reset mechanism is captured in the Fokker–Planck equation (6.22) with the source term at $V = V_R$, $\nu(t) \delta(V - V_R)$, with $\nu(t)$ being the rate of absorption at $V = V_T$. Finally, to relate $\nu(t)$ to $P(V, t)$ we compute the flux of $S(V, t)$ across V_T :

$$\begin{aligned} \nu(t) &= S(V_T, t) \\ &= -\frac{\sigma^2(t)}{2} \frac{\partial P(V, t)}{\partial V} \Big|_{V=V_T}. \end{aligned} \quad (6.26)$$

In the second line we have used the absorbing condition (6.25) in the definition of $S(V, t)$, removing the explicit dependence of $\nu(t)$ on $\mu(t)$. Finally, $\nu(t)$ is determined by the normalization condition:

$$\int_{-\infty}^{V_T} P(V, t) dV = 1. \quad (6.27)$$

Inspection of Eqn (6.26) immediately shows that $\nu(t)$ tracks $\sigma^2(t)$ instantaneously, offering an explanation of the experimental results in Fig. 6.5(b). This is in contrast to a rapid change in $\mu(t)$ needing to be integrated via Eqn (6.22) before it can influence $\nu(t)$ via Eqn (6.26), hence causing a lag in the $\nu(t)$ response.

The absorbing condition that causes this distinction between mean versus noise-coded signals is an abstraction of the spike generating mechanism in real neurons. However, the quadratic integrate-and-fire neuron does not require an absorbing boundary condition, since for sufficiently large $V(t)$, $V(t) \rightarrow \infty$ in finite time, allowing for a soft interpretation of spike threshold. This removes any instantaneous tracking of $\sigma^2(t)$ by $\nu(t)$ (Naundorf *et al.*, 2005). However, a more accurate IF model, when compared to real neural data, is the exponential IF model (Fourcaud-Trocmé *et al.*, 2003), which has an exponential in time explosion of $V(t) \rightarrow \infty$ rather than simply polynomial in time. This rapid explosion is well mimicked by the ad hoc threshold crossing and reset rule of the LIF model, better justifying the connection between Eqn (6.26) and the experimentally obtained Fig. 6.4.

6.6 Neural covariability

6.6.1 Experimental evidence of correlated variability in neural populations

The previous sections focused on the trial-to-trial variability of single units, and when constructing population scenarios tacitly assumed that any co-variability between pairs of cells was negligible. Recent advancements in experimental neuroscience readily permit simultaneous recording from multiple neurons during a single trial. An important observation from these experiments is that the trial-to-trial fluctuations of neurons are often weakly correlated. As an example, we review recent *in vivo* two-photon calcium imaging experiments in rat barrel cortex that permit the simultaneous optical recording of nearby cells (Kerr *et al.*, 2007). Figure 6.5(a) shows the calcium signal measured from an area of barrel cortex corresponding to a particular whisker. A small population of neurons (10–20) were easily identified based from their calcium transients (see Fig. 6.5a), and an accurate representation of their spiking activity in response to whisker deflection was constructed (see Fig. 6.5a right). Figure 6.5(b) shows the spiking activity of 10 neurons in response to four separate whisker deflections (orange regions labeled *a* through *d*). Individual cells respond primarily to either the onset (red) or offset (green) of the stimulus presentation, with varying degrees of spontaneous activity (black) between stimulus trials. It is immediately apparent that the population response to a whisker deflection differs significantly between any two trials. Further, a spatial labelling of the location of neurons responding to either the stimulus onset (Fig. 6.5c left) or the offset (Fig. 6.5c right) shows no apparent structure in the spatial organization of the population response. These results mimic the single cell variability reported earlier (see Fig. 6.1).

Using their population data, Kerr *et al.* (2007) also calculated the total population recruitment (as a percentage) during all trials (Fig. 6.5d) and estimated

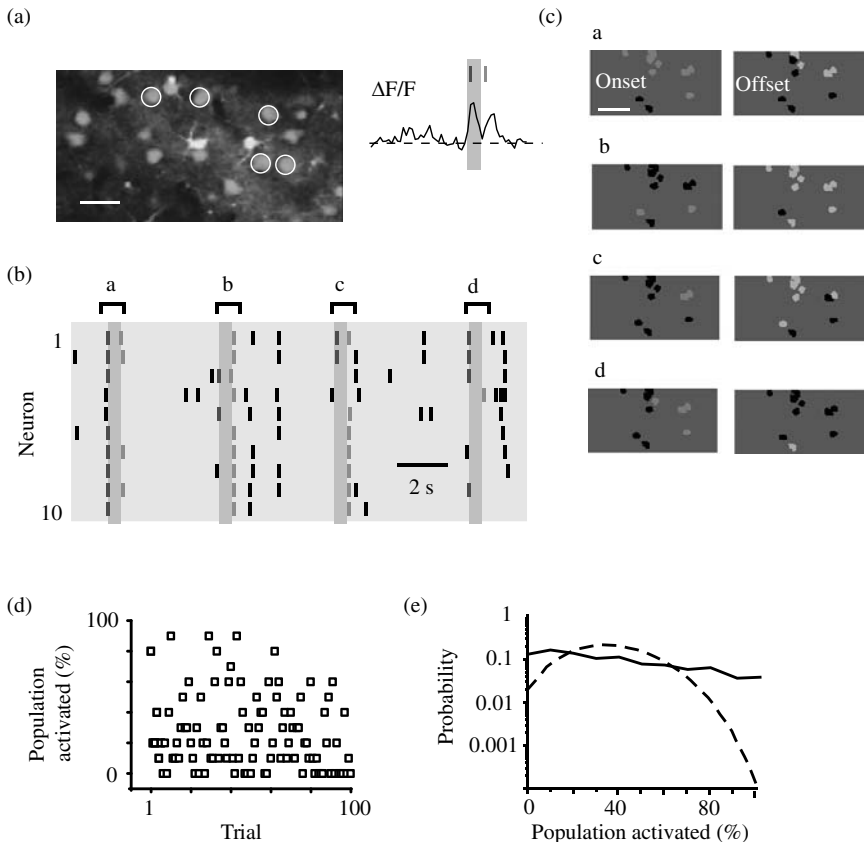


FIG. 6.5: Population variability in barrel cortex. (a) Optical calcium measurement from a population of neurons located in layer 2/3 of barrel cortex; the scale bar is 30 μm . The neurons have been bulk loaded with a calcium sensitive dye which fluoresces during neural activity (see right traces of the normalized fluorescence change). Fluorescence activity is thresholded and a putative spike train response is calculated for all neurons recorded. (b) Spike train rasters for a population of 10 neurons. Four whisker deflections are shown (*a* through *d*) and the stimulus duration is indicated in orange. Neurons responded primarily at stimulus onset (red) or offset (green); black spikes indicate spikes that were not correlated with the stimulus. (c) Spatial organization of onset (left) and offset (right) responses for each whisker deflection *a* through *d*; the scale bar is 50 μm . (d) The total population activity recruited at stimulus onset over 100 trials. (e) Estimated probability density of the amount of population activity for the actual data (solid) and assuming independence between neurons (dashed). We thank Jason Kerr for the donation of the figures – we refer the reader to Kerr *et al.* (2007) for the experimental details.

the probability density of the total population response across all trials (Fig. 6.5e, solid line). There are significant differences between the actual density and the one obtained from assuming that the variability in a single unit's recruitment is independent of all other cells in the population (Fig. 6.5e, dashed line). In particular, there is an excess of probability, as compared to the independent case, for a large fraction of the population to be either simultaneously silent or active. This indicates that the trial-to-trial variability is correlated across the neurons in the population. Similar correlated activity has been reported in retina (Mastronarde, 1983, Schneidman *et al.*, 2006, Shlens *et al.*, 2006), thalamus (Alonso *et al.*, 1996, Bruno and Sakmann, 2006), and primary sensory cortex (Zohary *et al.*, 1994, Kohn and Smith, 2005, deCharms and Merzenich, 1996, Gutnisky and Dragoi, 2008, Petersen *et al.*, 2001). The role of correlated variability in neural coding, either beneficial or deleterious, is a topic of much debate (Abeles, 1991, Schneidman *et al.*, 2003, Latham and Nirenberg, 2005, Averbeck *et al.*, 2006, Petersen *et al.*, 2001).

6.6.2 Population of correlated stochastic neurons

To motivate a mathematical description of correlated population activity, consider a representative pair of cells from a postsynaptic population, i and j , and write their respective input currents as:

$$\begin{aligned} I_i(t) &= a_E(P_{Ei}(t) + P_{Ec}(t)) + a_I(P_{Ii}(t) + P_{Ic}(t)), \\ I_j(t) &= a_E(P_{Ej}(t) + P_{Ec}(t)) + a_I(P_{Ij}(t) + P_{Ic}(t)). \end{aligned} \quad (6.28)$$

Here $P_{\alpha i}(t)$ and $P_{\alpha j}(t)$ are Poisson spike trains that are private to cells i and j , respectively, and $P_{\alpha c}(t)$ is a Poisson train common to both cells ($\alpha = E, I$). This dissection of inputs into private and common inputs can arise from partially overlapping presynaptic pools, as illustrated in Fig. 6.6(a). To separate changes in the correlation in synaptic drive from changes in overall synaptic drive we assume that the intensity of the excitatory and inhibitory inputs satisfy:

$$\begin{aligned} N_{Ei(j)}\nu_{Ei(j)}(t) + N_{Ec}\nu_{Ec}(t) &= N_E\nu_E(t), \\ N_{Ii(j)}\nu_{Ii(j)}(t) + N_{Ic}\nu_{Ic}(t) &= N_I\nu_I(t). \end{aligned} \quad (6.29)$$

Fixing $N_\alpha\nu_\alpha(t)$ requires that an increase in $N_{\alpha c}\nu_{\alpha c}(t)$ accompanies a decrease in $N_{\alpha i(j)}\nu_{\alpha i(j)}(t)$, so that the total synaptic drive across channel α is unchanged. In the appropriate diffusion limit $I_i(t)$ and $I_j(t)$ become:

$$\begin{aligned} I_i(t) &= \mu(t) + \sigma(t) [\sqrt{1-c} \xi_i(t) + \sqrt{c} \xi_c(t)], \\ I_j(t) &= \mu(t) + \sigma(t) [\sqrt{1-c} \xi_j(t) + \sqrt{c} \xi_c(t)]. \end{aligned} \quad (6.30)$$

Here $\xi_i(t)$, $\xi_j(t)$, and $\xi_c(t)$ are all uncorrelated white noise processes. We remark that the same realization of $\xi_c(t)$ appears in both I_i and I_j , thereby correlating the two currents. Similar to Eqn (6.2) we compute the statistics of $I_i(t)$

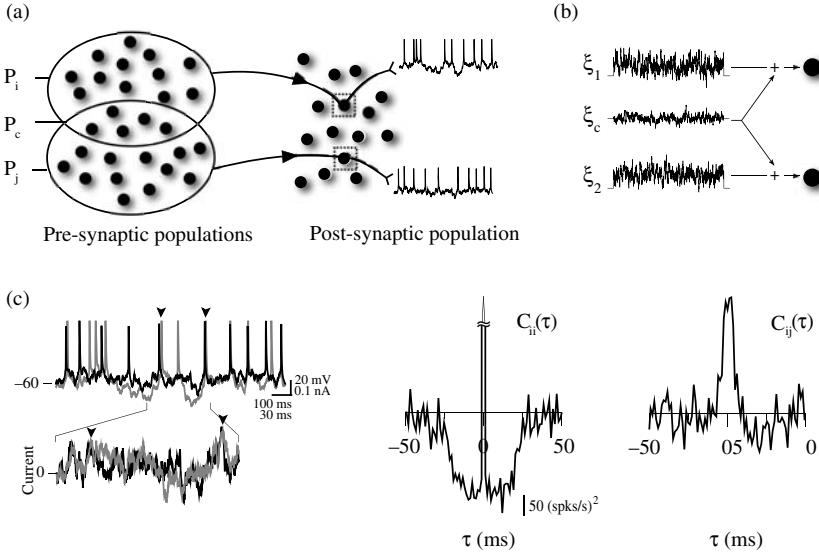


FIG. 6.6: Correlated inputs to a pair of cells. (a) Schematic of pools of presynaptic inputs afferent to two representative cells in a postsynaptic population; see Eqn (6.28). We dissect the activity of the presynaptic populations in private groups P_i and P_j , and a shared presynaptic pool P_c . (b) Reduction of panel (a) to a simplified stochastic setting (see Eqn (6.30)). (c) Example pair of correlated membrane traces (left), and computed autocovariance (middle) and cross-covariance (right) functions. Spike trains were generated from current driven cortical neurons *in vitro*. See de la Rocha *et al.* (2007) for details.

and $I_j(t)$ as:

$$\begin{aligned}\mu(t) &= a_E N_E \nu_E(t) + a_I N_I \nu_I(t), \\ \sigma^2(t) &= a_E^2 N_E \nu_E(t) + a_I^2 N_I \nu_I(t), \\ c(t) &= \frac{a_E^2 N_{Ec} \nu_{Ec}(t) + a_I^2 N_{Ic} \nu_{Ic}(t)}{\sigma^2(t)}.\end{aligned}\quad (6.31)$$

It is straightforward to show that the correlation coefficient between input currents ($i \neq j$) is:

$$\frac{\langle \Delta I_i \Delta I_j \rangle_{ijc}}{\sqrt{\langle \Delta I_i \rangle_{ijc} \langle \Delta I_j \rangle_{ijc}}} = c(t), \quad (6.32)$$

where $\Delta I_i = I_i(t) - \mu(t)$ and $\langle \cdot \rangle_{ijc}$ is an expectation over realizations of $\xi_i(t)$, $\xi_j(t)$, and $\xi_c(t)$. The diffusion framework of Eqn (6.30) is illustrated in Fig. 6.6(b). We remark that c is simply the proportion of shared presynaptic inputs relative to the total presynaptic pool.

The spike train responses from the pair of neurons are $y_1(t) = \sum_k \delta(t - t_{1k})$ and $y_2(t) = \sum_k \delta(t - t_{2k})$. To define a reasonable measure of spike train correlation we first define the covariance function (Cox and Lewis, 1966):

$$C_{ij}(t, t') = \langle y_i(t)y_j(t') \rangle_{ijc} - \langle y_i(t) \rangle_{ijc} \langle y_j(t') \rangle_{ijc}. \quad (6.33)$$

If we let the inputs' statistics $\mu(t)$, $\sigma(t)$, and $c(t)$ vary in time with frequencies upper bounded by f_U , then computing the spike train covariance function over times intervals of length $2T \ll 1/f_U$ allows us to centre the covariance function at t and replace t' with $t + \tau$ for $\tau \in (-T, T)$:

$$C_{ij}(t, \tau) = \langle y_i(t)y_j(t + \tau) \rangle_{ijc} - \nu^2(t). \quad (6.34)$$

This is effectively stating that over any time interval of length $2T$ the spike train is statistically stationary, also yielding for $t' \in (t - T, t + T)$ that $\langle y_i(t') \rangle_{ijc} = \langle y_j(t') \rangle_{ijc} = \nu(t)$. An example of the spike train autocovariance function, $C_{ii}(\tau)$, and the cross-covariance function, $C_{ij}(\tau)(i \neq j)$, is given in Fig. 6.6(c).

An integration over τ defines the spike train correlation coefficient over a window of length $2T$ centred at time t :

$$\rho_{ijT}(t) = \frac{\int_{-T}^T C_{ij}(t, \tau) \frac{T-|\tau|}{T} d\tau}{\sqrt{\int_{-T}^T C_{ii}(t, \tau) \frac{T-|\tau|}{T} d\tau \int_{-T}^T C_{jj}(t, \tau) \frac{T-|\tau|}{T} d\tau}}. \quad (6.35)$$

The coefficient $\frac{(T-|\tau|)}{T}$ in the integrand makes $\rho_{ijT}(t)$ equivalent to the spike count correlation coefficient:

$$\rho_{ijT}(t) = \frac{\langle \Delta n_{iT}(t) \Delta n_{jT}(t) \rangle_{ijc}}{\sqrt{\langle \Delta n_{iT}(t) \rangle_{ijc} \langle \Delta n_{jT}(t) \rangle_{ijc}}}. \quad (6.36)$$

Here $\Delta n_{iT}(t) = n_{iT}(t) - \langle n_{iT}(t) \rangle$ and $n_{iT}(t) = n_i(t - T, t + T)$ with $n_i(\cdot, \cdot)$ defined in Eqn (6.9). The proof of the equivalence between ρ_{ijT} defined by both Eqns (6.35) and (6.36) can be found in Cox and Lewis (1966). We remark that ρ_{ijT} is a normalized measure with values between 0 and 1 for $c > 0$. Finally, for stationary input statistics $\mu(t) = \mu$, $\sigma(t) = \sigma$, and $c(t) = c$ and in the limit $T \rightarrow \infty$ Eqn (6.35) becomes simply

$$\rho_{ij,\infty} = \frac{\int_{-\infty}^{\infty} C_{ij}(\tau) d\tau}{\sqrt{\int_{-\infty}^{\infty} C_{ii}(\tau) d\tau \int_{-\infty}^{\infty} C_{jj}(\tau) d\tau}}. \quad (6.37)$$

This is simply the area of the cross-covariance function normalized by the areas of the autocovariance functions. For the sake of notation we hereafter drop the ij notation.

6.6.3 Transfer of input correlation to spike train correlation

An important, though understudied, question is: how does $\rho_T(t)$ depend on the input statistics $\mu(t)$, $\sigma(t)$, and $c(t)$? An answer (or partial answer) will aid in the understanding of how correlations are transferred in spiking networks, a topic of much debate (Shadlen and Newsome, 1998, Reyes, 2003, Litvak *et al.*, 2003, Doiron *et al.*, 2006). Several experimental and theoretical studies have used the simple framework of Fig. 6.6 to study the c to ρ_T transfer (Svirskis and Hounsgaard, 2003, Galan *et al.*, 2006, Moreno-Bote and Parga, 2006, de la Rocha *et al.*, 2007, Shea-Brown *et al.*, 2008, Marella and Ermentrout, 2008). First, it is simple to show that for all T , $c = 0$ results in $\rho_T = 0$, and that for homogeneous model neurons $c = 1$ results in $\rho_T = 1$.⁵ However, for $c \neq 0, 1$ the nonlinearity inherent in spiking forces ρ_T to be less than c for all window sizes T . This means that $\rho_T(c)$ is a concave up function (Galan *et al.*, 2006, de la Rocha *et al.*, 2007, Marella and Ermentrout, 2008).

Recently, de la Rocha *et al.* (2007) have computed ρ_∞ for the case of stationary inputs, $\mu(t) = \mu$, $\sigma(t) = \sigma$, and $c(t) = c$. They used an *in vitro* cortical slice preparation and studied the simple framework of Fig. 6.6(b) for an ensemble of neuron pairs (see the example membrane potential traces in Fig. 6.7c). Rather than study the mapping between ρ and c with fixed μ and σ , they studied ρ_∞ with c fixed and varied μ and σ over a large range. Interestingly, a stereotyped relation appeared between the geometric mean of the output firing rates, $\sqrt{\nu_1\nu_2}$, and the output correlation ρ_∞ (Fig. 6.7a). As firing rates increased (through some combination of increasing μ and/or σ) the output correlation increased, even though the input correlation remained fixed. Assuming weak correlations ($c \ll 1$) they used perturbation theory on the spike train response (Doiron *et al.*, 2004) to obtain the compact formula relating ρ_∞ to μ , σ , and c :

$$\begin{aligned} \rho_\infty &\approx c \frac{\sigma^2 \left| \frac{d\nu}{d\mu} \right|^2}{\text{CV}^2 \nu} \\ &= c S(\mu, \sigma). \end{aligned} \tag{6.38}$$

The second line of (6.38) defines the *correlation susceptibility* $S(\mu, \sigma)$, which linearly relates input and output correlation. Restricting model neurons to be white noise driven LIF neurons, $\nu(\mu, \sigma)$, $\text{CV}(\mu, \sigma)$ (inter-spike interval coefficient of variation), and $d\nu(d\mu)/\mu, \sigma$ are all expressible in terms of first passage calculations (Tuckwell, 1988), making Eqn (6.38) tractable to compute. Firing rate, the gain of the firing rate transfer, spike train variability, and spike train correlation are all central measures of cortical response, and are thought to define, in part, the cortical code. The importance of Eqn (6.38) is that it relates these various quantities for the simple setting of Fig. 6.6(b).

⁵For real neuron pairs absolute homogeneity is impossible, and even if an applied current has $c = 1$ the intrinsic membrane fluctuations are uncorrelated across the pair, both causing $\rho_T < 1$ even when $c = 1$.

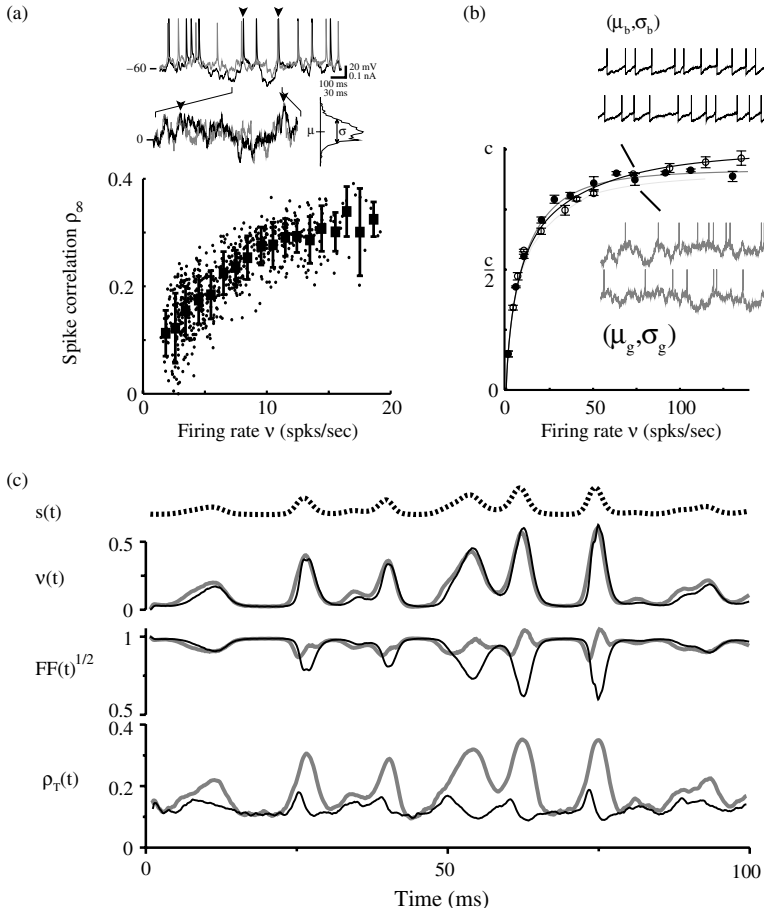


FIG. 6.7: Spike train correlation co-varies with firing rate. (a) *In vitro* cortical neurons ($n = 20$) were stimulated with correlated input currents with a fixed correlation, $c = 0.5$ and over a wide range of μ and σ . The top plots are sample membrane and current traces for a pair of neurons during a single trial. The bottom plot is ρ_∞ plotted against $\sqrt{\nu_1\nu_2}$; the large squares are ensemble averages over $\sqrt{\nu_1\nu_2}$ collapsed into 1 Hz bins, with error bars being \pm one standard deviation. (b) In the limit of small c , Eqn (6.38) (solid curves), matches simulations from a pair of LIF neurons (data points). The black curve and open circles have a fixed σ while μ varies; the grey curve and closed circles have a fixed μ while σ varies. Sample membrane traces for two selected points on each curve, (μ_b, σ_b) and (μ_g, σ_g) , are shown. (c) Stimulus $s(t)$ (top) drives a pair of neurons either through $\mu(t) \propto s(t)$ with fixed σ (black curves), or $\sigma^2(t) \propto s(t)$ with fixed μ (grey curves). For each case the firing rate $\nu(t)$, the Fano factor $FF(t)$, and the correlation coefficient $\rho_T(t)$ are shown. We thank Jaime de la Rocha, Eric Shea-Brown, and Kresimir Josic for the donation of the Figures.

Using LIF neuron models and fixing σ and varying μ (black curve in Fig. 6.7b), or fixing μ and varying σ (grey curve Fig. 6.7b), gave similar trends to the data and the theoretical relation in Eqn (6.38) matched simulation results well (compare simulation data points versus theoretical curves in Fig. 6.7b). To see why a relation between ν and ρ_∞ is surprising we focus on two (μ, σ) pairs, one on the black curve (μ_b, σ_b) and the other on the grey curve (μ_g, σ_g) . The point (μ_b, σ_b) has $\mu_b > 1$, meaning that the neurons will fire spikes even if $\sigma = 0$. With σ_b small, the spike train is very rhythmic, yielding a $CV \approx 0.3$ (see black spike train insert in Fig. 6.7b). In contrast, the point (μ_g, σ_g) has $\mu_g < 1$, implying that only for $\sigma > 0$ will the neurons fire spikes. Since σ_g is large, the spike train is very erratic having a $CV \approx 1$ (see grey spike train insert in Fig. 6.7b). Despite these spike trains being very distinct from the perspective of single train variability (as measured by CV), the trains have almost exactly the same ν and ρ_∞ . Furthermore, the black and grey curves nearly coincide over the whole ν axis, meaning there is a continuum of (μ_b, σ_b) and (μ_g, σ_g) where a similar analysis can be performed. Thus, the correlation between two spike trains, ρ_∞ , is approximately independent of the variability of the trains, CV , yet depends sensitively on the firing rates ν of the trains. This permits us to rewrite the correlation susceptibility S as:

$$S(\mu, \sigma) \approx S(\nu), \quad (6.39)$$

making, from Eqn (6.38), ρ_∞ and ν related via:

$$\rho_\infty \approx cS(\nu). \quad (6.40)$$

Equation (6.40) is an output–output relation – relating one output statistic (ν) to another (ρ). We remark that the approximation in Eqn (6.39) is not from a principled derivation, but from an empirical observation that ν and ρ_∞ co-vary with one another (see Fig. 6.7a). However, using standard asymptotic techniques Eqn (6.39) can be derived in the limit of small ν with $\mu < 1$ (Shea-Brown *et al.*, 2008). The approximate independence of ρ_T from spike train variability breaks down when T approaches the membrane time constant of the neuron pair (Shea-Brown *et al.*, 2008). For these small T values, only when σ is large and $\mu < 1$ (meaning that the Fano factor FF is large), is the relation in Eqn (6.40) preserved. We mention that a large FF is appropriate for cortical neurons (Softky and Koch, 1993). However, for large μ and relatively low σ (yielding $FF < 1$), it is the case that $\rho_T \ll c$ and ρ_T shows little ν dependence; this is due in part to $C_{ij}(\tau)$ and $C_{ii}(\tau)$ having significant structure beyond the domain given by $\tau \in (-T, T)$.

A relationship between spike train correlation and rate has a straightforward functional consequence. It is well known that the firing rate of neurons is tuned to specific stimuli (Hubel and Wiesel, 1959), so that for a fixed stimulus s we have $\nu(s)$. Equation (6.40) implies that even for fixed input correlation c we have that $\rho_T(s) = cS(\nu(s))$, meaning that correlation will also be tuned to the stimulus s . This final conclusion must be read with caution: Eqn (6.40) neglects any

potential stimulus dependence of c which in principle could distort the stimulus dependence of ρ . This caveat may explain conflicting data sets either supporting (Kohn and Smith, 2005) or contradicting (Gutnisky and Dragoi, 2008, Kohn and Smith, 2005) Eqn (6.40).⁶

6.6.4 Coding dynamic stimuli with correlation

In this last section we consider the coding of $s(t)$ by the joint spike train response of a representative pair of neurons; this is an extension of the uncorrelated population coding presented in Section 6.3. Specifically, we consider the following stimulus transduction:

$$\begin{aligned}\mu(t) &= \bar{\mu} + \Delta\mu s(t), \\ \sigma(t) &= \bar{\sigma} + \Delta\sigma s(t).\end{aligned}\tag{6.41}$$

Here $\bar{\mu}$ and $\bar{\sigma}$ are baseline values and $\Delta\mu$ and $\Delta\sigma$ are signal induced deviations from baseline. Figure 6.7c shows a sample $s(t)$ and $\nu(t)$ computed for two cases: the mean coded signal where $\Delta\mu > 0$ and $\Delta\sigma = 0$ (black curves in Fig. 6.7c), and the noise coded signal where $\Delta\mu = 0$ and $\Delta\sigma > 0$ (grey curves in Fig. 6.7c). The particular model and signal parameters were chosen so that $\nu(t)$ is nearly identical for the two cases (Fig. 6.7c).⁷ While $\nu(t)$ is transparent to the signal being mean coded versus noise coded, the variability versus co-variability of the spike train output clearly disambiguates the two cases (Fig. 6.7). When the signal is mean coded the time periods where $\mu(t) > 1$ force a rhythmicity in the spike train, which subsequently lowers $FF(t)$. By contrast, when $\mu(t) < 1$, $FF(t)$ increases due to the baseline noise $\bar{\sigma}$ inducing spike time variability over the ensemble. Thus, for mean coded signals, in addition to $\nu(t)$ tracking $s(t)$, $FF(t)$ is also an excellent indicator of $s(t)$, providing another channel by which to code.

However, for mean coded signals the correlation coefficient ρ_T (with $T = 0.5\tau_m$) shows little stimulus tracking and remains relatively low throughout the stimulus presentation. In contrast, when $\sigma(t)$ carries information about $s(t)$, $\rho_T(t)$ is stimulus locked while $FF(t)$ is both high and relatively stimulus independent. Thus, for spike time correlations measured over small time windows, e.g. synchrony, to code for a stimulus there is significant advantage when the stimulus influences the variability of the membrane response across a group of cells, rather than the mean membrane response.

⁶The V1 data set presented by Kohn and Smith (2005) follows Eqn (6.39) when $T < 100$ ms, and does not for larger T . The discrepancy here is likely due to slow non-stationarities shaping $C_{ij}(\tau)$; however, this remains to be shown.

⁷This requires that $s(t)$ be sufficiently slow that the fast transfer of a noise-coded signal, as presented in Section 6.5.2, does not outperform the mean coded signal transfer.

6.7 Conclusion and outlook

In this chapter we advocate a framework modelling the transduction between input statistics $\mu(t)$, $\sigma(t)$, and $c(t)$ and the complementary spike train statistics $\nu(t)$, $\text{FF}(t)$, and $\rho_T(t)$. This approach has led to significant results, yet there are still many unknowns. Primary among them is how a stimulus is actually encoded in input current statistics. Any answer to this question will likely require intracellular recording from single, or multiple, neurons during both spontaneous and evoked activity (Anderson *et al.*, 2000, Lampl *et al.*, 1999, Okum and Lampl, 2008). Furthermore, there is undoubtedly no single answer to this question, with signal transfer being contingent on the exact stimulus being coded, the brain areas involved in stimulus coding, and the previous history before stimulus presentation.

Representing the input current from a large presynaptic pool with a reasonable continuous stochastic process is also an area that requires continued investigation. The framework presented in Eqns (6.2)–(6.3) and (6.30)–(6.32) neglects the time-scale of both synaptic transmission, and any inherited due to spike train patterning in the presynaptic ensemble (Moreno *et al.*, 2002, Câteau and Reyes, 2006). We also focused exclusively on pairwise correlation, and did not discuss the higher order statistics between more than two neurons. Higher order statistics can dominate population behaviour (Kuhn *et al.*, 2003), however, recent studies in retina (Schneidman *et al.*, 2006, Shlens *et al.*, 2006) suggest that the full statistical structure of neural ensembles can be well approximated by knowledge of only weak pairwise statistics. Nevertheless, even a transient network synchronization amongst many neurons (influencing statistics at high order) can be very effective in propagating across layered networks (Reyes, 2003), and thus dominate information transfer.

Trial-to-trial variability in neurons, and populations of neurons, is an unavoidable reality of neural response. Elucidating the impact of variability on the performance of the nervous system is a difficult, yet critical, problem for the next generation of neuroscientists to solve. Successfully incorporating fluctuations within a neural coding paradigm will also address state- (anesthetized versus unanesthetized) or context- (attended versus unattended) dependent coding, where often the co-variability over a population of neurons is greatly affected. Finally, using fluctuations to enhance system performance is a radical new approach in the general theory of computation. The brain is both a source of inspiration for sophisticated processing, and an extremely stochastic organ. Uncovering the relationships between the ideas presented here promises new advances in the way computation is performed in many areas of science, engineering, and medicine.

References

- Abeles, M. (1991). *Corticonics: Neural Circuits of the Cerebral Cortex*. Cambridge Univ. Press, New York.

- Alonso, J.M., Usrey, W.M., and Reid, W.M. (1996). Precisely correlated firing in cells of the lateral geniculate nucleus. *Nature*, **383**, 815–819.
- Anderson, J.S., Lampl, I., Gillespie, D.C., and Ferster, D. (2000). The contribution of noise to contrast invariance of orientation tuning in cat visual Cortex. *Science*, **290**(5498), 1968–1972.
- Arsiero, M., Luscher, H.-R., Lundstrom, B.N., and Giugliano, M. (2007). The impact of input fluctuations on the frequency-current relationships of layer 5 pyramidal neurons in the rat medial prefrontal cortex. *J.Neurosci.*, **27**, 3274–3284.
- Averbeck, B.B., Latham, P.E., and Pouget, A.P (2006). Neural correlations, population coding and computation. *Nat. Rev. Neurosci.*, **7**, 358–366.
- Britten, K.H., Shadlen, M.N., Newsome, W.T., and Movshon, J.A. (1993). Response of neurons in macaque mt to stochastic motion signals. *Vis. Neurosci.*, **10**, 157–1169.
- Bruno, R.M. and Sakmann, B. (2006). Cortex is driven by weak but synchronously active thalamocortical synapses. *Nature*, **312**, 1622–1627.
- Bryant, H.L. and Segundo, J.P. (1976). Spike initiation by transmembrane current: a white-noise analysis. *The Journal of Physiology*, **260**(2), 279–314.
- Burkitt, A.N., Meffin, H., and Grayden, D.B. (2003). Study of neuronal gain in a conductance-based leaky integrate-and-fire neuron model with balanced excitatory and inhibitory synaptic input. *Biological Cybernetics*, **89**, 119–125.
- Carandini, M. (2004). Amplification of trial-to-trial response variability by neurons in visual cortex. *PLoS Biology*, **2**, 1483–1493.
- Câteau, H. and Reyes, A.D. (2006). Relation between single neuron and population spiking statistics and effects on network activity. *Physical Review Letters*, **96**, 058101.
- Chance, F.S., Abbott, L.F., and Reyes, A.D. (2002). Gain modulation from background synaptic input. *Neuron*, **35**, 773–782.
- Cover, T.M. and Thomas, J.A. (1991). *Elements of Information Theory*. John Wiley, New York.
- Cox, D.R. and Lewis, P.A.W. (1966). *The Statistical Analysis of Series of Events*. Methuen, London.
- de la Rocha, J., Doiron, B., Shea-Brown, E., Josic, K., and Reyes, A. (2007). Correlation between neural spike trains increases with firing rate. *Nature*, **448**, 802–806.
- deCharms, R.C. and Merzenich, M.M. (1996). Primary cortical representation of sounds by the coordination of action-potential timing. *Nature*, **381**, 610–613.
- Doiron, B., Lindner, B., Longtin, A., Maler, L., and Bastian, J. (2004). Oscillatory activity in electrosensory neurons increases with the spatial correlation of the stochastic input stimulus. *Physical Review Letters*, **96**, 048101.
- Doiron, B., Longtin, A., Berman, N., and Maler, L. (2001). Subtractive and divisive inhibition: Effect of voltage-dependent inhibitory conductances and noise. *Neural Comput.*, **13**, 227–248.

- Doiron, B., Rinzel, J., and Reyes, A. (2006). Stochastic synchronization in finite size spiking networks. *Physical Review E*, **74**, 030903.
- Fourcaud-Trocmé, N., Hansel, D., van Vreeswijk, C., and Brunel, N. (2003). How spike generation mechanisms determine the neuronal response to fluctuating inputs. *J. Neurosci.*, **23**, 11628–11640.
- Galan, R.F., Fourcaud-Trocmé, N., Ermentrout, G.B., and Urban, N.N. (2006). Correlation-induced synchronization of oscillations in olfactory bulb neurons. *Journal of Neuroscience*, **26**(14), 3646.
- Gerstner, W. (2000). Population dynamics of spiking neurons: fast transients, asynchronous states, and locking. *Neural Computation*, **12**, 43–89.
- Gutnisky, D.A. and Dragoi, V. (2008). Adaptive coding of visual information in neural populations. *Nature*, **452**, 220–224.
- Heeger, D.J. (1992). Normalization of cell responses in cat striate cortex. *Vis. Neuroscience*, **9**, 181–198.
- Heggelund, P. and Albus, K. (1978). Response variability and orientation discrimination of single cells in striate cortex of cat. *Exp. Brain Res.*, **32**, 197–211.
- Higgs, M.H., Slee, S.J., and Spain, W.J. (2006). Diversity of gain modulation by noise in neocortical neurons: Regulation by the slow afterhyperpolarization conductance. *Journal of Neuroscience*, **26**(34), 8787.
- Holt, G.R. and Koch, C. (1997). Shunting inhibition does not have a divisive effect on firing rates. *Neural Computation*, **9**, 1001–1013.
- Hubel, D.H. and Wiesel, T.N. (1959). Receptive fields of neurones in the cat's striate cortex. *J. Physiol.*, **148**, 574–591.
- Kerr, J.N.D., de Kock, C.P.J., Greenberg, D.S., Bruno, R.M., Sakmann, B., and Helmchen, F. (2007). Spatial organization of neuronal population responses in layer 2/3 of rat barrel cortex. *J. Neurosci.*, **27**, 13316–13328.
- Knight, B. (1972a). The relation between the firing rate of a single neuron and the level of activity in a population of neurons. *J. Gen. Physiol.*, **59**, 767–778.
- Knight, B.W. (1972b). Dynamics of encoding in a population of neurons. *Journal of General Physiology*, **59**, 734–766.
- Kohn, A. and Smith, M.A. (2005). Stimulus dependence of neuronal correlation in primary visual cortex of the macaque. *J. Neurosci.*, **25**, 3661–3673.
- Kuhn, A., Aertsen, A., and Rotter, S. (2003). Higher-order statistics of input ensembles and the response of simple model neurons. *Neural Comp.*, **15**, 67–101.
- Lampl, I., Reichova, I., and Ferster, D. (1999, Feb). Synchronous membrane potential fluctuations in neurons of the cat visual cortex. *Neuron*, **22**(2), 361–374.
- Lapicque, L. (2007). Quantitative investigations of electrical nerve excitation treated as polarization (translation). *Biol. Cyber.*, **97**, 341–349.
- Latham, P.E. and Nirenberg, S. (2005). Synergy, redundancy, and independence in population codes, revisited. *J. Neurosci.*, **25**(21), 5195–5206.

- Lindner, B. and Schimansky-Geier, L. (2001). Transmission of noise coded versus additive signals through a neuronal ensemble. *Physical Review Letters*, **86**(14), 2934–2937.
- Litvak, V., Sompolinsky, H., Segev, I., and Abeles, M. (2003). On the transmission of rate code in long feedforward networks with excitatory-inhibitory balance. *J. Neurosci.*, **95**, 3006–3015.
- Lundstrom, B.N., Hong, S., Higgs, M.H., and Fairhall, A.L. (2008). Two computational regimes of a single-compartment neuron separated by a planar boundary in conductance space. *Neural Computation*, **20**, 1239–1260.
- Mainen, Z. and Sejnowski, T. (1995). Reliability of spike timing in neocortical neurons. *Science*, **268**, 1503–1506.
- Marella, S. and Ermentrout, G.B. (2008). Class-II neurons display a higher degree of stochastic synchronization than class-I neurons. *Physical Review E*, **77**(4), 041918.
- Mastronarde, D.N. (1983). Correlated firing of cat retinal ganglion cells. i. spontaneously active inputs to x- and y- cells. *J. Neurophysiol.*, **49**, 303–324.
- Masuda, N. and Aihara, K. (2002). Bridging rate coding and temporal spike coding by effects of noise. *Phys. Rev. Lett.*, **88**, 248101.
- McAdams, C.J. and Maunsell, J.H.R. (1999). Effects of attention on orientation tuning functions of single neurons in macaque cortical area v4. *J. Neuroscience*, **19**, 431–441.
- Moreno, R., de la Rocha, J., Renart, A., and Parga, N. (2002). Response of spiking neurons to correlated inputs. *Physical Review Letters*, **89**, 288101.
- Moreno-Bote, R. and Parga, N. (2006). Auto- and crosscorrelograms for the spike response of leaky integrate-and-fire neurons with slow synapses. *Phys. Rev. Lett.*, **96**, 028101.
- Naundorf, B., Geisel, T., and Wolf, F. (2005). Action potential onset dynamics and the response speed of neuronal populations. *J. Comput. Neurosci.*, **18**, 297–309.
- Okum, M. and Lampl, I. (2008). Instantaneous correlation of excitation and inhibition during ongoing and sensory-evoked activities. *Nat. Neurosci.*, **11**, 535–537.
- Petersen, R.S., Panzeri, S., and Diamond, M.E. (2001). Population coding of stimulus location in rat somatosensory cortex. *Neuron*, **32**, 503–514.
- Pouget, A. and Sejnowski, T.J. (1997). Spatial transformations in the parietal cortex using basis functions. *J. Cognitive Neuroscience*, **9**, 222–237.
- Reyes, A.D. (2003). Synchrony-dependent propagation of firing rate in iteratively constructed networks in vitro. *Nat. Neurosci.*, **6**, 593–599.
- Ricciardi, L. (1977). *Diffusion-Processes and Related Topics in Biology*. Springer, Berlin.
- Risken, H. (1996). *The Fokker-Planck Equation: Methods of Solutions and Applications*. Springer-Verlag, New York.
- Salinas, E. and Thier, P. (2000). Gain Modulation: A major computational principle of the central nervous system. *Neuron*, **27**, 15–21.

- Schneidman, E., Berry, M.J. II., R., Segev, and B., William (2006). Weak pairwise correlations imply strongly correlated network states in a neural population. *Nature*, **440**(20), 1007–1012.
- Schneidman, E., Bialek, W., and Berry, M.J., II (2003). Synergy, redundancy, and independence in population codes. *J. Neurosci.*, **23**(37), 11539–11553.
- Shadlen, M.N. and Newsome, W.T. (1998). The variable discharge of cortical neurons: implications for connectivity, computation, and information coding. *J. Neurosci.*, **18**, 3870–3896.
- Shea-Brown, E., Josić, K., de la Rocha, J., and Doiron, B. (2008). Correlation and synchrony transfer in integrate-and-fire neurons: basic properties and consequences for coding. *Phys. Rev. Lett.*, **100**, 108102.
- Shlens, J., Field, G.D., Gauthier, J.L., Grivich, M.I., Petrusca, D., Sher, A., Litke, A.M., and Chichilnisky, E.J. (2006). The structure of multi-neuron firing patterns in primate retina. *J. Neurosci.*, **26**, 8254–8266.
- Silberberg, G., Bethge, M., Markram, H., Pawelzik, K., and Tsodyks, M. (2004). Dynamics of population rate codes in ensembles of neocortical neurons. *J. Neurophysiol.*, **91**, 704–709.
- Softky, W. and Koch, C. (1993). The highly irregular firing of cortical cells is inconsistent with temporal integration of random epsp's., **13**, 334–350.
- Stein, R.B. (1967). The information capacity of neurons using a frequency code. *Biophysical Journal*, **7**, 797–826.
- Stocks, N.G. (2000). Suprathreshold stochastic resonance in multilevel threshold systems. *Phys. Rev. Lett.*, **84**, 2310–2314.
- Stocks, N.G. and Mannella, R. (2001). Generic noise-enhanced coding in neuronal arrays. *Phys. Rev. E*, **64**, 030902.
- Svirskis, G. and Hounsgaard, J. (2003). Influence of membrane properties on spike synchronization in neurons: theory and experiments. *Network: Computation in Neural Systems*, **14**, 747–763.
- Thorpe, S., Fize, D., and Marlot, C. (1996). Speed of processing in the human visual system. *Nature*, **381**, 520–522.
- Tuckwell, H.C. (1988). *Introduction to Theoretical Neurobiology: Volume 2, Non-linear and Stochastic Theories*, Chapter 9. Cambridge University Press, New York.
- van Rossum, M., Turrigiano, G.G., and Nelson, S.B. (2002). Fast propagation of firing rates through layered networks of neurons. *J. Neurosci.*, **22**, 1956–1966.
- Zohary, E., Shadlen, M., and Newsome, W. (1994). Correlated neuronal discharge rate and its implications for psychophysical performance. *Nature*, **370**, 140–143.

POPULATION DENSITY METHODS IN LARGE-SCALE NEURAL NETWORK MODELLING

Daniel Tranchina

7.1 Introduction

Population density (also called probability density) methods have a rich history in theoretical and computational neuroscience. In earlier years, these methods were used in large part to study the statistics of spike trains (Tuckwell, 1988b, Wilbur and Rinzel, 1983). Starting in the 1990s (Kuramoto, 1991, Abbott and van Vreeswijk, 1993), population density function (PDF) methods have been used as an analytical and computational tool to study neural network dynamics. In this chapter, we will discuss the motivation and theory underlying PDF methods and a few selected examples of computational and analytical applications in neural network modelling. Chapter 6 of Gerstner and Kistler (2002) on population equations includes an integral-equation approach for population activity, not covered here.

7.2 Motivation for population density methods

7.2.1 Stochastic behaviour of neurons

Neurons in the central nervous system exhibit stochastic behaviour as a consequence of membrane channel noise and synaptic noise. One physiological role of stochastic behaviour is suggested by simulations of large-scale neural network activity. Models that do not include stochastic elements exhibit unphysiological synchronous activity with intrinsic network dynamics that code poorly the external input. Another role was suggested by Koch (1999), who pointed out that stochastic synaptic failure, with a probability that can be modulated, provides a mechanism for synaptic plasticity.

7.2.2 The large n problem

Simulation and mathematical analysis of electrical activity in large-scale neural networks can complement physiological experiments in developing an understanding of various parts of the brain, such as cortical areas involved in visual information processing (Ursino and La Cara, 2005, Rangan *et al.*, 2005, McLaughlin *et al.*, 2003, Krukowski and Miller, 2001, McLaughlin *et al.*, 2000, Somers *et al.*, 1995) and working memory (Miller and Wang, 2006, Teramae and Fukai, 2005, Wang, 1999). The number of individual neurons required in a neural

network model can be estimated by the number of neurons in a ‘functional sub-unit’ of the system being modelled. For example, an orientation hypercolumn in primary visual cortex (V1) in the primate is roughly $0.5 \times 0.5 \text{ mm}^2$, which represents an area in visual space of $0.25 \times 0.25 \text{ deg}^2$ in a parafoveal area. Each hypercolumn contains tens of thousands of neurons (Mountcastle, 1997) with several thousand synapses per neuron. Because there is extensive crosstalk between hypercolumns, numerous hypercolumns are required to make a realistic and useful model of function. The whole of the primary visual cortex contains roughly 4×10^8 neurons (Dorph-Petersen *et al.*, 2007).

If the stochastic behaviour of thousands of individual neurons and millions of synapses must be followed, the number of corresponding ordinary differential equations is huge. The enormous computation time and computer memory required to solve these equations can hinder progress that may emerge from realistic neural network simulations. Continuing progress in speeding up the computation time in models involving large numbers of individual neurons (Rangan and Cai, 2007, Rangan *et al.*, 2005) might obviate extensive further development of population density methods as a computational tool, but the analytical virtues of population density remain.

7.2.3 Many stochastic individual units turned to advantage

The population density method can in principle turn the liability of a large number of stochastic individual units into an advantage. If one can group together large numbers of biophysically similar neurons with similar network connectivity, one can track the distribution of neurons over state space instead of tracking the individual neurons. The distribution of neurons over state space is described by the *population density function* (PDF).

In the case of sparse connectivity among the populations, one grand density equation for the state variables of all populations is usually approximated by a system of separate density equations for each population. The populations are coupled through population firing rates.

The evolution equation for the density function of each population is a partial differential equation or a partial differential-integral equation. The number of state variables, i.e. the dimension of the state space, depends on the specifics of the underlying single-neuron model. In general, the population firing rate is given by the flux of probability across a surface in phase space. In the case of an integrate-and-fire (IF) neuron with instantaneous synaptic kinetics, there is only one state variable, the membrane voltage V , and the population firing rate is given by the flux of probability across the threshold voltage, v_{th} . The integrate-and-fire-or-burst (IFB) neuron model with instantaneous synaptic kinetics has two state variables, membrane voltage, and the calcium current inactivation variable, h (Casti *et al.*, 2002, Huertas and Smith, 2006). Synaptic kinetics add dimensions. For an IF neuron receiving excitatory synaptic input only, in which the unitary (elementary) postsynaptic conductance event has a single exponential time course (first-order kinetics), there are two state variables, membrane

voltage, V , and excitatory synaptic conductance, G_e (Apfaltter *et al.*, 2006). The population firing rate is given by the integral of the flux of probability per unit conductance across the threshold voltage v_{th} . If inhibitory synaptic input with first-order kinetics is added, there is an additional state variable for the inhibitory conductance G_i . More complex models add additional state variables.

7.3 Population density formulation for a single population with current driven synapses

We begin our exposition with a population density formulation that was introduced by Bruce Knight, Larry Sirovich and colleagues (Knight *et al.*, 1996, 2000, Omurtag *et al.*, 2000*a,b*, Knight, 2000). Their approach was novel in three ways: they considered postsynaptic potentials of physiological magnitude; they applied their methods to large-scale modelling of a physiological neural network (Omurtag *et al.*, 2000*a*); and their method served as a time-saving computational tool. Contemporaneous applications of PDF methods utilized Fokker–Planck approximations (Brunel and Hakim, 1999, Brunel, 2000) and highlighted insights that could be obtained by analytical techniques. Plessner and Gerstner (2000) further simplified the model for synaptic noise by replacing diffusive noise in the Fokker–Planck equation by a carefully chosen escape noise.

7.3.1 Poisson synaptic input

In population density methods it is usually assumed that the arrival times of the *unitary* postsynaptic input events are governed by a Poisson process (Gerstein and Mandelbrot, 1964). A unitary or elementary event is a postsynaptic response to the release of a synaptic transmitter at a single axon terminal upon the arrival of an action potential there. Strictly speaking, a composite train of synaptic input events can only be Poisson if all the spike trains of the input neurons are Poisson. The Poisson approximation is justified in the regime where each neuron receives input from neurons with low firing rates, whose firing times are conditionally independent (Câteau and Reyes, 2006). In practice, the conditional independence of synaptic inputs can only be approximated when the network connectivity is sparse. Fortunately, simulations comparing results obtained by direct Monte Carlo simulations to corresponding population density results have shown that in some network settings at least, connectivity need not be terribly sparse, and that violation of the Poisson assumption does not always cause large errors (Nykamp and Tranchina, 2000, 2001, Apfaltter *et al.*, 2006). See also Chapter 8 of this book. An example where the Poisson approximation fails dramatically is demonstrated by Câteau and Reyes (2006).

7.3.2 The integrate-and-fire (IF) model neuron

In the leaky *integrate-and-fire*, single-compartment model (Tuckwell, 1988*a*, Dayan and Abbott, 2001, Koch, 1999, Burkitt, 2006*a,b*, Brunel and van Rossum, 2007), all spatially extended parts of a neuron are approximated as a single isopotential compartment, and the fast dynamics of the voltage and voltage-dependent

conductances when an action potential is generated are collapsed into one instantaneous event. Models based on phase reduction (Ermentrout and Kopell, 1984; Gutkin and Ermentrout, 1998) have also been widely used in PDF methods (Brown *et al.*, 2004). Such models, or the quadratic integrate-and-fire model (Brunel and Latham, 2003), might turn out to be equally or more suitable.

In the IF model the membrane voltage evolves according to a simple ordinary differential equation. When the stochastic membrane potential, $V(t)$, reaches a threshold voltage v_{th} , the neuron is said to fire an action potential or *spike*. If a refractory period is included in the model, it is a period immediately after the neuron fires in which the membrane potential is undefined, but the conductances evolve as usual; once this period has elapsed the voltage is reset to v_{reset} .

7.3.3 Current-driven instantaneous excitatory synaptic input only

We begin by discussing the simple model in which synaptic input consists of excitatory pulses of current that cause the voltage to jump. This treatment follows closely that of Omurtag *et al.* (2000b). If we shift and normalize voltage so that $v = 0$ and $v = 1$ correspond to the resting and threshold voltage, respectively, the random differential equation for V is

$$\frac{dV}{dt} = -\frac{1}{\tau_m} V + I(t), \quad \text{for } 0 \leq V < 1 \quad (7.1)$$

where

$$I(t) = a \sum_k \delta(t - T^k); \quad (7.2)$$

$I(t)$ is scaled current (units, s^{-1}); τ_m is the membrane time constant; T^k are the random arrival times of the unitary postsynaptic current events; a is the fixed jump in voltage; and T^k are governed by a modulated Poisson process with rate $\nu(t)$. Later, to be more realistic, we will make the unitary event magnitude a random variable (Omurtag *et al.*, 2000b).

In this model, the state of a neuron is completely determined by its membrane voltage, because the synaptic input consists of instantaneous events that occur at discrete time points.

7.3.4 Evolution equation for the population density function

The population density function $\rho(v, t)$ is defined by

$$\Pr(V(t) \in (v_1, v_2)) = \int_{v_1}^{v_2} \rho(v, t) dv. \quad (7.3)$$

The evolution equation for $\rho(v, t)$ is found by a conservation-of-probability argument. We define an arbitrary interval (v_0, v) and compute the rate of change of total probability in this interval. To do so, we define a probability flux $J(v, t)$, which is the probability per unit time crossing v from below/above for $J(v, t)$

positive/negative. With this definition, in the absence of sources of probability within the interval (v_0, v) ,

$$\frac{d}{dt} \int_{v_0}^v \rho(v', t) dv' = J(v_0, t) - J(v, t),$$

or

$$\int_{v_0}^v \frac{\partial}{\partial t} \rho(v', t) dv' = J(v_0, t) - J(v, t). \quad (7.4)$$

Equation (7.4) states that the rate of change of probability in an interval is given by the rate at which probability enters, minus the rate at which probability leaves the interval. The general 1-D evolution equation is obtained by taking the partial derivative of Eqn (7.4) with respect to v to obtain

$$\frac{\partial}{\partial t} \rho(v, t) = -\frac{\partial}{\partial v} J(v, t). \quad (7.5)$$

The generalization when there is a vector of state variables is $\partial \rho(\vec{x}, t)/\partial t = -\nabla \cdot \vec{J}$, where \vec{J} is a probability flux vector with components in each direction of \vec{x} .

The probability flux can be decomposed into two parts:

$$J(v, t) = J_l(v, t) + J_e(v, t). \quad (7.6)$$

$J_l(v, t)$ is a drift or advection part stemming from the decay of voltage towards rest in the absence of any synaptic inputs. $J_e(v, t)$ is an excitatory part stemming from the jumps in voltage upon arrival of unitary postsynaptic events with rate $\nu(t)$. The advective flux, $J_l(v, t)$, is the velocity of the state variable v multiplied by the probability density

$$J_l(v, t) = \left(-\frac{1}{\tau_m}v\right) \rho(v, t). \quad (7.7)$$

We continue by deriving the excitatory flux, $J_e(v, t)$. Because a synaptic input event causes a voltage jump $\Delta v = a$, any neuron with starting voltage v' between $v - a$ and v will contribute to the flux of probability across v in the time interval $(t, t + dt)$ if it receives an input in this time interval. According to the Poisson assumption, the probability of an event in $(t, t + dt)$ is $\nu(t) dt$. The probability that a neuron is in voltage interval $(v', v' + dv')$ and experiences a synaptic input event in $(t, t + dt)$ is simply $(\rho(v', t) dv')(\nu(t) dt)$; the probabilities are multiplied because these two probabilistic events are independent by assumption. The total probability of crossing v from below in $(t, t + dt)$ is obtained by summing over the mutually exclusive ways this event can be realized, and it is equal to

$$\left(\int_{\max(0, v-a)}^v \rho(v', t) dv' \right) (\nu(t) dt).$$

The probability crossing v per unit time, $J_e(t)$, is obtained by dividing by the width of the time interval, dt :

$$J_e(v, t) = \nu(t) \int_{\max(0, v-a)}^v \rho(v', t) dv'. \quad (7.8)$$

The population firing rate $r(t)$ is the probability per unit time that a neuron crosses threshold; so it is given by the excitatory flux evaluated at the threshold voltage, v_{th} (equal to 1 according to the present definition of v):

$$\begin{aligned} r(t) &= J_e(1, t) \\ &= \nu(t) \int_{\max(0, 1-a)}^1 \rho(v', t) dv'. \end{aligned} \quad (7.9)$$

Putting together Eqns (7.5)–(7.8) gives

$$\frac{\partial}{\partial t} \rho = -\frac{\partial}{\partial v} \left(-\frac{1}{\tau_m} v \rho(v, t) + \nu(t) \int_{\max(0, v-a)}^v \rho(v', t) dv' \right) + \delta(v)r(t). \quad (7.10)$$

The source term, $\delta(v)r(t)$ in Eqn (7.10) reflects the resetting of voltage to rest ($v = 0$) after a neuron crosses threshold.

When one allows for a random unitary event size, A , the excitatory flux $J_e(v, t)$ is somewhat different, because any neuron with voltage $v' < v$ can contribute to the flux across v provided that $A > v - v'$. If we define $f_A(x)$ as the probability density function for A , and $\tilde{F}_A(x) \equiv \Pr(A > x)$ as the corresponding complementary cumulative distribution function, the evolution equation with random unitary events is

$$\frac{\partial}{\partial t} \rho = -\frac{\partial}{\partial v} \left(-\frac{1}{\tau_m} v \rho(v, t) + \nu(t) \int_0^v \tilde{F}_A(v - v') \rho(v', t) dv' \right) + \delta(v)r(t), \quad (7.11)$$

where

$$r(t) = \int_0^1 \tilde{F}_A(1 - v') \rho(v', t) dv'. \quad (7.12)$$

It can be proven that the stochastic processes that give rise to Eqns (7.11) and (7.10) give $\rho(v_{\text{th}}, t) = 0$ (where $v_{\text{th}} = 1$ in the present units).

7.3.5 Fokker–Planck approximation: instantaneous current-driven synapses and correspondence to white noise input

In the regime where the unitary event magnitude is small enough, and the rate of events ν is high enough, Eqn (7.10) or (7.11) can be approximated by a

Fokker–Planck (drift-diffusion) equation (Risken, 1996). Fokker–Plank equations are generally more amenable to mathematical analysis and easier to solve numerically than their exact equation counterparts. The basic idea of modelling Poisson synaptic inputs this way goes back to Gerstein and Mandelbrot (1964). Following Omurtag *et al.* (2000b) the Fokker–Planck equation can be obtained formally by approximating $\rho(v', t)$ in Eqn (7.10) or (7.11) by a truncated first-order Taylor series centred on $v' = v$. The result, after carrying out the integration over v' , is:

$$\frac{\partial}{\partial t} \rho = -\frac{\partial}{\partial v} \left(\left[-\frac{1}{\tau_m} v + \nu(t) \alpha(v) \right] \rho - \nu(t) \frac{\beta^2(v)}{2} \frac{\partial \rho}{\partial v} \right) + \delta(v) r(t). \quad (7.13)$$

In the case of a deterministic unitary event (Eqn (7.10)), $\alpha(v) = H(v - a) a + H(a - v) v$ and $\beta^2(v) = [H(v - a) a + H(a - v) v]^2$, where $H(\cdot)$ is the Heaviside step function. For random unitary events (Eqn (7.11)),

$$\alpha(v) = \mu_A + \left[v \tilde{F}_A(v) - \int_v^\infty x f_A(x) dx \right],$$

and

$$\beta^2(v) = \mu_{A^2} + \left[v^2 \tilde{F}_A(v) - \int_v^\infty x^2 f_A(x) dx \right].$$

In the population density literature, the voltage dependences of α and β are usually ignored. For the case of deterministic unitary events, $\alpha(v)$ and $\beta^2(v)$ are approximated as a and a^2 , respectively; and, in the case of random unitary events, by μ_A and μ_{A^2} , respectively, where we use μ_X to denote the expected value $\mathbf{E}[X]$. The diffusion term in Eqn (7.13) and the absorbing boundary at $v = v_{\text{th}}$ require the boundary condition $\rho(v_{\text{th}}, t) = 0$. This boundary condition is consistent with $\rho(v_{\text{th}}, t) = 0$ for the problems with voltage jumps above, Eqns (7.10) and (7.11). Consequently, the firing rate (probability flux at $v = v_{\text{th}}$) is given by

$$r(t) = -\nu(t) \frac{\beta^2(v_{\text{th}})}{2} \frac{\partial \rho}{\partial v}(v_{\text{th}}, t) \quad (7.14)$$

The Fokker–Planck equation (7.13) corresponds to the evolution equation (7.1) for V in which the injected current is

$$I(t) = \nu(t) \alpha(v) + \sqrt{\nu(t)} \beta(v) Z(t), \quad (7.15)$$

where $Z(t)$ is stationary zero-mean Gaussian white noise with autocorrelation function $\mathbf{E}[Z(t_0)Z(t_0 + t)] = \delta(t)$ (Risken, 1996). In the classical literature, the evolution equation for V is written as the Itô stochastic differential equation

$$dV = \left(-\frac{1}{\tau_m} V + \nu(t) \alpha(V) \right) dt + \sqrt{\nu(t)} \beta(V) dW, \quad (7.16)$$

where $W(t)$ is a standard Wiener process. See also Fourcaud and Brunel (2002).

7.4 Population firing rate and distribution of neurons over voltage in the steady state

The inclusion of synaptic noise in the population density approach has a dramatic effect on the relationship between the rate of synaptic input and the output population firing rate. Figure 7.1(a) compares steady-state firing rates for stochastic and deterministic synaptic input. The population density firing rate was computed for stochastic input with $\mu_A = 0.05$ (thick grey line), so that, on average, 20 simultaneous events would suffice to kick a neuron over the firing threshold from the resting voltage. The deterministic limit (thin black line) corresponds to $a \rightarrow 0$, $\nu \rightarrow \infty$, with $\nu \mu_A$ held fixed. As this limit is approached, the Fokker–Planck approximation applies, and the diffusion term in Eqn (7.13) becomes zero, because $\nu \mu_{A^2} \rightarrow 0$. In the steady state, where $\partial \rho / \partial t = 0$, Eqn (7.13) becomes

$$0 = -\frac{\partial}{\partial v} \left\{ \left[-\frac{1}{\tau_m} v + (\nu \mu_A) \right] \rho \right\}. \quad (7.17)$$

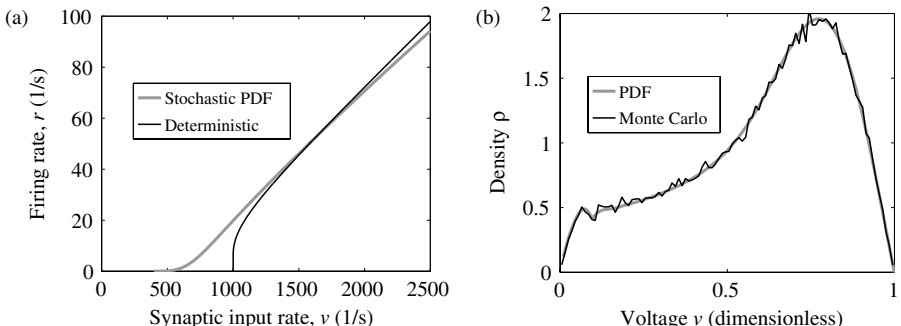


FIG. 7.1: Population firing rate and distribution of neurons over voltage. (a) Comparison of population firing rate versus synaptic input rate for random and deterministic synaptic input. The population density curve (thick grey) was computed for unitary postsynaptic current events that cause a random jump A in voltage, with density function (Apfaltlter *et al.*, 2006) $f_A(x) = 3x(2\mu_A - x)/(4\mu_A^3)$, $\mu_A = 0.05$, and coefficient of variation $\sigma_A/\mu_A = 0.45$. The thin black line corresponds to the deterministic limit $a \rightarrow 0$, $\nu \rightarrow \infty$, with $\mu_A \nu$ held fixed. Synaptic noise in the population density function approach smoothes the input–output curve. Noise causes the population firing rate to encode synaptic input over a wider range of inputs and in a more graded manner. (b) Distribution of neurons over voltage in the steady state with $\nu = 1000/\text{s}$. Same parameters as in (a). The thick grey curve is from the solution of Eqn (7.11). The thin black curve is a relative frequency estimate of the population density from direct Monte Carlo simulation with 100 000 neurons and 100 voltage bins of uniform width.

The term in curly brackets in Eqn (7.17) is still the excitatory flux. Equation (7.17) states that this flux is constant; therefore it must be equal to the flux at $v = 1$, which is the firing rate, r . Setting the term in curly brackets in Eqn (7.17) equal to r gives the solution for the steady density in terms of r , $\rho(v) = \tau_m r / [(\nu\mu_A)\tau_m - v]$, for $(\nu\mu_A)\tau_m > 1$. Note that $(\nu\mu_A)\tau_m > 1$ is the steady-state voltage in the absence of resetting voltage after crossing the threshold voltage. The constraint that the integral over v of $\rho(v)$ equals 1 gives an explicit expression for r (Sirovich *et al.*, 2000):

$$r = \frac{-1}{\tau_m \log \left(1 - 1 / [(\nu\mu_A)\tau_m] \right)}, \quad \text{for } \nu > 1 / (\tau_m \mu_A). \quad (7.18)$$

It is worth noting that the same equation for firing rate can be derived by computing the time T required for a neuron's voltage to evolve from $v = 0$ to $v = 1$, and then setting $r = 1/T$. For ν falling below threshold, i.e. $\nu < 1 / (\tau_m \mu_A)$, the firing rate $r = 0$, and $\rho(v) = \delta(v - \nu\mu_A\tau_m)$. The deterministic firing rate curve in Fig. 7.1(a) displays a firing threshold. At the threshold rate of synaptic input ($\nu = 1000/s$) the firing rate curve has infinite slope. The effect of synaptic noise, captured by the population density approach, is to smooth the input-output curve and to make the population firing rate encode synaptic input in a more graded manner over a wider range of inputs.

Figure 7.1(b) shows the distribution of neurons over voltage in the steady state with $\nu = 1000/s$. The other parameters are the same as those in panel (a). The thick grey curve is from solution of the PDF, Eqn (7.11). The thin black curve is a relative frequency estimate of the population density from direct Monte Carlo simulation with 100 000 neurons and 100 voltage bins of uniform width. In the Monte Carlo simulation all neurons started from resting voltage and were allowed to respond to Poisson synaptic inputs for 200 ms. The relative frequency estimate (thin black line) represents a snapshot at $t = 200$ ms.

7.5 Population firing rate dynamics with instantaneous synaptic kinetics: approach to a new equilibrium state

Population density methods have been used to analyse the dynamics of the population firing rate in the presence of synaptic noise. Population density firing rate dynamics are more complex than the dynamics given by deterministic rate models based on simple systems of ordinary differential equations.

For the purposes of analysing dynamics, it is useful to write Eqn (7.11) as

$$\frac{\partial \rho}{\partial t} = \mathcal{L}(\nu(t)) \rho, \quad (7.19)$$

where \mathcal{L} is a linear operator depending on $\nu(t)$ (Knight *et al.*, 2000, Knight, 2000, Brunel and Hakim, 1999). Furthermore, the population firing rate can be thought of as a linear functional of ρ with explicit dependence on $\nu(t)$:

$$r(t) = \mathcal{M}(\nu(t))\{\rho\} \quad (7.20)$$

This way of writing the evolution equation for ρ and the firing rate equation generalizes in a straightforward fashion to more realistic underlying single-neuron models (Apfaltre *et al.*, 2006). The linear-operator perspective is useful both from theoretical and computational standpoints (Knight *et al.*, 2000, Knight, 2000, Brunel and Hakim, 1999, Sirovich, 2003, Apfaltre *et al.*, 2006).

When Eqns (7.19) and (7.20) are discretized for purposes of numerical solution, the function $\rho(v, t)$ becomes a time-dependent vector $\vec{\rho}(t)$, whose elements correspond to the discretized voltage points; the linear operator becomes a matrix; and the linear functional becomes an inner product. Thus, Eqn (7.19) becomes a system of first-order ordinary differential equations. The evolution equation for $\vec{\rho}$ is of the form

$$\frac{d}{dt}\vec{\rho} = \mathbf{Q}(\nu(t))\vec{\rho}, \quad (7.21)$$

and the firing rate is given by

$$r(t) = \vec{b}(\nu(t)) \cdot \vec{\rho}, \quad (7.22)$$

where this notation indicates that \mathbf{Q} is a matrix and \vec{b} is a vector, and that both depend on the synaptic input rate $\nu(t)$. The discretization of the original evolution equation and boundary condition builds the boundary condition into the matrix \mathbf{Q} .

Knight *et al.* (2000) considered the special case of a piecewise-constant excitatory synaptic input rate. In the following, we will drop the argument ν with the understanding that ν is a constant parameter. As explained by Knight (2000), the generic situation is one where the matrix \mathbf{Q} and its transpose have a complete set of bi-orthonormal eigenvectors, $\vec{\phi}_n$ and $\vec{\psi}_n$, respectively; i.e. $\vec{\psi}_j^* \cdot \vec{\phi}_k = \delta_{jk}$, where the asterisk denotes complex conjugate. Furthermore, the eigenvalues corresponding to $\vec{\phi}_j$ and $\vec{\psi}_j$ are identical. The zero eigenvalue corresponds to the eigenvector that is the steady state solution of Eqn (7.21). The non-zero eigenvalues all have negative real part, and some come in complex-conjugate pairs. Sirovich (2003) presented a thorough discussion of eigenfunction theory for PDF equations.

Let us define Φ as the matrix whose columns are the eigenvectors of \mathbf{Q} , and Ψ as the matrix whose rows are the eigenvectors of \mathbf{Q}^T . When a coordinate system change is made using the eigenvectors of \mathbf{Q} as a basis, one writes

$$\vec{\rho}(t) = \Phi \vec{c}(t). \quad (7.23)$$

After substituting Eqn (7.23) into Eqn (7.21), and multiplying both sides on the left by Ψ^* , one obtains,

$$\frac{d}{dt}\vec{c} = \Lambda \vec{c}, \quad (7.24)$$

where $\mathbf{\Lambda}$ is a diagonal matrix whose elements are eigenvalues of the matrix \mathbf{Q} . Thus, Eqn (7.21) is transformed into a system of uncoupled first-order ordinary differential equations for the time-dependent coefficients, $c_j(t)$. Equation (7.24) has exponential solutions

$$c_j(t) = c_j(0) e^{\lambda_j t}. \quad (7.25)$$

The coefficients $c_j(0)$ must be chosen to satisfy the initial condition

$$\Phi \vec{c}(0) = \vec{\rho}(0). \quad (7.26)$$

Multiplying both sides of Eqn (7.26) on the left by Ψ^* determines

$$\vec{c}(0) = \Psi^* \vec{\rho}(0). \quad (7.27)$$

The solutions for $\vec{\rho}(t)$ is found by substituting Eqns (7.27) and (7.25) into Eqn (7.23) to give

$$\vec{\rho}(t) = \sum_j \left(\vec{\psi}_j^* \cdot \vec{\rho}(0) \right) e^{\lambda_j t} \vec{\phi}_j. \quad (7.28)$$

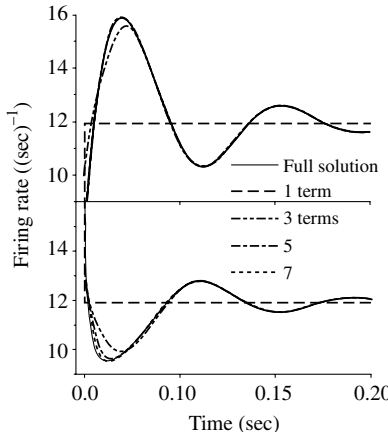


FIG. 7.2: Population firing rate response to a step in synaptic input rate. The rate of excitatory synaptic input has been held constant for $t < 0$, so that the population is in a steady state at $t = 0^-$; at time $t = 0$ the synaptic input rate is stepped to a higher (upper panel) or lower (lower panel) value. As the legend indicates, the full solution is compared to those using only one term (eigenvector with zero eigenvalue corresponding to the new steady-state solution), three, five, and seven terms in the eigenvector expansion in Eqn (7.28). The full solution is approximated very well by only seven terms. Figure taken from Knight *et al.* (2000).

Finally, the firing rate is obtained by substituting (7.28) into Eqn (7.22) to give

$$r(t) = \sum_j \left(\vec{\psi}_j^* \cdot \vec{\rho}(0) \right) \left(\vec{b} \cdot \vec{\phi}_j \right) e^{\lambda_j t}. \quad (7.29)$$

Figure 7.2 (Fig. 3 of Knight *et al.* 2000) shows results for the population firing rate response to a step change in synaptic input rate. In this figure, the rate of excitatory synaptic input has been held constant for $t < 0$, so that the population is in a steady state at $t = 0^-$. At $t = 0$ the synaptic input rate is stepped to a higher (upper panel) or lower (lower panel) value. A remarkable finding of Knight *et al.* (2000) is that one needs only the first few eigenvectors, those whose eigenvalues have real parts smallest in magnitude, in Eqn (7.29), to do a good job of approximating the exact solution. In Fig. 7.2 the full solution is compared to those using only one term (the eigenvector with zero eigenvalue, corresponding to the new steady-state solution), three, five, and seven terms. The full solution is well approximated by keeping only seven terms.

7.6 Conductance driven excitatory and inhibitory synapses

A more realistic single-neuron model for neural network modelling is one with conductance-driven excitatory and inhibitory synaptic input. For the sake of clarity here, we will retain the units and absolute value of the membrane voltage difference v . The evolution equation for the random membrane potential $V(t)$ for an IF neuron when there are excitatory and inhibitory synapses is given by

$$c \frac{dV}{dt} + g_r(V - \varepsilon_r) + \hat{G}_e(t)(V - \varepsilon_e) + \hat{G}_i(t)(V - \varepsilon_i) = 0, \quad (7.30)$$

between firing events, where c is the membrane capacitance, g_r is the resting conductance, ε_r is the resting potential and ε_e and ε_i are the excitatory and inhibitory equilibrium potentials, respectively. In this model, the membrane voltage $V \in (\varepsilon_i, v_{th})$, and $\varepsilon_i < \varepsilon_r < v_{th} \ll \varepsilon_e$. The excitatory and inhibitory conductances $\hat{G}_e(t)$ and $\hat{G}_i(t)$ are time-dependent random variables because the times and magnitudes of the underlying unitary postsynaptic events are taken to be random.

After dividing Eqn (7.30) by g_r we obtain

$$\tau_m \frac{dV}{dt} + (V - \varepsilon_r) + G_e(t)(V - \varepsilon_e) + G_i(t)(V - \varepsilon_i) = 0 \quad (7.31)$$

where $G_{e/i}(t) = \hat{G}_{e/i}/g_r$ is the normalized excitatory/inhibitory conductance and $\tau_m = c/g_r$ is the membrane time constant.

For the sake of concreteness, we will assume that the synaptic conductances obey first-order kinetics, where the rise in conductance upon arrival of a unitary synaptic event is instantaneous and the decline is exponential. Therefore,

the evolution of each synaptic conductance is given by an equation of the form (Apfaltre *et al.*, 2006)

$$\tau_s \frac{d}{dt} G_s(t) + G_s(t) = \sum_k A_s^k \delta(t - T_s^k), \quad (7.32)$$

where the subscript $s = e$ for excitatory or $s = i$ for inhibitory conductance; T_s^k is the random arrival time of the k th such input; A_s^k/τ_s is the (non-dimensional) jump in conductance upon arrival of a unitary event; and A_s^k is the area under the unitary event waveform, i.e. the integral of the normalized conductance change. We treat A_s^k as independent identically distributed random variables, with a specified probability density function $f_{A_s}(x)$. The random unitary postsynaptic event magnitude reflects the random number of neurotransmitter molecules per synaptic vesicle and the stochastic transmission at each of several synapses that a presynaptic neuron typically makes on a postsynaptic target.

With the single-neuron description above, the state variables are the membrane voltage V , and the excitatory and inhibitory conductances G_e and G_i , respectively.

7.6.1 Instantaneous synaptic conductances

To reduce the complexity of computational and analytical problems, the number of state variables can be reduced from 3 to 1 by taking the limit $\tau_s \rightarrow 0$ in Eqn (7.32). With this approximation the synaptic conductances are always zero except at a discrete set of time points. Consequently, each synaptic conductance is a sum of delta functions,

$$G_s(t) = \sum_k A_s^k \delta(t - T_s^k), \quad (7.33)$$

and the evolution equation for the membrane voltage at all times except those at which the synaptic events arrive is given by

$$\frac{dV}{dt} = -\frac{1}{\tau_m} (V - \varepsilon_r). \quad (7.34)$$

We follow the presentations of Omurtag *et al.* (2000b) and Nykamp and Tranchina (2000). The probability flux can be decomposed into three components. The leakage component $J_l(v, t)$ in this case is given by

$$J_l(v, t) = -\frac{1}{\tau_m} (v - \varepsilon_r) \rho(v, t). \quad (7.35)$$

The excitatory component, $J_e(v, t)$ stems from the jump in voltage upon arrival of a unitary postsynaptic conductance event. In principle, any neuron with starting voltage $v' < v$ can contribute to the flux of probability across v as long as the synaptic conductance event is large enough to cause a jump $\Delta v > v - v'$.

To determine the voltage jump upon arrival of an excitatory event, consider an infinitesimal time interval surrounding the event time T . If we combine Eqns (7.33) and (7.31) and consider a single excitatory event only, we have

$$\frac{dv}{dt} = -\frac{1}{\tau_m} \left[(v - \varepsilon_r) + A_e \delta(t - T) (v - \varepsilon_e) \right]. \quad (7.36)$$

To compute the jump in voltage, we divide (7.36) by $(v - \varepsilon_r)$, integrate from T^- to T^+ , and solve for $\Delta v \equiv v(T^+) - v(T^-)$. The result is

$$\Delta v = \Gamma_e (\varepsilon_e - v(T^-)), \quad (7.37)$$

where $\Gamma_s \equiv 1 - \exp(-A_s/\tau_m)$ for $s = i$ or e . Thus, if a neuron has a starting voltage v' , an excitatory synaptic input event will cause its voltage to jump across v if

$$\Delta v = \Gamma_e (\varepsilon_e - v') > v - v',$$

which implies

$$\Gamma_e > \frac{v - v'}{\varepsilon_e - v'}. \quad (7.38)$$

The total excitatory flux across v is obtained by summing up contributions from all infinitesimal intervals between ε_i and v :

$$J_e(v, t) = \nu_e(t) \int_{\varepsilon_i}^v \tilde{F}_{\Gamma_e} \left(\frac{v - v'}{\varepsilon_e - v'} \right) \rho(v', t) dv', \quad (7.39)$$

where $\tilde{F}_{\Gamma_e/(i)}(x) \equiv \Pr(\Gamma_{e/i} > x)$.

Because a neuron can only cross threshold as a consequence of an excitatory synaptic input, the population firing rate, $r(t)$, is the excitatory flux evaluated at $v = v_{th}$, as in the simpler current injection model above.

The inhibitory component of the probability flux $J_i(v, t)$ is computed in a similar manner. This flux is negative, because neurons experiencing an inhibitory input cross v from above. Any neuron with voltage v' such that $v < v' < v_{th}$ can contribute to this flux if the voltage jump is large enough.

$$J_i(v, t) = -\nu_i(t) \int_v^{v_{th}} \tilde{F}_{\Gamma_i} \left(\frac{v' - v}{v' - \varepsilon_i} \right) \rho(v', t) dv'. \quad (7.40)$$

The explicit evolution equation for $\rho(v, t)$, corresponding to Eqn (7.4) with

$$J(v, t) = J_l(v, t) + J_e(v, t) + J_i(v, t), \quad (7.41)$$

including the source term that comes from resetting voltage to v_{reset} upon crossing v_{th} , is

$$\begin{aligned} \frac{\partial}{\partial t} \rho(v, t) = & -\frac{\partial}{\partial v} \left\{ -\frac{1}{\tau_m} (v - \varepsilon_r) \rho(v, t) + \nu_e(t) \int_{\varepsilon_i}^v \tilde{F}_{\Gamma_e} \left(\frac{v - v'}{\varepsilon_e - v'} \right) \rho(v', t) dv' \right. \\ & \left. - \nu_i(t) \int_v^{v_{\text{th}}} \tilde{F}_{\Gamma_i} \left(\frac{v' - v}{v' - \varepsilon_i} \right) \rho(v', t) dv' \right\} + r(t) \delta(v - v_{\text{reset}}), \end{aligned} \quad (7.42)$$

where

$$r(t) = \nu_e(t) \int_{\varepsilon_i}^{v_{\text{th}}} \tilde{F}_{\Gamma_e} \left(\frac{v - v'}{\varepsilon_e - v'} \right) \rho(v', t) dv'. \quad (7.43)$$

If a refractory period with duration τ_{ref} is included in the model, the term $r(t)$ in Eqn (7.42) is replaced by $r(t - \tau_{\text{ref}})$. An equivalent way to write Eqn (7.42) is to omit the source term, state that Eqn (7.42) applies for $v \neq v_{\text{reset}}$, and impose the condition that the jump in flux at $v = v_{\text{reset}}$ is equal to the firing rate, i.e. $J(v_{\text{reset}}^+) - J(v_{\text{reset}}^-) = r(t)$, in the case of no refractory period, or $r(t - \tau_{\text{ref}})$ with a refractory period.

The evolution equation for the population density function, Eqn 7.42, is exact regardless of the magnitudes or rates of synaptic input. This allows one to consider physiological unitary postsynaptic conductance events that give postsynaptic potentials that are typically on the order of 0.1–1 mV.

7.6.2 Fokker–Planck approximation with instantaneous excitatory and inhibitory synaptic conductances

In the regime of tiny unitary synaptic events and high rates, Eqn (7.42) can be approximated by a Fokker–Planck equation. As in the current injection problem above, it is obtained by a first-order truncated Taylor series approximation of $\rho(v', t)$, centred on $v' = v$, for each integrand in Eqn (7.42). The boundaries at $v = \varepsilon_i$ and at $v = v_{\text{th}}$ affect the drift term and diffusion coefficient in the neighbourhood of each boundary, in the Fokker–Planck equation (Nykamp and Tranchina, 2000). If we ignore the effects of the boundaries on the drift and diffusion coefficients, and use the fact that $\Gamma_s \approx A_s/\tau_m$ when A_s is small, we obtain the following approximate form of the exact Fokker–Planck equation:

$$\begin{aligned} \frac{\partial}{\partial t} \rho(v, t) = & -\frac{\partial}{\partial v} \left\{ -\frac{1}{\tau_m} \left[(v - \varepsilon_r) + \nu_e(t) \mu_{A_e}(v - \varepsilon_e) + \nu_i(t) \mu_{A_i}(v - \varepsilon_i) \right] \rho(v, t) \right. \\ & \left. - \left[\frac{1}{2} \frac{\nu_e(t) \mu_{A_e}^2}{\tau_m^2} (v - \varepsilon_e)^2 + \frac{1}{2} \frac{\nu_i(t) \mu_{A_i}^2}{\tau_m^2} (v - \varepsilon_i)^2 \right] \frac{\partial \rho}{\partial v} \right\} \\ & + r(t) \delta(v - v_{\text{reset}}). \end{aligned} \quad (7.44)$$

This Fokker–Plank equation (Eqn (7.44)) corresponds to random synaptic conductances with deterministic and Gaussian white-noise components:

$$G_s(t) = \nu_s(t)\mu_{A_s} + \sqrt{\nu_s(t)\mu_{A_s^2}} Z_s(t) \quad (7.45)$$

where $Z_s(t)$ are independent Gaussian white-noise sources, as defined above, for $s = e, i$.

7.7 Application to neural network simulations: general principles

Neural network simulation in the population density framework, as originally envisioned by Knight *et al.* (1996), involves defining a population density function for each population, so that $\rho^k(v, t)$ is the density function for population k , and $r^k(t)$ is the corresponding population firing rate. Neurons within each population have similar biophysical properties and similar network connectivity. We define a connectivity matrix with elements W_{jk} which gives the number of synapses made by neurons in population j onto each individual neuron in population k . In a direct Monte Carlo simulation with individual neurons, W_{jk} can be interpreted probabilistically as the expected number of synapses. In some neural network models an external input from another brain area is specified by a separate model for that input, and each population of neurons receives external input and/or input from other populations in the model. In the context of a model in which neurons within a population receive excitatory/inhibitory input through only one class of excitatory/inhibitory postsynaptic receptors, and in which all excitatory/inhibitory unitary postsynaptic events are statistically equivalent, each population is simply classified as either excitatory (E) or inhibitory (I).

As each population, with density $\rho^k(v, t), k = 1, 2, \dots, m$, is either excitatory or inhibitory, we denote the set of excitatory indices by Λ_E and the set of inhibitory indices by Λ_I , i.e. $\{\rho^k(v, t) \mid k \in \Lambda_{E/I}\}$ is the set of density functions for excitatory/inhibitory populations.

If the excitatory and inhibitory external input rates to population k are $\nu_{e,o}^k(t)$ and $\nu_{i,o}^k(t)$, then the total input rates to population k are obtained by simply summing up the various components:

$$\nu_{e/i}^k(t) = \nu_{e,i,o}^k(t) + \sum_{j \in \Lambda_{E/I}} W_{jk} \int_0^\infty \alpha_{jk}(t') r^j(t - t') dt', \quad (7.46)$$

where $\alpha_{jk}(t')$ is the probability density function for the random synaptic delay between the firing of an action potential in population j and the arrival time of the resulting unitary postsynaptic conductance event in a neuron in population k .

7.8 Orientation tuning in primary visual cortex

Our purposes here are to show a specific numerical implementation of population density methods, and to address the practical question of to what extent these

methods can approximate networks in which the populations contain only a modest number of neurons with connectivity that is not sparse.

Neurons in the primary visual cortex (V1) respond preferentially to oriented bars, edges, or gratings over a narrow range of orientations, and each orientation around the clock is represented by some subset of neurons within an orientation hypercolumn. Salient features of orientation tuning in the visual cortex are that the sharpness of tuning is almost independent of stimulus contrast, and the tuning of cortical neurons is sharper than that expected from the feed-forward input from neurons in the lateral geniculate nucleus (LGN) of the thalamus alone.

Omurtag *et al.* (2000a) implemented a population density model of the input layer in one isolated hypercolumn of the primary visual cortex (V1). They applied their PDF methods to simulate an experimental study of the dynamics of orientation tuning that used a spike-triggered averaging technique (Ringach *et al.*, 1997). Omurtag *et al.* (2000a) found good agreement between theory and experiment.

Nykamp and Tranchina (2000) presented a similar PDF model which was loosely based on the model of orientation tuning in the cat visual cortex by Somers *et al.* (1995). In the Nykamp and Tranchina (2000) model, neurons in the hypercolumn received input from the same part of visual space but had different preferred orientations that spanned the full set of 180°. In this model cortical neurons had broad orientation tuning in the absence of cortical–cortical interactions as a consequence of anisotropic projections from the LGN to the cortical neurons. Neurons were grouped into populations with similar preferred orientation by dividing the orientation space into a set of 18 discrete orientations. At each ‘preferred’ orientation, one excitatory (E) and one inhibitory (I) population density function was defined. As in the Somers *et al.* (1995) model, cortical interaction strength depended on differences in preferred orientation. The synaptic connectivity weight function was a clipped Gaussian function of the preferred orientation difference, with the maximum connectivity in the same population. In the individual-neuron model, synaptic connections were made probabilistically based on the number of neurons in the presynaptic population and the expected number of connections to each postsynaptic population. The total number of synapses onto each cortical neuron was on the order of 100. Synaptic delays between cortical populations were gamma distributed with a mean of 3 ms and a standard deviation of 1 ms. The unitary postsynaptic conductances in the model were random with a coefficient of variation of 0.5. The average excitatory postsynaptic potentials in excitatory and inhibitory neurons were 0.5 and 1.2 mV, respectively, while the corresponding average inhibitory postsynaptic potentials were -0.3 and -0.7 mV. In the Nykamp and Tranchina (2000) model, as in the model of Somers *et al.* (1995), an individual LGN neuron simply mirrored its input from a single retinal ganglion cell neuron, and the firing rates of these cells were computed in a manner similar to that of Somers *et al.* (1995). The synaptic input events from each LGN neuron to each cortical neuron in the individual-neuron model were generated by a modulated Poisson

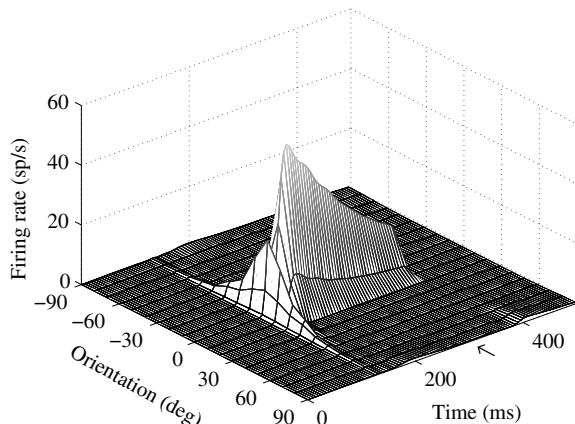


FIG. 7.3: A 3D view of excitatory-population responses to a flashed dark bar at 0° , demonstrating the orientation tuning of the cortical neurons. The bar appeared at $t = 100$ ms, with a duration of 250 ms. Firing rate across preferred orientations is plotted vs. time. The initial transient reflects the orientation bias of the input from the LGN. Afterwards, the tuning sharpens dramatically as a consequence of cortical–cortical interactions. Figure taken from Nykamp and Tranchina (2000).

process with a rate given by a deterministic model for the firing rates of the LGN neurons.

Figure 7.3 shows the firing rates of the excitatory populations in response to the presentation of a flashed dark bar oriented at 0° . The presentation duration was 250 ms beginning at $t = 100$ ms. The initial transient of the response is broadly tuned across the preferred orientations. This response reflects the weak orientation bias of the input from the LGN (not shown). The later response is much more sharply tuned – only neurons within 20° of zero fire significantly – as a consequence of cortical–cortical interactions.

Figure 7.4 shows the full set of excitatory-neuron probability density functions at $t = 300$ ms. At this time there is sharp orientation tuning in the population firing rates, centred at 0° , as shown in Fig. 7.3. The probability density functions for neurons with preferred orientations near 0° show distributions with peaks close to v_{th} (-55 mV); these are the populations with high firing rates in Fig. 7.3.

Nykamp and Tranchina (2000) compared population density results to those obtained by direct Monte Carlo simulation in a corresponding individual-neuron model with 100 neurons per population. Spikes for all neurons in each population were put into bins phased to the stimulus cycle over 20 passes of the stimulus. The resulting histogram approximations of the population firing rates (not shown here) were still somewhat ragged, so a comparison of computation times

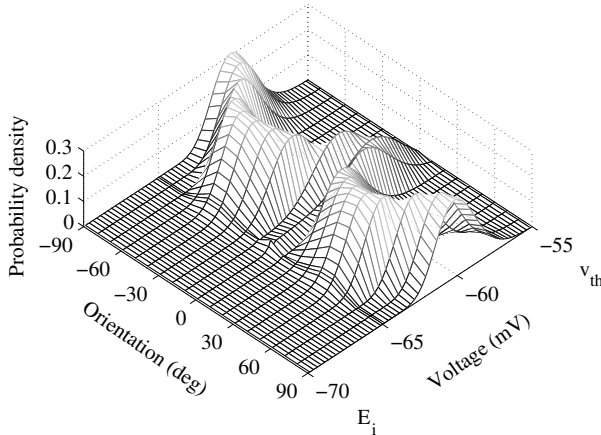


FIG. 7.4: Snapshot of the distribution of excitatory neurons over voltage at $t = 300$ ms in Fig. 7.3. Neurons with preferred orientation near 0° , corresponding to those that are firing in Fig. 7.3, are distributed closer to v_{th} than those at other orientations, corresponding to neurons that are not firing. Figure taken from Nykamp and Tranchina (2000).

for population density and direct simulation under these conditions provided a conservative estimate of the time-saving advantage of the population density method. They found that Monte Carlo and population density results matched reasonably well, but they observed some systematic discrepancies with only 100 neurons per population. There was some variation from realization to realization of the network due to the random connections, but averaging over 10 passes of the stimulus for each of 10 realizations of the network did not dramatically improve agreement. However, the same direct simulation with 1000 neurons per population, where the connectivity was sparse, rather than 100, considerably improved the match between Monte Carlo and population density results (Nykamp and Tranchina, 2000, Fig. 21). This implies that further development of population density methods is required for small populations and non-sparse connectivity. The population density simulations with 36 populations took 30 seconds for a 500 ms run and 0.5 ms time step, while individual neuron simulation took 530 s, 17 times longer.

7.9 Role of synaptic kinetics in population firing rate dynamics

The approximation of instantaneous synaptic kinetics provides for population density formulations that are tractable analytically and computationally. However, as pointed out in the introductions of Fourcaud and Brunel (2002) and Apfaltrer *et al.* (2006), this approximation is often unwarranted. Excitatory postsynaptic conductance events gated by ‘fast’ AMPA (α -amino-3-hydroxy-5-methyl-4-isoxazolepropionic acid) receptors are diverse (Edmonds *et al.*, 1995,

Koch, 1999) and sometimes not so fast compared to the membrane time constants. The same is true for ‘fast’ inhibitory synaptic events gated by GABA_A (γ -amino butyric acid type A) receptors. Excitatory postsynaptic conductance events gated by NMDA (*N*-methyl-*D*-aspartic acid) receptors (Fain, 1999, Edmonds *et al.*, 1995) are typically even slower, with decay time constants in the tens of ms. Postsynaptic conductances gated by the metabotropic class of synaptic receptors (both excitatory and inhibitory), where channel gating occurs through a second-messenger system (Fain, 1999), can have particularly slow kinetics.

7.9.1 Temporal frequency response of population firing rate: injected current as the input

Knight (1972) computed the temporal frequency response for the transduction from synaptic current input to population firing rate output, in the absence of noise. In the context of Section 7.3.3, the results of Knight (1972) correspond to the deterministic limit where $a \rightarrow 0$, $\nu(t) \rightarrow \infty$, $a\nu(t) = \alpha(t)$, $\alpha(t)$ is fixed, and $\alpha(t)$ is regarded as the input. In this chapter, we are concerned with the physiological ramifications of synaptic noise.

Brunel *et al.* (2001) and Fourcaud and Brunel (2002) examined the effect of synaptic kinetics on the input–output properties of a population of postsynaptic neurons. They considered a population of neurons receiving a noisy background barrage of unitary postsynaptic current events at a steady rate. They performed perturbation analysis in which the population firing rate was regarded as the output, and a small deterministic current injected into each and every neuron in the population was taken as the input. The elegant analysis of Brunel *et al.* (2001) and Fourcaud and Brunel (2002) compared temporal frequency responses for the case of instantaneous synaptic kinetics to frequency responses for the case of exponential unitary postsynaptic current waveforms. They used a Fokker–Planck approximation for the evolution equation of the population density function in both cases. In order to maintain some consistency with the notation used in sections above, we do not adhere to the notation of Brunel *et al.* (2001) or Fourcaud and Brunel (2002). To obtain the Fokker–Planck approximation (Fourcaud and Brunel, 2002), the evolution equation for the background postsynaptic current input, $I_s(t)$, is approximated by

$$\tau_s \frac{d}{dt} I_s = -I_s + \mu_{I_s} + \beta Z(t), \quad (7.47)$$

where μ_{I_s} is the mean postsynaptic current; $Z(t)$ is zero-mean Gaussian white noise with autocorrelation function $\delta(t)$; and τ_s is the time constant of the exponential decay of the unitary postsynaptic current event. The case of instantaneous synaptic kinetics corresponds to setting $\tau_s = 0$ in Eqn (7.47). The total injected membrane current, $i_{\text{in}}(t)$, is the sum of the synaptic input current and the external injected perturbing current, i.e. $i_{\text{in}}(t) = I_s(t) + \epsilon i_1(t)$. The evolution equation

for the random membrane voltage is given by

$$\frac{dV}{dt} = -\frac{1}{\tau_m} V + \frac{1}{c} [\epsilon i_1(t) + I_s(t)], \quad (7.48)$$

where resting voltage is defined to be $V = 0$. To compute the temporal frequency response for injected current one considers $\epsilon i_1(t)$ in Eqn (7.48) to be of the form $\epsilon i_1(t) = \epsilon \operatorname{Re}(e^{i\omega t}) = \epsilon \cos(\omega t)$ (units, A), where $\omega = 2\pi f$; and f is the temporal frequency of sinusoidal modulation in Hz. Then, when the population density equation corresponding to Eqns (7.47) and (7.48) are linearized around the steady state, where $i_1(t) = 0$, the first-order component of the population firing rate is of the form $r_1(t) = \epsilon \operatorname{Re}[R(\omega)e^{i\omega t}]$, where $R(\omega)$ is the complex-valued frequency response. The response $r_1(t)$ can be written as $r_1(t) = \epsilon r(\omega) \cos[\omega t + \phi(\omega)]$, where $r(\omega)$ is the gain of the frequency response (modulus of the complex-valued $R(\omega)$); and $\phi(\omega)$ is the phase difference between input and output sinusoids (argument of $R(\omega)$). The corresponding impulse response function is the first-order (in ϵ) response to a perturbing current $\epsilon i_1(t) = \epsilon \delta(t)$. A fundamental fact in linear systems theory is that the impulse response function, call it $h(t)$, and temporal frequency response function are a Fourier transform pair. That is, $R(\omega) = \mathcal{F}\{h(t)\}$ and $h(t) = \mathcal{F}^{-1}\{R(\omega)\}$, where \mathcal{F} indicates Fourier transform. It is also important to keep in mind for the analysis below that $\mathcal{F}\{\delta(t)\} = 1$.

In the case of instantaneous synaptic kinetics, where $I_s = \mu_{I_s} + \beta Z(t)$, and there is only one state variable, the membrane voltage, the 1-D Fokker–Planck equation for $\rho(v, t)$ is

$$\frac{\partial}{\partial t} \rho = -\frac{\partial}{\partial v} \left\{ \left[-\frac{1}{\tau_m} v + \frac{1}{c} (\mu_{I_s} + \epsilon i_1(t)) \right] \rho - \frac{1}{2} \left(\frac{\beta}{c} \right)^2 \frac{\partial \rho}{\partial v} + r(t) \delta(v) \right\}. \quad (7.49)$$

Again, the boundary condition $\rho(v_{\text{th}}, t) = 0$ implies that $r(t) = -(1/2)(\beta/c)^2 \partial \rho / \partial v$, evaluated at $v = v_{\text{th}}$. The next step in computing the frequency response is to write $\rho = \rho_0 + \epsilon \rho_1$, where ρ_0 is the steady state solution to Eqn (7.49) with $i_1(t) = 0$, and $\epsilon \rho_1$ is the first-order perturbation in the response due to $\epsilon i_1(t)$. The steady state solution ρ_0 is well known (Brunel and Hakim, 1999). When one substitutes the expression $\rho = \rho_0 + \epsilon \rho_1$ into Eqn (7.49) and collects first-order terms in ϵ , the result is

$$\frac{\partial}{\partial t} \rho_1 = -\frac{\partial}{\partial v} \left\{ \left[-\frac{1}{\tau_m} v + \frac{1}{c} (\mu_{I_s}) \right] \rho_1 + \frac{i_1(t)}{c} \rho_0 - \frac{1}{2} \left(\frac{\beta}{c} \right)^2 \frac{\partial \rho_1}{\partial v} \right\} + r_1(t) \delta(v), \quad (7.50)$$

where $r_1(t) = -(1/2)(\beta/c)^2 \partial \rho_1(v_{\text{th}}, t) / \partial v$.

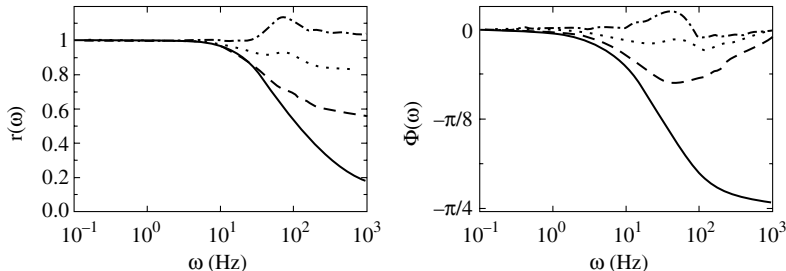


FIG. 7.5: Population firing rate frequency response for sinusoidal modulation of injected current. The left panel plots the gain and the right panel plots the phase. Each curve represents a different value of τ_s : $\tau_s = 0$ ms (solid); 2 ms (dashed); 5 ms (dotted); 10 ms (dot-dashed). For all cases $\tau_m = 20$ ms, and the synaptic current noise was fixed at a value quantified by $\sqrt{(\beta/c)^2 \tau_m} = 5$ mV. Figure taken from Fig. 6C of Fourcaud and Brunel (2002).

Brunel *et al.* (2001) and Fourcaud and Brunel (2002) used the method of Brunel and Hakim (1999) for oscillatory $i_1(t)$, i.e. $i_1(t) = e^{i\omega t}$, to solve analytically for the frequency response. The analytical results highlight the virtues of the Fokker–Planck approximation.

Brunel *et al.* (2001) and Fourcaud and Brunel (2002) found that the gain of the temporal frequency response in the 1-D case decays to zero like $1/\sqrt{\omega}$ (Fig. 7.5, left panel, solid line). The phase lag of the response approaches $\pi/4$ as $\omega \rightarrow \infty$ (Fig. 7.5, right panel, solid line). A salient implication of the decay of gain to zero is that there is no instantaneous component of the population firing rate response to externally injected current. This feature is expected if one considers the impulse response function (Fourier transform of the temporal frequency response). When a brief current that delivers a total charge of order ϵ is injected into every neuron in the population ($\epsilon i_1(t) = \epsilon q \delta(t)$), the voltage of every neuron jumps instantaneously by Δv , where $\Delta v = \epsilon q/c$. Thus, the voltage of any neuron within the interval between v_{th} and $v_{\text{th}} - \epsilon q/c$ jumps instantaneously across threshold. The total probability (fraction of neurons in the population) that crosses threshold instantaneously is given by the corresponding area under the density curve. This area is of order ϵ^2 because of the zero-density boundary condition at v_{th} . Consequently there is no first-order (order ϵ) instantaneous component of the impulse response function. This implies that the temporal frequency response does not converge to a constant, but rather decays to zero (Fig. 7.5, left panel, solid line). It is important to note that the zero-density boundary condition at v_{th} is not an artifact of the Fokker–Planck approximation; $\rho(v_{\text{th}}, t) = 0$ for the problem with non-infinitesimal voltage jumps as well.

In the case of non-instantaneous synaptic kinetics ($\tau_s \neq 0$), there are two state variables, the membrane voltage and synaptic current. For the sake of notational convenience, let us refer to the particular values that the random synaptic current can take on as x . The 2-D Fokker–Plank equation for $\rho(v, x, t)$ is

$$\begin{aligned} \frac{\partial}{\partial t} \rho = & -\frac{\partial}{\partial v} \left[\left(-\frac{1}{\tau_m} v + \frac{1}{c} [\epsilon i_1(t) + x] \right) \rho \right] \\ & - \frac{\partial}{\partial x} \left\{ -\frac{1}{\tau_s} (x - \mu_{I_s}) \rho - \frac{1}{2} \frac{\beta^2}{\tau_s^2} \frac{\partial \rho}{\partial x} \right\}, \end{aligned} \quad (7.51)$$

and the population firing rate $r(t)$ is given by

$$r(t) = \int_0^\infty dx \left(-\frac{1}{\tau_m} v_{\text{th}} + \frac{1}{c} [\epsilon i_1(t) + x] \right) \rho(v_{\text{th}}, x, t). \quad (7.52)$$

Equation (7.52) reflects the fact that neurons fire by advection across v_{th} , and it implies that the density at v_{th} cannot be equal to zero for all x if $r(t) > 0$.

Brunel *et al.* (2001) and Fourcaud and Brunel (2002) used asymptotic methods to compute an approximate analytical solution for the temporal frequency response in the case of non-instantaneous synaptic kinetics (2-D). They found that the gain of the temporal frequency response in the 2-D case does not decay to zero, but, rather, approaches an asymptotic value as $\omega \rightarrow \infty$ (Fig. 7.5, left panel, non-solid curves). Furthermore, the phase lag approaches zero as $\omega \rightarrow \infty$ (Fig. 7.5, right panel, non-solid curves). An implication is that there is an instantaneous component of the population firing rate response in the case of non-instantaneous synaptic kinetics (2-D). The asymptotic value of the gain (as $\omega \rightarrow \infty$) relative to the gain at a fixed low frequency is higher for larger values of τ_s (Fig. 7.5, left panel). This means that larger synaptic time constants τ_s give less temporal frequency filtering in the transduction from the injected current to the population firing rate.

This instantaneous component of the response is again expected if one considers the impulse response function. Because the density is not zero at $v = v_{\text{th}}$, when a brief current delivering a total charge of order ϵ is injected into every neuron in the population ($\epsilon i_1(t) = \epsilon q \delta(t)$), the voltage of every neuron jumps instantaneously by $\Delta v = \epsilon q/c$. The total probability (fraction of neurons in the population) that crosses threshold instantaneously is of order ϵ , because the density function at v_{th} is not equal to zero for all x .

7.9.2 Frequency response of population firing rate: rate of synaptic events as the input

Intuition suggests that a population with instantaneous synaptic kinetics should respond to ‘input’ faster than a population with slow synaptic kinetics. This is indeed the case when one regards the rate of unitary postsynaptic events as the

input. The transduction from synaptic event rate as input to population firing rate as output (Apfaltrer *et al.*, 2006) is the appropriate one to consider if one is interested in the dynamics of the population response to a synaptic event superimposed on top of an ongoing background barrage at a steady rate. The impulse response function for this transduction is the first-order (in ϵ) response to a perturbing input $\epsilon \nu_1(t) = \epsilon \delta(t)$. Integrating this rate $\epsilon \nu_1(t)$ between $t = 0^-$ and $t = 0^+$ gives the number of additional synaptic events provided to the population per neuron at $t = 0$. When $\epsilon \leq 1$ the input perturbation can be interpreted as delivering one additional synaptic event at $t = 0$ to a fraction of neurons in the population equal to ϵ . Apfaltrer *et al.* (2006) considered synapses driven by conductance rather than current, but this distinction is of no importance here.

In the case of instantaneous synaptic kinetics (1-D), the voltage jumps upon the arrival of a synaptic input event by an amount that is independent of ϵ . Instead, in contrast to the deterministic current injection problem above, ϵ determines the fraction of neurons that experience a perturbing input, i.e. an additional synaptic input event at $t = 0$. All neurons that are close enough to v_{th} jump across v_{th} at $t = 0$, upon receiving a perturbing synaptic input, and that fraction is proportional to ϵ . Consequently, there is an instantaneous component of the population firing rate response to modulation of the synaptic input rate.

In the case of non-instantaneous synaptic kinetics, the conductance of a neuron jumps upon arrival of a synaptic input event, but not the voltage. Therefore the fraction of neurons that cross threshold instantaneously at $t = 0$ in response to $\epsilon \nu_1(t) = \epsilon \delta(t)$ is zero. There is no first-order instantaneous component of the response in this case.

Apfaltrer *et al.* (2006) took a different approach from Brunel *et al.* (2001) and Fourcaud and Brunel (2002) to compute the frequency response for the transduction from synaptic input rate to population firing rate. In this problem, like that above, there are two state variables, the membrane voltage and the excitatory synaptic conductance rather than the synaptic current. When the problem is discretized over the two state variables, the density at each point in time can be represented as a matrix in which voltage varies over the rows, and conductance varies over the columns. If one concatenates all columns of the matrix into one grand density vector $\vec{\rho}$, the evolution equation is of the form given in Eqn (7.21). As in Knight (2000), Apfaltrer *et al.* (2006) expressed the temporal frequency response in terms of the eigenvectors and eigenvalues of the matrix \mathbf{Q} evaluated at the steady background synaptic input rate. A disadvantage of this method is that it does not give elegant analytical expressions for the frequency responses as in the work of Brunel *et al.* (2001) and Fourcaud and Brunel (2002) above. It seems that the Fokker–Planck form of Apfaltrer *et al.* (2006) would be amenable to the same techniques used by Brunel *et al.* (2001) and Fourcaud and Brunel (2002).

The results of Apfaltrer *et al.* (2006) were, in a sense, opposite to those of Brunel *et al.* (2001) and Fourcaud and Brunel (2002). Apfaltrer *et al.* (2006)

found that the gain of the frequency response for the case of instantaneous synaptic kinetics approached a constant value as $\omega \rightarrow \infty$, and the corresponding phase lag of the response approached zero. The implication is that in the case of instantaneous synaptic kinetics, there is an instantaneous component in the population firing rate response to a brief perturbing pulse in the synaptic input rate. This result is expected from the argument above. In the case of non-instantaneous synaptic kinetics Apfaltre *et al.* (2006) found that the gain of the frequency response approached zero as $\omega \rightarrow \infty$, and the corresponding phase lag approached $\pi/2$. In the case of non-instantaneous synaptic kinetics, there is no instantaneous component in the population firing rate response to a brief perturbing pulse in the synaptic input rate. Again this result is as expected from the argument above. Apfaltre *et al.* (2006) explored only two values for τ_s , 0 and 5 ms, but one expects the gain of the temporal frequency response to decline more rapidly with larger values of τ_s for the transduction from synaptic input rate to population firing rate.

7.10 Outstanding problems in the population density approach

7.10.1 *The dimension problem with realistic underlying single-neuron models*

Because synaptic kinetics play an important role in network dynamics, population density methods must ultimately include accurate descriptions of synaptic kinetics to be widely applicable. It seems that three state variables in the population density framework would be the bare minimum. Three variables would allow one to model the unitary excitatory and inhibitory postsynaptic event time courses as single exponentials.

The problem of characterizing population firing rate gain and dynamics for neurons receiving non-instantaneous excitatory and inhibitory synaptic input is an important open problem. It would be particularly interesting to see the effects of balanced background excitatory and inhibitory synaptic conductance input on the gain and dynamics of the response to superimposed synaptic inputs (Chance *et al.*, 2002). Burkitt *et al.* (2003) presented analytical results for the steady state with balanced instantaneous excitatory and inhibitory synaptic conductances.

Still more realistic synaptic kinetics and/or the inclusion of several types of excitation and/or inhibition would require even more state variables. The computation time for the numerical solution of population density equations grows as the dimension of the state space increases. In the case of two state variables, population density methods are still faster than Monte Carlo simulations (Casti *et al.*, 2002, Huertas and Smith, 2006, Apfaltre *et al.*, 2006). See Section 8.7 of this book for another example comparison.

It is likely that adding just one more state variable would make direct Monte Carlo simulations, with fewer than 100 or so neurons per population, faster. Continuing progress in speeding up computation time in direct simulations of

large neural networks (Rangan and Cai, 2007, Rangan *et al.*, 2005) further challenges the population density alternative.

Good dimension reduction methods might make population density methods practical in state spaces with three or higher dimensions and could also speed up computations for state spaces of lower dimension. A goal of dimension reduction techniques is to find a low-dimensional dynamical system that approximates a truly high-dimensional system. Wilson-Cowan type models (Wilson and Cowan, 1972, 1973), based on a system of ordinary differential equations for population firing rates and auxiliary variables such as synaptic conductances and synaptic depression/facilitation terms (Dayan and Abbott, 2001, Shelley and McLaughlin, 2002) can provide great insight. Rate models with only a few dynamic variables per population might not be able to capture complex population dynamics that arise in models that handle noise in a more detailed way. However, new methods for deriving rate models from spiking models (Aviel and Gerstner, 2006) seem promising.

Apfalterer *et al.* (2006) showed that a dimension reduction method based on using a small subset of a moving eigenvector basis, along the lines suggested by Knight (2000), can save considerable computation time for 1-D and 2-D population density problems. However, this method might not generalize well to higher dimensions because of the expense of computing eigenvectors of large matrices.

Dimension reduction by a particular moment closure method (Cai *et al.*, 2004, 2006, Rangan and Cai 2006) seemed promising when it was first introduced, but Ly and Tranchina (2007) have shown that this method gives ill-posed problems, in the sense that solutions do not exist for a wide range of physiological parameters. It is possible that other moment closure methods like those applied fruitfully in statistical physics (Dreyer *et al.*, 2001, 2004, Junk and Unterreiter, 2002, Bardos *et al.*, 1991, 1993) might work well in the population density framework for neural network modelling, but this has not yet been demonstrated.

7.10.2 Non-sparse coupling and correlations between inputs from presynaptic populations

Most applications of population density methods in neural network settings have involved the implicit assumption of conditionally independent synaptic inputs: once the population firing rate of a particular presynaptic population is given, the random arrival times of synaptic events from that population are independent of the previous arrival times of events from that population and from all other populations. This principle is violated when postsynaptic neurons in a population have a substantial number of presynaptic partners in common.

de la Rocha *et al.* (2007) recently studied how a pair of uncoupled neurons with instantaneous synaptic kinetics transfers correlation in synaptic inputs to correlations in their spike train outputs. They presented elegant analytical results that were first-order in the correlation coefficient between the two synaptic input trains.

An exact population density approach for a simple model of two neurons that share synaptic input involves a joint probability density $\rho(v_1, v_2, t)$ for the random voltages of the two neurons, V_1 and V_2 , respectively. The population density function in this context represents the distribution of an ensemble of pairs of neurons over all possible configurations in all possible realizations of the sequence of synaptic input events. There are independent Poisson synaptic input events to neurons 1 and 2, with rates $\nu_1(t)$ and $\nu_2(t)$, respectively, and there are common, simultaneous, Poisson synaptic events to both neurons with rate $\nu_{12}(t)$. Because common synaptic input events cause simultaneous voltage jumps in the two neurons – say $\Delta V_1 = a$ and $\Delta V_2 = b$ – there is a component of the total probability flux vector that is in the (a, b) direction. The magnitude of this probability flux vector at (v_1, v_2) is given by $\nu_{12}(t)$ times the integral of $\rho(v_1, v_2, t)$ over the line segment with end-points $(v_1 - a, v_2 - b)$ and (v_1, v_2) . Three firing rates (probability per unit time of crossing threshold voltage for the ensemble of pairs of neurons) can be distinguished in this problem: the rate at which neuron 1 is driven to fire by events with rate $\nu_1(t)$; the rate at which neuron 2 is driven to fire by events with rate $\nu_2(t)$; and the rate at which neurons 1 and 2 are driven to fire simultaneously by common events with rate $\nu_{12}(t)$. The simultaneous firing rate is given by $\nu_{12}(t)$ times the integral of $\rho(v_1, v_2, t)$ over a rectangular region in the upper right-hand corner of the $v_1 - v_2$ plane; it is defined by vertices $(1 - a, 1)$, $(1 - a, 1 - b)$, $(1, 1 - b)$, and $(1, 1)$. Any pair of neurons with voltages in this region of the $v_1 - v_2$ phase plane will simultaneously jump across threshold when they receive simultaneous synaptic inputs.

Generalizing population density methods to take into account correlations among synaptic inputs from numerous coupled populations is a challenging open problem.

7.10.3 Non-Poisson synaptic input

Câteau and Reyes (2006) demonstrated the emergence of population firing rate synchrony in a multi-layered feed-forward network model with sparse connectivity. The stimulus was a step in the steady rate of synaptic input events to the first (input) layer. The synchrony in successive layers became progressively more pronounced and longer lasting (Fig. 7.6). They showed that this behaviour was not captured by a population density modelling approach unless they included temporal correlations in the synaptic input train (lacking in the Poisson description). Câteau and Reyes (2006) proved that – contrary to popular belief – the composition of many uncorrelated spike trains does not necessarily approach a Poisson process on the relevant physiological time-scale; see also Lindner (2006). Câteau and Reyes (2006) used a population density equation that accounted for non-trivial autocorrelation in the input spikes for populations in each layer of their network. The statistics and rate of synaptic input were specified for their input layer. For each higher layer, the input was determined by the output population firing rate of the layer below it.

Figure 7.6 shows the population firing rates for the first five layers in the Câteau and Reyes (2006) model, computed in three ways: direct simulation with individual neurons (panel (a), histogram and raster); population density approach with Poisson synaptic input assumption (panel (b), grey line); and modified population density approach taking into account temporal correlations in synaptic input events (panel (b), black line).

For the purposes of our discussion of the work of Câteau and Reyes (2006), the fast excitatory synaptic kinetics ($\tau_e = 1\text{ ms}$ vs. $\tau_m = 20\text{ ms}$) in their underlying single-neuron model can be assumed to be instantaneous. Their voltage evolution equation is the same as Eqn (7.31) above, with excitation only and ε_r defined to be zero,

$$\frac{dV}{dt} = -\frac{1}{\tau_m} [V + G_e(t)(v - \varepsilon_e)]. \quad (7.53)$$

Câteau and Reyes (2006) proposed that for each layer in the network, the random train of synaptic input events in the quasi-steady-state, where the rate of events is changing slowly, can be thought of as a renewal process with random interspike intervals drawn from a population with a gamma density function. Our discussion will be further streamlined if we think of the synaptic input rate ν_e as constant for now. In our paraphrasing of the work of Câteau and Reyes (2006)

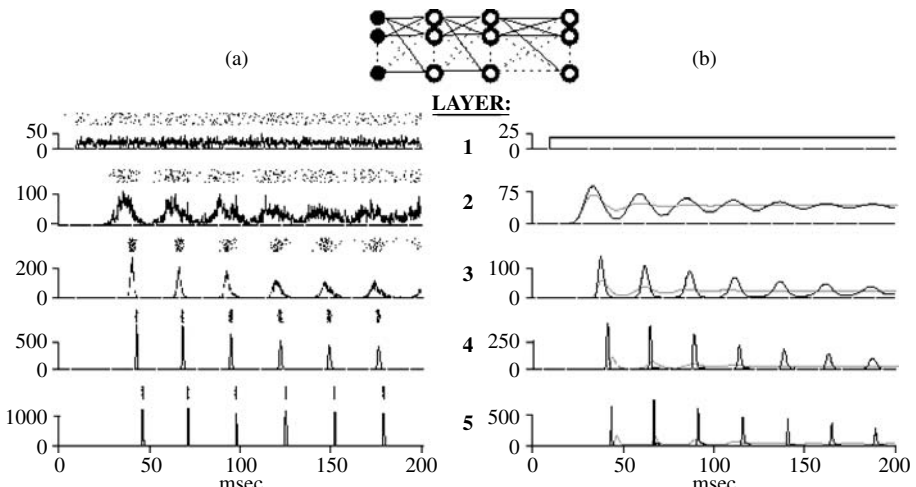


FIG. 7.6: Population firing rates for the first five layers in the multi-layered feed-forward model of Câteau and Reyes (2006). Firing rates were computed in three ways: (a) direct simulation with individual neurons, histogram, and dot rasters; (b) population density approach (Fokker–Planck equation) with Poisson synaptic input assumption, grey line; modified Fokker–Planck equation taking into account temporal correlations in synaptic input events, black line. Figure taken from Fig. 2 of Câteau and Reyes (2006).

we will restore the t argument for ν_e at the end the derivation of a Fokker–Planck equation.

The gamma probability density function for a random inter-event interval T is of the form $f_T(t) = (1/\theta)(t/\theta)^{n-1} e^{-t/\theta}/(n-1)!$, where n (assumed to be integer here) is the shape parameter, $\theta = 1/(n\nu)$ is the time-scale parameter, and ν is the rate of events. A special case is the Poisson renewal process, where $n = 1$ and the inter-event interval is exponentially distributed. The *random rate* of synaptic events, $R(t)$, corresponding to a random realization of the train of synaptic events, can be defined as a sum of delta functions centred on the random event times. This random rate function $R(t)$ is to be distinguished from the average rate ν . The autocovariance function, $c_{RR}(t) \equiv \mathbf{E}[(R(t_0) - \mu_R)(R(t_0+t) - \mu_R)]$ can be expressed as $c_{RR}(t) = \nu \mathcal{F}^{-1}\{\hat{f}_T(\omega)/[1 - \hat{f}_T(\omega)] - \nu/[i\omega]\} + \nu \delta(t)$, where \mathcal{F}^{-1} denotes the inverse Fourier transform operation, and $\hat{f}_T(\omega)$ is the Fourier transform of $f_T(t)$. The autocovariance function (Câteau and Reyes, 2006; Peskin, 1981) has a continuous part that is a damped oscillatory function with a prominent first negative lobe when $n \neq 1$. For example: for $n = 2$, $c_{RR}(t) = \nu[\delta(t) - \nu e^{-4\nu t}]$; for $n = 3$, $c_{RR}(t) = \nu[\delta(t) - \nu 2 \sin(3\sqrt{3}\nu t/2 + \pi/6)e^{-9\nu t/2}]$. The autocovariance function of the synaptic conductance is mirrored by the autocovariance function of the synaptic input rate. Câteau and Reyes (2006) approximated only the first negative lobe of the measured autocovariance function of the rate of synaptic input to their first layer. They did so by incorporating a cleverly chosen zero-mean noise component, $L(t)$, in their synaptic conductance. One can think of $L(t)$ as being produced by passing Gaussian white noise $Z(t)$ through a causal filter with biphasic impulse response function; call it $q(t)$. They chose $q(t)$ to be a delta function minus an exponential function. Their excitatory postsynaptic conductance was of the form

$$G_e(t) = \mu_{G_e} + \mu_{A_e} \sqrt{\nu_e} L(t), \quad (7.54)$$

where

$$L(t) = \int_{-\infty}^{+\infty} dt' Z(t') q(t-t'); \quad (7.55)$$

$$q(t) = \delta(t) - \frac{\alpha}{\tau_{\text{neg}}} \exp\left(-\frac{t}{\tau_{\text{neg}}}\right) H(t); \quad (7.56)$$

$\mu_{G_e} = \nu_e \mu_{A_e}$ is the mean excitatory conductance; and $H(t)$ is the Heaviside step function. The resulting autocorrelation function of the noise, $C_{LL}(t) \equiv \mathbf{E}[L(t_0)L(t_0+t)]$, is given by

$$\begin{aligned} c_{LL}(t) &= \int_{-\infty}^{\infty} q(t') q(t'+t) dt' \\ &= \delta(t) - \frac{1}{2\tau_{\text{neg}}} \left(1 - (1-\alpha)^2\right) e^{(-|t|/\tau_{\text{neg}})}. \end{aligned} \quad (7.57)$$

This $c_{LL}(t)$ gives the desired form for the autocovariance function for the synaptic conductance, because Eqn (7.54) implies that the autocovariance function for the synaptic conductance is $\mu_{A_e}^2 \nu_e c_{LL}(t)$. Câteau and Reyes (2006) say that they chose the exponential time constant τ_{neg} to be equal to the mean time between synaptic events – i.e. $\tau_{\text{neg}} = 1/\nu_e$ – in order to approximate the first negative lobe of the true autocovariance function of the synaptic input rate.

Câteau and Reyes (2006) represented the noise term $L(t)$ in an equivalent way with the pair of equations:

$$\begin{aligned} L(t) &= Z(t) - \alpha X(t) \\ \tau_{\text{neg}} \frac{dX}{dt} &= -X + Z(t). \end{aligned} \quad (7.58)$$

There are two state variables in this problem, the membrane voltage V , and X . After putting together the equations above for $V(t)$, $G_e(t)$, $L(t)$, and $X(t)$, with $\tau_{\text{neg}} = 1/\nu_e$, the dynamical system of Câteau and Reyes (2006) can be described by a pair of stochastic differential equations for V and X :

$$\frac{dV}{dt} = \mu_v(V, X) + \sigma_v(V, X) Z(t) \quad (7.59)$$

$$\frac{dX}{dt} = \mu_x(V, X) + \sigma_x(V, X) Z(t), \quad (7.60)$$

where the vector $\vec{\mu}(V, X)$ has components

$$\mu_v(V, X) = -\frac{1}{\tau_m} \left[V + \left(\nu_e \mu_{A_e} - \alpha \mu_{A_e} \sqrt{\nu_e} X \right) (V - \varepsilon_e) \right], \quad (7.61)$$

$$\mu_x(V, X) = -\nu_e X \quad (7.62)$$

and $\vec{\sigma}(V, X)$ has components

$$\sigma_v(V, X) = \frac{1}{\tau_m} \mu_{A_e} \sqrt{\nu_e} (\varepsilon_e - V), \quad (7.63)$$

$$\sigma_x(V, X) = \nu_e. \quad (7.64)$$

If we define the vector \vec{X} with components V and X , then Eqns (7.59) and (7.60) can be written more compactly as

$$d\vec{X}/dt = \vec{\mu}(\vec{X}) + \vec{\sigma}(\vec{X}) Z(t). \quad (7.65)$$

The corresponding probability flux in the v - x plane has an advective part, $\vec{J}_a = \vec{\mu}(\vec{x}) \rho$. The diffusion part \vec{J}_d is in the direction of $\vec{\sigma}(\vec{x})$ and is proportional to the corresponding directional derivative of ρ ; it can be written as $\vec{J}_d = -(1/2)(\nabla \rho \cdot \vec{\sigma}) \vec{\sigma}$. The total flux vector \vec{J} is given by $\vec{J} = \vec{J}_a + \vec{J}_d$.

The evolution for the probability density function $\rho(v, x, t)$, $\partial\rho/\partial t = -\nabla \cdot \vec{J}$, can now be simply written as

$$\frac{\partial}{\partial t}\rho = -\nabla \cdot \left(\vec{\mu} \rho - \frac{1}{2} \vec{\sigma} (\nabla \rho \cdot \vec{\sigma}) \right). \quad (7.66)$$

There is one such equation for the population in each layer of the network. The population firing rate at each level is the total flux of probability across the threshold voltage, and the input to the next layer above is proportional to this rate.

Câteau and Reyes (2006) found that their modified Fokker–Planck equation (7.66), taking correlation into account (FPE_C), gave substantial improvement over the results given by the conventional Fokker–Planck equation that assumes Poisson synaptic event trains (Fig. 7.6). However oscillations in the population firing rate in deep layers given by their FPE_C died out more rapidly than those in their direct simulations. This implies that further improvements are needed in modelling correlated synaptic inputs by population density methods when such correlations play an important role in network dynamics.

7.11 Diversity of past applications of PDF methods and beyond

We have touched on only a few applications of PDF methods in neural network modelling. We close this chapter by directing the reader to a number of other selected applications. In the early 1990s PDF methods were used to study the issue of synchronous versus asynchronous behaviour in networks of pulse coupled oscillators with excitatory interactions (Kuramoto, 1991, Abbott and van Vreeswijk, 1993, Strogatz and Mirollo, 1991, Gerstner and van Hemmen, 1993). Brunel and Hakim (1999) used PDF methods to study the emergence of synchronous oscillatory behaviour in a network of sparsely coupled inhibitory neurons. Brunel (2000) presented a thorough analysis of the dynamics of a sparsely coupled network of inhibitory and excitatory neurons. Brunel and Latham (2003) used asymptotic methods to determine the steady-state firing rate of quadratic integrate-and-fire neurons receiving one type of excitatory synaptic input, in which the unitary synaptic events had a single-exponential time course. Moreno-Bote and Parga (2004) applied similar methods for IF neurons with one type of slow synaptic input, and also for the combination of one fast and one slow synaptic input. Sirovich (2008) used PDF methods to study tightly coupled retinal ganglion cells (RGCs) and LGN neurons, where the LGN neuron is driven primarily by one RGC with large excitatory postsynaptic potentials. Chapter 8 of this book covers applications of PDF methods to modelling the physiology of the dorsal lateral geniculate nucleus and its inputs.

Future extensions of PDF methods to neural networks with more realistic underlying neurons and general connectivity will require solutions to the interesting and challenging problems discussed above in Section 7.10. The field of

PDF methods continues to provide a rich source of analytical and computational problems. It also provides great opportunities for collaborations between mathematicians, physicists, and neuroscientists.

References

- Abbott, L. F. and van Vreeswijk, C. (1993). Asynchronous states in networks of pulse-coupled oscillators. *Physical Review E*, **48**, 1483–1490.
- Apfaltrer, F., Ly, C., and Tranchina, D. (2006). Population density methods for stochastic neurons with a 2-D state space: Application to neural networks with realistic synaptic kinetics. *Network: Computation in Neural Systems*, **17**, 373–418.
- Aviel, Y. and Gerstner, W. (2006). From spiking neurons to rate models: a cascade model as an approximation to spiking neuron models with refractoriness. *Physical Review E*, **73**, 051908.
- Bardos, C., Galose, F., and Levermore, D. (1991). Fluid dynamic limit of kinetic equations 1: Formal derivations. *Journal of Statistical Physics*, **63**, 323–344.
- Bardos, C., Galose, F., and Levermore, D. (1993). Fluid dynamic limit of kinetic equations 2: Convergence proofs for the boltzmann equation. *Communication on Pure and Applied Math*, **46**, 667–753.
- Brown, E., Moehlis, J., and Holmes, P. (2004). On the phase reduction and response dynamics of neural oscillator populations. *Neural Computation*, **16**, 673–715.
- Brunel, N. (2000). Dynamics of sparsely connected networks of excitatory and inhibitory spiking neurons. *Journal of Computational Neuroscience*, **8**, 183–208.
- Brunel, N., Chance, F. S., Fourcaud, N., and Abbott, L. F. (2001). Effects of synaptic noise and filtering on the frequency response of spiking neurons. *Physical Review Letter*, **86**, 2186–2189.
- Brunel, N. and Hakim, V. (1999). Fast global oscillations in networks of integrate-and-fire neurons with low firing rates. *Neural Computation*, **11**, 1621–1671.
- Brunel, N. and Latham, P. E. (2003). Firing rate of the noisy quadratic integrate-and-fire neuron. *Neural Computation*, **15**, 2281–2306.
- Brunel, N. and van Rossum, C. W. (2007). Lapicque's 1907 paper: from frogs to integrate-and-fire. *Biological Cybernetics*, **97**, 337–339.
- Burkitt, A. N. (2006a). A review of the integrate-and-fire neuron model: I. Homogeneous synaptic input. *Biological Cybernetics*, **95**, 1–19.
- Burkitt, A. N. (2006b). A review of the integrate-and-fire neuron model: II. Inhomogeneous synaptic input and network properties. *Biological Cybernetics*, **95**, 27–12.
- Burkitt, A. N., Meffin, H., and Grayden, D. B. (2003). Study of neuronal gain in a conductance-based leaky integrate-and-fire neuron model with balanced excitatory and inhibitory synaptic input. *Biological Cybernetics*, **89**, 119–125.

- Cai, D., Tao, L., Rangan, A., and McLaughlin, D. (2006). Kinetic theory for neuronal network dynamics. *Communications in Mathematical Sciences*, **4**, 97–127.
- Cai, D., Tao, L., Shelley, M., and McLaughlin, D. (2004). An effective kinetic representation of fluctuation-driven neuronal networks with application to simple and complex cells in visual cortex. *Proceedings of the National Academy of Science*, **101**, 7757–7762.
- Casti, A. R., Omurtag, A., Sornborger, A., Kaplan, E., Knight, B., Victor, J., and Sirovich, L. (2002, May). A population study of integrate-and-fire-or-burst neurons. *Neural Comput*, **14**(5), 957–986.
- Câteau, H. and Reyes, A. D. (2006). Relation between single neuron and population spiking statistics and effects on network activity. *Physical Review Letters*, **96**, 058101.
- Chance, F. S., Abbott, L. F., and Reyes, A. D. (2002). Gain modulation from background synaptic input. *Neuron*, **35**, 773–782.
- Dayan, P. and Abbott, L. F. (2001). *Theoretical Neuroscience: Computational and Mathematical Modeling of Neural Systems*. MIT Press, Cambridge, MA.
- de la Rocha, J., Doiron, B., Shea-Brown, E., Josic, K., and Reyes, A. (2007). Correlation between neural spike trains increases with firing rate. *Nature*, **448**, 802–806.
- Dorph-Petersen, K.-A., Pierri, J. N., Wu, Q., Sampson, A. R., and Lewis, D. A. (2007). Primary visual cortex volume and total neuron number are reduced in schizophrenia. *Journal of Comparative Neurology*, **501**, 290–301.
- Dreyer, W., Herrmann, M., and Kunik, M. (2004). Kinetic solutions of the Boltzmann-Peierls equation and its moment systems. *Continuum Mechanics and Thermodynamics*, **16**, 453–469.
- Dreyer, W., Junk, M., and Kunik, M. (2001). On the approximation of the Fokker-Planck equation by moment systems. *Nonlinearity*, **14**, 881–906.
- Edmonds, B., Gibb, A. J., and Colquhoun, D. (1995). Mechanisms of activation of glutamate receptors and the time course of excitatory synaptic currents. *Annual Review of Physiology*, **57**, 495–519.
- Ermentrout, G. B. and Kopell, N. (1984). Frequency plateaus in a chain of weakly coupled oscillators, I. *SIAM Journal on Mathematical Analysis*, **15**, 215–237.
- Fain, G. L. (1999). *Molecular and Cellular Physiology of Neurons*, Chapter 9-11. Harvard University Press, Cambridge, MA.
- Fourcaud, N. and Brunel, N. (2002). Dynamics of the firing probability of noisy integrate-and-fire neurons. *Neural Computation*, **14**, 2057–2110.
- Gerstein, G. and Mandelbrot, B. (1964). Random walk models for spike activity of a single neuron. *Biophysical Journal*, **4**, 41–68.
- Gerstner, W. and Kistler, W. (2002). *Spiking Neuron Models: Single Neurons, Populations, Plasticity*. Cambridge University Press, Cambridge.
- Gerstner, W. and van Hemmen, J. L. (1993). Coherence and incoherence in a globally coupled ensemble of pulse-emitting units. *Physical Review Letters*, **71**, 312–315.

- Gutkin, B. and Ermentrout, G. B. (1998). Dynamics of membrane excitability determine inter-spike interval variability: A link between spike generation mechanisms and cortical spike train statistics. *Neural Computation*, **10**, 1047–1065.
- Huertas, M. A. and Smith, G. D. (2006). A multivariate population density model of the dLGN/PGN relay. *Journal of Computational Neuroscience*, **21**, 171–189.
- Junk, M. and Unterreiter, A. (2002). Maximum entropy moment systems and Galilean invariance. *Continuum Mechanics and Thermodynamics*, **14**, 563–576.
- Knight, B. W. (1972). Dynamics of encoding in a population of neurons. *Journal of General Physiology*, **59**, 734–766.
- Knight, B. W. (2000). Dynamics of encoding in neuron populations: Some general mathematical features. *Neural Computation*, **12**, 473–518.
- Knight, B. W., Manin, D., and Sirovich, L. (1996). Dynamical models of interacting neuron populations. In *Symposium on Robotics and Cybernetics: Computational Engineering in Systems Applications* (ed. E. C. Gerf), Lille, France. Cite Scientifique.
- Knight, B. W., Omurtag, A., and Sirovich, L. (2000). The approach of a neuron population firing rate to a new equilibrium: an exact theoretical result. *Neural Computation*, **12**, 1045–1055.
- Koch, C. (1999). *Biophysics of Computation : Information Processing in Single Neurons*. Oxford University Press, New York.
- Krukowski, A. E. and Miller, K. D. (2001). Thalamocortical NMDA conductances and intracortical inhibition can explain cortical temporal tuning. *Nature Neuroscience*, **4**, 424–430.
- Kuramoto, Y. (1991). Collective synchronization of pulse-coupled oscillators and excitable units. *Physica D*, **50**, 15–30.
- Lindner, B. (2006). Superposition of many spike trains is generally not a Poisson process. *Physical Review E*, **73**, 022901.
- Ly, C. and Tranchina, D. (2007). Critical analysis of dimension reduction by a moment closure method in a population density approach to neural network modeling. *Neural Computation*, **19**, 2032–2092.
- McLaughlin, D., Shapley, R., and Shelley, M. (2003). Large-scale modeling of the primary visual cortex: Influence of cortical architecture upon neuronal response. *Journal of Physiology-Paris*, **97**, 237–252.
- McLaughlin, D., Shapley, R., Shelley, M., and Wielaard, D. J. (2000). A neuronal network model of Macaque primary visual cortex (V1): orientation selectivity and dynamics in the input layer 4C α . *Proceedings of National Academy of Science*, **97**, 8087–8092.
- Miller, P. and Wang, X. J. (2006). Power-law neuronal fluctuations in a recurrent network model of parametric working memory. *Journal of Neurophysiology*, **95**, 1099–1114.
- Moreno-Bote, R. and Parga, N. (2004). Role of synaptic filtering on the firing response of simple model neurons. *Physical Review Letters*, **92**, 028102.

- Mountcastle, V. B. (1997). The columnar organization of the neocortex. *Brain*, **120**, 701–722.
- Nykamp, D. Q. and Tranchina, D. (2000). A population density approach that facilitates large-scale modeling of neural networks: Analysis and an application to orientation tuning. *Journal of Computational Neuroscience*, **8**, 19–50.
- Nykamp, D. Q. and Tranchina, D. (2001). A population density approach that facilitates large-scale modeling of neural networks: Extension to slow inhibitory synapses. *Neural Computation*, **13**, 511–546.
- Omurtag, A., Kaplan, E., Knight, B., and Sirovich, L. (2000a). A population approach to cortical dynamics with an application to orientation tuning. *Network: Computation in Neural Systems*, **11**, 247–260.
- Omurtag, A., Knight, B. W., and Sirovich, L. (2000b). On the simulation of large populations of neurons. *Journal of Computational Neuroscience*, **8**(1), 51–63.
- Peskin, C. (1981). The stochastic auditory code. In *Mathematical Aspects of Physiology* (ed. F. C. Hoppensteadt), American Mathematical Society, Volume 19, pp. 59–67.
- Plesser, H. E. and Gerstner, W. (2000). Noise in integrate-and-fire neurons: from stochastic input to escape rates. *Neural Computation*, **12**, 367–384.
- Rangan, A. and Cai, D. (2006). Maximum-entropy closures for kinetic theories of neuronal network dynamics. *Physical Review Letters*, **96**, 178101.
- Rangan, A. and Cai, D. (2007). Fast numerical methods for simulating large-scale integrate-and-fire neuronal networks. *Journal of Computational Neuroscience*, **22**, 81–100.
- Rangan, A., Cai, D., and McLaughlin, D. (2005). Modeling the spatiotemporal cortical activity associated with the line-motion illusion in primary visual cortex. *Proceedings of the National Academy of Science*, **102**, 18793–18800.
- Ringach, D. L., Hawken, M. J., and Shapley, R. (1997). Dynamics of orientation tuning in Macaque primary visual cortex. *Nature*, **387**, 281–284.
- Risken, H. (1996). *The Fokker-Planck Equation: Methods of Solutions and Applications*. Springer-Verlag, New York.
- Shelley, M. and McLaughlin, D. (2002). Coarse-grained reduction and analysis of a network model of cortical response I. Drifting grating stimuli. *Journal of Computational Neuroscience*, **12**, 97–122.
- Sirovich, L. (2003). Dynamics of neuronal populations: Eigenfunction theory; Some solvable cases. *Network: Computational Neural Systems*, **14**, 249–272.
- Sirovich, L. (2008). Populations of tightly coupled neurons: the RGC/LGN system. *Neural Computation*, **20**, 1179–1210.
- Sirovich, L., Omurtag, A., and Knight, B. W. (2000). Dynamics of neuronal populations: the equilibrium solution. *SIAM Journal of Applied Mathematics*, **60**, 2009–2028.
- Somers, D. C., Nelson, S. B., and Sur, M. (1995). An emergent model of orientation selectivity in cat visual cortical simple cells. *Journal of Neuroscience*, **15**, 5448–5465.

- Strogatz, S. H. and Mirollo, R. E. (1991). Stability of incoherence in a population of coupled oscillators. *J. Stat. Phys.*, **63**, 613–635.
- Teramae, J. and Fukai, T. (2005). A cellular mechanism for graded persistent activity in a model neuron and its implications on working memory. *Journal of Computational Neuroscience*, **18**, 105–121.
- Tuckwell, H. C. (1988a). *Introduction to Theoretical Neurobiology: Volume 1, Linear Cable Theory and Dendritic Structure*, Chapter 3. Cambridge University Press, New York, NY.
- Tuckwell, H. C. (1988b). *Introduction to Theoretical Neurobiology: Volume 2, Nonlinear and Stochastic Theories*, Chapter 9. Cambridge University Press, New York, NY.
- Ursino, M. and La Cara, G. (2005). Dependence of visual cell properties on intracortical synapses among hypercolumns: analysis by a computer model. *Journal of Computational Neuroscience*, **19**, 291–310.
- Wang, X. J. (1999). Synaptic basis of cortical persistent activity: The importance of NMDA receptors to working memory. *Journal of Neuroscience*, **19**, 9587–9603.
- Wilbur, W. J. and Rinzel, J. (1983). A theoretical basis for large coefficient of variation and bimodality in neuronal interspike interval distributions. *Journal of Theoretical Biology*, **105**, 345–368.
- Wilson, H. R. and Cowan, J. D. (1972). Excitatory and inhibitory interactions in localized populations of model neurons. *Biophysical Journal*, **12**, 1–24.
- Wilson, H. R. and Cowan, J. D. (1973). A mathematical theory of the functional dynamics of cortical and thalamic nervous tissue. *Kybernetik*, **13**, 55–80.

A POPULATION DENSITY MODEL OF THE DRIVEN LGN/PGN

Marco A. Huertas and Gregory D. Smith

8.1 Thalamocortical relay nuclei

The thalamus has been called the gateway to the cortex because it transmits sensory information from the periphery to the neocortex through so-called first-order relay nuclei (Sherman and Guillery, 1996). Examples of first-order relays are the dorsal lateral geniculate nucleus (LGN) and the ventral posterior medial (VPM) nucleus of the thalamus. The LGN is a major recipient of retinal ganglion cell (RGC) afferents and represents the first non-retinal stage of visual processing in the mammalian central visual pathway (Sherman and Koch, 1990). The VPM is the main recipient of axonal projections from trigeminal cells that respond to mechanical stimulation of the whiskers in the rat's mystacial pad (Woolsey and der Loos, 1970, Castro-Alamancos, 2004). For recent comprehensive reviews of the neurobiology of the thalamus and the role of the thalamus in cortical function see Sherman and Guillery (2005) and Jones (2007).

Sensory thalamic nuclei such as the LGN and VPM act as state-dependent gateways between the sensory periphery and higher cortical centres (McCormick and Bal, 1997). During sleep, for example, the principal cells of the LGN exhibit rhythmic bursts of action potentials which do not reflect the excitatory glutamatergic drive they receive from spontaneously active retinal ganglion cells (RGCs). This rhythmic bursting may thus be interpreted as a 'closure' of the LGN gate. During arousal, this gateway 'opens' as thalamocortical (TC) relay neurons of the LGN cease rhythmic bursting, enter tonic mode, and fire conventional action potentials, the timing of which reflects excitatory post-synaptic potentials (EPSPs) received from visually stimulated RGCs.

Several different lines of investigation indicate that it is an oversimplification to view first-order thalamic relay nuclei as passive units that simply relay information to the cortex (Sherman and Koch, 1986, 1990, Sherman and Guillery, 1996, Sherman, 1996). For example, anatomical evidence indicates that only approximately 15% of synapses on LGN relay cells are from RGCs. The remainder originate from subcortical areas, GABAergic local interneurons (IN) of the LGN, GABAergic thalamic reticular (RE) neurons, and striate cortex. Indeed, the neuroanatomical observation that the majority of LGN synapses derive from cortex suggests that the thalamic visual processing may not even be predominantly feed-forward. Instead, visual cortex projecting to the LGN and PGN may actively gate retinogeniculate transmission.

There is also a growing body of evidence that LGN relay neurons in awake-behaving and anesthetized cats exhibit transient (as opposed to rhythmic) bursts of action potentials in response to visual stimulation (Guido, Lu, and Sherman, 1992, Weyand, Boudreux, and Guido, 2001, Guido and Weyand, 1995). When objective criteria are used to divide extracellular records into ‘burst’ and ‘tonic’ responses, it has been observed that LGN relay neurons in both modes can be visually driven (Guido *et al.*, 1995). While tonic responses show little nonlinear distortion and faithfully relay retinal input, relay cells in burst mode have lower spontaneous activity, resulting in an improved signal-to-noise ratio. One bold hypothesis is that these transient, visually driven bursts may signal the presence of stimuli in receptive fields to which attention is not currently directed (Sherman, 1996).

While this specific hypothesis may not be validated, the above observations certainly suggest that the LGN is a dynamic filter under cortical and subcortical control rather than a gateway that can be only completely open (during arousal) or completely closed (during sleep). Indeed, although the classical receptive field properties of LGN relay neurons do not differ markedly from those of the RGCs that innervate them, investigators utilizing spatial and temporal frequency analysis of LGN and PGN cell response properties have long suggested that the thalamus has an important dynamic role to play in visual processing, e.g., in contrast gain control (Kaplan, Purpura, and Shapley, 1987, Kaplan, Mukherjee, and Shapley, 1993). However, precisely how stimulus-dependent recruitment of inhibitory mechanisms of the LGN determine what retinal information is filtered out, and what retinal information is faithfully relayed to cortex, is an open question of current research (Casti *et al.*, 2008).

8.2 Sleep oscillations, rhythmic bursts, and arousal

Experimental and theoretical investigations of thalamic activity during sleep have provided an understanding of the biophysical basis of rhythmic oscillations in thalamus that are associated with sleep and certain forms of epilepsy (Destexhe and Sejnowski, 2001, Rush and Rinzel, 1994, Golomb, Wang, and Rinzel, 1996b, Wang, Golomb and Rinzel, 1995, Rinzel *et al.*, 1998). In particular, the 7- to 14-Hz spindle oscillation, which is observed during the onset of sleep, is a well-known phenomenon of coherent brain waves (Steriade and McCarley, 1990, Buzsaki, 2006). Spindle oscillations are an emergent network property of thalamic origin that involve synaptic interactions between excitatory (glutamatergic) thalamocortical (TC) relay neurons and inhibitory (GABAergic) neurons of the thalamic reticular (RE) nucleus, and the intrinsic low-threshold Ca^{2+} current (I_T) that both TC and RE cells express (see Fig. 8.1). The details of the mechanisms subserving rhythmic bursting are relevant to thalamic visual processing, because they are also responsible for transient bursts of LGN and PGN cells, and may be involved in other aspects of the gating of retinogeniculate transmission.

In TC cells at rest, the low-threshold Ca^{2+} current I_T is largely inactivated; however, I_T becomes de-inactivated upon hyperpolarization. This allows TC cells

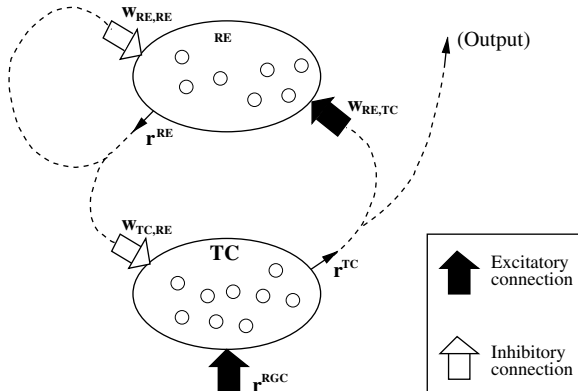


FIG. 8.1: Schematic diagram of the interaction between the RE and TC populations (*large ellipses*) in the Monte Carlo and population density simulations of driven LGN/PGN. The *small arrows* indicate the population firing rates r^{TC} and r^{RE} in the population density approach (Eqn (8.20)). The large arrows represent the interaction between populations (Eqn (8.24)) that is proportional to the average number of connections between pre- and post-synaptic cells (*small circles*). Excitatory drive from retinal ganglion cells (RGC) to TC cells is denoted by r^{RGC} . Reproduced with permission from Huertas and Smith (2006b).

to respond to release from hyperpolarization with a Ca^{2+} spike that triggers conventional action potentials on its crest. In the simulation shown in Fig. 8.2(c), a minimal TC-like integrate-and-fire-or-burst (IFB) model (Smith *et al.*, 2000) exhibits a post-inhibitory rebound burst in response to *hyperpolarizing* current injection (details of the IFB model are presented below). While TC cells hyperpolarized from rest may respond with a burst, TC cells depolarized from rest fire tonic spikes. Conversely, RE cells depolarized from rest respond with a burst, and if depolarized further can fire tonic spikes. RE cells burst in response to depolarization rather than hyperpolarization because they differentially express I_T and several other currents. This is illustrated in Fig. 8.2(d), which shows a voltage trace of a RE-like IFB model exhibiting a burst of action potentials in response to *depolarizing* current injection. In network oscillations of the sleeping thalamus, each cell type provides a synaptic conductance that may cause the other to burst. RE cells periodically provide (through GABAergic synapses) the hyperpolarization necessary for TC cells to respond with post-inhibitory rebound bursts. These TC cell rebound responses then excite RE cells through AMPA synapses and the cycle repeats.

Computational modelling has played an important role in the characterization and analysis of the dynamics of TC and RE neuron membrane currents,

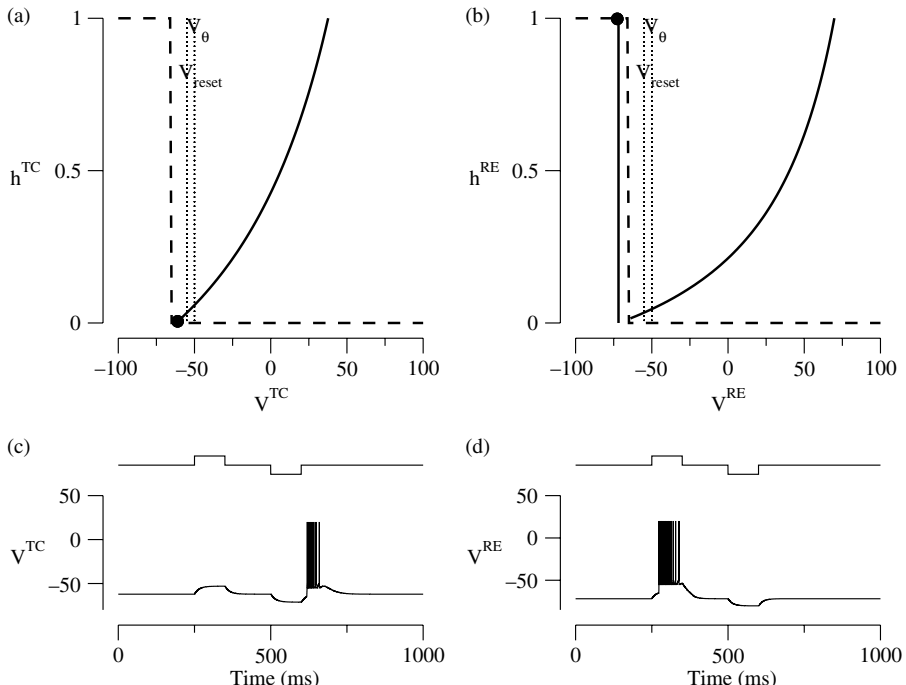


FIG. 8.2: (a), (b): (V, h) phase planes for the TC-like and RE-like IFB models (solid lines, $dV/dt = 0$; dashed lines, $dh/dt = 0$; see Eqns (8.1) and (8.2)). Filled circles indicate resting membrane potentials located at the intersection of the V and h nullclines ($E_L^{RE} = -71.8$ and $E_L^{TC} = -62.1$ mV). (c): Applied current pulse of $\pm 0.6 \mu\text{A}/\text{cm}^2$ (upper solid line) and corresponding voltage trace (lower solid line) of TC-like IFB model exhibiting a post-inhibitory rebound (PIR) burst in response to the hyperpolarizing current pulse. (d): Voltage trace (lower solid line) of RE-like IFB model exhibiting a burst of action potentials in response to depolarizing current injection (upper solid line). Parameters as in Table 8.1 save $C = 1 \mu\text{F}/\text{cm}^2$, $g_T^{TC} = 0.08 \text{ mS}/\text{cm}^2$, $g_{KL}^{TC} = 0.016 \text{ mS}/\text{cm}^2$, $g_{KL}^{RE} = 0.031 \text{ mS}/\text{cm}^2$. Adapted with permission from Huertas, Groff, and Smith (2005b).

in particular, the low-threshold Ca^{2+} current, I_T , and the hyperpolarization-activated nonspecific cation current, I_h (Destexhe *et al.*, 1996, Destexhe *et al.*, 1998, Zhan *et al.*, 1999, Gutierrez *et al.*, 2001). While the biophysical basis of rhythmic bursting in the thalamus has been extensively modelled (Destexhe, McCormick, and Sejnowski, 1993, Destexhe, Babloyantz, and Sejnowski, 1993, Destexhe *et al.*, 1994a, Destexhe *et al.*, 1994b, Rush and Rinzel, 1994, Wang, Golomb, and Rinzel, 1995, Golomb, Wang, and Rinzel, 1996a, Lytton, Destexhe,

and Sejnowski, 1996, Destexhe *et al.*, 1996, Rinzel *et al.*, 1998), there are comparatively few computational studies of the dynamic filter properties of thalamic relay nuclei during states of arousal. Kaplan and co-workers published two early studies of the burst and tonic response properties of driven LGN relay cells that included Hodgkin–Huxley (HH)-style simulations emphasizing the role of T-channel kinetics (Mukherjee and Kaplan, 1995, 1998). Firing rate models of retinogeniculate transmission have included feedback from primary visual cortex to the dLGN, but this modelling approach does not account for low-threshold currents or distinguish between burst and tonic spikes (Hayot and Tranchina, 2001). Our own prior work has focused on input/output properties of individual TC neurons (Smith *et al.*, 2000, 2006, Smith and Sherman, 2002) and network studies of the role of feedback inhibition from RE cells in shaping visually-driven TC responses (Huertas, Groff, and Smith, 2005a, 2005b, Huertas and Smith, 2006a, 2006b). Other investigators have used the TC- and RE-like IFB models (Fig. 8.2) as a starting point for computational analysis of the input/output properties of minimal thalamic circuits (Babadi, 2005). In this chapter, we will describe how a large-scale model of sensory relay by the LGN/PGN can be implemented using TC- and RE-like IFB models and the population density methods presented in Chapter 7.

8.3 The integrate-and-fire-or-burst model

Because the integrate-and-fire-or-burst (IFB) model originally presented by Smith *et al.* (2000) reproduces the salient response properties of TC cells driven by sinusoidal current injection, it is a reasonable starting point for network simulations of LGN/PGN responses driven by RGC input. Briefly, a TC-like IFB model is constructed by adding a slow variable to a classical integrate-and-fire (IF) neuron,

$$C \frac{dV_{TC}}{dt} = -I_L - g_T m_\infty h_{TC} (V_{TC} - E_T) \quad (8.1)$$

$$\frac{dh_{TC}}{dt} = \begin{cases} (1 - h_{TC}) / \tau_h^+ & \text{for } V_{TC} < V_h \\ -h_{TC} / \tau_h^- & \text{for } V_{TC} \geq V_h \end{cases} \quad (8.2)$$

where we have expressed the leakage current, I_L , as the sum of potassium and non-specific currents

$$I_L = I_{KL} + I_{NL} = -g_{KL} (V_{TC} - E_{KL}) - g_{NL} (V_{TC} - E_{NL}).$$

A spike occurs when V_{TC} reaches the threshold $V_\theta = -50$ mV, and subsequently an absolute refractory period of length $t_R = 4$ ms is imposed during which $V_{TC}=V_{\text{reset}} = -55$ mV. The activation of I_T is idealized here as an instantaneous step function of voltage given by

$$m_\infty (V_{TC}) = \begin{cases} 0 & \text{for } V_{TC} < V_h \\ 1 & \text{for } V_{TC} \geq V_h \end{cases}$$

with the activation parameter $V_h = -65$ mV corresponding to an all-or-none low-threshold voltage. The slow variable h_{TC} represents de-inactivation of I_T and satisfies Eqn (8.2). When V_{TC} is hyperpolarized below V_h , h_{TC} relaxes to 1 with time constant $\tau_h^+ = 100$ ms. When V_{TC} is depolarized above V_h , h_{TC} exponentially decays with time constant $\tau_h^- = 20$ ms.

Modification of several important parameters converts the TC-like IFB model into an RE-like version. While most of the parameters remain unchanged (e.g. V_θ and V_h), the RE cell leakage reversal potential (E_L^{RE}) is approximately 9 mV more hyperpolarized than the TC cell leakage reversal potential (E_L^{TC}). This difference makes the TC-like model resting membrane potential E_L^{TC} more depolarized than V_h , while the RE-like model E_L^{RE} is more hyperpolarized than V_h . The parameters chosen lead to the (V_{TC}, h_{TC}) and (V_{RE}, h_{RE}) phase planes shown in Fig. 8.2(a) and (b). The *solid* and *dashed lines* indicate the nullclines for voltage ($dV_{TC}/dt = 0$ and $dV_{RE}/dt = 0$) and I_T de-inactivation ($dh_{TC}/dt = 0$ and $dh_{RE}/dt = 0$), respectively. The vertical branch of the h_{TC} and h_{RE} nullcline (i.e. the *vertical dashed line*) corresponds to the burst threshold V_h and the *vertical dotted lines* show the location of the spike threshold (V_θ) and reset (V_{reset}) voltage. The *filled circle* located at the intersection of the V_{TC} and h_{TC} and V_{RE} and h_{RE} nullclines shows the resting state of the TC- and RE-like IFB neurons in the absence of synaptic input.

The simulated voltage traces of Fig. 8.2(c) showing the TC-like IFB model exhibiting a PIR burst in response to hyperpolarizing current injection can be understood using the phase plane of Fig. 8.2(a) as a consequence of the resting membrane potential (E_L^{TC} , *filled circle*) being more depolarized than the burst threshold (V_h , *vertical dashed line*). On the other hand, Fig. 8.2(d) shows simulated voltage traces of an RE-like IFB model exhibiting a burst of action potentials in response to depolarizing current injection. Here also the relative location of the resting membrane potential (E_L^{RE}) with respect to V_h explains this behaviour (see Fig. 8.2b). Because the maximum conductance for the low-threshold Ca^{2+} current is greater in the RE-like IFB model ($g_T^{RE} = 0.2\text{mS/cm}^2$) than in the TC-like version ($g_T^{TC} = 0.08\text{mS/cm}^2$), the RE cell burst response exhibits more action potentials (compare Figs. 8.2c and d).

8.4 Synaptic interactions and network connectivity

The LGN/PGN network model presented here is made up of two populations of neurons – one composed of TC-like and the other of RE-like IFB neurons – that interact through excitatory and inhibitory synapses (Fig. 8.1). The TC cells receive excitatory drive from retinal ganglion cells (RGCs) and provide an excitatory input to the RE population, while active RE cells provide feedback inhibition to the TC cells as well as recurrent inhibition to other RE cells (Golomb, Wang, and Rinzel, 1996b; Sanchez-Vives, Bal, and McCormick, 1997; Sanchez-Vives and McCormick, 1997). The response of the TC population that results from these interactions, either in the presence or absence of retinal drive, constitutes the network output. For simplicity, we include neither feed-forward

nor feedback inhibitory action of local interneurons (Cox, Zhou, and Sherman, 1998, Cox and Sherman, 2000, Cox, Reichova, and Sherman, 2003, Govindaiah and Cox, 2004).

Following Omurtag *et al.* (2000a and 2000b) and Nykamp and Tranchina (2000), the excitatory and inhibitory effects of presynaptic action potentials are modelled as instantaneous changes in the membrane potential of postsynaptic neurons. As discussed in Section 7.6.1 of this book, the effect on the postsynaptic cell of an action potential arriving at time \tilde{t} is an instantaneous change in membrane potential with magnitude,

$$\Delta\tilde{V} = \tilde{V}(\tilde{t}^+) - \tilde{V}(\tilde{t}^-) = [1 - \exp(-\tilde{\gamma}_{e/i})] [E_{e/i} - \tilde{V}(\tilde{t}^-)], \quad (8.3)$$

where $\tilde{\gamma}_{e/i}$ is a dimensionless random variable given by

$$\tilde{\gamma}_{e/i} = \frac{1}{C} \int \tilde{g}_{e/i}(t) dt.$$

In these expressions, tildes indicate random variables, $\tilde{g}_{e/i}(t)$ is the change in conductance due to the synaptic input at time \tilde{t} , and $E_{e/i}$ is the reversal potential of the corresponding excitatory (e) or inhibitory (i) synaptic current. Note that the random variable $\tilde{\gamma}_{e/i}^* = 1 - \exp(-\tilde{\gamma}_{e/i})$ takes values in the range of 0 to 1 and gives the change in the membrane potential ($\Delta\tilde{V}$) as a fraction of the difference between the membrane potential at the time of the arriving spike and the excitatory or inhibitory reversal potential, that is,

$$\tilde{\gamma}_{e/i}^* = \frac{\tilde{V}(\tilde{t}^+) - \tilde{V}(\tilde{t}^-)}{E_{e/i} - \tilde{V}(\tilde{t}^-)}. \quad (8.4)$$

This formulation assumes that changes in membrane potential due to the arrival of an action potential occur on a time-scale much shorter than the membrane's time-constant. Consequently, the model includes RE-to-TC inhibition mediated by fast (ionotropic) GABA_A receptors, but does not include slower (metabotropic) inhibition mediated by metabotropic GABA_B receptors.

In simulations presented below, the random variable $\tilde{\gamma}_{e/i}$ that corresponds to the magnitude of synaptic events is assumed to be gamma distributed with order $n = 4$ and mean $na_{e/i}$ (see Table 8.1). That is, the continuous probability distribution function $f_{\tilde{\gamma}_{e/i}}(\gamma)$ is given by

$$f_{\tilde{\gamma}_{e/i}}(\gamma) = \frac{\exp(-\gamma/a_{e/i})}{a_{e/i}(n-1)!} \left(\frac{\gamma}{a_{e/i}} \right)^{n-1}, \quad (8.5)$$

from which it follows that the random variable $\tilde{\gamma}_{e/i}^*$ is distributed according to

$$f_{\tilde{\gamma}_{e/i}^*}(\gamma) = \frac{1}{1-\gamma} f_{\tilde{\gamma}_{e/i}}(\gamma') \quad \text{where } \gamma' = -\ln(1-\gamma). \quad (8.6)$$

Interactions between presynaptic and postsynaptic cells also include random synaptic latencies ($\tilde{\tau}$) representing the finite speed of action potential propagation. These latencies are drawn from a truncated gamma distribution that would otherwise be order $n = 9$ with mean $n\alpha = 3$ ms (Nykamp and Tranchina, 2000), that is,

$$f_{\tilde{\tau}}(\tau) = \begin{cases} \alpha_{\text{norm}} \frac{\exp(-\tau/\alpha)}{\alpha(n-1)!} \left(\frac{\tau}{\alpha}\right)^{n-1} & 0 \leq \tau \leq \alpha_{\text{max}} \\ 0 & \text{otherwise,} \end{cases} \quad (8.7)$$

where $\alpha_{\text{max}} = 7.5$ ms and α_{norm} is a normalization constant. For physiological realism, the relationship between the excitatory and inhibitory synaptic reversal potentials and the spike threshold of the IFB model is assumed to be $E_i < V_\theta < E_e$. Thus, when Eqns (8.1) and (8.2) are driven by random synaptic input as described by Eqns (8.3)–(8.6), the state of a neuron initially satisfying $E_i \leq \tilde{V} \leq V_\theta$ and $0 \leq \tilde{h} \leq 1$ will remain in this range for all time.

To complete the model formulation, we assume that the TC and RE populations each contain N identical IFB neurons (Eqns (8.1) and (8.2)) with the TC- and RE-like parameters of Table 8.1. The random connectivity of the RE and TC cell populations in the LGN/PGN model is specified by a 2×2 matrix

$$W = (w_{ij}) = \begin{pmatrix} w_{\text{RE,RE}} & w_{\text{RE,TC}} \\ w_{\text{TC,RE}} & 0 \end{pmatrix} \quad (8.8)$$

with elements indicating the mean number of postsynaptic neurons in population j influenced by the spiking of a presynaptic neuron in population i . Typical values of w_{ij} are in the range of 5–50 with the exception of $w_{\text{TC,TC}}$ which is always zero. In the simulations presented below, we do not instantiate a $2N \times 2N$ connectivity matrix consistent with Eqn (8.8) and perform simulations using a fixed network topology. Instead, as suggested by Knight (1972) and Nykamp and Tranchina (2000), presynaptic spikes lead to a postsynaptic event in each and every postsynaptic neuron with probability $p = w_{ij}/N$. The number of postsynaptic potentials evoked by each presynaptic spike is thus a binomially distributed random variable with parameters N and p (and mean w_{ij}).

Figures 8.3(a) and (b) show the simulated membrane potential and de-inactivation gating variable as a function of time for two representative RE cells during a 2×100 neuron Monte Carlo simulation of the LGN/PGN network described above. Panel (e) shows the same traces in the (v, h) -plane along with *vertical dashed lines* indicating the burst threshold (V_h), the resting potential (E_L), and the reset potential (V_{reset}) of the RE cells. Panels (c), (d), and (f) show the corresponding results for two representative TC cells. As depicted in Fig. 8.1, the LGN/PGN network model is stimulated by excitatory synaptic drive from a population of RGC neurons to the TC population. The RGC-to-TC interaction is one-to-one and the event times for RGC action potentials are simulated as a Poisson point process with an average rate of 60 Hz (not shown). The

TABLE 8.1. Parameters for the LGN/PGN population density model following previous experimental and theoretical work (Smith *et al.*, 2000, Huertas *et al.*, 2005b). The parameters representing the magnitude of synaptic events ($a_{e/i}$ in Eqn (8.5)) were chosen to be consistent with experimental estimates. For example, the value of a_e^{RGC} was chosen so that in the absence of feedback inhibition the TC output correspond to a 50% transfer ratio (Kaplan, Purpura, and Shapley, 1987, Kaplan, Mukherjee, and Shapley, 1993). The values of a_e^{RE} (TC-to-RE excitation) and a_i^{TC} (RE-to-TC feedback inhibition) lead to average postsynaptic potentials shown in parentheses when the postsynaptic neuron is at rest. Experimental estimates of the mean number of synaptic connections between populations were used as upper limits on the w_{ij} (Kim and McCormick, 1998).

Parameter	Value	Unit	Description
Cellular parameters common to the TC- and RE-like IFB models:			
C	2	$\mu\text{F}/\text{cm}^2$	membrane capacitance
V_θ	-50	mV	integrate-and-fire spike threshold
V_{reset}	-55	mV	integrate-and-fire reset voltage
t_R	4	ms	absolute refractory period
V_h	-65	mV	I_T activation and inactivation threshold
τ_h^+	100	ms	I_T de-inactivation time constant
τ_h^-	20	ms	I_T inactivation time constant
E_T	120	mV	I_T reversal potential
E_{NL}	-50	mV	I_{NL} reversal potential
E_{KL}	-100	mV	I_{KL} reversal potential
Cellular parameters specific to RE:			
$g_{\text{NL}}^{\text{RE}}$	0.04	mS/cm^2	non-specific leak conductance
$g_{\text{KL}}^{\text{RE}}$	0.027	mS/cm^2	potassium leak conductance
g_T^{RE}	0.2	mS/cm^2	low-threshold Ca^{2+} conductance
Cellular parameters specific to TC:			
$g_{\text{NL}}^{\text{TC}}$	0.05	mS/cm^2	non-specific leak conductance
$g_{\text{KL}}^{\text{TC}}$	0.02	mS/cm^2	potassium leak conductance
g_T^{TC}	0.08	mS/cm^2	low-threshold Ca^{2+} conductance
Synaptic parameters:			
E_{AMPA}	0	mV	reversal potential of excitatory synaptic current
E_{GABA_A}	-85	mV	reversal potential of inhibitory synaptic current
a_e^{RE}	0.0047	-	magnitude of TC to RE excitation (+1.3 mV)
a_i^{TC}	0.0119	-	magnitude of RE to TC inhibition (-1.0 mV)
a_i^{RE}	0.0119	-	magnitude of RE to RE inhibition (-0.7 mV)
a^{RGC}	0.045	-	magnitude of RGC to TC excitation (+10.6 mV)
$w^{\text{TC,TC}}$	0	-	mean number of TC-to-TC synaptic connections
$w^{\text{TC,RE}}$	5–50	-	mean number of TC-to-RE synaptic connections
$w^{\text{RE,TC}}$	5–50	-	mean number of RE-to-TC synaptic connections
$w^{\text{RE,RE}}$	5–50	-	mean number of RE-to-RE synaptic connections

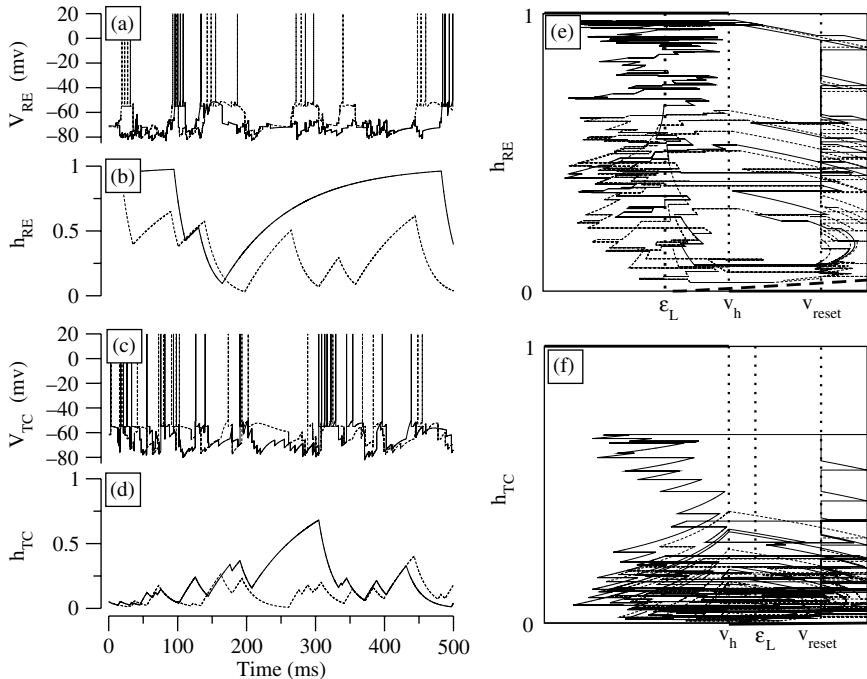


FIG. 8.3: Panels (a) and (b) show the membrane potential and de-inactivation gating variable as a function of time for two representative RE cells during a 2×100 neuron Monte Carlo simulation of the LGN/PGN network. Panel (e) shows the same traces in the (v, h) -plane. Panels (c), (d), and (f) show the corresponding results for two representative TC cells. Reproduced with permission from Huertas and Smith (2006b).

magnitude of the change in membrane potential due to each synaptic event is distributed according to Eqn (8.5). Note that during burst responses in Fig. 8.3, the gating variable for the low-threshold Ca^{2+} current of the representative RE and TC neurons decreases (inactivation of I_T) with an exponential time constant of $\tau_h^- = 20$ ms and increases (de-inactivation) with time constant $\tau_h^+ = 100$ ms. The instantaneous changes in membrane potential observed in panels (a) and (b) due to the arrival of a presynaptic spike can be observed in panels (e) and (f) as horizontal lines of variable length. Between spikes the trajectories followed by each cell type correspond to solutions to Eqns (8.1) and (8.2). The network connectivity used in this representative simulation is $w_{RE,RE} = w_{RE,TC} = w_{TC,RE} = 5$ and the 60 spikes/s spontaneous retinal input results in population firing rates of 170 and 110 spikes/s for the RE and TC cell populations, respectively.

8.5 Population density formulation

Because the Monte Carlo network simulation of the LGN/PGN presented in the previous section describes the time-evolution of each neuron in the population (either TC or RE), the method faces a computational disadvantage when the number of cells in the population is very large. However, because the neurons in each population are *homogeneous* in their cell properties – e.g. all RE-like IFB neurons possess the same membrane capacitance, resting membrane potential, and so on – an alternative population density approach can be employed that uses probability density functions to track the distribution of state variables (V and h) within each population (Knight, 1972, Omurtag *et al.*, 2000a, Omurtag *et al.*, 2000b, Nykamp and Tranchina, 2000).

Beginning with Eqns (8.1) and (8.2) we identify the drift rates $F_v(V, h)$ and $F_h(V, h)$ such that

$$\frac{dV}{dt} = F_v(V, h) \quad (8.9)$$

$$\frac{dh}{dt} = F_h(V, h) \quad (8.10)$$

where $F_v = -(I_L + I_T)/C$, and for clarity we have dropped the superscript TC. As discussed by Casti *et al.* (2002), an infinite *homogeneous* population of IFB neurons whose state variables satisfy Eqns (8.9) and (8.10) can be described by a two-dimensional probability density function

$$\rho(V, h, t) dV dh = \mathbb{P}\{V < \tilde{V}(t) < V + dV \text{ and } h < \tilde{h}(t) < h + dh\}. \quad (8.11)$$

Assuming the probability density function is initially restricted to the domain $E_i \leq V \leq V_\theta$ and $0 \leq h \leq 1$, these densities satisfy a conservation equation of the form

$$\frac{\partial}{\partial t} \rho(V, h, t) = -\nabla \cdot \vec{J}(V, h, t) + \delta(V - V_{\text{reset}}) \vec{J}_{\text{reset}} \cdot \hat{e}_v \quad (8.12)$$

where the ∇ operator is given by

$$\nabla = \hat{e}_v \frac{\partial}{\partial V} + \hat{e}_h \frac{\partial}{\partial h},$$

$\hat{e}_{v/h}$ are unit vectors in the (V, h) -plane, and the \vec{J}_{reset} term is defined below. In Eqn (8.12), the *total probability flux* $\vec{J}(V, h, t)$ is composed of two terms:

$$\vec{J}(V, h, t) = \vec{J}_{\text{int}} + \vec{J}_{\text{ext}}. \quad (8.13)$$

The first term (\vec{J}_{int}) represents the changes in the probability density due to the intrinsic membrane dynamics of the IFB model,

$$\vec{J}_{\text{int}}(V, h, t) = [F_v(V, h)\hat{e}_v + F_h(V, h)\hat{e}_h] \rho(V, h, t), \quad (8.14)$$

where F_v and F_h are the advection rates in the v - and h -directions (Eqns (8.9) and (8.10)). The second term in Eqn (8.13) (\vec{J}_{ext}) is the extrinsic probability flux that accounts for changes in membrane potential due to synaptic input (Nykamp and Tranchina, 2000),

$$\begin{aligned} \vec{J}_{\text{ext}} = & \hat{e}_v \left[\eta_e(t) \int_{E_i}^V \bar{F}_{\gamma_e^*} \left(\frac{V - V'}{E_e - V'} \right) \rho(V', h, t) dV' \right. \\ & \left. - \eta_i(t) \int_V^{V_\theta} \bar{F}_{\gamma_i^*} \left(\frac{V - V'}{E_i - V'} \right) \rho(V', h, t) dV' \right]. \end{aligned} \quad (8.15)$$

In this expression, $E_{e/i}$ is the reversal potential of excitatory/inhibitory synaptic currents and $\eta_{e/i}$ is the rate of excitatory/inhibitory synaptic events arriving to the population of IFB neurons. To understand the integrals, consider the case of excitatory connections, in which the quantity $\bar{F}_{\gamma_e^*}$ is the complementary cumulative distribution function of the random variable $\gamma_{e/i}^*$ (Eqn (8.4)) that gives the increase in voltage as a fraction of the distance to the reversal potential of the excitatory synaptic current,

$$\bar{F}_{\tilde{\gamma}_{e/i}^*}(\gamma) = P\{\tilde{\gamma}_{e/i}^* > \gamma\} = \int_\gamma^1 f_{\tilde{\gamma}_{e/i}^*} d\gamma = \int_\gamma^1 \frac{f_{\tilde{\gamma}_{e/i}^*}\{-\ln(1-\gamma')\}}{1-\gamma'} d\gamma', \quad (8.16)$$

where the last equality is given by Eqn (8.6), that is, evaluating $\bar{F}_{\gamma_e^*}$ as in Eqn (8.15) gives the probability that $\tilde{\gamma}_e^* > (V - V')/(E_e - V')$. Integrating the product of this quantity and the density $\rho(V', h, t)$ from E_i to V and scaling by $\eta_e(t)$ gives the probability flux of neurons jumping to a membrane potential beyond V upon receiving excitatory input.

Note that the probability density function evolves in time according to Eqn (8.12) and must remain confined to the physiological region $E_i \leq V \leq V_\theta$ and $0 \leq h \leq 1$. This requirement imposes boundary conditions on $\rho(V, h, t)$ that correspond to vanishing probability density flux (see Eqn (8.13)). These are

$$\rho(V = E_i, 0 \leq h \leq 1, t) = 0 \quad (8.17)$$

$$\rho(E_i \leq V < V_h, h = 0, t) = 0 \quad (8.18)$$

$$\rho(V_h \leq V \leq V_\theta, h = 1, t) = 0, \quad (8.19)$$

while $\rho(E_i \leq V < V_h, h = 1, t)$ and $\rho(V_h \leq V \leq V_\theta, h = 0, t)$ are not required to be zero since on those boundaries the drift rates vanish exactly, and $\rho(V = V_\theta, 0 \leq h \leq 1, t)$ is also not necessarily zero since even in the absence of external input there can be a net flux through $V = V_\theta$ from neurons firing in burst mode.

The component of the total probability flux \vec{J} in the voltage direction (\hat{e}_v) at $V = V_\theta$ corresponds to the fraction of neurons per unit time crossing the

spike threshold and becoming refractory. Thus, the population firing rate $r(t)$ is given by

$$r(t) = \int_0^1 \vec{J}_{\text{spike}}(h, t) \cdot \hat{e}_v dh \quad \text{where } \vec{J}_{\text{spike}}(h, t) = \vec{J}(V = V_\theta, h, t). \quad (8.20)$$

It is sometimes convenient to choose a particular value of the de-inactivation gating variable of the low-threshold current (e.g. $\bar{h} = 0.05$) and thereby distinguish burst and tonic portions of the firing rate,

$$r_{\text{tonic}}(t) = \int_0^{\bar{h}} \vec{J}_{\text{spike}}(h, t) \cdot \hat{e}_v dh \quad r_{\text{burst}}(t) = \int_{\bar{h}}^1 \vec{J}_{\text{spike}}(h, t) \cdot \hat{e}_v dh \quad (8.21)$$

where $r(t) = r_{\text{tonic}}(t) + r_{\text{burst}}(t)$.

Finally, the probability flux $\vec{J}_{\text{reset}}(h, t)$ in Eqn (8.12) represents neurons leaving the refractory state and becoming responsive again at the membrane potential $V = V_{\text{reset}}$. Because the gating variable for the low-threshold Ca^{2+} current continues to inactivate during the refractory time τ_r , the flux $\vec{J}_{\text{reset}}(h, t)$ is given by

$$\vec{J}_{\text{reset}}(h, t) = \begin{cases} e^{\tau_r/\tau_h^-} \vec{J}_{\text{spike}} \left(h e^{\tau_r/\tau_h^-}, t - \tau_r \right) & \text{for } h e^{\tau_r/\tau_h^-} \leq 1 \\ 0 & \text{otherwise.} \end{cases} \quad (8.22)$$

When this expression is used in Eqn (8.12), the boundary conditions given by Eqns (8.17)–(8.19) imply that the probability densities are conserved, that is,

$$\int_{E_i}^{V_\theta} \int_0^1 \rho(V, h, t) dh dV + \int_{t-\tau_r}^t r(t') dt' = 1, \quad (8.23)$$

where the second integral gives the fraction of neurons in the population that are refractory at time t .

To complete the population density formulation of the LGN/PGN network depicted in Fig. 8.1, we distinguish between the density functions describing the RE and TC populations by writing $\rho^p(V, h, t)$ where $p = \text{TC, RE}$. Each density solves equations of the form (8.12)–(8.22) with TC- or RE-like cellular parameters, respectively (Table 8.1). As diagrammed in Fig. 8.1, the network is constructed by associating the rate of excitatory and inhibitory synaptic events with the population firing rate of the presynaptic neuronal populations. The rates $\eta_{e/i}^p(t)$ in Eqn (8.15) are given by

$$\eta_{e/i}^p(t) = \eta_{e/i}^{p,0}(t) + \sum_{q=\text{TC,RE}} w_{qp} \int_0^\infty f_{\tilde{\tau}}(t') r^q(t - t') dt' \quad (8.24)$$

where $\eta_{e/i}^{p,0}(t)$ represents external drive to the population p , and the quantities w_{ij} are the mean synaptic connectivities (Eqn (8.8)), $f_{\tilde{\tau}}(t)$ is the probability

distribution function for the synaptic delays (Eqn (8.7)), and $r^q(t)$ is the firing rate of presynaptic population q (Eqn (8.20)). In the LGN/PGN model $\eta_{i}^{\text{TC},0} = \eta_{e/i}^{\text{RE},0} = 0$ and $\eta_e^{\text{TC},0}(t) = r^{\text{RGC}}(t)$ because the only external drive is the excitatory retinal input to the TC cell population.

8.6 Numerical method and model parameters

Numerical solution of the population density model described in the previous section can be performed using the total variation diminishing (TVD) scheme described in Casti *et al.* (2002) that is here presented with some important modifications. First, note that Eqn (8.12) can be rewritten in conservative form,

$$\frac{\partial}{\partial t}\rho(V, h, t) = -\nabla \cdot \left[\vec{J}(V, h, t) + \Theta(V - V_{\text{reset}})\vec{J}_{\text{reset}}(h, t) \right] \quad (8.25)$$

where the δ -function reaction term is responsible for the Heaviside function (Θ) inside the divergence operator and we have dropped the superscripted p 's for clarity. Next, we discretize the membrane voltage as $V_j = j\Delta V + E_i$ where $j = 0, 1, \dots, N_v$, the number of mesh-points in the v -direction, and $\Delta V = (V_\theta - E_i)/N_v$. Similarly, the low-threshold Ca^{2+} current gating variable is discretized as $h_j = j\Delta h$ where $j = 0, 1, \dots, N_h$ and $\Delta h = 1/N_h$. The total probability flux evaluated at V_i and h_j is denoted here as \vec{f}_{ij} and identified as

$$\vec{f}_{ij}(t) = f_{ij}^v \hat{e}_v + f_{ij}^h \hat{e}_h = \vec{J}(V_i, h_j, t) + \Theta(V_i - V_{\text{reset}})\vec{J}_{\text{reset}}(h_j, t). \quad (8.26)$$

where the second equality defines f_{ij}^v and f_{ij}^h . With these preliminaries, the numerical scheme can be written as

$$\frac{d\rho_{ij}}{dt} = -\frac{1}{\Delta V} [g_{ij}^v - g_{i-1,j}^v] - \frac{1}{\Delta h} [g_{ij}^h - g_{i,j-1}^h] \quad (8.27)$$

where g_{ij}^v , $g_{i-1,j}^v$, g_{ij}^h , and $g_{i,j-1}^h$ are given by

$$g_{ij}^v = f_{i+\frac{1}{2},j}^* + \frac{1}{2}\psi_{i-\frac{1}{2},j}^+(f_{i,j} - f_{i-\frac{1}{2},j}^*) + \psi_{i+\frac{3}{2},j}^-(f_{i+1,j} - f_{i+\frac{3}{2},j}^*) \quad (8.28)$$

$$g_{ij}^h = f_{i,j+\frac{1}{2}}^* + \frac{1}{2}\psi_{i,j-\frac{1}{2}}^+(f_{i,j} - f_{i,j-\frac{1}{2}}^*) + \psi_{i,j+\frac{3}{2}}^-(f_{i,j+1} - f_{i,j+\frac{3}{2}}^*) \quad (8.29)$$

and the terms $f_{i+\frac{1}{2},j}^*$ and $f_{i,j+\frac{1}{2}}^*$ are first-order Roe fluxes defined by (Casti *et al.*, 2002, Hundsdorfer and Verwer, 2003),

$$f_{i+\frac{1}{2},j}^* = \frac{1}{2}(f_{i,j} + f_{i+1,j}) - \frac{1}{4}|F_{i,j}^v + F_{i+1,j}^v|(\rho_{i+1,j} - \rho_{i,j}) \quad (8.30)$$

$$f_{i,j+\frac{1}{2}}^* = \frac{1}{2}(f_{i,j} + f_{i,j+1}) - \frac{1}{4}|F_{i,j}^h + F_{i,j+1}^h|(\rho_{i,j+1} - \rho_{i,j}), \quad (8.31)$$

where F_{ij}^v and F_{ij}^h are the discretized v - and h -components of the advection rate due to the intrinsic membrane properties of the IFB model (cf. Eqns (8.9) and (8.10)). The quantities ψ^+ and ψ^- occurring in Eqns (8.28) and (8.29) are flux limiters given by

$$\begin{aligned}\psi_{i-\frac{1}{2},j}^+ &= \psi \left[\frac{f_{i+1,j} - f_{i+\frac{1}{2},j}^*}{f_{i,j} - f_{i-\frac{1}{2},j}^*} \right] & \psi_{i+\frac{3}{2},j}^- &= \psi \left[\frac{f_{i,j} - f_{i+\frac{1}{2},j}^*}{f_{i+1,j} - f_{i+\frac{3}{2},j}^*} \right] \\ \psi_{i,j-\frac{1}{2}}^+ &= \psi \left[\frac{f_{i,j+1} - f_{i,j+\frac{1}{2}}^*}{f_{i,j} - f_{i,j-\frac{1}{2}}^*} \right] & \psi_{i,j+\frac{3}{2}}^- &= \psi \left[\frac{f_{i,j} - f_{i,j+\frac{1}{2}}^*}{f_{i,j+1} - f_{i,j+\frac{3}{2}}^*} \right]\end{aligned}$$

where

$$\psi[r] = \max [0, \min(2r, 1), \min(r, 2)]. \quad (8.32)$$

Note that the discretized probability flux in the v -direction given by f_{ij}^v in Eqn (8.26) includes contributions due to synaptic input and the reset flux ($f_{ij}^v = F_{ij}^v \rho_{ij} + J_{ij}^v$) and these fluxes contribute $\frac{1}{2}(J_{i,j}^v + J_{i+1,j}^v)$ to the Rho flux $f_{i+\frac{1}{2},j}^*$.

Figure 8.4 shows details of the numerical implementation of the boundary conditions given by Eqns (8.17)–(8.19). As required by the five-point stencil used in Eqns (8.25)–(8.32), two rows and two columns of ‘ghost’ points are shown in addition to the interior and boundary mesh points of the (V, h) -plane. The *open circles* and *squares* of Figure 8.4 indicate the unknown probability densities updated using Eqns (8.25)–(8.32), while the *filled circles* and *squares* indicate mesh points where the probability density is known to be zero. The *open squares* located at the $h = 1$ boundary for $V < V_h$ and the $h = 0$ boundary for $V \geq V_h$ are unique in that they are located at the reversal of the h -component of the advection rate $F_h(V, h)$ due to the intrinsic dynamics of the IFB model (Eqn (8.10)) and, consequently, probability density can accumulate at these points. To guarantee conservation of probability, it is important to set the advection rate to zero at the *filled squares* located external to the boundaries. Conservation of probability also requires that the ghost points external to boundaries where the advection rate is not reversing (*filled circles*) use F_{ij}^v and F_{ij}^h given by Eqns (8.9) and (8.10).

Note that g_{ij}^v in Eqn (8.28) corresponds to the magnitude of the total probability flux in the V -direction at the (V_i, h_j) mesh point. Evaluating this at the $V = V_\theta$ boundary ($i = N_v$), it provides an approximation to the spiking flux of Eqn (8.20) (as a function of h_j). Numerical integration along the h -direction gives the population firing rate (Eqn (8.20)) which is used to calculate the reset flux (Eqn (8.12)) and the rate of synaptic input (Eqn (8.24)). In the simulations presented below, integration in time is performed using Euler’s method with a

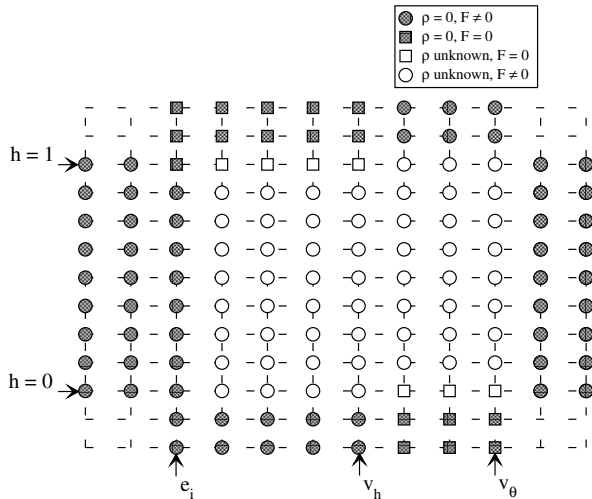


FIG. 8.4: Schematic representation of the mesh used to solve the discretized population density model (Eqns (8.25)–(8.32)). Internal and boundary points in the (v, h) -plane are shown as well as two rows and columns of ghost points. *Open symbols* indicate unknowns while *filled symbols* indicate points where the probability density is known to be zero. *Open squares* indicate boundary points where the advection rate of the probability flux evaluates to zero and *filled squares* indicate ghost points where this advection rate is set to zero to conserve probability. Reproduced with permission from Huertas and Smith (2006b).

fixed time step Δt so that the probability density function at the ij -mesh point advances according to

$$\rho_{ij}(t + \Delta t) = \rho_{ij}(t) + \Delta t \left(\frac{d\rho_{ij}}{dt} \right) \quad (8.33)$$

where $d\rho_{ij}/dt$ is the right-hand side of Eqn (8.27) at time t . We use a 100×100 mesh, $\Delta V = 0.35$ mV, $\Delta h = 0.01$, and $\Delta t = 0.01$ ms.

8.7 Representative Monte Carlo and population density simulations

A representative simulation of the probability density model of the driven LGN/PGN is shown in Fig. 8.5(a) (*solid lines*). The external drive to the network was chosen to be a complicated function of time varying in the range $0 \leq r^{\text{RGC}}(t) \leq 200$ spikes per second per cell (lower trace). This time-dependent excitatory input drives the TC cell population – it corresponds to the term $\eta_e^{\text{TC},0}(t)$ in Eqn (8.24) – and the resulting TC cell activity in turn evokes the

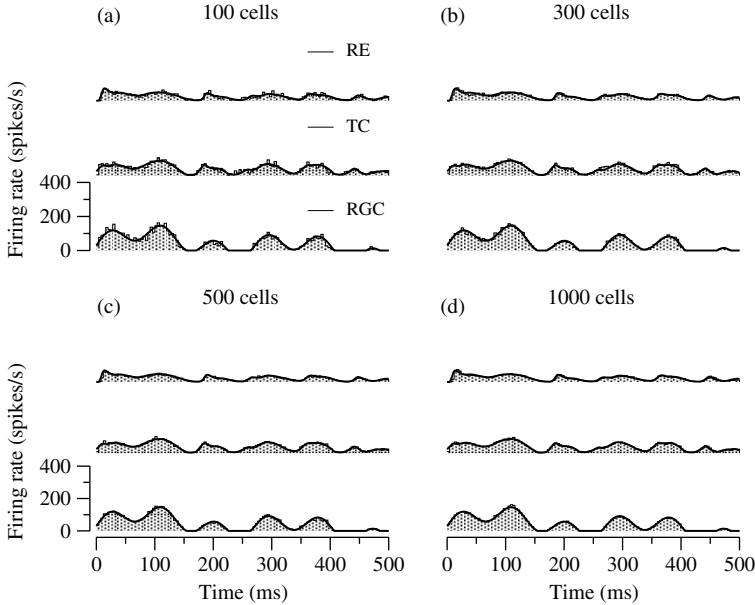


FIG. 8.5: Convergence of Monte Carlo simulations (*histograms*) of the driven LGN/PGN network to the population density model (*solid lines*) as the number of cells in the TC and RE populations increases from $N = 100$ (a) to 1000 (d). The firing rates $r^{\text{RGC}}(t)$ of retinal ganglion cells presynaptic to the TC cell population (lower trace) are shown along with the resulting TC and RE population response (middle and upper traces). Network connectivity is as shown in Fig. 8.1 with $w_{\text{TC},\text{RE}} = w_{\text{RE},\text{TC}} = w_{\text{RE},\text{RE}} = 5$, $a_e^{\text{RE}} = 0.01$, $a_i^{\text{TC}} = a_i^{\text{RE}} = 0.12$, and $a_e^{\text{RGC}} = 0.1$. Reproduced with permission from Huertas and Smith (2006b).

RE cell population response (middle and upper traces, respectively). As shown in Fig. 8.1, feedback inhibition from RE to TC cells and reciprocal RE-to-RE inhibition is also included in these simulations.

In Fig. 8.5(a) the probability density calculation (*solid lines*) is compared to Monte Carlo simulations of the driven LGN/PGN using the same parameters and 100 cells per population (*grey histograms*). As expected, the RGC input and the TC and RE responses of the Monte Carlo simulations fluctuate around the population density result (the largest deviation is approximately 28 spikes/s in the TC population). Importantly, Fig. 8.5 (b)–(d) shows that these fluctuations become smaller in Monte Carlo calculations involving 300, 500, and 1000 cells per population. That is, as the number of neurons in each population increases, the Monte Carlo result converges to the population density calculation (shown on each panel).

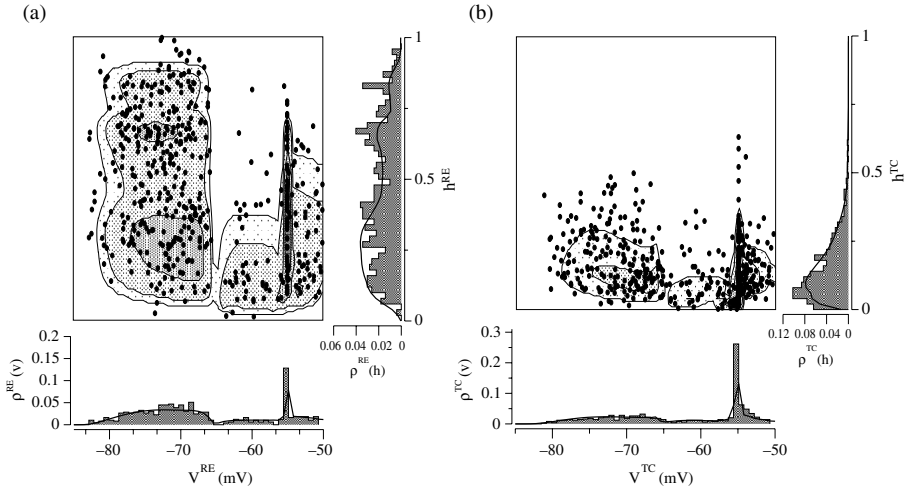


FIG. 8.6: Snapshot of the Monte Carlo and probability density calculations of Fig. 8.5 at $t = 300$ ms for the RE (a) and TC (b) cell populations. Contour plots in (a) and (b) show the probability density functions ρ^{RE} and ρ^{TC} , respectively, while the *filled circles* show the state of 500 RE and 500 TC neurons in the corresponding Monte Carlo simulation. The marginal distribution functions $\rho_v^p(V, t)$ and $\rho_h^p(h, t)$ (Eqns (8.34) and (8.35)) for the membrane potential and low-threshold Ca^{2+} current gating variable confirm that the probability density (*solid lines*) and Monte Carlo (*grey histograms*) models are in agreement. Parameters as in Fig. 8.5(c). Reproduced with permission from Huertas and Smith (2006b).

A different type of validation can be obtained by comparing the instantaneous distribution of cells in each population in the phase-plane (V, h) obtained from both methods. This is shown in Fig. 8.6 and corresponds to a snapshot taken at time $t = 300$ ms of the simulation shown in Fig. 8.5(c). The *filled contour lines* of panels (a) and (b) show the probability density functions ρ^{RE} and ρ^{TC} , respectively, while the *filled circles* show the state of 500 RE and 500 TC neurons in the corresponding Monte Carlo simulation (Fig. 8.5c). In both cases refractory neurons are included and shown at $V = V_{\text{reset}}$ (12 and 22% of the RE and TC populations cells, respectively). The offset graphs in Fig. 8.6(a) and (b) show that the marginal distribution functions for V and h calculated from both the probability density (*solid lines*) and Monte Carlo (*grey histograms*) models are also in agreement. These marginal distributions are defined by the equations

$$\rho_v^p(V, t) dV = \mathbb{P}\{V < \tilde{V}(t) < V + dV\} = \int_0^1 \rho^p(V, h, t) dh \quad (8.34)$$

and

$$\rho_h^p(h, t) dh = \mathbb{P}\{h < \tilde{h}(t) < h + dh\} = \int_{\varepsilon_i}^{v_\theta} \rho^p(V, h, t) dV. \quad (8.35)$$

where the superscript p can be either TC or RE.

The marginal distribution function for RE and TC cell voltage presented in Fig. 8.6 shows a significant fraction of both populations hyperpolarized below the burst threshold V_h , with the low-threshold Ca^{2+} current more de-inactivated in the TC population. Notice also that the marginal densities show both cell types have a non-zero probability density at $V = V_\theta$ indicating advection across the firing threshold mediated by the T-current (Eqn (8.14)). While this drift of probability density across the spike threshold corresponds to intrinsic membrane properties generating burst spikes, the significant population firing rate of both the TC (67 spikes/s) and RE (39 spikes/s) populations also includes the RGC-to-TC and TC-to-RE excitation fluxes (Eqn (8.15)).

8.8 Oscillatory responses of the LGN/PGN model

As discussed in Section 8.1, potassium leakage conductances ($g_{\text{KL}}^{\text{TC/RE}}$) representing increased or decreased cholinergic neuromodulatory action of the brain stem lead to changes in the resting membrane potential of both TC and RE cells. These changes are such that during sleep states the mutual action of both cell populations favour the appearance of self-sustaining oscillatory responses composed of bursts of action potentials. On the other hand, during states of vigilance, the changes in g_{KL} decrease the sustainability of such oscillatory responses.

Figure 8.7 shows that in the absence of retinal input the LGN/PGN model is capable of rhythmic bursting. These rhythmic oscillations (*solid lines* in both panels) are composed almost entirely of burst spikes (Eqn (8.21)) and their occurrence is not particularly sensitive to the average number of connections between TC and RE populations, but the frequency of oscillation is influenced by changes in $w_{\text{TC,RE}}$ and $w_{\text{RE,TC}}$ (Eqn (8.24)). When the potassium leakage conductance in both TC and RE cells ($g_{\text{KL}}^{\text{TC/RE}}$) is changed to represent arousal of the LGN/PGN network, the rhythmic oscillations may be eliminated or persist depending on the strength of the network connectivity. In Fig. 8.7(b) we observe an example where the network connectivity of the model allows rhythmic oscillations to be sustained even in the aroused state. These oscillatory responses are indicated by the *dotted lines*. On the other hand, in Fig. 8.7(a) the network connectivity allowed rhythmic oscillations only when the values of $g_{\text{KL}}^{\text{TC/RE}}$ corresponded to the sleep state, while in the aroused state no oscillations are observed.

When the LGN/PGN network model is driven by constant retinal input, and the values of the potassium leakage conductances are chosen to correspond to the awake state, the response of the system depends strongly on the strength of the driving input and the magnitude of the synaptic connections between the TC and RE populations. Parameter studies varying the average

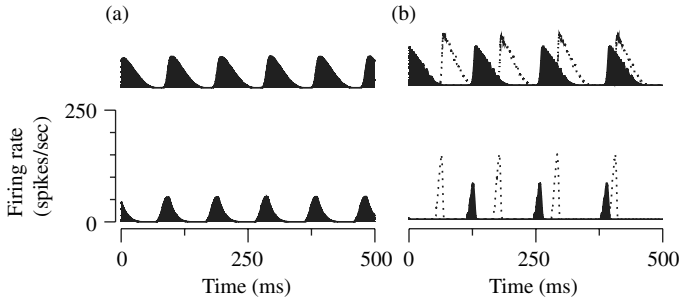


FIG. 8.7: Rhythmic bursting of the LGN/PGN population density model in the absence of retinal drive. Each panel shows the population firing rate (*thick black line*) for RE cells (upper panels) and TC cells (lower panels). Network connectivity is $[w_{RE,RE}, w_{RE,TC}, w_{TC,RE}] = [10, 5, 5]$ in (a) and $[10, 50, 5]$ in (b). When $g_{KL}^{TC/RE}$ is changed to represent arousal of the LGN/PGN network (Table 8.1), the rhythmic oscillations still persist in (b) (*black dotted lines*) but are eliminated in (a), which is clear from the absence of dotted lines. Adapted with permission from Huertas and Smith (2006b).

number of synaptic connections – i.e. changing the entries of the W matrix defined in Eqn (8.8) – show that at high retinal input ($r^{RGC} \approx 200$ spikes/s) the network response is often time-independent. In these simulations the RE population firing rate is composed mostly of tonic spikes while the TC population response always contained a mixture of both burst and tonic spikes (not shown). However, at more moderate values of time-homogeneous retinal drive ($r^{RGC} \approx 30$ spikes/s), the response of each population depends dramatically on the mean number of synaptic connections. Interestingly, network connectivities can be found where the TC and RE populations exhibit oscillatory responses in response to constant retinal input. For example, a 17 Hz oscillation emerges in the presence of constant retinal input of 15 spikes/s when the mean number of TC-to-RE synaptic connections is $w_{TC,RE} = 10$ and the mean number of RE-to-TC and RE-to-RE inhibitory connections are $w_{RE,TC} = 50$ and $w_{RE,RE} = 10$, respectively.

Figure 8.8 presents another interesting example: a low-frequency oscillatory response that emerges in the presence of constant retinal input of 15 spikes/s when the mean number of TC-to-RE synaptic connections is $w_{TC,RE} = 20$ and the mean number of inhibitory connections are $w_{TC,RE} = w_{RE,RE} = 10$. In this figure, the *thick black lines* indicate population firing rates and the *dark* and *light grey* areas represent burst and tonic spikes, respectively (Eqn (8.21)). Such low-frequency oscillatory responses are not exhibited in the absence of retinal input and are clearly distinguishable from the sleep spindle-like responses shown in Fig. 8.7. These low-frequency oscillations are also not observed in the absence of the reciprocal RE-to-RE connection, and this feedback inhibition appears to be responsible for the decrease in RE population firing rate that occurs

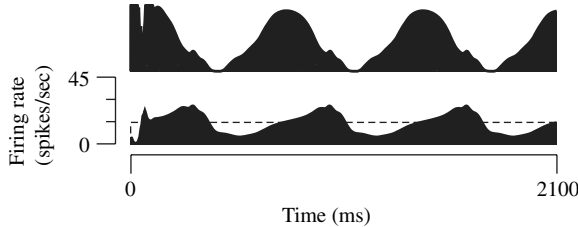


FIG. 8.8: Responses of the aroused LGN/PGN population density model to constant retinal input at 15 spikes/s (*dashed lines*). Network connectivity is $[w_{RE,RE}, w_{RE,TC}, w_{TC,RE}] = [10, 10, 20]$. The population firing rate of both RE (top) and TC (bottom) cells (*solid lines*) is decomposed into burst and tonic components (*dark and light grey*, respectively). Adapted with permission from Huertas and Smith (2006b).

during a phase of the oscillation where the TC population firing rate is increasing (Fig. 8.8). However, it is unclear how the long time-scale of these slow oscillations arises, because the synaptic latencies are only a few milliseconds and the full de-inactivation of the T-current requires only several hundred milliseconds.

8.9 Conclusion

We have shown how the population density modelling approach, discussed in more detail in Chapter 7, can be used to simulate a large-scale network model of the LGN/PGN (Fig. 8.4). This approach accurately computes the distribution of membrane potential V and de-inactivation variable h of a large number of cells in each population (Fig. 8.6). As discussed in Chapter 7, the computational efficiency of this multivariate population density approach is not as dramatic as that observed in univariate simulations (in our hands approximately 30-fold). An important open question is whether dimension reduction techniques can be successfully applied in this context (Ly and Tranchina, 2007).

It is also important to note the exclusive use of fast synapses in the LGN/PGN network model presented here. While interactions mediated through fast (ionotropic) GABA_A and AMPA receptors are sufficient for our present purposes, the dynamics of slow (metabotropic) synaptic interactions such as those associated with GABA_B receptors play important physiological roles in the LGN/PGN network (Cox, Zhou, and Sherman, 1998, Cox and Sherman, 2000, Cox, Reichova, and Sherman, 2003, Govindaiah and Cox, 2004). Such slow kinetics could be implemented using an additional dynamic variable (say q) to the IFB model. This would increase the dimensionality of the probability densities, $\rho^p(V, h, q, t)$, and lead to computationally more demanding numerical integration of the resulting advection-reaction equations (Eqn (8.12)). Alternative implementations that do not increase the number of dimensions might also be employed (Haskell, Nykamp, and Tranchina, 2001).

References

- Babadi, B. (2005). Bursting as an effective relay mode in a minimal thalamic model. *Journal of Computational Neuroscience*, **18**(2), 229–43.
- Buzsaki, G. (2006). *Rhythms of the Brain*. Oxford University Press, Oxford.
- Casti, A., Hayot, F., Xiao, Y., and Kaplan, E. (2008). A simple model of retinal-LGN transmission. *Journal of computational neuroscience*, **24**(2), 235–252.
- Casti, A.R., Omurtag, A., Sornborger, A., Kaplan, E., Knight, B., Victor, J., and Sirovich, L. (2002, May). A population study of integrate-and-fire-or-burst neurons. *Neural Comput*, **14**(5), 957–986.
- Castro-Alamancos, M.A. (2004, Nov). Dynamics of sensory thalamocortical synaptic networks during information processing states. *Progress in neurobiology*, **74**, 213–47.
- Cox, C.L., Zhou, Q., and Sherman, S.M. (1998, Aug). Glutamate locally activates dendritic outputs of thalamic interneurons. *Nature*, **394**, 478–82.
- Cox, C.L., Reichova, I., and Sherman, S.M. (2003, Aug). Functional synaptic contacts by intranuclear axon collaterals of thalamic relay neurons. *J Neurosci*, **23**(20), 7642–6.
- Cox, C.L. and Sherman, S.M. (2000, Sep). Control of dendritic outputs of inhibitory interneurons in the lateral geniculate nucleus. *Neuron*, **27**(3), 597–610.
- Destexhe, A., Babloyantz, A., and Sejnowski, T.J. (1993). Ionic mechanisms for intrinsic slow oscillations in thalamic relay neurons. *Biophys. J.*, **65**(4), 1538–52.
- Destexhe, A., Bal, T., McCormick, D.A., and Sejnowski, T.J. (1996, Sep). Ionic mechanisms underlying synchronized oscillations and propagating waves in a model of ferret thalamic slices. *J. Neurophysiol.*, **76**(3), 2049–70.
- Destexhe, A., Contreras, D., Sejnowski, T.J., and Steriade, M. (1994a, Aug). A model of spindle rhythmicity in the isolated thalamic reticular nucleus. *J. Neurophysiol.*, **72**(2), 803–18.
- Destexhe, A., Contreras, D., Sejnowski, T.J., and Steriade, M. (1994b, Nov). Modeling the control of reticular thalamic oscillations by neuromodulators. *Neuroreport*, **5**(17), 2217–20.
- Destexhe, A., Contreras, D., Steriade, M., Sejnowski, T.J., and Huguenard, J.R. (1996). In vivo, in vitro, and computational analysis of dendritic calcium currents in thalamic reticular neurons. *J Neurosci*, **16**(1), 169–85.
- Destexhe, A., McCormick, D.A., and Sejnowski, T.J. (1993). A model for 8–10 Hz spindling in interconnected thalamic relay and reticularis neurons. *Biophys. J.*, **65**(6), 2473–7.
- Destexhe, A., Neubig, M., Ulrich, D., and Huguenard, J. (1998). Dendritic low-threshold calcium currents in thalamic relay cells. *J Neurosci*, **18**(10), 3574–88.
- Destexhe, A. and Sejnowski, T.J. (2001). *Thalamocortical Assemblies: How Ion Channels, Single Neurons and Large-Scale Networks Organize Sleep Oscillations*. Oxford University Press, Oxford.

- Golomb, D., Wang, X.-J., and Rinzel, J. (1996a). Propagation of spindle waves in a thalamic slice model. *J. Neurophysiol.*, **72**(2), 750–769.
- Golomb, D., Wang, X.-J., and Rinzel, J. (1996b). Synchronization properties of spindle oscillations in a thalamic reticular nucleus model. *J. Neurophysiol.*, **72**(3), 1109–1126.
- Govindaiah and Cox, C.L. (2004, Feb). Synaptic activation of metabotropic glutamate receptors regulates dendritic outputs of thalamic interneurons. *Neuron*, **41**(4), 611–23.
- Guido, W., Lu, S.-M., and Sherman, S.M. (1992). Relative contributions of burst and tonic responses to the receptive field properties of lateral geniculate neurons in the cat. *J. Neurophysiol.*, **68**, 2199–2211.
- Guido, W., Lu, S.-M., Vaughan, J.W., Godwin, D.W., and Sherman, S.M. (1995). Receiver operating characteristic (ROC) analysis of neurons in the cat's lateral geniculate nucleus during tonic and burst response mode. *Vis. Neurosci.*, **12**, 723–741.
- Guido, W. and Weyand, T. (1995, Oct). Burst responses in thalamic relay cells of the awake behaving cat. *J. Neurophysiol.*, **74**(4), 1782–6.
- Gutierrez, C., Cox, C.L., Rinzel, J., and Sherman, S.M. (2001, Feb). Dynamics of low-threshold spike activation in relay neurons of the cat lateral geniculate nucleus. *J. Neurosci.*, **21**(3), 1022–32.
- Haskell, E., Nykamp, D.Q., and Tranchina, D. (2001). Population density methods for large-scale modelling of neuronal networks with realistic synaptic kinetics: cutting the dimension down to size. *Network: Comput. Neural. Syst.*, **12**, 141–174.
- Hayot, F. and Tranchina, D. (2001, Nov). Modeling corticofugal feedback and the sensitivity of lateral geniculate neurons to orientation discontinuity. *Vis. Neurosci.*, **18**(6), 865–77.
- Huertas, M.A., Groff, J.R., and Smith, G.D. (2005a, Apr). The effect of feedback inhibition on throughput properties of the dorsal lateral geniculate nucleus. *Neurocomputing*, **65–66**, 499–505.
- Huertas, M.A., Groff, J.R., and Smith, G.D. (2005b). Feedback inhibition and throughput properties of an integrate-and-fire-or-burst network model of retinogeniculate transmission. *J. Comput. Neurosci.*, **19**(2), 147–180.
- Huertas, M.A. and Smith, G.D. (2006a, Feb). A two-dimensional population density approach to modeling the dLGN/PGN network. *Neurocomputing*, **69**(10–12), 1286–1290.
- Huertas, M.A. and Smith, G.D. (2006b). A multivariate population density model of the dLGN/PGN relay. *Journal of Computational Neuroscience*, **21**, 171–189.
- Hundsdorfer, W. and Verwer, J.G. (2003). *Numerical Solution of Time-Dependent Advection-Diffusion-Reaction Equations*. Springer-Verlag, Berlin.
- Jones, E.G. (2007). *The Thalamus*, 2nd edn. Cambridge University Press, Cambridge.

- Kaplan, E., Mukherjee, P., and Shapley, R.M. (1993). Information filtering in the lateral geniculate nucleus. In *Contrast Sensitivity* (ed. R. Shapley and D. Lam), Volume 5, Cambridge, Massachusetts, pp. 183–200. The MIT Press.
- Kaplan, E., Purpura, K., and Shapley, R.M. (1987). Contrast affects the transmission of visual information through the mammalian lateral geniculate nucleus. *J. Physiol. (London)*, **391**, 267–288.
- Kim, U. and McCormick, D.A. (1998). The functional influence of burst and tonic firing mode on synaptic interactions in the thalamus. *J. Neurosci.*, **18**(22), 9500–16.
- Knight, B.W. (1972). Dynamics of encoding in a population of neurons. *Journal of General Physiology*, **59**, 734–766.
- Ly, C., and Tranchina, D. (2007, Jun). Critical analysis of dimension reduction by a moment closure method in a population density approach to neural network modeling. *Neural computation*, **19**, 2032–92.
- Lytton, W.W., Destexhe, A., and Sejnowski, T.J. (1996, Feb). Control of slow oscillations in the thalamocortical neuron: a computer model. *Neuroscience*, **70**(3), 673–84.
- McCormick, D.A. and Bal, T. (1997). Sleep and arousal: thalamocortical mechanisms. *Ann. Rev. Neurosci.*, **20**, 185–215.
- Mukherjee, P. and Kaplan, E. (1995). Dynamics of neurons in the cat lateral geniculate nucleus: in vivo electrophysiology and computational modeling. *J. Neurophysiol.*, **74**(3), 1222–1243.
- Mukherjee, P. and Kaplan, E. (1998). The maintained discharge of neurons in the cat lateral geniculate nucleus: spectral analysis and computational modeling. *Vis. Neurosci.*, **15**, 529–539.
- Nykamp, D.Q. and Tranchina, D. (2000). A population density approach that facilitates large-scale modeling of neural networks: Analysis and an application to orientation tuning. *Journal of Computational Neuroscience*, **8**, 19–50.
- Omurtag, A., Kaplan, E., Knight, B., and Sirovich, L. (2000a). A population approach to cortical dynamics with an application to orientation tuning. *Network: Computation in Neural Systems*, **11**, 247–260.
- Omurtag, A., Knight, B.W., and Sirovich, L. (2000b). On the simulation of large populations of neurons. *Journal of Computational Neuroscience*, **8**(1), 51–63.
- Rinzel, J., Terman, D., Wang, X., and Ermentrout, B. (1998). Propagating activity patterns in large-scale inhibitory neuronal networks. *Science*, **279**(5355), 1351–5.
- Rush, M.E. and Rinzel, J. (1994). Analysis of bursting in a thalamic neuron model. *Biol. Cybern.*, **71**(4), 281–291.
- Sanchez-Vives, M.V., Bal, T., and McCormick, D.A. (1997, Nov). Inhibitory interactions between perigeniculate gabaergic neurons. *The Journal of Neuroscience*, **17**, 8894–908.

- Sanchez-Vives, M.V., and McCormick, D.A. (1997, Nov). Functional properties of perigeniculate inhibition of dorsal lateral geniculate nucleus thalamocortical neurons in vitro. *The Journal of Neuroscience*, **17**, 8880–93.
- Sherman, S.M. (1996). Dual response modes in lateral geniculate neurons: mechanisms and functions. *Vis. Neurosci.*, **13**, 205–213.
- Sherman, S.M. and Guillory, R.W. (1996). The functional organization of thalamocortical relays. *J. Neurophysiol.*, **76**, 1367–1395.
- Sherman, S.M. and Koch, C. (1986). The control of retinogeniculate transmission in the mammalian lateral geniculate nucleus. *Exp. Brain Res.*, **63**, 1–20.
- Sherman, S.M. and Koch, C. (1990). Thalamus. In *Synaptic Organization of the Brain, Third Edition* (ed. G. Shepherd), Oxford University Press, New York, pp. 246–278.
- Sherman, S.M. and Guillory, R.W. (2005). *Exploring the Thalamus and Its Role in Cortical Function*, 2nd edn. The MIT Press, Cambridge, MA.
- Smith, G.D., Cox, C.L., Sherman, M.S., and Rinzel, J. (2006). A firing-rate model of spike-frequency adaptation in sinusoidally-driven thalamocortical relay neurons. *Thalamus and Related Systems*, **1**(02), 135–156.
- Smith, G.D. and Sherman, S.M. (2002). Detectability of excitatory versus inhibitory drive in an integrate-and-fire-or-burst thalamocortical relay neuron model. *Journal of Neuroscience*, **22**(23), 10242.
- Smith, G.D., Cox, C.L., Sherman, S.M., and Rinzel, J. (2000, Jan). Fourier analysis of sinusoidally driven thalamocortical relay neurons and a minimal integrate-and-fire-or-burst model. *J. Neurophysiol.*, **83**(1), 588–610.
- Steriade, M.M. and McCarley, R. (1990). *Brainstem Control of Wakefulness and Sleep*. Springer, New York.
- Wang, X.-J., Golomb, D., and Rinzel, J. (1995). Emergent spindle oscillations and intermittent burst firing in a thalamic model: specific neuronal mechanisms. *Proc. Nat. Acad. Sci.*, **92**(12), 5577–5581.
- Weyand, T.G., Boudreaux, M., and Guido, W. (2001, Mar). Burst and tonic response modes in thalamic neurons during sleep and wakefulness. *J. Neurophysiol.*, **85**(3), 1107–18.
- Woolsey, T.A. and der Loos, H. Van (1970, Jan). The structural organization of layer IV in the somatosensory region (SI) of mouse cerebral cortex. the description of a cortical field composed of discrete cytoarchitectonic units. *Brain research*, **17**, 205–42.
- Zhan, X.J., Cox, C.L., Rinzel, J., and Sherman, S.M. (1999, May). Current clamp and modeling studies of low-threshold calcium spikes in cells of the cat's lateral geniculate nucleus. *J. Neurophysiol.*, **81**(5), 2360–73.

SYNAPTIC ‘NOISE’: EXPERIMENTS, COMPUTATIONAL CONSEQUENCES AND METHODS TO ANALYSE EXPERIMENTAL DATA

Alain Destexhe and Michelle Rudolph-Lilith

9.1 Introduction

The cerebral cortex is characterized by an extremely dense connectivity, with each pyramidal neuron receiving between 5000 and 60 000 synaptic contacts. A large part of this connectivity originates from the cortex itself (Braitenberg and Schüz, 1998, DeFelipe and Fariñas, 1992). In awake animals, neurons in different cortical structures display high spontaneous firing rates (Evarts, 1964, Steriade and McCarley, 1990). As a consequence, many synaptic inputs are simultaneously active onto cortical neurons in intact networks. Indeed, intracellular recordings in awake animals reveal that cortical neurons are subjected to an intense synaptic bombardment and, as a result, are depolarized and have a low input resistance (Baranyi, Szente, and Woody, 1993, Matsumura, Cope, and Fetz, 1988, Steriade, Timofeev, and Grenier, 2001) compared to brain slices kept *in vitro*. This activity is also responsible for a considerable amount of subthreshold fluctuations, called ‘synaptic noise’. Together these properties are described as the ‘high-conductance state’ of cortical neurons. How such high-conductance and high-noise conditions affect the integrative properties of neurons remains an intense subject of research (reviewed in Destexhe, 2007, Destexhe *et al.*, 2003).

In this chapter, we give an overview of the experimental measurements of synaptic noise in cortical neurons *in vivo*. We next review computational models with which to explore the impact of synaptic noise on integrative properties, and to determine what sort of computational advantages can be conferred by noise. Finally, we review experimental methods derived from the stochastic modelling of synaptic noise, and discuss how such methods could be tested experimentally.

9.2 Experimental characterization of synaptic noise

9.2.1 *The noisy subthreshold activity in different brain states*

The intracellular recording shown in Fig. 9.1(a) (awake) shows the membrane potential (V_m) activity of a cortical neuron in an awake cat. The V_m activity is characterized by a considerable amount of synaptic activity and fluctuations which give rise to irregular firing. Although this fact is well known, it was only characterized recently. Most of the data have been obtained in intracellular

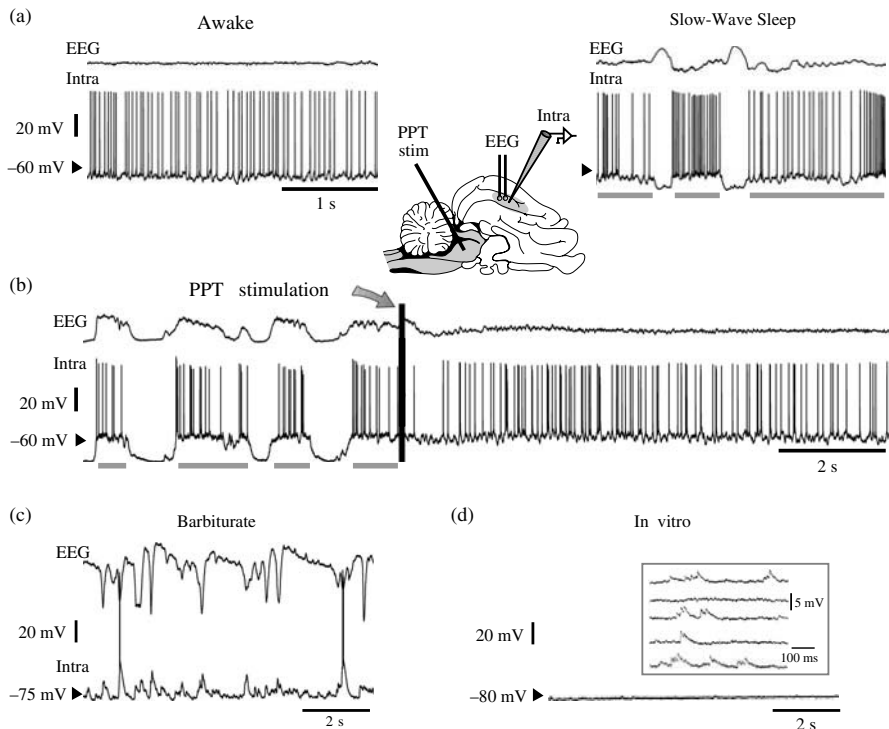


FIG. 9.1: Membrane potential activity during different states of the cerebral cortex. (a) Intracellular recordings and electroencephalogram (EEG) in the association cortex of cats (area 5-7, see scheme), during the waking state (left) and during slow-wave sleep (right). The activity during sleep consists of up- and down-states (up-states indicated by grey bars; modified from Steriade, Timofeev, and Grenier (2001)). (b) Activity during ketamine-xylazine anesthesia. The spontaneous activity (up and down states) switches to a prolonged up-state with desynchronized EEG after stimulation of the PPT (vertical bar; grey bars indicate up-states; modified from Rudolph *et al.* (2005)). (c) Activity during barbiturate anesthesia. The membrane is mostly hyperpolarized, with occasional depolarizations. (d) Activity in cortical slices (*in vitro*). Synaptic activity is diminished and mostly consists of unitary synaptic potentials (see inset at higher time resolution; (c)–(d) modified from Paré *et al.*, 1998).

recordings under anesthesia, and, in some cases, in awake or naturally sleeping animals (reviewed by Destexhe, Rudolph, Paré *et al.* (2003)). In awake animals, the cerebral cortex (and more generally the entire brain) displays an 'activated' state, with distinct characteristics compared to other states like slow-wave sleep or anesthesia. These characteristics include a low-amplitude 'desynchronized'

electroencephalogram (EEG), a depolarized V_m and irregular firing activity, all visible in Fig. 9.1(a) (awake). During slow-wave sleep, the EEG and V_m activity follow low-frequency rhythms (Fig. 9.1a, slow-wave sleep). The most prominent rhythm consists of slow-wave complexes in the EEG, which are paralleled with up/down-state dynamics in the V_m . During the up-state (grey bars in Fig. 9.1a), the V_m is depolarized and the activity is similar to wakefulness; during the down-state, all cortical neurons are hyperpolarized and do not fire. Several anesthetics, such as urethane or ketamine-xylazine, induce EEG and V_m dynamics very similar to slow-wave sleep. For instance, ketamine-xylazine anesthesia induces up/down states very similar to sleep (grey bars Fig. 9.1b). For recent reviews on EEG and V_m dynamics during activated and sleep states, see Steriade, (2001, 2003), McCormick and Bal (1997) and Steriade and McCarley (1990).

One of the main interesting aspects of up/down states is that there is good evidence that the up-states follow dynamics very close to the activated states of the brain (for a recent review, see Destexhe *et al.*, 2007). At the level of EEG and intracellular activities, the dynamics seen during up-states are extremely similar to that during wakefulness. An illustrative example of this similarity is that electrical stimulation of the brain stem (pedonculopontine tegmentum, or PPT) can transform the up/down-state dynamics into the typical desynchronized EEG of activated states (Fig. 9.1b). Following the PPT stimulation, this artificial activated state appears as a ‘prolonged’ up-state (Steriade, Amzica, and Nunez, 1993, Rudolph *et al.*, 2005). Thus, it seems that the up-states constitute a relatively good approximation of the network state during activated states. It is important to stress that these states are close, but not identical, as shown for example by conductance measurements (Destexhe *et al.*, 2007).

Other types of anesthetics, such as barbiturates, do not induce dynamics comparable to either activated or slow-wave sleep states but rather depress cortical activity and induce an EEG dominated by slow waves (Fig. 9.1c). In this case, the V_m is hyperpolarized, and rarely makes excursions to depolarized values. The most depressed state is obtained *in vitro* (Fig. 9.1d), where the V_m is at rest with rare synaptic events (Fig. 9.1d, inset). In some cases, manipulations are possible to excite cortical activity, resulting in the spontaneous generation of up/down-state dynamics *in vitro* (Sanchez-Vives and McCormick, 2000).

9.2.2 Conductance measurements

The first way to characterize synaptic noise is to build V_m distributions, as shown in Fig. 9.2(a) and (b). From such distributions at different levels of DC injection, one can grossly evaluate the conductance underlying each phase of the oscillation. In ketamine-xylazine anesthesia (Fig. 9.2a), the V_m distributions are bimodal, with left and right peaks corresponding to the down- and up-states, respectively. By injecting different levels of current, it is apparent that the current has a much more powerful effect in shifting the down-states, whereas it produces only a minor shift of the up-states (compare different curves in Fig. 9.2a). In other words,

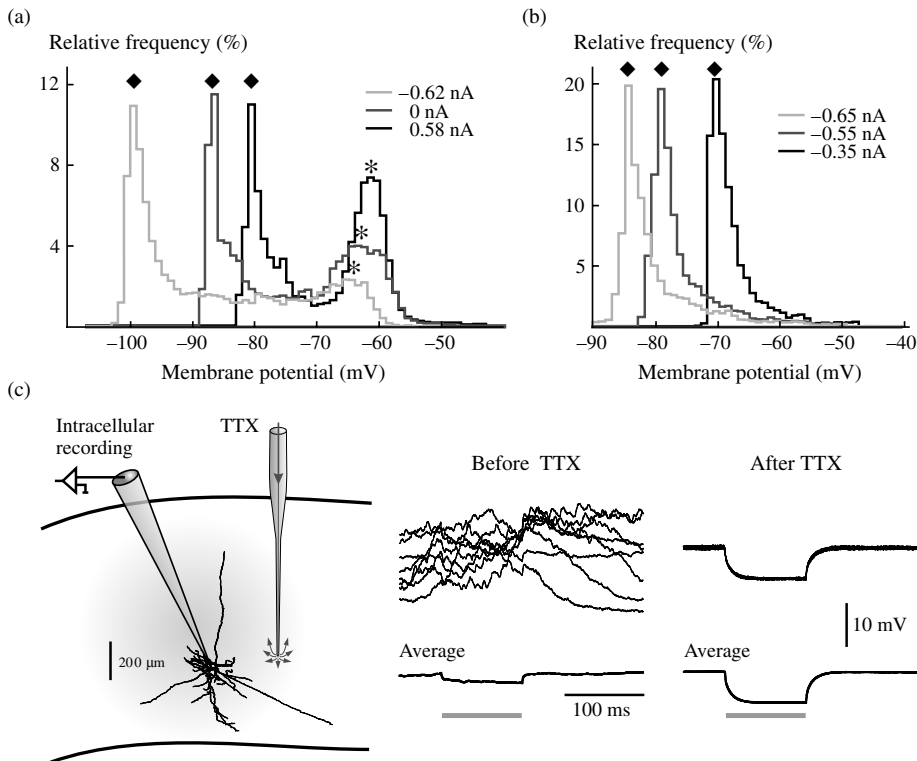


FIG. 9.2: Conductance measurements in different cortical states. (a) Different levels of current injection during ketamine-xylazine anesthesia reveal that the up-states (right peaks) have a much larger overall conductance compared to down-states (left peaks). (b) During barbiturate anesthesia, the behaviour was similar to down-states. (c) Quantification of the conductance state of the membrane in up-states by microperfusion of TTX to cortex (see scheme). Hyperpolarizing current pulses were injected during up-states (before TTX), and later after total suppression of network activity (after TTX), in the same neurons. The overall conductance was about five times lower after TTX for this particular cell (modified from Paré *et al.*, 1998).

the up-state has a much larger conductance compared to the down-state. The behaviour during barbiturate anesthesia (Fig. 9.2b) reminds one of the down-state, in agreement with the recordings shown in Fig. 9.1(b) and (c). These measurements (Paré *et al.*, 1998) constitute a first indication that the up-states correspond to a high-conductance state. The same results were obtained with purely subthreshold activity, showing that they are not due to the conductances of action potentials.

A second, more direct, measurement was obtained by comparing the intracellular recording during up-states and after total suppression of network activity using TTX (Fig. 9.2c; Paré *et al.*, 1998). Because TTX blocks all sodium channels, it completely suppresses all action-potential dependent activity and reveals the resting state of the neuron. Input resistance (R_{in}) measurements revealed that taking the up-states of ketamine-xylazine anesthesia as reference, these active states have about five times more synaptic conductance compared to the resting state of the cell (Fig. 9.2c; Destexhe and Paré, 1999, Paré *et al.*, 1998). These results are not affected by the V_m level nor by spiking activity (identical results are obtained at hyperpolarized, subthreshold levels) and R_{in} measurements correspond to the linear portion of the I - V curve, suggesting little or no contamination by intrinsic voltage-dependent currents (Destexhe and Paré, 1999; see also discussion in Monier, Fournier and Frégnac, 2008).

Measurements have also been obtained during active states *in vivo* in other preparations, usually by comparing up- and down-states under various anesthetics such as ketamine-xylazine or urethane. Such estimates are very variable, ranging from up to several-fold smaller R_{in} in up-states (Contreras, Timofeev, and Steriade, 1996, Leger *et al.*, 2005, Paré *et al.*, 1998, Petersen *et al.*, 2003), to nearly identical R_{in} between up- and down-states or even larger R_{in} in up-states (Metherate and Ashe, 1993, Waters and Helmchen, 2006, Zou *et al.*, 2005). The latter paradoxical result may be explained by voltage-dependent rectification (Waters and Helmchen, 2006) or by the presence of potassium currents in down-states (Zou *et al.*, 2005). Consistent with the latter, cesium-filled electrodes have negligible effects on the up-state, but largely abolish the hyperpolarization during the down-states (Timofeev, Grenier, and Steriade, 2001). Moreover, the R_{in} of the down-state differs from that of the resting state (after TTX) by about two-fold (Paré *et al.*, 1988). It is thus clear that at least the down-state is very different from the true resting state of the neuron. Finally, conductance measurements in awake and naturally sleeping animals have revealed a wide diversity between cells in cat cortex (Rudolph *et al.*, 2007), ranging from large (much larger than the leak conductance) to moderate (smaller or equal to the leak) synaptic conductances. On average, the synaptic conductance was estimated to be about three times the resting conductance, with division into about one-third excitatory and two-thirds inhibitory conductance (Rudolph *et al.*, 2007). Strong inhibitory conductances were also found in artificially evoked active states using PPT stimulation (Rudolph *et al.*, 2005), such as that shown in Fig. 9.1(b).

In conclusion, the data reviewed here indicate that when the EEG is desynchronized, neocortical neurons are in a ‘high-conductance state’ characterized by the following features: (i) a large membrane conductance, which corresponds to a three- to five-fold decrease in input resistance; (ii) an average membrane potential (around -65 to -60 mV), which is significantly depolarized compared to the natural resting level (-70 to -80 mV); and (iii) large-amplitude membrane potential fluctuations (σ_V of 2–6 mV), which are at least 10-fold larger than those seen in the absence of network activity. In addition, the data indicate

that these characteristics are attributable mostly to network activity, and that inhibitory conductances account for most of the large membrane conductance.

Thus, experiments show that synaptic activity has a tremendous influence on cortical neurons, and this is true for activated states such as wakefulness, so presumably it is an important factor in understanding awake neuronal processing. Computational models are needed to investigate the consequences of synaptic noise on integrative properties, as we review in the next section.

9.3 Computational consequences of synaptic noise

9.3.1 *Models of synaptic noise*

There is a long tradition of theoretical studies aimed at understanding the impact of noise on the integrative properties of neurons. The notion of a high-conductance state, as well as the fact that neurons could integrate differently in such states, was first suggested by modelling studies. By integrating the sustained synaptic conductance arising from network activity into models, Barrett (1975) for motoneurons, and later Holmes and Woody (1989) for pyramidal cells, predicted that synaptic activity could have a profound impact on dendritic integration. This theme was then investigated using biophysically and morphologically more precise models in cortex (Bernander *et al.*, 1991, Destexhe and Paré, 1999) and cerebellum (De Schutter and Bower, 1994, Rapp, Yarom, and Segev, 1992). Such models have predicted a number of computational consequences of background activity and high-conductance states in neurons (see Section 9.3.2 below).

In addition to morphologically precise models, a large number of theoretical studies have designed simplified models to study the effect of noise on neurons. Synaptic activity is usually modelled by a source of current noise in the neuron (Levitin *et al.*, 1968, Tuckwell, 1988), and thus the membrane potential is described by a stochastic process. More recently, the background activity has been modelled by fluctuating conductances instead of fluctuating currents (Destexhe *et al.*, 2001). In this case, the synaptic conductances are stochastic processes, which in turn influence V_m dynamics. The advantage of this representation is that the high-conductance state of the membrane can be specifically reproduced and modulated. The realism and simplicity of those models also enables injection into real neurons in order to recreate high-conductance states artificially (see Section 9.4 below).

Another advantage is that those models are simple enough to allow mathematical treatment. Various mathematical studies of the firing dynamics of neurons with conductance-based inputs were proposed (see for example, Moreno-Bote and Parga (2005), Muller *et al.* (2007), Burkitt, Meffin, and Grayden (2003)) and have consequences on network dynamics with conductance-based inputs (Meffin, Burkitt, and Grayden, 2004; see also Shelley *et al.*, 2002).

We will consider here in more detail the ‘point-conductance’ stochastic process. According to this model, the membrane potential dynamics is described by

the following set of equations (Destexhe *et al.*, 2001):

$$C \frac{dV}{dt} = -G_L(V - E_L) - g_e(V - E_e) - g_i(V - E_i) + I_{\text{ext}}, \quad (9.1)$$

$$\frac{dg_e(t)}{dt} = -\frac{1}{\tau_e} [g_e(t) - g_{e0}] + \sqrt{\frac{2\sigma_e^2}{\tau_e}} \xi_e(t), \quad (9.2)$$

$$\frac{dg_i(t)}{dt} = -\frac{1}{\tau_i} [g_i(t) - g_{i0}] + \sqrt{\frac{2\sigma_i^2}{\tau_i}} \xi_i(t), \quad (9.3)$$

where C denotes the membrane capacitance, I_{ext} a stimulation current, G_L the leak conductance, and E_L the leak reversal potential. $g_e(t)$ and $g_i(t)$ are stochastic excitatory and inhibitory conductances with respective reversal potentials E_e and E_i . The excitatory synaptic conductance is described by Ornstein–Uhlenbeck (OU) stochastic processes (Eqn. (9.2)), where g_{e0} and σ_e^2 are, respectively, the mean value and variance of the excitatory conductance, τ_e is the excitatory time constant, and $\xi_e(t)$ is a Gaussian white noise source with zero mean and unit standard deviation (see Chapter 1 for a discussion on OU processes). The inhibitory conductance $g_i(t)$ is described by an equivalent equation (9.3) with parameters g_{i0} , σ_i^2 , τ_i and noise source $\xi_i(t)$.

This conductance-based stochastic process has been extremely useful in studying synaptic noise both in models and real neurons, as will be shown in the next sections.

9.3.2 Impact of synaptic noise on integrative properties

Computational models have predicted several interesting computational consequences for high-conductance states and synaptic noise (reviewed by Destexhe (2007) and Destexhe *et al.* (2003)).

9.3.2.1 Probabilistic responses. A first straightforward consequence is that neuronal responses in high-conductance states are fundamentally probabilistic because of the high variability of responses due to the presence of synaptic noise (Fig. 9.3a). In the presence of synaptic noise, it is necessary to use repeated trials for any given response, and calculate the probability of spiking. This variability and the use of probabilities are well-known by *in vivo* electrophysiologists, who routinely calculate ‘post-stimulus time histograms’ (PSTH) from their data. Integrating the probability of response after the stimulus gives the total probability that a spike is emitted (the total ‘output’ of the neuron; Fig. 9.3b). This measure will be used throughout this chapter.

9.3.2.2 Noise-induced enhanced responsiveness. A second consequence of high-conductance states is that not only do they transform neurons to probabilistic

devices, but they also profoundly change their response properties. The response curve, which is obtained by plotting the total response probability (integrated over time after stimulus) against stimulus amplitude, is all-or-nothing for a deterministic neuron (Fig. 9.3b, grey), reflecting the presence of a spike threshold. In this case, the spike can only indicate whether or not the stimulus is larger than the threshold. In the presence of synaptic noise, the response curve is different – it is smooth and spans a whole range of input amplitudes (Fig. 9.3b, black). In this case, the probability of spiking is indicative of the whole range of input amplitudes. In particular, for small-amplitude inputs (those in the physiological range), which are normally

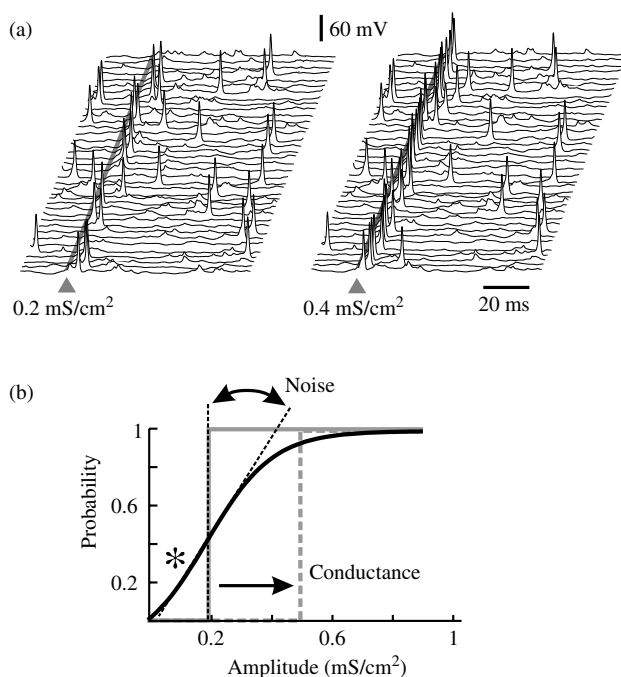


FIG. 9.3: Increased responsiveness in the presence of synaptic noise. (a) In the presence of synaptic noise, the response to additional inputs is highly variable, and spikes are evoked at different latencies at each trial (40 trials are shown for two different input amplitudes). (b) Modulation of the response curve. The response curve (probability of evoking spikes as a function of input amplitude) is all-or-nothing in quiescent conditions (grey). Decomposing synaptic activity into ‘conductance’ and ‘noise’ components shows that conductance shifts the curve rightward (grey dashed), while the noise changes its slope (gain modulation; black). The response of the neuron is a combination of these effects, showing enhanced responsiveness (star) for otherwise subthreshold input regime (modified from Hô and Destexhe, 2000).

subthreshold, the neuron's response probability is enhanced (Fig. 9.3b, star). This enhanced responsiveness is a very robust feature of neurons in the presence of synaptic background activity (Hô and Destexhe, 2000, Shu *et al.*, 2003). A similar phenomenon has also been called 'gain modulation' (Chance, Abbott, and Reyes, 2002), reflecting the fact that the slope of the response curve is modulated by synaptic noise.

With models, it is possible to decompose synaptic noise into its conductance component and the 'noise' component. The conductance alone shifts the response curve (rightward arrow in Fig. 9.3b), while the noise component alone modulates the slope (gain) of the response curve (Hô and Destexhe, 2000, Mitchell and Silver, 2003, Prescott and De Koninck, 2003, Shu *et al.*, 2003, Chance, Abbott, and Reyes, 2002). It is important to note that the type of modulation by noise will depend strongly on the intrinsic properties of the neurons. An inverse gain modulation can be observed (Fellous *et al.*, 2003) and may be explained by the presence of potassium conductances (Higgs, Slee, and Spain, 2006). Similarly, the dual response (burst versus single-spike) of thalamic relay neurons is also strongly affected by the presence of synaptic noise and the two modes may no longer be distinguishable (Wolfart *et al.*, 2005) (see Section 9.4 below).

The phenomenon of enhanced responsiveness is similar to that of stochastic resonance, which has been thoroughly studied by physicists (reviewed by Wiesenfeld and Moss, 1995, Gammaitoni *et al.*, 1998; see Chapter 4 in this volume). Stochastic resonance (SR) is a noise-induced enhancement of the signal-to-noise ratio in nonlinear systems. It usually appears as a peak of the signal-to-noise ratio as a function of noise amplitude, thus the system appears to 'resonate' or to respond optimally for an intermediate but non-vanishing amount of noise. While neurons can also show such behaviour if subject to noise (Levin and Miller, 1996, Stacey and Durand, 2000), the situation is more complex than for classic stochastic resonance phenomena, because in neurons the noise source is also a conductance source, and conductances have an additional shunting effect (see details in Rudolph and Destexhe, 2001*b*). As we will see below, this modulation of neuronal responsiveness by noise is the basis for the explanation of other neuronal response properties.

9.3.2.3 Equalization of synaptic efficacies. A third consequence of synaptic noise states is that it may fundamentally change dendritic integration properties, as illustrated in Fig. 9.4. An inherent property of dendrites and other cable structures is voltage attenuation. This is true in particular for pyramidal neurons: synaptic inputs can experience strong attenuation in the neuron's resting state (Fig. 9.4a, left). If the high-conductance state of the membrane is integrated as a static conductance component (i.e. increasing the leak conductance of the membrane), the attenuation is much more severe (Fig. 9.4a, middle): inputs arising at 400 microns or more from the soma are almost totally attenuated, and post-synaptic potentials (PSPs) at the soma are undetectable. This phenomenon is perfectly predictable by cable theory. Remarkably, if the full high-conductance

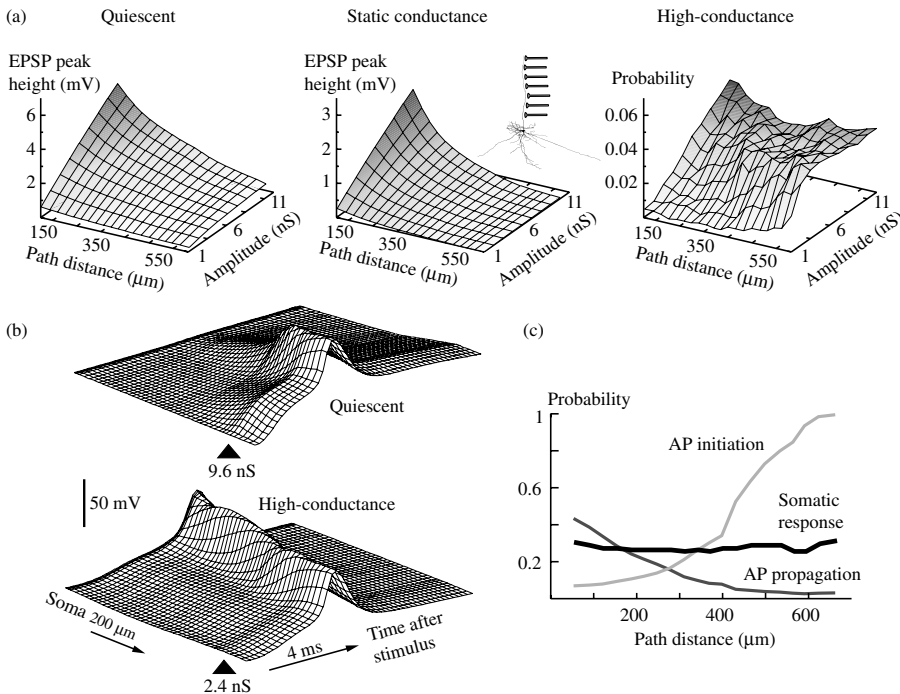


FIG. 9.4: Location independence of synaptic inputs in high-conductance states.

(a) Somatic response amplitudes for inputs located at different positions in dendrites. In a quiescent neuron (left), somatic input amplitudes decrease as a function of distance to soma. With a static conductance (middle), this attenuation is stronger. By including both conductance and noise (right), the probability of somatic spikes becomes much less dependent of the position of the input in dendrites. (b) Illustration of forward propagating spike in a quiescent neuron (top), and in the presence of background activity (bottom). (c) Explanation for location independence based on probabilities of action potential (AP) initiation and propagation (modified from Rudolph and Destexhe, 2003a).

state is simulated, the spiking probability shows a surprisingly low dependence on the location of inputs in dendrites (Fig. 9.4a, right).

How does one explain this equalization of synaptic efficacy? Dendritic excitability, combined with noise, plays a critical role. In quiescent conditions, synaptic inputs arising in distal dendrites can elicit a local dendritic spike, but such a spike is hard to evoke and typically does not propagate well across the dendritic structure (Fig. 9.4b, top). With synaptic noise, as shown above, the behaviour is highly variable, and there is a small probability that evoked spikes propagate all the way to the soma (Fig. 9.4b, bottom). The probability that

a local dendritic spike propagates to the soma and evokes a somatic spike decreases with distance (Fig. 9.4c, dark grey). Conversely, the probability that synaptic inputs evoke a local dendritic spike increases with distance (because the local input resistance is higher for distal dendrites; see Fig. 9.4c, light grey). The product of these two probabilities gives the spike probability of synaptic inputs and is necessarily less dependent on location (Fig. 9.4c, black). Thus, according to this ‘stochastic integrative mode’ (Rudolph and Destexhe, 2003a), the neuron could solve one long-standing problem, namely how to equally integrate inputs situated at different locations in extended dendritic trees. This equalization mechanism depends on both intrinsic properties (dendritic excitability) and the presence of synaptic noise.

9.3.2.4 Sharper temporal processing. Another important consequence of synaptic noise concerns temporal processing. The large conductance is necessarily associated with a reduced membrane time constant, which is visible in the faster response to injected current (Fig. 9.2c, averaged traces). As proposed more than 30 years ago (Barrett, 1975), this reduced time constant should favour finer temporal discrimination (Bernander *et al.*, 1991, Destexhe and Paré, 1999, Holmes and Woody, 1989). In excitable dendrites, small membrane time constants also promote fast-propagating action potentials, resulting in a reduced location-dependence of EPSP timing (Fig. 9.5a; Rudolph and Destexhe, 2003a). This property is likely to facilitate the association of synaptic inputs arising at different locations. The neuron also has a superior ability to distinguish and process high-frequency inputs, compared to low-conductance states. This is illustrated in Fig. 9.5(b), which shows the temporal resolution of a neuron plotted against the input frequency. In quiescent or low-conductance states, neurons can follow inputs (i.e. produce a spike) up to a maximal frequency which is usually around 40–50 Hz (Fig. 9.5b, grey). With synaptic noise, the neuron can lock its response to higher frequencies (up to more than 100 Hz in the example of Fig. 9.5b, black).

Other computational advantages of synaptic noise on temporal processing have been noted by modelling studies. If both excitatory and inhibitory conductances are large during high-conductance states, slight variations of either excitation or inhibition can be very effective in modifying spiking probability. As a consequence, neurons can reliably detect faint changes in temporal correlation of the random activity of their inputs (Halliday, 2000, Salinas and Sejnowski, 2000, Rudolph and Destexhe, 2001a). This type of response is interesting, because changes in correlation do not change the average conductance nor the average V_m , but they appear as changes of the level of fluctuations (variances) of the conductances and of the V_m . In this case, neurons respond to a signal which is not carried by the mean activity of conductances, which is an example of a paradigm that cannot be modelled by rate-based models.

High-conductance states also have an impact on the operating mode of cortical neurons. Neurons can operate either as coincidence detectors or as temporal

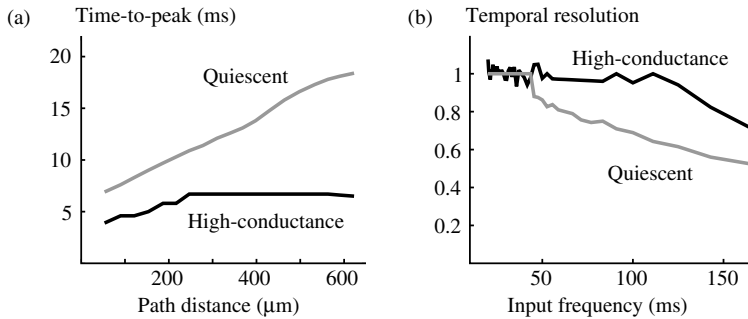


FIG. 9.5: Increased temporal resolution with synaptic noise. (a) Location-dependence of the timing of EPSPs. A similar stimulation paradigm as in Fig. 9.4(a) was used, except that the time-to-peak of averaged synaptic responses is plotted against distance to soma. In quiescent conditions (grey), the time-to-peak of EPSPs increased approximately linearly with distance from soma. This location dependence was markedly reduced in the high-conductance state (black). (b) Enhanced temporal resolution of synaptic inputs during high-conductance state. AMPA-mediated synaptic inputs were delivered at different frequencies. The temporal resolution was quantified by computing the ratio between the stimulus interval and the mode of the corresponding interspike interval histogram. In quiescent conditions (grey), the model could respond reliably up to a stimulus frequency of about 50 Hz. In high-conductance states (black), the frequency following was reliable up to much higher frequencies (beyond 100 Hz). (a) modified from Rudolph and Destexhe (2003a); (b) modified from Destexhe *et al.* (2003).

integrators, which determines whether the cortex encodes information by the precise timing of spikes, or by average firing rates. Modelling studies monitored the spike output of neurons subject to a full spectrum of multisynaptic input patterns, from highly coincident to temporally dispersed (Kisley and Gerstein, 1999, Marsalek, Koch, and Maunsell, 1997). It was found that generally the spike output jitter is less than the input jitter, indicating that neurons tend to synchronize the responses and reduce their temporal dispersion. In high-conductance states, however, the temporal dispersion was found to be nearly identical between input and output (Rudolph and Destexhe, 2003c), suggesting that both operating modes can be used robustly in cortical networks in such states.

9.4 Testing the impact of synaptic noise using dynamic-clamp experiments

A particularly elegant way to evaluate the impact of synaptic noise on neurons is to recreate synaptic noise in a controlled fashion in neurons in brain slices. Because such an experiment requires adding artificial conductances to the

neuron, one needs to use an appropriate technique, called *dynamic-clamp*. This technique was introduced in 1993 independently by two laboratories (Robinson and Kawai, 1993, Sharp *et al.*, 1993) and is now well-established (Prinz, Abbott, and Marder, 2004). The dynamic-clamp consists of injecting computer-generated conductances into a real neuron through the recording electrode. Because the injected current depends not only on the conductance, but also on voltage ($I = g[V - E]$), one needs to continuously update the current to be injected as a function of the constantly changing voltage. Thus, a computer is required to run the conductance models in real time in order to communicate in a perfectly timed fashion with the recording setup, and in particular the amplifier of the intracellular signal.

The first study to inject synaptic noise in cortical neurons using dynamic-clamp and artificially recreate high-conductance states was proposed in 2001 (Destexhe *et al.*, 2001), and this was followed by a number of studies which investigated different aspects of high-conductance states using this technique (Fellous *et al.*, 2003, Higgs, Slee, and Spain, 2006, Piwkowska *et al.*, 2008, Prescott and De Koninck, 2003, Shu *et al.*, 2003, Wolfart *et al.*, 2005, Chance, Abbott, and Reyes, 2002). To this end, one needs first to generate an appropriate model of stochastic synaptic activity because thousands of synapses releasing randomly cannot be simulated in real time. The ‘point-conductance’ stochastic process outlined above (Eqns. (9.1)–(9.3)) constitutes a possible basis of such experiments (Fig. 9.6a). This stochastic process is adjusted to match the total conductance seen at the soma in the presence of synaptic noise *in vivo*. These conductances are then injected in dynamic-clamp (Fig. 9.6a) in order to reproduce, for instance, the conductance measurements in TTX experiments (Fig. 9.6b; compare with Fig. 9.2c). Other properties such as the mean and standard deviation of the V_m , the spontaneous firing rate, the variability of spiking, or the power spectrum of the V_m fluctuations, can also be used to better constrain the model.

One of the properties of high-conductance states, namely the enhanced responsiveness, was thoroughly tested in dynamic-clamp experiments. Injection of stochastic conductances into cortical neurons *in vitro* profoundly altered their responsiveness, or equivalently, neuronal gain (Fellous *et al.*, 2003, Prescott and De Koninck, 2003, Shu *et al.*, 2003, Chance, Abbott, and Reyes, 2002). The ‘noise’ component of background activity was found to reduce the gain in most cases, as illustrated in Fig. 9.6(c). However, in some cases, noise may increase the gain (Fellous *et al.*, 2003), a property which could be explained by the presence of strong after-hyperpolarization conductances (Higgs, Slee, and Spain, 2006).

The effect of synaptic noise was also studied in neuronal types which express strong and prominent intrinsic properties, such as the bursting neurons of the thalamus. Thalamic relay cells classically display two modes of firing (Llinás and Jahnsen, 1982): at depolarized potentials, they respond to excitatory stimuli rather classically, by producing regular trains of spikes (‘tonic mode’); at hyperpolarized potentials, the same stimuli evoke full-blown bursts

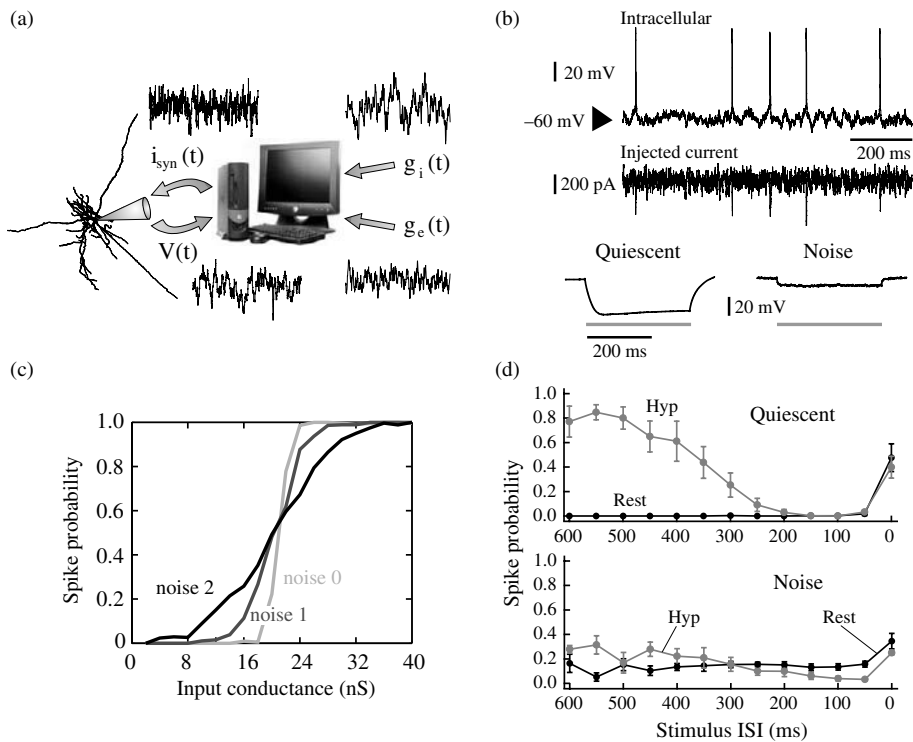


FIG. 9.6: Dynamic-clamp addition of synaptic noise in cortical and thalamic neurons *in vitro*. (a) Scheme of the dynamic-clamp experiment, in which computer-generated stochastic conductances are injected in the neuron *in vitro*. (b) Injection of conductances in cortical neurons can recreate high-conductance states compatible with *in vivo* measurements (modified from Destexhe *et al.*, 2001). (c) Effect of controlling the amount of noise on the slope of the response curve of cortical neurons (modified from Shu *et al.*, 2003). (d) Effect of synaptic noise in thalamic neurons. The conductance noise interacts with burst generation to generate response curves that are roughly independent of the V_m (modified from Wolfart *et al.*, 2005).

of action potentials ('burst mode'). However, this classification has been challenged recently in a dynamic-clamp study where high-conductance states were reproduced in thalamic neurons (Wolfart *et al.*, 2005). Instead of responding in two distinct modes, thalamic relay neurons with noise mixed single-spikes and burst responses at all membrane potentials. This suggests that both single-spikes and bursts participate equally in transmitting information. Consistent with this, if one calculates spiking probabilities by mixing bursts and single-spikes, the responsiveness is independent of both the V_m level and the frequency of the input

(Fig. 9.6d). In this case, this situation is possible only because of the presence of the calcium current generator of bursts. It was suggested that this constitutes an efficient ‘relay’ for thalamic neurons (Wolfart *et al.*, 2005), and this relay is possible only because of the interaction between intrinsic neuronal properties and synaptic noise.

In summary, dynamic-clamp experiments support the idea that stochastic conductances stemming from intense network activity are responsible for an enhancement of responsiveness in cortical neurons, and more generally, a fundamental change of responsiveness in all neuronal types. Moreover, the amount of conductance and V_m fluctuations identified *in vivo* are mostly in the range needed to drastically alter the responsiveness of neurons, which suggests that these phenomena occur well within the physiological situation. It is also one of the bases by which different ‘states’ of activity of the network can yield different responsiveness (reviewed by Destexhe and Contreras, 2006). This is in agreement with previous observations that state changes induced by stimulating the ascending activating systems lead to enhanced responsiveness (Singer, Tretter, and Cynader, 1976, Steriade, 1970).

9.5 Methods of analysing experimental data

We have seen above that the point-conductance stochastic process (Eqns. (9.1)–(9.3)) not only models the conductance fluctuations during background activity *in vivo*, but can also be used to recreate *in vivo*-like states in real neurons. In this section, we will go one step further and show that the same model can also be used as the basis for methods to analyse experimental data.

9.5.1 The VmD method to extract conductances from V_m activity

9.5.1.1 Outline of the VmD method. The model described by Eqns (9.1)–(9.3) has been thoroughly studied theoretically and numerically. Using the Fokker–Planck formalism (see Chapter 1), different analytic approximations have been proposed to describe the steady-state distribution of the V_m activity of the PC model (Lindner and Longtin, 2006, Richardson, 2004, Rudolph and Destexhe, 2003b, 2005); for a comparative study, see Rudolph and Destexhe (2006). One of these expressions is invertible (Rudolph and Destexhe, 2003b, 2005), which enables one to directly estimate the synaptic conductance parameters (g_{e0} , g_{i0} , σ_e , σ_i) from experimentally obtained V_m distributions. This constitutes the basis of the VmD method (Rudolph *et al.*, 2004), which we outline below.

The essential idea behind the VmD method is to fit an analytic expression to the steady-state subthreshold V_m distribution obtained experimentally, and obtain estimates of the parameters (mean, variance) of the underlying synaptic conductances. Among the different analytic expressions outlined above, we consider the following steady-state probability distribution $\rho(V)$ for the membrane

potential V (Rudolph and Destexhe, 2005, 2003b):

$$\rho(V) = N \exp \left[A_1 \ln \left[\frac{u_e(V - E_e)^2}{(aC_m)^2} + \frac{u_i(V - E_i)^2}{(aC_m)^2} \right] \right. \\ \left. + A_2 \arctan \left[\frac{u_e(V - E_e) + u_i(V - E_i)}{(E_e - E_i)\sqrt{u_e u_i}} \right] \right], \quad (9.4)$$

where the following constants were defined: $k_L = 2a^2 C_m g_{L0}$, $k_e = 2aC_m g_{e0}$, $k_i = 2aC_m g_{i0}$, $u_e = \sigma_e^2 \tilde{\tau}_e$, $u_i = \sigma_i^2 \tilde{\tau}_i$, as well as the following voltage-independent terms:

$$A_1 = -\frac{k_L + k_e + k_i + u_e + u_i}{2(u_e + u_i)}$$

and

$$A_2 = 2aC_m \frac{(g_{e0}u_i - g_{i0}u_e)(E_e - E_i) - ag_L u_e(E_e - E_L) - ag_L u_i(E_i - E_L) + I_{ext}(u_e + u_i)}{(E_e - E_i)\sqrt{u_e u_i}(u_e + u_i)}.$$

Here, N denotes a normalization constant such that $\int_{-\infty}^{\infty} dV \rho(V) = 1$. $\tilde{\tau}_{\{e,i\}}$ are effective time constants given by (Rudolph and Destexhe, 2005; see also Richardson, 2004):

$$\tilde{\tau}_{\{e,i\}} = \frac{2\tau_{\{e,i\}}\tilde{\tau}_m}{\tau_{\{e,i\}} + \tilde{\tau}_m}, \quad (9.5)$$

where $\tilde{\tau}_m = C/(G_L + g_{e0} + g_{i0})$ is the effective membrane time constant.

Due to the multiplicative coupling of the stochastic conductances to the membrane potential, the V_m probability distribution (9.4) takes in general an asymmetric form. However, $\rho(V)$ shows only small deviations from a Gaussian distribution, suggesting an approximation by a symmetric distribution. To this end, the first- and second-order terms in the power series expansion of the exponent in Eqn. (9.4) around the maximum \bar{V} of the probability distribution $\rho(V)$

$$\bar{V} = \frac{S_1}{S_0}, \quad (9.6)$$

with $S_0 = k_L + k_e + k_i + u_e + u_i$ and $S_1 = k_L E_L + k_e E_e + k_i E_i + u_e E_e + u_i E_i$ are considered. This yields the following Gaussian distribution

$$\rho(V) = \frac{1}{\sqrt{2\pi\sigma_V^2}} \exp \left[-\frac{(V - \bar{V})^2}{2\sigma_V^2} \right] \quad (9.7)$$

with the standard deviation given by

$$\sigma_V^2 = \frac{S_0^2(u_e E_e^2 + u_i E_i^2) - 2S_0 S_1(u_e E_e + u_i E_i) + S_1^2(u_e + u_i)}{S_0^3}. \quad (9.8)$$

This expression provides an excellent approximation of the V_m distributions obtained from models and experiments (Rudolph *et al.*, 2004), because the V_m distributions obtained experimentally show little asymmetry (for up-states and activated states; for specific examples, see Piwkowska *et al.*, (2008) and Rudolph *et al.*, (2004, 2005, 2007)).

The main advantage of this Gaussian approximation is that it can be inverted, which leads to expressions for the synaptic noise parameters as a function of the V_m measurements, specifically \bar{V} and σ_V . By fixing the values of τ_e and τ_i , which are related to the decay time of synaptic currents and which can be estimated from voltage-clamp data and/or current-clamp by using power spectral analysis (see Section 9.5.2.2), we have four parameters remaining: the means (g_{e0}, g_{i0}) and standard deviations (σ_e, σ_i) of excitatory and inhibitory synaptic conductances. To extract these four conductance parameters from the membrane probability distribution, Eqn. (9.7) is, however, insufficient because it is characterized by only two parameters (\bar{V}, σ_V). To solve this problem, one possibility is to consider two V_m distributions obtained at two different constant levels of injected current I_{ext1} and I_{ext2} . In this case, the Gaussian approximation of the two distributions gives two mean V_m values, \bar{V}_1 and \bar{V}_2 , and two standard deviation values, σ_{V1} and σ_{V2} . The resulting system of four equations relating V_m parameters to conductance parameters can now be solved for four unknowns, yielding

$$g_{\{e,i\}0} = \frac{(I_{ext1} - I_{ext2}) [\sigma_{V2}^2 (E_{\{i,e\}} - \bar{V}_1)^2 - \sigma_{V1}^2 (E_{\{i,e\}} - \bar{V}_2)^2]}{[(E_e - \bar{V}_1)(E_i - \bar{V}_2) + (E_e - \bar{V}_2)(E_i - \bar{V}_1)] (E_{\{e,i\}} - E_{\{i,e\}}) (\bar{V}_1 - \bar{V}_2)^2} - \frac{(I_{ext1} - I_{ext2})(E_{\{i,e\}} - \bar{V}_2) + [I_{ext2} - G_L(E_{\{i,e\}} - E_L)] (\bar{V}_1 - \bar{V}_2)}{(E_{\{e,i\}} - E_{\{i,e\}}) (\bar{V}_1 - \bar{V}_2)}, \quad (9.9)$$

$$\sigma_{\{e,i\}}^2 = \frac{2C(I_{ext1} - I_{ext2}) [\sigma_{V1}^2 (E_{\{i,e\}} - \bar{V}_2)^2 - \sigma_{V2}^2 (E_{\{i,e\}} - \bar{V}_1)^2]}{\tilde{\tau}_{\{e,i\}} [(E_e - \bar{V}_1)(E_i - \bar{V}_2) + (E_e - \bar{V}_2)(E_i - \bar{V}_1)] (E_{\{e,i\}} - E_{\{i,e\}}) (\bar{V}_1 - \bar{V}_2)^2}. \quad (9.10)$$

These relationships allow one to estimate global characteristics of network activity such as mean excitatory (g_{e0}) and inhibitory (g_{i0}) synaptic conductances, as well as their respective variances (σ_e^2, σ_i^2), from the knowledge of only the V_m distributions obtained at two different levels of injected current. This VmD method was tested using computational models (Fig. 9.7a) and dynamic-clamp experiments (Fig. 9.7b,c; Rudolph *et al.*, 2004; see below) and was also used to extract conductances from different experimental conditions *in vivo* (Rudolph *et al.*, 2005, 2007, Zou *et al.*, 2005). This will be examined in more detail in the next sections.

9.5.1.2 Testing the VmD method with dynamic-clamp. Taking advantage of the possibility given by the dynamic-clamp technique (see above) to mimic in a

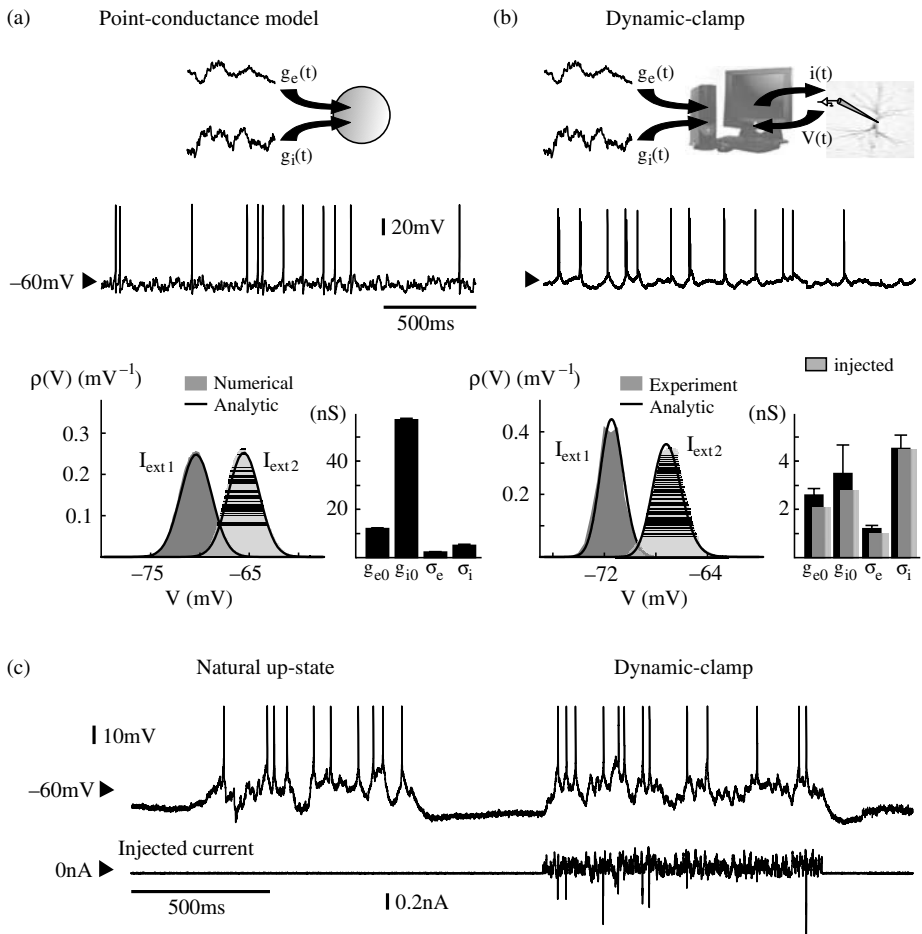


FIG. 9.7: Numerical and dynamic-clamp test of the VmD method to extract conductances. (a) Simulation of the point-conductance model (top trace) and comparison between numerically computed V_m distributions (bottom; left) and the analytic expression (black; conductance values shown in the bar graph). (b) Dynamic-clamp injection of the point-conductance model in a real neuron. Right: conductance parameters are re-estimated (black bars; error bars are standard deviations obtained when the same injected conductance parameters are re-estimated in different cells) from the V_m distributions and compared to the known parameters of the injected conductances (grey bars). Left: the experimental V_m distributions are compared to the analytic distributions calculated using the re-estimated conductance parameters. (c) Comparison of a spontaneous up-state (natural up-state) with an artificial up-state recreated using conductance injection (dynamic-clamp). Modified from Rudolph *et al.* (2004).

finely controlled way the fluctuating conductances g_e and g_i in biological neurons, *in vitro* tests of the VmD method were performed (Piwkowska *et al.*, 2008, Piwkowska *et al.*, 2005, Rudolph *et al.*, 2004). In a first test (in five neurons), V_m distributions were computed selectively during periods of subthreshold activity collected within up-states recorded in ferret cortical slices, conductance parameters were subsequently extracted from Gaussian fits to these distributions, and finally we used the estimated parameters to inject fluctuating conductances in dynamic-clamp in the same cell, during down-states. Figure 9.7(c) shows a typical example of a real up-state and, shortly after, an up-state recreated in dynamic-clamp. It was confirmed that the V_m distributions are very similar in the two cases (see Rudolph *et al.*, 2004, for more details). This test shows that the V_m distributions observed experimentally *in vitro* during recurrent cortical activity can be accounted for by the proposed point-conductance model. Also known parameters of synaptic conductances (g_{e0} , g_{i0} , σ_e , σ_i) injected in dynamic-clamp from the resulting V_m distributions were re-estimated: the match between actual and estimated values is shown in Fig. 9.7(b). This second test indicates that the passive approximation for the membrane behaviour holds in the case studied. In these tests, we did not consider the issue of the estimation of τ_e and τ_i and assumed these values were known.

9.5.1.3 Application of the VmD method to analyse intracellular recordings *in vivo*. The VmD method was applied to analyse intracellular recordings in anaesthetized (Rudolph *et al.*, 2005), as well as naturally sleeping and awake cats (Rudolph *et al.*, 2007). We illustrate the latter study here. The VmD method was applied to several cells recorded in either awake or sleep states (Fig. 9.8a), sometimes displaying both states in the same cell. The analysis was based on V_m distributions computed at different DC levels corresponding to the linear portion of the I - V curve of the recorded neurons (Fig. 9.8b). For both awake and sleep states, in the majority of cells analysed, especially during slow-wave-sleep up-states, the inhibitory conductances were larger than excitatory ones, for both mean and variance (Fig. 9.8c). At the population level, the ratio of inhibition to excitation was higher during slow-wave-sleep up-states compared to the awake state. In three neurons that were recorded from across several states, both average conductances together with their variances decreased in the awake state compared to slow-wave-sleep up-states. In addition, especially during the awake state, some cells displayed comparable excitation and inhibition or even a dominant excitation (2 out of 11 cells in the awake state). There was an important diversity in the absolute values of the estimated conductance parameters (Fig. 9.8d).

9.5.2 Other methods derived from the point-conductance stochastic model

9.5.2.1 Extraction of spike-triggered average conductances from V_m activity. We recently developed a procedure to extract the spike-triggered averages (STAs) of conductances from recordings of the V_m (Pospischil *et al.*, 2007). The basis

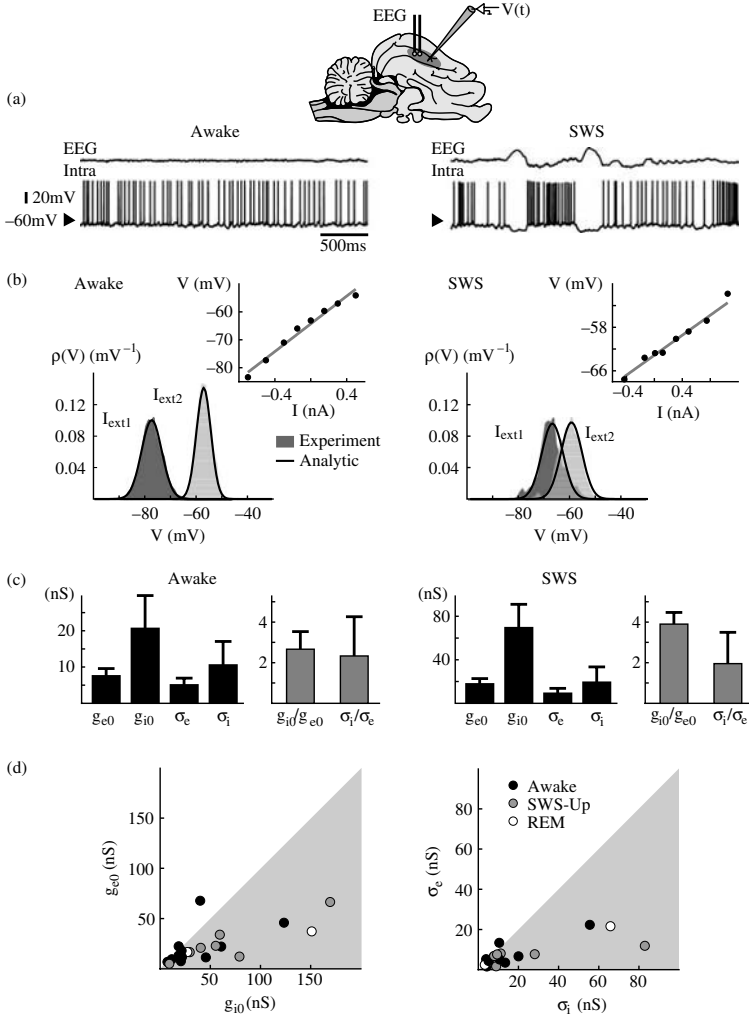


FIG. 9.8: VmD estimates of conductances from intracellular recordings in awake and naturally sleeping cats. (a) Intracellular recordings in awake and naturally sleeping (SWS) cats. Recordings were made in association cortex (area 5-7). (b) Examples of V_m distributions computed during wakefulness (awake) and slow-wave sleep up-states (SWS). The black lines show analytic fits of the experimental distributions. Insets: current–voltage relations obtained for these particular neurons. (c) Conductance values estimated using the VmD method. Results for the means (g_{e0} , g_{i0}) and standard deviations (σ_e , σ_i) of excitatory and inhibitory conductances, respectively, as well as their ratios are shown (error bars: standard deviations obtained by repeating the analysis using different pairs of injected current levels). (d) Grouped data showing the means and standard deviations of the conductances for different cells across different behavioural states (REM = rapid eye movement sleep). Modified from Rudolph *et al.* (2007).

of the STA method is to, first, calculate the STA of the V_m activity, and then search for the ‘most likely’ spike-related conductance time courses ($g_e(t)$, $g_i(t)$) that are compatible with the observed voltage STA. This problem is non-trivial because the membrane equation must be inverted, which is in general not possible because of the multiplicative coupling of conductances. However, assuming that the conductances are Gaussian stochastic processes (as in the point-conductance model), and by discretizing the time axis, it is possible to estimate the most probable conductance time course (‘maximum likelihood’ approach). To do this, one discretizes time, leading to sequences $\{g_e^k, g_i^k\}_{k=1,\dots,n}$, denoting the time course of conductances giving rise to the voltage STA V^k . For a given time k , there is a continuum of combinations $\{g_e^k, g_i^k\}$ that can advance the membrane potential from V^k to V^{k+1} , each pair occurring with a probability denoted p_k . If the initial condition $\{g_e^0, g_i^0\}$ is known (if the duration of the STA is long enough, one can safely assume $g_e^0 = g_{e0}$ and $g_i^0 = g_{i0}$), one can write down the probability p for certain series of conductances $\{g_e^j, g_i^j\}_{j=0,\dots,n}$ to occur that reproduce a given voltage trace $\{V^l\}_{l=1,\dots,n+1}$:

$$p = \prod_{k=0}^{n-1} p^k , \quad (9.11)$$

where it can be shown (Pospischil *et al.*, 2007) that

$$p_k = \frac{1}{2\pi} \exp \left(-\frac{1}{4\Delta t} X^k \right) \quad (9.12)$$

with

$$X^k = \frac{\tau_e}{\sigma_e^2} \left(g_e^{k+1} - g_e^k \left(1 - \frac{\Delta t}{\tau_e} \right) - \frac{\Delta t}{\tau_e} g_{e0} \right)^2 + \frac{\tau_i}{\sigma_i^2} \left(g_i^{k+1} - g_i^k \left(1 - \frac{\Delta t}{\tau_i} \right) - \frac{\Delta t}{\tau_i} g_{i0} \right)^2 , \quad (9.13)$$

where Δt is a fixed time bin. This system can be solved by finding the extremum of p_k :

$$\left\{ \frac{\partial p}{\partial g_e^k} = 0 \right\}_{k=1,\dots,n} ,$$

leading to a simple linear system solvable by traditional methods (Pospischil *et al.*, 2007).

Thus, as can be seen from Eqn. (9.13), the STA of the conductances can be evaluated from a voltage trace at a single current level, but it requires prior knowledge of the parameters g_{e0} , g_{i0} , σ_e , and σ_i , which can be estimated using the VmD method (see above).

Similarly to the VmD method, the STA method was tested in two ways: First, using computational models, it was verified that the procedure applied

to the V_m activity reproduces the STA of the conductances calculated from the model (Pospischil *et al.*, 2007). Secondly, the dynamic-clamp technique was used to inject known conductance patterns in real neurons. From the analysis of the V_m activity, one could check that the STA method successfully estimates the correct conductance patterns related to spikes (Pospischil *et al.*, 2007).

The STA method was applied to intracellular recordings in awake and naturally sleeping cats (Rudolph *et al.*, 2007). It was found that for the majority of neurons, the spike is correlated with a decrease of inhibitory conductance, suggesting that inhibition is most effective in determining spiking activity. This observation matches the dominance of inhibition observed using the VmD method in the same neurons (see above).

9.5.2.2 Extraction of synaptic time constants from the power spectrum of the V_m
 Another important way of analysing V_m recordings is through the power spectral density (PSD). The PSD of the V_m fluctuations of the point-conductance stochastic process can be well approximated by the following expression (Destexhe and Rudolph, 2004):

$$S_V(\omega) = \frac{4}{G_T^2} \frac{1}{1 + \omega^2 \tilde{\tau}_m^2} \left[\frac{\sigma_e^2 \tau_e (E_e - \bar{V})^2}{1 + \omega^2 \tau_e^2} + \frac{\sigma_i^2 \tau_i (E_i - \bar{V})^2}{1 + \omega^2 \tau_i^2} \right], \quad (9.14)$$

where $\omega = 2\pi f$, f is the frequency, $G_T = G_L + g_{e0} + g_{i0}$ is the total membrane conductance, $\tilde{\tau}_m = C/G_T$ is the effective time constant, and $\bar{V} = (G_L E_L + g_{e0} E_e + g_{i0} E_i)/G_T$ is the average membrane potential. The ‘effective leak’ approximation used to derive this equation consisted of incorporating the average synaptic conductances into the total leak conductance, and then assuming that fluctuations around the obtained mean voltage are subjected to a constant driving force (Destexhe and Rudolph, 2004).

Fitting this template to experimentally recorded PSDs should provide estimates of the synaptic time constants τ_e and τ_i . This procedure was first tested by comparing the prediction to numerical simulations of a single-compartment model subject to fluctuating synaptic conductances (Eqns. (9.1)–(9.3)). The matching between the analytic expression and the PSD obtained numerically was nearly perfect (Destexhe and Rudolph, 2004). The same procedure was also tested in dynamic-clamp (Piwkowska *et al.*, 2008). In this case, the theoretical template provided an excellent fit up to frequencies of about 500 Hz, above which the mismatch was presumably due to instrumental noise.

This procedure was also used to fit *in vivo* recordings of V_m activity (Rudolph *et al.*, 2005). In this case, the matching was more approximate: the PSD presents a frequency scaling region at high frequencies (>100 Hz) which scales as $1/f^\alpha$ with an exponent $\alpha = 4$ predicted by the theory. The experimental PSDs show a different scaling at high frequencies, with an exponent close to $\alpha = 2.5$ (Destexhe *et al.*, 2003, Rudolph *et al.*, 2005). This different scaling may be due to the attenuation of synaptic inputs occurring on dendrites, as well as to the non-ideal aspect of the membrane capacitance (Bedard and Destexhe, 2008). Nevertheless,

the matching of the expression above to the low-frequency end (<100 Hz) of the PSD yielded values of time constants of $\tau_e = 3$ ms and $\tau_i = 10$ ms. Small variations (around 20–30%) around these values of τ_e and τ_i yielded equally good fits (Rudolph *et al.*, 2005). Thus, one can conclude that this PSD method cannot be used to precisely estimate those parameters, but can nevertheless be used to broadly estimate them with an error of the order of 30%.

9.6 Conclusions

In this chapter we have given an overview of the use of stochastic processes in the study of synaptic noise in cortical neurons. We first reviewed experimental results (Section 9.2), showing that cortical neurons *in vivo* are subject to a considerable amount of synaptic noise. In Section 9.3, we reviewed models of synaptic noise, and in particular the point-conductance stochastic process. This and other models have predicted a number of computational consequences of synaptic noise on neuronal processing. The rest of the chapter was devoted to illustrating the usefulness of the point-conductance stochastic process: it can be used to add artificial synaptic noise in neurons *in vitro* using the dynamic-clamp technique (Section 9.4). This technique is of primary importance, because it allows one to directly test the predictions of the models in real neurons. It can also be used to realize experiments that would not be possible *in vivo*, such as controlling the amount of synaptic noise. Another important application of the point-conductance model is that it can form the basis of the design of methods to analyse experimental data (Section 9.5). These methods include the estimation of synaptic conductances (the VmD method), spike-triggered average conductances (the STA method), or synaptic time constants (the PSD method). These quantities are evaluated from the knowledge of only the V_m activity, which makes it applicable to the standard intracellular recording conditions. Each of these methods was tested using computational models, as well as on real neurons using the dynamic-clamp technique.

Thus, the drastic effect of noise on neurons, which was predicted by theoretical and computational studies, is now at the stage of being investigated in real neurons in two ways. First, the nature of synaptic noise is being characterized from experimental data using appropriate methods, which characterize different quantities such as the V_m distributions and PSD, and derive the characteristics of the underlying synaptic conductances. Second, predictions of the models are being tested in real neurons, as we examine in more detail below.

The first prediction, namely that the gain and responsiveness of neurons is enhanced by noise, was first reported from modelling studies (Hô and Destexhe, 2000), and then investigated experimentally using dynamic-clamp injection of *in vivo*-like synaptic noise (Destexhe *et al.*, 2001, Fellous *et al.*, 2003, Higgs, Slee, and Spain, 2006, Piwkowska *et al.*, 2008, Prescott and De Koninck, 2003, Shu *et al.*, 2003, Wolfart *et al.*, 2005, Chance, Abbott, and Reyes, 2002), confirming some of the predictions formulated by models. Enhanced responsiveness was also tested using real network activity, but contradictory results were obtained

when comparing responses in up- and down-states (see Section 9.2). A possible reason for the discrepancies is that some of these studies used a unique input amplitude which is insufficient (inputs can be either more or less responsive depending on their amplitude; see Fig. 9.3b). More experiments are needed, using a range of different input amplitudes. A fascinating possible consequence is that the enhanced responsiveness due to synaptic noise could be used as an attentional mechanism (Hö and Destexhe, 2000, Shu *et al.*, 2003). By modulating the amount of synaptic noise, it should be possible to switch entire networks from unresponsive to responsive states. This possibility should be investigated by designing appropriate experiments and models.

A second aspect concerns the modulation of intrinsic neuronal properties. Synaptic noise affects neuronal responsiveness, but what happens when neurons express dominant intrinsic properties, such as bursting? This question has been addressed so far only for thalamic neurons (Wolfart *et al.*, 2005). This study revealed that the classic 'tonic' and 'burst' modes of firing in thalamic relay cells were profoundly altered. With synaptic noise, these modes are no longer distinguishable because bursts and single-spikes participate to all responses. It was also shown that strong potassium conductances can change the sign of gain modulation in cortical neurons (Higgs, Slee, and Spain, 2006). How extrinsic noise interacts with intrinsic neuronal properties is at present only partially understood, and certainly constitutes a field where much remains to be done.

A third prediction is that synaptic noise modulates dendritic integration. The phenomenon of enhanced responsiveness also influences local dendritic processing. The interplay between excitable properties (dendritic spikes) and synaptic noise can result in an equalization of the efficacy of individual synapses (Fig. 9.4). These predictions have so far not been tested experimentally; it would require one to recreate the correct conductance state all along the cable structure, which is at present difficult to achieve. More generally, how synaptic noise influences dendritic integration is a complex problem only partially understood, and which will also require further modelling and experimental studies.

A fourth prediction is that synaptic noise enhances the temporal resolution of neurons. This type of temporal processing was the first consequence put forward by modelling studies (Barrett, 1975, Bernander, Douglas, Martin, and Koch, 1991, Holmes and Woody, 1989, Rudolph and Destexhe, 2003a, 2003c). Neurons in high-conductance states necessarily have a smaller time constant which allows sharp temporal processing (see example in Fig. 9.5). Surprisingly, few experimental studies have investigated this aspect, which also constitutes a very interesting direction to be explored in the future.

As a conclusion, the exploration of synaptic noise and its effect on neurons and networks is a fascinating subject, which can have far-reaching consequences. The understanding of how the state of a network in general modulates the integrative properties and information flow (and vice versa) is only at its early stage, and will require a continuous association of experiments and computational models.

9.6.1 Acknowledgments

The experimental data reviewed here were obtained by Drs. T. Bal, D.A. McCormick, D. Paré, Z. Piwkowska and I. Timofeev. Research supported by the Centre National de la Recherche Scientifique (CNRS, France), Agence Nationale de la Recherche (ANR), Future and Emerging Technologies (FET, European Union) and the Human Frontier Science Program (HFSP). Additional information is available at <http://cns.iaf.cnrs-gif.fr>

References

- Baranyi, A., Szente, M.B., and Woody, C.D. (1993). Electrophysiological characterization of different types of neurons recorded *in vivo* in the motor cortex of the cat. II. Membrane parameters, action potentials, current-induced voltage responses and electrotonic structures. *Journal of Neurophysiology*, **69**(6), 1865–1879.
- Barrett, J.N. (1975). Motoneuron dendrites: role in synaptic integration. *Fed Proc*, **34**(5), 1398–407.
- Bedard, C. and Destexhe, A. (2008). A modified cable formalism for modeling neuronal membranes at high frequencies. *Biophysical Journal*, **94**(4), 1133.
- Bernander, O., Douglas, R.J., Martin, K.A., and Koch, C. (1991). Synaptic background activity influences spatiotemporal integration in single pyramidal cells. *Proceedings of the National Academy of Sciences of the United States of America*, **88**(24), 11569.
- Braitenberg, V. and Schüz, A. (1998). *Cortex: Statistics and Geometry of Neuronal Connectivity*. Springer-Verlag, New York.
- Burkitt, A.N., Meffin, H., and Grayden, D.B. (2003). Study of neuronal gain in a conductance-based leaky integrate-and-fire neuron model with balanced excitatory and inhibitory synaptic input. *Biological Cybernetics*, **89**, 119–125.
- Chance, F.S., Abbott, L.F., and Reyes, A.D. (2002). Gain modulation from background synaptic input. *Neuron*, **35**, 773–782.
- Contreras, D., Timofeev, I., and Steriade, M. (1996). Mechanisms of long-lasting hyperpolarizations underlying slow sleep oscillations in cat corticothalamic networks. *The Journal of Physiology*, **494**(1), 251–264.
- De Schutter, E. and Bower, J.M. (1994). Simulated responses of cerebellar Purkinje cells are independent of the dendritic location of granule cell synaptic inputs. *Proceedings of the National Academy of Sciences of the United States of America*, **91**(11), 4736.
- DeFelipe, J. and Fariñas, I. (1992). The pyramidal neuron of the cerebral cortex: morphological and chemical characteristics of the synaptic inputs. *Prog Neurobiol*, **39**(6), 563–607.
- Destexhe, A. (2007). High-conductance state. *Scholarpedia*, **2**(11), 1341.
- Destexhe, A. and Contreras, D. (2006). Neuronal computations with stochastic network states. *Science*, **314**(5796), 85–90.

- Destexhe, A., Hughes, S.W., Rudolph, M., and Crunelli, V. (2007). Are corticothalamic upstates fragments of wakefulness? *Trends in Neurosciences*, **30**(7), 334–342.
- Destexhe, A. and Paré, D. (1999). Impact of network activity on the integrative properties of neocortical pyramidal neurons *in vivo*. *Journal of Neurophysiology*, **81**(4), 1531–1547.
- Destexhe, A. and Rudolph, M. (2004). Extracting information from the power spectrum of synaptic noise. *Journal of Computational Neuroscience*, **17**(3), 327–345.
- Destexhe, A., Rudolph, M., Fellous, J.M., and Sejnowski, T.J. (2001). Fluctuating synaptic conductances recreate *in vivo*-like activity in neocortical neurons. *Neuroscience*, **107**(1), 13–24.
- Destexhe, A., Rudolph, M., Paré, D. et al. (2003). The high-conductance state of neocortical neurons *in vivo*. *Nature Reviews Neuroscience*, **4**, 739–751.
- Evarts, E.V. (1964). Temporal patterns of discharge of pyramidal tract neurons during sleep and waking in the monkey. *Journal of Neurophysiology*, **27**(2), 152–171.
- Fellous, J.M., Rudolph, M., Destexhe, A., and Sejnowski, T.J. (2003). Synaptic background noise controls the input/output characteristics of single cells in an *in vitro* model of *in vivo* activity. *Neuroscience*, **122**(3), 811–829.
- Gammaconi, L., Hänggi, P., Jung, P., and Marchesoni, F. (1998). Stochastic resonance. *Reviews of Modern Physics*, **70**(1), 223–287.
- Halliday, D.M. (2000). Weak, stochastic temporal correlation of large-scale synaptic input is a major determinant of neuronal bandwidth. *Neural Computation*, **12**(3), 693–707.
- Higgs, M.H., Slee, S.J., and Spain, W.J. (2006). Diversity of gain modulation by noise in neocortical neurons: Regulation by the slow afterhyperpolarization conductance. *Journal of Neuroscience*, **26**(34), 8787.
- Hö, N. and Destexhe, A. (2000). Synaptic background activity enhances the responsiveness of neocortical pyramidal neurons. *Journal of Neurophysiology*, **84**(3), 1488–1496.
- Holmes, W.R. and Woody, C.D. (1989). Effects of uniform and non-uniform synaptic ‘activation-distributions’ on the cable properties of modeled cortical pyramidal neurons. *Brain Res*, **505**(1), 12–22.
- Kisley, M.A. and Gerstein, G.L. (1999). The continuum of operating modes for a passive model neuron. *Neural Computation*, **11**(5), 1139–1154.
- Leger, J.F., Stern, E.A., Aertsen, A., and Heck, D. (2005). Synaptic integration in rat frontal cortex shaped by network activity. *Journal of Neurophysiology*, **93**(1), 281–293.
- Levin, J.E. and Miller, J.P. (1996). Broadband neural encoding in the cricket cercal sensory system enhanced by stochastic resonance. *Nature*, **380**(6570), 165–168.
- Levitin, H., Segundo, J.P., Moore, G.P., and Perkel, D.H. (1968). Statistical analysis of membrane potential fluctuations: relation with presynaptic spike train. *Biophysical Journal*, **8**(11), 1256.

- Lindner, B. and Longtin, A. (2006). Comment on: ‘Characterization of sub-threshold voltage fluctuations in neuronal membranes’ by M. Rudolph and A. Destexhe. *Neural Computation*, **18**, 1896–1931.
- Llinas, R. and Jahnse, H. (1982). Electrophysiology of mammalian thalamic neurons *in vitro*. *Nature*, **297**(5865), 406–408.
- Marsalek, P., Koch, C., and Maunsell, J. (1997). On the relationship between synaptic input and spike output jitter in individual neurons. *Proceedings of the National Academy of Sciences*, **94**(2), 735.
- Matsumura, M., Cope, T., and Fetz, E.E. (1988). Sustained excitatory synaptic input to motor cortex neurons in awake animals revealed by intracellular recording of membrane potentials. *Experimental Brain Research*, **70**(3), 463–469.
- McCormick, D.A. and Bal, T. (1997). Sleep and arousal: thalamocortical mechanisms. *Ann. Rev. Neurosci.*, **20**, 185–215.
- Meffin, H., Burkitt, A.N., and Grayden, D.B. (2004). An analytical model for the large, fluctuating synaptic conductance state typical of neocortical neurons *in vivo*. *Journal of Computational Neuroscience*, **16**(2), 159–175.
- Metherate, R. and Ashe, J.H. (1993). Ionic flux contributions to neocortical slow waves and nucleus basalis-mediated activation: whole-cell recordings *in vivo*. *Journal of Neuroscience*, **13**(12), 5312.
- Mitchell, S.J. and Silver, R.A. (2003). Shunting inhibition modulates neuronal gain during synaptic excitation. *Neuron*, **38**(3), 433–445.
- Monier, C., Fournier, J., and Frégnac, Y. (2008). *In vitro* and *in vivo* measures of evoked excitatory and inhibitory conductance dynamics in sensory cortices. *Journal of Neuroscience Methods*, **169**(2), 323–365.
- Moreno-Bote, R. and Parga, N. (2005). Membrane potential and response properties of populations of cortical neurons in the high conductance state. *Physical Review Letters*, **94**(8), 088103.
- Muller, E., Buesing, L., Schemmel, J., and Meier, K. (2007). Spike-frequency adapting neural ensembles: Beyond mean adaptation and renewal theories. *Neural Computation*, **19**(11), 2958–3010.
- Paré, D., Shink, E., Gaudreau, H., Destexhe, A., and Lang, E.J. (1998). Impact of spontaneous synaptic activity on the resting properties of cat neocortical pyramidal neurons *in vivo*. *Journal of Neurophysiology*, **79**(3), 1450–1460.
- Petersen, C.C.H., Hahn, T.T.G., Mehta, M., Grinvald, A., and Sakmann, B. (2003). Interaction of sensory responses with spontaneous depolarization in layer 2/3 barrel cortex. *Proceedings of the National Academy of Sciences*, **100**(23), 13638.
- Piwowska, Z., Pospischil, M., Brette, R., Sliwa, J., Rudolph-Lilith, M., Bal, T., and Destexhe, A. (2008). Characterizing synaptic conductance fluctuations in cortical neurons and their influence on spike generation. *Journal of Neuroscience Methods*, **169**(2), 302–322.

- Piwkowska, Z., Rudolph, M., Badoual, M., Destexhe, A., and Bal, T. (2005). Re-creating active states *in vitro* with a dynamic-clamp protocol. *Neurocomputing*, **65**, 55–60.
- Pospischil, M., Piwkowska, Z., Rudolph, M., Bal, T., and Destexhe, A. (2007). Calculating event-triggered average synaptic conductances from the membrane potential. *Journal of Neurophysiology*, **97**(3), 2544.
- Prescott, S.A. and De Koninck, Y. (2003). Gain control of firing rate by shunting inhibition: Roles of synaptic noise and dendritic saturation. *Proceedings of the National Academy of Sciences*, **100**(4), 2076.
- Prinz, A.A., Abbott, L.F., and Marder, E. (2004). The dynamic clamp comes of age. *Trends in Neurosciences*, **27**(4), 218–224.
- Rapp, M., Yarom, Y., and Segev, I. (1992). The impact of parallel fiber background activity on the cable properties of cerebellar Purkinje cells. *Neural Computation*, **4**(4), 518–533.
- Richardson, M.J.E. (2004). Effects of synaptic conductance on the voltage distribution and firing rate of spiking neurons. *Physical Review E*, **69**(5), 051918.
- Robinson, H.P. and Kawai, N. (1993). Injection of digitally synthesized synaptic conductance transients to measure the integrative properties of neurons. *J Neurosci Methods*, **49**(3), 157–65.
- Rudolph, M. and Destexhe, A. (2001a). Correlation detection and resonance in neural systems with distributed noise sources. *Physical Review Letters*, **86**(16), 3662–3665.
- Rudolph, M. and Destexhe, A. (2001b). Do neocortical pyramidal neurons display stochastic resonance? *Journal of Computational Neuroscience*, **11**(1), 19–42.
- Rudolph, M. and Destexhe, A. (2003a). A fast-conducting, stochastic integrative mode for neocortical neurons *in vivo*. *Journal of Neuroscience*, **23**(6), 2466.
- Rudolph, M. and Destexhe, A. (2003b). Characterization of subthreshold voltage fluctuations in neuronal membranes. *Neural Computation*, **15**(11), 2577–2618.
- Rudolph, M. and Destexhe, A. (2003c). Tuning neocortical pyramidal neurons between integrators and coincidence detectors. *Journal of Computational Neuroscience*, **14**(3), 239–251.
- Rudolph, M. and Destexhe, A. (2005). An extended analytic expression for the membrane potential distribution of conductance-based synaptic noise. *Neural Computation*, **17**(11), 2301–2315.
- Rudolph, M. and Destexhe, A. (2006). On the use of analytical expressions for the voltage distribution to analyze intracellular recordings. *Neural Computation*, **18**(12), 2917–2922.
- Rudolph, M., Pelletier, J.G., Paré, D., and Destexhe, A. (2005). Characterization of synaptic conductances and integrative properties during electrically induced EEG-activated states in neocortical neurons *in vivo*. *Journal of Neurophysiology*, **94**(4), 2805–2821.

- Rudolph, M., Piwkowska, Z., Badoual, M., Bal, T., and Destexhe, A. (2004). A method to estimate synaptic conductances from membrane potential fluctuations. *Journal of Neurophysiology*, **91**(6), 2884–2896.
- Rudolph, M., Pospischil, M., Timofeev, I., and Destexhe, A. (2007). Inhibition determines membrane potential dynamics and controls action potential generation in awake and sleeping cat cortex. *Journal of Neuroscience*, **27**(20), 5280.
- Salinas, E. and Sejnowski, T.J. (2000). Impact of correlated synaptic input on output firing rate and variability in simple neuronal models. *J. Neurosci.*, **20**(16), 6193–6209.
- Sanchez-Vives, M.V. and McCormick, D.A. (2000). Cellular and network mechanisms of rhythmic recurrent activity in neocortex. *Nat Neurosci.*, **3**(1), 1027–1034.
- Sharp, A.A., O’Neil, M.B., Abbott, L.F., and Marder, E. (1993). The dynamic clamp: artificial conductances in biological neurons. *Trends Neurosci.*, **16**(10), 389–94.
- Shelley, M., McLaughlin, D., Shapley, R., and Wielaard, J. (2002). States of high conductance in a large-scale model of the visual cortex. *Journal of Computational Neuroscience*, **13**(2), 93–109.
- Shu, Y., Hasenstaub, A., Badoual, M., Bal, T., and McCormick, D.A. (2003). Barrages of synaptic activity control the gain and sensitivity of cortical neurons. *J Neurosci.*, **23**(32), 10388–401.
- Singer, W., Tretter, F., and Cynader, M. (1976). The effect of reticular stimulation on spontaneous and evoked activity in the cat visual cortex. *Brain Res.*, **102**(1), 71–90.
- Stacey, W.C. and Durand, D.M. (2000). Stochastic resonance improves signal detection in hippocampal CA1 neurons. *Journal of Neurophysiology*, **83**(3), 1394–1402.
- Steriade, M. (1970). Ascending control of thalamic and cortical responsiveness. *Int Rev Neurobiol*, **12**, 87–144.
- Steriade, M. (2001). Impact of network activities on neuronal properties in corticothalamic systems. *J. Neurophysiol.*, **86**, 1–39.
- Steriade, M. (2003). *Neuronal Substrates of Sleep and Epilepsy*. Cambridge University Press, Cambridge.
- Steriade, M., Amzica, F., and Nunez, A. (1993). Cholinergic and noradrenergic modulation of the slow (approximately 0.3 Hz) oscillation in neocortical cells. *Journal of Neurophysiology*, **70**(4), 1385–1400.
- Steriade, M., Timofeev, I., and Grenier, F. (2001). Natural waking and sleep states: A view from inside neocortical neurons. *Journal of Neurophysiology*, **85**(5), 1969–1985.
- Steriade, M.M. and McCarley, R. (1990). *Brainstem Control of Wakefulness and Sleep*. Springer, New York.
- Timofeev, I., Grenier, F., and Steriade, M. (2001). Disfacilitation and active inhibition in the neocortex during the natural sleep-wake cycle: An intracellular study. *Proceedings of the National Academy of Sciences*, **98**(4), 1924.

- Tuckwell, H.C. (1988). *Introduction to Theoretical Neurobiology*. Cambridge University Press, Cambridge.
- Waters, J. and Helmchen, F. (2006). Background synaptic activity is sparse in neocortex. *Journal of Neuroscience*, **26**(32), 8267.
- Wiesenfeld, K. and Moss, F. (1995). Stochastic resonance and the benefits of noise: from ice ages to crayfish and SQUIDs. *Nature*, **373**(6509), 33–36.
- Wolfart, J., Debay, D., Le Masson, G., Destexhe, A., and Bal, T. (2005). Synaptic background activity controls spike transfer from thalamus to cortex. *Nat Neurosci*, **8**(12), 1760–7.
- Zou, Q., Rudolph, M., Roy, N., Sanchez-Vives, M., Contreras, D., and Destexhe, A. (2005). Reconstructing synaptic background activity from conductance measurements *in vivo*. *Neurocomputing*, **65**, 673–678.

STATISTICAL MODELS OF SPIKE TRAINS

Liam Paninski, Emery N. Brown, Satish Iyengar, and Robert E. Kass

10.1 Introduction

Spiking neurons make inviting targets for analytical methods based on stochastic processes: spike trains carry information in their temporal patterning, yet they are often highly irregular across time and across experimental replications. The bulk of this volume is devoted to mathematical and biophysical models useful in understanding neurophysiological processes. In this chapter we consider *statistical models* for analysing spike train data.

Strictly speaking, what we would call a statistical model for spike trains is simply a probabilistic description of the sequence of spikes. But it is somewhat misleading to ignore the data-analytical context of these models. In particular, we want to make use of these probabilistic tools for the purpose of scientific inference.

The leap from simple descriptive uses of probability to inferential applications is worth emphasizing for two reasons. First, this leap was one of the great conceptual advances in science, taking roughly two hundred years. It was not until the late 1700s that there emerged any clear notion of inductive (or what we would now call *statistical*) reasoning; it was not until the first half of the twentieth century that modern methods began to be developed systematically; and it was only in the second half of the twentieth century that these methods became well understood in terms of both theory and practice. Second, the focus on inference changes the way one goes about the modelling process. It is this change in perspective we want to highlight here, and we will do so by discussing one of the most important models in neuroscience, the stochastic integrate-and-fire (IF) model for spike trains.

The stochastic IF model has a long history (Gerstein and Mandelbrot, 1964, Stein, 1965, Knight, 1972, Burkitt, 2006a, 2006b): it is the simplest dynamical model that captures the basic properties of neurons, including the temporal integration of noisy subthreshold inputs, all-or-nothing spiking, and refractoriness. Of course, the IF model is a caricature of true neural dynamics (see, e.g. Ermentrout and Kopell, 1986, Brunel and Latham, 2003, Izhikevich, 2007, for more elaborate models) but, as demonstrated in this book and others (Ricciardi, 1977, Tuckwell, 1989, Gerstner and Kistler, 2002), it has provided much insight into the behaviour of single neurons and neural populations.

In this chapter we explore some of the key *statistical* questions that arise when we use this model to perform inference with real neuronal spike train data.

How can we efficiently fit the model to spike train data? Once we have estimated the model parameters, what can the model tell us about the encoding properties of the observed neuron? We also briefly consider some more general approaches to statistical modelling of spike train data.

We begin in Section 10.2 by discussing three distinct useful ways of approaching the IF model, via the language of stochastic (diffusion) processes, hidden Markov models, and point processes. Each of these viewpoints comes equipped with its own specialized analytical tools, and the power of the IF model is most evident when all of these tools may be brought to bear simultaneously. We discuss three applications of these methods in Section 10.3, and then close in Section 10.4 by indicating the scope of the general point process framework of which the IF model is a part, and the possibilities for solving some key outstanding data-analytic problems in systems neuroscience.

10.2 The IF model from three different points of view

The leaky stochastic IF model is defined, in the simplest case, in terms of a one-dimensional stochastic voltage process $V(t)$ that follows the linear stochastic dynamics

$$dV(t) = (-g(t)V(t) + I(t))dt + \sigma dB_t, \quad (10.1)$$

where the random term B_t denotes a standard Brownian motion.¹ We model the observed spike train as the passage times of the random process $V(t)$ through the threshold voltage V_{th} ; after each threshold crossing, $V(t)$ is reset to $V_{\text{reset}} < V_{\text{th}}$.

Here $I(t)$ and $g(t)$ denote the input current and membrane conductance at time t , respectively. In the simplest case, we take the membrane conductance and input current to be constant, $g(t) = g, I(t) = I$. However, it is natural to consider the time-varying case as well. For example, in the popular ‘spike-response’ model (Gerstner and Kistler, 2002, Paninski, Pillow, and Simoncelli, 2004b), we include a time-varying current $h(t - t_i)$ flowing into the cell after each spike time t_i , i.e. $I(t) = I + \sum_{t_i < t} h(t - t_i)$; this post-spike current models the lumped effects of all currents that enter a real neuron following an action potential. By changing the shape and magnitude of $h(\cdot)$, we can model a variety of interspike interval (ISI) behaviour. For example, a negative but sharply time-limited $h(\cdot)$ can extend the relative refractory period of the IF neuron, since it will take longer for the voltage V to climb back up to the threshold V_{th} ; this in turn leads to firing rate saturation or spike-rate adaptation, since increasing the input current I will just increase the hyperpolarizing effect of the total spike history effect $\sum_{t_i < t} h(t - t_i)$. Similarly, a positive or biphasic $h(\cdot)$ can induce burst effects in the spike train; see Gerstner and Kistler (2002) and Paninski, Pillow, and Simoncelli (2004b) for further examples. It is also natural to consider similar

¹Or in discrete time,

$$V(t + dt) - V(t) = (-g(t)V(t) + I(t))dt + \sigma\sqrt{dt}\epsilon_t,$$

where ϵ_t is an i.i.d. standard normal random variable.

models for the conductance $g(t)$ following a spike time (Stevens and Zador, 1998, Jolivet, Lewis, and Gerstner, 2004).

Just as importantly, we would like to model the effects of an external stimulus on the observed spike train. One natural way to include stimulus effects in the model is to let the input current $I(t)$ depend on the stimulus $\vec{x}(t)$. In the simplest case, this dependence could be linear,

$$I(t) = \sum_i a_i x_i(t), \quad (10.2)$$

but of course it is possible to include nonlinear effects as well (Paninski, Pillow, and Simoncelli, 2004b).

When we turn to fitting models to data, and using them for scientific inference, there are various approaches we may consider. Some of the most powerful methods are based on the *likelihood function* which, in turn, is defined in terms of the joint probability density function (PDF) for the spike train. Let us write the PDF for the sequence of spike times $\{t_i\}$ as $p(\{t_i\}|\theta)$, where θ is a multi-dimensional parameter vector. In the setting described above, θ could include $\{V_{\text{th}}, V_{\text{reset}}, \sigma, \vec{a}, h(\cdot), g\}$. The likelihood function reverses the dependence displayed in the PDF: the PDF is a function of $\{t_i\}$ for each fixed θ , while the likelihood function is a function of θ for each fixed $\{t_i\}$. In other words, the PDF fixes the parameter θ and assigns probability to the spike trains that might then occur, while the likelihood function fixes the spike train that was actually observed, and assigns relative likelihood to the parameter values that might have produced it. Because likelihood-based methods use the information in the data as efficiently as possible (see, e.g. Brown, Barbieri, Eden and Frank, 2003, Kass, Ventura and Brown, 2005 and the references therein), a great deal of effort has been devoted to developing such methods and for carrying out the relevant computations. In the next subsections we discuss three different conceptual approaches for performing statistical inference with the IF model via likelihood-based methods.

However, before we dive into these different approaches for computing and maximizing the likelihood, it is worth noting a surprising and important fact about the likelihood in this model: the logarithm of the likelihood turns out to be *concave* as a function of many of the model parameter values θ (Paninski, Pillow, and Simoncelli, 2004b, Paninski, 2005, Mullowney and Iyengar, 2007). This makes model fitting via maximum likelihood or Bayesian methods surprisingly tractable, since concave functions lack any suboptimal local maxima that could trap a numerical optimizer. (This concavity property is also extremely useful in the context of *decoding*, i.e. inferring the stimulus \vec{x} given the observed spike train data $\{t_i\}$ (Pillow and Paninski, 2007, Ahmadian, Pillow, and Paninski, 2008); we will discuss some simple decoding applications of the IF model below.) Indeed, without this concavity property the IF model would be much less attractive from a statistical point of view.

10.2.1 The IF model as a diffusion process

The most direct, and probably best-explored, view of the IF model is as a linear *diffusion process* (Ricciardi, 1977, Tuckwell, 1989, Burkitt, 2006a, 2006b). This connection allows us to apply powerful tools from stochastic calculus (Karatzas and Shreve, 1997) to understand the behaviour of this model. For example, in the non-leaky case ($g(t) = 0$) with constant current input ($I(t) = I$), we may employ the ‘reflection principle’ from the basic theory of Brownian motion to derive the so-called ‘inverse Gaussian’ first passage time density (Gerstein and Mandelbrot, 1964, Seshadri, 1998, Iyengar and Liao, 1997, Brown, 2005); denoting $p(\tau|\theta)$ as the probability density that the next interspike interval will be of length τ , we may explicitly calculate

$$p(\tau|\theta) = \frac{V_{\text{th}} - V_{\text{reset}}}{\sqrt{2\pi\sigma^2\tau^3}} e^{-[(V_{\text{th}} - V_{\text{reset}}) - I\tau]^2/2\sigma^2\tau}.$$

In this simplest case, each interspike interval is independent and identically distributed (this point process is a special case of a ‘renewal’ process, since it resets itself after each spike), and therefore the likelihood of a full spike train is obtained by taking the product over the observed interspike intervals $\tau_i = t_{i+1} - t_i$:

$$p(\{t_i\}|\theta) = \prod_i p(\tau_i|\theta).$$

This explicit analytical formula for the spike train likelihood allows us, for example, to derive closed-form expressions for the maximum likelihood estimate of the model parameters θ here (Seshadri, 1998); thus the classical stochastic process theory makes model fitting in this simple case quite straightforward.

In the more general case of non-constant $I(t)$ and non-zero $g(t)$, things are somewhat more complicated; we have no explicit general formula for $p(\tau|\theta)$, for example. However, the stochastic calculus leads directly to partial differential equation (Risken, 1996, Paninski, Pillow, and Simoncelli, 2004b) or integral equation (Siebert, 1951, Buoncore, Nobile, and Ricciardi, 1987, Plesser and Tanaka, 1997, Burkitt and Clark, 1999, DiNardo *et al.*, 2001, Paninski, Haith, and Szirtes, 2008, Mullowney and Iyengar, 2007) methods for computing the likelihood. For example, it is well-known (Tuckwell, 1989) that the probability density of the next spike satisfies

$$p(\tau|\theta) = -\frac{\partial}{\partial t} \left(\int P(v, t) dv \right) \Big|_{t=\tau},$$

where the density $P(v, t) = \Pr(V(t) = v, \tau_i > t)$ satisfies the Kolmogorov ‘forward’ (Fokker–Planck) PDE

$$\frac{\partial P(v, t)}{\partial t} = \frac{\sigma^2}{2} \frac{\partial^2 P(v, t)}{\partial v^2} + g(t) \frac{\partial [(v - I(t)/g(t)) P(v, t)]}{\partial v} \quad (10.3)$$

with boundary conditions

$$P(v, t_{i-1}^+) = \delta(v - V_{\text{reset}}),$$

corresponding to the fact that the voltage resets to V_{reset} following the last spike, and

$$P(V_{\text{th}}, t) = 0,$$

corresponding to the fact that the voltage $V(t)$ is never greater than the threshold V_{th} . In the constant-current, zero-leak case this PDE may be solved explicitly by the method of images (Daniels, 1982, Paninski, 2006b); more generally, we may solve the PDE numerically via efficient implicit techniques such as the Crank–Nicholson method (Press *et al.*, 1992, Paninski, Pillow, and Simoncelli, 2004b). These methods are mathematically closely related to techniques developed to understand the behaviour of populations of neurons (Brunel and Hakim, 1999, Nykamp and Tranchina, 2000, Knight, Omurtag, and Sirovich, 2000, Fourcaud and Brunel, 2002) (and see Chapter 7 of this volume), though the application here is very different.

Alternatively, $p(\tau|\theta)$ solves a number of integral equations of the form

$$f(t) = \int_0^t K(\tau, t)p(\tau|\theta)d\tau$$

(Siebert, 1951, Ricciardi, 1977, Plesser and Tanaka, 1997, Burkitt and Clark, 1999, DiNardo *et al.*, 2001, Paninski, Haith, and Szirtes, 2008, Mullowney and Iyengar, 2007), where the kernel function $K(\tau, t)$ and the left-hand-side $f(t)$ may be computed as simple functions of the model parameters θ . In the case of constant current and conductance ($I(t) = I, g(t) = g$), this integral equation may be solved efficiently by Laplace transform techniques (Mullowney and Iyengar, 2007); more generally, the equation may be solved by numerical integration methods (Plesser and Tanaka, 1997, DiNardo *et al.*, 2001) or by direct matrix inversion methods (Paninski, Haith, and Szirtes, 2008) (the latter methods also lead to simple formulas for the derivative of the likelihood with respect to the model parameters; this gradient information is useful for optimization of the model parameters, and for assessing the accuracy of the parameter estimates).

Thus, to summarize, stochastic process methods may be used to derive efficient schemes for computing the likelihood in this model. However, this approach leaves some questions open. For example, it is unclear how to use the methods described above to obtain various *conditional* quantities of interest given observed spike train data. One such important quantity is the probability $p(V(t)|\{t_i\}, \theta)$ that the voltage at time t is at a certain level, given the observed spike sequence $\{t_i\}$ and model parameters θ . To address these questions, we adopt a ‘state-space’ approach to the IF model.

10.2.2 The IF model as a state-space model

A second way to approach the IF model is by considering a broader class of statistical models, known as ‘state space’, or ‘hidden Markov’ models. As the name implies, this model consists of two processes: an unobserved (‘hidden’) Markovian process, and an observed process which is related to the hidden process in a simple instantaneous manner (Rabiner, 1989).

Because this hidden Markov framework is natural in a wide variety of contexts, from speech recognition to genetic transcription, statisticians have developed a number of useful inference tools for models of this form. State-space models have recently been introduced in a number of neural contexts (Brown *et al.*, 1998, Smith and Brown, 2003, Czanner *et al.*, 2008, Yu *et al.*, 2006, Srinivasan *et al.*, 2006, Kulkarni and Paninski, 2007, Huys and Paninski, 2007, Dombeck *et al.*, 2007, Vogelstein and Paninski, 2007), with applications ranging from neural prosthetic design to signal processing of calcium imaging data.

The IF model may be cast in this framework easily. $V(t)$ is a hidden Markovian process which we observe only indirectly, through the spike times $\{t_i\}$, which may be considered a simple function of $V(t)$: the observed spike variable at time t is zero if $V(t)$ is below threshold, and one if $V(t) = V_{\text{th}}$. Now we may easily exploit standard methods from the state-space literature for computing the likelihood: for example, the standard ‘forward recursion’ for the computation of the likelihood in hidden Markov models (Rabiner, 1989) corresponds exactly to the computation of the Kolmogorov forward density $P(v, t)$ discussed in the previous section (Paninski, Pillow, and Simoncelli, 2004b, Nikitchenko and Paninski, 2007).

The standard method for computing the maximum likelihood estimate for the model parameter θ in a hidden Markov model is based on the so-called ‘Expectation-Maximization’ (EM) algorithm (Dempster, Laird, and Rubin, 1977, Rabiner, 1989). This algorithm is guaranteed to increase the likelihood with each iteration (i.e. EM serves as a likelihood ascent algorithm – though interestingly, the basic algorithm does not require a direct computation of the likelihood itself). In a nutshell, the EM algorithm applied to the IF model iterates between two conceptually straightforward steps (Czanner and Iyengar, 2004, Nikitchenko and Paninski, 2007). In the expectation step, we compute the *conditional expectation* $E[V(t)|\{t_i\}, \theta]$ of the voltage $V(t)$ at each time t , given all the observed spike data, via the standard ‘forward–backward’ recursive algorithm from hidden Markov models (we will discuss an interesting application of this conditional expectation computation below, in Section 10.3.1); in the maximization step, we fit the parameters of model (10.1) directly, using the inferred conditional expectations $E[V(t)|\{t_i\}, \theta]$ as a substitute for the expectations (sufficient statistics) computed from the actual subthreshold voltages $V(t)$. This M step is straightforward because it is much easier to fit model (10.1) given direct voltage observations; in this case, the model reduces to a fairly standard autoregressive model, for which the estimation theory is quite well-established. See, for example Jolivet, Lewis, and Gerstner (2004), Paninski, Pillow, and Simoncelli (2004a), Huys, Ahrens,

and Paninski (2006), Lansky, Sanda, and He (2006) for some examples in which autoregressive models similar to our equation (10.1) have been fitted directly to intracellularly recorded voltage data.

Thus the state-space setting provides a very useful framework for optimizing the IF model parameters θ , and for making inferences about the hidden subthreshold voltage $V(t)$ (see Section 10.3.1 below). One additional major advantage of the state-space representation is its flexibility: it turns out to be fairly straightforward to generalize these techniques to include other important dynamical biophysical variables in our model beyond just the voltage $V(t)$. We will discuss some of these extensions in Section 10.4 below.

10.2.3 Approximating the IF model via simpler point-process models

The diffusion- and state-space-based approaches above are conceptually elegant but computationally somewhat expensive. A third approach for performing inference with integrate-and-fire data is not to fit the IF model at all, but rather to use a simpler model that retains the IF model's key properties. (It is worth recalling here the adage that all models are wrong, but some are useful. In other words, when performing statistical analysis we are not bound to any one model in particular; instead, we should choose the model which best suits our needs.) A particularly simple framework for analysis of point process data involves likelihood methods based on the *conditional intensity function* $\lambda(t|H_t, \theta)$, the instantaneous firing rate at time t given H_t , the complete stimulus and spiking history preceding time t (see Brown, Barbieri, Eden and Frank, 2003, Brown, 2005, Kass, Ventura and Brown, 2005 and references therein for further discussion). To be concrete, we define $p(\text{spike at time } t|H_t) = \lambda(t|H_t, \theta)dt$ or, more precisely,

$$\lambda(t|H_t, \theta) = \lim_{\Delta t \rightarrow 0} \frac{Pr(\text{spike in } (t, t + \Delta t)|H_t, \theta)}{\Delta t}.$$

The point-process likelihood function is then given by the simple and explicit PDF (Snyder and Miller, 1991, Brown *et al.*, 2003, Paninski, 2004, Brown, 2005, Truccolo *et al.*, 2005)

$$p(\{t_i\}|\theta) = e^{-\int_0^T \lambda(t|H_t, \theta)dt} \prod_i \lambda(t_i|H_{t_i}, \theta), \quad (10.4)$$

where $[0, T]$ indicates the time interval over which the spike train is observed. With this formula in hand it becomes natural to approach the fitting of spike-train data by trying to find tractable and useful forms for the conditional intensity function.

With this in mind, let us write the time of the spike preceding t as $s_*(t)$, and note that the usual stimulus-driven IF model (without effects $h(\cdot)$) that involve spikes prior to $s_*(t)$) depends only on the experimental clock time t , relative to

stimulus onset, and the elapsed time $t - s_*(t)$, i.e. it satisfies

$$\lambda(t|H_t, \theta) = \lambda(t, t - s_*(t)) \quad (10.5)$$

for a suitable non-negative function $\lambda(\cdot, \cdot)$. (More generally, this equation is a good approximation whenever the spike history effect $h(\tau)$ is negligible for τ larger than the typical interspike interval in the data.) Models of the general form of Eqn (10.5) have been called ‘inhomogeneous Markov interval (IMI) models’ by Kass and Ventura (2001).

We may consider three special cases of Eqn (10.5):

- The multiplicative IMI (m-IMI) model:

$$\lambda(t, s_*(t)) = \lambda_0(t)r(t - s_*(t)). \quad (10.6)$$

Here, $\lambda_0(t)$ modulates the firing rate only as a function of the experimental clock time, while $r(t - s_*(t))$ represents non-Poisson spiking behaviour. See Kass and Ventura (2001) and references therein.

- The time-rescaled renewal process (TRRP) model:

$$\lambda(t, s_*(t)) = \lambda_0(t)r(\Lambda_0(t) - \Lambda_0(s_*(t))), \quad (10.7)$$

where r is the hazard function of a renewal process (basically, a non-negative function such that $\lim_{t \rightarrow \infty} \int^t r(s)ds = \infty$), and $\Lambda_0(t)$ has the time-rescaling form (Brown, Barbieri, Ventura, Kass and Frank, 2002)

$$\Lambda_0(t) = \int_0^t \lambda_0(u)du. \quad (10.8)$$

- The additive IMI model:

$$\lambda(t, s_*(t)) = f[y(t) + h(t - s_*(t))], \quad (10.9)$$

where $f(\cdot)$ is some smooth non-negative function, $y(t)$ is a scalar function of time, and the spike-history effect $h(\cdot)$ only looks back at the last spike time $s_*(t)$, instead of over the full spike history as discussed in the models above.

Of course, Eqn (10.5) may be generalized to include multi-spike history effects (see, e.g. Kass and Ventura, 2001).

Each of these models separate the dependence on t from the dependence on the time since the last spike $t - s_*(t)$, but they do so differently. Here, we may call λ_0 or $f[y(t)]$ the *excitability function* to indicate that this modulates the amplitude of the firing rate, and r the *recovery function*, since it affects the way the neuron recovers its ability to fire after generating an action potential. The fundamental difference between the models is the way the excitability interacts with

the recovery function. In the m-IMI model, for example, the refractory period represented in the recovery function is not affected by excitability or firing rate variations, while in the TRRP model the refractory period is no longer fixed but is scaled by the firing rate (Reich, Victor, and Knight, 1998, Barbieri *et al.*, 2001).

Koyama and Kass (2008) investigated the relationship of m-IMI and TRRP models to the stimulus-driven IF model. Specifically, given a joint probability distribution of spike trains generated by an IF model, they asked how close this distribution is to each of the best-fitting m-IMI and TRRP models. Some of the main results in Koyama and Kass (2007) are provided in Fig. 10.1. The authors considered the case that the input to the IF neuron was periodic, and numerically computed the probability that a test (specifically, a time-rescaled Kolmogorov–Smirnov test, as described by Brown *et al.*, 2002) will reject the (false) hypothesis that the data were generated by a Poisson, m-IMI, or TRPP model, instead of the true IF model. Figure 10.1 displays the rate of rejecting the models as a function of the number of spikes. It takes very little data to reject the inhomogeneous Poisson process, while it takes much larger data sets to reject the m-IMI model and the TRRP. Because the recovery functions in the m-IMI and TRRP models allow us to mimic the interspike interval distributions

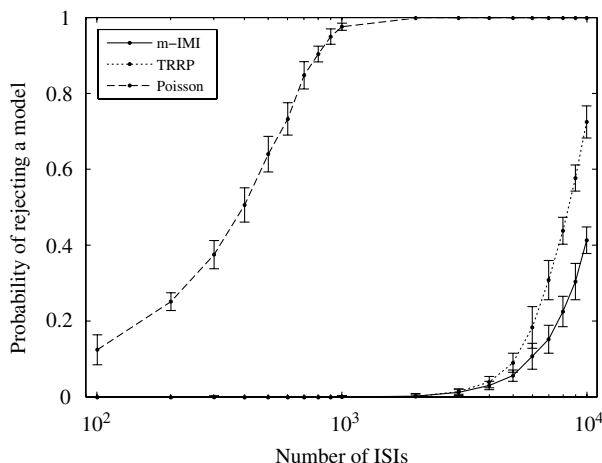


FIG. 10.1: Probability of rejecting three statistical models as a function of the number of ISIs. The spike trains were generated from a IF neuron with periodic input. The solid, dotted, and dashed lines represent the m-IMI model, the TRRP model, and the inhomogeneous Poisson process, respectively. The mean and the standard deviation at each point were calculated with 10 repetitions. With relatively small sample sizes it can be easy to reject the hypothesis of Poisson firing, but impossible to distinguish either the m-IMI model or the TRRP model from the IF model. Even after 10 000 spikes the m-IMI model is, for practical purposes, statistically indistinguishable from the IF model. Modified from Koyama and Kass (2008).

of the IF cell, for many data-analytic applications the results using the m-IMI, TRRP, and IF models will be very similar to one another – but very different from those based on a Poisson model.

Clearly these three model classes overlap somewhat. For example, if the nonlinearity $f(\cdot)$ in Eqn (10.9) is taken to be the exponential function, then the multiplicative and additive IMI models coincide. The additive formulation has become popular recently (Brillinger, 1988, Chornoboy, Schramm, and Karr, 1988, Brillinger, 1992, Paninski, 2004, Truccolo *et al.*, 2005, Paninski, Pillow, and Lewi, 2007), largely because stimulus terms (e.g. if we set $y(t) = \sum a_i x_i(t)$, given the stimulus $\vec{x}(t)$) and spike history terms are treated in a unified, linear manner within the nonlinear function $f(\cdot)$ (for this reason, the additive model is often described as a ‘generalized linear model’). It is worth making the connection between the IF and this additive model more explicit. Consider the inhomogeneous Poisson process with rate given by $f[V(t)]$, where $V(t)$ is the solution of the leaky-integrator differential equation $dV/dt = -gV(t) + I(t)$, starting at the initial value V_{reset} after every spike. This model is a simple version of the ‘escape-rate’ approximation to the noisy integrate-and-fire (IF) model described by Gerstner and Kistler (2002). Since this differential equation is linear, $V(t)$ may be written (up to boundary conditions) as the convolution of $I(t)$ with the exponential function e^{-gt} ; that is, this soft-threshold IF model is just a version of the additive IMI model (with the input current redefined suitably); see Paninski (2004) and Paninski, Pillow, and Lewi (2007) for details, and therefore the additive parameters may be indirectly interpreted in biophysical terms. See Paninski, Pillow, and Lewi (2007) for an explicit comparison of the additive and IF models applied to data from a retinal ganglion neuron; again, as in Fig. 10.1, the additive model provides an excellent approximation to the behaviour of the IF neuron.

Thus, to summarize, these point process models may be used to provide good approximations to the IF model. Some biophysical interpretability may be lost, because the ‘intracellular’ noise in the IF model (due to the diffusion term) is replaced by ‘point-process’ variability (due to the randomness of the spike times). What we gain is a simpler, more tractable, and more general framework; in particular, the explicit likelihood formula (10.4) makes various inference tasks much more straightforward and computationally tractable (Paninski, Pillow, and Lewi, 2007).

10.3 Applications

10.3.1 Computing the spike-triggered average and the most likely voltage path

The simplicity of the IF model allows us to analytically compute certain quantities of great theoretical interest. A key question in neural coding is: what does a single spike ‘mean’ (Rieke *et al.*, 1997)? More generally, what does a pattern of spikes mean (de Ruyter van Steveninck and Bialek, 1988)? We may make this question quantitative by computing the conditional distribution of a

behaviourally relevant signal given the observation of a spike pattern; if we can characterize these conditional distributions for every conceivable spike pattern, we can reasonably say that we have answered the question: ‘what is the neural code?’

As is well-known, these questions may be answered explicitly in the case of simple ‘cascade’ Poisson-based models (Chichilnisky, 2001, Schnitzer and Meister, 2003, Simoncelli *et al.*, 2004). It turns out that we can also solve this problem in the case of some of the more biophysical encoding models we have been working with so far. For a concrete example, let’s look at the ‘doublet-triggered density’ $P(V(t)|[t_1, t_2])$, the probability density on voltage of a non-leaky integrate-and-fire cell that has been observed to fire at times t_1 and t_2 (with $t_2 > t_1$, and no spikes observed in the intervening period).

This density may be computed exactly (Paninski, 2006b) by applying simple stochastic calculus tools, similar to those we have discussed above in Section 10.2.1. We condition the voltage to start at $V(t_1^+) = V_{\text{reset}}$ and end at $V(t_2^-) = V_{\text{th}}$, because we observed spikes at time t_1 and t_2 . The non-leaky IF model with constant current inputs may be described in terms of a Brownian motion with constant drift (Gerstein and Mandelbrot, 1964, Karatzas and Shreve, 1997). Because the Brownian motion is a Gaussian process, and our constraints are linear equality constraints, the conditioned process (known as a ‘Brownian bridge’) is also Gaussian, with mean and variance which may be calculated by the usual Gaussian conditioning formulas. We denote the marginal density of the Brownian bridge at time t as

$$P(V(t)|V(t_1) = V_{\text{reset}}, V(t_2) = V_{\text{th}}) = \mathcal{N}(V_{\text{reset}} + m(t), s(t)),$$

where $\mathcal{N}(\mu, \sigma^2)$ denotes the Gaussian density with mean μ and variance σ^2 , and we have made the abbreviations $m(t) = (t - t_1)(V_{\text{th}} - V_{\text{reset}})/(t_2 - t_1)$ and $s(t) = \sigma^2(t - t_1)(t_2 - t)/(t_2 - t_1)$.

Now we know not only that the cell has fired at two specific times t_1 and t_2 , but also that the voltage is below threshold for all times $t_1 < t < t_2$. Thus we need to compute the conditional density of the Brownian bridge given that the process lies below threshold,

$$P(V(t)|[t_1, t_2]) = P(V(t)|V(t_1) = V_{\text{reset}}, V(t_2) = V_{\text{th}}, V(t) < V_{\text{th}}, t_1 < t < t_2).$$

Now we may apply the method of images, as in the unconditioned case, to obtain the remarkably simple solution

$$P(V(t)|[t_1, t_2]) = \frac{1}{Z} [\mathcal{N}(V_{\text{reset}} + m(t), s(t)) - \mathcal{N}(V_{\text{th}} + (V_{\text{th}} - V_{\text{reset}}) - m(t), s(t))].$$

This solves our doublet-triggered density problem for the simple non-leaky, linear integrate-and-fire model. What about the leaky case, or more generally if the

neuron obeys nonlinear and/or multidimensional subthreshold dynamics (Badel, Richardson, and Gerstner, 2006)? Here we may apply the state-space techniques discussed in Section 10.2.2 above: we use a version of the forward–backward method to obtain (Paninski, 2006b):

$$P(V(t)|[t_1, t_2]) = \frac{1}{Z(t)} P_f(V, t) P_b(V, t)$$

where $P_f(V, t) = P(V(t), \tau_1 > t)$ satisfies the forward Kolmogorov PDE discussed in Section 10.2.1, and $P_b(V, t) = P(\tau_1 = t_2 | V(t))$ satisfies a corresponding Kolmogorov ‘backward’ PDE. See Paninski (2006b) for further details of the computation of these forward and backward probabilities; Fig. 10.2 illustrates the components of this solution.

Once we have obtained the doublet-triggered average voltage $E[V(t)|[t_1, t_2]]$, it turns out to be straightforward to apply renewal theory techniques (recalling that the spike trains of the IF model with constant coefficients may be described as a renewal model, as mentioned in Section 10.2.1) to obtain the single-spike-triggered average $E[V(t)|[t_1]]$; again, see Paninski (2006b) for details.

While obtaining the conditional average voltage $E[V(t)|\{t_i\}]$ given some observed spike data $\{t_i\}$ is conceptually straightforward, it does require some numerical computation in the case of a non-constant input current $I(t)$, or a non-zero membrane conductance $g > 0$. It turns out to be even easier to obtain the most likely conditional voltage path,

$$\mathbf{V}_{\text{ML}} = \arg \max_{\mathbf{V} \in C} p(\mathbf{V}|\{t_i\}),$$

than to compute the conditional average path. Here the optimization is taken over the constraint space

$$C = \{\mathbf{V} : V(t) \leq V_{\text{th}} \ \forall t; \ V(t_i^-) = V_{\text{th}}; \ V(t_i^+) = V_{\text{reset}}\}$$

of all subthreshold voltage paths consistent with the observed spike train $\{t_i\}$. By using the state-space representation, it is straightforward to show that $p(\mathbf{V}|\{t_i\})$ is in fact just a linearly constrained quadratic function of \mathbf{V} , and may therefore be optimized quite easily (Paninski, 2006a, Koyama, Kass, and Paninski, 2008). In fact, it turns out to be possible to obtain the most likely path analytically in greater generality than is possible for the conditional average path $E[V(t)|\{t_i\}]$; further, one can prove that the conditional average and conditionally most likely voltage paths coincide in the case of small noise σ (Paninski, 2006a, Badel, Richardson, and Gerstner, 2006). See Fig. 10.3 for an application to real data, in which the most likely voltage path provides a very accurate prediction of the unobserved subthreshold voltage $V(t)$, given the superthreshold observed spike train $\{t_i\}$ and the input current $I(t)$ (Paninski, 2006a).

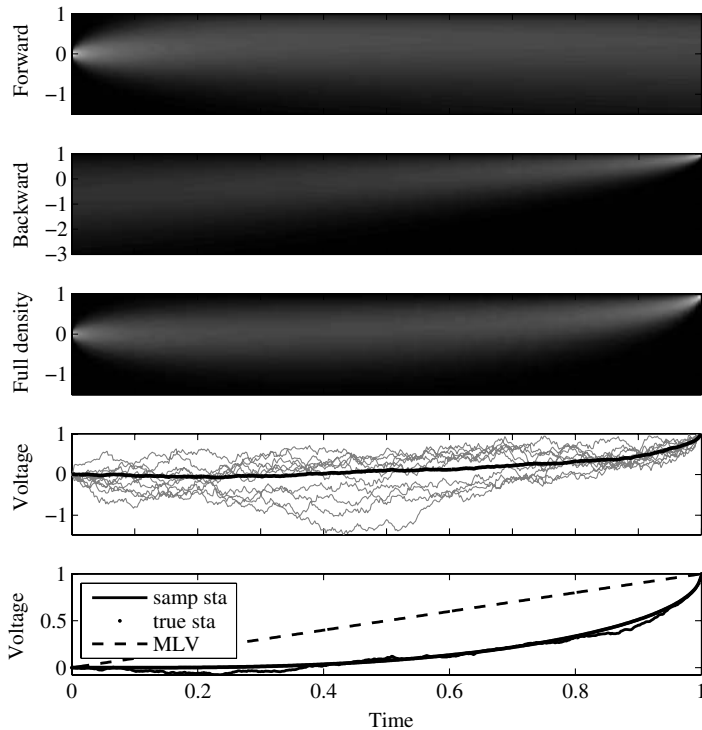


FIG. 10.2: The doublet-triggered average of the non-leaky IF model (adapted from Paninski, 2000b). Panels 1–3 show the evolution of densities $P_f(t)$, $P_b(t)$, and $P(V(t)|[t_1, t_2])$, for $t \in [0, 1]$; greyscale indicates height of density. Panel 4 shows some samples from the conditional voltage path distribution given spikes at $t_1 = 0$ and $t_2 = 1$ (the standard forward–backward sampling method for hidden Markov models was employed here, after discretizing the state space $V(t)$), with the empirical mean conditional voltage given 100 samples shown in black. The bottom panel shows the most likely path (dotted trace), the analytical doublet-triggered average (dashed), and the empirical doublet-triggered average (solid). Parameters: $V_{\text{th}} = 1$, $V_{\text{reset}} = 0$, $\sigma^2 = 1$, $I = 1$, $t_1 = 0$, $t_2 = 1$. Note that the conditional mean voltage ‘sags’ below V_{th} , since voltage paths that cross V_{th} are killed and are therefore subtracted out of the expectation $E(V(t)|[t_1, t_2])$; see Paninski (2006b) for further discussion of this effect.

10.3.2 Tracking plasticity in hippocampal place fields

Neural receptive fields are frequently plastic: a neural response to a stimulus can change over time as a result of experience. Frank *et al.* (2002) used a multiplicative IMI model to characterize spatial receptive fields of neurons from both the CA1 region of the hippocampus and the deep layers of the entorhinal cortex (EC)

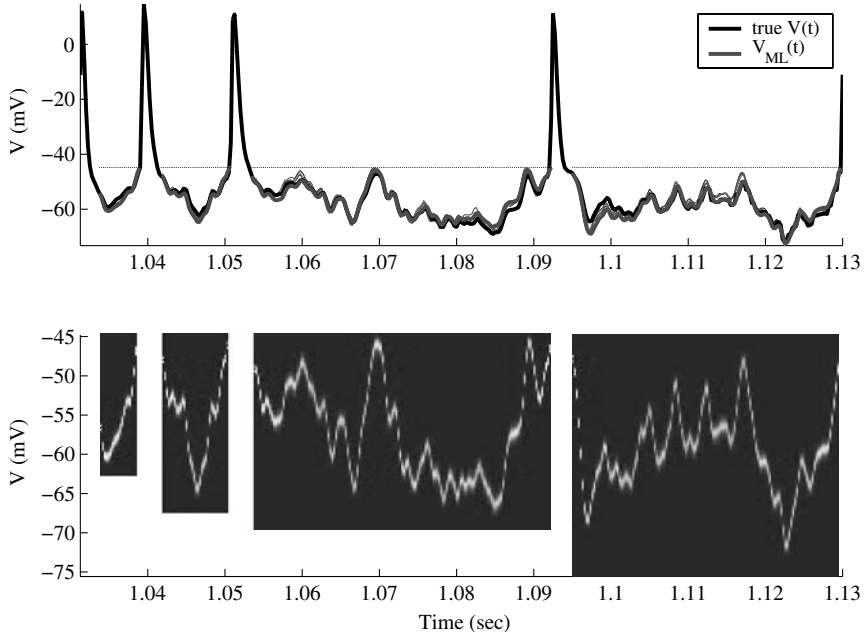


FIG. 10.3: Computing the most likely voltage path given *in vitro* physiological data. Top: comparison of true voltage path (bold black trace) with computed $V_{ML}(t)$ (bold grey trace) and samples from conditional distribution $p(V(t)|\text{spikes}, \{I(t)\}_{0 \leq t \leq T}, \hat{\theta})$ (thin traces, partially obscured; here $\hat{\theta}$ denotes the IF model parameters estimated from a separate sequence of training data, and $I(t)$ is the observed fluctuating input current). Trace shown is a randomly chosen segment of a 25-second long white noise experiment; dashed trace indicates estimated threshold. Bottom: conditional distributions $p(V(t)|\text{spikes}, \{I(t)\}_{0 \leq t \leq T}, \hat{\theta})$. White space indicates gaps in time where voltage was superthreshold, and thus not modelled. Note the small scale of estimated noise σ (Mainen and Sejnowski, 1995). Adapted from Paninski (2006a).

in awake, behaving rats. In their model, each neuronal spike train was described in terms of a conditional intensity function

$$\lambda(t|H_t, \theta) = \lambda^S(x(t))r(t - s_*), \quad (10.10)$$

which is of the form (10.6), except that the spatial intensity factor λ^S has replaced the temporal factor λ_0 . In Eqn (10.6), both the factors $\lambda^S(x(t))$ and $r(t - s_*)$ are dynamic, evolving simultaneously according to a state-space model specified by a point process adaptive filter (Brown *et al.*, 2001, Brown *et al.*, 2003). This allowed the authors to describe the way the receptive fields evolve across space and time. They found consistent patterns of plasticity in both CA1

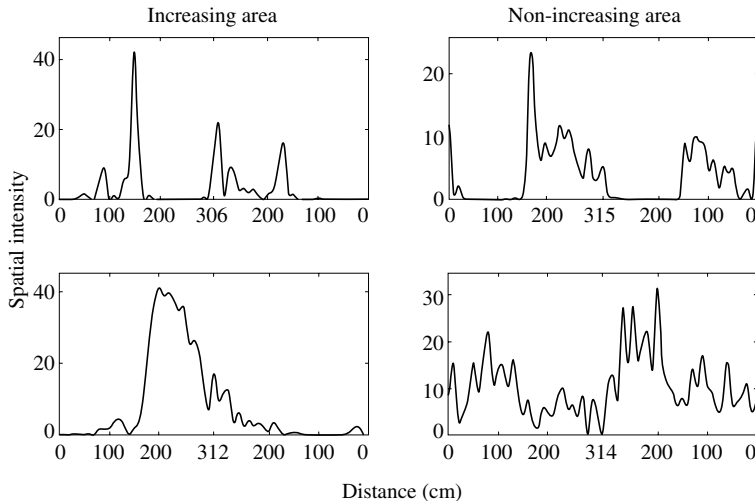


FIG. 10.4: The instantaneous spatial intensity function for a CA1 neuron at the outset of the experiment (upper left) and at the end of the experiment (lower left) illustrating the increase in the spatial firing pattern typical of these neurons in this experiment. The instantaneous spatial intensity function for a deep EC neuron at the outset of the experiment (upper right) and at the end of the experiment (lower right) illustrating the decrease in the spatial firing pattern typical of these neurons in this experiment. Reprinted with permission of the *Journal of Neuroscience*.

and deep EC neurons, which were distinct: the spatial intensity functions of CA1 neurons showed a consistent increase over time, whereas those of deep EC neurons tended to decrease (Fig. 10.4). They also found that the ISI-modulating factor $r(t - s_*(t))$ of CA1 neurons increased only in the ‘theta’ region (75–150 milliseconds), whereas those of deep EC neurons decreased in the region between 20 and 75 milliseconds. In addition, the minority of deep EC neurons whose spatial intensity functions increased in area over time fired in a significantly more spatially specific manner than non-increasing deep EC neurons. This led them to suggest that this subset of deep EC neurons may receive more direct input from CA1 and may be part of a neural circuit that transmits information about the animal’s location to the neocortex.

10.3.3 Encoding and decoding spike train information in the retina

Our final application illustrates that the IF model may be tractably fit to data via maximum likelihood, and that the model allows us to: (1) predict the spike times of a sensory neuron at near-millisecond precision; and (2) decode the responses of these sensory neurons with an accuracy greater than is possible

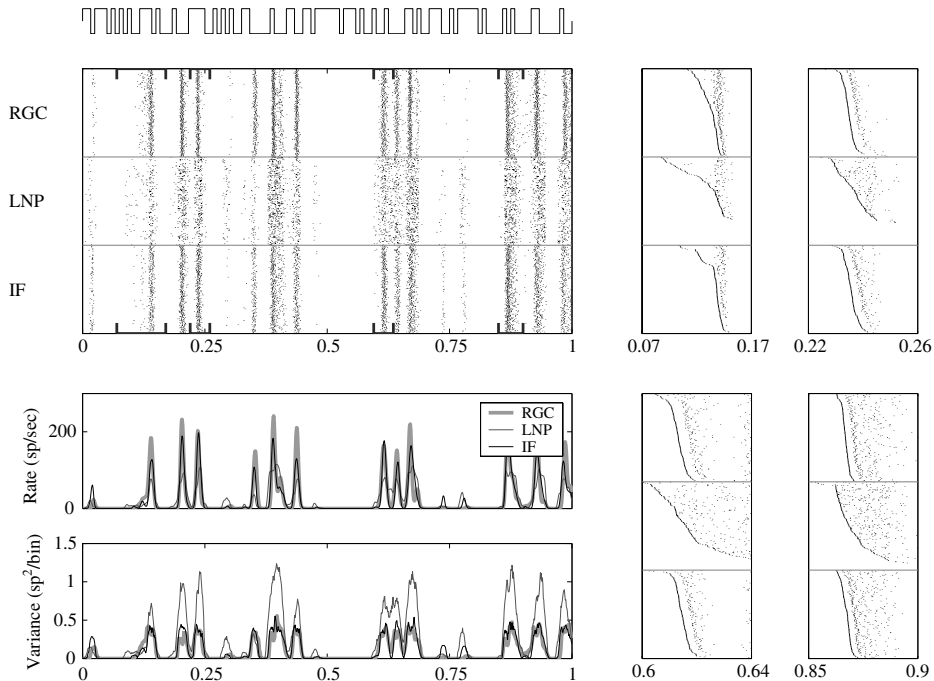


FIG. 10.5: Responses of an OFF-type retinal ganglion cell (RGC) to a repeated stimulus. Top left: recorded responses of a single macaque RGC to repeated full-field temporally varying light stimulus (top; inset trace indicates light intensity as a function of time), simulated inhomogeneous Poisson model (middle; LNP), and IF model (bottom) spike trains. (Both the IF and Poisson models were based on covariates including multiple time lags of the temporally varying stimulus; the models were fit via ML to a non-overlapping, nonrepeating segment of training data not shown here.) Each row corresponds to the response during a single stimulus repeat; 167 repeats are shown. Bottom left: peri-stimulus time histogram (mean observed spike rate) and variance for the RGC, Poisson model, and IF model. For this cell, the IF model accounts for 91% of the variance of the PSTH, whereas the Poisson model accounts for 75%. Right: magnified sections of rasters, with rows sorted in order of first spike time within the window. The four sections shown are indicated by black brackets in the upper left panels. Note that the IF model matches the true precision of the spike train much more accurately than does the Poisson model, as expected, since the Poisson model does not incorporate any spike-history effects. See Pillow *et al.* (2005) for details. Reprinted with permission of the *Journal of Neuroscience*.

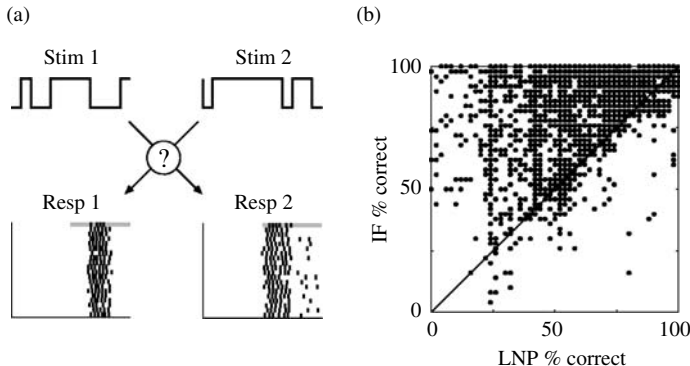


FIG. 10.6: Decoding responses using model-derived likelihoods. (a) Two stimulus (Stim) fragments and corresponding fragments of the RGC response (Resp) raster. Grey boxes highlight a 50 ms interval of the first row of each response raster. A two-alternative forced-choice (2AFC) discrimination task was performed on these response fragments, in which the task was to determine which stimulus gave rise to each response. The IF and Poisson (LNP) models were used to compute the likelihood of these responses given the ‘correct’ and ‘incorrect’ pairing of stimuli and responses, and the pairing with the higher likelihood was selected. This discrimination procedure was applied to each row of the response raster and used to obtain the percentage correct for the discrimination performance of each model. (b) Discrimination performance of the IF and Poisson models. Each point corresponds to the percentage correct of a 2AFC discrimination task using two randomly selected 50 ms windows of the response. Although both models attain perfect performance (100%) for a majority of such randomly selected response windows, the scatter of points above the diagonal shows that when discrimination performance is imperfect, the IF model is far better at decoding the neural spike responses. See Pillow *et al.* (2005) for full details. Reprinted with permission of the *Journal of Neuroscience*.

with a Poisson model of the responses (Pillow *et al.*, 2005). The basic results are illustrated in Figs. 10.5 and 10.6. The authors recorded the spike train responses of primate retinal ganglion cells which were stimulated with a temporally varying full-field light stimulus. Data from a long sequence of non-repeated training stimuli were used to fit both the IF model and a simpler inhomogeneous Poisson model; Fig. 10.5 compares the predictions of these two models given a novel repeated test stimulus. The IF model does a significantly better job of capturing the true neuron’s time-varying mean response, variability, and fine spike timing details.

See also Keat *et al.* (2001) for some related results using a similar model fit using non-likelihood-based methods, and Iyengar and Liao (1997) for an illustration of a generalized inverse Gaussian model's ability to capture the interspike interval properties of a goldfish retinal ganglion cell under constant illumination (i.e. no time-varying stimulus).

Figure 10.6 illustrates an important application of the likelihood-based approach. Once we have obtained an accurate approximation for $p(\{t_i\}|\vec{x})$, the probability of a spike response $\{t_i\}$ given the stimulus \vec{x} (namely, the approximation is provided by our estimated model, $p(\{t_i\}|\vec{x}) \approx p(\{t_i\}|\vec{x}, \hat{\theta})$, with $\hat{\theta}$ denoting our estimate of the parameter), we may invert this likelihood via Bayes' rule to obtain the *decoding* posterior probability,

$$p(\vec{x}|\{t_i\}) \propto p(\{t_i\}|\vec{x})p(\vec{x}).$$

In many cases the prior probability $p(\vec{x})$ is known, allowing us to compute the posterior $p(\vec{x}|\{t_i\})$ explicitly, and we may then use this posterior distribution to decode \vec{x} optimally, given the observed data $\{t_i\}$. This is what was done in the experiment illustrated in Fig. 10.6. The authors asked how well could one discriminate two possible stimuli, given a short observed segment of the retinal spike train response. As expected, the IF model permits more accurate posterior decoding than does the inhomogeneous Poisson model, since (as we saw in Fig. 10.5) the IF model provides a better approximation to the true likelihood $p(\{t_i\}|\vec{x})$.

10.4 Conclusion

Integrate-and-fire models play a distinguished role in theoretical neuroscience, but only recently have they been taken seriously as statistical models for analysing spike train data. We have placed the IF neuron within a more general point process modelling framework, and have described several useful variations on the general likelihood-based modelling theme. In particular, the three applications we reviewed show how this class of models may be used to describe stimulus-related effects: the first and third via IF models, the second via an explicit conditional-intensity model.

Statistical models may have varying degrees of interpretability and biophysical plausibility. The primary goal of any statistical analysis of neural data is to develop an accurate and parsimonious description of the experimental data that is interpretable and consistent to the extent possible with known neurophysiological principles. The accuracy of the data description should be guided by formal goodness-of-fit assessments (Brown *et al.*, 2002) and the standard model selection approaches (Burnham and Anderson, 2002, Truccolo *et al.*, 2005). From the point of view of analysing a particular set of spike-train data, the decision whether to rely on IF models must consider interpretation, computational effort, and ability to account for apparent features of the data.

Several extensions of the IF models presented here are possible. In principle, the random term in Eqn (10.1) could be replaced by a more realistic random term with positive temporal correlations, although this introduces substantial new computational issues (Haskell, Nykamp, and Tranchina, 2001, Fourcaud and Brunel, 2002, Moreno *et al.*, 2002). However, the state-space methods discussed above may still be applied in a straightforward manner. One interesting application is to model not just the voltage in a single somatic compartment, as we have discussed here, but also other dynamical variables (Badel, Richardson, and Gerstner, 2006, Vogelstein and Paninski, 2007) or the voltage in other unobserved compartments (Huys and Paninski, 2007). Along similar lines, state-space techniques may be used to include synaptic conductance noise effects in the IF model, though the Gaussian noise assumption needs to be modified somewhat here, since conductances are non-negative.

The general conditional-intensity framework allows inclusion of a wide variety of measured effects, including trial-to-trial variation terms, the local field potential (LFP), etc. In informal schematic form, we would have

$$\begin{aligned} \text{log conditional intensity} \\ = \text{stimulus} + \text{stimulus history} + \text{spiking history} + \text{trial} + \text{LFP}. \end{aligned}$$

History effects may be of the IMI form discussed here, or they may reach back further in time, incorporating effects of many spikes (Kass and Ventura, 2001, Paninski, 2004, Kass, Ventura, and Brown, 2005, Truccolo *et al.*, 2005, Paninski, Pillow, and Lewi, 2007), while trial-to-trial variation may be accommodated using slowly-varying, trial-dependent contributions to the firing rate (Ventura, Cai, and Kass, 2005, Czanner *et al.*, 2008). The advantages of this sort of model become more apparent when one considers multiple simultaneously-recorded spike trains (Brown, Kass, and Mitra, 2004), where interactions among neurons may be modelled by inclusion of additional terms that define the conditional intensity (Chornoboy, Schramm, and Karr, 1988, Paninski *et al.*, 2004, Okatan, Wilson, and Brown, 2005, Truccolo *et al.*, 2005, Kulkarni and Paninski, 2007, Pillow *et al.*, 2008, Czanner *et al.*, 2008). IF models have been successfully employed, for example, to explore the cross-correlation properties of pairs of simultaneously-recorded neurons (Iyengar, 1985, de la Rocha *et al.*, 2007, Carandini, Horton, and Sincich, 2007). We expect the future of spike train data analysis to be driven by insightful extensions of these point process modelling techniques.

Acknowledgements

We thank J. Pillow, E. Simoncelli, E.J. Chichilnisky, and S. Koyama for their collaboration on the work described here. LP is partially supported by an NSF CAREER award and an Alfred P. Sloan Research Fellowship; EB is partially supported by NIH grants R01MH59733 and R01DA015644; SI is partially supported by NIMH grant MH041712-20; RK is partially supported by NIMH grant RO1-MH064537-04.

References

- Ahmadian, Y., Pillow, J., and Paninski, L. (2008). Efficient Markov chain Monte Carlo methods for decoding population spike trains. *Under review, Neural Computation*.
- Badel, L., Richardson, M. J. E., and Gerstner, W. (2006). Dependence of the spike-triggered average voltage on membrane response properties. *Neurocomputing*, **69**, 1062–1065.
- Barbieri, R., Quirk, M., Frank, L., Wilson, M., and Brown, E. (2001). Construction and analysis of non-poisson stimulus-response models of neural spiking activity. *Journal of Neuroscience Methods*, **105**, 25–37.
- Brillinger, D. (1988). Maximum likelihood analysis of spike trains of interacting nerve cells. *Biological Cybernetics*, **59**, 189–200.
- Brillinger, D. (1992). Nerve cell spike train data analysis: a progression of technique. *Journal of the American Statistical Association*, **87**, 260–271.
- Brown, E. (2005). The theory of point processes for neural systems. In *Methods and Models in Neurophysics* (ed. C. Chow, B. Gutkin, D. Hansel, C. Meunier, and J. Dalibard), Elsevier, Amsterdam, pp. 691–726.
- Brown, E., Barbieri, R., Eden, U., and Frank, L. (2003). Likelihood methods for neural data analysis. In *Computational Neuroscience: A Comprehensive Approach* (ed. J. Feng), CRC Press, Boca Raton, pp. 253–286.
- Brown, E., Barbieri, R., Ventura, V., Kass, R., and Frank, L. (2002). The time-rescaling theorem and its application to neural spike train data analysis. *Neural Computation*, **14**, 325–346.
- Brown, E., Frank, L., Tang, D., Quirk, M., and Wilson, M. (1998). A statistical paradigm for neural spike train decoding applied to position prediction from ensemble firing patterns of rat hippocampal place cells. *Journal of Neuroscience*, **18**, 7411–7425.
- Brown, E., Kass, R., and Mitra, P. (2004). Multiple neural spike train data analysis: state-of-the-art and future challenges. *Nature Neuroscience*, **7**, 456–461.
- Brown, E., Nguyen, D., Frank, L., Wilson, M., and Solo, V. (2001). An analysis of neural receptive field plasticity by point process adaptive filtering. *PNAS*, **98**, 12261–12266.
- Brunel, N. and Hakim, V. (1999). Fast global oscillations in networks of integrate-and-fire neurons with low firing rates. *Neural Computation*, **11**, 1621–1671.
- Brunel, N. and Latham, P. E. (2003). Firing rate of the noisy quadratic integrate-and-fire neuron. *Neural Computation*, **15**, 2281–2306.
- Buoncore, A., Nobile, A., and Ricciardi, L. (1987). A new integral equation for the evaluation of first-passage-time probability densities. *Adv. Appl. Prob.*, **19**, 784–800.
- Burkitt, A. and Clark, G. (1999). Analysis of integrate-and-fire neurons: synchronization of synaptic input and spike output. *Neural Computation*, **11**, 871–901.
- Burkitt, A. N. (2006a). A review of the integrate-and-fire neuron model: I. Homogeneous synaptic input. *Biological Cybernetics*, **95**, 1–19.

- Burkitt, A. N. (2006b). A review of the integrate-and-fire neuron model: II. Inhomogeneous synaptic input and network properties. *Biological Cybernetics*, **95**, 27–12.
- Burnham, K. and Anderson, D. (2002). *Model Selection and Multimodel Inference: A Practical Information-Theoretic Approach*. Springer, New York.
- Carandini, M., Horton, J., and Sincich, L. (2007). Thalamic filtering of retinal spike trains by postsynaptic summation. *Journal of Vision*, **7**, 1–11.
- Chichilnisky, E. J. (2001). A simple white noise analysis of neuronal light responses. *Network: Computation in Neural Systems*, **12**, 199–213.
- Chornoboy, E., Schramm, L., and Karr, A. (1988). Maximum likelihood identification of neural point process systems. *Biological Cybernetics*, **59**, 265–275.
- Czanner, G., Eden, U., Wirth, S., Yanike, M., Suzuki, W., and Brown, E. (2008). Analysis of between-trial and within-trial neural spiking dynamics. *Journal of Neurophysiology*, **99**, 2672–2693.
- Czanner, G. and Iyengar, S. (2004). Expectation-Maximization (EM) estimation of an integrate-and-fire model with spike-frequency adaptation. *COSYNE*, presented at the Computational and Systems Neuroscience meeting, Cold Spring Harbor, NY, 2004.
- Daniels, H. (1982). Sequential tests contructed from images. *Annals of Statistics*, **10**, 394–400.
- de la Rocha, J., Doiron, B., Shea-Brown, E., Josic, K., and Reyes, A. (2007). Correlation between neural spike trains increases with firing rate. *Nature*, **448**, 802–806.
- de Ruyter van Steveninck, R. and Bialek, W. (1988). Real-time performance of a movement-sensitivie neuron in the blowfly visual system: coding and information transmission in short spike sequences. *Proc. R. Soc. Lond. B*, **234**, 379–414.
- Dempster, A., Laird, N., and Rubin, D. (1977). Maximum likelihood from incomplete data via the EM algorithm. *Journal Royal Stat. Soc., Series B*, **39**, 1–38.
- DiNardo, E., Nobile, A., Pirozzi, E., and Ricciardi, L. (2001). A computational approach to first-passage-time problems for Gauss–Markov processes. *Advances in Applied Probability*, **33**, 453–482.
- Dombeck, D. A., Khabbaz, A. N., Collman, F., Adelman, T. L., and Tank, D. W. (2007, Oct). Imaging large-scale neural activity with cellular resolution in awake, mobile mice. *Neuron*, **56**(1), 43–57.
- Ermentrout, G. and Kopell, N. (1986). Parabolic bursting in an excitable system coupled with a slow oscillation. *SIAM Journal on Applied Math*, **46**, 233–253.
- Fourcaud, N. and Brunel, N. (2002). Dynamics of the firing probability of noisy integrate-and-fire neurons. *Neural Computation*, **14**, 2057–2110.
- Frank, L., Eden, U., Solo, V., Wilson, M., and Brown, E. (2002). Contrasting patterns of receptive field plasticity in the hippocampus and the entorhinal cortex: An adaptive filtering approach. *J. Neurosci.*, **22**(9), 3817–3830.

- Gerstein, G. and Mandelbrot, B. (1964). Random walk models for spike activity of a single neuron. *Biophysical Journal*, **4**, 41–68.
- Gerstner, W. and Kistler, W. (2002). *Spiking Neuron Models: Single Neurons, Populations, Plasticity*. Cambridge University Press, Cambridge.
- Haskell, E., Nykamp, D. Q., and Tranchina, D. (2001). Population density methods for large-scale modelling of neuronal networks with realistic synaptic kinetics: cutting the dimension down to size. *Network: Comput. Neural. Syst.*, **12**, 141–174.
- Huys, Q., Ahrens, M., and Paninski, L. (2006). Efficient estimation of detailed single-neuron models. *Journal of Neurophysiology*, **96**, 872–890.
- Huys, Q.J.M. and Paninski L. (2009). Smoothing of, and Parameter Estimation from, Noisy Biophysical Recordings. *PLoS Comput Biol* 5(5): e1000379.
- Iyengar, S. (1985). Hitting lines with two-dimensional Brownian motion. *SIAM Journal on Applied Mathematics*, **45**, 983–989.
- Iyengar, S. and Liao, Q. (1997). Modeling neural activity using the generalized inverse Gaussian distribution. *Biological Cybernetics*, **77**, 289–295.
- Izhikevich, E. (2007). *Dynamical Systems in Neuroscience*. MIT Press, Cambridge MA.
- Jolivet, R., Lewis, T., and Gerstner, W. (2004). Generalized integrate-and-fire models of neuronal activity approximate spike trains of a detailed model to a high degree of accuracy. *Journal of Neurophysiology*, **92**, 959–976.
- Karatzas, I. and Shreve, S. (1997). *Brownian Motion and Stochastic Calculus*. Springer, Berlin.
- Kass, R. and Ventura, V. (2001). A spike-train probability model. *Neural Comp.*, **13**, 1713–1720.
- Kass, R. E., Ventura, V., and Brown, E. N. (2005). Statistical issues in the analysis of neuronal data. *J. Neurophysio.*, **94**, 8–25.
- Keat, J., Reinagel, P., Reid, R., and Meister, M. (2001). Predicting every spike: a model for the responses of visual neurons. *Neuron*, **30**, 803–817.
- Knight, B. W. (1972). Dynamics of encoding in a population of neurons. *Journal of General Physiology*, **59**, 734–766.
- Knight, B. W., Omurtag, A., and Sirovich, L. (2000). The approach of a neuron population firing rate to a new equilibrium: an exact theoretical result. *Neural Computation*, **12**, 1045–1055.
- Koyama, S. and Kass, R. (2008). Spike train probability models for stimulus-driven leaky integrate-and-fire neurons. *Neural Computation*, **20**(7), 1776–1795.
- Koyama, S., Kass, R., and Paninski, L. (2008). Efficient computation of the most likely path in integrate-and-fire and more general state-space models. *COSYNE*.
- Kulkarni, J. and Paninski, L. (2007). Common-input models for multiple neural spike-train data. *Network: Computation in Neural Systems*, **18**, 375–407.
- Lansky, P., Sanda, P., and He, J. (2006). The parameters of the stochastic leaky integrate-and-fire neuronal model. *Journal of Computational Neuroscience*, **21**, 211–223.

- Mainen, Z. and Sejnowski, T. (1995). Reliability of spike timing in neocortical neurons. *Science*, **268**, 1503–1506.
- Moreno, R., de la Rocha, J., Renart, A., and Parga, N. (2002). Response of spiking neurons to correlated inputs. *Physical Review Letters*, **89**, 288101.
- Mullowney, P. and Iyengar, S. (2007). Parameter estimation for a leaky integrate-and-fire neuronal model from ISI data. *Journal of Computational Neuroscience*, **24**, 179–194.
- Nikitchenko, M. and Paninski, L. (2007). An expectation-maximization Fokker–Planck algorithm for the noisy integrate-and-fire model. *COSYNE*, presented at the Computational and Systems Neuroscience meeting, Salt Lake City, UT 2007.
- Nykamp, D. Q. and Tranchina, D. (2000). A population density approach that facilitates large-scale modeling of neural networks: Analysis and an application to orientation tuning. *Journal of Computational Neuroscience*, **8**, 19–50.
- Okatan, M., Wilson, M., and Brown, E. (2005). Analyzing functional connectivity using a network likelihood model of ensemble neural spiking activity. *Neural Computation*, **17**, 1927–1961.
- Paninski, L. (2004). Maximum likelihood estimation of cascade point-process neural encoding models. *Network: Computation in Neural Systems*, **15**, 243–262.
- Paninski, L. (2005). Log-concavity results on Gaussian process methods for supervised and unsupervised learning. *Advances in Neural Information Processing Systems*, **17**.
- Paninski, L. (2006a). The most likely voltage path and large deviations approximations for integrate-and-fire neurons. *Journal of Computational Neuroscience*, **21**, 71–87.
- Paninski, L. (2006b). The spike-triggered average of the integrate-and-fire cell driven by Gaussian white noise. *Neural Computation*, **18**, 2592–2616.
- Paninski, L., Fellows, M., Shoham, S., Hatsopoulos, N., and Donoghue, J. (2004). Superlinear population encoding of dynamic hand trajectory in primary motor cortex. *J. Neurosci.*, **24**, 8551–8561.
- Paninski, L., Haith, A., and Szirtes, G. (2008). Integral equation methods for computing likelihoods and their derivatives in the stochastic integrate-and-fire model. *Journal of Computational Neuroscience*, **24**, 69–79.
- Paninski, L., Pillow, J., and Lewi, J. (2007). Statistical models for neural encoding, decoding, and optimal stimulus design. In *Computational Neuroscience: Progress in Brain Research* (ed. P. Cisek, T. Drew, and J. Kalaska). Elsevier, Amsterdam.
- Paninski, L., Pillow, J., and Simoncelli, E. (2004a). Comparing integrate-and-fire models estimated using intracellular and extracellular data. *Neurocomputing*, **65**, 379–385.
- Paninski, L., Pillow, J., and Simoncelli, E. (2004b). Maximum likelihood estimation of a stochastic integrate-and-fire neural model. *Neural Computation*, **16**, 2533–2561.

- Pillow, J. and Paninski, L. (2007). Model-based decoding, information estimation, and change-point detection in multi-neuron spike trains. *Under review, Neural Computation*.
- Pillow, J., Paninski, L., Uzzell, V., Simoncelli, E., and Chichilnisky, E. J. (2005). Prediction and decoding of retinal ganglion cell responses with a probabilistic spiking model. *Journal of Neuroscience*, **25**, 11003–11013.
- Pillow, J., Shlens, J., Paninski, L., Simoncelli, E., and Chichilnisky, E. J. (2008). Visual information coding in multi-neuronal spike trains. *Nature*, **454**, 995–999.
- Plesser, H. and Tanaka, S. (1997). Stochastic resonance in a model neuron with reset. *Physics Letters A*, **225**, 228–234.
- Press, W., Teukolsky, S., Vetterling, W., and Flannery, B. (1992). *Numerical recipes in C*. Cambridge University Press, Cambridge.
- Rabiner, L. (1989). A tutorial on hidden Markov models and selected applications in speech recognition. *Proceedings of the IEEE*, **77**, 257–286.
- Reich, D., Victor, J., and Knight, B. (1998). The power ratio and the interval map: Spiking models and extracellular recordings. *The Journal of Neuroscience*, **18**, 10090–10104.
- Ricciardi, L. (1977). *Diffusion Processes and Related Topics in Biology*. Springer, Berlin.
- Rieke, F., Warland, D., de Ruyter van Steveninck, R., and Bialek, W. (1997). *Spikes: Exploring the Neural Code*. MIT Press, Cambridge, MA.
- Risken, H. (1996). *The Fokker-Planck equation: Methods of Solutions and Applications*. Springer-Verlag, New York.
- Schnitzer, M. and Meister, M. (2003). Multineuronal firing patterns in the signal from eye to brain. *Neuron*, **37**, 499–511.
- Seshadri, V. (1998). *The Inverse Gaussian Distribution*. Springer, Berlin.
- Siegent, A. (1951). On the first passage time probability problem. *Physical Review*, **81**, 617–623.
- Simoncelli, E., Paninski, L., Pillow, J., and Schwartz, O. (2004). Characterization of neural responses with stochastic stimuli. In *The Cognitive Neurosciences* (3rd edn) (ed. M. Gazzaniga). MIT Press, Cambridge, MA.
- Smith, A. and Brown, E. (2003). Estimating a state-space model from point process observations. *Neural Computation*, **15**, 965–991.
- Snyder, D. and Miller, M. (1991). *Random Point Processes in Time and Space*. Springer-Verlag, New York.
- Srinivasan, L., Eden, U., Willsky, A., and Brown, E. (2006). A state-space analysis for reconstruction of goal-directed movements using neural signals. *Neural Computation*, **18**, 2465–2494.
- Stein, R. (1965). A theoretical analysis of neuronal variability. *Biophysical Journal*, **5**, 173–194.
- Stevens, C. and Zador, A. (1998). Novel integrate-and-fire-like model of repetitive firing in cortical neurons. *Proc. 5th joint symp. neural computation, UCSD*.

- Truccolo, W., Eden, U., Fellows, M., Donoghue, J., and Brown, E. (2005). A point process framework for relating neural spiking activity to spiking history, neural ensemble and extrinsic covariate effects. *Journal of Neurophysiology*, **93**, 1074–1089.
- Tuckwell, H. (1989). *Stochastic Processes in the Neurosciences*. SIAM, Philadelphia.
- Ventura, V., Cai, C., and Kass, R. (2005). Trial-to-trial variability and its effect on time-varying dependence between two neurons. *Journal of Neurophysiology*, **94**, 2928–2939.
- Vogelstein, J. and Paninski, L. (2009). Model-based optimal inference of spike times and calcium dynamics given noisy and intermittent calcium-fluorescence imaging. *Biophysical Journal*, in press.
- Yu, B., Afshar, A., Santhanam, G., Ryu, S., Shenoy, K., and Sahani, M. (2006). Extracting dynamical structure embedded in neural activity. *Advances in Neural Information Processing Systems*, **18**, 1545–1552.

STOCHASTIC SIMULATION OF NEURONS, AXONS, AND ACTION POTENTIALS

A. Aldo Faisal

11.1 Why model neurons stochastically?

Variability is inherent in our brains and our behaviour. This variability is not captured by conventional deterministic models, which capture some average behaviour over many or repeated events. To account for variability we have to make use of stochastic models. We will take a look at this more biologically realistic approach by studying the fundamental signal of our brain's neurons, the action potential. We will discuss how to model the action potential stochastically and discuss what this has taught us about the function, structure, and limits of action potential signalling in neurons. The most surprising insight is that the stochastic effects of individual molecules becomes relevant for whole-cell behaviour, making stochastic approximations or algorithmic short-cuts infeasible as a bottom-up explanation of neuronal variability.

At the biochemical and biophysical level there are many stochastic processes at work in neurons (Faisal, Selen, and Wolpert, 2008): protein production and degradation, opening and closing of ion channels, fusing of synaptic vesicles and diffusion and binding of signalling molecules. However, it is often implicitly assumed that averaging large numbers of such small stochastic elements effectively wipes out the randomness of individual elements at the level of neurons and neural circuits. This assumption requires reassessment for two reasons. First, neurons perform highly nonlinear operations involving high gain amplification and positive feedback. Therefore, small biochemical and electrochemical fluctuations of a random nature can significantly change whole-cell responses. Second, many neuronal structures are very small. This implies that they are sensitive to (and require only) a relatively small number of discrete signalling molecules to affect the whole. These molecules, such as voltage-gated ion channels or neurotransmitters, are invariably subject to thermodynamic fluctuations and hence their behaviour will have a stochastic component which may affect whole-cell behaviour.

Taking this view Faisal, Selen, and Wolpert (2008) suggest that random variability or ‘noise’ produced by thermodynamic (e.g. diffusion of signalling molecules) or quantum mechanisms (e.g. photon absorption in vision) has a deep and lasting influence on the evolution and development of the nervous system, and contrasts with the deterministic understanding of the nervous system traditionally taught (Kandel, Schwartz and Jessell, 2000). Classically, large neuronal

structures such as the squid giant axon have been key in understanding and explaining neural mechanisms such as the action potential, which, given their scale, are experimentally easily accessible and appear to function deterministically. This is because random variability averages out quickly as size increases: the standard deviation of variability over the mean activity of a set of signalling molecules will go as the inverse square root of the number of involved molecules.

However, neurons and synapses in many pathways are tiny: In comparison to squid giant axon neuronal connections in our brains can be over 10 000 times smaller. Cerebellar parallel fibres have 0.2 μm average diameter, C-fibres involved in sensory and pain transmission range between 0.1 and 0.2 μm , while the unmyelinated pyramidal cell axon collaterals which form the vast majority of local cortico-cortical connections have an average diameter of 0.3 μm (Faisal, White, and Laughlin, 2005). Thus, as few as a hundred ion channels will be involved in transmitting the action potential per unit length of axon, in contrast to several millions over the same unit length in squid giant axon.

Similarly, the majority of central nervous system synapses (spiny- or bouton-type) are below a micrometre in size, and biochemical processes and concentrations occur within volumes smaller than picolitres. For example, in the classic synaptic preparation of the frog neuromuscular junction several thousand post-synaptic receptors will be ‘listening’ to incoming neurotransmitters released by hundreds of vesicles. However, in the much smaller bouton-type synapses found in mammalian cortex as few as three post-synaptic receptors have to detect the release of a single vesicle (containing some 1000–2000 neurotransmitter molecules), triggered by a single action potential.

The action potential (AP) is the fundamental signal used for communication in the brain’s neural networks. Measuring the timing of APs *in vivo* and *in vitro* shows that neuronal activity displays considerable variability both within and across trials (Shadlen and Newsome, 1998; Strong *et al.*, 1998). This variability can have statistical characteristics that match those of simple random processes such as Poisson or Bernoulli processes. However, just because neuronal activity has some of the same statistics as a random process, it does not necessarily follow that neuronal activity is generated by a random process. In fact, Shannon’s theory of information (Shannon, 1948) suggests that to maximize information transmission the optimal way to encode (neural) signals will be to make the stream of signals appear like a random process (Rieke *et al.*, 1997). Thus, to what extent neuronal variability is part of meaningful processing rather than meaningless noise remains a fundamental problem in neuroscience.

There are multiple sources contributing to neuronal trial-to-trial variability: deterministic ones, such as changes in internal states of neurons and networks, as well as stochastic ones, noise inside and across neurons (White, Rubinstein, and Kay, 2000; Faisal, Selen, and Wolpert, 2008). To what extent each of these sources makes up the total observed trial-to-trial variability still remains unclear. To solve this question it is not sufficient to study neuronal behaviour experimentally (as this measures only the total variability), but also requires stochastic

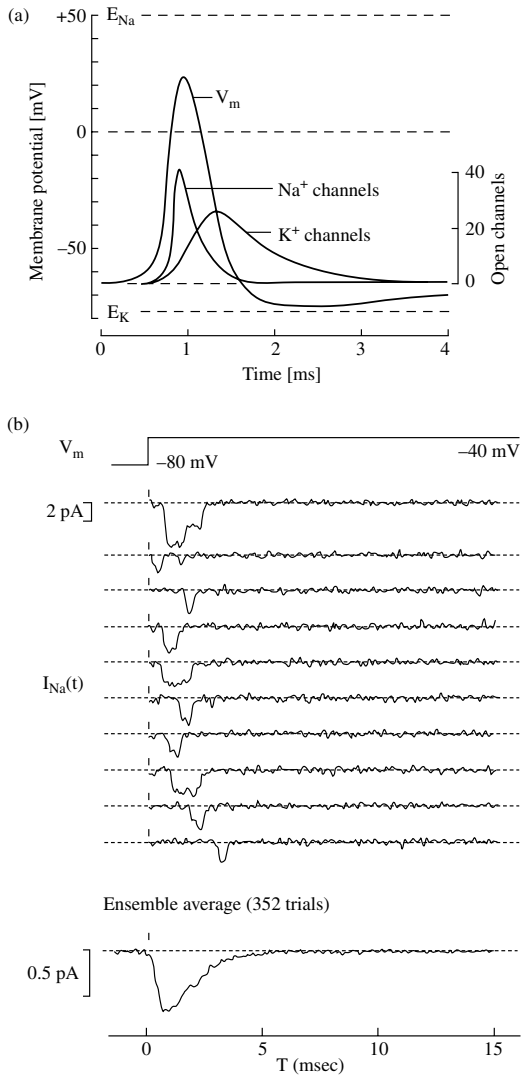


FIG. 11.1: (a) Schematic model of the action potential and the mediating Na^+ and K^+ currents. Note that here the idealized deterministic ion channel behaviour is drawn. For a small number of ion channels a more accurate picture would be like that in (b). (b) Illustration of ion channel variability in repeated identical voltage-step trials. Patch-clamp recording of a few unitary Na^+ channels in mouse muscle during a 40 mV voltage step. The ensemble average – averaging over 352 repeated identical trials – approaches the idealized deterministic description, akin to the ‘ Na^+ channels’ curve in (a). Note that the average single channel current of 2.2 pA corresponds to a single channel conductance of 19 pS and thus the step-like structure in the traces reflects the opening and closing of an individual ion channel. Figure reproduced from Hille (2001) based on experiments by Patlak and Ortiz (1986).

modelling, as this allows one to control and assess the impact of each source of (random) variability. We will illustrate this approach by looking at the initiation and propagation of the AP.

The action potential is carried by the spread of membrane potential depolarization along the membrane and is mediated by voltage-gated ionic conductances (Fig. 11.1a). The depolarization of the membrane potential is (re)generated by the nonlinear voltage-gated Na^+ conductances that open at low levels of membrane depolarization, which depolarize the membrane further, thereby recruiting more Na^+ conductances. Thus, Na^+ conductances act like positive feedback amplifiers. The resting membrane potential is then restored by the inactivation of the Na^+ conductance and is assisted by the (delayed) opening of K^+ and membrane leak conductances (and the two to three order of magnitude slower $\text{Na}^+ \text{-} \text{K}^+$ pumps) that repolarize the membrane. Thus K^+ channels and leak conductances provide negative feedback (Koch, 1999, Hille, 2001).

The patch-clamp technique showed that these ionic conductances result from populations of discrete and stochastic voltage-gated ion channels (Sakmann and Neher, 1995, Katz, 1971); see Fig. 11.1(b). These ion channels are transmembrane proteins that act as pores which can open and close in response to changes in the membrane potential ('channel gating') across the channel, thus acting like protein 'transistors'. These voltage-gated ion channels operate with an element of randomness due to thermodynamic effects. This stochastic behaviour produces random electrical currents, called channel noise (White, Rubinstein, and Kay, 2000), which is by one to two orders of magnitude the most dominant source of intracellular noise in neurons¹ (Manwani and Koch, 1999, Faisal, White, and Laughlin, 2005). What are the effects of channel noise on the AP?

To answer this question we require first a stochastic model of the AP. We will begin by outlining how to model a spatially extended (i.e. not point-like) neuron with stochastic ionic conductances. In most cases such stochastic models cannot be solved analytically, and require computational approaches, through stochastic or Monte Carlo simulation. At the cellular level our stochastic simulations will use data on the responses of individual molecules (in our case the properties of voltage-gated ion channels) to derive the responses of systems of interacting molecules (here, the response of a neuron's excitable membrane) and thus take into account the inherent variability of molecular mechanisms. Once the methodological concepts and terminology have been established we will review the progress made in understanding the AP through stochastic models and simulations.

11.2 How to model the stochastic nature of the action potential

The first simulation of the AP model by Hodgkin and Huxley (1952) required hand-operated calculators (Hodgkin, 1964). Over a decade later, Cooley, Dodge,

¹We ignore here synaptic input as a form of electrical 'noise' and note that the common use of the term 'synaptic background noise' denotes the (not necessarily random) variability produced by massive synaptic input in cortical neurons (Faisal, Selen, and Wolpert, 2008).

Jr. and Cohen (1965) and Cooley and Dodge, Jr. (1966) devised the first computer based simulation. Since then computer simulations have become more complex, computer performance has increased, and deterministic neuron simulators (e.g. NEURON, GENESIS) have been commonly used to model the morphology of neurons and recreate their averaged behaviour at a physiological level (Bower and Beeman 1995, Hines and Carnevale 1997, 2001). Experimental studies have begun to reveal the role played by neuronal variability in information processing, requiring more realistic models of neuronal behaviour. A first step towards a more accurate model treats the behaviour of single ion channels as a multi-state Markovian process (Fitzhugh, 1965), which is by now a well-established biophysical technique and based on direct recordings of single ion channel behaviour (Sakmann and Neher, 1995).

In general, models of neurons that reproduce a neuron's neurophysiological and electrical characteristics have to capture two important aspects: First, a description of electrical excitability of the neuronal membrane in biophysical terms and secondly, a description of the geometry of the neuron and the spread of electrical excitation over its membrane in biophysical and neurophysiological terms. The classic example for such a model is the work of Hodgkin and Huxley (1952). For the purposes of this chapter a neuron or parts of a neuron are modelled as acyclical graphs of interconnected electrical membrane compartments. These compartments are typically rendered as spheres or (tapered) cylinders which approximate the shape of neurons. The differences in membrane potential within a compartment are assumed to be small enough that it is reasonable to approximate the potential as constant throughout the compartment (iso-potential compartments). The use of compartments allows us to describe the electrical function of a neuron in terms of an equivalent electrical circuit representing the membrane of each compartment. For deterministic systems this is a well-established approach (Hodgkin and Huxley, 1952, Jack, Noble, and Tsien, 1983, Koch, 1999, Dayan and Abbott, 2001), referred to in the engineering literature as finite element modelling, and therefore we shall be brief here and just pick up, on the way, the necessary ingredients and note the differences when modelling stochastic systems. The construction of a biologically accurate neuron model requires several parameters that are often not directly measured or explicitly computed in the experimental literature. It is therefore essential to be aware of the problems one might encounter when extracting such parameters from published experimental data; we will point out three common issues in the footnotes.

11.2.1 Modelling excitable neuronal membranes

Electrical activity in neurons arises from the selective movement of charged ions across the membrane – membrane excitability. However, in most cases the number of ions flowing through ion channels during episodes of electrical activity is minute compared to the number of ions present in the respective medium (Hodgkin, 1964). In the following we ignore the changes in ionic concentration

due to signalling, thus instead of a microscopic description of the neuron in terms of ions, a macroscopic description is used: individual ions and local concentration gradients are ignored, and replaced by a description of the membrane potential based on electrical circuit elements, including batteries and ionic currents (which are related to individual ion flows via Faraday's constant and the ionic charge). An equivalent electrical circuit description (see Fig. 11.2a for details and nomenclature) is derived by equating the currents inside and through the membrane compartment according to Kirchhoff's current law. This method balances all currents flowing through the membrane and to other compartments (including at branch points). Each transmembrane circuit describes an iso-potential patch of membrane and is represented by a membrane compartment. It is therefore possible to mimic a neuron's morphology using tree-like networks of cylindrical or spherical compartments (Rall 1969*a*, 1969*b*).

The cylindrical description reduces the modelling of cylindrical segments to that of a line segment. The corresponding one-dimensional cable equation is the partial differential equation (PDE) describing the spatio-temporal dynamics of the membrane potential $V(x, t)$ for a cylindrical neuron of diameter d (Hodgkin and Huxley, 1952, Jack, Noble, and Tsien, 1983, Koch, 1999):

$$C_m \frac{\partial V(x, t)}{\partial t} = \frac{d}{4R_a} \frac{\partial^2 V(x, t)}{\partial x^2} + J(x, t) \quad (11.1)$$

$$J(x, t) = g_{\text{Leak}}(E_{\text{Leak}} - V(x, t)) + J_{\text{ion}}(x, t) + J_{\text{inj}}(x, t) \quad (11.2)$$

$$J_{\text{ion}}(x, t) = \sum_i \bar{g}_i p_i(x, t)(E_i - V(x, t)). \quad (11.3)$$

Equation (11.1) has the dimension of current density or current flux (J), i.e. the amount of current flowing through a given area. For the sake of simplicity we will refer to the current density terms used here simply as 'currents', as the membrane area of each compartment is known for modelling purposes. The first term in Eqn (11.2) is $g_{\text{Leak}}(E_{\text{Leak}} - V(x, t)) = J_{\text{leak}}$ and corresponds to a leak current per unit area flowing through the membrane (g_{Leak}) and driven by the 'Leak reversal potential' E_{Leak} , a free parameter that allows one to set the resting membrane potential. E_{Leak} should remain within physiologically realistic bounds of the Na^+ , K^+ , Cl^- and Ca^{2+} reversal potentials (typically between -100 and 200 mV relative to the membrane resting potential). The term J_{ion} in Eqn (11.2) corresponds to the current flowing through voltage-gated ionic conductances, where i indexes the conductances. Each is modelled as a battery in series with a variable resistance and is mathematically the product of the total ionic conductance \bar{g}_i , the probability p_i of the channel to be open (see below), and the potential difference between the ionic reversal potential E_i and the membrane potential V that acts as a battery, Eqn (11.3). Synaptic input can be incorporated by a term in J_{ion} capturing synaptic conductances. Finally, the

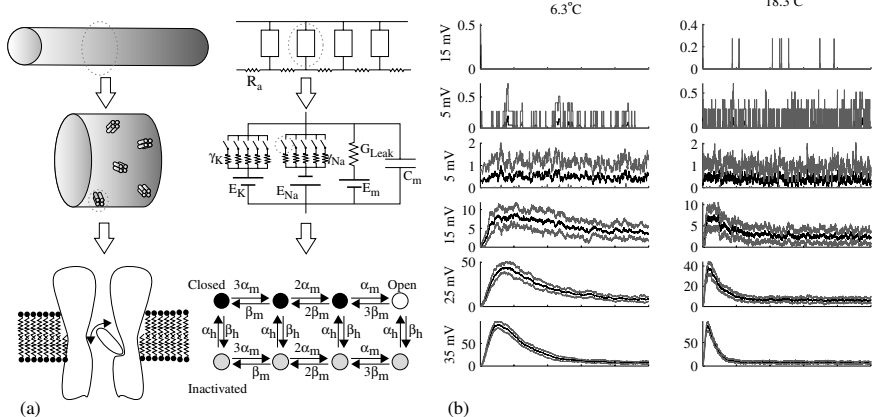


FIG. 11.2: (a) Stochastic modelling of a neuron (axon shown here). Top: the axon can be modelled as a sequence of cylindrical membrane segments. The segments are electrically coupled through the axial resistance R_a . Middle: each segment of axon membrane contains populations of voltage-gated ion channels. The electrical circuit of a membrane segment can be represented by switchable resistance $\gamma_{\text{Na}, \text{K}}$ (equivalent to Na^+ and K^+ voltage-gated ion channels) followed in series by batteries $E_{\text{Na}, \text{K}}$ (ionic driving force across the membrane), membrane leakage (membrane resistance g_{Leak} and driving force E_m) and a capacitor C_m (representing the membrane acting as a separator of intra- and extracellular ions). Bottom: each ion channel is voltage-dependent, and can be modelled in this illustration as a finite state Markov random process, reflecting discrete states of the channel protein. Transition rates between states depend on the membrane potential of the membrane compartment defined by kinetic rate functions (α, β). We depict here a Na^+ -channel model which has a single open state (unfilled circle), three closed (black filled circles) and four inactivated states (grey filled circles). Figure adapted from Faisal, White, and Laughlin 2005. (b) Voltage-step responses of the number of open squid Na^+ channels at two different temperatures. The data are visualized in a plot matrix, where each row contains data resulting from stepping the membrane potential at time $t = 0$ from a resting potential (set here to $V = 0 \text{ mV}$) to a target potential indicated at the left of the plots. Each plot column corresponds to a different temperature (6.3°C and 18.3°C). Individual plots show the number of open channels, mean (black line) \pm standard deviation (red line), versus time for 20 repeated trials using a stochastic population of 1000 ion channels (modelled as depicted in (a)). Temperature dependence of all channel kinetics was $Q_{10} = 3$, as measured by Hodgkin and Huxley (1952). The stochastic simulation data were obtained using the Modigliani stochastic neuron simulator operating in Binomial Algorithm mode ($\Delta t = 1 \mu\text{s}$) (Faisal, 2004, unpublished PhD Thesis, University of Cambridge).

term J_{inj} denotes currents per unit area arising from microelectrodes or other explicit current sources.

If the ionic current terms are zero, Eqn (11.1) reduces to the heat or diffusion equation. In this case ‘diffusion’ refers to the spread of membrane potential along the axon and not to the thermal random walk of ions, which occurs several orders of magnitude slower. By rearranging terms in Eqn (11.1) we can identify a diffusion coefficient which is commonly referred to as a steady state length constant or passive length constant of the neuronal axon (‘cable’)

$$\lambda_m = \sqrt{\frac{d R_m}{4 R_a C_m}}$$

(with units of length). In an infinite cable the steady-state voltage from constant current injection at a single point decays to $1/e$ of its value over a distance λ_m . The length constant is useful when comparing the length of cylindrical segments of different diameters and choosing suitable discretization parameters for simulations.

If the ionic currents are dependent on the voltage, Eqn (11.1) corresponds to a reaction-diffusion equation which can support a stable travelling wave (Hodgkin and Huxley, 1952) – the action potential. Multiplying Eqn (11.1) by the membrane resistance R_m results in the PDE expressed in terms of membrane potential. The left-hand side of Eqn (11.1) has the form $C_m R_m \partial V(x, t) / \partial t$. The factor $C_m R_m$ has units of time and describes to first order how fast the membrane potential can change. This characteristic of the membrane is called the membrane time constant: $\tau_m \equiv C_m R_m$.

Strictly speaking λ_m and τ_m are only valid for the resting neuron, as the common assumption made is that the membrane resistance (which may vary due to voltage-gated channels) is equated to the membrane leak resistance (the resistance of the membrane in absence of voltage-gated channels)² and care

²The membrane leak conductance g_{Leak} is often interchangeably used with the reciprocal of the (specific) membrane resistance $1/R_m = g_{\text{Leak}}$. Strictly speaking the reciprocal of the leak conductance is the membrane leak resistance and not the membrane resistance $R_m = R_m(V)$, which is voltage-dependent. The difference arises when ionic conductances that have been explicitly accounted for in the term J_{ion} contribute to the membrane resistance $R_m(0)$ at resting potential, e.g. when ionic conductances g_i are not fully closed at the resting potential. Thus

$$R_m(V) = \frac{1}{g_{\text{Leak}} + \sum_i g_i(V)} \neq R_{\text{Leak}} = \frac{1}{g_{\text{Leak}}}.$$

One should consequently use parameters for the membrane leak resistance only from experimental data where the description removes voltage-gated conductances in the calculation of the leak conductance, as was done by Hodgkin and Huxley (1952) or compensate for it by subtracting the voltage-dependent component of the leak conductance (as determined by modelling) at rest.

has to be taken when extracting these parameters from published experimental data.

The only potential sources of noise which would require stochastic modelling so far are the membrane resistance, which produces thermal noise several orders of magnitude smaller than channel noise (Manwani and Koch, 1999), and fluctuations in capacitance, probably negligible unless very small structures involving vesicle release, which changes membrane area in discrete increments, have to be considered. This concludes our brief outline of how we can model the passive electrical properties of neurons. Membrane excitability requires the introduction of state-dependent ionic conductances.

11.2.2 Modelling the ionic conductance

Hodgkin and Huxley (1952) postulated that the observed ionic currents within an iso-potential patch of membrane or more specifically, a single cylindrical compartment of axon with iso-potential membrane, could be modelled by voltage-dependent ionic membrane conductances. The activation of a conductance was determined by the binding of ‘gating particles’ to the conductance (or in modern terms the ion channel). An ion channel would only open if all necessary ‘gating particles’ have bound to it. This enabled Hodgkin and Huxley to model the ratio of open channels using chemical reaction schemes for Na^+ and K^+ conductances by fitting experimental data. Although the gating-particle approach is probabilistic in nature (being binomial/multinomial) the resulting model of the conductance is not and describes the average behaviour.

We now know that these conductances are made up of populations of ion channels. Assuming a large number of channels within a given area of membrane the probability p_i of a single channel being open corresponds to the ratio of open channels to all channels of the specific kind in that part of the membrane. In deterministic simulations the open channel ratio and the open channel probability are interchangeable, but when we account for stochastic effects there can be considerable, persistent deviations between the two (Faisal and Laughlin, 2007). To simplify the notation we will use p_i as notation for both the open channel ratio and the open channel probability and highlight the differences where necessary.

The ionic conductance per unit membrane area, g_i , is the product of the total ionic membrane conductance per unit membrane area \bar{g}_i and the time- and voltage-dependent ratio of open channels p_i

$$g_i(V, t) = \bar{g}_i p_i(V, t). \quad (11.4)$$

\bar{g}_i is the product of the single channel conductance γ_i and the number of channels per unit membrane area (channel density) ρ_i – determining these parameters is important for stochastic simulations, as both the number of channels present

and their individual conductance determine the level of noise³

$$\bar{g}_i = \gamma_i \rho_i. \quad (11.5)$$

Inserting Eqn (11.5) into Eqn (11.4) and interpreting p_i as a channel open probability yields a microscopic description of the ionic conductance per unit membrane area

$$g_i(V, t) = \gamma_i \rho_i p_i(V, t). \quad (11.6)$$

In the gating particle model the probability that a channel will be open is given by the probability that all gating particles are simultaneously bound. The gating-particle model assumes independence of the gating particles and the open channel probability p_i is therefore the product of the probabilities of each particle being bound. With q_j being the probability that a gating particle of type j is bound and $l(j)$ being the multiplicity of particles of type j that have to bind to support channel opening we can write

$$p_i(V, t) = \prod_j q_j(V, t)^{l(j)}. \quad (11.7)$$

In the case of the standard squid axon Na⁺channel (Hodgkin and Huxley, 1952) we have $q_j \in \{m, h\}$ and $l(m) = 3$ and $l(h) = 1$, thus $p(V, t) = m^3 h$. The q_j themselves are governed by linear differential equations of the form

$$\dot{q}_j(V, t) = \alpha_j(V)(1 - q_j) - \beta_j(V)q_j. \quad (11.8)$$

³The channel density ρ_i is often calculated by dividing the maximum ionic conductance \bar{g}_i , typically measured in voltage-clamp experiments, by the single channel conductance γ_i , typically measured in patch-clamp experiments, $\rho_i = \bar{g}_i/\gamma_i$. It is important to note that \bar{g}_i is the largest value over the set of all ‘slope’ conductances $\bar{g}_i = \max\{g_i(V, t)\}$ measured in voltage step experiments (Koch, 1999). Consequently the parameter \bar{g}_i depends critically on the experimental protocol exploring the space of possible conductances g_i sufficiently well to find the maximum. In the case of squid giant axon this procedure yields a Na⁺channel density $\rho_i = 60 \mu\text{m}^{-2}$ given $\bar{g}_i = 120 \text{ mS cm}^{-2}$ (Hodgkin and Huxley, 1952) and $\gamma_i = 19\text{--}20 \text{ pS}$ (Hille, 2001). This leaves a second problem in estimating channel density when using data for \bar{g}_i other than squid axon, as the implicit assumption often made is that \bar{g}_i corresponds to the state where all ion channels are open ($p_i = 1$). However, the ratio p_i of open Na⁺channels during the action potential is less than 1 (Hodgkin and Huxley, 1952). This is because, as discussed further below, in squid axon the gating particle probabilities q_j never approached unity and the steady state voltage-clamp open probability $q_{j\infty}$ is by construction below unity (cf. Eqn (11.10)). It is reasonable to assume that p_i will always be less than 1 for all voltage-gated ion channels. Consequently \bar{g}_i and channel density must be correspondingly larger and corrected by a factor $1/p_i$. Historically, Na⁺channel density measurements in squid axon varied from $170 \pm 20 \mu\text{m}^{-2}$ to $530 \pm 120 \mu\text{m}^{-2}$ using protein labelling methods (Levinson and Meves, 1975, Strichartz, Rogart, and Ritchie, 1979), to $125\text{--}160 \mu\text{m}^{-2}$ (Armstrong and Bezanilla, 1974, Keynes and Rojas, 1974) using another labelling method, while a statistical method suggested a density of $330 \mu\text{m}^{-2}$ (Conti and Wanke, 1975, Sigworth, 1980). These large variations in estimates are reflected in the modelling literature over the years and were due largely to uncertainty in the single channel conductance prior to the development of the patch-clamp technique.

The reaction's kinetic rate functions $\alpha_j(V)$, $\beta_j(V)$ describe the rate of change of the probability q_j , Eqn (11.8). These rate functions are particular to the ion channel protein (and gene) studied (Hille, 2001), so they can be identified from whole-cell behaviour (e.g. Faisal and Niven 2006, Faisal 2007, but see Prinz, Bucher, and Marder 2004b). These rate functions are either sigmoidal or exponential functions empirically fitted to voltage-clamp data (e.g. Hodgkin and Huxley 1952) or Boltzmann functions derived from the channel's voltage sensor behaviour in a constant, uniform electrical field (Patlak, 1991, Hille, 2001). Temperature is a key factor not only in determining the speed of channel behaviour but also the amount of variability. Therefore, channel kinetics and simulations should be always accompanied by appropriate temperature-dependent scaling factors and base temperatures (or assumed to be temperature invariant). In the first case, temperature-dependence can be accounted for by scaling the transition rates $\alpha(V)$ and $\beta(V)$ by the factor

$$Q_{10}^{\frac{\theta-6.3}{10^{\circ}C}},$$

where Q_{10} is an empirically determined, channel-specific parameter and θ is the temperature in degrees Celsius.⁴ In the second case, the Boltzmann function should account for temperature-dependence explicitly, however other parameters depend on temperature as well (Patlak, 1991), thus making the Q_{10} based models currently the more feasible ones to use.

We can define a voltage-dependent ion channel time constant τ_j characterizing the time in which sudden changes in membrane potential will affect ion channel gating

$$\tau_j(V) = \frac{1}{\alpha_j(V) + \beta_j(V)}. \quad (11.9)$$

Directly related to the time constant is the voltage-dependent steady-state value, $q_{j\infty}$, to which the q_j will converge for a constant membrane potential V .

$$q_{j\infty}(V) = \frac{\alpha_j(V)}{\alpha_j(V) + \beta_j(V)} = \frac{\alpha_j(V)}{\tau_j(V)}. \quad (11.10)$$

The q_j are probabilities and have to satisfy $q_j \in [0, 1]$. This purely mathematical requirement must be enforced by the kinetic rate functions and the dynamics of the membrane potential. Any violation of this requirement during

⁴Temperature has to be treated carefully in simulations, especially when using the Q_{10} relationship. It is the special case of Arrhenius's law for simple chemical reactions (Arrhenius, 1967) and thus itself an explicit function of temperature. Each kinetic function therefore may scale differently with temperature and have multiple Q_{10} factors over different ranges of temperatures (e.g. compare Hodgkin and Huxley 1952 with Schwarz and Eikhof 1987). Activation and inactivation rate functions can have different Q_{10} values and channel kinetics have often been measured well below their actual operating temperature in the organism.

simulations typically suggests unsuitable rate functions, too large a time step in the integration process, or a lack of precision in the algorithm integrating the corresponding differential equations.

11.2.3 Modelling each ion channel – Markov models

A biophysically more rigorous approach to describing membrane excitability is to model the underlying behaviour of individual ion channels, instead of describing the kinetics of their lumped ionic conductance. Ion channel based models describe conductance changes in terms of populations of ion channels where each ion channel is modelled as an individual stochastic process. Hodgkin and Huxley's original conductance-based model, although being macroscopic, introduced the concept of gating particles that control individual transmembrane conductances. The underlying rationale is compatible with the modern understanding of ion channels and can even be used to construct ion channel based models (see below), where a physical interpretation of gating would correspond to basic conformation changes of the channel protein.

One way to describe the gating behaviour of individual channels is through the use of Markov chains (Markov 1906, 1971) describing the channel as a finite state stochastic process (see Hille 2001 for biophysics and Gillespie 1992, van Kampen 1992 regarding Markov processes). These Markov models use linear chemical kinetic schemes to determine transition rates between discrete channel states. The individual states can be carefully interpreted as local energy minima of the channel protein conformation and state transitions correspond to crossings of activation energy barriers (Johnston and Wu, 1995). Markov models are the class most commonly used by biophysicists and highly detailed patch-clamp-based methods are available fitting the data to an excellent degree (e.g. Patlak 1991, Kuo and Bean, 1994).

Markov models can be recovered from gating-particle type models of conductances (Conti and Wanke, 1975, Hille, 2001) – the most common model-type measured and used by neurophysiologists (Koch, 1999, Dayan and Abbott, 2001). The deterministic gating-particle model is reformulated as a specific subclass of Markov model as described in the following (for illustration see Fig. 11.2(a), bottom right). Every possible combination of bound and unbound gating particles corresponds to a discrete ion channel state. The deterministic kinetic functions that describe the binding and unbinding rate of gating particles are correspondingly used to describe the probability of transition per unit time between individual ion channel states. Each transition corresponds to the binding or unbinding of one gating particle. The Markov states and the associated transition probability rate functions together form a Markovian kinetic gating scheme.

A central assumption of the gating-particle models is that individual gating particles of the same type are indistinguishable and independent of each other. Multiple states, therefore, may have the same set of numbers of bound particles for each particle type. Without loss of generality these multiple, yet indistinguishable states are lumped together into one Markov state. (See also Chapter 2 for more on Markov models.)

To account for lumped states the transition rates are multiplied by a factor k , which is determined as follows. A transition corresponding to the unbinding of a gating particle of type j has a factor k that equals the number of particles of type j bound to the state where the transition originated. A transition corresponding to the binding of a gating particle of type j has a k that equals the multiplicity $l(j)$ minus the j particles bound at the target state. This procedure allows one to transform any deterministic gating-particle model of conductances into a stochastic model of ion channel gating. The Markovian kinetic scheme derived for the gating-particle model for the squid axon m^3h -type gating-particle model of Na^+ channels is shown in Fig. 11.2(a) (bottom right). For example, the transition rate from the third closed state to the open state is $\alpha_m(V)$, the inverse transition has rate $3\beta_m(V)$ and the transition probability away from the open state is $3\beta_m(V)+\beta_h(V)$ (towards the two adjacent closed and inactivated states). Figure 11.2(b) shows voltage-step responses of a population of Hodgkin–Huxley Na^+ channels, whose stochastic model was obtained in the way described above (compare the *in vitro* trace in Fig. 11.1(b), bottom, with the simulated trace in Fig. 11.2(b), bottom).

11.2.4 Alternative models of ion channels

Alternative ways of describing channel kinetics – which are mathematically more complicated, and less popular among electrophysiologists – exist, but for only a few types of ion channels. For example, channel kinetics can be described using a simple two-state ion channel model with an open and closed state, where the complexity of gating behaviour, such as inactivation, is placed in the transition rates (Hoyt, 1984). The transition rates are in this case described by a set of nonlinear differential equations controlled by membrane potential, instead of being just instantaneous functions of the membrane potential.

A similar two-state model was recently proposed to describe ion channels in cortical neurons. These neurons show a variable threshold and a sudden rise in membrane potential at action potential initiation. It was argued (Naundorf, Wolf, and Volgushev, 2006) that the rapid, massive opening of Na^+ channels required to achieve the sudden rise in membrane potential could not be explained by traditional multi-state Na^+ ion channel models. This is because ion channels are thought to only indirectly affect each other's opening via the membrane potential. Thus, the speed of positive feedback would be limited and too slow to account for the observed data. These authors suggested instead that such a sudden rise in membrane potential could arise from two-state Na^+ channels which would have to be directly coupled (cooperative gating), instead of influencing each other indirectly via the membrane potential. However, there is no direct biological evidence to support this form of cooperative gating. Moreover, taking into account neuronal geometry, i.e. the interaction between neighbouring compartments, and the spike initiation properties of cortical neurons, is sufficient to explain the observed sudden rise of the action potential with traditional, non-cooperatively gating ion channels (McCormick, Shu, and Yu, 2007, Faisal and Laughlin, 2007).

Another ion channel modelling approach considered the fact that the probability density function (PDF) of the time ion channels spend in the open and closed states displays scaling behaviour across time-scales. This behaviour can arise from time-dependent changes in the energy barriers between a large number of conformational states having a continuous distribution of activation energy barriers. Ion channels could, therefore, have a continuum of states, show a lack of time-scales and display long-term memory. Fractal channel models were proposed to capture this type of behaviour (Liebovitch *et al.*, 1987, Liebovitch and Toth 1990, 1991, Liebovitch, Selector, and Kline 1992). Fractal models suggest that channel behaviour is the result of deterministic, chaotic dynamics that just appears to be random (Cavalcanti and Fontanazza, 1999) and can explain time-scale free activity patterns observed in neurons (Lowen and White, 1999). However, such fractal neuronal firing behaviour could be mediated by other cellular processes such as second messenger systems or gene-expression control of ion channels, and a proposed experimental test of the fractal approach remains to be conducted (Roncaglia, Mannella and Grigolini, 1994).

The behaviour of ion channels can be described in a variety of ways. The kinetic scheme and the kinetic functions determining the gating behaviour are individual to each ion channel. To form a complete model of ion channel behaviour, the model's kinetics (transfer rate functions and gating scheme) have to be complemented by the electrical parameters of the ion channel – i.e. single channel conductance γ_i , channel density ρ_i , and the ionic reversal potential E_i .

11.3 How to simulate the stochastic action potential

We now proceed in our quick tour of the action potential from modelling to simulating the models. Much previous work on neuron simulation algorithms addressed deterministic simulation of spatially extended neurons (Cooley and Dodge, Jr., 1966, Hines, 1984, Abbott, 1992, Bower and Beeman, 1995, Hines and Carnevale, 1997, Mascagni and Sherman, 1998, Hines and Carnevale, 2001, Koch, 1999, Dayan and Abbott, 2001) or stochastic simulation of membrane patches (point-like neurons) (Skaugen and Walloe, 1979, Strassberg and DeFelice, 1993, Chow and White, 1996, Mino, Rubinstein, and White, 2002). Here, we provide a description of the most important algorithms which can (and cannot) be used for stochastic simulation of neurons.

To this end let us take the point of view of somebody wishing to implement a stochastic neuron simulator from scratch, as we did when implementing the Modigliani (see www.modigliani.co.uk) stochastic simulation framework. The membrane potential dynamics of an iso-potential membrane patch are described by an ordinary differential equation (ODE). Its solution is a scalar value at any point in time. In an experiment this is equivalent to the trace of the membrane potential recorded by an electrode in an electrically compact neuron. In contrast, spatially extended membranes (i.e. not point-like iso-potential membranes), such as axons, dendrites, or entire neurons, are represented by a deterministic partial differential equation (PDE).

A membrane patch with stochastic ion channels is modelled by a stochastic ODE. The solution at a given instant in time is a probability distribution of possible scalar solutions. It results from integrating a PDE which describes how the probability distribution of all possible solutions (membrane potential traces) develops over time (van Kampen, 1992, Gillespie, 1992). This is equivalent to conducting identical repeated trials in an experiment (which may be difficult to realize) and recording the membrane potential trace repeatedly so as to form histograms of membrane potentials over time.

Spatially extended membranes with stochastic ion channels are modelled by using a stochastic PDE (SPDE). Integrating this equation up to a certain point in time yields a probability density of solution trajectories, i.e. a probability distribution over possible curves (the membrane potential along the neuron) rather than the probability distribution of a single value (the membrane potential at a point-like neuron). It is generally impossible to find analytical solutions of SPDEs, with the exception of few, simple cases (Walsh, 1986), and therefore Monte Carlo methods are usually employed. The idea of Monte Carlo methods is to sample the solution, the probability density function, through repeated stochastic simulations (Metropolis *et al.*, 1953, Hastings, 1970). This approach is especially feasible if the stochastic terms satisfy simplifying assumptions that reduce the number of necessary simulations. Therefore, SPDEs have been mostly studied where the stochasticity results from a perturbation of white-noise type, i.e. noise which is uncorrelated in time (Walsh, 1986).

However, ion channel stochasticity can only be described to a limited degree in this way, as we shall see below, thus realistic modelling of ion channel stochasticity in a spatially extended neuron can become numerically complicated. Fortunately, solving neuronal models with stochastic voltage-gated ion channels can be separated into two independent algorithmic tasks which significantly reduces computational demands. The first task consists of the solution of the deterministic PDE describing the interaction between the membrane potential and transmembrane currents along the neurons for one time step, which is possible once the (stochastic) currents have been determined. The second task is to integrate the stochastic currents in an appropriate manner once the membrane potential at each point of the neuron has been updated.

11.3.1 Solving the deterministic cable equation

The one-dimensional cable equation (11.1) is a parabolic PDE and more specifically a reaction-diffusion type differential equation.

$$C_m \frac{\partial V(x, t)}{\partial t} = \frac{d}{4R_a} \frac{\partial^2 V(x, t)}{\partial x^2} + J(x, t).$$

This type of PDE can be solved by direct integration under several restricting assumptions (Press *et al.*, 1996), e.g. by setting a constant propagation velocity of the action potential (reducing the neuronal cable PDE to an ODE) as was originally done (Hodgkin and Huxley, 1952), or by finite difference discretization (Reynolds, Jr., 1972). The latter is the commonly used approach for numerical

solution and several related algorithms exist for solving the discretized cable equation in linear (Cooley, Dodge, Jr. and Cohen, 1965, Cooley and Dodge, Jr., 1966) or arbitrary neuronal geometries (Hines, 1984, Abbott, 1992). This technique assumes that time and space are discretised as $V(x, t) \approx V(i\Delta x, n\Delta t)$, where Δx and Δt are spatial and temporal steps, respectively.

The stochastic integration of neuronal PDEs can be performed efficiently in a fairly straightforward manner for the case of stochastic voltage-gated ion channels. Efficiency is ensured because each compartment can undergo independent stochastic integration, as the continuity of the membrane potential is the only quantity that couples membrane compartments. Each compartment's ionic currents are conditionally linear with respect to the compartmental membrane potential. Given the compartment's membrane potential at time step n we can compute the (stochastic) currents for that time step by solving the stochastic ODE of ion channel behaviour in that compartment. We can then solve the deterministic PDE with the membrane compartment's currents. This reduces the problem of SPDE integration to that of solving stochastic ODEs in each compartment with efficient stochastic algorithms (see below) and then coupling the results by solving the cable equation PDE in a deterministic way.

The use of an efficient and accurate PDE solver is paramount for this approach. There are three standard methods to solve the discretized PDE with deterministic transmembrane currents $J(x, t)$. We will only briefly comment on their suitability for stochastic transmembrane currents and refer the reader here to the literature (e.g. Hines 1984, Abbott 1992, Mascagni and Sherman 1998, Koch 1999, Faisal, Laughlin, and White 2002). The first method is the *backward Euler* method. It has numerical accuracy of $O(\Delta t) + O(\Delta x^2)$ and the discretization parameters Δt and Δx can be chosen independently of each other. The backward Euler method is unconditionally stable and was proven to converge towards the solution for neuron-type partial differential equations (Mascagni, 1989). The second method is the *forward Euler* method. This method determines V at the new time step explicitly in terms of V at the previous time step. It can become unstable for unsuitable choices of Δt and Δx , as the two quantities are linked to each other. The third and most popular method in deterministic neuronal simulation is the *Crank–Nicolson* (or time-step staggered) method (Juncosa and Young, 1957). The magnitude of the discretization parameters Δt and Δx can be set independently of each other and the numerical accuracy is $O(\Delta t^2) + O(\Delta x^2)$. However, variables which are explicitly dependent on the membrane potential, such as intracellular Ca^{2+} flux or in our case stochastic ion channels, should not be solved with this method (Pearlmutter and Zador, 1999). Care has to be taken when upgrading or using deterministic neural simulators to account for stochastic ion channels.

11.3.2 Solving for the dynamics of stochastic compartments

Once we know the membrane potential in all membrane compartments after a time step, the behaviour of each ion channel population in each compartment can be treated separately for the next time step. The following algorithms

describe how to update the stochastic open probability p_i of a compartment's ionic conductances J_{ion} for the next time step.

These stochastic algorithms can be divided into two classes depending on how stochastic events are taken into account. Synchronous algorithms update the model's state at a common time interval. The effects of all events occurring during this period are lumped together, ignoring their order or repetition of occurrence. This assumption is reasonable as the low-pass filtering characteristics of the membrane will blur the event's individual effects given small enough time steps. The performance of synchronous algorithms is insensitive to the number of potential stochastic event sources (here the number of ion channels) and thus makes them suitable for large-scale simulations. Each compartment can be efficiently solved independently of, and in parallel with, the other compartments.

In contrast, asynchronous algorithms update the state of the model as events occur and are sensitive to the number of event sources. The time steps are determined by the time-scale of the stochastic events, which can result in very small time steps. This makes them less suitable for large-scale simulations. However, these mathematically accurate algorithms should be used when the precise timing or coincidence of a few, individual events can influence the entire system.

11.3.2.1 Synchronous stochastic algorithms Algorithms that solve conductance based models are synchronous by nature, since individual stochastic event sources (ion channels) are not accounted for in these models. The two conductance-based models of ion channels discussed here are a deterministic algorithm similar to Cooley, Dodge, Jr. and Cohen (1965) and Cooley and Dodge, Jr. (1966) and a Langevin-type stochastic algorithm based on Fox (1997).

Deterministic Algorithm 1 solves the standard deterministic class of conductance-based ion channel models (Hodgkin and Huxley, 1952). Forward Euler integration is sufficient to integrate the linear ODE of the gating particle q (Eqn (11.8)). If the gating particle bound state probability q exceeds its physically interpretable bounds of 0 and 1, q is clamped to the extreme value in the assumption that the evolution of the system dynamics will drive it back in subsequent iterations. If the necessity to clamp the values arises, this is typically

Algorithm 1 Deterministic integration step of bound gating particle probability.

Ensure: $0 \leq q \leq 1$

- 1: $q \leftarrow q + \Delta t(\alpha_q(1 - q) - \beta_q q)$ {Make sure that deterministic integration keeps q within bounds}
 - 2: **if** $q > 1$ **then**
 - 3: $q \leftarrow 1$
 - 4: {Issue warning to reduce time step size}
 - 5: **else if** $q < 0$ **then**
 - 6: $q \leftarrow 0$
 - 7: {Issue warning to reduce time step size}
 - 8: **end if**
-

an indication that the time step is too large for accurate integration and should be reduced. Once all the gating particle probabilities q are updated the channel open probability p_i is computed using Eqn (11.7). The complexity of this algorithm grows linearly with the number of compartments and the number of ion channel populations per compartment.

Langevin The Langevin algorithm, Algorithm 2, make a stochastic approximation of an underlying Markovian channel-gating process and describes the resulting stochasticity in terms of continuous conductance fluctuations. The stochastic channel kinetics are reduced to a Fokker–Planck-type equation (van Kampen, 1992, Gillespie, 1992). This Langevin approximation (for a derivation and description see Fox 1997) adds to the deterministic gating particle ODE (11.8) a Gaussian noise term ϵ (Langevin, 1908).

$$\dot{q}_j(V, t) = \alpha_j(V)(1 - q_j) - \beta_j(V)q_j + \epsilon. \quad (11.11)$$

This additive Gaussian noise ϵ has no temporal correlation, zero mean and variance proportional to

$$\frac{\alpha_q(V)(1 - q) + \beta_q(V)q}{N}$$

where N is the number of ion channels in the compartment that have a gating particle q . The underlying deterministic algorithm is correspondingly augmented by the (Langevin) noise term (line 17). The term's randomness depends on the

Algorithm 2 Langevin integration step of bound gating particle probability.

Ensure: $0 \leq q \leq 1$

- 1: $okFlag \Leftarrow \text{true}$
 - 2: $q \Leftarrow q + \Delta t(\alpha_q(1 - q) - \beta_q q)$
 - 3: **repeat**
 - 4: $X \Leftarrow \text{Random}(\text{Gaussian}, \mu = 0, \sigma = 1)$
 - 5: $\Delta q^* \Leftarrow \Delta t X \sqrt{(\alpha_q(1 - q) + \beta_q q)/N}$
 - 6: **if** $q + \Delta q^* > 1$ **then** {Make sure that integration keeps q within bounds}
 - 7: $q \Leftarrow 1$
 - 8: $okFlag = \text{false}$
 - 9: {Issue warning to reduce time step size}
 - 10: **else if** $q + \Delta q^* < 0$ **then**
 - 11: $okFlag = \text{false}$
 - 12: $q \Leftarrow 0$
 - 13: {Issue warning to reduce time step size}
 - 14: **end if**
 - 15: **until** $okFlag == \text{true}$ {Retry with new noise term if q outside bounds}
 - 16: $q^* \Leftarrow q^* + \Delta q^*$
 - 17: $q \Leftarrow q + \Delta t q^*$
-

rate of change of q (line 5). The noise term could push the gating particle variable out of its probabilistically interpretable bounds of 0 and 1. If this happens (line 3, 15), the noise term is regenerated. The algorithm's performance is comparable in speed to the deterministic system, as it requires only two uniform random numbers per time step per ion channel population in each compartment.

The complexity of this algorithm grows linearly with the number of compartments and the number of ion channel populations per compartment. The algorithm results in an underestimation of the expected channel noise (Fig. 11.6, left and right), especially in small neurons. This is because the continuous approximation of ionic conductances breaks down as the discrete nature of ion channels produces detectable discrete jumps. In these cases much of the current variability of the Langevin approximation is smaller than the conductance of an open channel. For example, the relatively frequent event of a second channel opening randomly produces large jumps in transmembrane conductance, while the Langevin approximation produces such large jumps in conductances only very infrequently. Thus, the white noise term used by the Langevin approximation cannot capture all of the characteristic properties of channel noise. Mathematically speaking, this is because the stochastic master equation model governing the channel openings has significant drift and jump terms due to memory and nonlinear effects, such that the Langevin description and the underlying Fokker–Planck equation breaks down (van Kampen, 1992). We will discuss the specific limits and the lesson learned using this approach in the last section.

Instead of developing more complicated conductance-based approximations of the underlying discrete-state process which describes channel gating, better results are obtained using stochastic algorithms for Markovian state-based models of single channels or populations thereof.

Single channel The single channel algorithm (see Algorithm 3) models each channel separately. The algorithm accounts for the transition probability $p(i, j)$ of each channel to transit from one state to the next during a fixed time step, to determine with a single uniform random number (line 4) which state the channel will be in at the next time step (lines 6–11). The transition probability $p(i, j)$ is the product of the transition rate for the Markov model to move from state i to state j , and the time step size. The membrane compartment's dynamics is affected by the number of ion channels in the open state. Each open channel adds γ_i conductance to the compartment, as described by Eqn (11.6).

The complexity of this algorithm grows linearly with the number of compartments and the total number of channels per compartment. It requires a number of uniform random numbers proportional to the number of compartments and to the total number of channels per compartment. For very small time steps the algorithm is as exact as an asynchronous algorithm in simulating the stochasticity of the system, but it is very slow for large numbers of channels and compartments. Its speed, however, exceeds that of Gillespie's algorithm for a large number of compartments, as the time step is constant (typically 1 μ s), and only depends on the total number of channels per compartment.

Binomial population The binomial population algorithm (Algorithm 4) assumes that all of the ion channels of the same type in each compartment are part of an independently and identically distributed (iid) population. As in the case of the single channel algorithm, the membrane compartment's dynamics is affected by the number of ion channels in the open state. Each open channel adds γ_i

Algorithm 3 Single channel integration step of channel population given state transition probabilities $P(i, j)$ and state occupancy $S(i)$.

```

1:  $S_{\text{old}} \leftarrow S$ 
2: for all Markov states  $i$  do
3:   for channels in state  $i$ ,  $u = 1S_{\text{old}}(i)$  do
4:      $X \leftarrow \text{Random}(\text{Uniform}, \text{min} = 0, \text{max} = 1)$ 
5:      $Q = 0$ 
6:     for all Markov states  $j \neq i$  and  $P(i, j) \neq 0$  do
7:        $Q \leftarrow Q + P(i, j)$ 
8:       if  $X \leq Q$  then
9:          $S(i) \leftarrow S(i) - 1$ 
10:         $S(j) \leftarrow S(j) + 1$ 
11:        break
12:     end if {Note, transitions  $i \mapsto i$  are implicitly handled}
13:   end for{j}
14: end for{u}
15: end for{i}
```

Algorithm 4 Binomial population integration step of channel states given state transition probabilities $P(i, j)$ and state occupancy $S(i)$.

Ensure: $\sum_i S(i) = N$ {Number of channels N has to be conserved}

- 1: $Counter \leftarrow 0$
- 2: $S_{\text{old}} \leftarrow S$
- 3: **repeat**
- 4: $Counter \leftarrow Counter + 1$
- 5: **for all** State transition pairs (i, j) and $P(i, j) \neq 0$ **do**
- 6: $X \leftarrow \text{Random}(\text{Binomial}, p = P(i, j), n = S_{\text{old}}(i))$
- 7: $S(i) \leftarrow S(i)_{\text{old}} - X$
- 8: $S(j) \leftarrow S(j)_{\text{old}} + X$
- 9: **end for**
- 10: **if** $Counter \geq 100$ **then** {Stop satisfying condition, break repeat loop and emit warning}
- 11: $S \leftarrow S_{\text{old}}$
- 12: **break**
- 13: **end if**
- 14: **until** $\sum_i S(i) = N$

conductance to the compartment, as described by Eqn (11.6). A specific transition from one state i to another state j is calculated here over the entire population of ion channels, instead of each channel by itself, which implies a binomially distributed number B of channels switching states from i to j (Skaugen and Wallace, 1979, Schneidman, Freedman, and Segev, 1998). A single binomially distributed random variable (B_{nl}) (e.g. as found in Press *et al.* 1996) can be used to determine how many channels switch from a state i to another state j , $n_{ij} = B_{nl}(\text{Number of channels in state } i, \text{transition rate}(i \rightarrow j) \times \Delta t)$.

Several transitions lead independently away from each state. Because no sequence can be imposed on these transitions, the same number of channels in the state has to be used when computing the binomial random numbers B for each transition. If the integration time step Δt is oversized and transition probabilities (proportional to Δt) become large, then the sum of channels switching away from a state can become larger than the number of channels that were originally in the state. This is biologically implausible and prevented by an integration quality criterion (line 14). If the sum of channels switching away from a state should be greater than the actual number of channels in that state, the procedure is repeated until a physically realistic set of state transitions is found. The number of repeats (lines 10 and 11) can be used as a signal for appropriateness of the time step and level of stochastic accuracy. The range of transition rates in typical Na^+ channels suggests time steps of 1–2 μs , as integration step sizes of 10 μs (Schneidman, Freedman, and Segev, 1998) lead to frequent (every 10–100 steps) repetitions during action potentials.

The binomial population algorithm is faster than the single channel algorithm as it uses many fewer random numbers ('number of states' random numbers in contrast to 'number of channels' random numbers). However, generation of binomial random numbers is computationally expensive, involving calculating the logarithm of the gamma function. For small channel populations (< 100 channels) the single channel algorithm will be both faster and more accurate, while for larger populations (100–10 000 channels) the Binomial algorithm can become faster, especially if the logarithm of the gamma function is precomputed in a look-up table for integers 0 to 10 000 000.

11.3.2.2 Asynchronous stochastic algorithms – compartmentalized Gillespie

Gillespie's algorithm (Gillespie 1976, 1977) is an asynchronous stochastic algorithm that is driven by stochastic events and reflects the physical process in a more natural manner than the above synchronous algorithms. The stochastic properties of individual ion channel states can be treated as statistically independent and memoryless random variables and it is sufficient to track state occupancies for the whole population of ion channels (Skaugen and Wallace, 1979). Channel kinetics are described by Markov processes and the probability for a single channel to remain in its present state decreases exponentially with time. One can thus determine the transition rate for all transitions within a single population of ion channels and determine how long the state of the population should persist. We can determine with one random number when this state ends and a transition occurs, and then with a second random number which transitions occurred.

We propose a simple extension of the Gillespie algorithm (Faisal, Laughlin, and White, 2002, Faisal, White, and Laughlin, 2005) by applying it to our compartmentalized neuronal PDE. A channel k of ionic conductance type j in compartment i has a probability p_{ijk} of remaining in its state given by (last state change was at $t = 0$):

$$p_{ijk}(t) = \frac{1}{\tau_{\text{state } a}} \exp \left[-\frac{t}{\tau_{\text{state } a}} \right] \quad (11.12)$$

where $\tau_{\text{state } a} = 1 / (\text{Escape rate from present state } a)$.

The escape rate is given by the sum of transition rates (in units ms^{-1}) from a parent state a to all adjacent states b_i in the Markov model. For a squid Na^+ channel in the penultimate closed state (cf. right-most black node in the graph of Fig. 11.2(a), bottom right) the escape rate would be $\alpha_m + \beta_h + 2\beta_m$. In a stochastic simulation, where the state transitions have to be explicitly computed, the time until the next state transition Δt_{ijk} can be generated using a uniformly distributed random variable $u_1 \in [0, 1]$ with the transformation

$$\Delta t_{ijk} = \ln \left(\frac{1}{u_1} \right) / \tau_{ijk}. \quad (11.13)$$

The probability of transition from a parent state a to adjacent states b_i is given by

$$p(a \rightarrow b_i) = \frac{\text{transition rate } a \rightarrow b_i}{\tau_{\text{state } a}}.$$

Using a uniform random variable $u_2 \in [0, 1]$, one then determines towards which state l , of the L possible states, the transition occurred, by

$$\sum_{i=1}^{l-1} p(a \rightarrow b_i) < u_2 < \sum_{i=l}^L p(a \rightarrow b_i).$$

One could simulate the entire neuron by computing all of the Δt_{ijk} and determining the smallest one, solve the PDE with that smallest temporal step size and subsequently determine which state transition occurred.

A more efficient approach is to compute the total combined life time of all channels, by propagating the information about the individual neuron's channel life times up to the level of the entire neuron⁵ (Algorithm 5). Next the

⁵The transition rate of a channel to persist in the same state, the self-transition rate, expresses the probability per unit time that a channel will not change state. The probability of a population of channels persisting in their states is calculated by summing the probabilities of each state persisting, weighted by the number of channels in that state. Similarly, the probability of all channels in a compartment persisting in their state is the sum of the population persistence probability. Finally, the probability that all channels in a neuron persist in their state is the sum of the compartmental persistence probabilities and the inverse of the sum is the life time τ of the entire neuron's state. This aggregation process is reflected in the nested loops of Algorithm 5.

Algorithm 5 Spatially extended Gillespie integration of compartment model – Time step determination.

Require: Global variables ΔT

```

1: for all Membrane compartments  $c$  do
2:   for all types  $k$  of voltage-gated conductances in compartment  $c$  do
3:     Compute self-transition rate  $R_k$  to remain in present channel states in voltage-
   gated conductance population  $k$ 
4:    $R \Leftarrow 0$ 
5:   for all states  $i$  do
6:      $R \Leftarrow R + \frac{S(i)P(i,i)}{\Delta T}$ 
7:   end for{i}
8:    $R_c \Leftarrow \sum_k R_k$  {Compute self-transition rate for all channel states in
   compartment  $c$ }
9: end for{k}
10: end for{c}
11:  $R_n \Leftarrow \sum_c R_c$  {Compute self-transition rate for all channel states in neuron
   model}
12:  $\tau \Leftarrow \frac{1}{P_n}$  {Life-time for all channels in neuron to remain in the same state}
13:  $X \Leftarrow$  Random (Uniform, min = 0, max = 1)
14:  $\Delta T \Leftarrow \frac{1}{\tau} \ln(\frac{1}{X})$  {Determine when the next state transition occurs}

```

system is integrated for the determined time step and recursively the channel transition that occurred is determined by picking the compartment, the channel population, and respective channel and finally its transition is determined⁶ (Algorithm 6). Finally, the neuron's PDE is deterministically integrated for the calculated time step if a channel opening or closing event has occurred, otherwise another stochastic integration step is calculated.

This synchronous algorithm is suited to parallel and distributed implementation and requires only six random numbers to be generated at each time step for the entire neuron. The simulated system is by construction a solution without stochastic approximations of the SPDE (Gillespie, 1992). This algorithm is extremely fast for a small number (≤ 10) of compartments, however it becomes inefficient for large numbers of compartments (≥ 50), as the time steps between

⁶This state transition is determined by drawing a uniform unit interval random number and assigning each compartment a set on the unit interval proportional to the compartment state persistence probability (lines 4 and 5). This procedure is repeated at the level of the chosen compartment to determine in which ion channel population the state change occurred (lines 10 and 11). Finally, the procedure is repeated again to determine within the chosen ion channel population which state transitions occurred (lines 15 and 16). Then, the channel states are updated correspondingly (lines 18–29). If a channel opened or closed due to state transition a channel gating event is flagged and has to be accounted for by the next integration step (lines 23–27). The previously computed life time τ is used to draw an exponentially distributed random variable which is used as the time step Δt for the next integration step (line 34). Integration using the time step given by this algorithm in solving the PDE is (virtually) exact as the flow of ionic currents does not change during an integration step.

Algorithm 6 Spatially extended Gillespie integration of compartment model – State transition determination.

```

1:  $X \leftarrow \text{Random}(\text{Uniform}, min = 0, max = 1)$ 
2:  $valC \leftarrow 0$ 
3: for all Membrane compartments  $c$  do
4:    $valC \leftarrow valC + P_n$ 
5:   if  $X < valC/P_n$  then {determine compartment}
6:      $valK \leftarrow 0$ 
7:      $X \leftarrow \text{Random}(\text{Uniform}, min = 0, max = 1)$ 
8:     for all types  $k$  of voltage-gated conductances in compartment  $c$  do
9:        $valC \leftarrow valK + P_c$ 
10:      if  $X < valK/P_c$  then {determine conductance type}
11:         $valS \leftarrow 0$ 
12:         $X \leftarrow \text{Random}(\text{Uniform}, min = 0, max = 1)$ 
13:        for all states  $i$  do {determine transition origin}
14:           $valS \leftarrow valK + P_c$ 
15:          if  $X < valS/P_k$  then
16:             $val \leftarrow 0$ 
17:             $X \leftarrow \text{Random}(\text{Uniform}, min = 0, max = 1)$ 
18:            for all states  $j$  with  $P(i, j) \neq 0$  do {determine transition target}
19:               $val \leftarrow val + P(i, j)$ 
20:              if  $X < val$  then {update state}
21:                 $S(i) \leftarrow S(i) - 1$ 
22:                 $S(j) \leftarrow S(j) + 1$ 
23:                if State transition  $i \mapsto j$  opened or closed channel then
24:                   $ChannelGating = true$ 
25:                else
26:                   $ChannelGating = false$ 
27:                end if
28:                break
29:              end if
30:            end for{j}
31:            break
32:          end if
33:        end for{i}
34:         $\Delta T \leftarrow \ln(1/X)\tau_n$ 
35:        if  $\Delta T > 1$  ms then
36:           $\Delta T \leftarrow 1$ 
37:          break
38:        end if
39:        break
40:      end if
41:    end for{k}
42:    break
43:  end if
44: end for{c}

```

individual transitions become smaller than a nanosecond (Faisal, White, and Laughlin, 2005).

11.3.2.3 Choice of stochastic algorithm Among the five integration algorithms discussed here one will typically be most efficient for the competing goals of accuracy and speed. The choice depends also on the number of compartments and the number of ion channels per compartment when solving a neuron model as a whole. An overview of the five algorithms in terms of complexity is shown in Table 11.1, which are sorted top to bottom (worst to best) by the biological/biophysical accuracy with which they account for stochastic events. The performance of these algorithms in spatially extended membranes is the opposite of how these algorithms perform in iso-potential, point-like membrane patches (Mino, Rubinstein, and White, 2002). Further gains in efficiency or accuracy are possible by applying different algorithms to different parts of a model and allowing for automatic switching between algorithms based on the state of the system. Note that while we discussed the algorithms with multi-compartment models in mind, it should be straightforward to use all of the above algorithms for single-compartment models, i.e. iso-potential membrane patches, by setting the number of compartments to 1.

This concludes our tour of the most commonly used mathematical models and algorithms for the simulation of stochastic action potentials. We now look at the scientific questions addressed by the fundamental stochastic nature of neurons with these stochastic methods at our disposal.

TABLE 11.1. Overview of algorithms for stochastic integration of compartments in terms of membrane conductance model ('chan' – channel-based, 'cond' – conductance-based), update strategy ('sync' – synchronous, 'asyn' – asynchronous) and computational complexity per compartment (see text for details). N_{pop} is the number of ion channel populations per compartment N_{chan} is the number of channels per ion channel population, and N_{state} is the number of states per ion channel population. The term N_{state}^x , with the exponent $x \in \{1, 2\}$ accounts for the number of possible state transitions based on the number of states.

Algorithm	Model	Update	Complexity
Deterministic (see Alg. 1)	cond	sync	$\mathbf{O}(N_{\text{pop}})$
Langevin (see Alg. 2)	cond	sync	$\mathbf{O}(N_{\text{pop}})$
Binomial population (see Alg. 4)	chan	sync	$\mathbf{O}(N_{\text{pop}} N_{\text{state}}^x)$
Single channel (see Alg. 3)	chan	sync	$\mathbf{O}(N_{\text{pop}} N_{\text{chan}})$
Compartmental Gillespie (see Alg. 5 & 6)	chan	async	$\mathbf{O}(N_{\text{pop}} N_{\text{chan}} N_{\text{state}})$

11.4 Lessons learned: neuroscience

In general, developing stochastic models of biological and especially nervous systems is important, as this can further our understanding in at least three different ways. First of all, novel properties may emerge, such as stochastic resonance (SR), see Chapter 4. Secondly, stochastic effects produce noise – random variability – which is a limiting factor in the design of any information processing system and may be critical for the evolution and development of brains. The nervous system may not have evolved from simple neurons to complex circuits without having been influenced in its design by the constraints imposed by noise. Thirdly, it remains an open question as to what extent the observed trial-to-trial variability in both the nervous system and behaviour is caused by noise, and in what part it may be due to ‘unfathomable’ complex dynamics (reflecting chaotic dynamics and myriads of ever changing internal states). Noise will inevitably increase neuronal variability and we can thus compare the amount of variability produced by noise to the total experimentally observed variability. Stochastic models allow us to trace stochastic effects, from their sources at the molecular level to the level of neuronal function at the cellular and circuit level.

Early work: Probabilistic models of neuronal activity The AP mechanism and its theory is arguably the most successful quantitatively modelled system in biology. Reliability and noise in AP generation has been studied for almost as long as the ionic basis underlying membrane excitability (Blair and Erlanger, 1933, Pecher, 1939). Reliability of AP generation in response to a current step input was measured at the Nodes of Ranvier (Verveen, 1962, Derksen and Verveen, 1966, Verveen, Derksen, and Schick, 1967). Here, the probability of triggering an action potential was fitted by a Gaussian cumulative probability function, parameterized by the stimulus amplitude. This phenomenological model embodied the idea that the stimulus had to drive the membrane over a fluctuating threshold to trigger an action potential. Threshold fluctuations were postulated to result from an internal noise source of possibly ionic origins and it was concluded that the threshold’s coefficient of variation must depend on axon diameter. Using dynamical system theory it was subsequently possible (Lecar and Nossal, 1971a,b) to derive an analytical relationship between an assumed transmembrane noise source and action potential threshold fluctuations. These studies considered both thermal resistance noise produced by the neuronal membrane’s resistance and noise resulting from discrete, stochastic ion channels, which at the time were not yet experimentally proven to exist. Noise that could result from ion channels was estimated to have an over 20 times larger effect on threshold fluctuations than thermal resistance noise (see also Hille, 2001).

Early work: Stochastic simulation of membrane patches The landmark stochastic simulation study by Skaugen and Walløe (1979) investigated the impact of discrete, stochastic ion channels on action potential initiation in squid-giant-axon type iso-potential membrane patches. They found that inputs that were below AP threshold in the deterministic Hodgkin–Huxley model could trigger spikes. The highly nonlinear input-current versus firing-rate characteristic was

linearized (when averaged over many trials) proportional to the amount of channel noise present (the relative amount of channel noise increased as membrane area was reduced). In other words, channel noise could increase and linearize the signalling range of neurons (Skaugen and Walloe, 1979). To be able to conduct this study with the limited computer power of the time they adapted the celebrated Gillespie algorithm (Gillespie 1976, 1977, 1992), developed for simulating chemical reactions, to obtain a fast yet mathematically accurate simulation of the stochastic system. The model neuron was formed by combining the known deterministic voltage dynamics of an iso-potential patch of membrane, as described by the ODEs of Hodgkin and Huxley (1952). To introduce channel noise they replaced the deterministic linear kinetic equations representing the voltage-gated ion channels with stochastic Markov processes over populations of discrete ion channels (see Chapter 8). Both the findings and methods of this work were ahead of many subsequent simulation studies in terms of methods and accuracy. In fact, the Gillespie-based implementation provides the most accurate implementation of stochastic integration methods and ion channel models in iso-potential membrane patches (see Fig. 11.6a below).

The nature of ion channels and action potential threshold fluctuations Experimental methods leaped ahead with the development of the patch-clamp technique (Sakmann and Neher, 1995) and it became possible to demonstrate the discrete and stochastic nature of individual Na^+ -ion channels (Sigworth and Neher, 1980). Experimental data showed that Na^+ -channel fluctuations could be large enough to account for the observed threshold fluctuations in Nodes of Ranvier (several μm diameter, Na^+ -channel densities $> 1000 \mu\text{m}^{-2}$) (Sigworth, 1980). Finally, Monte Carlo simulations, in which stochastic models of Na^+ -channels were the only source of variability, confirmed that the Na^+ -channel noise alone produced action potential threshold fluctuations which compared well with experimental data (Clay and DeFelice, 1983, Rubinstein, 1995). Variability in the experimental context could be quantified as the coefficient of variation, defined as the standard deviation over the mean of a variable. The studies suggested that the action potential threshold's coefficient of variation was dependent on the square root of the number of Na^+ -channels, N , present in the membrane. For large N this would imply that channel noise should have only a small impact on spike-based information processing, as fluctuations in the number of open channels ΔN would have been small in most cells, because they are proportional to

$$\Delta N \propto \frac{\sqrt{N}}{N} = \sqrt{\frac{1}{N}}.$$

For Hodgkin and Huxley's squid giant axon this was certainly true as it measured several millimetres in diameter and possessed millions of ion channels per unit length. Similarly the myelinated nerves' Nodes of Ranvier considered in these studies, although about a hundred-fold smaller in diameter than squid giant axon, featured hundred-fold higher channel densities. Nodes of Ranvier were, thus, comparable to squid axon in terms of the expected variability. The general validity of this assumption required reconsideration for most neurons, as we shall see in the following.

Random initiation of action potentials Stochastic simulations of large iso-potential membrane patches showed that super-threshold inputs could fail to generate an action potential and, more importantly, make random APs appear in the absence of any external input (Strassberg and DeFelice, 1993, Chow and White, 1996). Chow and White (1996) were able to derive analytically the rate at which these random action potentials were triggered in an iso-potential membrane patch by interpreting it as Kramer's double-well problem. They assumed that the membrane potential was like a particle sitting in a well, the bottom of the well being analogous to the resting state of the neurons, and the local maximum of the well representing the action potential threshold. Channel noise would act on the membrane potential like random perturbations moving the particle, so that eventually the particle could escape the well – which was analogous to a random action potential being triggered. Their analytical result was derived from first principles knowledge of the Na^+ channel kinetics and basic biophysics of neuronal membranes. They assumed that it was sufficient to model Na^+ channel noise (slower K^+ channel fluctuations were ignored) using a Fokker–Planck-type approximation (which reduced the nature of channel noise to that of a white noise source of randomness). Their analytical derivation of random action potential rate versus membrane area matched their stochastic simulations of membrane patches. Because they had implemented the Gillespie algorithm to simulate ion channel behaviour, they were able to see that their analytical approximation would break down as channel numbers decreased.

The noise triggered action potentials found by Chow and White were named ‘spontaneous action potentials’ (Chow and White, 1996, Faisal, White, and Laughlin, 2005), a term that may be confounded with ‘spontaneously activity’ of neurons, which describes neurons that are actively spiking in the absence of synaptic input. Such ‘spontaneous activity’ can result from a purposeful instability of a neuron’s resting state (e.g. when the action potential threshold is below resting potential), and can thus appear independently of noise in deterministically modelled neurons. To help disambiguate the two we will use henceforth the term ‘random action potentials’ to refer to the noise-generated action potentials. *Action potential initiation is affected by channel noise* Random action potentials constitute a major disruption of neuron-to-neuron communication. While the presence or absence of APs does carry information, the precise timing of each action potential also carries information (e.g. Rieke *et al.* 1997). The trial-to-trial variability of AP timing *in vivo* and *in vitro* in many systems can be on the order of milliseconds (1–10 ms) and the timing of individual APs on the millisecond scale was shown to be behaviourally relevant in perception and movement of invertebrates (see Faisal, Selen, and Wolpert, 2008, for review). The effects of channel noise on neural activity are likely to affect the dynamics of cortical neural networks as suggested by dynamic-clamp experiments (White *et al.*, 1998, Dorval Jr. and White, 2005). Therefore, we aim to make quantitative predictions about the effects of channel noise on AP timing and assess axonal reliability in the densely connected CNS – 4 km of unmyelinated axons per mm^3 (Braitenberg

and Schütz, 1998). Ideally, we would like to establish the influence of channel noise on neuronal design. Historically, modelling of realistic neural noise focused on the influence of ion channel stochasticity on action potential generation in a patch of neuronal membrane (Skaugen and Wallace, 1979, Strassberg and DeFelice, 1993, Chow and White, 1996, Schneidman, Freedman, and Segev, 1998) and the effects of channel noise in dendrites (Steinmetz *et al.*, 2000).

To what extent would channel noise affect the timing of action potentials? Schneidman, Freedman, and Segev (1998) showed (using stochastic simulations with the Binomial algorithm) that in neurons with a large numbers of ion channels, channel noise can play a significant role for a neuron's spike time reliability, i.e. the timing precision with which an action potential is initiated (see also Fig. 11.3, top two plots). This is because during action potential generation the instant when the membrane potential crosses AP threshold is determined by the small probability and thus small number of ion channels open around action potential threshold $N^* = p_{\text{open}}N$ and not, as was often implicitly assumed, the much larger number N of ion channels present in total. The magnitude of the fluctuations of N^* could be considerable even for large N and were better described by a binomial random variable:

$$\Delta N^* \propto \frac{\sqrt{N p_{\text{open}}(1 - p_{\text{open}})}}{N p_{\text{open}}} = \sqrt{\frac{1 - p_{\text{open}}}{N p_{\text{open}}}}.$$

This implied that many neurons in the cerebral cortex, e.g. pyramidal cells, could be influenced by channel noise. The study was able to generate comparable spike time variability as found in cortical neurons *in vitro*. Furthermore, spike initiation had high temporal precision when the sizes of ionic current fluctuations near AP threshold were small compared to the injected stimulus current. Thus, weaker stimuli will produce more unreliable spiking in agreement with experimental data (Schneidman, Freedman, and Segev, 1998). These results were extrapolated to AP propagation in axons, where the current flowing ahead of the AP (re)generates the action potential driving it forward. It was assumed that this axial current constituted a strong driving input and, hence, it was inferred that APs should propagate very reliably in axons; however, as we shall discuss shortly, conduction velocity will fluctuate significantly in thin axons due to channel noise (Faisal and Laughlin, 2007).

Propagation variability of the action potential While a neuron will contain many ion channels, typically these ion channels do not interact instantaneously (neurons are not iso-potential) and thus their fluctuations do not average out, as much smaller (and thus noisier) subsets of ion channels are responsible for driving activity locally in the neuron. However, little was known about how the stochasticity of ion channels influences spikes as they travel along the axon to the synapse and how much information arrives there. Experimentally, axonal spike time jitter has previously been measured only *in vitro* at myelinated cat and frog axons of several μm diameter and was on the order of 0.01 ms (Lass and Abeles, 1975*a*, 1975*b*).

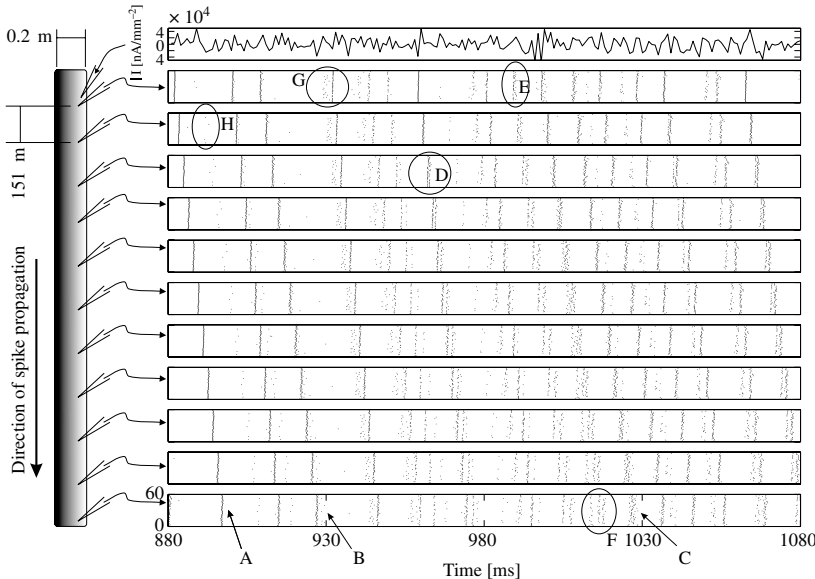


FIG. 11.3: The stacked raster plot shows travelling APs produced by identical repeated trials and is organized as follows. The top-most row shows the white noise current input. Below that, each row contains a spike raster plot recorded at equally spaced axonal positions (from the proximal stimulus site at the top to the distal end of the axon at the bottom). In each spike raster plot, the precise timing of a spike is marked by a dot on an invisible time line. These time lines are stacked over each other for the $N = 60$ repeated trials. The linear shift visible in the overall spike pattern across rows reflects the APs travelling along the axon. The top-most raster plot reflects the spike initiation variability, all subsequent plots reflect variability produced during propagation which quickly exceed that of initiation. Data based on 10 s trial length, squid axon of $0.2 \mu\text{m}$ diameter (average diameter of cerebellar parallel fibers) with a frozen noise current stimulus (zero mean, 0.01nA SD , 1kHz corner frequency) injected at the proximal end. See text for details. Figure adapted from Faisal and Laughlin (2007).

Biologically accurate stochastic simulations (using the Binomial channel algorithm for most data and the Gillespie algorithm for verification) of axons showed (Faisal and Laughlin, 2007) that the variability of AP propagation (measured as spike time jitter) in unmyelinated axons between 0.1 and $0.5 \mu\text{m}$ diameter was on the order of 0.1 – 1 ms SD over distances of millimetres (cf. Fig. 11.3). Thus, axonal variability can grow several orders of magnitude larger than previously expected and have considerable impact on neural coding. Why can action potential propagation become so variable? The spatial spread of membrane potential follows different input-response relationships than for point-like

iso-potential membrane patches (Faisal, White, and Laughlin, 2005). In fact, the current driving the AP ahead is one to two orders of magnitude smaller than the minimum stimulus current ('rheobase') required to trigger an action potential in a resting axon (Faisal and Laughlin, 2007). Consequently the driving axial current is a weak input that is susceptible to channel noise. Channel noise acts in two ways that affect the action potential mechanism (see Fig. 11.4 for illustration). Firstly, only a small number of Na^+ channels are involved in driving the AP when the membrane is between resting potential and AP threshold, and these small Na^+ currents are thus subject to large fluctuations. Secondly, the resting membrane ahead of the AP is far from being at rest, but fluctuates considerably.

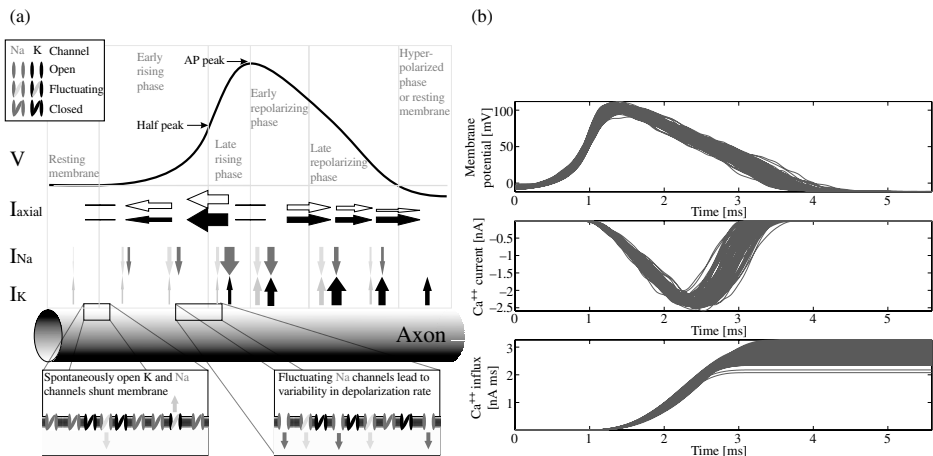


FIG. 11.4: (a) Diagrammatic representation of an action potential travelling on an axon, based on Faisal and Laughlin (2007). Stacked over each other, the leftward travelling membrane potential wave form of the AP (V), axial currents flowing along the axon (I_{axial}), Na^+ and K^+ currents (I_{Na} , I_{K}) and the representation of the axon itself. Axial, Na^+ and K^+ currents are denoted by black, red, and blue arrows scaled to represent the relative size of the current in the various phases. Hollow and light shaded arrows denote the size of the current fluctuations relative to the average currents. The action potential wave form is subdivided into six phases: resting membrane, early rising phase, late rising phase, early repolarizing phase, late repolarizing phase, and an optional hyperpolarized phase. See text for details. (b) Synaptic variability from axonal variability. Top: wave forms of 713 consecutive APs arriving at the terminal end of a 1.6 mm long unmyelinated axon of 0.2 μm diameter. Middle and bottom: Ca^{++} current and total Ca^{++} influx resulting from the integration of the above AP wave forms into a model of a Calyx-of-Held type synapse. Figure adapted from Faisal and Laughlin (2003). See Plate 3.

Inspection of Fig. 11.3 shows that APs generated by the same stimulus are not precisely aligned across trials, and the misalignment ('jitter') in this action potential set grows considerably as the APs propagate further. In general, four distinct stochastic effects of channel noise on APs propagating in axons can be identified. To describe these effects the portion of the input stimulus which triggers an AP will be called a *stimulus event*. APs which were triggered across trials by the same stimulus event form an *AP set*.

The timing of APs in a set is jittered but remains unimodally distributed (Fig. 11.3, arrows A,B,C), or grows and is markedly multimodally distributed (Fig. 11.3, D, fourth row) – splitting into distinct groups of APs across trials. For a stimulus event we quantify the jitter at a given position on the axon as the standard deviation (SD) of spike timing in its corresponding AP set. For a 0.2 μm axon (shown in Fig. 11.3) AP generation at the proximal end of the axon had on average a SD of 0.38 ms, similar to spike generation in simulated membrane patches (Schneidman, Freedman, and Segev, 1998). However, spike time jitter increases over relatively short distances, such that at 2 mm the average jitter over all AP sets has increased to ~ 0.6 ms SD. This jitter implies that post-synaptic coincidence detection windows cannot be more precise than 2–3 ms at this short distance. Furthermore, at the site of spike generation the timings within each action potential set are unimodally distributed (Fig. 11.3, top raster plot). However, during propagation the spike time distribution can become multimodal, with the different peaks several milliseconds apart. In other words, the AP set splits into distinct groups (Fig. 11.3, D, fourth row). Thus, axonal channel noise sets limits on the precision with which neurons in the densely wired cortex can communicate with each other over a given distance. These effects become relevant in unmyelinated axons below 0.5 μm , as commonly found in the tightly packed circuits of the central nervous system.

Memory effects of ion channel populations Propagating APs splitting into distinct groups across trials (Fig. 11.3, D, fourth row) was the only stochastic effect that was not observed in a separate set of simulations, where a single action potential was triggered per trial instead of a spike train (Faisal and Laughlin, 2007). Therefore, splitting must depend on the temporal pattern of the spike train conditioning the stochastic behaviour of ion channels, and the timing reliability of APs can become dependent on the axon's activity history. These memory effects cannot be captured by Langevin models, which ignore the temporal correlation and structure of channel noise.

Previously, such axonal memory effects have been measured in axons (Debanne, 2004), where selective conduction of APs was, for example, dependent on inactivation of a K^+ channel (Debanne *et al.*, 1997). However, this stochastic population effect is different, as it arises from the generic property of any voltage-gated ion channel with multiple states (Faisal and Laughlin, 2007). Because spike time reliability depends on the temporal pattern of spikes (splitting effect), dendritic and somatic mechanisms of AP initiation could be tuned to generate spike patterns which propagate particularly reliably, such as bursts of APs.

Conduction safety in the presence of channel noise Although channel noise provides a means for APs to fail, stochastic simulations⁷ show (Faisal and Laughlin, 2007) that conduction failures are rare – 1% in axons of the smallest known diameter and thus the noisiest axons – while empirically observed failure rates can be as high as 50%. Several neuronal mechanisms that purposely produce conduction failure are known, acting through membrane hyperpolarization, shunting effects, and spike-frequency dependent block of APs at axonal branch points (Debanne, 2004). In contrast, channel noise has the opposite effect of promoting action potential generation, because of the strong positive feedback of Na^+ channels. This suggests that channel noise cannot account for the AP failures observed in many systems and that other factors must be responsible. This suggests that when propagation failures occur in the healthy nervous system, this is due to purposely designed mechanisms for pre-synaptic information processing, which allow the incorporation of local information not available at the site of spike initiation (Faisal and Laughlin, 2007).

A novel mode of signal propagation – stochastic microsaltatory conduction Some APs in thin axons travel faster than a continuously moving wave front, where the AP wave front suddenly jumps ahead (Fig. 11.5.a). This novel mode of conduction results from a collaborative channel effect, where random opening of nearby Na^+ channels pre-depolarize the membrane by a few millivolts. The axial current from an incoming AP then triggers the AP threshold and the AP jumps several hundred micrometres ahead to the pre-depolarized region. Thus, the spike time at a given position of the axon appears to be shifted on the order of a millisecond. This stochastic microsaltatory conduction effect resembles saltatory conduction between the morphologically specialized Nodes of Ranvier in myelinated nerve fibres. Here, however, it is produced by the stochastic behaviour of individual channels embedded in an axon of uniform morphology and it occurs randomly. This adds considerable variability across trials and will enhance the effects of jitter and can initiate the following effect.

Synaptic variability from axonal noise Action potential timing precision is bound to decrease the further the AP travels, thus long-range communication is in this respect noisier than short-range communication, given the same axon diameter. Axonal channel noise may also have an effect on information transmission in short-range synaptic connections in unmyelinated axons of up to 1 μm diameter, because the shape of the AP wave form is perturbed by channel noise (Faisal and Laughlin, 2003). The wave form of the presynaptic AP is of fundamental importance in determining the strength of synaptic transmission. It determines the calcium signal that controls synaptic transmitter vesicle release, by both controlling the opening of voltage-gated Ca^{2+} channels and the driving force for Ca^{2+} influx (Augustine, 2001). Stochastic simulations show that the travelling AP wave form fluctuates considerably (see Fig. 11.4) (Faisal and

⁷Using the Binomial channel algorithm for most data and the Gillespie algorithm for verification.

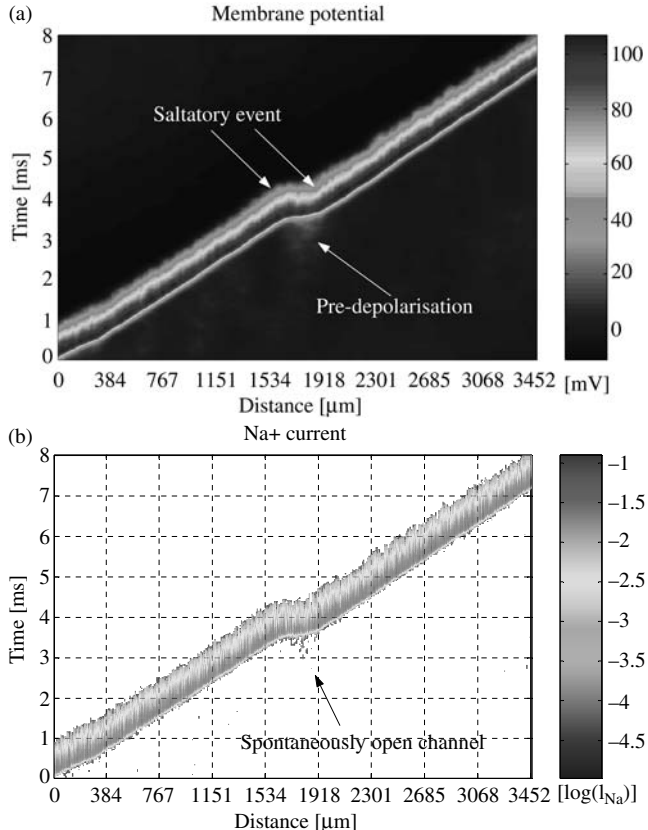


FIG. 11.5: A stochastic microsaltatory conduction event in a $0.1\text{ }\mu\text{m}$ diameter squid axon. A continuously propagating action potential wave front (note the jitter in propagation speed) suddenly jumps from position $x = 1550\text{ }\mu\text{m}$ to $x = 1900\text{ }\mu\text{m}$. (a) A space-time plot of the membrane potential on the axon. (b) The corresponding space-time plot of the transmembrane Na^+ current. The regions where no Na^+ current was flowing were not colour coded, making ionic currents from spontaneously open channels clearly visible. Figure adapted from Faisal and Laughlin (2007). See Plate 4.

Laughlin, 2003) and the wave form of an action potential mid-way down the axon and at the terminal end were little correlated. Thus in thin axons below $1\text{ }\mu\text{m}$ somatically triggered APs are unlikely to carry much information in the action potential wave form to the synapse, as has been measured in the soma of cortical neurons (de Polavieja *et al.*, 2005).

Stochastic modelling from the soma to the synapse is essential, as synaptic reliability and variability has been in general attributed to mechanisms inside the cortical synapse, but knowledge is typically based on paired soma recordings or

large synapses, while most of our brain's synapses are very small. Thus, it is difficult to dissociate synaptic and axonal stochastic effects in these preparations. Furthermore, most studies so far ignored synaptic channel noise at presynaptic Ca^{2+} channels, which may produce spontaneous postsynaptic potentials and further increase trial-to-trial transmission variability.

Dynamic-clamp: stochastic versus deterministic channels *in vitro* While the discussion so far has dealt with findings based on simulations, the difference between deterministic and stochastic channel behaviour was recently investigated in living neurons using the dynamic-clamp method. Dynamic-clamp is an electrophysiological technique that uses a real-time interface between neurons and a computer to simulate dynamic processes of neurons (Sharp *et al.*, 1993, Robinson and Kawai, 1993, Prinz, Abbott, and Marder, 2004a). It reads the membrane potential of the neuron and calculates the transmembrane current produced by virtual, simulated voltage-gated or synaptic conductances. The simulated current is injected into the neuron, which therefore receives the same current as if it biologically contained the virtual conductances.

Dorval and White used this technique to study the role of channel noise in cortical neurons *in vitro*, allowing them to investigate what happens if ion channels were to act deterministically in a real neuron (Dorval Jr. and White, 2005). A Na^+ channel population was blocked pharmacologically and using dynamic-clamp replaced by an equivalent virtual population of Na^+ channels. The virtual channels were simulated either deterministically or stochastically.⁸ These neurons showed near-threshold oscillations of the membrane potential, characteristic of their morphological class *in vitro*, and were able to phase lock their activity with other neurons, if and only if the virtual Na^+ channels were simulated stochastically. Neurons lost these two properties with deterministically stimulated Na^+ channels. These experimental results provide the first direct demonstration that physiological levels of channel noise can produce qualitative changes in the integrative properties of neurons. This suggests that channel noise could even have a profound effect on the evolution and development of neurons.

Why cell size has a lower limit set by noise (critical stochasticity) How small can neurons be made before channel noise effects disrupt action potential signalling? Hille (1970) suggested that in very fine axons the opening of a small number of Na^+ channels could generate an AP. This idea was subsequently used to highlight the fact that channel noise could generate random action potentials (RAPs) posing limits to myelinated axons (Franciolini, 1987). Based on a probabilistic argument predicting a RAP rate of 1 Hz in myelinated axons, it was suggested that RAPs would discourage the use of Nodes of Ranvier below 1 μm diameter. Unfortunately the calculation was flawed because ion channel state transition probabilities were confused with ion channel state transition rates. Furthermore, it was previously shown that in the mammalian nervous system myelinated Nodes of Ranvier exist with diameters as fine as 0.2 μm .

⁸Using the Gillespie algorithm described.

(Waxman and Bennett, 1972). The first stochastic simulations of unmyelinated axons (Horikawa, 1991), using simplified channel kinetics (discussed elsewhere in this chapter), showed that in fine axons more APs arrived at the distal end than were generated at the proximal end. Based on this single finding a lower limit to axon diameter of 0.2 μm was postulated. The relationship between diameter, biophysical parameters, and RAP rate, however, was not studied and the findings were not related to anatomical data. Anatomists had previously shown that axons as fine as 0.1 μm are commonly found in the central nervous system.

Detailed stochastic simulations⁹ (Faisal, White, and Laughlin, 2005) showed that spontaneous opening of Na^+ channels can, in theory, trigger RAPs below a critical axon diameter of 0.15–0.2 μm . This is because at these diameters the input resistance of a Na^+ channel is comparable to the input resistance of the axon. The single, persistent opening of a single Na^+ channel can therefore depolarize the axon membrane to threshold. Below this diameter, the rate at which randomly generated APs appear increases exponentially as the diameter decreases. This will disrupt signalling in axons below a limiting diameter of about 0.1 μm , as RAPs cannot be distinguished from signal-carrying APs. This limit is robust with respect to parameter variation, as two contrasting axon models, mammalian cortical axon collaterals and the invertebrate squid axon, show that the limit is mainly set by the order of magnitude of the properties of ubiquitous cellular components, conserved across neurons of different species. The occurrence of RAPs and the exponential increase in RAP rate as the diameter decreases is an inescapable consequence of the AP mechanism. The stochasticity of the system becomes critical when its inherent randomness makes its operation unfeasible.

Electrically passive neurites of 0.05 μm diameter (which do not contain Na^+ channels or sustain action potential conduction) are known to exist. A steric (volume-exclusion) argument shows that an axon of 0.05 μm diameter can be constructed, as the cross-sectional area of an axon can fit all required components to sustain AP conduction (i.e. Na^+ channels and $\text{Na}^+ \text{-K}^+$ pumps protruding into the axon, the thickness of the actin feltwork supporting cell shape, microtubules, motorproteins and vesicles supplying synapses); (Faisal, White, and Laughlin, 2005). Furthermore, other molecular limits to axon diameter are well below the limiting diameter of 0.1 μm , thus action potential conducting axons finer than 0.1 μm could, in theory, exist. Yet anatomical data across many species, invertebrate and vertebrate, extremely small insects and large mammals, shows an identical lower limit of diameter for AP conducting axons of 0.1 μm .¹⁰ This suggests that channel noise limits axon diameter and thus the wiring density of the central nervous system and thus ultimately the size of the cortex.

⁹Using the Binomial algorithm and Gillespie algorithm for cross-validation.

¹⁰Historical note: Although the published anatomical data demonstrated a common lower value for the diameter of axons for almost 30 years, this was not noticed, until the study on stochastic limits to cell size prompted us to search for the smallest known axon diameters (Faisal, White, and Laughlin, 2005).

Body temperature reduces the impact of noise Temperature-dependent stochasticity can produce some counterintuitive effects, whereby increasing temperature can lower noise levels. While commonly overlooked, temperature, and its effects on the kinetics of ion channels, can vary greatly across the nervous system: cold-blooded insects can warm up their body to over 40 °C prior to taking flight, while human extremities and the sensory and motoneurons therein can be exposed to temperature differences of up to 10 °C or more between their dendrites, cell bodies and axon terminals, as they connect the (cold) extremities and the (warmer) spinal cord.

The rate of RAPs triggered by channel noise counterintuitively decreases as temperature increases, unlike what one would expect from electrical Johnson noise. Stochastic simulations (Faisal, White, and Laughlin, 2005) showed that RAP rate is inversely temperature dependent in the cortical pyramidal cell, and in the squid axon which operates at 6.3° and 36°. The rate of random activity falls with increasing temperature because when ion channel kinetics speed up, the duration of spontaneous depolarizing currents decreases and the membrane is less likely to reach action potential threshold (this effect prevails over the increased rate of spontaneous channel openings). In other words, increasing temperature shifts channel noise to higher frequencies where it is attenuated by the low-pass characteristics of the axon (Steinmetz *et al.*, 2000, Faisal, White, and Laughlin, 2005). This finding suggest an evolutionary advantage to increasing body temperature. It allows homeothermic animals, such as mammals, to sustain more reliable, smaller, and thus more densely connected neural circuits, than the older poikilotherms' nervous systems.

Implications of axon channel noise for the interpretation of experiments The findings from stochastic simulations of the AP prompt careful experimental consideration in thin axons, because typical experimental protocols are not geared to distinguish post-synaptic variability due to synaptic transmission from variability caused by axonal noise ('axonal variability'). Optical methods and extracellular recordings have limited stimulus control and signal resolution, thus intra-cellular paired-cell recordings, as used to study small synapses innervated by thin axons, would be more suitable. However, the impact of axonal channel noise in circuits may have gone so far unnoticed, because paired cell measurements which could reveal axonal variability are difficult to obtain. This is because typical cell-to-cell distances are limited by the microscope's field of view and the probability of finding two mono-synaptically connected neurons with standard techniques is low. This limits the potential cell pairs to about 500 µm distance, where conduction jitter standard deviation is small, on the order of about 0.1 ms. However, cortico-cortical axon collaterals and cerebellar parallel fibres, which are below 0.5 µm in diameter, can extend up to a centimetre away from the soma, suggesting that jitter will limit the minimum width of reliable coincidence detection windows to 5–10 ms at their terminals.

The question as to what extent channel noise generates variability in the brain and ultimately behaviour will probably require researchers to combine

both experimental studies, where total variability can be assessed, and stochastic modelling, where each source of variability can be controlled for. Noise levels set both hard limits on the central nervous system, such as the degree of miniaturization of the brain's circuits (Faisal, White, and Laughlin, 2005) and soft constraints such as the achievable spike time reliability (Schneidman, Freedman, and Segev, 1998, Faisal, 2007).

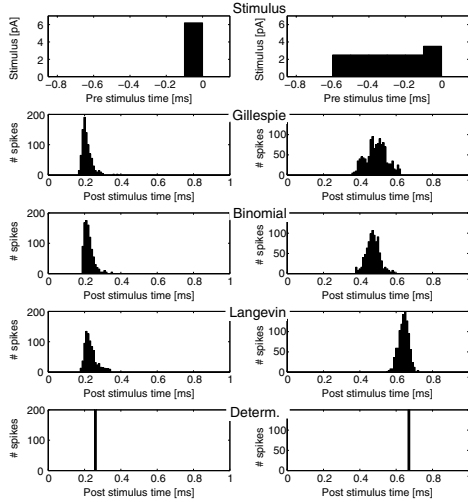
11.5 Lessons learned: stochastic methods

Theoretical and simulation-based studies of the action potential have shown that stochastic modelling of individual ion channels captures essential properties and provides constraints on whole-cell behaviour. A key advance has been the understanding that stochastic models operating at the microscopic level can explain the experimentally observed macroscopic variability and enable cellular mechanisms to be characterized in a more detailed (and often simpler) manner than deterministic models.

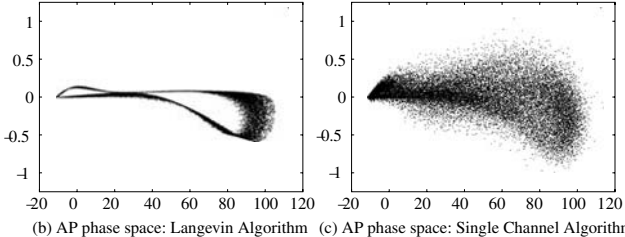
The multi-state nature of ion channels induces an activity-history dependence on the response of a population of ion channels to new activity. These effects cannot be accounted for by deterministic (e.g. jitter) or approximative (Langevin-type) stochastic models. Schneidman, Freedman, and Segev (1998) showed that the initiation of the AP is sensitive to channel noise even in large neurons, because the small number of ion channels determining the timing of action potential initiation is a fraction of the total number of ion channels present.

This effect can only be captured by biologically accurate models and algorithms. For example, triggering an AP in a membrane patch with a single pulse produces comparable variability in AP initiation across Gillespie, Binomial, and Langevin algorithms (Fig. 11.6a left). However, a two-stage stimulus, where the first stage causes a mere subthreshold response, demonstrates that the subthreshold activation of ion channels has significant effects on the variability of AP initiation (Fig. 11.6a right). These differences reflect the varying amount of stimulus history captured by the stochastic algorithm and its implied channel model (deterministic conductance-based with additive noise versus Markov based single channel model).

The impact of individual ion channel stochasticity is further increased if, instead of modelling an iso-potential membrane (i.e. modelling membrane potential by an ODE), one accounts for spatial interactions in the filigree morphology of neurons (i.e. modelling membrane potential by a PDE). Conclusions based on ODE studies suggest that noise in AP propagation is negligible. However, accounting for spatial interaction reveals a quite different picture. The spike time variability in thin axons was found to have an SD (Standard Deviation) between 0.1 and 1 ms over mm distances (Faisal and Laughlin, 2007). These findings contrast with the extrapolations from iso-potential membrane patches and early stochastic axon simulations by Horikawa (1991) which reported spike time variability SD 0.001–0.01 ms over a distance of a few millimetres (thus, an



(a) AP initiation variability



(b) AP phase space: Langevin Algorithm (c) AP phase space: Single Channel Algorithm

FIG. 11.6: Comparison of stochastic algorithms in simulating action potential initiation. (a) Sensitivity of stochastic integration methods to stimulus history. Spike-time histograms ($N = 1000$) in an iso-potential membrane patch containing 1000 Na^+ channels driven by repeated identical current stimuli. Left column: single-pulse suprathreshold current stimulus. Right column: two-step current stimulus: the first step is subthreshold and the second step's amplitude is the same as in the left column stimulus. Top row: injected stimulus current. Second row to bottom: spike-time histograms for simulations using Gillespie, Binomial, Langevin and Deterministic (i.e. Hodgkin–Huxley conductance-based) algorithms, respectively. The time step size for the three synchronous algorithms was $\Delta t = 1 \mu\text{s}$. Note, the post stimulus time diagram is offset with respect to the pre-stimulus diagram. Data extracted from Mino, Rubinstein, and White (2002). Phase space comparison of squid axon membrane potential dynamics using the (b) Langevin and (c) Single Channel algorithms. Spike trains with uniform distributed interspike intervals were generated at the proximal end of a $2.5 \mu\text{m}$ diameter and $50 \mu\text{m}$ long squid-like axon. The instantaneous ionic transmembrane currents and membrane potential were measured in the mid-way membrane compartment, sampling at 10 kHz. The phase space plots show the membrane current (horizontal axis) and membrane potential (vertical axis) in a scatter plot. Membrane resting potential was set to 0 mV. Each phase space plot displays 100 000 data points from stochastic simulation using the Modigliani stochastic neuron simulator (Faisal, 2004, unpublished PhD Thesis, University of Cambridge).

order of magnitude smaller than the aforementioned *in vitro* measurements in axons over tenfold larger). There are two model-related reasons for this underestimation of variability. Firstly, the simulations used spatial compartments and time steps that were on the order of 0.1–0.01 ms (probably to overcome computational constraints) which averages out noise (Faisal and Laughlin, 2007). Secondly, the stochastic channel model was oversimplified, as transitions between the open and the nearest closed states were stochastic, but all other state transitions were deterministic. Thus, only the instantaneous effects of membrane potential changes were stochastic; temporal effects could not emerge. In fact, the spike time variability in these simulations matched those simulations which used deterministic conductance models with additive Gaussian noise (Horikawa, 1991) (related to the Langevin algorithm described above). Both approaches generate noise uncorrelated in time, and cannot capture the correlation in time resulting from the sequence of transitions between conformational states in the channel protein. These correlations can only be captured by stochastic simulations using full-kinetic models of channels which capture correlations of channel gating in time and across spatial locations.

The unsuitable additive Gaussian channel noise model corresponds to a (first-order) Langevin approximation of the Markov process of channel gating (Fox, 1997). In general, theoretical and simulation work shows that Langevin approximations break down in iso-potential membrane patches with fewer than about 800 channels (Fox, 1997), but their limitations have not been assessed in non-iso-potential (i.e. spatially extended) models of neurons since the number of channels involved dynamically varies with distance, membrane potential, and conductance. These findings suggest that the Langevin algorithm is inadequate for simulations used in studying neuronal response properties (Faisal and Laughlin, 2007), signal reliability (Faisal, 2007), or effects near membrane resting potential (Faisal, White, and Laughlin, 2005). For typical neuronal Na^+ channel densities ($< 120 \mu\text{m}^{-2}$, excluding Nodes of Ranvier in myelinated axons) and assuming that the average membrane area affected by the action potential corresponds to an axon cylinder about a length constant long, the breakdown of the Langevin approximation in spatially extended models occurs at about an order of magnitude larger density of channels. Thus, Langevin-type approximations of channel noise are unsuitable for ion channel populations smaller than 8000 channels or neuronal compartments smaller than $10\text{--}20 \mu\text{m}$ in diameter. The underestimation of noise effects is clearly visible in the phase space occupied by repeated APs, where the amount of phase space occupied is a direct measure of the variability of the underlying neuronal dynamics. The Langevin algorithm markedly underestimates the variability in the current–voltage relationship due to channel noise (cf. Fig. 11.6b and c).

Similarly, stochastic models of smaller arborized neurons will break down using the Langevin approximation because they ignore both spatial and temporal correlations, as individual ion channels have a large impact on membrane potential. This is confirmed by two analytical calculations (see Supplemental

Information in Faisal, White, and Laughlin 2005) that showed that the Langevin approximation underestimated noise limits to axon diameter by over an order of magnitude, while a deterministic worst-case approximation (assuming that the worst stochastic effect is that a Na^+ channel that should be closed at resting potential remained opened indefinitely) was within 20% of the noise limit to axon diameter, as determined by detailed stochastic simulations and supported by anatomical data across species.

Stochastic simulation and simulators Stochastic whole neuron simulation relies on an algorithmic framework which combines the integration of the compartmentalized, deterministic PDE describing the membrane potential dynamics and the stochastic ODEs describing the ionic transmembrane current dynamics. The underlying PDE should be integrated using Euler steps, as it is incorrect to use the Crank–Nicolson algorithm for stochastic simulations. Extending existing simulator code with custom-built code that handles stochastic ion channels can yield incorrect stochastic simulations if the core simulation engine is not adjusted accordingly. In other words, even a flawless implementation of a deterministic neuron simulator and stochastic ion channels can produce in combination mathematically unsound results. This emphasizes the advantage of designing the simulation engine with stochastic simulation in mind. The algorithms presented in this chapter are an essential part of the Modigliani simulator that was developed specifically to simulate whole neuron models stochastically (see www.modigliani.co.uk).

Conclusion Stochastic simulations have contributed to developing our bottom-up understanding of how noise present at the molecular level, channel noise in neuronal membranes, and biochemical noise at synapses (Franks, Stevens, and Sejnowski, 2003), affects information processing at macroscopic levels – whole neurons, neuronal circuits, and behaviour (Faisal, Selen, and Wolpert, 2008). The appropriate choice of algorithms for simulation is essential both in terms of resource efficiency and the accuracy of the results, since in many neurons, modelling single ion channel behaviour is important.

Here, we used stochastic methods to study the role of internal noise in setting constraints on the function and structure of a typical cell signalling system, the action potential (Hartwell *et al.*, 1999). Similar effects, constraints, and limits due to stochasticity, will apply to other wave-based cell signalling systems, as they have to rely on inherently noisy protein switches to generate and propagate signals.

References

- Abbott, L. F. (1992). Simple diagrammatic rules for solving dendritic cable problems. *Physica A*, **185**, 343–356.
- Armstrong, C. M. and Bezanilla, F. (1974, May). Charge movement associated with the opening and closing of the activation gates of the na channels. *J Gen Physiol*, **63**(5), 533–552.

- Arrhenius, S. A. (1967). On the reaction velocity of the inversion of cane sugar by acids (english translation). In *Selected Readings in Chemical Kinetics* (ed. M. H. Back and K. J. Laidler), p. 226. Pergamon Press. Original citation: *Zeitschrift für Physikalische Chemie* **4**, 226 (1889).
- Augustine, G. J. (2001, Jun). How does calcium trigger neurotransmitter release? *Curr. Opin. Neurobiol.*, **11**(3), 320–326.
- Blair, E. A. and Erlanger, J. (1933). A comparison of the characteristics of axons through their individual electric responses. *Am. J. Physiol.*, **106**, 524–564.
- Bower, J. M. and Beeman, D. (1995). *The book of GENESIS: Exploring Realistic Neural Models with the GEneral NEural SImulation System*. TELOS/Springer-Verlag, New York.
- Braitenberg, V. and Schütz, A. (1998). *Cortex: Statistics and Geometry of Neuronal Connectivity* (2nd edn). Springer, Hamburg.
- Cavalcanti, S. and Fontanazza, F. (1999, Sep). Deterministic model of ion channel flipping with fractal scaling of kinetic rates. *Ann. Biomed. Eng.*, **27**(5), 682–695.
- Chow, C. C. and White, J. A. (1996, Dec). Spontaneous action potentials due to channel fluctuations. *Biophys. J.*, **71**, 3012–3021.
- Clay, J. R. and DeFelice, L. J. (1983, May). Relationship between membrane excitability and single channel open-close kinetics. *Biophys J.*, **42**(2), 151–157.
- Conti, F. and Wanke, E. (1975). Channel noise in nerve membranes and lipid bilayers. *Q. Rev. Biophys.*, **8**, 451–506.
- Cooley, J. W. and Dodge, Jr., F. A. (1966). Digital computer solutions for excitation and propagation of the nerve impulse. *Biophysic. J.*, **6**, 583–599.
- Cooley, J. W., Dodge, Jr., F. A., and Cohen, H. (1965). Digital computer solution for excitable membrane models. *J. Cell. and Comp. Physiol.*, **66**, 99–110.
- Dayan, P. and Abbott, L. F. (2001). *Theoretical Neuroscience*. Computational Neuroscience. MIT Press, Cambridge, MA.
- de Polavieja, G. G., Harsch, A., Kleppe, I., Robinson, H. P. C., and Juusola, M. (2005). Stimulus history reliably shapes action potential waveforms of cortical neurons. *J. Neurosci.*, **25**(23), 5657–5665.
- Debanne, D. (2004, Apr). Information processing in the axon. *Nat. Rev. Neurosci.*, **5**(4), 304–316.
- Debanne, D., Guérineau, N. C., Gähwiler, B. H., and Thompson, S. M. (1997, Sep). Action-potential propagation gated by an axonal IA-like K^+ conductance in hippocampus. *Nature*, **389**(6648), 286–289.
- DerkSEN, H. E. and Verveen, A. A. (1966). Fluctuations of resting neural membrane potential. *Science*, **12**, 1388–1389.
- Dorval Jr, A. D. and White, J. A. (2005, Oct). Channel noise is essential for perithreshold oscillations in entorhinal stellate neurons. *J. Neurosci.*, **25**(43), 10025–10028.
- Faisal, A. A. and Laughlin, S. B. (2003). Effect of channel noise on the propagating ap wave form and its potential impact on synaptic transmission. *J. Physiol.*

- Faisal, A. A. and Laughlin, S. B. (2007, May). Stochastic simulations on the reliability of action potential propagation in thin axons. *PLoS Comput. Biol.*, **3**(5).
- Faisal, A. A., Laughlin, S. B., and White, J. A. (2002). How reliable is the connectivity in cortical neural networks? In *Proceedings of the IEEE Intl. Joint. Conf. Neural Networks 2002* (ed. D. Wunsch), pp. 1–6. INNS.
- Faisal, A. A. and Niven, J. E. (2006). *A Simple Method to Simultaneously Track the Numbers of Expressed Channel Proteins in a Neuron. Lecture Notes in Computer Science*, **4216**, 257. Springer-Verlag, Berlin.
- Faisal, A. A., Selen, L. P., and Wolpert, D. M. (2008, Apr). Noise in the nervous system. *Nat. Rev. Neurosci.*, **9**(4), 292–303.
- Faisal, A. A., White, J. A., and Laughlin, S. B. (2005, Jun). Ion-channel noise places limits on the miniaturization of the brain's wiring. *Curr Biol*, **15**(12), 1143–1149.
- Faisal, A. A. (2007). Studying channelopathies at the functional level using a system identification approach. In *CompLife* (ed. A. P. J. M. Siebes, M. R. Berthold, R. C. Glen, and A. J. Feelders), AIP, Volume 940, pp. 113–126.
- Fitzhugh, R. (1965). A kinetic model of the conductance changes in nerve membrane. *J. Cell. Comp. Physiol.*, **66**, 111–118.
- Fox, R. F. (1997, May). Stochastic versions of the Hodgkin–Huxley equations. *Biophysical J.*, **72**, 2068–2074.
- Franciolini, F. (1987). Spontaneous firing and myelination of very small axons. *J. Theor. Biol.*, **128**, 127–134.
- Franks, K. M., Stevens, C. F., and Sejnowski, T. J. (2003, Apr). Independent sources of quantal variability at single glutamatergic synapses. *J. Neurosci.*, **23**(8), 3186–3195.
- Gillespie, D. T. (1976). A general method for numerically simulating the stochastic time evolution of coupled chemical reactions. *J. Comp. Phys.*, **22**, 403–434.
- Gillespie, D. T. (1992). *Markov Processes – An Introduction for Physical Scientists*. Academic Press, San Diego, CA.
- Gillespie, D. T. (1977). Exact stochastic simulation of coupled chemical reactions. *J. Phys. Chem.*, **81**(25), 2340–2361.
- Hartwell, L. H., Hopfield, J. J., Leibler, S., and Murray, A. W. (1999, Dec). From molecular to modular cell biology. *Nature*, **402** Supplement, C47–C42.
- Hastings, W. K. (1970). Monte Carlo sampling methods using markov chains and their applications. *Biometrika*, **57**, 97–109.
- Hille, B. (1970). Ionic channels in nerve membranes. *Prog. Biophys. Molec. Biol.*, **21**, 3–28.
- Hille, B. (2001). *Ion Channels of Excitable Membranes* (3rd edn). Sinauer Associates, Sunderland, MA.
- Hines, M. (1984). Efficient computation of branched nerve equations. *Int. J. Bio-Medical Computing*, **15**, 69–76.

- Hines, M. L. and Carnevale, N. T. (1997). The neuron simulation environment. *Neural Comp.*, **9**, 1179–1209.
- Hines, M. L. and Carnevale, N. T. (2001, Apr). Neuron: a tool for neuroscientists. *Neuroscientist*, **7**(2), 123–135.
- Hodgkin, A. L. (1964, Sep). The ionic basis of nervous conduction. *Science*, **145**(3637), 1148–1154.
- Hodgkin, A. L. and Huxley, A. F. (1952). Quantitative description of membrane current and its application to conduction and excitation in nerve. *J. Physiol. (London)*, **117**, 500–544.
- Horikawa, Y. (1991). Noise effects on spike propagation in the stochastic Hodgkin-Huxley models. *Biol. Cybern.*, **66**, 19–25.
- Hoyt, R. C. (1984). A model of the sodium channel. *Biophys. J.*, **45**, 55–57.
- Jack, J. J. B., Noble, D., and Tsien, R. W. (1983). *Electric Current Flow in Excitable Cells* (2nd edn). Oxford University Press, Oxford.
- Johnston, D. and Wu, S. M.-S. (1995). *Foundations of Cellular Neurophysiology*. MIT Press, Cambridge, MA.
- Juncosa, M. L. and Young, D. (1957). On the crank-nicolson procedure for solving parabolic partial differential equations. *Cambridge Philos. Soc. Trans.*, **53**, 448–461.
- Kandel, E. R., Schwartz, J. H., and Jessell, T. M. (2000). *Principles of Neural Science*. McGraw-Hill/Appleton & Lange, New York.
- Katz, B. (1971, Jul). Quantal mechanism of neural transmitter release. *Science*, **173**(992), 123–126.
- Keynes, R. D. and Rojas, E. (1974, Jun). Kinetics and steady-state properties of the charged system controlling sodium conductance in the squid giant axon. *J. Physiol.*, **239**(2), 393–434.
- Koch, C. (1999). *Biophysics of Computation*. Computational Neuroscience. Oxford University Press, Oxford.
- Kuo, C. C. and Bean, B. P. (1994, Apr). Na⁺ channels must deactivate to recover from inactivation. *Neuron*, **12**(4), 819–829.
- Langevin, P. (1908). Sur la théorie du mouvement brownien. *Comptes-Rendus de l'Académie des Sciences*, **146**, 530–532.
- Lass, Y. and Abeles, M. (1975a). Transmission of information by the axon: 1. noise and memory in the myelinated nerve fiber of the frog. *Biol. Cybernetics*, **19**, 61–67.
- Lass, Y. and Abeles, M. (1975b). Transmission of information by the axon: 2. The channel capacity. *Biol. Cybernetics*, **19**, 121–125.
- Lecar, H. and Nossal, R. (1971a). Theory of threshold fluctuations in nerves: 2. analysis of various sources of membrane noise. *Biophys. J.*, **11**, 1068–1084.
- Lecar, H. and Nossal, R. (1971b, Dec). Theory of threshold fluctuations in nerves. i. relationships between electrical noise and fluctuations in axon firing. *Biophys. J.*, **11**(12), 1048–67.
- Liebovitch, L. S., Fischbarg, J., Koniarek, J. P., Todorova, I., and Wang, M. (1987). Fractal model of ion-channel kinetics. *Biochim. Biophys. Acta*, **896**, 173–180.

- Levinson, S. R. and Meves, H. (1975, Jun). The binding of tritiated tetrodotoxin to squid giant axons. *Philos. Trans. R. Soc. Lond. B. Biol. Sci.*, **270**(908), 349–352.
- Liebovitch, L. S., Selector, L. Y., and Kline, R. P. (1992, Dec). Statistical properties predicted by the ball and chain model of channel inactivation. *Biophys. J.*, **63**(6), 1579–1585.
- Liebovitch, L. S. and Toth, T. I. (1990). Using fractals to understand the opening and closing of ion channels. *Ann. Biomed. Eng.*, **18**(2), 177–194.
- Liebovitch, L. S. and Toth, T. I. (1991, Jan). A model of ion channel kinetics using deterministic chaotic rather than stochastic processes. *J. Theor. Biol.*, **148**(2), 243–267.
- Lowen, S. B., L. S., Liebovitch, and White, J. A. (1999, May). Fractal ion-channel behavior generates fractal firing patterns in neuronal models. *Phys. Rev. E*, **59**(5), 5970–5980.
- Manwani, A. and Koch, C. (1999). Detecting and estimating signals in noisy cable structures, II: information theoretic analysis. *Neural Comp.*, **11**, 11831–11873.
- Markov, A. A. (1906). Rasprostranenie zakona bol'shih chisel na velichiny, zavisimysaschie drug ot druga. *Izvestiya Fiziko-matematicheskogo obschestva pri Kazanskem universitete*, **15**(2-ya seriya), 135–156.
- Markov, A. A. (1971). Extension of the limit theorems of probability theory to a sum of variables connected in a chain (translation). In *Dynamic Probabilistic Systems* (ed. R. Howard), Volume 1: Markov Chains. John Wiley, New York. Reprinted in Appendix B.
- Mascagni, M. (1989). An initial-boundary value problem of physiological significance for equations of nerve conduction. *Comm. Pure Appl. Math.*, **42**, 213–227.
- Mascagni, M. V. and Sherman, A. S. (1998). Numerical methods for neuronal modeling. In *Methods in Neuronal Modeling* (ed. I. Segev and C. Koch), MIT Press, Cambridge, MA, pp. 569–606.
- McCormick, D. A., Shu, Y., and Yu, Y. (2007, Jan). Neurophysiology: Hodgkin and Huxley model – still standing? *Nature*, **445**(7123), 1–2.
- Metropolis, N., Rosenbluth, A. W., Rosenbluth, M. N., Teller, A. H., and Teller, E. (1953). Equations of state calculations by fast computing machines. *J. Chem. Phys.*, **21**, 1087–1091.
- Mino, H., Rubinstein, J. T., and White, J. A. (2002, Apr). Comparison of algorithms for the simulation of action potentials with stochastic sodium channels. *Ann. Biomed. Eng.*, **30**(4), 578–587.
- Naundorf, B., Wolf, F., and Volgshev, M. (2006, Apr). Unique features of action potential initiation in cortical neurons. *Nature*, **440**(7087), 1060–1063.
- Patlak, J. (1991, Oct). Molecular kinetics of voltage-dependent Na^+ channels. *Physiol. Rev.*, **71**(4), 1047–1080.
- Patlak, J. B. and Ortiz, M. (1986). Two modes of gating during late Na^+ channel currents in frog sartorius muscle. *J. Gen. Physiol.*, **87**, 305–326.

- Pearlmutter, B. A. and Zador, A. (1999). Appendix C. In *Biophysics of Computation* (Oxford edn) (ed. C. Koch), Computational neuroscience. OUP, Oxford University Press.
- Pecher, C. (1939). La fluctuation d'excitabilité de la fibre nerveuse. *Arch. Int. Physiol. Biochem.*, **49**, 129–152.
- Press, W. H., Teukolsky, S. A., Vetterling, W. T., and Flannery, B. P. (1996). *Numerical recipes in C* (2nd corrected edn). Cambridge University Press, Cambridge.
- Prinz, A. A., Abbott, L. F., and Marder, E. (2004a, Apr). The dynamic clamp comes of age. *Trends Neurosci.*, **27**(4), 218–224.
- Prinz, A. A., Bucher, D., and Marder, E. (2004b, Dec). Similar network activity from disparate circuit parameters. *Nat. Neurosci.*, **7**(12), 1345–1352.
- Rall, W. (1969a, Dec). Distributions of potential in cylindrical coordinates and time constants for a membrane cylinder. *Biophys. J.*, **9**(12), 1509–1541.
- Rall, W. (1969b, Dec). Time constants and electrotonic length of membrane cylinders and neurons. *Biophys. J.*, **9**(12), 1483–1508.
- Reynolds, Jr., A. C. (1972). Convergent finite difference schemes for nonlinear parabolic equations. *SIAM J. Numerical Analysis*, **9**(4), 523–533.
- Rieke, F., Warland, D., de Ruyter van Steveninck, R. R., and Bialek, W. (1997). *Spikes: Exploring the Neural Code*. Computational Neuroscience. MIT Press, Cambridge, MA.
- Robinson, H. P. and Kawai, N. (1993, Sep). Injection of digitally synthesized synaptic conductance transients to measure the integrative properties of neurons. *J. Neurosci. Methods.*, **49**(3), 157–165.
- Roncaglia, R., Mannella, R., and Grigolini, P. (1994, Sep). Fractal properties of ion channels and diffusion. *Math. Biosci.*, **123**(1), 77–101.
- Rubinstein, J. T. (1995, Mar). Threshold fluctuations in an N sodium channel model of the node of ranvier. *Biophys. J.*, **68**(3), 779–785.
- Sakmann, B. and Neher, E. (1995). *Single-Channel Recording* (2nd edn). Plenum Press, New York.
- Schneidman, E., Freedman, B., and Segev, I. (1998). Ion channel stochasticity may be critical in determining the reliability and precision of spike timing. *Neural Computation*, **10**, 1679–1703.
- Schwarz, J. R. and Eikhof, G. (1987). Na currents and action potentials in rat myelinated nerve fibres at 20 and 37 degrees C. *Pflügers Arch.*, **409**, 569–577.
- Shadlen, M. N. and Newsome, W. T. (1998, May). The variable discharge of cortical neurons: implications for connectivity, computation, and information coding. *J. Neurosci.*, **18**(10), 3870–3896.
- Shannon, C. E. (1948). A mathematical theory of communication. *Bell Systems Technical Journal*, **27**, 373–423, 623–656.
- Sharp, A. A., O'Neil, M. B., Abbott, L. F., and Marder, E. (1993, Mar). Dynamic clamp: computer-generated conductances in real neurons. *J. Neurophysiol.*, **69**(3), 992–995.
- Sigworth, F. J. (1980, Oct). The variance of sodium current fluctuations at the node of ranvier. *J. Physiol.*, **307**, 97–129.

- Sigworth, F. J. and Neher, E. (1980, Oct). Single Na^+ channel currents observed in cultured rat muscle cells. *Nature*, **287**(5781), 447–449.
- Skaugen, E. and Walløe, L. (1979). Firing behaviour in a stochastic nerve membrane model based upon the Hodgkin-Huxley equations. *Acta Physiol. Scand.*, **107**, 343–363.
- Steinmetz, P. N., Manwani, A., Koch, C., London, M., and Segev, I. (2000, Sep). Subthreshold voltage noise due to channel fluctuations in active neuronal membranes. *J. Comput. Neurosci.*, **9**(2), 133–148.
- Strassberg, A. F. and DeFelice, L. J. (1993). Limitation of the Hodgkin-Huxley formalism: Effects of single channel kinetics on transmembrane voltage dynamics. *Neural. Comp.*, 843–855.
- Strichartz, G. R., Rogart, R. B., and Ritchie, J. M. (1979, Aug). Binding of radioactively labeled saxitoxin to the squid giant axon. *J. Membr. Biol.*, **48**(4), 357–364.
- Strong, S. P., Koberle, R., de Ruyter van Steveninck, R. R., and Bialek, W. (1998, Jan). Entropy and information in neural spike trains. *Phys. Rev. Lett.*, **80**(1), 197–200.
- van Kampen, N. G. (1992). *Stochastic Processes in Physics and Chemistry*. Elsevier Science, Amsterdam.
- Verveen, A. A. (1962). Axon diameter and fluctuation in excitability. *Acta Morphol. Neerl. Scand.*, **5**, 79–85.
- Verveen, A. A., Derksen, H. E., and Schick, K. L. (1967, Nov). Voltage fluctuations of neural membrane. *Nature*, **216**(115), 588–589.
- Walsh, J. B. (1986). *An Introduction to Stochastic Partial Differential Equations*, Volume 1180 of *Lecture Notes in Math*. Springer, Berlin.
- Waxman, S. G. and Bennett, M. V. (1972, Aug). Relative conduction velocities of small myelinated and non-myelinated fibres in the central nervous system. *Nat. New Biol.*, **238**(85), 217–219.
- White, J. A., Klink, R., Alonso, A., and Kay, A. R. (1998). Noise from voltage-gated ion channels may influence neuronal dynamics in the entorhinal cortex. *J. Neurophysiol.*, **80**, 262–269.
- White, J. A., Rubinstein, J. T., and Kay, A. R. (2000). Channel noise in neurons. *Trend Neurosci.*, **23**(3), 131–137.

NUMERICAL SIMULATIONS OF SDES AND SPDES FROM NEURAL SYSTEMS USING *SDELab*

Hasan Alzubaidi, Hagen Gilsing, and Tony Shardlow

12.1 Introduction

Many physical phenomena can be described by systems of ordinary or partial differential equations. Moreover, some of the parameters or initial conditions of such systems are often not completely known. To compensate for this lack of information and to obtain a more realistic description, the effects of randomness are taken into account by modelling an external source interacting with the system. The resulting equations are called *Stochastic Differential Equations* (SDEs) if the original system was an ordinary differential equation and *Stochastic Partial Differential Equations* (SPDEs) if the original system was a partial differential equation.

Mathematically, the Itô SDE is an object of the following type:

$$dx(t) = f(t, x(t))dt + g(t, x(t))dw(t), \quad x(t_0) = x_0 \quad (12.1)$$

and the counterpart Stratonovich SDE can be written as

$$dx(t) = \underline{f}(t, x(t))dt + g(t, x(t)) \circ dw(t), \quad x(t_0) = x_0 \quad (12.2)$$

where the notation ‘ \circ ’ in (12.2) denotes the use of Stratonovich calculus. $f, \underline{f} : \mathbb{R} \times \mathbb{R}^d \rightarrow \mathbb{R}^d$ are *drift* functions and $g : \mathbb{R} \times \mathbb{R}^d \rightarrow \mathbb{R}^{d \times p}$ is a *diffusion* function. $w(t)$ is an \mathbb{R}^p -valued Brownian motion. The initial condition $x(t_0) = x_0$ is deterministic data. The solution $x(t)$ of the above SDEs is a stochastic process satisfying

$$x(t) = x(t_0) + \int_0^t f(s, x(s))ds + \int_0^t g(s, x(s))dw(s) \quad (12.3)$$

and

$$x(t) = x(t_0) + \int_0^t \underline{f}(s, x(s))ds + \int_0^t g(s, x(s)) \circ dw(s), \quad (12.4)$$

in Itô and Stratonovich senses, respectively. We now briefly look at the definition of the stochastic integrals.

Stochastic integrals cannot be interpreted as the Riemann or Lebesgue integral because $w(t)$ is nowhere differentiable in the ordinary sense. Itô overcame

this problem by defining a stochastic integral using mean square convergence. Thus, the Itô integral $\int_0^T g dw$ over the interval $[0, T]$ is defined as the mean square limit of the sum

$$S_n = \sum_{j=0}^n g(\tau_j) \{w(t_{j+1}) - w(t_j)\}$$

with evaluation points $\tau_j = t_j$ for partitions $0 = t_0 < t_1 < \dots < t_{n+1} = T$, in the limit $\delta = \max_{0 \leq j \leq n} (t_{j+1} - t_j) \rightarrow 0$ and $n \rightarrow \infty$. In general, the evaluation point τ_j is

$$\tau_j = (1 - \lambda)t_j + \lambda t_{j+1}, \quad 0 \leq \lambda \leq 1.$$

When $\lambda = 0$ this leads to the Itô integral, and the case of the Stratonovich integral $\int_0^T g \circ dw$ as in (12.4) can be obtained when $\lambda = \frac{1}{2}$ (Kloeden and Platen, 1999). To understand more about the differences between two calculi, set $g = w$ in the sum S_n , yielding (Kloeden and Platen, 1999)

$$\int_0^T w(t)dw(t) = \frac{1}{2}w(T)^2 + \left(\lambda - \frac{1}{2}\right)T.$$

Thus, in the Itô case ($\lambda = 0$), we have $\int_0^T w(t)dw(t) = \frac{1}{2}w(T)^2 - \frac{1}{2}T$, which contains an additional term $(-\frac{1}{2}T)$ not present in the classical calculus. In contrast, Stratonovich calculus ($\lambda = \frac{1}{2}$) gives the same result for the integral $\int_0^T w(t)dw(t) = \frac{1}{2}w(T)^2$. This property of obeying the transformation rules of classical calculus is the main reason for using the Stratonovich calculus in many applications, for which the white noise is used as an idealization of a real noise process, whereas the Itô type is convenient to model external noise arising in many biological and physical systems where the noise is independent of the current state. Furthermore, the Itô integral satisfies the powerful martingale properties whereas the Stratonovich approach does not. Therefore, the Itô calculus is more appropriate for theoretical work and proofs. However, it is possible to move between the calculi (Itô and Stratonovich) using a simple transformation, since the solution of the Itô equation (12.1) can be written as the solution of the Stratonovich equation (12.2) with the modified drift function defined component-wise by

$$\underline{f}^i = f^i - \frac{1}{2} \sum_{j=1}^d \sum_{k=1}^p g_{jk} \frac{\partial g_{ik}}{\partial x_j} \quad i = 1, 2, \dots, d.$$

In the case of additive noise, $f = \underline{f}$ and the Itô and Stratonovich SDEs have the same solutions. Further information can be found in Kloeden and Platen (1991, 1999).

SDEs have many applications in fields such as chemistry, physical and engineering sciences, computational neuroscience, and finance. Unfortunately, being

able to solve an SDE explicitly is rare, so accurate numerical solutions play a crucial role. The main approach for numerical solutions is based on discrete time approximations, and either strong or weak numerical schemes (Kloeden, Platen, and Schurz, 1994). Strong approximations involve computing individual sample paths, while weak approximations involve computing approximations to the probability distribution of the solution, or, in general, a functional of the solution, such as the first or second moment.

Various software packages can be used to solve and analyse SDEs. For instance, MATLAB provides an ideal environment for numerical computation. Some examples can be found in Higham (2001). There is also a Maple package for both symbolic manipulation and numerical analysis of SDEs (Cyganowski, Grune, and Kloeden, 2001).

Recently, Gilsing and Shardlow (2007) created *SDELab*, a package for solving SDEs within MATLAB. *SDELab* features explicit and implicit integrators for a general class of Itô and Stratonovich SDEs. The current version of *SDELab* offers several standard numerical methods for the computation of strong solutions of (12.1)–(12.2) and generates configurable plots and subplots on demand. The *SDELab* package and instructions on its use can be found at either www.ma.ac.uk/~sdelab or www.mathematik.hu-berlin.de/~gilsing/sdelab.

One important class of methods is the Euler methods, with parameter α ; see (12.5). When $\alpha = 0$ we obtain the Euler–Maruyama method; when $\alpha = 1/2$ we obtain the trapezium rule; and when $\alpha = 1$ we obtain the implicit Euler–Maruyama method. This class of methods is referred to as the *Strong Itô Euler method with parameter α* in *SDELab*. Mathematically, the Euler approximation to the Itô process x satisfying (12.1) is defined as the sequence y_n given by the iterative scheme:

$$y_{n+1} = y_n + [(1 - \alpha)f(t_n, y_n) + \alpha f(t_{n+1}, y_{n+1})]\Delta t + g(t_n, y_n)\Delta w_n, \quad (12.5)$$

where $0 \leq \alpha \leq 1$, $t_n = t_0 + n\Delta t$, $n = 0, 1, \dots, N - 1$, where $N \in \mathbb{N}$. Δt is the time step and $\Delta w_n = w(t_{n+1}) - w(t_n)$ are increments of the Brownian motion which are normally distributed, with initial data $y_0 = x_0$. If the drift function f and the diffusion function g are well behaved, then the solution y_n of (12.5) converges strongly to the solution x of (12.1) at time t_n with strong order $1/2$, which means that

$$(\mathbb{E}[\|x(t_n) - y_n\|^2])^{1/2} = O(\Delta t^{1/2}) \quad \forall t_0 \leq t_n \leq T,$$

where $\mathbb{E}[\cdot]$ denotes expectation with respect to the law of the Brownian motion.

The Euler scheme is obtained by considering the first three terms of the Itô–Taylor expansion which is obtained by repeatedly applying Itô’s formula (Kloeden and Platen, 1999) (the Itô version of the chain rule) to the integrand functions in (12.3)–(12.4). The Euler method represents the simplest strong Taylor approximation, and more accurate strong Taylor schemes can be obtained by including further multiple stochastic integrals from the Itô–Taylor

expansion into the scheme (Kloeden and Platen, 1999). The basic example is the Milstein method, which is implemented in *SDELab* as the *Strong Itô Milstein method with parameter α* (Gilsing and Shardlow, 2007)

$$\begin{aligned} y_{n+1} = y_n + [(1 - \alpha)f(t_n, y_n) + \alpha f(t_{n+1}, y_{n+1})]\Delta t + g(t_n, y_n)\Delta w_n \\ + \sum_{j=1}^p \frac{\partial}{\partial y} g_j(t_n, y_n)(g(t_n, y_n)\xi_j), \quad y_0 = x_0 \end{aligned} \quad (12.6)$$

where $g_j(t, y)$ is the j th column of $g(t, y)$, $\xi_j = (I_{1j,n}, \dots, I_{pj,n})^T$ and

$$I_{ij,n} = \int_{t_n}^{t_{n+1}} \int_{t_n}^r dw_i(s)dw_j(r).$$

To derive this method, just one more term is added to the Euler scheme which raises the strong convergence order to 1 under regularity on f and g (Kloeden and Platen, 1999, Higham, 2001). More information about implementing this method and approximating ξ_j can be found in Gilsing and Shardlow (2007).

SDELab also provides an efficient method for small noise problems called the *second-order Backward Differentiation Formula* which is referred to as *Strong Itô BDF2* in *SDELab*:

$$\begin{aligned} y_{n+1} = \frac{4}{3}y_n - \frac{1}{3}y_{n-1} + \frac{2}{3}f(t_{n+1}, y_{n+1})\Delta t \\ + g(t_n, y_n)\Delta w_n - \frac{1}{3}g(t_{n-1}, y_{n-1})\Delta w_{n-1} \end{aligned} \quad (12.7)$$

for $n \geq 2$, with initial values given by

$$y_1 = y_0 + \left[\frac{1}{2}f(t_0, y_0) + \frac{1}{2}f(t_1, y_1) \right] \Delta t + g(t_0, y_0)\Delta w_0, \quad y_0 = x_0.$$

Thus, if we consider (12.1) with diffusion function $\sigma g(t, x)dw$ where σ is a small parameter, then its solution y_n obtaining from the Euler method with $\alpha = 0.5$ and the BDF2 method satisfies $(\mathbb{E}[\|x(t_n) - y_n\|^2])^{1/2} = O(\Delta t^2 + \sigma\Delta t + \sigma^2\Delta t^{1/2})$ $\forall t_0 \leq t_n \leq T$. So if the noise $\sigma \ll \Delta t$ then the error is of order $O(\Delta t^2 + \sigma\Delta t)$ where $O(\sigma^2\Delta t^{1/2})$ becomes negligible (Gilsing and Shardlow, 2007).

The main aim of this chapter is to illustrate using the Hodgkin–Huxley (HH) and FitzHugh–Nagumo (FHN) equations how SDEs and SPDEs can be solved numerically, and to give the reader tools to solve their own SDEs and SPDEs in *SDELab*.

The HH model forms the basis for all models of excitable membrane behaviour, although it was originally developed by Hodgkin and Huxley (1952) to explain the action potential in the long giant axon of squid nerve cells. FitzHugh

(1960, 1961) studied the model and then reduced it to a two-variable model in order to apply phase plane analysis. Later, Nagumo, Arimoto, and Yosizawa (1962) constructed a circuit using tunnel diodes for the nonlinear channels modelled by the FitzHugh equations, and thus these equations have become known as the FitzHugh–Nagumo model.

There are many sources of noise which can be modelled for these systems (Mishra *et al.*, 2005). For instance, the noise may come from the randomness of opening and closing times of ionic channels. It may also come from synaptic events in the form of additive noisy synaptic current, which we consider for the models in the present chapter.

This chapter is arranged as follows. In Section 12.2, we consider the stochastic space-clamped HH model and study some of the effects of additive noise on spike generation using the *SDELab* package. In Section 12.3, we consider an SPDE system given by the FHN model with additive space-time white noise and discuss how we can simulate this system using the *SDELab* package. The effectiveness of small noise algorithms is also considered.

12.2 Stochastic HH model with space-clamp technique

The Hodgkin–Huxley model is a mathematical description of electrical excitation and propagation along a nerve axon. In response to a stimulus, the cell membrane elicits an action potential (spike) which propagates along the nerve axon. The current flow across the cell membrane depends on the capacitance of the membrane and the conductance of ion channels, in particular the voltage-dependent conductances (sodium and potassium) as well as a leakage conductance. The voltage and current flow are assumed to obey Ohm's law. In this section, we consider the HH model without the extra complication of spatial variation in the membrane potential (known as the space-clamped model) and with additive Gaussian noise input current. In the literature, there has been interest in the stochastic activity of neurons and the influence of noise on generating spikes in regard to understanding neuronal information processing (Tuckwell, 1986). Several works have studied the effects of noise on the HH model. See, for example, Tuckwell (2005), Tuckwell and Wan (2005), Tuckwell and Roderigues (1998), Horikawa (1991), Pankratova, Polovinkin, and Mosekilde (2005), Zhou and Kurths (2003), Rowat (2007). Here we consider the following stochastic version of the HH model (Tuckwell, 1986):

$$\begin{aligned} C_m dv &= (\bar{g}_k n^4 (v_k - v) + \bar{g}_{N_a} m^3 h (v_{N_a} - v) + \bar{g}_l (v_l - v) + \mu) dt + \sigma dw(t) \\ \frac{dn}{dt} &= \alpha_n(v)(1 - n) - \beta_n(v)n \\ \frac{dm}{dt} &= \alpha_m(v)(1 - m) - \beta_m(v)m \\ \frac{dh}{dt} &= \alpha_h(v)(1 - h) - \beta_h(v)h \end{aligned} \tag{12.8}$$

where μ and σ are constants representing the input current and the noise intensity respectively, and $\{w(t), t \geq 0\}$ is \mathbb{R} -valued Brownian motion. $n(t)$, $m(t)$, and $h(t)$ represent the fractions of potassium channel activation, sodium channel activation, and sodium channel inactivation respectively (see Fig. 12.1). The values of these conductance variables are between 0 and 1. C_m is the membrane capacitance in $\mu\text{F}/\text{cm}^2$ and $v(t)$ is the membrane potential in mV. \bar{g}_k , \bar{g}_{N_a} and \bar{g}_l represent the maximal values of membrane conductances for potassium, sodium and leakage ions respectively. v_k , v_{N_a} and v_l are the corresponding reversal potentials. The α and β functions are given by (Hodgkin and Huxley, 1952)

$$\begin{aligned}\alpha_n(v) &= \frac{10-v}{100(e^{(10-v)/10}-1)}, & \beta_n(v) &= \frac{1}{8}e^{-v/80}, \\ \alpha_m(v) &= \frac{25-v}{10(e^{(25-v)/10}-1)}, & \beta_m(v) &= 4e^{-v/18}, \\ \alpha_h(v) &= \frac{7}{100}e^{-v/20}, & \beta_h(v) &= \frac{1}{e^{(30-v)/10}+1}.\end{aligned}$$

Following Hodgkin and Huxley (1952), we set the parameters of this model to $C_m = 1 \mu\text{F}/\text{cm}^2$, $\bar{g}_k = 36 \text{ mS}/\text{cm}^2$, $\bar{g}_{N_a} = 120 \text{ mS}/\text{cm}^2$, $\bar{g}_l = 0.3 \text{ mS}/\text{cm}^2$, $v_k = -12 \text{ mV}$, $v_{N_a} = 115 \text{ mV}$ and $v_l = 10.613 \text{ mV}$, and hence the resting potential is 0 mV.

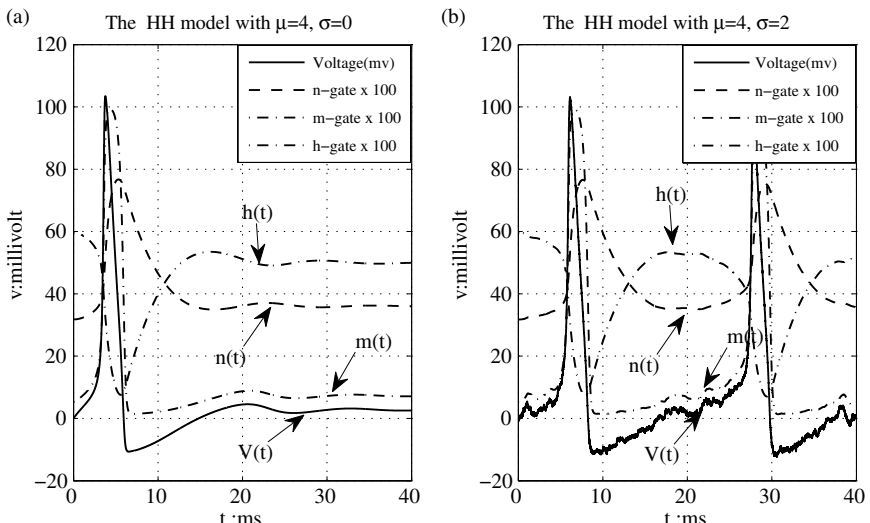


FIG. 12.1: The conductance variables $n(t)$, $m(t)$, and $h(t)$ for the HH model with $\mu = 4$ and (a) $\sigma = 0$, (b) $\sigma = 2$.

To solve the HH system using *SDELab*, we rewrite the model in the form (12.1), where $p = 1$ and $d = 4$:

$$dx(t) = f(t, x(t))dt + g(t, x(t))dw \quad (12.9)$$

where $x = [v, n, m, h]^T$, the drift function is

$$f(t, x) = \begin{bmatrix} C_1 n^4(v_k - v) + C_2 m^3 h(v_{N_a} - v) + C_3(v_l - v) \\ \alpha_n(v)(1 - n) - \beta_n(v)n \\ \alpha_m(v)(1 - m) - \beta_m(v)m \\ \alpha_h(v)(1 - h) - \beta_h(v)h \end{bmatrix}$$

and the diffusion function is $g(t, x) = [\sigma, 0, 0, 0]^T$. We use the initial condition $x_0 = [v_0, n_0, m_0, h_0]^T$, where $v_0 = 0$,

$$\begin{aligned} n_0 &= \frac{\alpha_n(v_0)}{\alpha_n(v_0) + \beta_n(v_0)}, \\ m_0 &= \frac{\alpha_m(v_0)}{\alpha_m(v_0) + \beta_m(v_0)} \end{aligned}$$

and

$$h_0 = \frac{\alpha_h(v_0)}{\alpha_h(v_0) + \beta_h(v_0)}.$$

The constants are $C_1 = \bar{g}_k/C_m$, $C_2 = \bar{g}_{N_a}/C_m$, and $C_3 = \bar{g}_l/C_m$.

Note that the noise intensity σ in the HH model is often large (Tuckwell, 2005, Tuckwell and Wan, 2005), and that the system is stiff, so the appropriate integrators are semi-implicit ($\alpha = 1/2$) or fully implicit ($\alpha = 1$) methods. Since we have chosen additive noise, the order of strong convergence of the Euler scheme is 1 under appropriate smoothness assumptions on the drift function (Kloeden and Platen, 1999). Moreover, the Milstein scheme in the case of additive noise is reduced to the Euler scheme which involves no multiple stochastic integrals. Hence, in this case, the Euler method should be selected.

12.2.1 Solving the HH system using SDELab

The codes of the HH model and its drift and diffusion functions for use in *SDELab* are shown below in codes 1, 2 and 3 respectively, and for simplicity, a 's and b 's are put in these codes instead of α 's and β 's.

To start using *SDELab* within MATLAB, type

```
sdelab_init;
```

and to find approximate paths (strong approximations) of (12.1) and (12.2), the following function can be used:

```
[t,y]= sdesolve_strong_solutions (fcn,tspan,y0,p,opt,params);
```

which requires basic information (arguments) in order to solve SDEs appropriately and returns values in $[t, y]$. In the following *SDELab* codes for the HH model we describe the functions and their arguments.

The first code (code 1) for the Hodgkin–Huxley model can be described as follows:

1. The first step involves setting up the problem dimension, time interval, and initial data

```
d = 4; %dimension of y
p = 1; % dimension of w(t)
tspan = [0,40]; % time interval
%%%%%%%%%%%%%%%%%%%%%%%%%%%%%%%%%%%%%
% compute initial data y0
%%%%%%%%%%%%%%%%%%%%%%%%%%%%%%%%%%%%%
a0_n=0.1/(exp(1)-1); b0_n=0.125;
a0_m=2.5/(exp(2.5)-1); b0_m=4;
a0_h=0.07; b0_h=1/(exp(3)+1);
y0=[0;a0_n/(a0_n+b0_n);a0_m/(a0_m+b0_m);a0_h/(a0_h+b0_h)]
```

The above information is used later in the function

```
sdesolve_strong_solutions(fcn,tspan,y0,p,opt,params);
```

where the interval time, initial data y_0 , and the dimension p of $w(t)$ are given as the second, third, and fourth arguments, respectively.

2. The second step involves defining the drift f and diffusion g functions which are specified by the single structure **fcn**. These coefficient functions can be specified in two styles in *SDELab*; MATLAB style functions and Dynamic Library (DL) style functions. Here, we concentrate on MATLAB style functions which can be passed as the first argument to **sdesolve_strong_solutions (fcn,tspan,y0,p,opt,params)** by setting

```
fcn.drift='HH_drift';
fcn.diff_noise='HH_diff_noise';
```

where **HH_drift** and **HH_diff_noise** are the names of m-files of drift and diffusion functions of the HH model (see codes 2 and 3 below).

3. Define the parameters of the drift and diffusion functions, which are the last argument for **sdesolve_strong_solutions** and are specified as **params**.

```
params.Mu=2.5;
params.sigma=0;
```

4. The fifth argument is **opt** which is a MATLAB structure whose fields set *SDELab* options. In our code, we set

```
opt.IntegrationMethod='StrongItoEuler';
opt.StrongItoEuler.Alpha=0.5;
opt.MaxStepSize=1e-3;
opt.MSISGenRNG.SeedZig = 23;
```

where the first option sets the integration method and the second sets the parameter α of the Euler method. In *SDELab*, the default integration method is **StrongItoEuler** and the options are (Gilsing and Shardlow, 2007)

StrongItoMilstein,	StrongItoBDF2,
StrongStratoEulerHeun,	StrongStratoMilstein

The parameter α in the Euler and Milstein methods for the Itô and the Stratonovich equations is controlled by

StrongItoEuler.Alpha,	StrongItoMilstein.Alpha,
StrongStratoEulerHeun.Alpha,	StrongStratoMilstein.Alpha

The third option (**MaxStepSize**) represents the maximum value of the time step Δt , which in our code is equal to 10^{-3} . If it is not specified the default value $((T - t_0)/100)$ is used.

The last option in our code is the seed for the random number generator. In fact, there are many other options which are used for the control of the nonlinear solver and for the control of the output and plot behaviour. For further information, see Gilsing and Shardlow (2007).

5. Finally, we find the strong numerical solutions using the solver function **sdesolve_strong_solutions** which has the above arguments and returns values in $[t, y]$. t represents the time points and y is a matrix of state vectors obtained as follows

```
[t,y]= sdesolve_strong_solutions (fcn,tspan,y0,p,opt,params)
```

Moreover, if $[t, y]$ is omitted, the MATLAB figure appears and the approximate paths are plotted as they are computed. The output plot of these results can be produced by a set of configurable options which are passed with an option structure as an argument to the calling *SDELab* function. For instance, the plot types can be controlled by the option:

```
opt.OutputPlotType='sdesolve_plot_path' %path plot (default)
opt.OutputPlotType='sdesolve_plot_phase' %phase plot
opt.OutputPlotType='sdesolve_plot_time_phase'%time-phase plot
opt.OutputPlotType='sdesolve_plot_phase3' %phase3 plot
```

The drift function of the HH model is defined by the following code.

Code2: m-file of the drift function of the HH model:

```
function z=HH_drift(t,y,varargin)
Mu=varargin{2}.Mu; % Extract parameters
%%%%%%%%%%%%%
% conductance variables of potassium,sodium and leakage
%%%%%%%%%%%%%
g_k=36;g_Na=120;g_L=0.3;
C_m=1; % the membrane capacitance

C1=g_k/C_m;C2=g_Na/C_m;C3=g_L/C_m;
%%%%%%%%%%%%%
% Constants of resting potential of such ions
v_k=-12;v_Na=115; v_L=10.613;
a_n=(10-y(1))/(100*(exp((10-y(1))/10)-1));
b_n=exp(-y(1)/80)/8;
a_m=(25-y(1))/(10*(exp((25-y(1))/10)-1));
b_m=4*exp(-y(1)/18);
a_h=(7*exp(-y(1)/20))/100;
b_h=1/(exp((30-y(1))/10)+1);
%%%%%%%%%%%%%
%Compute drift function of HH model
%%%%%%%%%%%%%
z1=(C1*(v_k-y(1))*(y(2)^4))+(C2*(v_Na-y(1))*(y(3)^3)*y(4))
+(C3*(v_L-y(1)))+ Mu;
z2=a_n*(1-y(2))-b_n*y(2);
z3=a_m*(1-y(3))-b_m*y(3);
z4=a_h*(1-y(4))-b_h*y(4);
z=[z1;z2;z3;z4]; %Return values of the drift function
%%%%%%%%%%%%%
```

The MATLAB style function describing the drift function of the HH model satisfies the call syntax

```
function z=HH_drift(t,y,varargin)
```

where its arguments are the time value t , a real vector y of length d representing the current state value, and a list of optional arguments `varargin`. The returned value z is a real vector of length d which represents the value of f at t and y . The solution of a stiff system with a nonlinear drift requires a nonlinear equation solver. In fact we need the nonlinear solver as we are using an implicit method. *SDELab* uses the freeware package MinPack-1.3 which provides software for solving nonlinear equations. To speed-up the solver MinPack-1.3, the user may provide spatial derivatives of the drift function which can be utilized in *SDELab* as the function `drift_dy`, which returns the *Jacobian* matrix of

f with entries $\partial f_i(t, y) / \partial y_j$ for $i, j = 1, 2, \dots, d$ (Gilsing and Shardlow, 2007). The MATLAB style function describing the spatial derivatives of the drift f satisfies the call syntax:

```
function z=HH_drift_dy(t,y,varargin)
```

and can be passed as an argument to `sdesolve_strong_solutions` by setting `fcn.drift_dy='HH_drift_dy'` where `HH_drift_dy` is the name of the m-file of the spatial drift of the HH model. However, `drift_dy` is optional, so if no spatial derivatives of f are passed, the algorithm with forward-difference approximations of the spatial derivative is used.

The diffusion function g of the HH model is defined by the following code:

Code3: m-file for the diffusion function of the HH model

```
function z=HH_diff_noise(t,y,dw,flag,varargin)
sigma=varargin{2}.sigma; %extract parameters
B=[sigma;0;0;0]; % compute the diffusion
if(flag)
    z=B;
else z=B*dw;
end
```

The MATLAB style function describing the diffusion function of the HH model satisfies the call syntax

```
function z=HH_diff_noise(t,y,dw,flag,varargin)
```

where its arguments are the time value t , a real vector y of length d representing the current state value, a real vector of length p representing Brownian increment values, a flag indication, and a list of optional arguments `varargin`. The returned value z is either a real vector of length d if $flag = 0$, representing the value of gdw (which is beneficial for sparse diffusion matrices), or if the flag is not zero, the same size as the matrix g . More details on the implementation for both Itô and Stratonovich can be found in Gilsing and Shardlow (2007).

12.2.2 The effectiveness of noise on generating spikes

Repetitive firing in the space-clamped HH model in response to an applied current has been studied and analysed in the literature, particularly in the noiseless case; see, for example Hassard (1978), Rinzel and Miller (1980), Guttman, Lewis, and Rinzel (1980), Stein (1967) and Koch (1999). Here, we present a numerical simulation in this context for the standard HH model, and our results can be summarized as follows:

1. In the absence of noise($\sigma = 0$).

The minimal current required to fire at least one spike is $\mu = 2.5 \mu\text{A}/\text{cm}^2$, and a threshold current required to elicit an infinite train of spikes is $I_0 = 6.25 \mu\text{A}/\text{cm}^2$, see Fig. 12.2.

According to Hassard (1978), Rinzel and Miller (1980), Guttman, Lewis, and Rinzel (1980) and Stein (1967), over a range of constant applied current

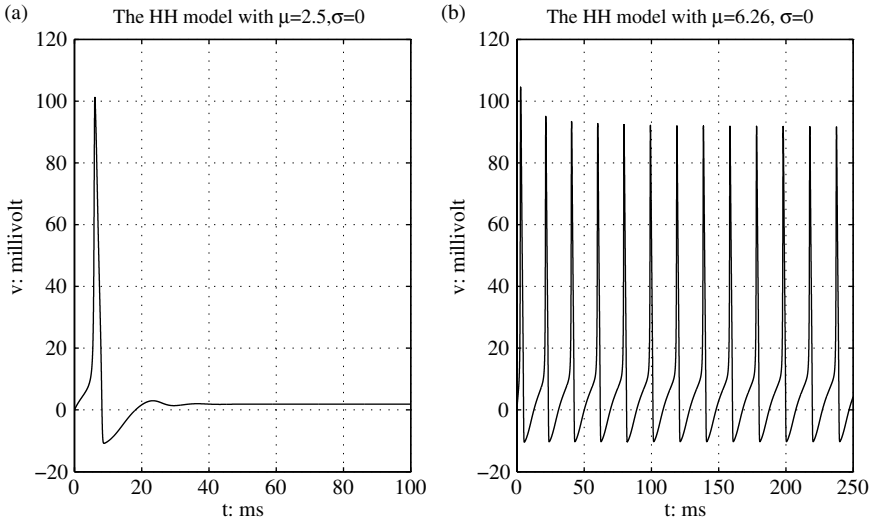


FIG. 12.2: In the absence of noise, (a) shows the current needed to fire a spike ($\mu = 2.5$) and (b) shows that the current required to produce an infinite train of spikes must be greater than $I_0 = 6.25$. In the figure, $\mu = 6.26$ is just above I_0 .

μ , the HH equations have limit cycle solutions when $I_0 < \mu < I_2$, where $I_2 = 154 \mu\text{A/cm}^2$ (Hassard, 1978). If $\mu < I_0$, no limit cycle solutions occur and the initial conditions go to a fixed point, see Fig. 12.3(a) for $\mu = 3 < I_0$. When μ is increased above I_0 , the HH equations start to generate an infinite train of spikes. I_0 is considered a critical current at which the firing frequency jumps sharply from zero to over 50 spike/s (Stein, 1967) as shown in Fig. 12.5.

Between I_0 and I_1 , where $I_1 \cong 9.8 < I_2$ (Hassard, 1978), the solutions either decay to the stable fixed point or grow to a stable limit cycle depending on the initial conditions. This coexistence of stable solutions may demand the existence of a surface containing unstable limit cycles which separates the domains of attractions of these two stable states, see Hassard (1978) and Rinzel and Miller (1980) for further details. If μ is increased towards I_1 , the domain of attraction of the fixed point becomes smaller and decreases to zero when μ reaches I_1 , as shown in Fig. 12.3(b) and Fig. 12.3(c). So the system has only periodic solutions for the current range $I_1 < \mu < I_2$ (Rinzel and Miller, 1980), see Fig. 12.3(c) and Fig. 12.4(a) for $\mu = 20$ as an example.

As μ is increased above I_1 , the spiking frequency also increases, as shown in Fig. 12.5. However, there is a limited range of frequencies, between 53 and 138 spike/s (Koch, 1999). Thus, if μ is further increased towards I_2 ,

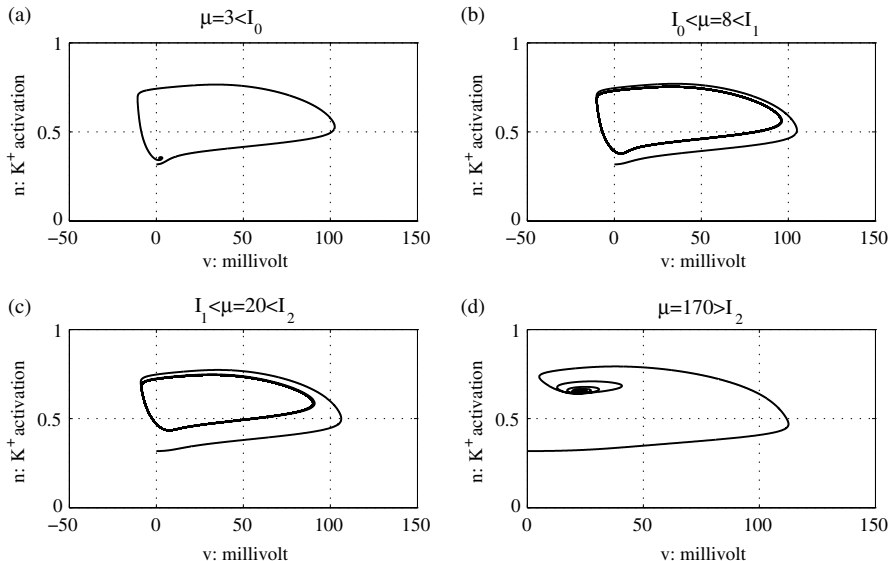


FIG. 12.3: Examples for the dynamic behaviour that the solutions of the HH equations can display: (a) $\mu = 3 < I_0$ (b) $I_0 < \mu = 8 < I_1$ (c) $I_1 < \mu = 20 < I_2$ and (d) $\mu = 170 > I_2$.

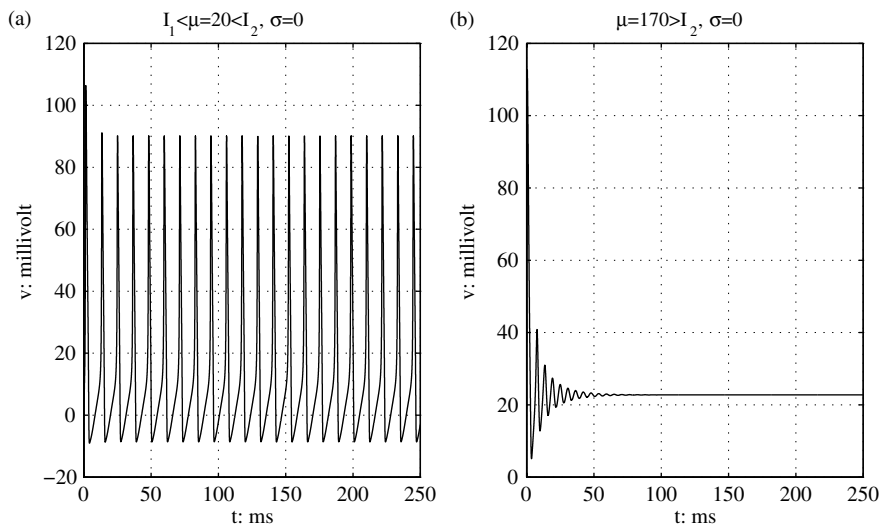


FIG. 12.4: (a) Periodic solutions that the system has when $I_1 < \mu < I_2$. (b) The case when $\mu > I_2$ where the system shows oscillatory behaviour but no true spikes due to the blocking of the nerve after a few spikes.

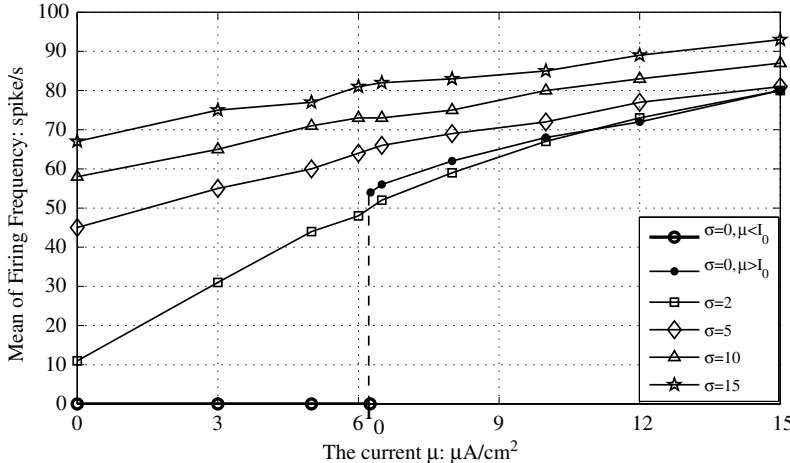


FIG. 12.5: The mean firing frequency versus the current μ for different values of noise σ .

the frequency begins to decrease and when μ passes I_2 , the nerve becomes blocked after a few spikes (Stein, 1967). This behaviour is due to the high injected current in the axon which causes the membrane to fail to repolarize sufficiently between spikes, in order to relieve sodium inactivation. The membrane shows oscillatory behaviour but no true action potentials (Koch, 1999) as shown in Fig. 12.4(b). The system has a stable fixed point, see Fig. 12.3(d). For further details about the dynamic behaviour of solutions of the HH equations, and the analysis of the stability near the parameters I_k , $k = 0, 1, 2$, see Hassard (1978) and Izhikevich (2000).

2. To investigate the influence of noise on the firing frequency of the HH model, different values of μ are chosen relative to the critical values I_0 , I_1 , and I_2 with different levels of noise σ . For $\mu < I_0$ we take $\mu = 0, 3, 5$, and 6 , and we choose $\mu = 6.5$ and 8 between I_0 and I_1 . For the current range $I_1 < \mu < I_2$, we choose $\mu = 10, 12$, and 15 , all of which are close to I_1 in order to avoid the decrease in the frequency when μ is very high. The results of our simulation are summarized in Fig. 12.5 where the mean firing frequency is plotted versus the current μ with different values of noise intensity $\sigma = 0, 2, 5, 10$, and 15 . The results are obtained from 25 trials for each value of μ over an interval of time $[0, 250]$.

In the absence of noise, no limit cycles are generated when $\mu < I_0$, and if μ is increased above I_0 , the firing frequency jumps from 0 to over 50 spikes/s. This discontinuity in the firing frequency (dashed line in Fig. 12.5 for the curve of $\sigma = 0$) is eliminated when suitable noise is added, as shown by the curves in Fig. 12.5 for other values of $\sigma = 2, 5, 10$, and 15 . Thus with noise, the input is strong enough to generate spikes with non-zero

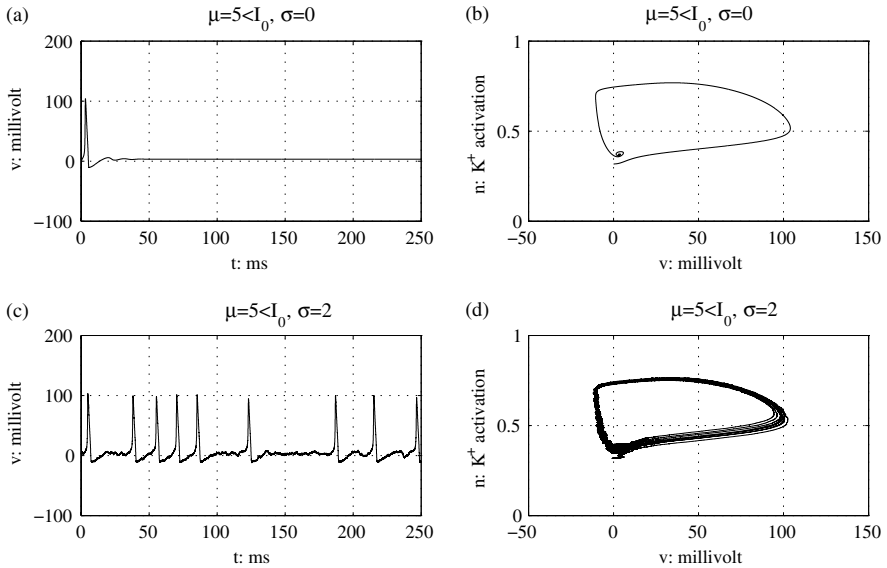


FIG. 12.6: Trajectories of voltage variable v of the HH system when $\mu = 5$ (less than the critical value I_0) with (a) $\sigma = 0$ (c) $\sigma = 2$, and (b) and (d): the projection v versus n for the corresponding cases, respectively.

average frequency even when $\mu < I_0$ (Koch, 1999, Rowat, 2007) as shown in Fig. 12.6. Furthermore, it is clear that additive noise also increases the frequency for values of μ above I_0 , see Fig. 12.5.

12.3 The FHN model with additive space-time white noise

SDELab can be used to solve and analyse some SPDEs such as the FHN equation with additive space-time white noise. This will be discussed in detail in this section. In practice, many kinds of dynamics with stochastic influence in nature can be modelled by SPDEs and the state spaces of their solutions are necessarily infinite dimensional.

A rich body of theoretical work has been developed for SPDEs (Prato and Zabczyk, 1992). Nevertheless, few of these equations have analytic solutions, so there is growing interest in producing numerical solutions for SPDEs. For instance, Shardlow (1999, 2005), Gaines (1995), Gyongy (1998) and Davie and Gaines (2001) study parabolic SPDEs that are discretized spatially, to obtain a system of SDEs which can be solved by numerical methods for SDEs. This approach will be implemented here for the stochastic FHN equations.

Consider the FHN model with additive space-time noise:

$$\begin{aligned} du &= (D\Delta u + F(u, v) + \mu)dt + \sigma dw(t, x) \\ dv &= G(u, v)dt \end{aligned} \tag{12.10}$$

with boundary conditions $u(0, t) = u(1, t) = 0$ and initial data $u(x, 0) = u_0$, $v(x, 0) = v_0$ and $F, G : \mathbb{R} \times \mathbb{R} \rightarrow \mathbb{R}$. μ and σ are real numbers. $\Delta = \partial^2 / \partial x^2$, and $D\Delta u$ represents the propagation of the potential u at a rate determined by the diffusion coefficient D . $w(t, x)$ is a Wiener process with covariance Q . To understand this consider $e_j = \sqrt{2} \sin(j\pi x)$, $j = 1, 2, \dots$, a complete orthonormal system for $L_2(0, 1)$. Then the Wiener process $w(t, x)$ with covariance Q can be written in terms of its Fourier series. If Q has an eigenvalue $\alpha_j > 0$ and corresponding eigenfunction $\sin(j\pi x)$, then

$$w(t, x) = \sum_{j=1}^{\infty} \sqrt{2\alpha_j} \sin(j\pi x) \beta_j(t),$$

where $\beta_j(t)$ is a sequence of independent real-valued Brownian motions. For our work, we consider a space-time white noise, so $Q = I$ and thus $\alpha_j = 1 \forall j = 1, 2, \dots$ Thus

$$w(t, x) = \sum_{j=1}^{\infty} \sqrt{2} \sin(j\pi x) \beta_j(t).$$

Following FitzHugh (1961), the function $F(u, v)$ is a cubic function which can be written as $F(u, v) = u(1-u)(u-a) - v$ where $0 < a < 1$ and $G(u, v) = b(u-\gamma v)$ where $b, \gamma \in \mathbb{R}$ (Tuckwell, 1986). To obtain a suitable suprathreshold response, a should be less than $1/2$ (Tuckwell and Roderigues, 1998). The variable u represents the fast (voltage-like) variable and v represents the slow or recovery variable (potassium gating variable). The initial data are chosen as the resting value of u ($u_0 = 0$) and the equilibrium state of v ($v_0 = n_0$).

We now discuss how to discretize the FitzHugh–Nagumo model spatially to get a system of SDEs which can be solved by *SDELab*. To do that, consider a time step Δt and a grid size $\Delta x = 1/d + 1$ where $d \in \mathbb{N}$. The Wiener process $w(t, x)$ can be approximated by truncating its Fourier expansion after d terms (Shardlow, 1999), so we consider the \mathbb{R}^d -valued process $\tilde{w}(t)$ with components

$$\tilde{w}_i(t) = \sum_{j=1}^d \sqrt{2} \sin(j\pi x_i) \beta_j(t)$$

where $x_i = i\Delta x$, $i = 1, 2, \dots, d$, is the spatial grid. Moreover, the standard three-point finite difference approximation A is used to approximate the Laplacian Δ , where A is a tridiagonal matrix $\in \mathbb{R}^d \times \mathbb{R}^d$ and $A_{ii} = -2$, $A_{i+1,i} = 1$ for $1 \leq i \leq d-1$ and $A_{i-1,i} = 1$ for $2 \leq i \leq d$. This leads to the following spatial discretization scheme:

$$\begin{aligned} d\tilde{u} &= \left[\frac{D}{(\Delta x)^2} A \tilde{u} + F(\tilde{u}, \tilde{v}) + \mu \right] dt + \sigma d\tilde{w}(t) \\ d\tilde{v} &= G(\tilde{u}, \tilde{v}) dt \end{aligned} \tag{12.11}$$

where $\tilde{u} \in \mathbb{R}^d$ with components $\tilde{u}_i = u(i\Delta x, t)$ and $\tilde{v} \in \mathbb{R}^d$ with components $\tilde{v}_i = v(i\Delta x, t)$, $F(\tilde{u}, \tilde{v})$ and $G(\tilde{u}, \tilde{v}) : \mathbb{R}^d \times \mathbb{R}^d \rightarrow \mathbb{R}^d$ where $F_i = (\tilde{u}_i(1 - \tilde{u}_i)(\tilde{u}_i - a) - \tilde{v}_i)$ and $G_i = b(\tilde{u}_i - \gamma \tilde{v}_i), i = 1, 2, \dots, d$. $d\tilde{w}(t) = Qd\beta(t)$ where $Q \in \mathbb{R}^d \times \mathbb{R}^d$ with components $Q_{ij} = \sqrt{2} \sin(ij\pi\Delta x)$ and $d\beta(t)$ are \mathbb{R}^d -valued Brownian motion since $d\beta(t) = [d\beta_1(t), d\beta_2(t), \dots, d\beta_d(t)]^T$.

12.3.1 Numerical Simulation of SPDEs of the FitzHugh–Nagumo model using SDELab

Spatially discretizing the system (12.10) of SPDEs for the FHN model yields a system (12.11) of SDEs which can be solved by *SDELab*. Firstly, we rewrite these as

$$dY = f(t, Y)dt + g(t, Y)d\beta(t) \quad (12.12)$$

where $Y = [\tilde{u}_1, \tilde{u}_2, \dots, \tilde{u}_d, \tilde{v}_1, \tilde{v}_2, \dots, \tilde{v}_d]^T \in \mathbb{R}^{2d}$, the drift function

$$f(Y, t) = \begin{bmatrix} \frac{D}{(\Delta x)^2} A\tilde{u} + F(\tilde{u}, \tilde{v}) + \mu \\ G(\tilde{u}, \tilde{v}) \end{bmatrix},$$

where $F(\tilde{u}, \tilde{v})$ and $G(\tilde{u}, \tilde{v})$ are interpreted as vectors with entries $F(\tilde{u}_1, \tilde{v}_1)$, $F(\tilde{u}_2, \tilde{v}_2)$, etc. and $g = \begin{bmatrix} \sigma Q \\ 0 \end{bmatrix}$ is a diffusion function, with initial condition

$$Y_0 = \begin{bmatrix} u_0 \\ v_0 \end{bmatrix} \in \mathbb{R}^{2d} \text{ since } u_0 = \begin{bmatrix} 0 \\ 0 \\ \vdots \\ 0 \end{bmatrix} \in \mathbb{R}^d \text{ and } v_0 = \begin{bmatrix} n_0 \\ n_0 \\ \vdots \\ n_0 \end{bmatrix} \in \mathbb{R}^d.$$

The codes for the FHN equations and their drift and diffusion functions are shown in Appendix A in codes 4, 5, and 6 respectively. The parameters of the model are specified as $D = 0.01$, $a = 0.05$, $\mu = 0.5$, $\gamma = 0.5$, and $b = 0.008$ with time step $\Delta t = 0.01$ and spatial step $\Delta x = 0.1$.

To avoid problems with stability and to deal efficiently with small intensity of noise for the FHN model where $\sigma \ll 1$, the Euler method with $\alpha = 1/2$ and the BDF2 method are suitable methods.

12.3.2 Trajectories

To investigate the influence of additive noise intensity σ on the trajectories of the fast variable u using our *SDELab* codes (see Appendix A), different values for the noise intensity σ are chosen with other parameters fixed. The results of such numerical simulations can be summarized as follows:

- When σ is very small, as shown in Fig. 12.7 for $\sigma = 0.001$, the paths are close to the deterministic case (shown in Fig. 12.8).
- If the noise parameter is increased to, for example, $\sigma = 0.01$, spikes can be realized although the paths are erratic as illustrated in Fig. 12.9.

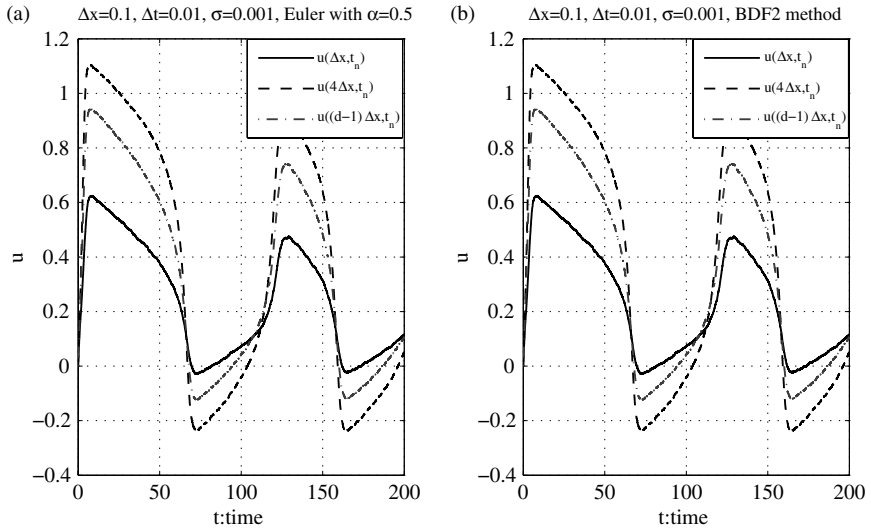


FIG. 12.7: Numerical simulation of the FHN model when $\sigma = 0.001 \ll 1$, for which the trajectories are very close to the deterministic case. The figure shows the trajectories of the fast variable: (a) when using the Euler method with $\alpha = 0.5$; (b) when using the BDF2 method.

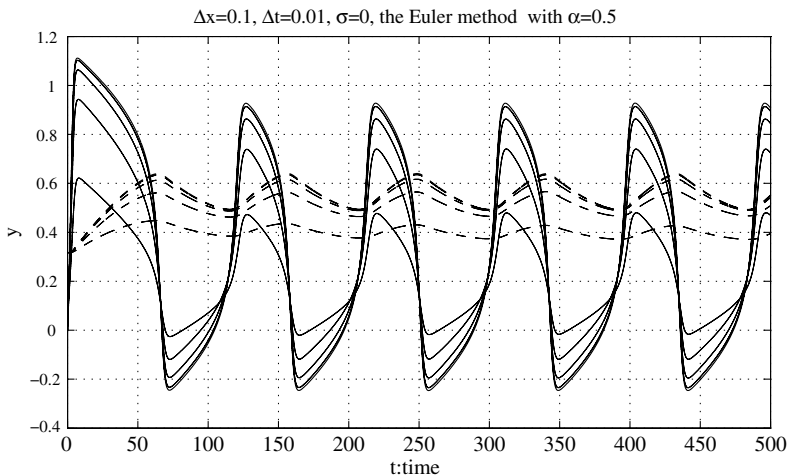


FIG. 12.8: An illustration of the spikes generated by numerical simulation of SPDEs for the FHN system using the Euler method ($\alpha = 0.5$) with $\Delta t = 0.01, \Delta x = 0.1$ and $\sigma = 0$. The fast variable $u(i\Delta x, t)$, where $i = 1, 2, \dots, d = 9$, is represented by solid lines and the recovery variable $v(i\Delta x, t)$, where $i = 1, 2, \dots, d$, by dashed lines.

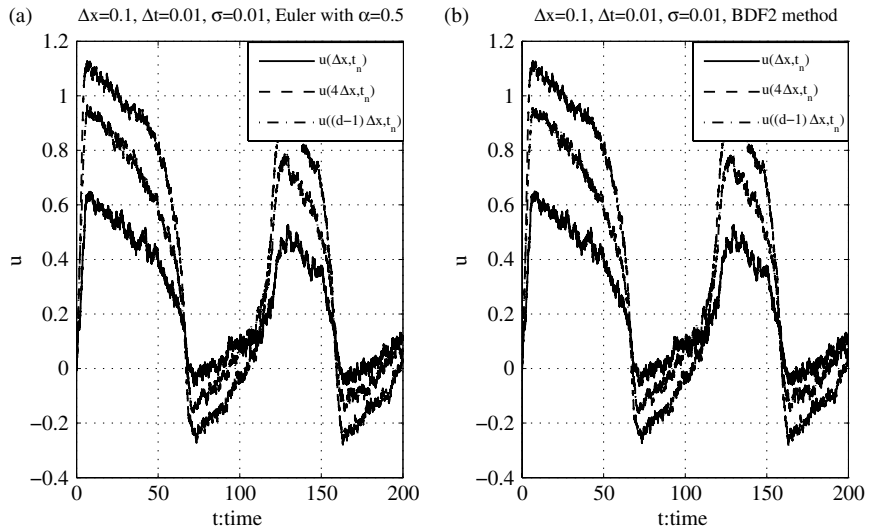


FIG. 12.9: Trajectories of the fast variable u when $\sigma = 0.01$ (a) using the Euler method with $\alpha = 0.5$ and (b) using the BDF2 method. The spikes can be recognized despite the irregularity in their paths.

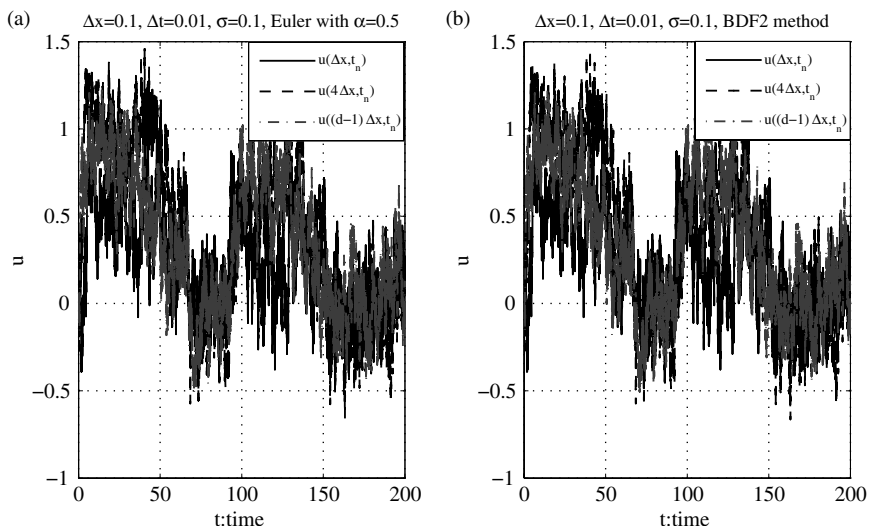


FIG. 12.10: Erratic paths of the fast variable u when $\sigma = 0.1$ (a) using the Euler method ($\alpha = 0.5$) and (b) using the BDF2 method. The noise is dominant so it is difficult to recognize the spikes.

- When the noise is further increased to $\sigma = 0.1$, the irregularity in paths is also increased. This is shown in Fig. 12.10, where the paths are very erratic and it is difficult to recognize the spikes very well.

The above numerical experiments give evidence of the sensitivity of such a model to noise. Therefore, the noise should be very small, $\sigma \ll 1$, in order to produce regular spikes.

Appendix A. Codes of FitzHugh–Nagumo model

Code 4: the FHN model with additive space-time noise

```
% M-file for the FHN model in space-time
d = 9; %dimension of y
p = 9; %dimension of w
tspan = [0,200]; %time interval
%%%%%%%%%%%%%
%Compute the initial condition
a0_n=0.1/(exp(1)-1); b0_n=0.125;
v0=a0_n/(a0_n+b0_n);
y0=[zeros(d,1);v0*ones(d,1)];
%%%%%%%%%%%%%
% Define the drift and diffusion functions
fcn.drift='spdefh_drift';
fcn.diff_noise='spdefh_diff_noise';
%%%%%%%%%%%%%
%Define the parameters of drift and diffusion functions
params.D=0.01;
params.a=0.05;
params.Mu=0.5;
params.b=0.008;
params.gamma=0.5;
params.sigma=0.005;
%%%%%%%%%%%%%
%Choice the integration method and other options
opt.IntegrationMethod ='StrongItoEuler';
opt.MaxStepSize=1e-2;
opt.StrongItoEuler.Alpha=0.5;
opt.MSIGenRNG.SeedZig = 23;
%%%%%%%%%%%%%
%Strong numerical solutions stored in [t,y]
[t,y]= sdesolve_strong_solutions (fcn,tspan,y0,p,opt,params)
```

Code 5: the drift function of the FHN model

```
% M-file drift function of \SPDEs of the FHN model
function z=spdefh_drift(t,y,varargin)
%%%%%%%%%%%%%
```

```
%Extract parameters
D=varargin{2}.D;
Mu=varargin{2}.Mu;
a=varargin{2}.a;
b=varargin{2}.b;
q=varargin{2}.gamma;
d=length(y)/2;
%%%%%%%%%%%%%
%Compt drift function
A=-gallery('tridiag',d); %tridiagonal matrix A
u=y(1:d); % u fast variable
v=y(d+1:end); % v recovery variable
F=(u.*((1-u).*(u-a))-v;
B=D*((d+1)^2)*A*u; % Approximation of Laplacian
z1=B+F+Mu;
z2=b*(u-(gamma*v));
z=[z1;z2]; %Return values of drift
```

Code 6: the diffusion function of FHN model

```
% M-file diffusion function of \SPDEs of the FHN model
function z=spdefh_diff_noise(t,y,dw,flag,varargin)
sigma=varargin{2}.sigma; % Extract parameter
p=length(dw);
d=p;
% Compute Q_ij=sqrt(2)*sin(i*j*pi/(d+1)), i,j=1,2,...,d.
Q=sqrt(d+1)*gallery('orthog', d,1);
%Compute the diffusion function
if(flag)
    z=[sigma*Q;zeros(m)];
else
    z=[sigma*(Q*dw);zeros(m,1)];
end
```

References

- Cyganowski, S., Grune, L., and Kloeden, P. E. (2001). Maple for stochastic differential equations. In *Theory and Numerics of Differential Equations*, Universitext, pp. 127–178. Springer, Berlin.
- Davie, A. M. and Gaines, J. G. (2001). Convergence of numerical schemes for the solution of parabolic stochastic partial differential equations. *Mathematics of Computation*, **70**(233), 121–134.
- FitzHugh, R. (1960). Thresholds and plateaus in the Hodgkin–Huxley nerve equations. *Journal of General Physiology*, **43**, 867–896.
- FitzHugh, R. (1961). Impulses and physiological states in theoretical models of nerve membrane. *Biophysical Journal*, **1**, 445–466.

- Gaines, J. G. (1995). Numerical experiments with S(P)DEs. In *Stochastic Partial Differential Equations* (ed. A. M. Etheridge), London Mathematical Society Lecture Note Series 216, pp. 55–71. Cambridge University Press, Cambridge.
- Gilsing, H. and Shardlow, T. (2007, August). *SDELab*: A package for solving stochastic differential equations in MATLAB. *Journal of Computational and Applied Mathematics*, **205**(2), 1002–1018.
- Guttman, R., Lewis, S., and Rinzel, J. (1980). Control of repetitive firing in squid axon membrane as a model for a neuroneoscillator. *Journal of Physiology*, **305**, 377–359.
- Gyongy, I. (1998). Lattice approximations for stochastic quasi-linear parabolic partial differential equations driven by space-time white noise I^* . *Potential Analysis*, **9**, 1–25.
- Hassard, B. (1978). Bifurcation of periodic solutions of the Hodgkin–Huxley model for the squid giant axon. *Journal of Theoretical Biology*, **71**, 401–420.
- Higham, D. J. (2001). An algorithmic introduction to numerical simulation of stochastic differential equations. *SIAM Review*, **43**(3), 525–546.
- Hodgkin, A. L. and Huxley, A. F. (1952). A quantitative description of membrane current and its application to conduction and excitation in nerve. *Journal of Physiology*, **117**, 500–544.
- Horikawa, Y. (1991). Noise effects on spike propagation in the stochastic Hodgkin–Huxley models. *Biological Cybernetics*, **66**, 19–25.
- Izhikevich, E. M. (2000). Neural excitability, spiking and bursting. *International Journal of Bifurcation and Chaos*, **10**, 1171–1266.
- Kloeden, P.E. and Platen, E. (1999). *Numerical Solution of Stochastic Differential Equations*. Springer-Verlag, Berlin.
- Kloeden, P. E. and Platen, E. (1991). Stratonovich and Itô stochastic Taylor expansion. *Mathematische Nachrichten*, **151**, 33–50.
- Kloeden, P. E., Platen, E., and Schurz, H. (1994). *Numerical Solution of SDE Through Computer Experiments*. Springer-Verlag, Berlin.
- Koch, C. (1999). *Biophysics of Computation: Information Processing in Single Neurons*, Chapter 6. Oxford University Press, Oxford.
- Mishra, D., Yadav, A., Sudipta, R., and Kalra, P. K. (2005). Effects of noise on the dynamics of biological neuron models. In *Soft Computing as Transdisciplinary Science and Technology*, Advances in Soft Computing, pp. 60–69. Springer. Proceedings of the Fourth IEEE Internation workshop, by Ajith Abraham, Institute of Electrical and Electronics Engineer, Muroran, Japan.
- Nagumo, J., Arimoto, S., and Yosizawa, S. (1962). An active pulse transmission line simulating nerve axon. *Proceedings of the IRE*, **50**, 2061–2070.
- Pankratova, E. V., Polovinkin, A. V., and Mosekilde, E. (2005). Resonant activation in a stochastic Hodgkin-Huxley model: Interplay between noise and suprathreshold driving effects. *The European Physical Journal B*, **45**, 391–397.
- Prato, G. Da and Zabczyk, J. (1992). *Stochastic Equations in Infinite Dimensions*, Volume 44 of *Encyclopedia of Mathematics and its applications*. Cambridge University Press, Cambridge.

- Rinzel, J. and Miller, R. (1980). Numerical calculation of stable and unstable periodic solutions to the Hodgkin–Huxley equations. *Mathematical Biosciences*, **49**, 27–59.
- Rowat, P. (2007). Interspike interval statistics in the stochastic Hodgkin–Huxley model: Coexistence of gamma frequency bursts and highly irregular firing. *Neural Computation*, **19**, 1215–1250.
- Shardlow, T. (1999). Numerical methods for stochastic parabolic PDEs. *Numerical Functional Analysis and Optimization*, **20**(1), 121–145.
- Shardlow, T. (2005). Numerical simulation of stochastic PDEs for excitable media. *Journal of Computational and Applied Mathematics*, **175**, 429–446.
- Stein, R. B. (1967). The frequency of nerve action potentials generated by applied currents. *Proceeding of the Royal Society of London. B*, **167**, 64–86.
- Tuckwell, H. C. (1986). Stochastic equations for nerve membrane potential. *J. Theoretical Neurobiology*, **5**, 87–99.
- Tuckwell, H. C. (2005). Spike trains in a stochastic Hodgkin–Huxley system. *BioSystems*, **80**, 25–36.
- Tuckwell, H. C. and Roderigues, R. (1998). Analytical and simulation results for stochastic FitzHugh–Nagumo neurons and neural networks. *Journal of Computational Neuroscience*, **5**, 91–113.
- Tuckwell, H. C. and Wan, F. Y. (2005). Time to first spike in stochastic Hodgkin–Huxley systems. *Physica A*, **351**, 427–438.
- Zhou, C. and Kurths, J. (2003). Noise-induced synchronization and coherence resonance of a Hodgkin–Huxley model of thermally sensitive neurons. *Chaos*, **13**(1), 401–409.

INDEX

- Action Potential (AP), 3, 251, 298, 300, 309, 311, 317, 322–330, 332–334, 336
Adjoint, 126, 128
Allosteric
 energy, 46, 56
 interaction, 45–49, 55
Alpha function, 24
AMPA, 199, 219, 237, 253
Anti-phase oscillation, 141, 142, 144
Arnold tongues, 110, 111
Autocorrelation, 5–7, 11, 13, 16, 187, 200, 207, 209
Autocovariance, 209, 210
Axon, 57, 183, 303, 304, 322, 325–330, 332, 348, 357
 myelinated, 325, 331, 336
 squid, 29, 30, 298, 305, 306, 309, 323, 326, 347
 unmyelinated, 298, 324, 326–329, 332

Barnacle, *see also* Morris–Lecar, 29, 65
Bifurcation, 66, 69, 70, 78–83, 86, 90, 91, 98, 145, 146, 150
Hopf, 70, 83, 88, 96, 99
Pitchfork, 70
Saddle-node, 67, 68, 70, 77–79, 81, 83, 85, 86
Saddle-Node on an Invariant Circle (SNIC), 83, 96, 127, 131
Binomial distribution, *see* Distribution, binomial
Brownian bridge, 282
Brownian motion, 68, 119, 275, 282, 344, 346, 349, 359, 360
Burst threshold, 222, 224, 235
Bursting/bursts, 23, 91, 120, 217–222, 226, 228, 229, 235–237, 250, 254–256, 265, 273, 328

Calcium, *see also* ion channels, calcium
 puffs, 29, 42, 48–51, 57
 sparks, 29, 42, 47–51, 54, 57
Canards, 88
Cat, 154, 197, 218, 242, 243, 246, 260, 261, 263, 325
Chaos, 94
Clusters, 29, 42, 43, 57, 148
Coefficient of Variation (CV), 22, 103, 118

Coherence Resonance (CR), 94, 97, 100, 101, 103, 104, 107–109, 117–119, 121
Coloured noise, *see* noise, coloured
Conditional intensity function, 278, 285
Correlation time, 7, 8, 14, 17, 22, 98, 100, 130, 131, 137, 138
Correlations, 17, 23, 25, 94, 120, 124, 130, 140, 143, 172, 175, 206–208, 211, 290, 336
Cortex, 124, 159, 161, 164, 169, 217, 242, 243, 245–247, 253, 261, 298, 325, 328, 332
 Barrel, 2, 167, 168
 CA1, 284–286
 Entorhinal Cortex (EC), 284, 286
 Visual, 154, 182, 196, 197, 217, 221, V1, 175, 182, 197
Covariance, 171, 359
Cycle histogram, 114

Dendrites, 57, 94, 250–252, 263, 310, 325, 333
Diffusion, 9, 29, 44, 74, 77, 99, 155, 169, 187, 188, 275, 278, 297, 344, 346, 354
Dimension reduction, 206, 237
Dirac delta function, 99, 131, 142, 147
Directional diagram, 33
Distribution
 binomial, 47, 48, 305, 316, 317, 325
 gamma, 197, 208, 209
 normal (Gaussian), 1, 8, 9, 25, 26, 97, 99, 100, 187, 196, 200, 257, 258, 273, 282, 289, 290
 Poisson, 22, 23, 155
 uniform, 15, 26, 27, 38, 44, 55, 135, 137, 143, 146, 315, 318, 319
Doublet-triggered average, 283, 284
Drift, 9, 68, 76, 119, 136, 141, 185, 195, 227, 282, 315, 344, 345
Dwell times, 34, 35, 39, 41, 44
Dynamic-clamp, 253–256, 258–260, 263, 264, 324, 331

EEG, 124, 243, 244, 246
Eigenvalue(s), 34, 88, 104, 147, 190–192, 204, 359
Eigenvector(s), 34, 54, 190–192, 206
Endoplasmic Reticulum (ER), 29, 44, 50

- Equilibrium branch(es), 67, 69, 76, 83, 86
 Equilibrium point/fixed point, 72, 77, 82,
 85–89, 95, 97, 98, 104, 105, 110, 142,
 146, 355, 357
 Ergodic, 9, 17, 136
 Euler–Maruyama, 100, 107, 346, 347, 350,
 360
 Excitability, 29, 48–50, 57, 83, 91, 95,
 251, 252, 279, 280, 301, 305,
 308, 322
 Excitatory Post Synaptic Potential
 (EPSP), 217, 252, 253
 Excitatory/inhibitory, 155, 159, 192,
 195–198, 211, 223, 228,
 246, 258
- f-I curve, 96, 115
 Fano factor, 158, 173, 174
 Fast–slow analysis, 65–67, 76, 81
 Feed-forward, 197, 208, 217, 222
 Feedback, 221, 222, 233, 236, 297, 300,
 309, 329
 Fenichel, 71
 Finite difference, 311, 359
 Firing rate, 96, 106, 107, 111, 114, 115,
 117, 120, 153–155, 157, 158, 160, 161,
 165, 172, 174, 183, 189, 190, 192, 195,
 197, 198, 207, 211, 219, 229, 273,
 278–280, 290
 FitzHugh–Nagumo (FHN), 65, 67, 81, 86,
 88, 96, 99, 347, 348, 359, 360, 363
 Fixed point, *see* Equilibrium point/fixed
 point
 Flux, 33, 35, 146, 166, 182, 184, 227, 228,
 231, 302, 312
 Fokker–Planck, 9–12, 26, 135, 146, 150,
 166, 183, 187, 188, 195, 200, 204, 208,
 209, 211, 256, 275, 315
 Fourier transform, 5–7, 11, 14, 23, 24,
 103, 201, 202, 209
 Fractional Brownian motion, 70
 Frog, *see also* *xenopus laevis*, 298, 325
- Gain, 158, 159, 172, 201, 205, 250, 254,
 264, 265, 297
 Gamma distribution, *see* distribution,
 gamma
 Gap junctions, 128
 Gating, 29–31, 38, 42, 45, 57, 200, 218,
 224, 300, 305, 308, 313, 336, 359
 Gaussian distribution, *see* Distribution,
 normal
 Gillespie’s algorithm, 38, 47, 315,
 317–319, 321, 323, 324, 326
 Goldfish, 289
- Hidden Markov, *see* Markov, hidden
 High-conductance state, 242, 245–248,
 254
 Hill’s method, 33
 Hillock, 94
 Hippocampal, 284
 Hodgkin–Huxley (HH), 1, 96, 99, 133,
 161, 221, 347
 Hopf bifurcation, *see* Bifurcation, Hopf
- Impulse response function, 201–203, 209
 Inference, 272, 274, 277, 278, 281
 Infinitesimal generator matrix, 31, 43, 51,
 55
 Information, 161, 162, 164, 175, 176, 298,
 301, 322, 323
 Inhibitory, *see* Excitatory/inhibitory
 Inhomogeneous Markov Interval (IMI)
 Model, 279–281, 284, 290
 Inner product, 31, 128, 190
 Integral equation, 137, 275, 276
 Integrate-and-fire, *see also*
 Leaky-integrate-and-fire, 182–184,
 192, 211, 221, 272, 273–278, 280–283,
 285–290
 Integrate-and-fire-or-burst, 182, 219–222,
 224, 227, 228, 231, 237
 Interneurons, 217, 223
 Interspike Interval (ISI), 21–25, 97, 98,
 101, 103, 109, 113, 114, 116, 119, 273,
 280, 286
 Ion channels
 calcium, 42, 44, 49, 55, 65, 182, 256, 329
 leak, 225, 246, 248, 250, 263, 300, 302,
 304
 potassium, 65, 99, 161, 221, 235, 246,
 250, 265, 348, 359
 sodium, 65, 99, 161, 246, 348, 357
 Irreducible, 32
 Isochrons, 125
 Itô, 107, 135, 187, 344–347, 352, 354
- Jacobian, 27, 353
- Kramer’s rate, 106, 108
 Kronecker, 9, 52, 54–56
- Langevin equation, 8, 9, 141
 Lattice, 44, 46, 47, 49, 55
 Leaky-integrate-and-fire, *see also*
 Integrate-and-fire, 97, 118
 Length constant, 304
 LGN(Lateral Geniculate Nucleus), 197,
 198, 211, 217–219, 221, 222, 224, 226
- Likelihood, *see also* maximum likelihood,
 274–276

- Limit cycle, *see* periodic orbit/limit cycle
 Linearization, 71, 76, 78, 87, 115, 126, 147
 Local field potential, 124, 290
 Lorentzian, 11, 16, 18, 19
 Lumping, 35
 Lyapunov exponent, 136, 137
- Markov, 273, 284, 303, 308, 315,
 318, 334
 chain, 29–31, 34, 39, 42, 49, 54, 308
 hidden, 277
 process, 4, 8, 15, 308, 317, 323, 336
- Master equation, *see also* Fokker–Planck equation, 15, 29,
 MATLAB, 346, 350
- Maximum likelihood, *see also* Likelihood, 40, 262, 274, 275, 277, 286
- Microsaltatory conduction, 3, 329, 330
- Milstein, 347, 350
- Monte Carlo, 49, 132, 144, 183, 189, 196, 199, 205, 224, 232–234, 311, 323
- Morris–Lecar, 65, 68, 85–87, 108
- Mouse, 299
- Mutual Information (MI), 162–164
- Nerve, 120, 329, 347, 348, 357
- Nodes of Ranvier, 322, 323, 329, 331, 336
- Noise
 coloured, 99, 100, 129, 130, 136, 137
 shot, 1, 20, 22, 26
 telegraph, 15–17, 20, 25
 thermal, 305
 white, 1, 8, 26, 68, 98–100, 105, 118, 128, 131, 132, 135, 140, 141, 164, 169, 186, 196, 200, 209, 248, 311, 315, 324, 345, 358
- Noisy oscillator, *see* Oscillator, noisy/stochastic
- Normal distribution, *see* Distribution, normal
- Normal form, 78, 83, 85, 86, 88, 108, 149
- Nullcline, 67, 68, 81, 83, 86, 91, 222
- Ordinary Differential Equation (ODE), 31, 125, 126, 310, 311, 313, 314, 334
- Orientation tuning, 197, 198
- Ornstein–Uhlenbeck (OU) process, *see also* Noise, coloured, 7, 8, 10, 11, 14, 16, 98–100, 105, 248
- Oscillator
 noisy/stochastic, 96, 104, 107, 130
 relaxation, 96, 99
 van der Pol, 81, 88
- Parameter estimation, 40
- Partial Differential Equation (PDE), 275, 276, 283, 302, 304, 310–312, 318, 319, 334, 337
- Patch clamp, 30, 300, 323
- Pedonculopontine tegmentum (brain stem), 235, 244, 246
- Perigeniculate Nucleus (PGN), 217–219, 221, 222, 224–227, 229, 230, 232, 233, 235–237
- Periodic orbit/limit cycle, 81–83, 88, 95, 98, 104, 109, 125, 126, 128, 355
- Perturbation theory, 131, 132, 137, 150
- Phase
 coherence, 96
 locking, 95, 96, 109–111, 119
 plane, 207, 222, 348
 resetting curve (PRC), 125–127, 130–132, 137, 139–141, 143–145
- Pitchfork bifurcation, *see* Bifurcation, pitchfork
- Plasticity, 121, 181, 284, 285
- Point process, 2, 19, 25, 103, 275, 278, 281, 285, 289
- Poisson, *see also* Distribution, Poisson inputs, 135, 136, 139
 model, 281, 288
 process, 19, 22–24, 85, 87, 89, 98, 99, 158, 183, 184, 197, 207, 280, 281
 spike train, 17, 26
- Population firing rate, 156, 182, 186, 188, 189, 192, 194, 196, 198, 200–207, 211, 226, 229, 231, 235–237
- Post Synaptic Potential (PSP), 250
- Post-Inhibitory Rebound (PIR), 219, 220, 222
- Posterior, 289
- Power spectral density, 103, 263, 264
- Power spectrum, 5, 6, 8, 11, 14, 18, 22, 23, 124, 254
- Probability density, 4, 5, 9, 15, 16, 19, 20, 22, 185, 207, 227, 231, 233–235, 275
- Probability Density Function (PDF), 138, 142, 181–184, 186, 189, 190, 196, 197, 211, 212, 227, 228, 232, 274, 310, 311
- Purkinje cell(s), 57
- Pyramidal cell(s), 138, 154, 165, 242, 247, 250, 298, 325, 333
- Quadratic Integrate-and-Fire (QIF), 105–109, 117, 118, 127
- Random Action Potential (RAP), 331–333

- Rapid Eye Movement (REM), 261
 Rat, 161, 167, 285
 Receptor
 acetylcholine, 32
 GABA, 200
 NMDA, 200
 Ryanodine (RyR), 29, 41, 42, 45, 46,
 51, 57
 Refractory period, 19, 23, 24, 97, 103,
 114, 118, 161, 184, 195, 273, 280
 Regularization, 108, 109, 118
 Relaxation oscillator, *see* Oscillator,
 relaxation
 Reticular (RE), 217–222, 224–227, 229,
 233–237
 Retinal Ganglion Cell (RGC), 211,
 217–219, 221, 222, 224, 233, 287, 288
 Rheobase, 95, 96, 327
 Rice's method, 11, 14

 Saddle-node bifurcation, *see* Bifurcation,
 saddle-node
 Scaling, 9, 85, 89, 91, 100, 108, 159, 160,
 263
 Shot noise, *see* Noise, shot
 Signal to Noise Ratio (SNR), 114–116,
 118, 119, 218, 250
 Sinusoidal, 104, 110, 114, 130, 201, 221
 Skipping, 94, 111, 114, 119, 121
 Sleep, 217, 218, 235, 236, 243, 244, 260
 Slow manifold, 67, 68
 SNIC, *see* Bifurcation, saddle-node on an
 invariant circle
 Soma, 94, 250, 251, 254, 330, 333
 Spike, *see also* Action potential (AP)
 time, 175, 273, 279, 325, 328, 329, 334
 time average (STA), 260, 262–264
 train, 2, 19, 23, 26, 98, 114, 119, 143,
 156, 161, 162, 171, 172, 176,
 206, 273, 274, 283, 285, 287,
 288, 328
 Squid, *see* Axon, squid
 State-transition diagram, 30, 31, 34, 38,
 40
 Stochastic
 attrition, 50
 differential Equation (SDE), 1, 14, 68,
 72, 73, 84, 107, 135, 141, 311,
 312, 337, 344–347, 351,
 358–360
 oscillator, *see* Oscillator, stochastic

 PDE(SPDE), 311, 344, 347, 348, 358,
 360, 361
 resonance (SR), 94, 96, 97, 100, 103,
 109, 112–121, 164, 250, 322
 Stratonovich, 107, 344–346, 352, 354
 Strong approximations, 351
 Symmetry, 55
 Synapses, 94, 99, 140, 158, 182, 186, 192,
 196, 197, 217, 219, 222, 237, 265, 298,
 331, 337
 Synchrony, 133, 136, 137, 141, 144, 148,
 162, 175, 207

 Telegraph/dichotomous noise, *see* Noise,
 telegraph
 Temperature, 120, 303, 307, 333
 Tetrodotoxin (TTX), 245, 246, 254
 Thalamocortical (TC), 217–219, 221, 222,
 224–227, 229, 230, 232–237
 Thalamus, 169, 197, 217–219, 254
 Theta neuron, 107, 108
 Tihonov, 71, 74, 76
 Time-rescaled renewal process (TRRP),
 279–281
 Tonic, 120, 217–219, 221, 229, 236, 254,
 265
 Tuning curve, 109
 Two-state process, 1, 14, 25
 Type I, *see also* Bifurcation, 95–98, 105,
 108, 117
 Type II, *see also* Bifurcation 95–97, 99,
 109, 113

 Uniform distribution, *see* Distribution,
 uniform
 Unitary event, 186, 193
 Up/down states, 244

 van der Pol oscillator, *see* oscillator, van
 der Pol
 Ventroposterior Medial Nucleus (VPM),
 217
 VmD method, 256, 258, 260

 Weak approximations, 346
 White noise, *see* Noise, white
 Wiener process, 9, 187, 359
 Wiener–Khinchin, 6, 7, 14

 Xenopus laevis, *see also* Frog, 42, 57

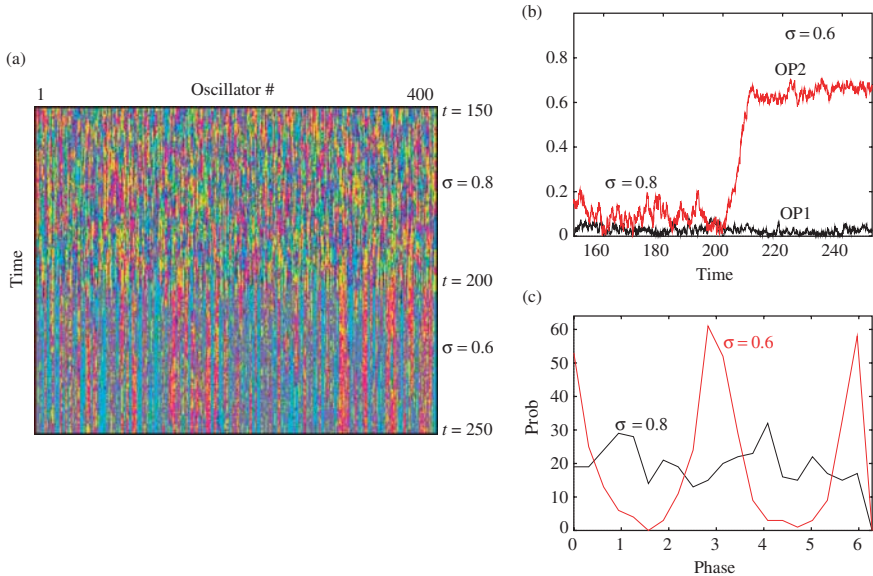


PLATE 1: Example of the destabilization of the asynchronous state as the noise is reduced leading to a two-cluster solution. ($H(\phi) = 0.25 \cos(\phi) - 0.5 \sin(\phi) + \sin(2\phi)$, $\sigma^* = 1/\sqrt{2} \approx 0.707$). (a) Space-time plot of the phases relative to oscillator 1. At $t = 200$, the noise is abruptly reduced from $\sigma = 0.8$ to $\sigma = 0.6$. The emergence of a two-cluster state (turquoise/red) is apparent. (b) Order parameters $OP_{1,2}$ showing the two-cluster instability. (c) Histogram of the relative phases during two different points in the simulation corresponding to the two different levels of noise. See page 149.

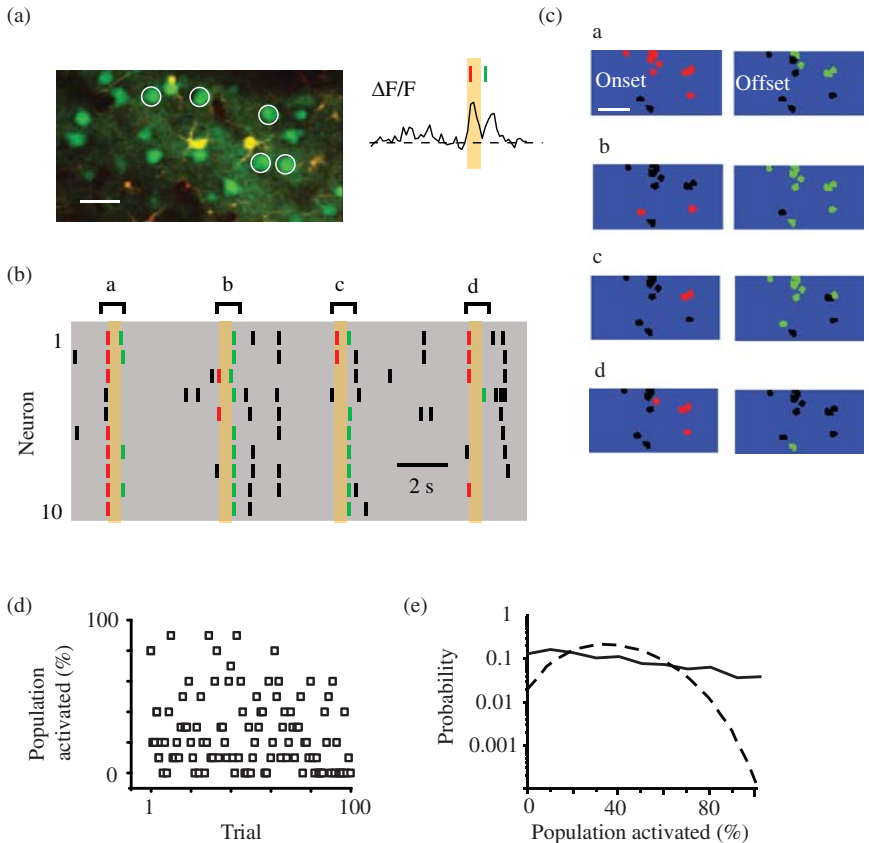


PLATE 2: Population variability in barrel cortex. (a) Optical calcium measurement from a population of neurons located in layer 2/3 of barrel cortex; the scale bar is 30 μ m. The neurons have been bulk loaded with a calcium sensitive dye which fluoresces during neural activity (see right traces of the normalized fluorescence change). Fluorescence activity is thresholded and a putative spike train response is calculated for all neurons recorded. (b) Spike train rasters for a population of 10 neurons. Four whisker deflections are shown (*a* through *d*) and the stimulus duration is indicated in orange. Neurons responded primarily at stimulus onset (red) or offset (green); black spikes indicate spikes that were not correlated with the stimulus. (c) Spatial organization of onset (left) and offset (right) responses for each whisker deflection *a* through *d*; the scale bar is 50 μ m. (d) The total population activity recruited at stimulus onset over 100 trials. (e) Estimated probability density of the amount of population activity for the actual data (solid) and assuming independence between neurons (dashed). We thank Jason Kerr for the donation of the figures – we refer the reader to Kerr et al. (2007) for the experimental details. See page 168.

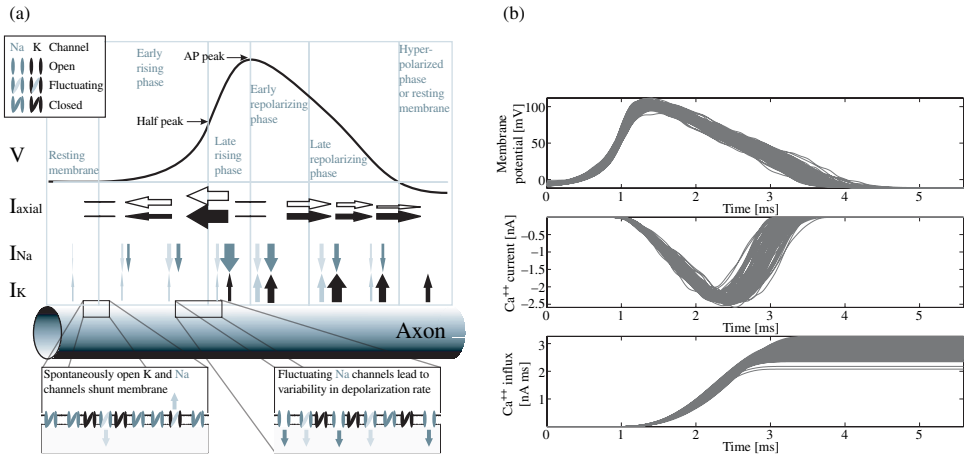


PLATE 3: (a) Diagrammatic representation of an action potential travelling on an axon, based on Faisal and Laughlin (2007). Stacked over each other, the leftward travelling membrane potential wave form of the AP (V), axial currents flowing along the axon (I_{axial}), Na^+ and K^+ currents ($I_{\text{Na}}, I_{\text{K}}$) and the representation of the axon itself. Axial, Na^+ and K^+ currents are denoted by black, red, and blue arrows scaled to represent the relative size of the current in the various phases. Hollow and light shaded arrows denote the size of the current fluctuations relative to the average currents. The action potential wave form is subdivided into six phases: resting membrane, early rising phase, late rising phase, early repolarizing phase, late repolarizing phase, and an optional hyperpolarized phase. See text for details. (b) Synaptic variability from axonal variability. Top: wave forms of 713 consecutive APs arriving at the terminal end of a 1.6 mm long unmyelinated axon of 0.2 μm diameter. Middle and bottom: Ca^{++} current and total Ca^{++} influx resulting from the integration of the above AP wave forms into a model of a Calyx-of-Held type synapse. Figure adapted from Faisal and Laughlin (2003). See page 327.

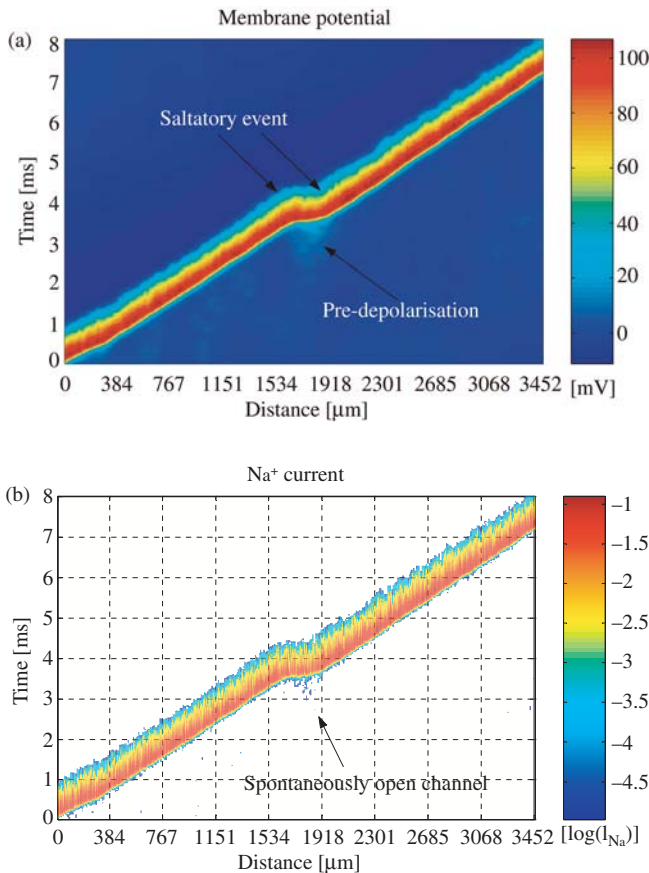


PLATE 4: A stochastic microsaltatory conduction event in a $0.1 \mu\text{m}$ diameter squid axon. A continuously propagating action potential wave front (note the jitter in propagation speed) suddenly jumps from position $x = 1550 \mu\text{m}$ to $x = 1900 \mu\text{m}$. (a) A space-time plot of the membrane potential on the axon. (b) The corresponding space-time plot of the transmembrane Na^+ current. The regions where no Na^+ current was flowing were not colour coded, making ionic currents from spontaneously open channels clearly visible. Figure adapted from Faisal and Laughlin (2003). See page 330.